No. 1, Vol. 51, 1985

PIBSBD 51 (1) 1-294

ISSN 0370-0046

Physical Sciences

Part A

PROCEEDINGS OF THE INDIAN NATIONAL SCIENCE ACADEMY

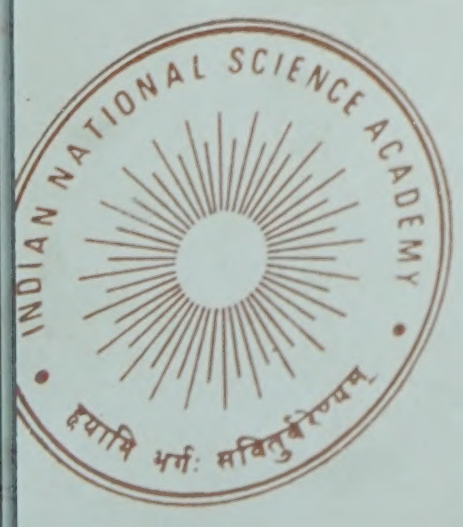

INDIAN NATIONAL SCIENCE ACADEMY
NEW DELHI

Proceedings of the Indian National Science Academy Part A

(Physical Sciences)

Editor

A N Mitra, *Department of Physics, University of Delhi, Delhi*

Editorial Board

Sadhan Basu, *Department of Chemistry, Calcutta University, Calcutta*

J C Bhattacharyya, *Indian Institute of Astrophysics, Bangalore*

T R Govindachari, *22 Cresent Park Street, T' Nagar, Madras*

P K Kaw, *Plasma Physics Programme, Physical Research Laboratory, Navrangpura, Ahmedabad*

A Mani (Miss), *Wind Energy Project, Indian Institute of Tropical Meteorology, Raman Research Institute, Bangalore*

G Mehta, *School of Chemistry, University of Hyderabad, Hyderabad*

K K Rohtagi Mukherjee (Mrs), *Department of Physical Chemistry, Faculty of Science, Jadavpur University, Calcutta*

A P B Sinha, *Physical Chemistry Division, National Chemical Laboratory, Pune*

B M Udgaonkar, *Tata Institute of Fundamental Research, Homi Bhabha Road, Bombay*

R C Mehrotra, *Department of Chemistry, University, of Rajasthan, Jaipur*

S P Pandya, *Director, Physical Research Laboratory, Navrangpura, Ahmedabad*

Assistant Executive Secretary
(Associate Editor/Publications)
M Dhara

Annual Subscription Rates
(*Including postage*)

Inland : **Rs 150.00**
Foreign : **US $ 50.00**

Single Issue

Inland : **Rs 30.00**
Foreign : **US $ 10.00**

Editorial Office

The Indian National Science Academy, Bahadur Shah Zafar Marg, New Delhi 110 002, India

© The Indian National Science Academy, 1985

Proceedings of the Indian National Science Academy, Part A, is published in alternate months, i.e., January, March, May, July, September and November.

Information to Contributors

Purpose and Scope

PART 'A' of the Proceedings of the Indian National Science Academy is an interdisciplinary Journal in Physical Sciences devoted to publication of papers embodying results of original research in any branch of Physics, Chemistry and Geology. Contributions in Biophysics, Biochemistry, Geochemistry, Hydrology, Meteorology, Radio-Physics, Soil Physics, Soil Chemistry, and Oceanography are also accepted.

Papers presented at the Academy's Symposia, Special Academy Lectures and Original Review articles relating to research and concepts fundamental to Physical Sciences would also be published in the Proceedings.

(Continued on inside back cover)

Proc. Indian natn. Sci. Acad., **51**, A, No. 1, 1985, pp. 1–16.

Printed in India.

EXPERIMENTAL SURFACE SCIENCE WITH ELECTRON SPECTROSCOPIES AND COGNATE TECHNIQUES*+

C N R Rao

Solid State and Structural Chemistry Unit, Indian Institute of Science, Bangalore-560 012, India

Experimental surface science has made major advances in the last decade due to the availability of a variety of sophisticated techniques, especially those of electron spectroscopy. Some of the important techniques are briefly described along with their applications. Interaction of carbon monoxide as well as of oxygen with metal surfaces are discussed.

Key Words : Surface Science; Electron Spectroscopy; Cognate Techniques; Surface Copography

Introduction

Study of surfaces has become exciting in the last decade or so because of the advent of new surface-sensitive techniques. These techniques are not only powerful in characterizing surfaces of solids in terms of electron states but also in examining adsorbed species. The most common surface techniques that are employed today are low-energy electron diffraction and the various electron spectroscopies. These techniques have become possible due to the ready availability of ultra-high vacuum and sophisticated instrumentation. Today, there are commercial instruments which offer several combinations of techniques. Electron spectroscopic techniques[1–6] generally involve the analysis of the kinetic energy of ejected or scattered electrons and some of the more important ones amongst these are, UV and X-ray photoelectron spectroscopy (UPS and XPS), Auger electron spectroscopy (AES) and electron energy loss spectroscopy (EELS). For examining problems related to corrosion, conversion Mössbauer spectroscopy has been employed; for problems related to adsorption and and catalysis, infrared spectroscopy especially in the FT mode with a reflection—absorption cell, has been found useful. Electron spectroscopy carried out at ambient or high pressures should also yield valuable information relevant to catalysis. New techniques continue to be developed for surface studies, a noteworthy addition being scanning tunnelling microscopy[7] which is useful for surface topography on an atomic scale. We shall briefly present the results of some of the recent experimental studies on surfaces to indicate the scope of the subject. While doing so, I can not help giving a more chemical orientation to the presentation because of my own interests.

Electron Spectroscopic Techniques

Techniques of electron spectroscopy and their applications to surface studies have been reviewed in the literature[1–6]. In photoelectron spectroscopy, a monochromatic

*Paper presented at the Symposium on Physics and Chemistry of Surfaces held at INSA, New Delhi from September 28-30, 1984.

+Contribution No. 275 from the Solid State and Structural Chemistry Unit.

photon beam impinges on a solid and the resulting photoelectrons are energy analysed. The binding energy of the electrons, E_B, originating from a given state is obtained by the energy balance equation,

$$h\nu = E_k + E_B + \phi \qquad \ldots(1)$$

where E_k is the kinetic energy of the electron and ϕ is the work function of the solid. A schematic diagram of an electron spectrometer is shown in Fig. 1. In UV photoelectron spectroscopy, HeI (21.22 eV) and HeII (40.8 eV) are the most common radiations employed. AlKα (1486.6 eV) and MgKα (1253.6 eV) are the common X-radiations used in XPS. While UPS is useful to study valence bands, XPS provides detailed information about the core electron levels as well. Angular dependence of photoelectrons is particularly useful in the study of surface species[8].

The advent of synchrotron radiation has further increased the potential of photoelectron spectroscopy to study surface phenomena. Synchrotron radiation permits the examination of surfaces with radiations of different energies. It may be recalled that the intensity I of the photoelectrons emerging at the surface is related to its intensity I_0 at a depth x from the surface by the relation,

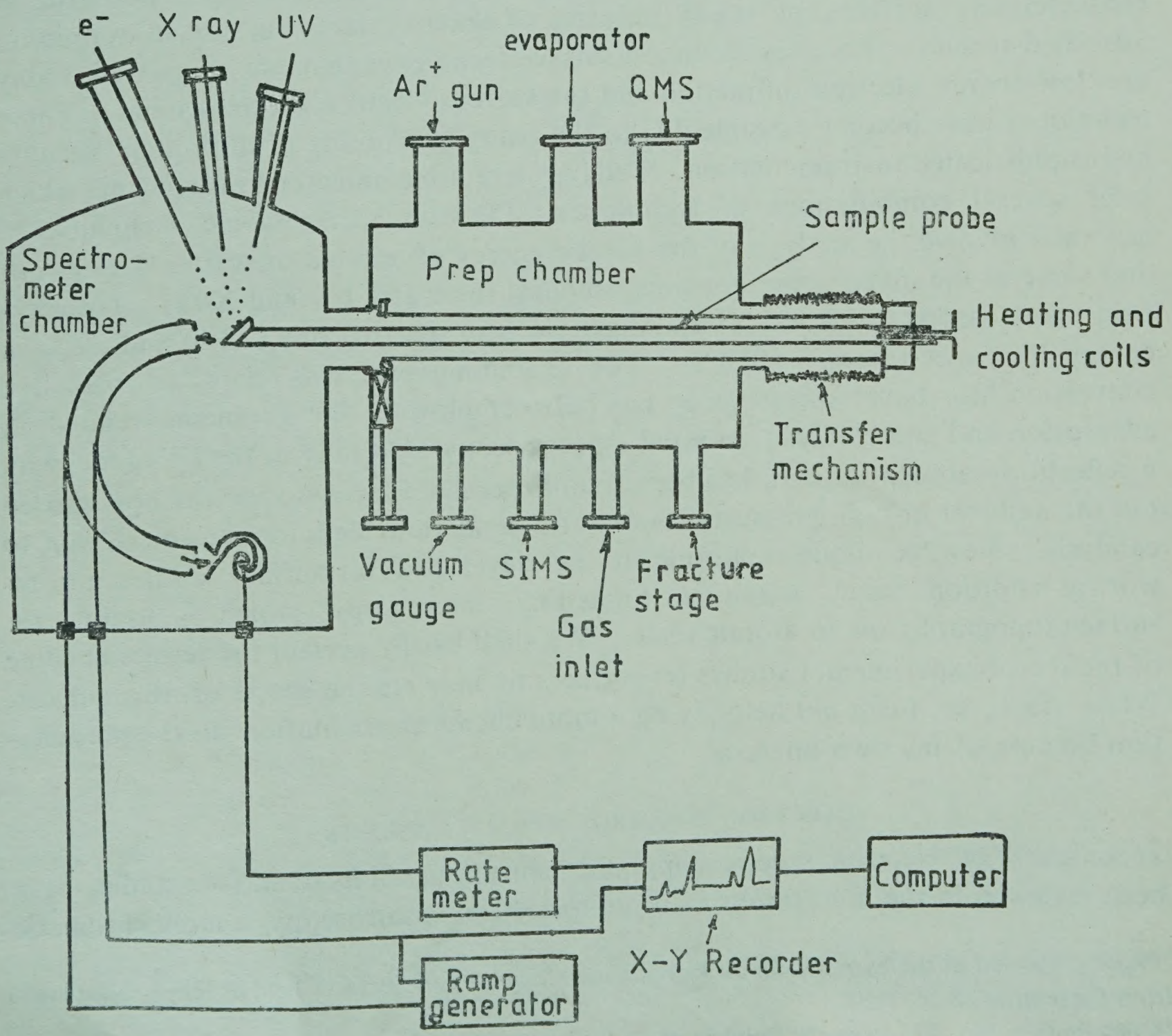

FIG. 1. Schematic diagram of an electron spectrometer.

$$I = I_0 \exp(-x/\lambda) \qquad \ldots(2)$$

where λ is the mean escape depth for the photoelectrons. The plot of $\lambda(E)$ vs E_k has a minimum around 70 eV (Fig. 2). Ordinarily, the mean escape depth in UPS is 5Å while it is 25 to 30Å in XPS. With variable photon energy, λ can be so chosen as to give information either on the surface or the bulk of the solid. With synchrotron radiation, it is possible to tune the radiation energy so as to have maximum cross-section for a particular band. Angular distribution of photoelectrons can be studied more effectively with synchrotron radiation. Photoelectron spectroscopy with synchrotron radiation has been reviewed by Spicer[9]. In Fig. 3, we show how the surface and bulk levels are delineated in III—V compounds[10].

In Auger spectroscopy, an impinging electron beam causes the ionisation of a core electron and this core level vacancy is filled by a non-radiative electron jump from a higher energy level with the simultaneous ejection of an Auger electron from

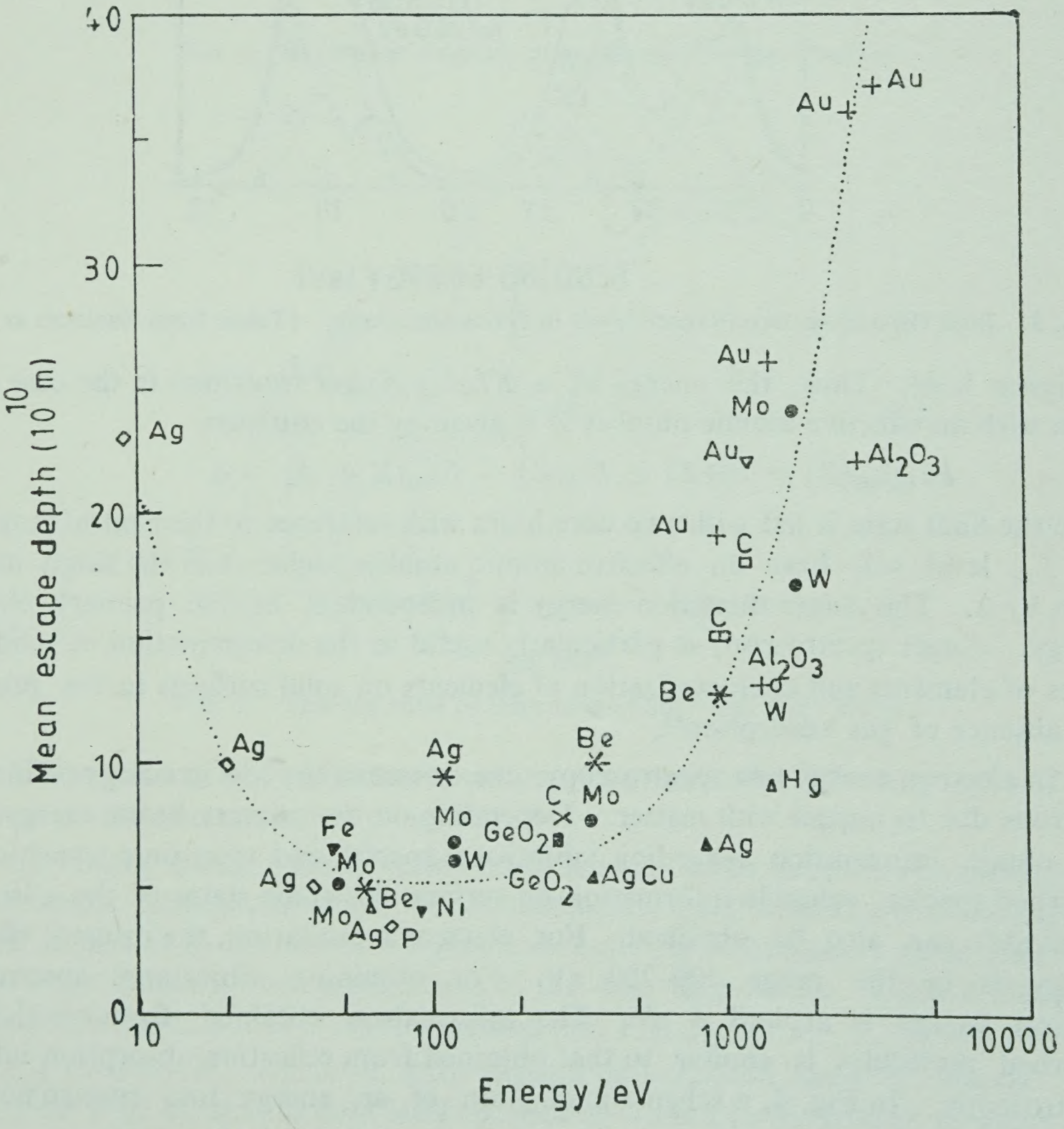

FIG. 2 Variation of escape depth with the energy of the radiation.

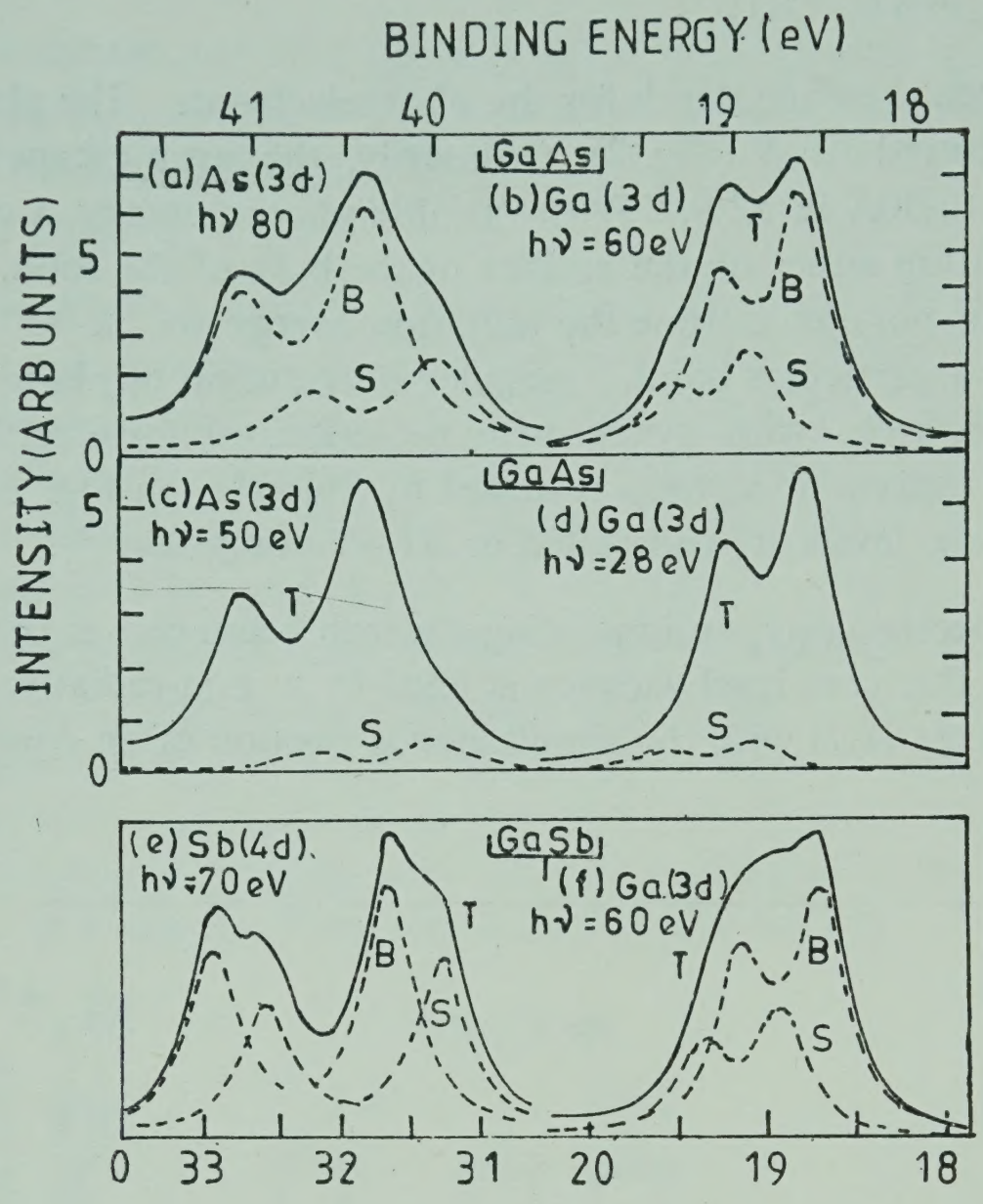

BINDING ENERGY (eV)

FIG. 3. Bulk (B) and surface (S) core levels in GaAs and GaSb. (Taken from Eastman *et al*[10])

a higher level. Thus, the energy of a KL_1L_{23} Auger transition in the case of an atom with an effective atomic number Z is given by the equation

$$E_{KL_1L_{23}}(Z) = E_K(Z) - E_{L_1}(Z) - E_{L_{23}}(Z + \Delta) - \phi \qquad \ldots(3)$$

Here the final state is left with two core holes with reference to the neutral atom and the L_{23} level will have an effective atomic number higher than the singly ionized atom by Δ. The Auger transition energy is independent of the primary electron energy. Auger spectroscopy is particularly useful in the determination of oxidation states of elements and characterization of elements on solid surfaces in the presence and absence of gas adsorption[11].

In electron energy loss spectroscopy, one measures the loss in energy of incident electrons due to impact with matter. Depending on the primary beam energy, one can obtain information regarding vibrational spectra and electronic transitions of adsorbed species; valuable information on surface electronic states of the adsorbent (substrate) can also be obtained. For electronic excitation, the primary electron energy is in the range 100–200 eV. For obtaining vibrational spectra, the electron energy is around 4 eV. The information obtained from EELS on adsorbed molecules is similar to that obtained from reflection-absorption infrared spectroscopy. In Fig. 4, a schematic diagram of an energy loss spectrometer is shown.

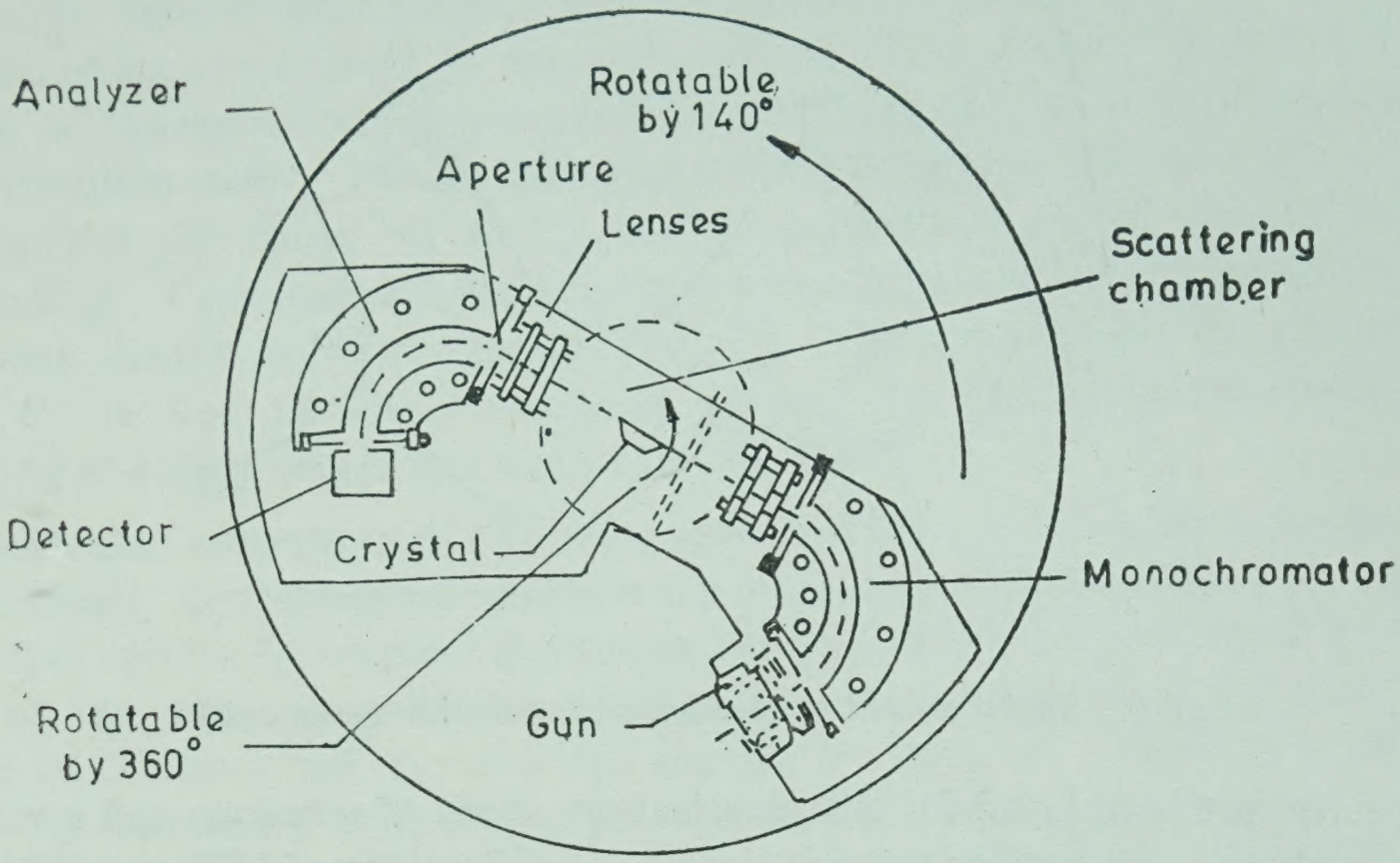

FIG. 4. Schematic diagram of an energy loss spectrometer.

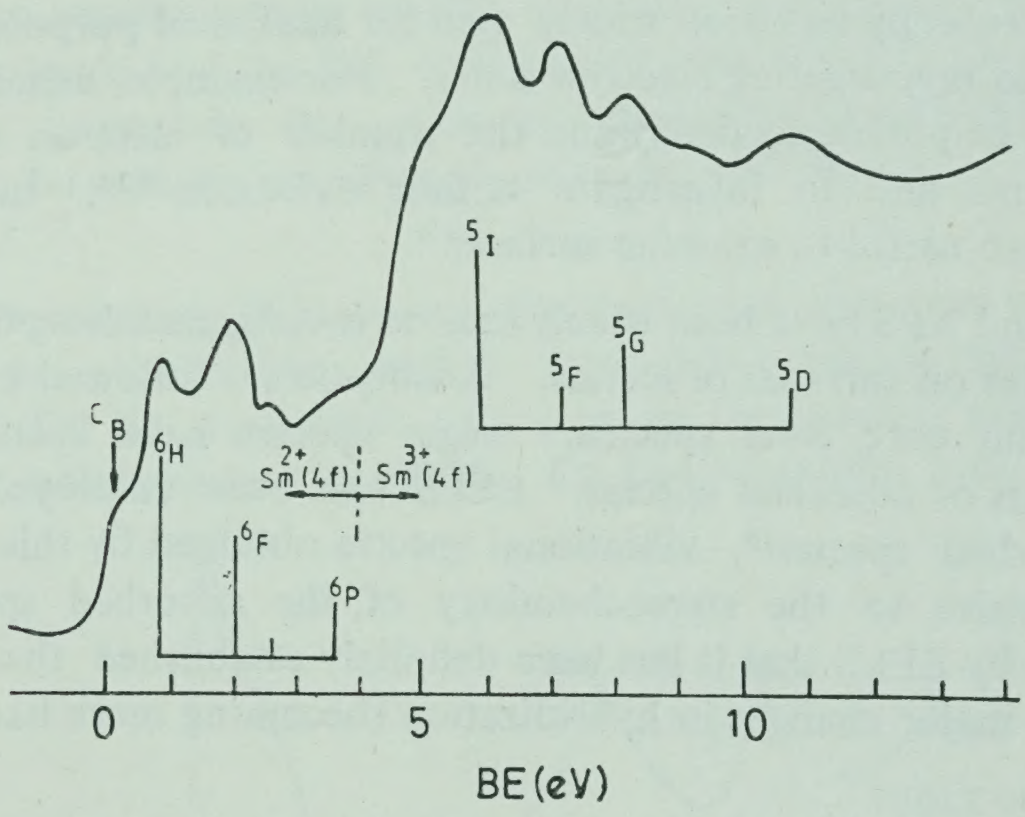

FIG. 5. Valence band of Sm showing Sm^{2+} and Sm^{3+} states.

UV and X-ray photoelectron spectroscopy provide the following types of information on the electron states of solids:

(i) *Valence bands* : Final state effects depend on the electronic configuration of the elements. Changes in valenec bands accompany metal-insulator transitions; Sharp cut-off is seen at E_f in metals. Spin-state equilibria of transition metal ions can be seen due to different final state effects of the two spin-states. Valence fluctuation (mixed valency) in solids is readily studied (see Fig. 5).

(ii) *Core levels* : Chemical shifts depend on oxidation states of metals. Satellites (see Fig. 6) next to core levels commonly found in the spectra of many of the transition metal compounds[12] crucially depend on the metal-ligand overlap. Core

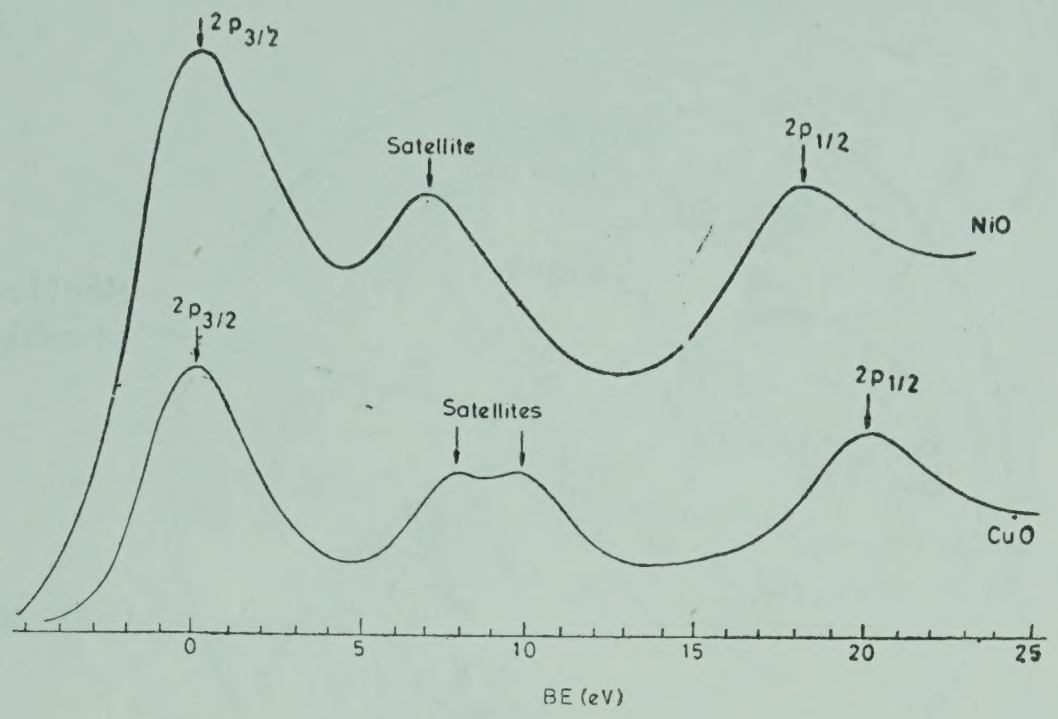

FIG. 6. Satellites next to core levels of transition metal oxides.

level spectra are employed for characterization, study of reactions and a variety of solid state phenomena such as mixed valency. Applications of UPS and XPS to the study of solids have been reviewed by Rao and Sarma[5].

Auger spectroscopy has been widely used for analytical purposes, but it is also of great value in investigating electron states. For example, metal Auger intensity ratios have been employed to determine the number of electron states in transition metal systems and to investigate surface oxidation[13,14]. Interatomic Auger transitions are also useful to examine surfaces [5].

Both UPS and XPS have been widely used to investigate adsorption of molecular and atomic species on surfaces of metals. Adsorption is followed by changes in the valence band and core level spectra. Auger spectra have been used recently to obtain fingerprints of adsorbed species. EELS has been employed extensively to investigate adsorbed species[16], vibrational spectra obtained by this technique being particularly sensitive to the stereochemistry of the adsorbed species or the site symmetry. It is by EELS that it has been definitely established that acetylene and ethylene undergo major changes in hybridization (becoming more like sp^3) on certain metal surfaces.

Adsorption of Carbon Monoxide on Transition Metal Surfaces

Adsorption of CO has been studied on a variety of transition metal surfaces by various techniques by several authors[17,18]. CO adsorbs dissociatively on the early transition metals (in the left of the periodic table) and molecularly on the late transition metals (in the right of the periodic table). Based on this observation Broden *et al.*[19] suggested a boundary line in the periodic table which separates metals exhibiting dissociative chemisorption from those exhibiting molecular chemisorption. Benziger[20] has attempted to rationalise this behaviour through a study of the heats of dissociative chemisorption. Dissociative chemisorption leads to the build-up of surface carbide and oxide[21], while molecular chemisorption has several interesting possibilities.

The HOMD of CO is a non-bonding orbital (5σ orbital) largely localised on the C atom. Immediately below it are the 1π and the 4σ orbitals that are responsible for bonding; the LUMO is the $2\pi^*$ orbital. The metal-CO bonding occurs through a synergetic bonding mechanism involving the $5\sigma \rightarrow$ metal and the metal $\rightarrow 2\pi^*$ charge transfer. Such a bonding scheme necessarily brings the 5σ level of the adsorbed CO closer to the 1π and 4σ levels which participate little in metal-CO bonding. Consequently, the ultraviolet photoelectron spectra of CO adsorbed on metals exhibit only two features (Fig. 7). The first of these features appearing at $\sim$ 7 eV is due to the overlapping 5σ and 1π bands and the second feature appearing at higher energies is due to the 4σ band[22].

Molecular adsorption of CO can occur on a variety of adsorption sites. While it is difficult to distinguish these in ultraviolet photoelectron spectra, studies of vibrational spectra by employing electron energy loss spectroscopy readily reveal the effect of the adsorption site[17,18]. In figure 8 we show typical electron energy loss spectra of CO adsorbed on polycrystalline Cu, Pt and Pd. While Cu exhibits a single CO stretching frequency close to 260 meV, Pt shows two bands at 260 and 248 meV (1 meV = 8.065 cm^{-1}). Pd shows only the 245 meV band, while Ni shows the 248 meV band at higher exposures. Based on the assignments of Sheppard and Nguyen[23], we can readily assign the 260 meV stretching band to the terminally adsorbed CO molecule and the 248 meV band to the two-fold bridge bonded CO molecule. It is interesting that while Pt shows the coexistence of different CO adsorption sites, Ni exhibits a surface phase transition[24] beyond a critical coverage value of $\theta > 0.5$.

In figure 9 we show EEL spectra illustrating the variation in metal reactivity to CO adsorption. While Mn exhibits dissociative chemisorption even at low temperatures (LT), Fe dissociates CO at room temperature and adsorbs it molecularly at lower temperatures ($<$ 100K). Co and Ni exhibit molecular adsorption

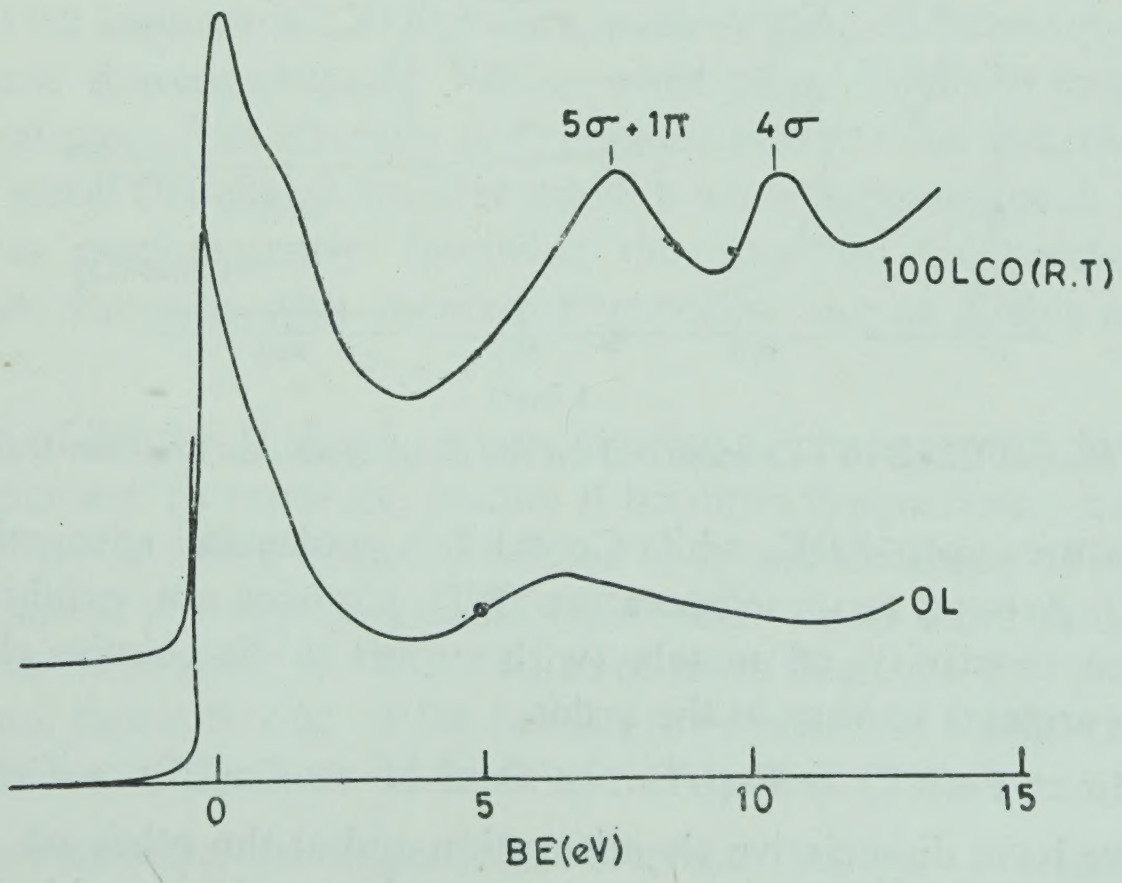

FIG. 7. HeII spectrum of CO adsorbed on a polycrystalline nickel surface.

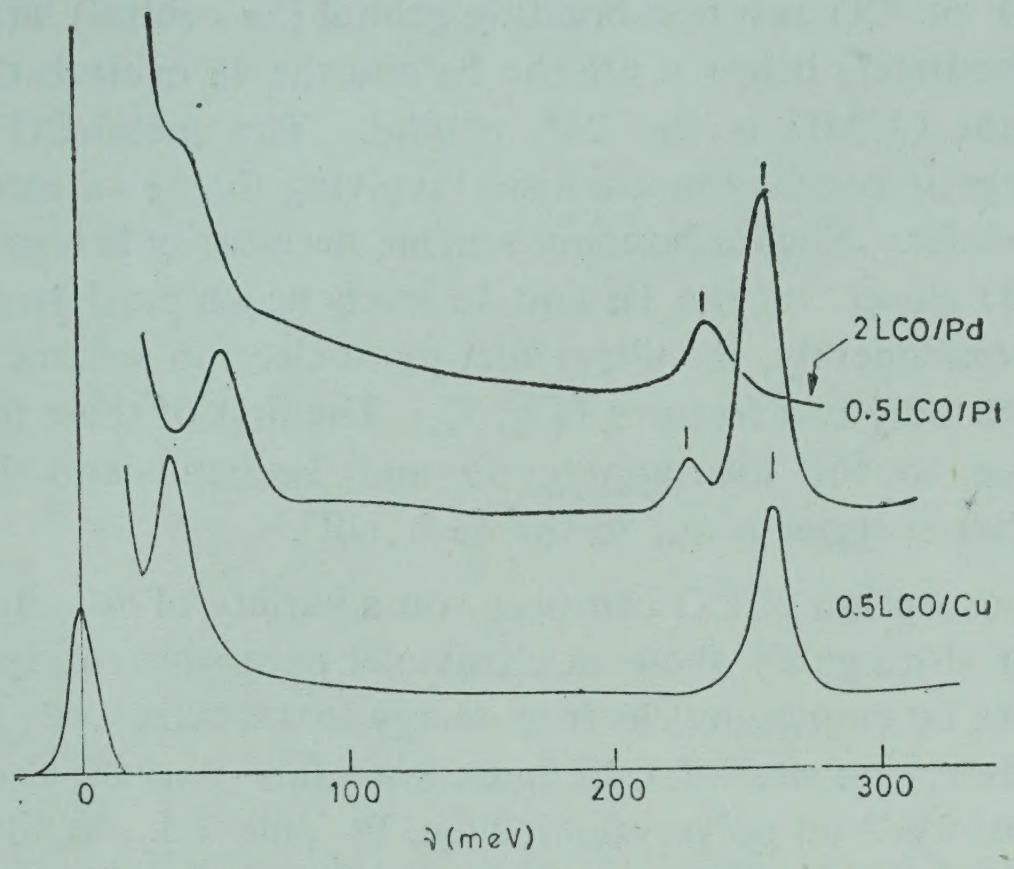

FIG. 8. Vibrational EELS of CO adsorbed on polycrystalline Cu, Pt and Pd.

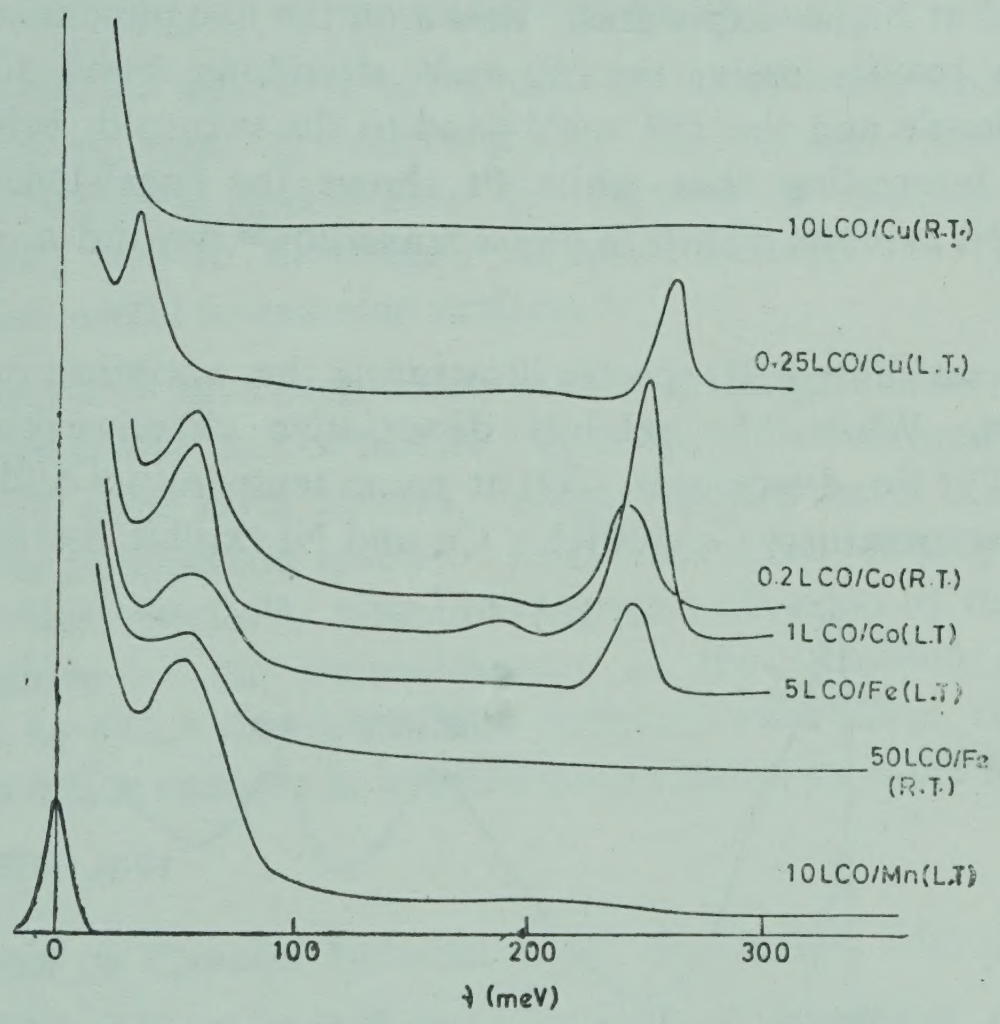

FIG. 9. Vibrational EELS of CO adsorbed on the polycrystalline first-row transitional metal.

at all temperatures upto 400K, while Cu exhibits molecular adsorption only at low temperatures. Around room temperature (RT), Cu does not exhibit any ad-layer build-up. The reactivity of metals (with respect to dissociative chemisorption of CO) therefore appears to vary in the order,

$$\text{Mn} \approx \text{Fe(RT)} > \text{Fe(LT)} > \text{CO} \approx \text{Ni} \approx \text{Cu(LT)} > \text{Cu(RT)}.$$

At one end, we have dissociative chemisorption and at the other no chemisorption. These results on polycrystalline metal foils are quite consistent with the single crystal

data reported in the literature for Cu(100), Ni(100), Ni(111), Pd(100), and Pt(111). It is generally found that the metal-carbon stretching frequency (appearing around 50 meV or lower) increases as the CO stretching frequency decreases. The heat of adsorption as well as the 5σ level of CO vary systematically with the C—O stretching frequency[16].

Using higher energy electron beams it is possible to observe electronic excitations in adsorbed CO. While the energy of the intramolecular transition (5σ, $1\pi \rightarrow 2\pi^*$) of the adsorbed CO changes little on adsorption, the metal $E_f \rightarrow 2\pi^*$ (CO) excitation varies widely from metal to metal, increasing with increase in the ΔH_{ads}. This suggests that an increase in the strength of the metal-carbon bond causes an increase in the transition energy[16].

X-ray photoelectron spectra in the C(1s) and O(1s) regions are also useful to investigate CO adsorption on metal surfaces. While dissociative chemisorption gives rise to C(1s) and O(1s) spectra similar to those of carbides and oxides, the corresponding features due to molecularly chemisorbed CO show a large variation from one metal to another. These variations have been related to heats of adsorption by Joyner and Roberts[25].

C(1s) and O(1s) levels of CO show extensive satellite structure (Norton *et al.* 1978). These satellites are due to metal adsorbate charge-transfer excitations. These assignments are supported by the fact that no satellite is observed in the spectrum of free CO in this energy range. We show in figure 10, spectra in the O(1s) region of CO adsorbed molecularly on Cu. We clearly see three features A, B and C in the spectra. These features could be delineated by decomposition of the O(1s) peaks into gaussians using an error minimisation procedure; this procedure enables us to estimate the intensity of each feature as a percentage of the total intensity. We have plotted these intensities against the logarithm of exposure in figure 10b. At low exposures, peak A is of low intensity while peak B is intense and broad. With increase in CO exposure, peak A gains in intensity till it becomes the predominant feature (beyond 100L), while peak B falls in intensity and gets substantially narrow. The intensity of C remains more or less constant. We assign peak B to a metal-CO charge transfer satellite while assigning peak C to a charge transfer process predominantly involving the adsorbed CO levels. Feature A, which becomes stronger with increasing exposure can be readily assigned to the main O(1s) line.

The width of feature B shows certain interesting changes with increasing exposure. With increase in exposure, feature B becomes progressively narrow (being 6 eV at 0.5L and 4 eV at 100L), while the widths of A and C remain almost unchanged. The broad feature at low exposure could arise from two or more peaks of comparable intensity corresponding to the presence of more than one species. On increasing the exposure, however, one of the peaks grows relatively faster than the other due to the preferential population of one of the species.

CO in sub-monolayer coverages forms clusters. At low coverages, the clusters are small and therefore the number of peripheral CO molecules is comparable to

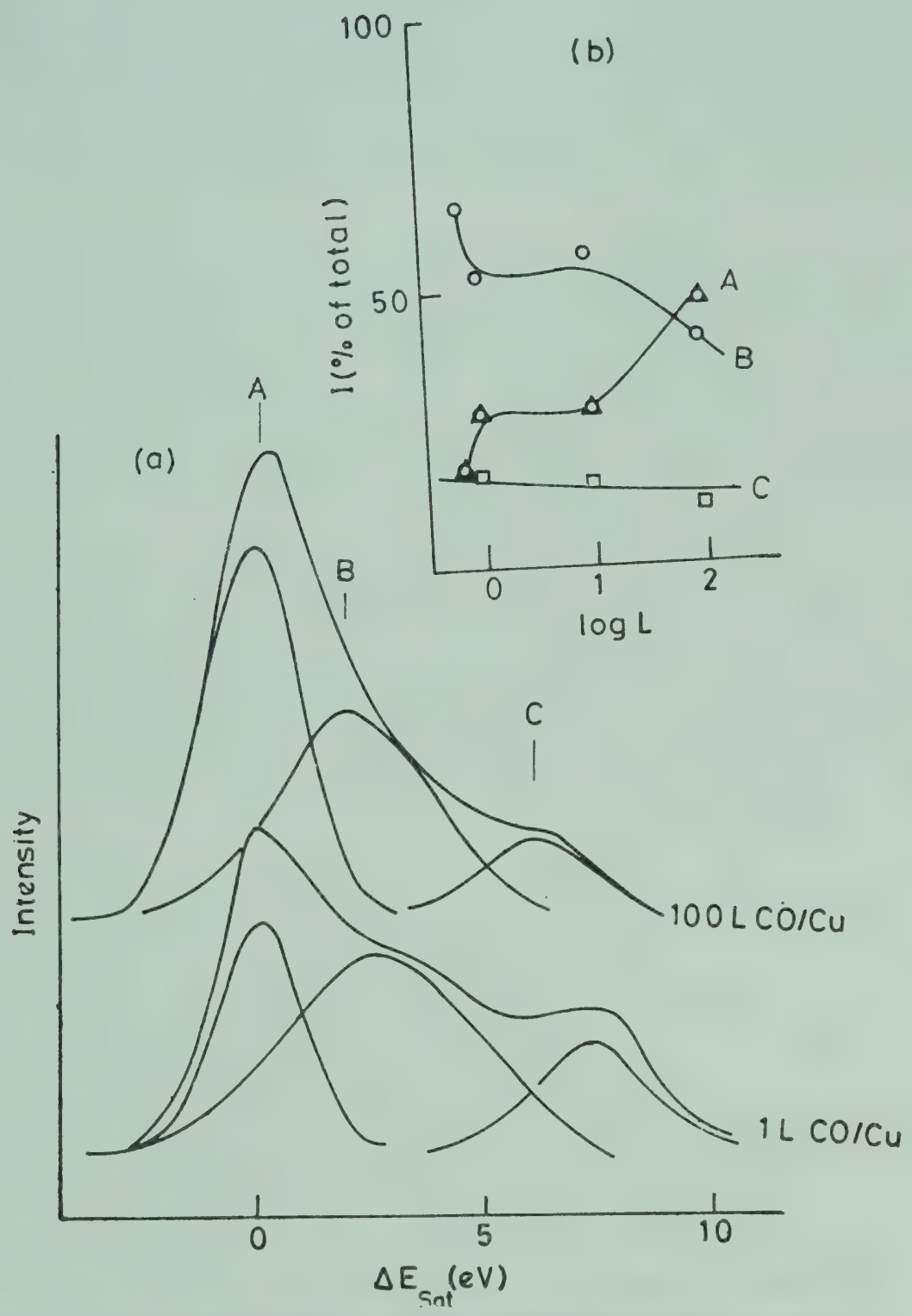

FIG. 10. O (1s) region of CO adsorbed on Cu showing satellites (B and C). Peak A is the main O(1s) signal.

the number of CO molecules within the cluster. On increasing the coverage, the clusters grow and thereby the number of molecules inside the cluster increases relative to the number of peripheral CO molecules.

Apart from dissociation and molecular adsorption, disproportionation (Boudouard's reaction) has also been observed on a number of first-row transition metals. This has been observed by UPS, XPS and by Auger electron spectroscopy. The reaction which can be written as $2CO \rightarrow C + CO_2$, leads to the formation of a surface carbide.

INTERACTION OF OXYGEN WITH TRANSITION METAL SURFACES

Adsorption of oxygen on transition metals has been extensively studied in the last decade[26]. Adsorption of oxygen on transition metal surfaces yields a variety of species ranging from the oxide (O^{2-}) to molecular oxygen O_2. These species can be distinguished clearly from a study of UV and X-ray photoelectron spectra.

Dissociation of oxygen on metal surfaces is a commonly observed phenomenon. Dissociated oxygen can exist in the form of weakly chemisorbed triplet atomic oxygen, strongly chemisorbed singlet atomic oxygen or as the oxide. Molecularly chemisorbed oxygen was unknown until 1980; the molecular species has been observed on Pt, Ag and other metal surfaces[27]. Molecularly adsorbed oxygen may occur in the physisorbed state as well. Physisorbed molecular oxygen has been observed on Pd and Ni at 80K.

The various oxygen species exhibit distinctly different features in their UV photoelectron spectra (Fig. 11). Molecular oxygen in the chemisorbed state shows three bands which can be assigned to the π_g^*, π_u and $2p\sigma_g$ levels. Since the bands of the chemisorbed species due to π_u and $2p\sigma_g$ do not split as in the case of physisorbed O_2 on Ga[28], this dioxygen species can be assigned to the singlet oxygen. Physisorbed O_2, on the other hand, shows a more complex five peak structure, due to the splitting of features due to the π_u and $2p\sigma_g$ levels. This splitting arises because photoionisation from these orbitals in triplet O_2 leads to two final states which differ in their spin.

The molecular oxygen species is stable only at low temperatures and on warming dissociates to give triplet atomic oxygen. The triplet atomic oxygen causes a splitting of the peak due to the 2p level. At higher temperatures (close to room temperature), we observe a single band in the UV photoelectron spectrum due to strongly chemisorbed singlet atomic oxygen. These species can be identified in the X-ray photoelectron spectra as well. XPS binding energies of the various oxygen

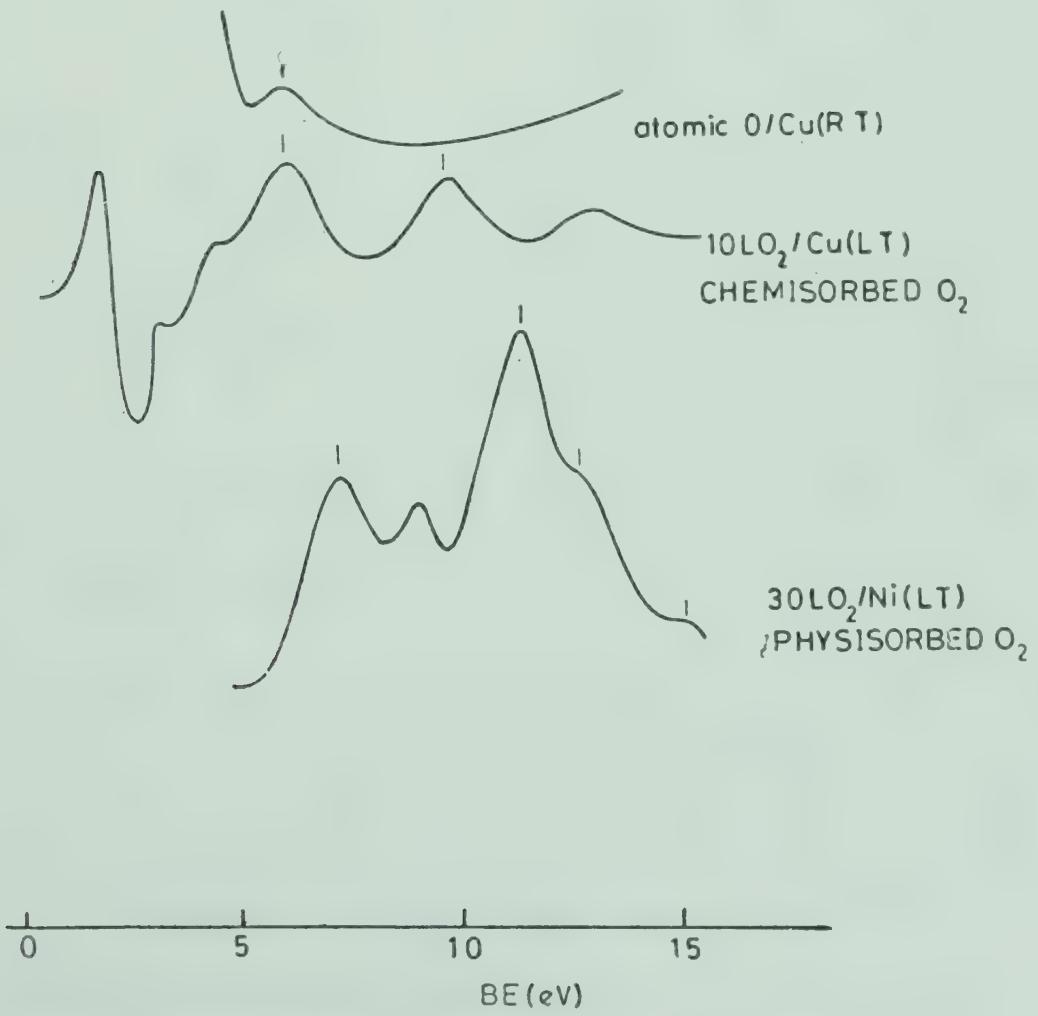

FIG. 11. HeII spectra of various adsorbed oxygen species.

species are: oxide, 529 eV; chemisorbed atomic oxygen, 530.5 eV; chemisorbed molecular oxygen, 533.0 eV; physisorbed molecular oxygen, > 533 eV.

Electron energy loss spectra obtained from surfaces covered with oxygen provide interesting information. Dissociated oxygen exhibits the low energy metal-oxygen stretching mode while molecular oxygen shows a band due to the O—O stretching mode in addition to the M—O stretching band. The O—O stretch of adsorbed oxygen is greatly shifted from that of the free O_2 molecule, and occurs in the range of 78 mev (1 meV = 8.065 cm^{-1}) in the case of silver to 105 meV in the case of platinum. These stretching frequencies are indicative of a bond order less than unity. On Pt, in addition to the 105 meV peak, another stretching frequency close to 80 meV is seen. This new species is considered to be the precursor to the dissociation of molecular oxygen[29].

There has been much interest of late in the adsorption of oxygen on alkali metal modified transition metal surfaces. Several interesting oxygen species have been characterised on such metal surfaces[30,31]. Unlike alkali metals which enhance the adsorption of oxygen on Ag, by enhancing the sticking coefficient, absorbed S, Cl and atomic oxygen are reported to passivate transition metal surfaces[32]. Chlorine preferentally favours the molecular species on Cu and Ag surfaces[33] as shown by the O(1s) spectra in (Fig. 12).

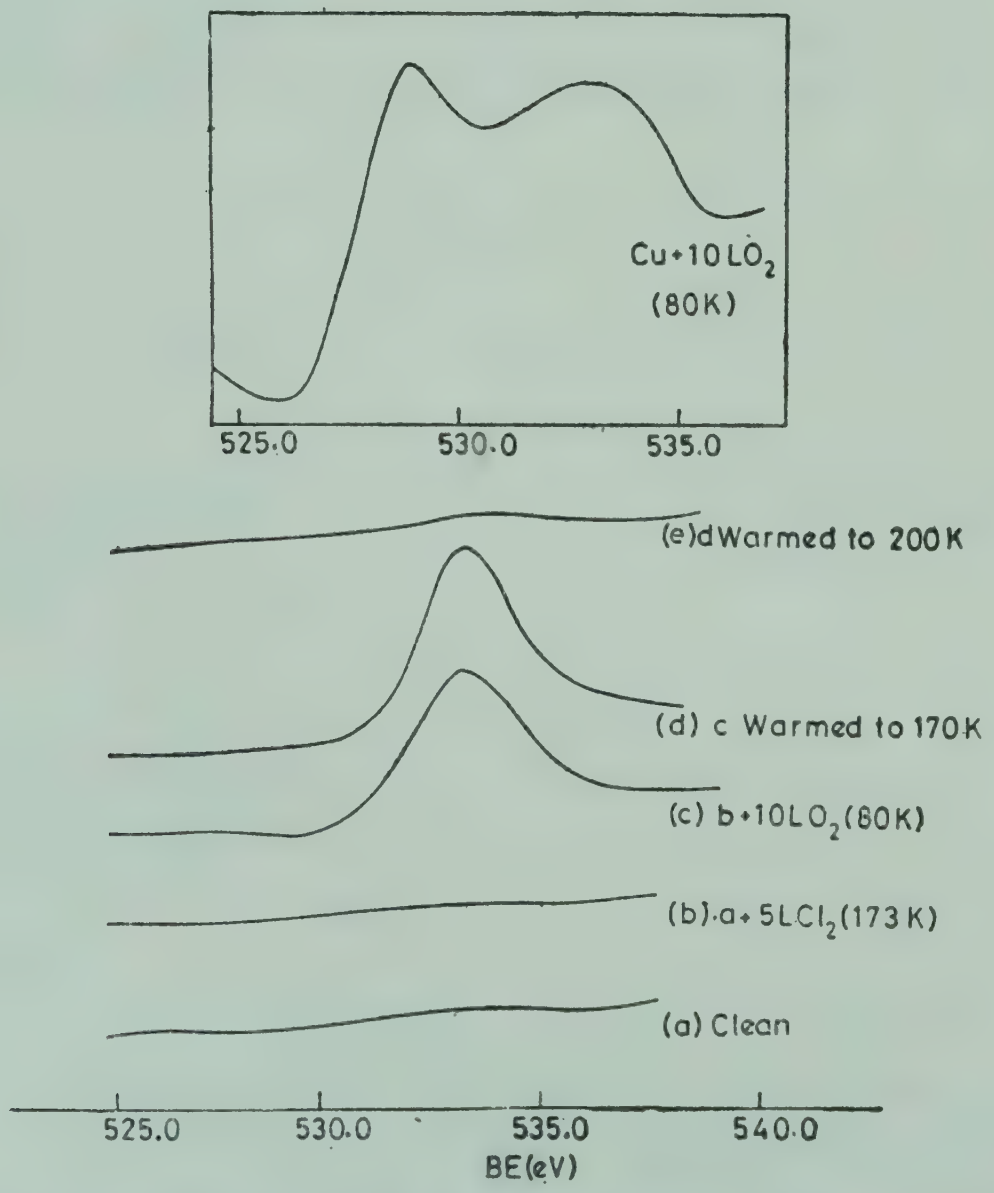

FIG. 12. Effect of presorbed chlorine on the adsorption of oxygen on Cu. Inset shows oxygen adsorbed on a clean Cu surface.

Surface oxidation of metals has been investigated widely by UPS, XPS and Auger spectroscopy. While in XPS, one follows the changes in the metal core level peaks as well as O(1s) peaks, Auger metal intensity ratios provide a novel means of following surface oxidation. In figure 13 we show how the oxidation of zirconium has been studied[34] by following changes in zirconium 4d peaks in XPS. Valence bands also give a clue to the nature of surface oxidation; for example in the surface oxidation of cerium, only the UPS band due to the 6s + 5d state diminishes in intensity or disappears on surface oxidation leaving the 4f peak unaffected suggesting thereby that the surface oxide is Ce_2O_3. Figure 14 shows how the metal Auger

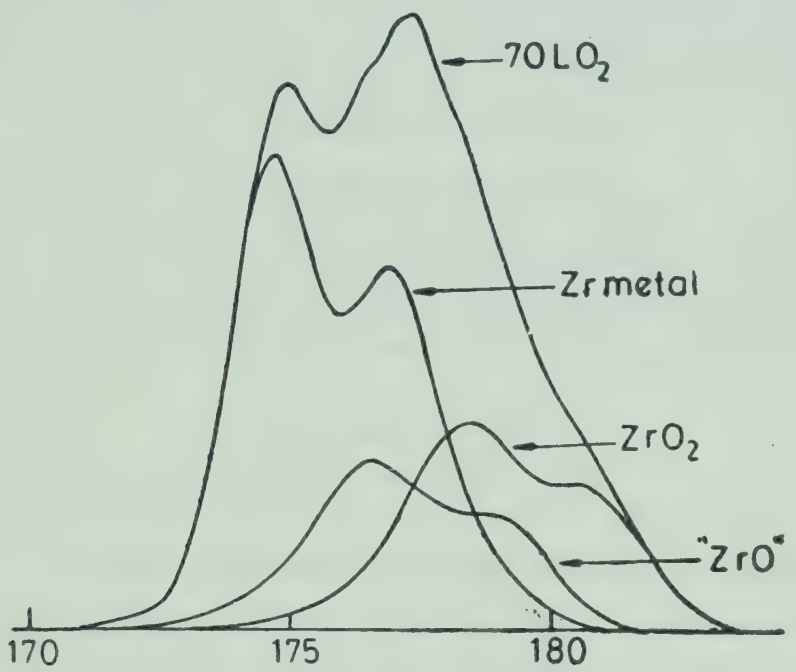

FIG. 13. Decomposition of Zr (3d) spectrum in terms of Zr, "ZrO" and ZrO_2 contributions.

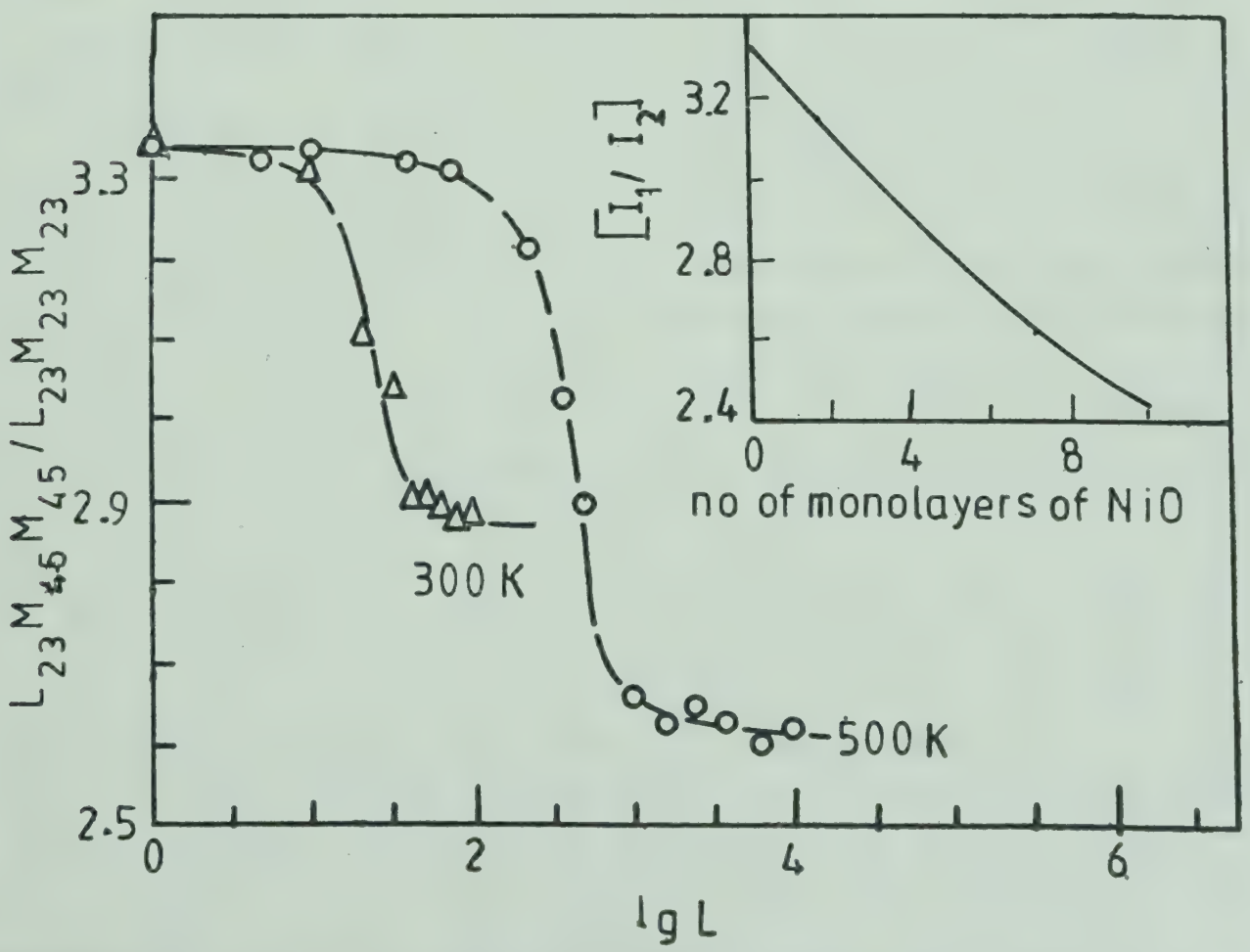

FIG. 14. Plot of the metal Auger intensity ratio of Ni against the logarithm of oxygen exposure. Inset shows the Auger intensity ratio *vs* the number of oxide layers.

intensity ratios provide quantitative information on surface oxidation of transition metals; metal Auger intensity ratios are directly related to the number of valence electron states. Amongst the large number of oxidation studies reported in the literature, the recent investigations of the oxidation of metallic glasses are specially significant[34,35]. The studies show the role of composition, the metalloid and the special nature of metglass surfaces.

Photon-stimulated desorption of metals covered with oxygen provides valuable information on surface oxygen layers. In the desorption process, O^+ ions are removed from oxygen covered metal surfaces and these ions are detected mass spectrometrically. The O^+ ion desorption occurs corresponding to different core levels of the metal and exhibits fine structure similar to EXAFS[36,37]. Both electron and photo-stimulated desorption studies have been employed to examine desorption of species such as OH^+ and F^+ from metal surfaces.

Ion scattering spectroscopy (ISS) is useful in examining the structure of surfaces. For example, ISS has shown that sulphur atoms stick out of the plane of Ni atoms when sulphur is adsorbed on Ni metal. The structure of UO_2 surfaces has been studied most effectively by this technique[38].

Concluding Remarks

Most of the studies referred to in the previous sections are on to single crystal surfaces. While results of such studies are undoubtedly of value in understanding surface phenomena and fundamental processes on surfaces, the conditions employed for the experiments are far removed from real situations. For example, in real life, we employ polycrystalline or amorphous catalysts, often metal particulates dispersed on surfaces of oxide supports. Adsorption studies on polycrystalline metal foils are useful, but these are still far removed from catalytic reactor conditions. Reactions are carried out at atmospheric pressure or higher and not in ultra-high vacuum. One has to therefore carry out studies on real systems by employing different or modified techniques. IRAS with high pressure cells appears to be one such technique. Thermal desorption, electron spectroscopies and IRAS combined together would probably provide much of the information on catalytic reaction mechanisms.

There will certainly be many new and improved techniques to study surfaces in the years to come. Scanning tunnelling microscopy[7] for surface topography at an atomic level was mentioned earlier. In experimental surface science, it becomes almost always necessary to employ more than one technique to investigate a problem. For example, the number of d-electron states in catalysts can be determined by Auger spectroscopy, X-ray absorption spectroscopy and EELS[39,40]. In order to investigate the interaction of carbon monoxide with metal surfaces, one generally employs UPS, XPS and vibrational EELS (CO and M–C stretching frequencies). Auger spectroscopy can be used to obtain finger prints of the adsorbed molecules while electronic EELS yields information on the electronic transitions. Similarly, interaction of oxygen with metals is readily investigated by UPS (valence bands) and XPS (oxygen 1s, metal core levels and plasmon peaks) as well as metal and oxygen Auger line

intensities; electronic EELS provides information on surface electronic states and vibrational EELS gives oxygen-oxygen and metal-oxygen stretching frequecies. In all such studies, LEED patterns are related to the surface structure (surface reconstruction, if any). Infrared reflection absorption spectroscopy is equally useful to study vibrations of CO, O_2 and other adsorbed molecules while Mössbauer spectroscopy gives, in the case of Fe, Sn and such metals, valuable information on the oxidation states. The nature of species on Pt surface when ethylene is adsorbed on it around room temperature was established to ethylidyne by a combination of vibrational EELS and optical (Raman and IR) spectroscopy carried out in comparison with cluster compounds[41]. With the availability of the variety of techniques, experimental surface science will undoubtedly continue to be a challenging and rewarding area of research in the years to come.

Acknowledgement

The author is thankful to his coworkers for fruitful collaboration and to the Department of Science and Technology, Government of India, for support of this research.

References

1. T A Carlson, *Photoelectron and Auger Sepectroscopy*, Plenum Press, New York (1975).
2. L Fiermans, *Electron and Ion Spectroscopy*, (J Vennik and W Dekeyser Eds.), Plenum Press, New York (1978).
3. C N R Rao, *Proc. Indian natn. Sci. Acad.* **47A** (1981) 111.
4. C N R Rao and M S Hegde, *Preparation and Characterization of Materials* (J. M. Honig and C N R Rao, Eds.), Academic Press, New York (1981).
5. C N R Rao and D D Sarma, *J. Solid. State Chem.* **45** (1982) 14.
6. J C Green, *Ann Rev. Phys. Chem.*, **28** (1977) 161.
7. G Binning, H Rohrer, Ch Gerber and E Weibel, *Phys. Rev. Lett.* **49** (1982) 57.
8. D R Lloyd, C M Quinn and N V Richardson, *Surface and Defect properties of Solids* (M W Roberts and J M Thomas, Eds.), Vol. 6, Specialist Periodic Report (1977).
9. W E Spicer, *Electron and Ion Spectroscopy of Solids* (L. Fiermans *et al.*, Eds.), Plenum Press, New York (1978).
10. D E Eastman, T C Chiang and F J Himpsel, *Phys. Rev. Lett.* **45** (1980) 656.
11. R W Joyner and M W Roberts, *Surface and Defect properties of Solids* (M W Roberts and J M Thomas, Eds.), Vol. 4, Specialist Periodic Report, The Chemical Society, London (1975).
12. D D Sarma, P V Kamath and C N R Rao, *Chem. Phys.* **73** (1982) 71.
13. C N R Rao, D D Sarma and M S Hegde, *Proc. Roy. Soc. London* **A370** (1981) 269.
14. S Yashonath, P Sen, M S Hegde and C N R Rao, *J. Chem. Soc. Faraday* 1 **79** (1983) 1229.
15. C N R Rao and D D Sarma, *Phys. Rev.* **B25** (1982) 2927.
16. C N R Rao, A Srinivasan and K Jagannathan, *Intnl. Rev. Phys. Chem.* **1** (1981) 45.
17. C N R Rao, P V Kamath, K Prabhakaran and M S Hegde, *Can. J. Chem.* (1984) In Print.
18. P V Kamath, D D Sarma and C N R Rao, *Proc. Indian Acad. Sci.* (Chem. Sci.) **93** (1984) 335 and the references cited therein.
19. G Broden, T N Rhodin, C Brucker, R Benbow and Z Huyrich, *Surf. Sci.* **59** (1976) 593.
20. J B Benziger, *Appl. Surf. Sci.* **6** (1980) 105.
21. J B Benziger, E I Koe and R J Madix, *J. Catal* **54** (1978) 414.
22. P M Williams, P Butcher, J Wood and K Jacobi, *Phys. Rev.* **B14** (1976) 3215.
23. N Sheppard and T Nguyen, *Advances in IR and Raman Spectroscopy* (R J H Clark and R E Hester, Eds.), Vol. 5, Heyden, London (1978).
24. S Andersson, *Solid State Commun.* **21** (1977) 75.

25. R W Joyner and M W Roberts, *Chem. Phys. Lett.* **29** (1974) 447.
26. K Wandelt, *Surf. Sci. Rep.* **2** (1982) 1.
27. P V Kamath and C N R Rao, *J. Phys. Chem.* **88** (1984) 464 and the references cited therein.
28. D Schmeisser and K Jacobi, *Surf. Sci.* **108** (1981) 421.
29. N R Avery, *Chem. Phys. Lett.* **96** (1983) 371.
30. P J Goddard and R M Lambert, *Surf. Sci.* **107** (1981) 519.
31. M Ayyoob and M S Hegde, *Surf. Sci.* **133** (1983) 516.
32. E I Koe and R J Madix, *Surf. Sci.* **112** (1982) 273.
33. P V Kamath, K Prabhakaran and C N R Rao, *Surf. Sci.* **146** (1984) 551.
34. P Sen, D D Sarma, R C Bhudhani, K L Chopra and C N R Rao, *J. Phys. F.* (*Metal Phys.*) **14** (1984) 565.
35. P Sen, A Srinivasan, M S Hegde and C N R Rao, *J. Mater. Sci.* **18** (1983) 173.
36. T E Madey, R. Stockbauer, J F van der Veen and D E Eastman, *Phys. Rev. Lett.* **45** (1980) 187.
37. R Jaeger, J Feldmans, J Haase, J Stohr, Z Hussain, D Menzal and D. Norman, *Phys. Rev. Lett.* **45** (1980) 1870.
38. W P Ellis and T N Taylor, *Surf. Sci.* **91** (1990) 409.
39. C N R Rao, T G Sparrow, B G Williams and J M Thomas, *J. C. S. Chem. Comm.* (1984) 1238.
40. C N R Rao, J M Thomas, T G Sparrow and B G Williams, *J. Phys. Chem.* (1984) In Print.
41. P Skinner, M W Howard, I A Oxton, S F A Kettle, D B Powell and N Sheppard, *J. Chem. Soc. Faraday* 2 77 (1981) 1203.

© *Proc. Indian natn. Sci. Acad.*, **51**, A, No. 1, 1985, pp. 17–26.
Printed in India.

THEORY OF SEMICONDUCTOR SURFACE RECONSTRUCTION*

K C Pandey

IBM Research Centre, Yorktown Heights, New York 10598, U.S.A.

We show that a π-like bonding between the broken bonds present at the surface is apparently the key to understanding several long-standing puzzles concerning the reconstruction of Si surfaces. To fully exploit the π-bonding mechanism, the surface atoms must rearrange themselves rather thoroughly namely, the surface topology and the ring structure must be altered. Based on the π-bonding mechanism we have arrived at a unique reconstruction model for the cleaved Si(111)–2 × 1 surface. The model consists of π-bonded chains of Si atoms at the surface. Of the reconstruction models proposed for the cleaved 2 × 1 surface, the π-bonded chain model leads to the largest total-energy benefit, and only the π-bonded chain model provides a natural interpretation of the various spectroscopic and other data on this surface. We show that one of the most widely used ideas in the context of semiconductor reconstruction, that of buckling, is inappropriate for homopolar semiconductors. Buckling, however, provides a valid reconstruction mechanism for heteropolar surfaces such as the GaAs(110). These conclusions are based on the total-energy and surface-band calculations using the self-consistent pseudopotentia method.

Key Words : Semiconductor; Atomic structure; Surface topology; Crystallography

Introduction

Remarkable as it might seem, with very few exceptions, the atomic structure of the bare surfaces of semiconductors are not known[1]. The fundamental problem is the following: At semiconductor surfaces, the covalent bonds that characterize the bulk solid are broken, leaving "dangling bonds" that are not energetically stable and distort or rebond in some way to reduce their energy; the question is, How? Because of the great importance of Si, the effort to understand its various crystallographic surfaces continues to be enormous.

In this paper we discuss two theoretical developments in the field of semiconductor surface reconstructions that have occurred over the last few years[2,3]. One is the analysis and discrediting of an old idea (the buckling model); the other is the introduction of a completely new idea (π-bonding). Prior to 1981, it was believed (essentially universally) that a broken-bond distortion consisting of displacements of surface atoms driven by charge transfer (buckled surface model) would lower the total energy. We showed[2,3] that buckling, which had been central to thinking about *all* semiconductor surfaces, is not a valid reconstruction mechanism for homopolar surfaces such as the Si(111)–2 × 1. In particular, we showed[3] that buckling actually raises the energy of this surface and it does not lead to a semiconducting surface as previously thought and known from experiments. In analyzing the reasons for the failure of buckling on the Si surface, we also showed[3] that buckling

*Paper presented at the Symposium on Physics and Chemistry of Surfaces held at INSA, New Delhi from September 28-30, 1984.

might be a valid reconstruction mechanism for heteropolar surfaces (such as the GaAs(110)).

The second development is the introduction of an alternative mechanism for surface reconstruction. We showed[2] that π-bonding, which plays no important role either in the bulk solid or in molecules containing Si, is an important means by which surfaces can lower their broken-bond energy and derived a unique atomic model for the cleaved Si(111)-2 × 1 surface. For the maximum utilization of π-bonding, we showed that the connectivity or topology of atoms near the surface must be changed. Thus the π-bonding reconstruction mechanism represents a complete and qualitative departure from the simple Jahn-Teller buckling mechanism.

When introdced, π-bonding mechanism aroused considerable skepticism. There were two reasons for this. First, the π-bonding ideas were in conflict with the prevailing ideas (charge transfer and magnetic ordering[4]) at the time. Second, the π-bonding idea was novel and not understood. The novelty of these ideas and the interest that they created have led to a number of experiments on the cleaved Si surface. These studies include angle-resolved photoemission[5], electron energy loss[6], ion-scattering[7], polarization-dependent reflectivity[8], low energy electron diffraction[9], and second harmonic generation[10], the sum of which confirms the validity of the π-bonding mechanism for the Si(110)-2 × 1 surface. The π-bonding ideas have also had a significant impact on theoretical work in the field, and these ideas have been confirmed by others[11].

Reconstruction Mechanisms : Buckling vs π-Bonding

The buckling and π-bonding reconstruction mechanisms are qualitatively distinct. This is illustrated schematically by Fig. 1. Buckling is a simple Jahn-Teller distor-

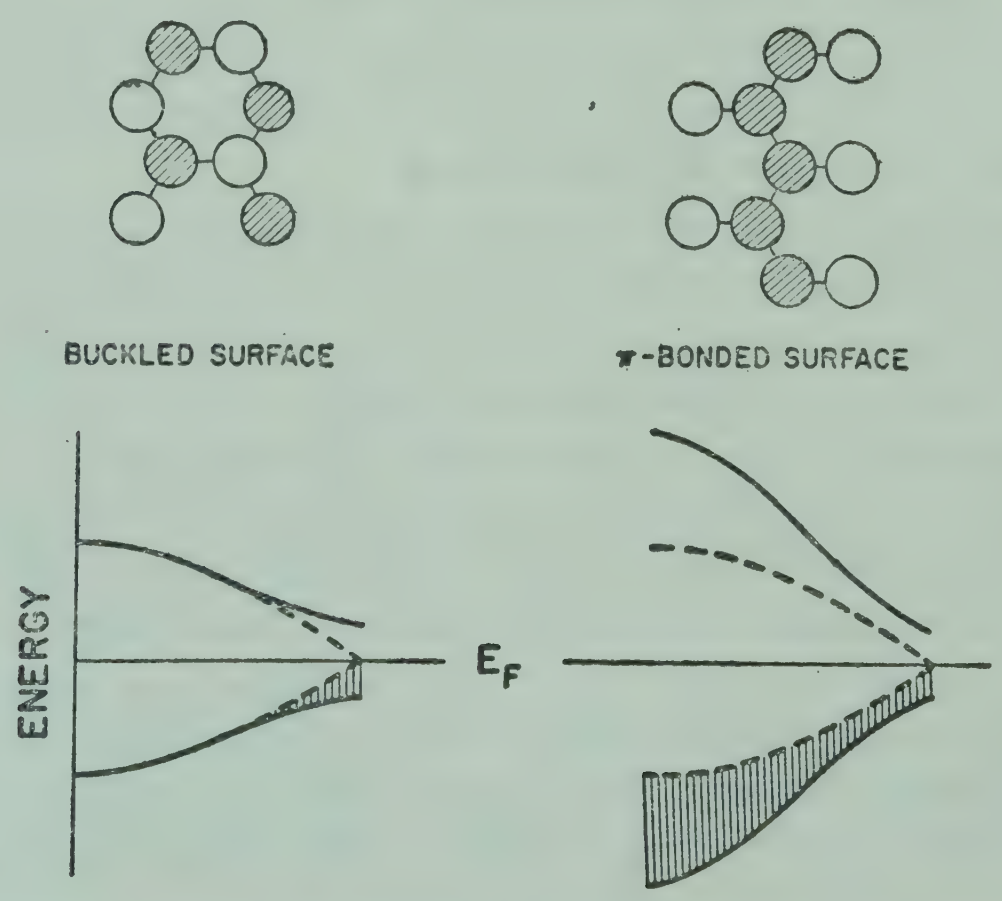

Fig. 1. A comparison of the essential geometrical and surface electronic features of the buckling and π-bonding models surface. Open circles represent surface atoms.

tion driven by the redistribution of only the electrons near the Fermi surface. It does not involve any drastic rearrangement of atoms. π-bonding, on the other hand, is not driven by the rearrangements of a few electrons at the Fermi surface. It is driven by the rearrangement of most of the electrons. It involves a very drastic rearrangement of atoms that even alters the topology.

The idea that buckling distortions energetically stabilize semiconductor surfaces has enjoyed great popularity since it was introduced in 1961 by Haneman[12]. Its popularity is due in part to its intuitive appeal and in part to estimates of the stabilization energy based on electronic-structure calculations that proved to be too crude and unreliable. The intuitive appeal of the buckling idea is easy to appreciate. The electrons in tetrahedral semiconductors reside in bond orbitals which project from each atom in the four tetrahedral directions. The diamond and zinc-blende crystal structures permit all the bond orbitals to be joined perfectly inside the semiconductor, but, at the surface one or more of these bond orbitals is left "dangling" from each atom. On the unreconstructed (111) surface of such systems, e.g., one such dangling bond projects directly into the vacuum from each atom (Fig. 1). Since there is one electron in each dangling bond, such a surface corresponds to a half-filled band and is therefore metallic, in conflict with experiment. It is very natural to think that such a system will spontaneously reduce its symmetry, so as to lower the energy of the states in the occupied half of the band, thereby energetically stabilizing the surface and, at the same time, introducing an energy gap between the occupied and unoccupied states, as is observed. This is the intuitive appeal of Jahn-Teller symmetry-breaking distortions in general and of the buckling idea, in particular.

According to the buckling idea, half of the surface atoms recede toward the bulk crystal; the remaining half move outward. A crucial aspect of buckling, fully appreciated by Haneman, is that the rehybridization of the atomic orbitals caused by the change in geometry leads to a substantial charge transfer from the receding atoms to the outwardly displaced atoms. This charge transfer can be understood with the help of Fig. 2. On the ideal surface the "dangling bonds" are sp_3-like and

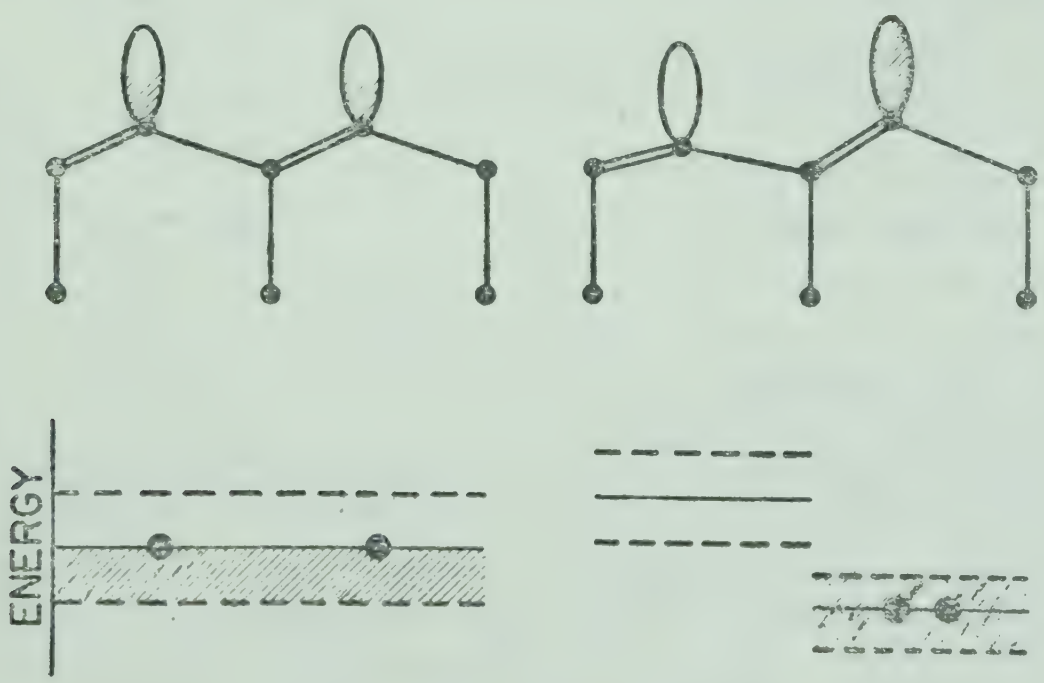

FIG. 2. Rehybridization and electron transfer on buckling.

they are all degenerate in energy. On buckling, the back bonds on the "in" atoms become planer and thus tend towards sp_2-like configuration. This leaves the broken bonds on these atoms more p-like thus raising their energies (Fig. 2). The opposite holds on the "out" atoms whose broken bonds become more s-like and their energy is lowered (Fig. 2). For an energy gain via buckling, the occupation of the lower-energy state must be increased. In order to achieve this, electrons must be transferred from the "in" atoms to "out" atom. Thus the buckling leads to an ionic surface.

In the π-bonding reconstruction, shown schematically in Fig. 1, the dangling bonds, which on the ideal truncated surface are placed on the second-neighbour atoms, are brought to the nearest neighbour atoms to form a one dimensional zig-zag chain. This is accomplished without any increase in the number of broken bonds and only with local rebonding that does not involve any diffusion of surface atoms. Both the increased overlap of the dangling bonds and formation of a one dimensional energy band, permitted by this geometry, contribute to the increased width of the dangling bond energy band. It is this increased bandwidth that is responsible for the large energy benefit due to the π-bonding (Fig. 1). Note that states near the Fermi level do not play any special role in this mechanism.

Figure 3 shows a detailed view of the π-bonded chain model for the Si(111)-2 $\times$ 1 surface. The model is shown nearly to the correct scale. The two important

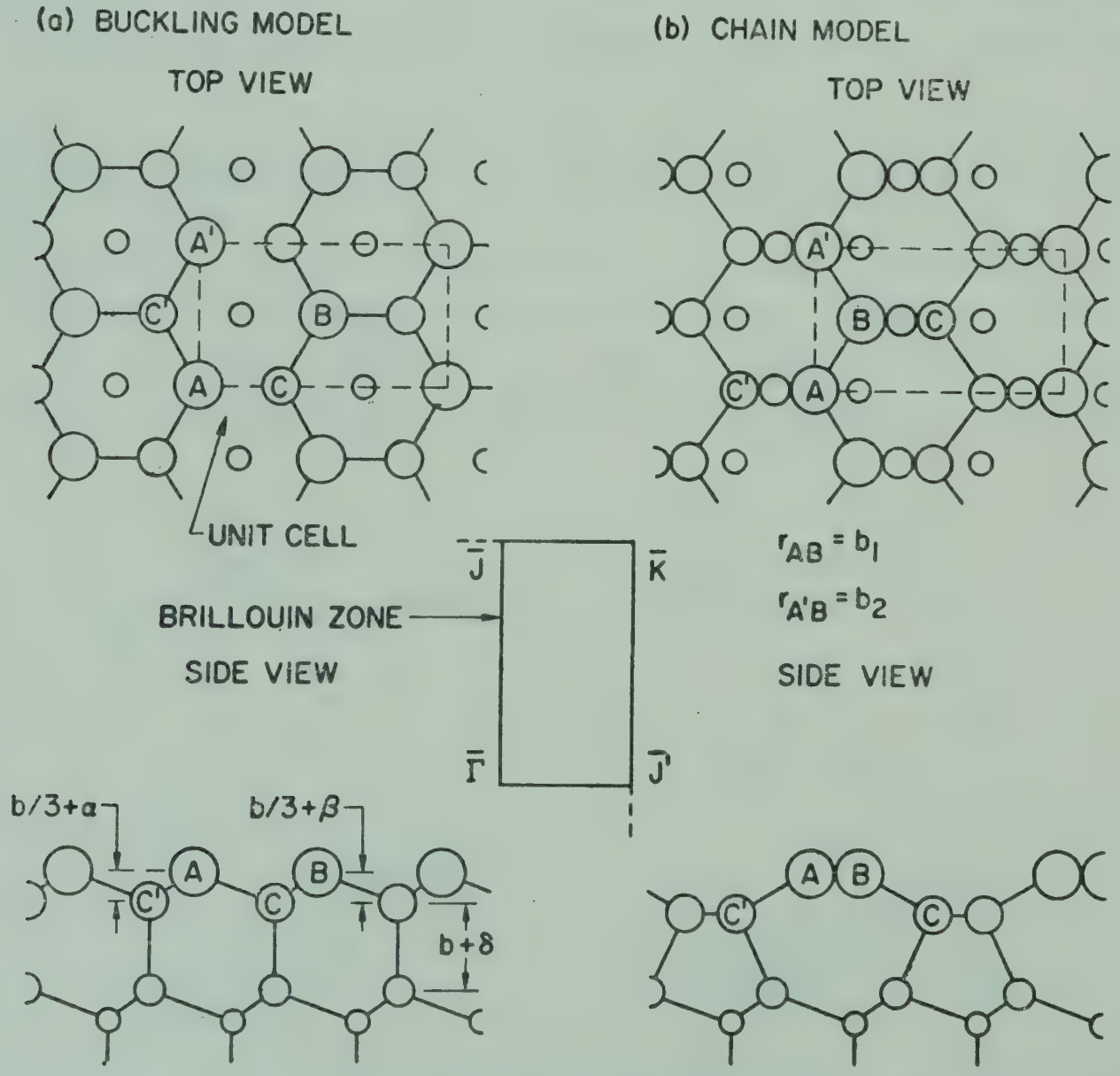

FIG. 3. The π-bonded chain model for the Si(111)-2 $\times$ 1 compared with the buckling model.

features of the model are: nearly parallel dangling bonds on nearest neighbour atoms and the chain structure. The topology of the zig-zag chain structure of the top two layers (shaded circles) is similar to that of the ideal (110) surface. Deeper layers are in their ideal positions. All bond lengths have their ideal values (2.35 Ang.) except for bonds along the chains in the top layer which are contracted by 0.1 Ang. The chains are slightly tilted with respect to the ideal surface. This tilt results from the asymmetry of the underlying substrate which makes the alternate atoms along the chains non equivalent. For comparison purposes, the buckling model for this surface with alternate rows of surface atoms (largest circles) displaced "in" and "out" are also shown. Both the models have a reflection symmetry about the (1–10) plane. The surface unit cell and the surface Brillouin zone are also shown.

There were two important reasons for questioning the validity of the buckling mechanism and introducing the π-bonding mechanism as an alternative. First, experimental developments, particularly, the measurement[13,14] of core level shifts of surface atoms relative to atoms in the bulk and an unambiguous determination[5] of the symmetry and energy band dispersions of surface states by polarization-dependent angle-resolved photoemission spectroscopic (ARUPS) measurements along symmetry directions on a cleaved surface with a single domain. From our extensive studies of the buckling model, with buckling parameters varying over a wide range, we were unable to find any buckling model which leads to a semiconducting surface with an observed band gap of at least 0.25 eV and which is still consistent with any of the observed features of surface-state energy bands (signs of dispersions, the large bandwidth, absence of states with odd parity with respect to the reflection plane) as well as small surface core level shifts. Second, on theoretical considerations of total energy of the surface, buckling seems a very nonphysical mechanism because of the large charge transfer involved.

Calculation of Surface Energy Bands and Total Energy

In this section, we discuss briefly the technical aspects of the calculation of the total energy and the surface energy bands that are presented in the section to follow. Calculations were carried out using the "local-density" description of exchange and correlation, implemented with self-consistent pseudopotential theory. We approximate the semi-infinite semiconductor by a "slab" of infinite extent in two directions, and of finite extent in the third[14,15]. All aspects of the theoretical approach have been tested previously. In particular, for both Si and GaAs, the calculated bulk properties[16] (the energy bands, lattice constant, cohesive energy, and bulk modulus) based on these potentials, are all in good agreement with experiment and, for Si, almost identical to the results reported by Yin and Cohen[17]. The pseudopotentials used are non-local and norm-conserving[18]. Several of the calculations were repeated using local pseudopotentials, without significant effect. Wave functions were expanded in plane waves and total-energy calculations were carried out in reciprocal space. We emphasize two technical points. First, all controllable approximations, the number of plane waves used to expand various quantities e.g., were held fixed as

the atomic geometry was varied. (For example, the reference calculation for the ideal Si 1 × 1 surface was performed using a 2 × 1 unit cell). Second, a very high degree of self-consistency was required and achieved in all the calculations. We estimate that the controllable errors in total-energy differences discussed below are smaller than 0.02 eV/surface atom. Since we use the "super-cell" technique to study the slab geometry, our above-mentioned bulk calculations constitute a test of our implementation of the theory. In addition, however, further tests have been carried out by repeating the surface band calculations of previous workers for the relaxed Si(111)–1 × 1 and GaAs(110) surfaces. Apart from small discrepancies due, we believe, to our greater self-consistency, the two sets of calculations agree well.

For the Si(111)–2 × 1 surface, ten-layer slabs separated by vacuum, with the (111) unit cell dimension of 41.26 a.u. were used. For GaAs(110) nine-layer slabs with the (110) unit cell dimension of 47.4 a.u. were used. All plane waves with kinetic energy less than 3 Ryd (approximately 325) were treated exactly and those with kinetic energy between 3 and 6 Ryd (approximately 500) were treated using Lowdin's perturbation scheme. Perturbation corrections to wave functions were also calculated. The exchange-correlation potentials were evaluated in real space at about 14000 uniformly spaced points in the unit cell. Calculations of charge density and Hartree potential in the self-consistency iteration were based on a sampling of 9 k-points in the irreducible section of the Brillouin zone. At no stage in our calculations were any cutoffs, either in potential or charge density, used.

Total Energy and Band Dispersion of Buckling and π-Bonding Models

We now consider the quantitative results of our calculations. In Fig. 4 we compare the total-energy benefit to the (111) surface of Si resulting from two types of surface reconstruction, buckling and relaxation (the uniform displacement of all surface-layer atoms toward the bulk). The reconstruction model of Ref. 20 labeled "Chadi" in Fig. 4 is the particular combination of buckling and relaxation that minimises the total energy calculated non-self-consistently[20]. The total-energy difference between the dashed and dotted lines in Fig. 4 isolates the effect of self-consistency (approximately 0.35 eV/atom) for this particular geometry. The aspect of Fig. 4 that we emphasize most strongly, however, is that buckling is seen to raise the total energy of the surface. This result is not restricted to the "Chadi" model; we obtained similar results for all of the buckling models in the literature.

Figure 5 deals with the second purported virtue of buckling, the creation of a gap separating the occupied and unoccupied states. Shown in Fig. 5 is the dispersion (dependence of the orbital energy on momentum parallel to the surface) of the dangling-bond surface state. Three surface geometries are considered: (1) unreconstructed, (2) small buckling, and (3) large buckling. All previous calculations find a gap proportional to the degree of buckling, in agreement with Haneman's analysis. We find no gap, even for large amounts of buckling. Here again, self-consistency is the distinguishing feature of the present analysis. The opening of the gap is resisted by the depedence of the self-consistent potential in the vicinity of

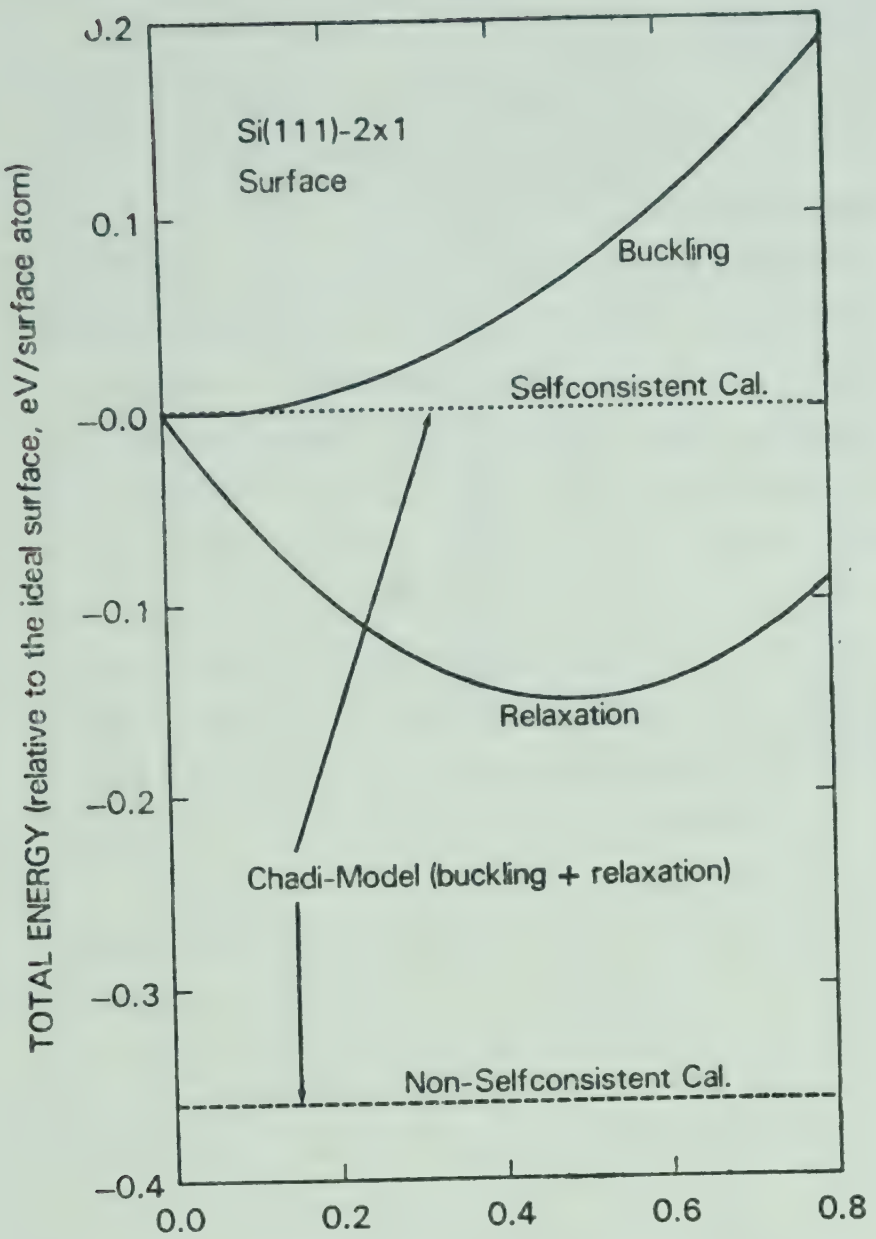

FIG. 4. Total-energy variation for buckling and relaxation distortions of the surface of a homopolar semiconductor. Note that the self-consistent result for the Chandi model (dotted line) is only coincidentally very close to zero.

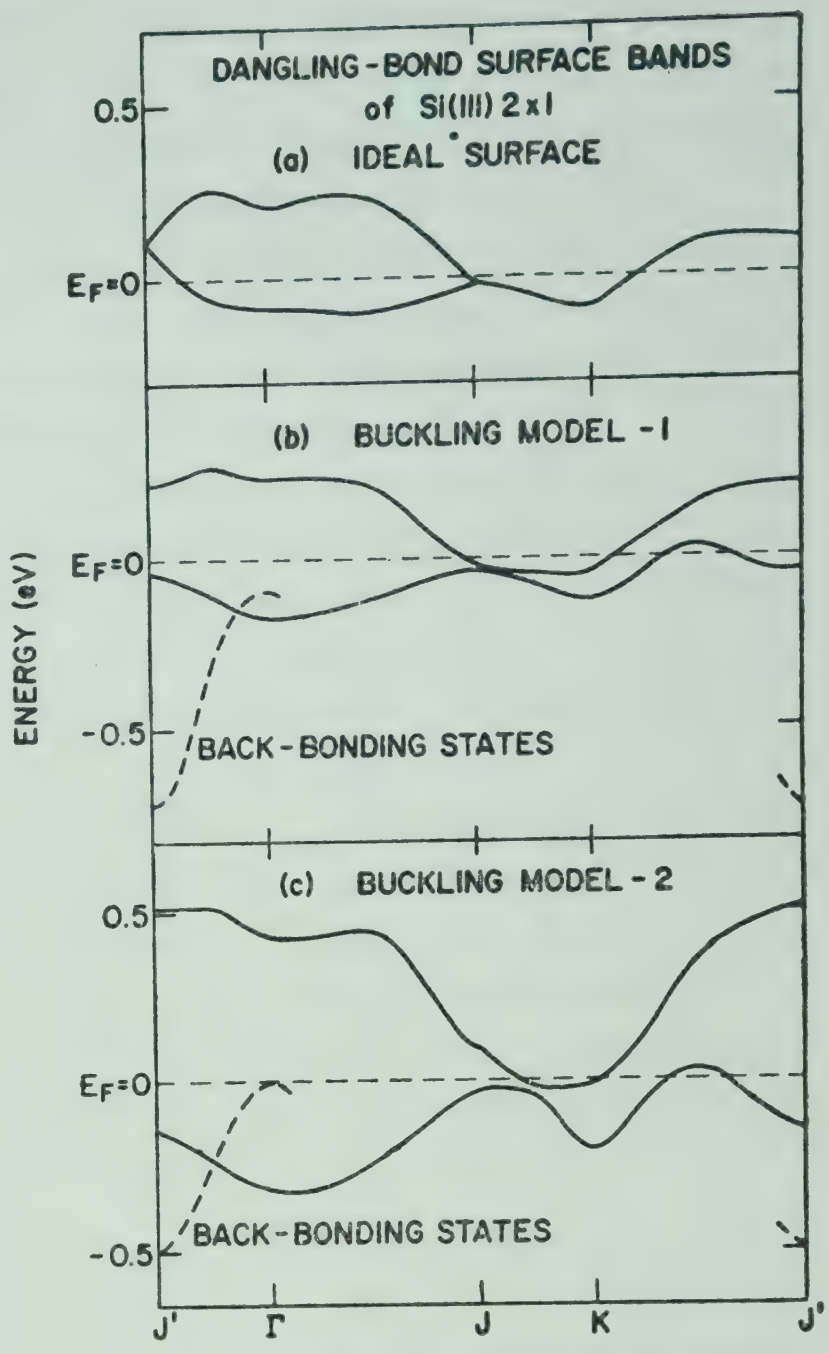

FIG. 5. Surface energy bands along the principal directions in the surface Brillouin zone for buckling models.

each atom on the number of electrons in that region; as electrons are removed (by buckling e.g.) the electrostatic potential in that region is lowered; the lowered potential attracts electrons to that region. Quantitatively, the dependence of the potential on atomic charge (the intra-atomic Coulomb integral) is large (approximately 5 eV/unit charge). Consistently, the calculations on which Fig. 5 is based exhibit very little charge transfer.

Consider now the alternative to buckling distortions offered by the π-bonded-chain model. The significant virtue of this model is that the bond topology of the surface is changed so that the dangling-bond orbitals reside on nearest-neighbour atoms. In this configuration, the bond orbitals are close enough to interact significantly, causing a substantial reduction of total-energy. This total-energy reduction is compared in Fig. 6 to the other types of reconstruction, buckling, relaxation and magnetic. In the magnetic reconstruction, the surface spontaneously reduces its

symmetry by permitting electrons of different spin to congregate on different surface atoms. Figure 6 shows that the π-bonded-chain model reduces the surface energy more than all the other models presently available.

In Fig. 7 we show the calculated energy band dispersion of the dangling bond surface state. Also shown in this figure are the bands derived from ARUPS measurements. Two independent sets of measurements are shown[5]. It is clear that within the experimental uncertainties the measurements agree with the calculated bands. The two quatitative features of the band dispersion—large dispersion along the length of the chains and almost no dispersion in the perpendicular direction—arise from the one dimensional nature of the π-bonded chains. With regard to the presence or absence of a gap in the excitation spectrum, we wish to point out that the gap (Fig. 7) arises because the alternate atoms in the chain are not equivalent. This is because of the underlying substrate (Fig. 3). We remind the reader that a principal motivation for the introduction of the chain model is its consistency with spectoscopic data. Consider for example the small surface core level shifts observed in ARUPS. This is precisely what one expects for the π-bonded chain model because, in contrast to buckling, charge transfer is not required by reconstructions of the π-bonded-chain type.

Finally, Fig. 8 demonstrates that buckling can be effective for surfaces of heteropolar semiconductors. Shown in Fig. 8 is the total energy of GaAs(110) as

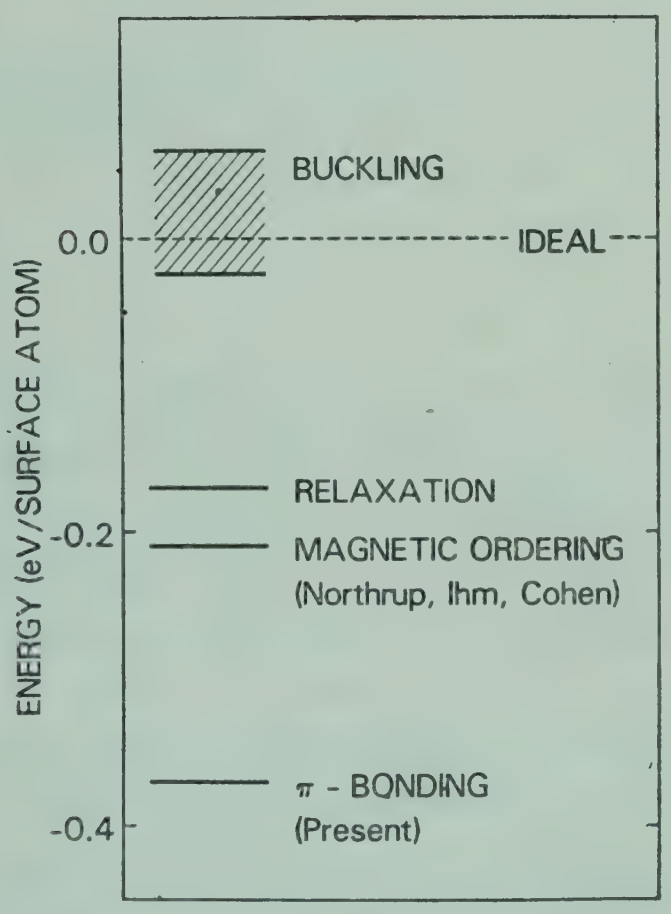

FIG. 6. Stabilization of Si(111)–2 × 1 surface by π-bonded-chain reconstruction.

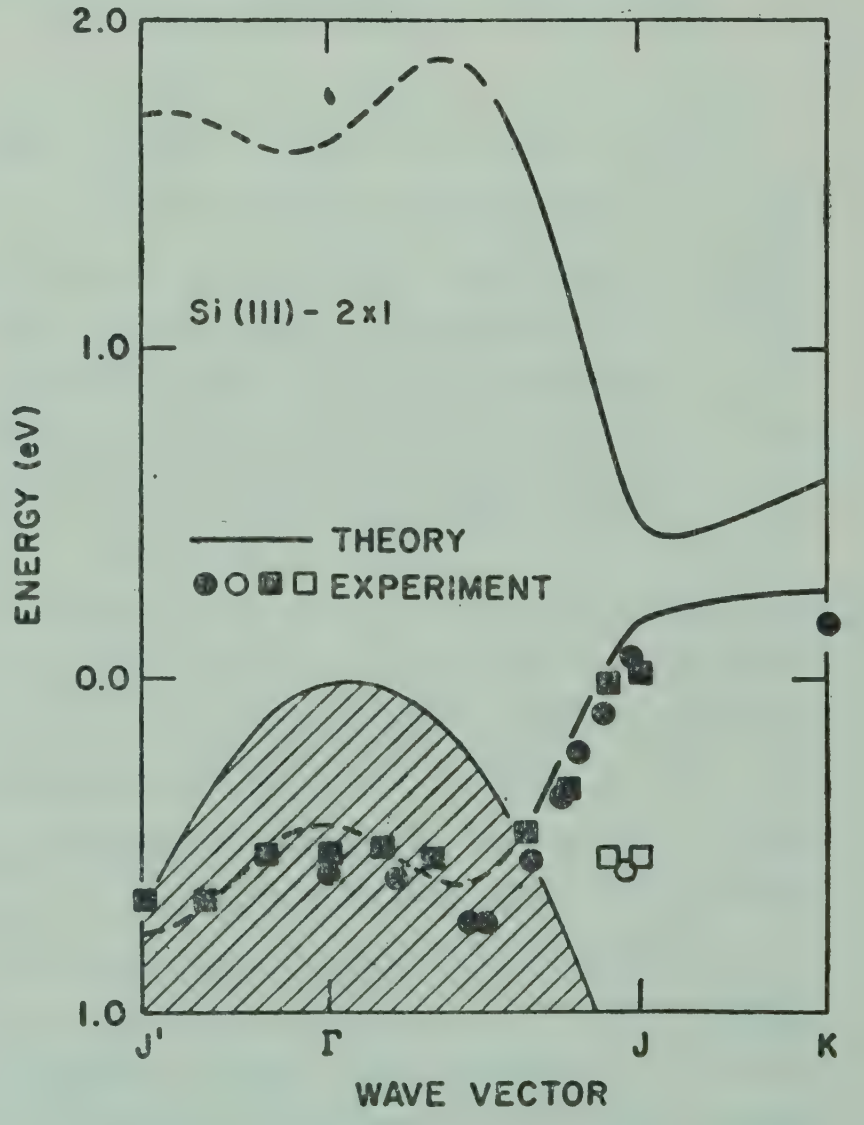

FIG. 7. Energy band dispersion for the π-bonded chain model compared with bands derived from photoemission measurements (Ref. 5).

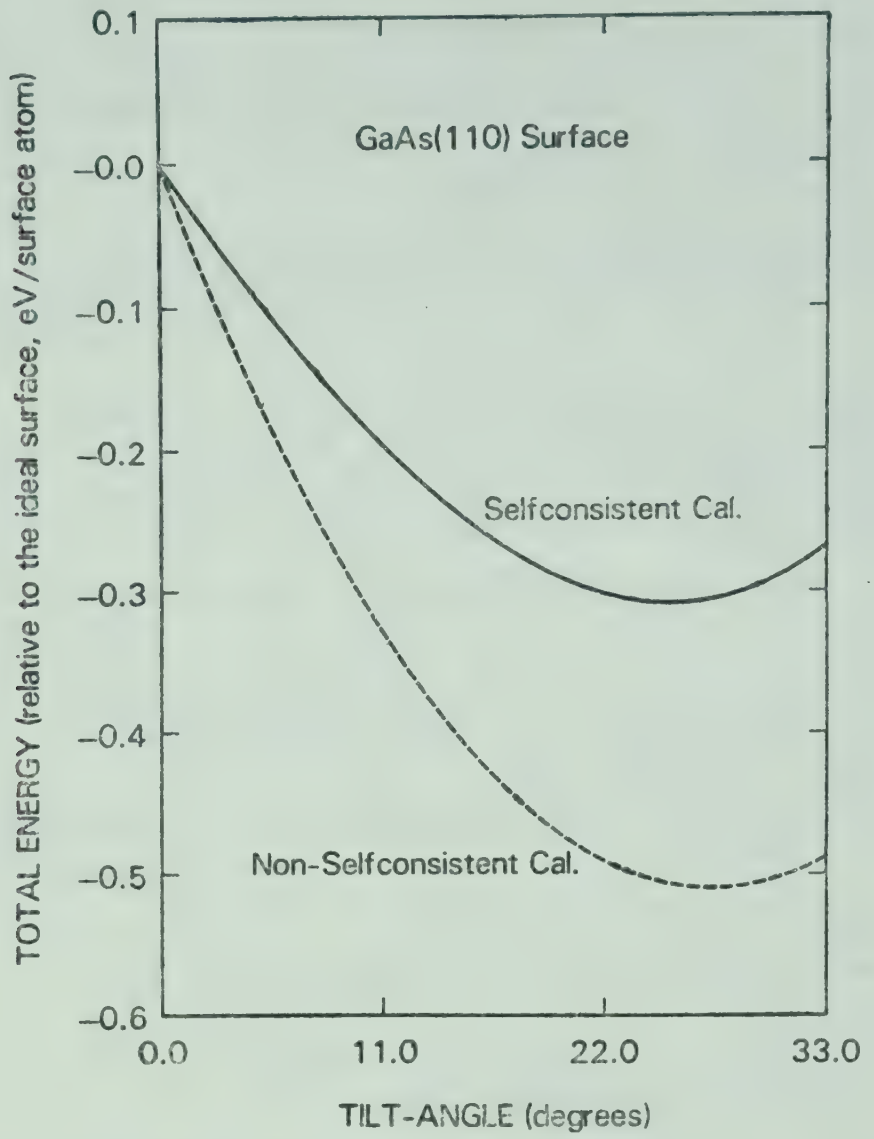

FIG. 8. Stabilization of the surface of a heteropolar semiconductor by buckling reconstruction.

a function of the degree of buckling. We see, in contrast to the homopolar system considered in Fig. 4, that both the present self-consistent and non-self-consistent calculations show an energy reduction, although the non-self-consistent analysis again overestimates the energy benefit by a large amount. Buckling is favourable on heteropolar semiconductors, because the bulk semiconductor is comprised of ions and the charge transfer associated with buckling provides a means by which the ions can be converted to neutral atoms at the surface.

CONCLUSIONS

We have shown by theoretical calculations and a critical evaluation of experimental data that buckling is not a valid reconstruction mechanism for homopolar surfaces such as the Si(111)-2 $\times$ 1 surface. We have that this is because the large intra-atomic Coulomb energy costs preclude charge transfers for homopolar surfaces. Heteropolar semiconductors, such as GaAs, are interestingly different in this regard because the bulk semiconductor is comprised of ions and the charge transfer associated with buckling provides a means by which the ions can be converted to neutral atoms at the surface. Our self-consistent calculations show that, for the surfaces of homopolar semiconductors, such as Si(111), the recently proposed π-bonded-chain reconstruction is much more effective in lowering the total energy of the surface. While the present study is confined to Si(111) and GaAs(110), we have studied the total-energy implications of a very large number of specific reconstruction models. The consistency of the results for all these models suggests that our important qualitative conclusions are quite general.

References

1. For a recent review see, e.g., e D E Eastman, *J. Vac. Sci. Technol.* **17** (1980) 492.
2. K C Pandey, *Phys. Rev. Lett.* **47** (1981) 1913.
3. K C Pandey, *Phys. Rev. Lett.* **49** (1982) 223.
4. J E Northrup and M L Cohen, *Phys. Rev. Lett.* **47** (1981) 1910.
5. F J Himpsel *et al.*, *Phys. Rev.* **B24** (1981) 2003; R I G Uhrberg *et al.*, *Phys. Rev. Lett.* **48** (1982) 1032.
6. R Matz *et al.*, *Solid State Comm.* **46** (1983) 343.
7. R M Tromp *et al.*, *Phys. Rev. Lett.* **51** (1983) 1672.
8. P Chiaradia *et al.*, *Phys. Rev. Lett.* **52** (1984) 1145; M A Olmstead and N M Amer, *Phys. Rev. Lett.* **52** (1984) 1148.
9. F J Himpsel *et al.*, *Phys. Rev.* **B30** (1984) 2257; R Feder and W Monch, *Solid State Comm.* **50** (1984) 311.
10. T F Heinz and M M Loy, *Phys. Rev. Lett.* (submitted).
11. J E Northrup and M L Cohen, *Phys. Rev. Lett.* **49** (1982) 1349.
12. D Haneman, *Phys. Rev.* **121** (1961) 1093.
13. F J Himpsel *et al.*, *Phys. Rev. Lett.* **45** (1980) 1112; S Brennan *et al.*, *Phys. Rev. Lett.* **45** (1980) 1414.
14. M Schluter *et al.*, *Phys. Rev.* **B12** (1975) 4200.
15. J R Chelikowsky and M L Cohen, *Phys. Rev.* **B20** (1979) 4150.
16. K C Pandey, unpublished.
17. M T Yin and M L Cohen, *Phys. Rev. Lett.* **45** (1980) 1004.
18. G B Bachelet *et al.*, *Phys. Rev.* **B24** (1981) 4745.
19. J Ihm *et al.*, *J. Phys.* **C. 12** (1979) 4409.
20. D J Chadi, *Phys. Rev. Lett.* **41** (1978) 1062.

© *Proc. Indian natn. Sci. Acad.*, **51**, A, No. 1, 1985, pp. 27–56.
Printed in India.

DYNAMICAL BEHAVIOUR OF ATOMIC MONOLAYERS ON SURFACES*

BAL K. AGRAWAL

Department of Physics, University of Allahabad, Allahabad–211 002

1. INTRODUCTION

UNIVERSAL energies known as dispersive energies which are attractive in nature exist between every pair of isolated atoms. They are responsible for the condensation of gas atoms into liquids of all elements. In addition to these dispersion energies, much larger energies such as valence energies are very often present. When an atom approaches the surface of a solid, it can become bound to the surface and the atom is said to be physically adsorbed. In case larger chemical energies are involved in the adsorption, the atom is said to be chemically adsorbed. It is difficult to have a sharp demarcation line between physisorbed and chemisorbed systems nevertheless adsorption involving energies lying below 10 kcal/mol is called physisorption and above it is named chemisorption. In the present lecture, we would study both the chemisorbed and physisorbed systems.

The study of the adsorbed surfaces is important primarily for two reasons. First, its technological applications in hetrogeneous catalysis, oxidation, crystal growth, corrosion, electroacoustic microelectronic devices etc. Second, man's desire to understand the fundamental principles of the behaviour of two dimensional (2–D) systems. In the field of hetrogeneous catalytic reactions, one faces the problem of understanding the nature of adsorbed atoms or molecules and reaction-intermediates. The energy transfer from atoms/molecules to phonons is fundamental to an understanding of accommodation coefficients, adsorption and desorption kinetics as well as the sticking coefficients. These are all important elementary steps in catalysis. We would study the well known W(001)H chemisorbed system in the present lecture.

Long wavelength Rayleigh waves at the clean or adsorbed surfaces find extensive applications in electroacoustic micro-electronic devices like delay lines and band pass filters because of their small damping, constant velocity and the accessibility provided by their surface localisation. In electronics industry, the thinness of the integrated circuits and the various steps in the device fabrication involve several physical and chemical processes occurring on the surfaces and interfaces.

Atomic or molecular films physisorbed on uniform solid surfaces form well-defined monolayers[1]. Many efforts have been made to understand the types of phase transitions taking place in these films, the nature of the phase involved, and the possible relationship between weakly bound surface monolayers and the idealized two-dimensional (2D) systems of the theory. The adsorbed atoms or molecules can exist in a variety of thermodynamic phases, in particular, in the submonolayer region, 2D gas, liquid, and solid phases may be either commensurate or incommensurate with the substrate surface. In a commensurate phase, one notes the lattice parameter

*Paper presented at the Symposium on Physics and Chemistry of Surfaces held at INSA, New Delhi from September 28-30, 1984.

of the 2D physisorbed layer as a multiple or submultiple of that of a normal plane of the substrate in bulk.

Near the surface one may observe relaxation bigger than in the bulk and the distance between an adsorbed monolayer and the substrate might increase with temperature. The two-dimensional order inside the monolayer may then overcome the three-dimensional order imposed by the substrate. This may enable a phonon to become soft at a certain temperature leading to reconstruction or superstructures. In the present lecture, we would look into the possibility of the occurrence of soft phonons in some systems, such as rare gas monolayers on different rare gas solids and on graphite.

Over the past few years, a number of experimental techniques with good resolution and surface sensitivity have been evolved for the study of the phonons of adsorbed layers. To name a few are, electron energy loss spectroscopy (EELS), inelastic electron tunneling spectroscopy (IETS), atom or molecular beam scattering, neutron scattering, reflection absorption infrared spectroscopy (IRAS) and surface enhanced Raman scattering etc. For a datailed discussion of these techniques, their merits and demerits, we refer the reader to recent review articles[2].

Adsorbed atoms modify many vibrational properties of surfaces and create new ones[3]. The adsorption entropies can be obtained by measuring the desorption rate of the adsorbed particles as a function of temperature or by analyzing the adsorption isotherms determined by Auger spectroscopy. The mean square displacements of adsorbed atoms can be measured in L.E.E.D. and Mössbauer experiments. The low temperature specific heat, the phonon free energies, the local phonon density of states are also modified by adsorption. The elastic and phonon contributions to the free energy of interacting adatom pairs are also of interest. The localized and resonant modes of vibration due to adsorption in the acoustical as well as in the optical region may also appear.

Our aim here is not to review and discuss all these properties but to focus on adsorbate induced phonons.

We first review the theoretical works done on this subject and discuss the main physical effects. Then we illustrate this lecture by going in more details through the theoretical studies of the systems, W(001) H, Ni(111) O and the acoustic phonons of rare monolayers on rare gas solids and on graphite, comparing them with the experimental results whenever available. The choice of these examples is somewhat arbitrary and due only to the fact that the author has worked on them.

2. A Short Review

The existence of adsorbate induced optical phonons was first shown on two-dimensional lattice models. Kaplan[4] and Hori *et al.*[5] put a row of isotopic impurities along one of the free edges of a two-dimensional lattice. They found that for the same wavevector, surface modes of frequencies higher than the bulk modes may appear. Adsorbate induced optical phonons on three dimensional crystals were studied by Dobrzynski *et al.*[5]. Rare gas monolayers on another rare gas b.c.c.

crystals were investigated by Alldredge *et al.*[7] and by Castiel *et al.*[8] The effect of relaxation of the monolayer from the substrate was also accounted for by Lawrence *et al.*[9] and more recently by Agrawal *et al.*[10] in an anharmonic theory.

Realistic systems have been investigated by several workers such as S and O on Ni(001) and (111) surfaces by Agrawal *et al.*[11] and by Bortolani *et al.*[12], H on W(001) by Bullet and Cohen[13] and by Agrawal[14]. Rare gas monolayers on graphite have recently been investigated by Agrawal[15] and deWette *et al*[16].

Lattice dynamical models deduced from the surface electronic band structure have been discussed by Bullet and Cohen[13] and by Allan and Lopez[17].

3. General Theory

The usual elastic theory is valid upto the angular frequencies of $\sim 10^{11}$ sec^{-1} and this limit is well above the frequencies of surface waves used in devices of technological interest. On the other hand, the phonon frequencies determining most of the other physical properties such as thermodynamic, response functions, atom-surface interactions etc. are typically of $\sim 10^{13}$ sec^{-1} and can be treated only by a lattice dynamical approach. Also, near a crystal surface clean or adsorbed, there may occur local relaxation of atoms and sometimes a reconstruction i.e., a surface structure which is different from that of bulk leading to altered values even for the bulk properties like elastic constants and density etc.

For a non-Bravais crystal lattice containing more than one atom in the unit cell, one may define the positions of the atoms, by the lattice vectors,

$$\vec{R}(l\kappa) = \vec{R}(l) + \vec{R}(\kappa),$$

with $$\vec{R}(l) = l_1\vec{a}_1 + l_2\vec{a}_2 + l_3\vec{a}_3,$$

and $$(l_1, l_2, l_3) = -\frac{L}{2}, \ldots, +\frac{L}{2}. \qquad \ldots(3.1)$$

Here the integer set (l_1, l_2, l_3) describes the positions of the unit cells in the lattice having $\vec{a}_j$ $(j = 1, 3)$ as the basis vectors and $\vec{R}(\kappa)$ denotes the positions of the atom of kind κ in the unit cell containing 's' atoms ($s = 1, 2, \ldots$). The number of unit cells in the crystal is L^3.

Choosing the basis vectors $(\vec{a}_1, \vec{a}_2)$ lying in the crystal surface and $\vec{a}_3$ pointing outside the surface (not necessarily normal to surface), we can write

$$\vec{R}(l\kappa) = \vec{R}(\bar{l}) + \vec{R}(l_3\kappa),$$

with $$\vec{R}(\bar{l}) = l_1\vec{a}_1 + l_2\vec{a}_2,\ \bar{l} \equiv (l_1, l_2), \qquad \ldots(3.2)$$

as the two-dimensional lattice vectors lying in the surface; the symbol l_3 now describes the various atomic layers parallel to the surface.

In adiabatic approximation, the atomic vibrations in the crystal can be analyzed by expanding the potential energy in powers of the atomic displacements from their equilibrium positions as

$$\Phi = \Phi_0 + \sum_{l,\kappa,\alpha} \Phi_\alpha(l\kappa)\, u_\alpha(l\kappa) + \frac{1}{2} \sum_{l\kappa\alpha} \sum_{l'\kappa'\beta} \Phi_{\alpha\beta}(l\kappa, l'\kappa')\, u_\alpha(l\kappa)\, u_\beta(l'\kappa') + \ldots\ldots + \frac{1}{6} \Sigma\Sigma\Sigma\, \Phi_{\alpha\beta\gamma}(l\kappa, l'\kappa', l''\kappa'')\, u_\alpha(l\kappa)\, u_\beta(l'\kappa')\, u_\gamma(l''\kappa'') + \ldots \quad \ldots(3.3)$$

The harmonic force constants are given by

$$\Phi_{\alpha\beta}(l\kappa, l'\kappa') = \left| \frac{\partial^2 \Phi}{\partial u_\alpha(l\kappa)\, \partial u_\beta(l'\kappa')} \right| \text{equi.} \quad \ldots(3.4)$$

The derivatives are to be evaluated in equilibrium conditions. The higher derivatives determine the anharmonic higher order force constants to be discussed later.

The equilibrium sites of the atoms are determined by the vanishing of the forces i.e., the first derivatives,

$$\Phi_\alpha(l\kappa) = \left| \frac{\partial \Phi}{\partial R_\alpha(l\kappa)} \right|_{\vec{R}(l\kappa) = \vec{R}^\circ(l\kappa)}, \quad \ldots(3.5)$$

where $\vec{R}^\circ(l\kappa)$' s are the equilibrium atomic position vectors. These equilibrium atomic positions would, in general, be different from those what they would have been in the bulk as a result of the relaxation or contraction of the atomic planes near the surface.

The various force constants obey the translational and rotational invariance conditions arising from the fact that the crystal potential energy should remain unchanged under arbitrary rigid-body translation or rotation of the lattice.

The equations of motion for a harmonic lattice read

$$M_\kappa(l_3) \frac{d^2}{dt^2} u_\alpha(\bar{l}, l_3\kappa) = - \sum_{l'\kappa'} \sum_{l_3'\beta} \Phi_{\alpha\beta}(\bar{l} - \bar{l}';\ l_3\kappa,\ l_3'\kappa') \times u_\beta\left(\bar{l}',\ l_3'\kappa'\right), \quad \ldots(3.6)$$

where $M_\kappa(l_3)$ denotes the mass of the atom 'κ' in the layer l_3.

As the periodicity is retained in the surface, one may seek plane wave solutions which travel along the surface as

$$\vec{u}\left[\vec{R}(\bar{l}),\ l_3\kappa\right] = \frac{1}{\sqrt{M_\kappa(l_3)}}\, \vec{e}(l_3\kappa|\vec{k}_\parallel) \exp i[\vec{k}_\parallel \cdot \vec{R}(\bar{l}) - \omega t], \quad \ldots(3.7)$$

where $\vec{e}(l_3\kappa|\vec{k}_\parallel)$ are the eigenvectors of the wave of frequency ω at atom κ lying in the atomic layer l_3 corresponding to the plane wavevector $\vec{k}_\parallel$.

One then obtains the secular equation as

$$\sum_{l'_3\kappa'\beta} D_{\alpha\beta}\left(l_3\kappa,\, l_3^1\,\kappa';\ \vec{k}_\parallel\right) e_\beta\left(l'_3\,\kappa'|\vec{k}_\parallel i\right)$$

$$= \omega_i^2\,(k_\parallel)\, e_\alpha(l_3\kappa|\vec{k}_\parallel^{\,i}), \qquad \ldots(3.8)$$

where the Fourier transformed Dynamical matrix is given by

$$D_{\alpha\beta}(l_3\kappa.l_3'\kappa';\kappa\vec{k}_{\parallel i}) = \frac{1}{\sqrt{M_\kappa(l_3)\, M_{\kappa'}(l_3')}} \sum_{\bar{l}'} \Phi_{\alpha\beta}(\bar{l} - \bar{l}';\ l_3\kappa,\, l_3'\kappa')$$

$$\times \exp i\vec{k}_\parallel:\{(\vec{R}\,(\bar{l}) - \vec{R}(\bar{l}')\} \qquad \ldots(3.9)$$

The index i labels the various eigenfrequencies whose total number for a fixed value of $\vec{k}_\parallel$ is $3s\ N_L$ with N_L as the number of the atomic planes in the slab. The spatial behaviour of the surface modes of wave vector $\vec{k}_\parallel$ is described by the values of the eigenvectors $\vec{e}(l_3\kappa|\vec{k}_\parallel)$ in the sublayers as one moves away from the surface into the bulk.

Direct Method

In the direct method, a slab containing a finite number of atomic layers (N_L) is chosen and Eq. (3.8) is solved on a high speed computer for a larger number of the wavevectors $\vec{k}_\parallel$. In order to keep the computation manageble, one consider, only a small number of layers (say $N_L \sim 15 - 20$). However, for gathering precise quantitative information on the vibrations of a semi-infinite lattice from the slab calculation one should consider a large value of N_L which is not practicable at present. This difficulty does not arise in Green's function method.

Green's Function Method

In Green's function method one describes a free surface/monolayer as a two-dimensional defect which induces perturbation in the behaviour of an infinite like three-dimensional crystal using cyclic boundary conditions. Free surfaces are created by cutting the infinite crystal along a plane and setting all the interatomic forces on the vacuum side to be zero.

The planar dynamical matrix $\underset{\approx}{D}$ for a crystal containing a surface may then be written as

$$\underset{\approx}{D} = \underset{\approx}{D}^\circ + \underset{\approx}{P}, \qquad \ldots(3.10)$$

where $\underset{\approx}{D}^{\circ}$ is planar dynamical matrix for the perfect three-dimensional lattice and $\underset{\approx}{P}$ is the perturbation matrix.

Eq. (3.8), then, reads as

$$(\underset{\approx}{D}^{\circ} + \underset{\approx}{P} - \omega^2 \underset{\approx}{I})\vec{e} = 0. \qquad \ldots(3.11)$$

One defines an unperturbed planar Green's function $\underset{\approx}{G}^{\circ}$ by the inverse matrix,

$$\underset{\approx}{G}(z) = (\underset{\approx}{D}^{0} - z\underset{\approx}{I})^{-1}, \qquad \ldots(3.12)$$

where $z = \omega^2 + i\delta$ which is the complex squared frequency in the limit $\delta \to 0$, takes care of the singular behaviour of the inverse matrix $\underset{\approx}{G}^{\circ}(\omega^2)$.

Eq. (3.11) can be written as

$$(\underset{\approx}{I} + \underset{\approx}{G}^{\circ}(z)\underset{\approx}{P})\vec{e} = \vec{0}. \qquad \ldots(3.13)$$

The surface wave solutions are obtained by the secular determinant,

$$|\underset{\approx}{I} + \underset{\approx}{G}^{\circ}(z)\underset{\approx}{P}| = \underset{\approx}{0}. \qquad \ldots(3.14)$$

Also, the perturbed Green's function,

$$G(z) = (D - zI)^{-1} \qquad \ldots(3.15)$$

is given by

$$\underset{\approx}{G} = (\underset{\approx}{I} + \underset{\approx}{G}^{\circ}\underset{\approx}{P})^{-1}\underset{\approx}{G}^{\circ}. \qquad \ldots(3.16)$$

Knowing $\underset{\approx}{G}$, one can determine the density of states and the various lattice response functions required for understanding the physical properties such as infrared absorption, Raman scattering, inelastic atom or neutron scattering, lattic specific heat, entropy etc.

4. Some General Results

We now discuss the main qualitative effects displayed in all the studied adsorbed systems.

Along some symmetry directions of the Brillouin zone, the eigenvectors are perfectly polarised either in the sagittal plane (the plane containing the direction of wave propagation and the normal to the surface) or perpendicular to the sagittal plane. The former modes are called longitudinal waves. The latter ones called transverse waves have atomic displacements lying in the surface but normal to $\vec{k}_{\parallel}$.

Adsorbed atoms lighter than the substrate atoms increase the frequencies of the surface modes and new modes may also appear above the bulk phonon bands for a given value of the propagation vector $\vec{k}_{\parallel}$.

An increase in the surface force constant has an effects similar to a light monolayer. Such increase in the force constants can, in particular, exist when the distances between the surface and the adsorbed atoms are contracted as has been seen in some real systems such as α-Fe(001), Ni(111) etc.

A. *Unreconstructed monolayer*

Consider first the case where the surface has no super-structure and examine the vibrational spectrum of the semi-infinite crystal with an adsorbed layer having the same symmetry as the (001) surface. The dispersion curves are shown in Fig. 1 for modes with wave vector $\vec{k}_{\parallel}$ directed along the y direction, $k_x = 0$. For each value of k_y, one has a range of frequencies associated with bulk vibrations (shaded areas). The width of these bulk bands for each value of k_y is due to the fact that for each value of $k_{\parallel}$, one has several values of $\omega(\vec{k}_{\parallel}, k_z)$ as a function of k_z which is still a good quantum number for bulk bands.

The low frequency modes called Rayleigh modes modified by the adsorbed atoms are represented by curve (1).

There may appear 'window gaps' within the sub-bands corresponding to acoustic bulk modes depicted as region (2) in Fig. 1. High frequency localised modes can be and usually are present within these gaps.

It is possible for surface modes to exist even within some bulk sub-bands. For example, the curve (2) is due to a localized mode polarized along the axis orthogonal to the propagation vector k_y and the normal z to the surface. This

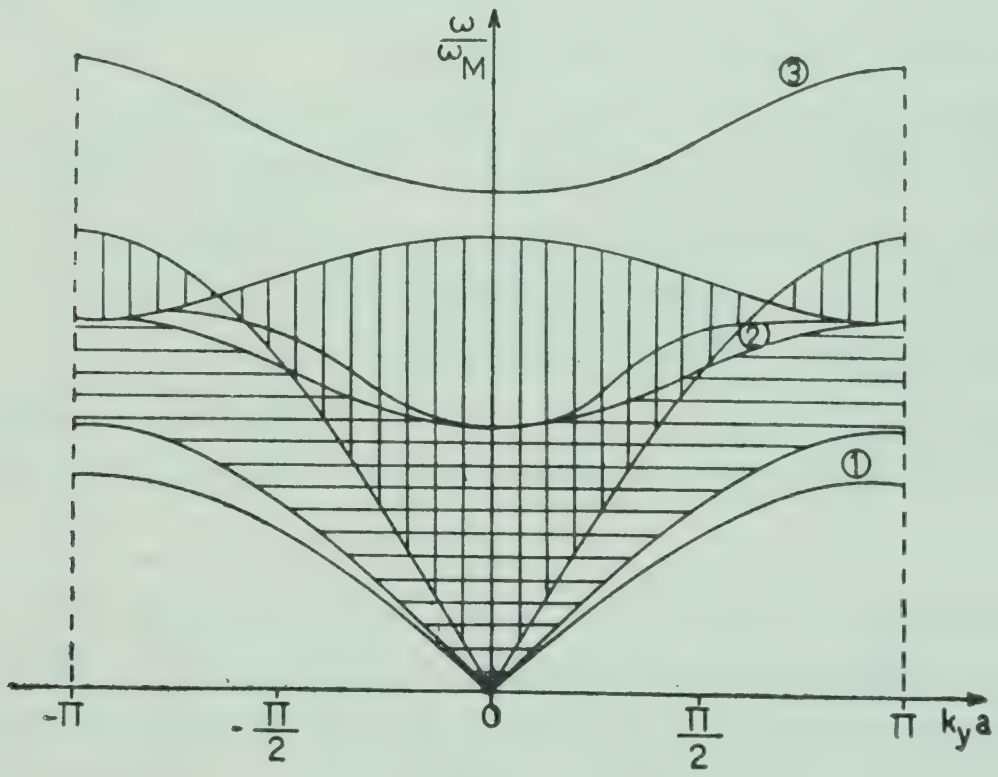

FIG. 1. Different types of surface waves due to adsorption of a monolayer in registry with the substrate. The shaded area give the bulk bands. Curve (1) represents the Rayleigh waves modified by adsorption. Curve (2) corresponds to localized waves falling partly into a window gap and partly into a bulk band where the atom displacements are orthogonal to those of this mode. Curve (3) shows an optical phonon branch situated above the bulk bands.

curve falls partly in a window gap and partly for smaller value of k_y within the bulk sub-band (vertically shaded area) corresponding to phonons polarized within the (y z) plane. Therefore these surface modes can remain decoupled from the bulk phonons having the same frequencies.

Finally, the optical surface phonon modes lying above the bulk phonon bands are shown by the dispersion curve (3) in Fig. 1.

Let us mention also that one can have localized surface phonos in one part of the two-dimensional Brillouin zone. Usually such a branch of localized modes can be prolongated by a branch of resonances, which may correspond to a sharp feature in the local phonon density of states. In particular, adsorption may cause that one part of a surface phonon branch falls in the bulk continuum or inversely that localized modes peel off the bulk bands only in a part of the two-dimensional surface Brillouin zone.

B. *Superstructures*

In a number of cases, the positions of the atoms in the surface region can be different from those one would see in the bulk structure. Evidence comes from the appearance of 'extra' spots in the LEED patterns originating from the reconstructed cell which is enlarged compared to the unreconstructed unit cell in one and/or two axial directions. To name a few examples are the $W(001)$ or $M_0(001)$ surfaces, both clean or H-covered where one observes (2×2) superstructures.

For metal surfaces, recent electronic structure calculations suggest that the driving mechanism for the displacive transition is either a Fermi surface instability leading to a charge density wave[18,19] or an intrinsic atomic instability with wave vector determined by the Fermi surface structure[20].

Another mechanism is based on the fact that interactions between surface induced dynamic effective charges present on the atoms can cause the surface region to become unstable via a soft surface phonon and the surface may then reconstruct. We would investigate the appearance of soft phonon having its origin in the relaxation of the surface layer or adsorbed monolayer.

One finds that a superstructure has two main qualitative effects on the properties of the localized phonons. These effects are illustrated in a schematic fashion in Figs. 1 and 2.

Now suppose the adsorbed monolayer has a superstructure, in such a manner that the new repeat distance parallel to the y axis assumes a value twice that appropriate to the (001) surface of the substrate. We can plot the normal mode spectrum in this case as indicated in Fig. 2.

The effect of the superstructure is to introduce new zone boundaries at $k_y = \pm\pi/2a$, respectively where a is the lattic parameter. The region $-\pi/2a < k_y < \pi/2a$ is now the first Brillouin zone and the two regions $\pi/2a < k_y < \pi/a$, and $-\pi/a < k_y < -\pi/2a$ correspond to the second Brillouin zone. Gaps in the surface mode dispersion relation open up at the zone boundaries, as indicated on

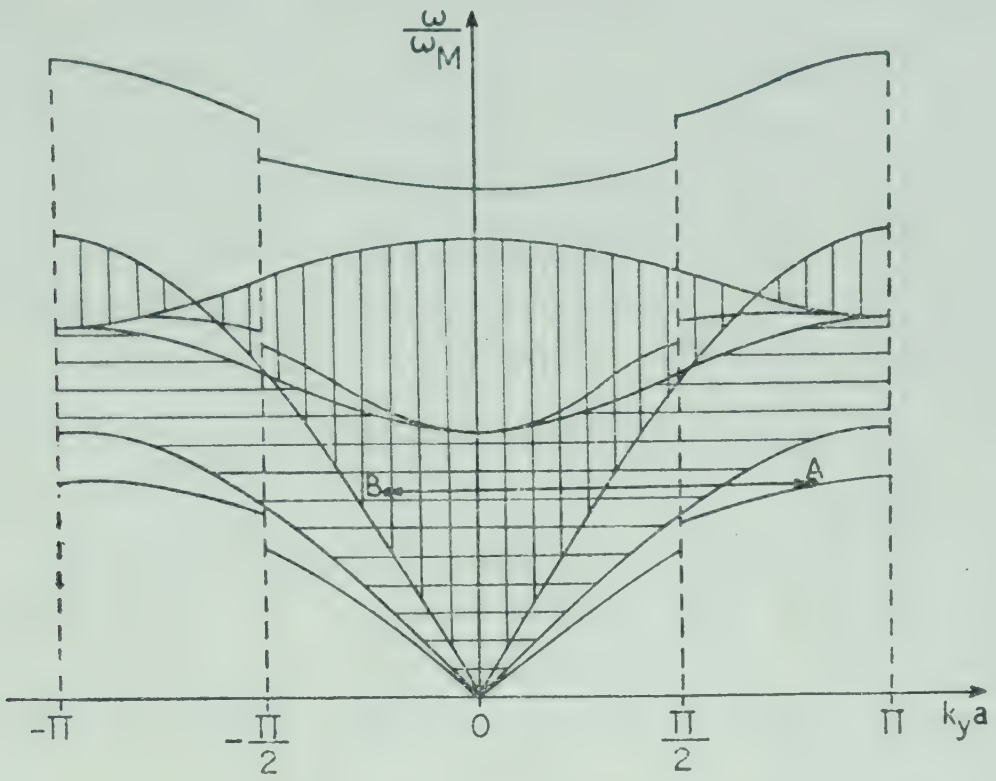

FIG. 2. Effect of a (1 × 2) superstructure in the adsorbed monolayer on the surface phonons given on Fig. 1.

Fig. 2. If the surface phonon dispersion relations are plotted in the reduced zone ($-\pi/2a < k_y < \pi/2a$), there are now twice as many distinct surface branches (six in this example).

The surface modes, which were at $k_y = \pi/a$ for the unreconstructed layer, are now at $k_\parallel = 0$ and can be detected by the usual spectroscopic experiments. In particular, the acoustic surface mode at $k_y = \pi/a$ is now detectable by the high frequency spectroscopic methods[17].

There is one other effect that is quite striking. Consider the surface made at point A in Fig. 2. This mode is well localized for the monolayer having the same symmetry as the surface. When the monolayer has its (1 × 2) superstructure, the resulting perturbation term in the dynamical matrix mixes this surface phonon A with the bulk phonon B displaced in $\vec{k}$ from A by the reciprocal lattice vector $\vec{G} = -\hat{y}\pi/a$. As a result of this admixture the mode A is no longer a true localized mode, but becomes a virtual state (also called resonance) since the displacement field is no longer localized at the surface. We will now illustrate this general discussion on some specific examples for which experimental results are available.

5. W(001) H

The (001) tungsten surface, clean or covered with hydrogen is a very good example of chemisorption and has been the subject of numerous experimental and theoretical investigations[21]. The desorption activation energy is ~30 kcal/mol. Very recently, LEED[22,23], EELS[24,25], high energy ion scattering (HEIS)[26] measurements, infrared surface-electromagnetic wave (SEW) spectroscopy[27], etc., have been reported in the literature. The clean $W(001)$ surface is unstable below 300°K and it reconstructs into a $c(2 \times 2)$ superstructure. This phase trasition is temperature-dependent and reversible. However, the $c(2 \times 2)$ superstructure can

be stabilised above 300°K by chemisorption of hydrogen. One finds a distinct LEED pattern corresponding to a $c(2 \times 2)$ super-structure at an adatom density of 2.5×10^{14} H cm^{-2}, namely β_2-phase. Further, increased coverage of H drives the $c(2 \times 2)$ super-structure back to the normal $p(1 \times 1)$ surface lattice similar to $a(001)$ plane in the bulk W. A distinct LEED pattern corresponding to the $p(1 \times 1)$ H lattice develops fully for a saturation coverage of H corresponding to a monolayer coverage of the β_1-phase, 17×10^{14} H cm^{-2}.

Keeping in view the existing C_{2v}-point group symmetry of the bridge sites of H atoms at all coverages and also the LEED spots intensity, mainly three models have been proposed for the $c(2 \times 2)$ superstructure: (i) Debe and King's model[23], (ii) Puckered layer model and (iii) Barker and Estrup's model[22]. The HEIS measurements reveal that only 50% surface atoms are displaced by about $\sim$ 0.2 Å in the reconstructed surface. A similar estimate of about 0.15 — 0.30 Å has been made in LEED experiments.

A model for the $c(2 \times 2)$ H structure for low coverage of H is still open and the mechanism driving the phase transition seems to remain unclear. We analyse the results of electron energy loss measurements on the basis of different models of the $c(2 \times 2)$ super-structure in a bid to extract information about the nature and strength of the interaction between the adatoms themselves, and the interaction between the H and W atoms lying on or below the surface. We employ[10] a lattice dynamical model which includes the $H - W$ central interactions up to third neighbours and angular interactions up to first second neighbours.

We study the unreconstructed $p(1 \times 1)$ H surface in Section 5*A* and the three structural models in Section 5*B* and include the conclusions in Section 5*C*.

A. Unreconstructed p (1 × 1) *W(001) H surface*

We refer to Fig. 3 for the geometry of the unreconstruted $W(001)$ surface with H-atoms.

In the saturated coverage, i.e. in β_1-phase, we have two H-atoms per square planar unit cell of lattice parameter 'a'. We assume three central pair potentials

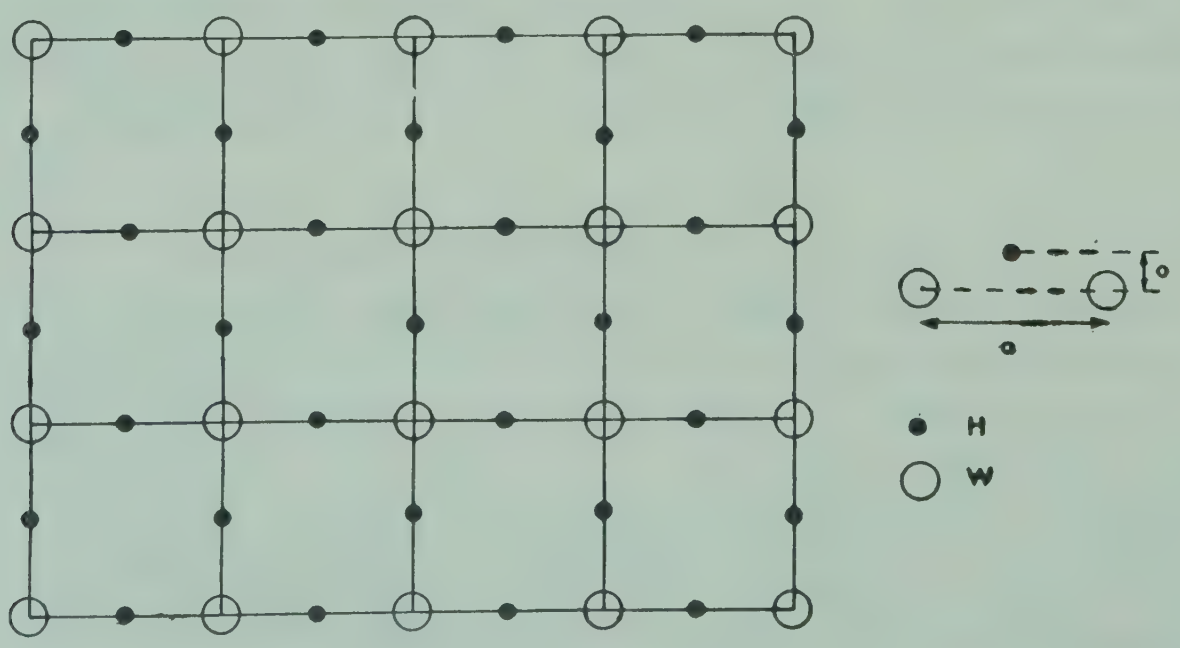

FIG. 3. Positions of atoms in the H monolayer and the unreconstructed $W(001)$ surface.

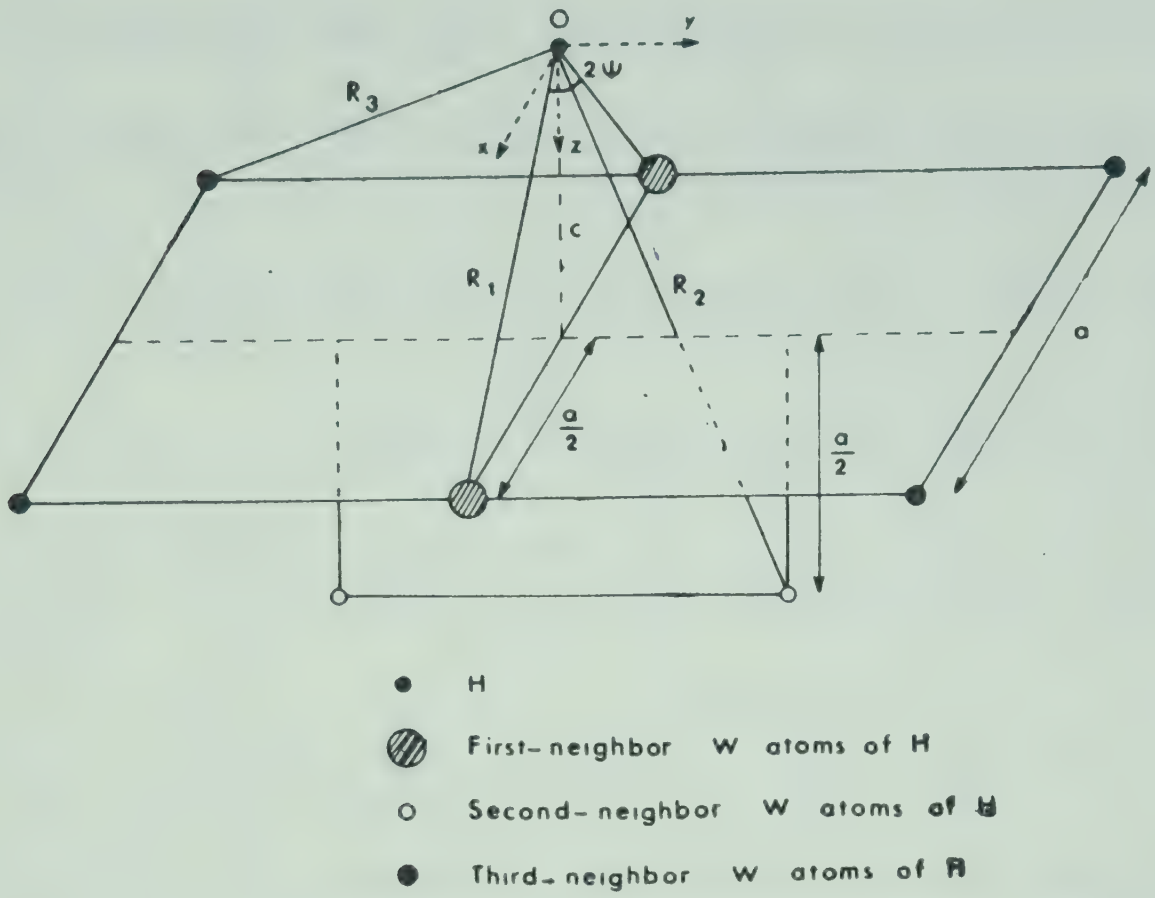

FIG. 4. First, second and third neighbouring *W*-atoms of a *H*-atom on the unreconstructed *W*(001) surface.

(Φ_1, Φ_2, Φ_3) between a *H*-atom and its first, second and third nearest neighbours. For the angular interactions, we assume an angular force constant γ for the $W - H - W$ angle, and another γ' for the two $H - W - W$ angles. Let 2ψ be the $W - H - W$ angle. For the adatom-adatom interactions, i.e. $H - H$ interactions, we assume a single central force constant β.

As the *H*-atom is much lighter ($\sim 1/180$) compared to the *W*-atom, its frequencies lie much above the *W*-bulk phonon bands and one may safely work in the frozen substrate approximation, i.e. all the *W*-atoms are fixed.

In a set of axes where the *x*-axis lies along the $W - W$ line, the *y*-axis normal to it, and the *z*-axis points downwards normal to the surface (see Fig. 4), the three Fourier-transformed equations of motion for a *H*-atom of mass *m* can be written as

$$(-m\omega^2 + 4\beta + K_x)\, e_x(1) = 4\beta \cos k_x \frac{a}{2} k_y \cos \frac{a}{2}\, e_x(2)$$

$$- 4\beta \sin k_x \frac{a}{2} \sin k_y \frac{a}{2}\, e_y\,(2), \qquad \ldots(5.1)$$

$$(-m\omega^2 + 4\beta + K_y)\, e_y(1) = -4\beta \sin k_x \frac{a}{2} \sin k_y \frac{a}{2}\, e_x(2)$$

$$+ 4\beta \cos k_x \frac{a}{2} \cos k_y \frac{a}{2}\, e_y(2), \qquad \ldots(5.2)$$

$$\text{and } (-m\omega^2 + K_z)\, e_z(1) = 0. \qquad \ldots(5.3)$$

Here $\vec{e}(1)$ and $\vec{e}(2)$ denote the eigenvectors of the two H-atoms of a planar unit cell; ω is the phonon frequency corresponding to the wave vector $\vec{k}(k_x, k_y, k_z)$ and the three diagonal force constants are given by

$$K_x = \frac{1}{2}\left(\frac{a}{R_1}\right)^2 \Phi''(R_1) + \frac{1}{4}\left(\frac{a}{R_3}\right)^2 \Phi''(R_3) + 2\left(\frac{c}{R_1}\right)^2 \gamma',$$

$$K_y = \frac{1}{2}\left(\frac{a}{R_2}\right)^2 \Phi''(R_2) + 4\left(\frac{a}{R_3}\right)^2 \Phi''(R_3),$$

$$K_z = 2\left(\frac{c}{R_1}\right)^2 \Phi''(R_1) + \frac{1}{2}\left(\frac{a}{R_1}\right)^2 (2\gamma + \gamma') + 2\left\{\frac{\left(c + \frac{a}{2}\right)}{R_2}\right\}^2 \Phi''(R_2) + 4\left(\frac{c}{R_3}\right)^2 \Phi''(R_3), \quad \ldots(5.4)$$

where $\Phi''(R)$'s are the second derivatives of the three pair potentials for the first, second and third W-atom neighbours of a H-atom. R_1, R_2 and R_3 denote the distances of the neighbours explicitly given by

$$R_1 = \left(c^2 + \frac{a^2}{4}\right)^{1/2}; \; R_2 = \left|\left(c + \frac{a}{2}\right)^2 + \frac{a^2}{4}\right|^{1/2}$$

and $$R_3 = \left(c^2 + \frac{5a^2}{4}\right)^{1/2}, \quad \ldots(5.5)$$

with c as the monolayer-substrate surface separation.

The frequency of the non-dispersive mode having displacements perpendicular to the surface is given by (Eq. 5.3)

$$m\omega_z^2 = K_z. \quad \ldots(5.6)$$

Equations similar to (5.1) and (5.2) can easily be written down for the second H-atom ($x = 2$) of the unit cell by interchanging the values of $x(= 1, 2)$ and also of $\alpha(= x, y)$ in the eigen-vectors $e_\alpha(x = 1, 2)$ and further, the x and y indices in the wave vector components k_α and in the parameters K_α.

The frequencies of the modes polarized parallel to the surface can then be obtained and are given by

$$m\omega_{1,2}^2 = \frac{1}{2}(K_x + K_y) + 4\beta\left(1 - \sin k_x \frac{a}{2} \sin k_y \frac{a}{2}\right) \pm \frac{1}{2}\left|(K_x - K_y)^2 + 64\beta^2 \cos k_x \frac{a}{2} \cos k_y \frac{a}{2}\right|^{1/2}, \quad \ldots(5.7a)$$

$$m\omega_{3,4}^2 = \frac{1}{2}(K_x + K_y) + 4\beta\left(1 + \sin k_x \frac{a}{2} \sin k_y \frac{a}{2}\right) \pm \frac{1}{2}\left|(K_x - K_y)^2 + 64\beta^2 \cos k_x \frac{a}{2} \cos k_y \frac{a}{2}\right|^{1/2}, \quad \ldots(5.7b)$$

where $-\frac{\pi}{a} < k_x < \frac{\pi}{a}$ and $-\frac{\pi}{a} < k_y < \frac{\pi}{a}$.

At the symmetry point $\Gamma(k_x = 0;\ k_y = 0)$, we have the following two doubly-degenerate different frequencies.

$$m\omega_{1,4}^2 = m\omega_{3,4}^2 = \frac{1}{2}(K_x + K_y) + 4\beta \pm \frac{1}{2}\left|(K_x - K_y)^2 + 64\beta^2\right|^{1/2} \quad \ldots(5.8)$$

At the symmetry point $\bar{X}(k_x = \frac{\pi}{a},\ k_y = 0)$, again, one has two doubly-degenerate different frequencies given by

$$m\omega_1^2 = m\omega_3^2 = K_x + 4\beta, \quad \ldots(5.9a)$$

and

$$m\omega_2^2 = m\omega_4^2 = K_y + 4\beta. \quad \ldots(5.9b)$$

One observes a lifting of the degeneracy at the symmetry point $M\left(k_x = k_y = \frac{\pi}{a}\right)$ where the four different frequencies are given by

$$m\omega_1^2 = K_x;\ m\omega_2^2 = K_y,$$

$$m\omega_3^2 = K_x + 8\beta;\ m\omega_4^2 = K_y + 8\beta. \quad \ldots(5.10)$$

It may be noted that the dispersion in all the H-modes is only due to the $H - H$ interactions β. The increments in frequencies at $\bar{X}$ over those of Γ point are

$$\Delta\left(m\omega_1^2\right) = \Delta\left(m\omega_3^2\right) = -\Delta\left(m\omega_2^2\right) = -\Delta\left(m\omega_4^2\right)$$

with

$$\Delta\left(m\omega_1^2\right) = \frac{1}{2}(K_x - K_y) - \frac{1}{2}\left|(K_x - K_y)^2 + 64\beta^2\right|^{1/2}, \quad \ldots(5.11)$$

Thus, the dispersion in the planer vibrations along the Δ-axis, i.e., line joining Γ and $\bar{X}$ points, have opposite curvatures. However, this behaviour has not been detected in experiment because of the small observed widths ($\sim$ 5 meV) of the H-atom phonon bands. One may infer that the adatom-adatom interaction is quite weak and we take $\beta = 0$ in our later calculations.

For an estimation of the monolayer substrate surface separation c, we neglect the angular force constants ($\gamma = \gamma' = 0$) and work in a nearest-neighbour approximation. The two frequencies ω_x and ω_z corresponding to the parallel and perpendicular polarizations of the modes lying in the plane of the molecule $W - H - W$ give

$$\frac{\omega_z^2}{\omega_x^2} = \frac{K_z}{K_x} = \frac{4c^2}{a^2} = \cot^2 \psi. \qquad \ldots(5.12)$$

By employing the two high experimental frequencies 160 meV and 130 meV for ω_x and ω_z, respectively, we find $\psi = 51°$ and for a lattice parameter $a = 3.16$Å, one obtains $c = 1.28$ Å and $R_1 = 2.03$ Å.

We use these values of c and R_1 in our future calculations.

We now extend the calculation to third neighbours and determine the values of the three derivatives $\Phi''(R_i)$, $i = 1, 2, 3$, by using the three experimental frequencies 80, 160 and 130 meV. The results have been shown in the first row of Table I.

We have also estimated the angular force constant and find that the role of the second derivative for the second neighbours, $\Phi''(R_2)$, and that of the angular force constant are analogous. Both of them have comparatively quite small negative values and may safely be neglected.

B. Reconstructed W(001) c(2 × 2) H surface

As the surface atoms move one may expect a change in the bond lengths between H and its W neighbours and also a change in c, A recent analysis[28] of infrared data for metal-hydrogen bond ($M - H$) stretching frequencies in metal hydride complexes has seen a relaxation in the bond length (5 ~ 10 per cent) with decreasing bond angle. We have, therefore, allowed the bond lengths to relax and estimate a new value of bond angle of 39° at H-atom and also of c'. It is assumed that the W-atoms undergo a maximum displacement such that the first W neighbours of H lie at a distance equal to the nearest neighbouring distance in the bulk (2.74Å).

Calculations have been performed for the $c(2 \times 2)$ superstructure in three models as shown in Fig. 5. In Debe and King's model, *all* the surface W-atoms move together laterally in a pairwise fashion to form zig-zig chains along $< 11 >$ direction. In the puckered layer model only 50 per cent of the surface atoms move both parallel and perpendicular to the original surface. Finally, in Barker and Estrup's model, which may be more reliable for M (001) H system, the surface W-atoms move along $< 10 >$ direction.

Results have been obtained for three arbitrary displacements of the surface atoms. As a typical example, we present the results in Debe and King's model in Table I. Here R_1', R_2', R_3', and R_4' denote the new distances of the first, second and the two types of the third neighbouring atoms of H, respectively. The results for the other two models are somewhat similar but for the puckered layer model, the displacement of surface W-atoms need to be large in contrast to an estimate of about (0.15 — 0.3) Å by LEED experiments or about ~ 0.2 Å by HEIS measurements. For details, we refer to Agrawal[14].

TABLE I

Values of the different qnantities used in Debe and King's model for the different displacements of W surface atoms. All distances are measured in Å, *the values of the second derivatives in* 10^4 *meV*^{2} *and the phonon frequencies in meV.*

d	ψ (°)	c'	R_1'	R_2'	R_3'	R_4'	$\frac{\hbar^2}{m}\phi''(R_1')$	$\frac{\hbar^2}{m}\phi''(R_2')$	$\frac{\hbar^2}{m}\phi''(R_3')$	$\frac{\hbar^2}{m}\phi''(R_4')$	ω_y (cal)	ω_x (cal)	ω_z (cal)	ω_y	ω_x ←Expt.→	ω_z
0.0	51	1.28	2.03	3.27	3.76	3.76	2.02	−0.075	0.24	0.24	80	160	130	80	60	130
0.32	39	1.70	2.19	3.64	3.84	4.20	1.80	0.05	0.24	0.10	61	127	155	60	125	155
0.2	45	1.45	2.04	3.41	3.76	3.99	1.80	0.05	0.24	0.16	73	141	141	70	142	142
0.1	45	1.51	2.14	3.47	3.82	3.93	1.80	0.05	0.24	0.18	74	140	140			

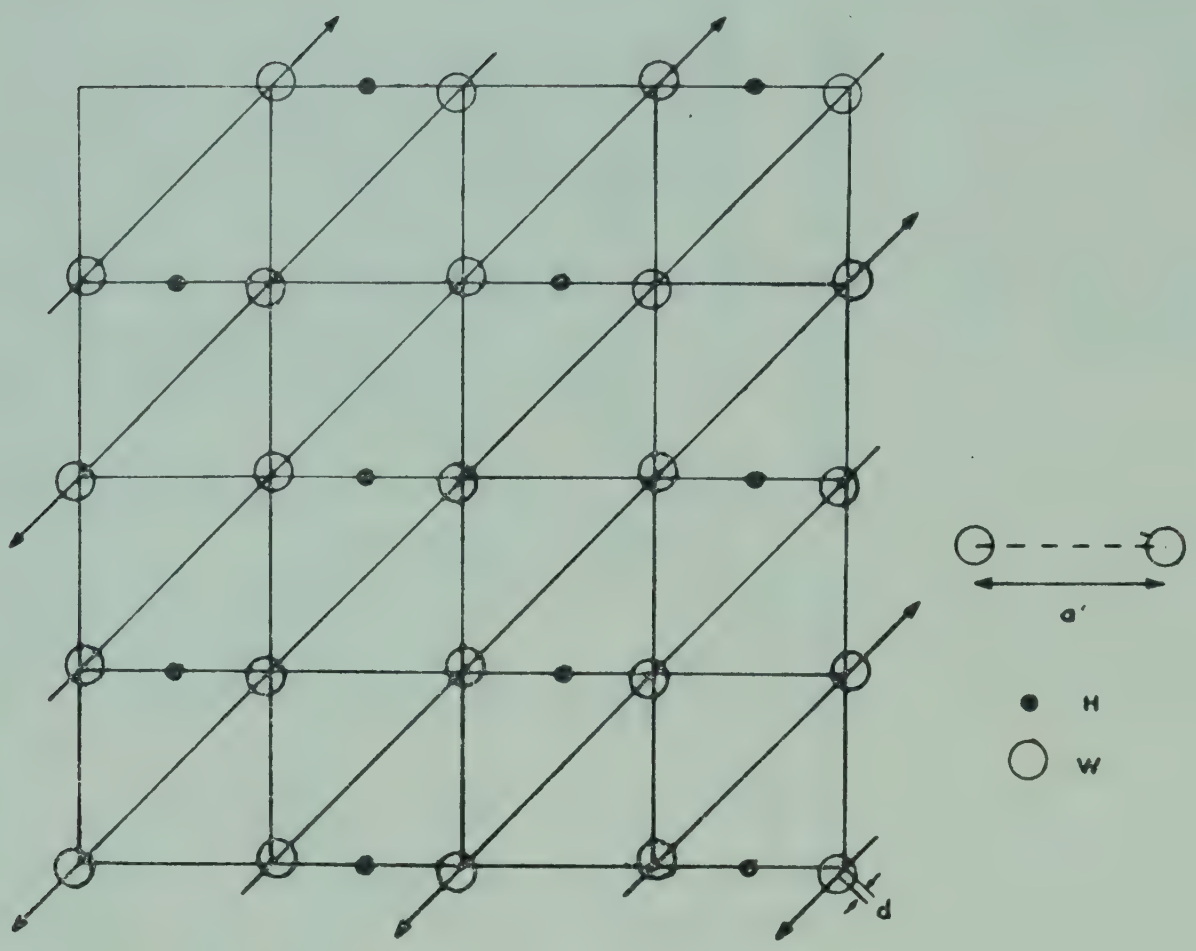

FIG. 5. (a) Debe and King's model for the reconstructed $W(001)$ $c(2 \times 2)$ H surface showing the displacements of W plane atoms along the <11> direction.

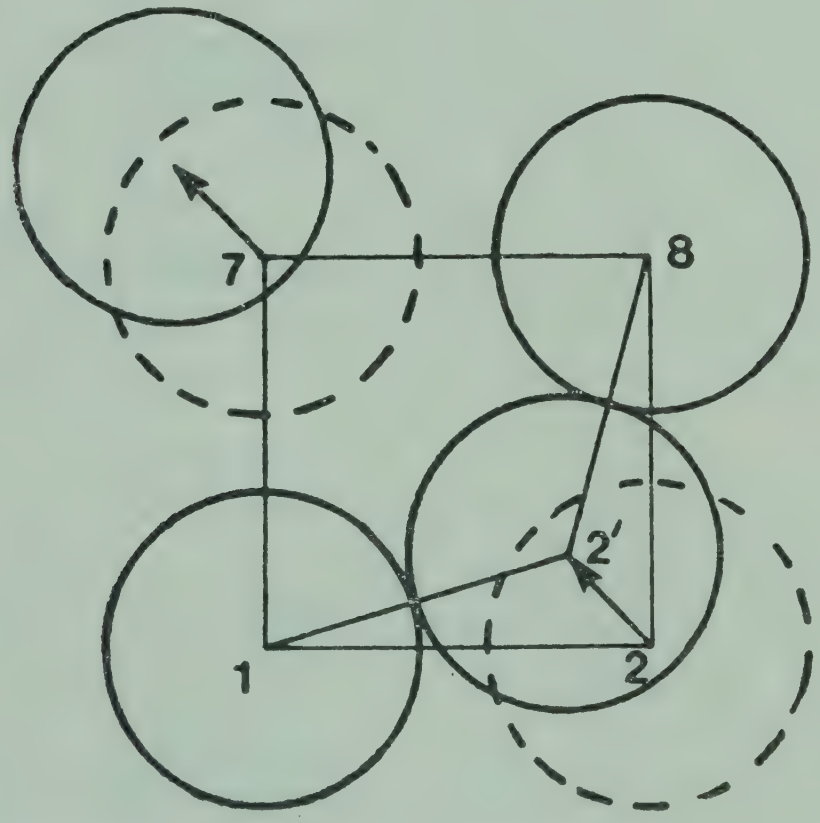

FIG. 5. (b) Puckered layer model. Position of W-atoms lying in a layer just below the H monolayer before (dotted circles) and after (full circles) reconstruction.

C. *Conclusions*

It is observed that the dispersion in the planar vibrations (i.e., the vibrations having eigenvectors parallel to the W-surface) arises due to the adatom $H - H$ interactions, and that along Δ-axis, the dispersions have opposite curvatures. These predictions could not be tested in the absence of experimental data. we find that the EELS data can well be understood in all the models with a coamparati-

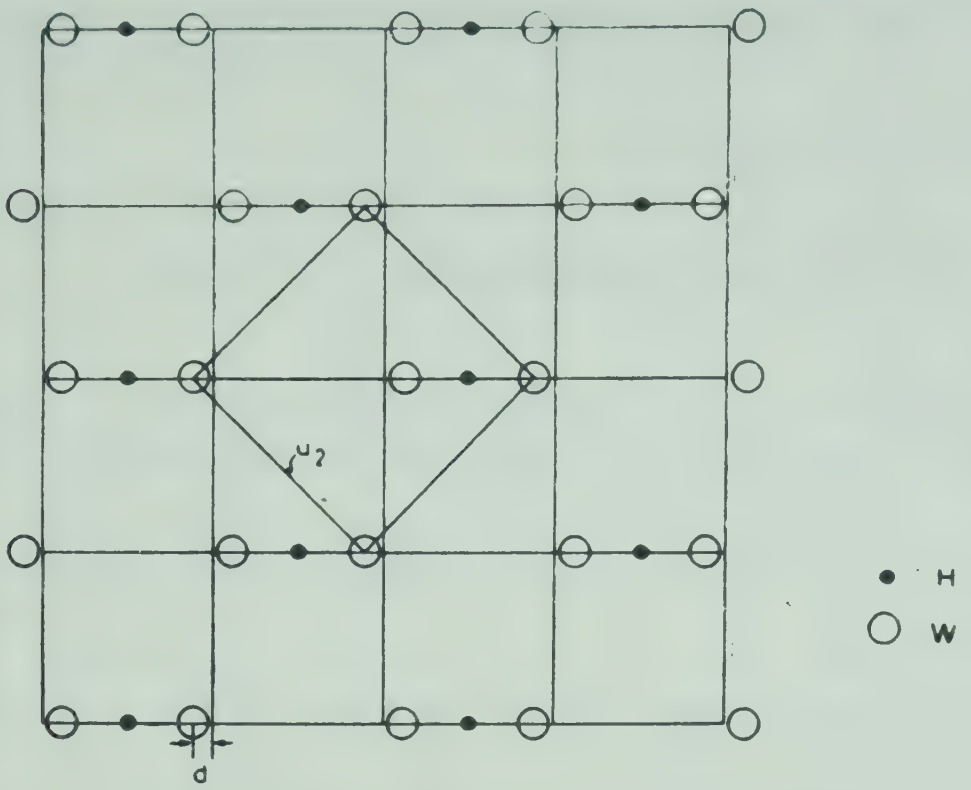

FIG. 5. (c) Barker and Estrup model where the surface *W*-atoms are shifted along the $< 01 >$ direction. U_2 indicates the unit cell.

vely small displacement of *W*-atoms ($d \sim 0.2 - 0.32$ Å), quite in agreement with the experimental measurements. Tha force constants between the *H*-atom and the surface *W*-atoms vary regularly with the distance. The interaction between the *H*-monolayer and the substrate bulk plane lying just below the surface is seen to be quite feeble, most probably due to a strong screening by the metal substrate's conduction electrons.

6. Ni(111) O

The preceding example shows that the surface-adatom distance is needed as well as the adsorption geometry before any quantitative fit of the adsorbate induced optical phonons can be made. This distance is for some systems known from LEED measurements, otherwise one may approximate it from molecular interatomic distances or by some simpler procedure as done above. Therefore a model which could give the vibration frequencies as well as the interatomic distances is of great interest. Starting from surface electronic structure calculations, such a model has been proposed recental by Allan *et al*[11,17].

The transition metal substrate is described by *d* states and the oxygen by *p* states within the tight-binding approximation.

Only two first moments of the local density of states are used to calculate the electronic energies. The local density of states on a given atom are fitted to a gaussian.

The hopping integrals β_{ij} between atoms *i* and *j* depend on the distance R_{ij} as

$$\beta_{ij} = \beta_{ij}^{0} \exp(-q_{ij} R_{ij}) \qquad \ldots(6.1)$$

The stability of the crystal is ensured by a Born-Mayer repulsive potential

$$C_{ij} = C^0_{ij} \exp(-p_{ij} R_{ij}) \qquad ...(6.2)$$

The β^0_{ij}, q^0_{ij}, c^0_{ji} and p_{ij} are parameters of this model.

A first and second order development of the energy as a function of atomic positions is used to minimize the energy, find the interatomic distances and the dynamical matrix. The eight parameters of this model are fitted to bulk transition metal properties, to molecular vibration frequencies or to the observed electron loss spectra.

Recent EELS measurements of 'O' chemisorbed on a Ni(111) surface show peaks which were assigned by Ibach *et al.*[29] to Ni surface phonons. Electron losses are only observed at the center of the surface Brillouin zone. However, two oxygen structures ($\sqrt{3} \times \sqrt{3}\ R\ 30°$) and $c(2 \times 2)$ are known.

All the experimental data were of a good accuracy, apart from the distance O — Ni at the (001) surface and the corresponding frequency for the $c(2 \times 2)$ structure. We show here only the results for the $p(2 \times 2)$ structure on the (111) surface.

The phonon spectra were calculated at the centre of the structure Brillouin zone using a slab of 6 to 12 Ni layers deposited on a frozen Ni substrate. The local phonon frequencies have been gaussian broadened to get a continuous spectrum. Figure 6 gives the spectra calculated for the (111) $p(2 \times 2)$ structure. The vibrating dipole $D(\omega)$ is represented on curve (A)

$$D(\omega) = \sum_n \sum_i Q_i |\, u_i(\omega_n)|\, \delta(\omega - \omega_n), \qquad ...(6.3)$$

where $Q_i = 1$ for the oxygen atom and $Q_i = -1/N$ for one of its nickel neighbours and $u_i(\omega_n)$ is the amplitude of vibration on atom i for the frequency ω_n. It is slightly different from the local density of phonons which is

$$n_i(\omega) = \sum_n |\, u_i(\omega_n)\,|^2\, \delta(\omega - \omega_n). \qquad ...(6.4)$$

Curves (B), (C) and (D) give, respectively the local phonon spectra on the oxygen adatom, on one of its nickel neighbours and on a nickel free surface atom. The peaks of $D(\omega)$ agree quite well with the experimental ones.

One can see on the curves (C) and (D) that the adsorption of oxygen modifies the local nickel surface atom phonon spectra. The localized surface vibration frequencies are slightly shifted. New force constants appear between the surface atoms and the oxygen atoms. Moreover, the oxygen adsorption destroys the contraction arising near a free nickel surface or even may change the relaxation sign.

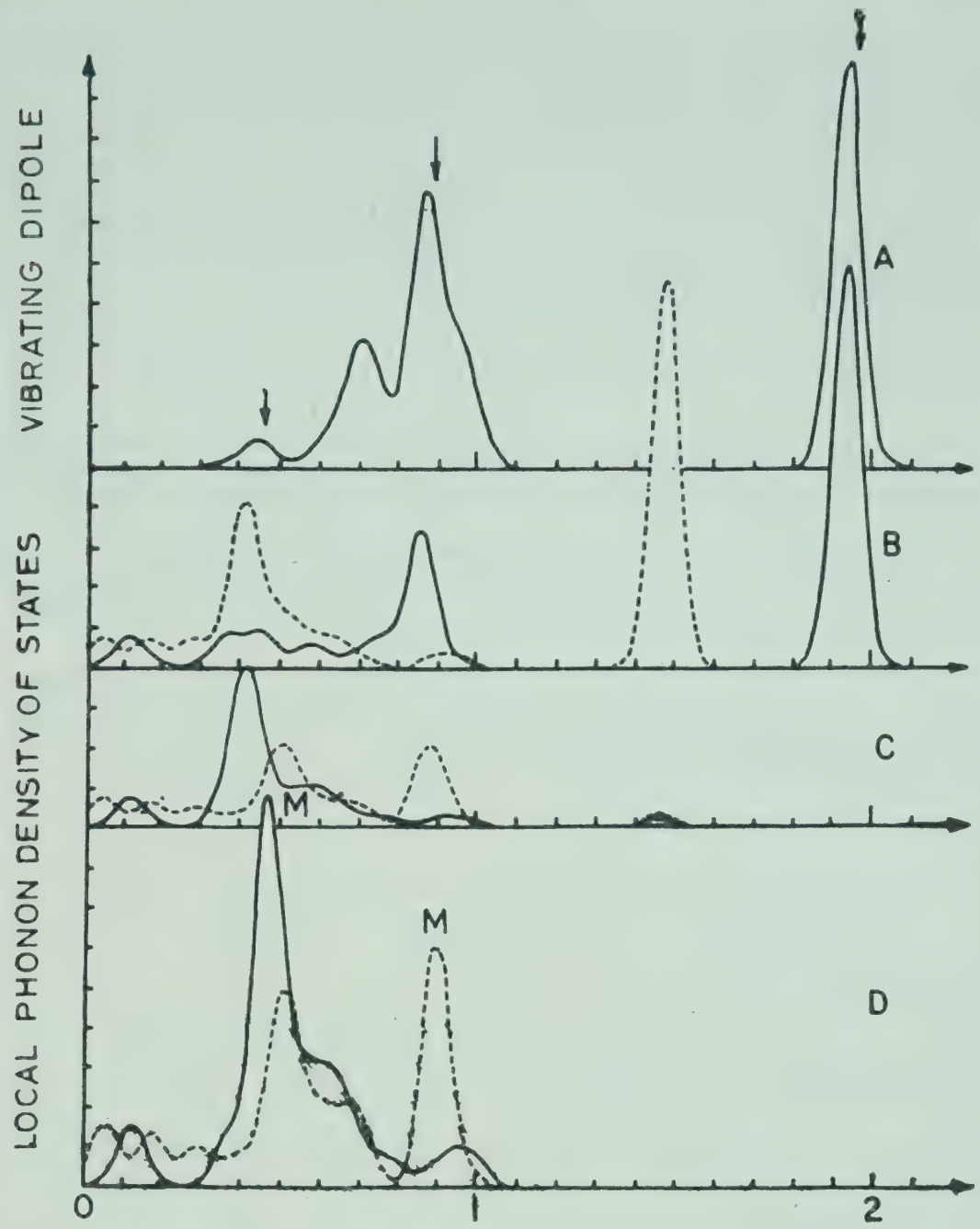

FIG. 6. Oxygen $p(2 \times 2)$ structure local phonon spectra on Ni(111) surface. The Curve (A) shows the vibration dipole. The curves (B), (C) and (D) give respectively the local phonon spectra on the oxygen atom, on one of its nickel neighbours and on a free nickel (111) surface. The arrows indicate the positions of the experimental electron loss peaks. The full lines are for vibrations perpendicular to thes urface and the dotted lines for vibrations in the surface plane.

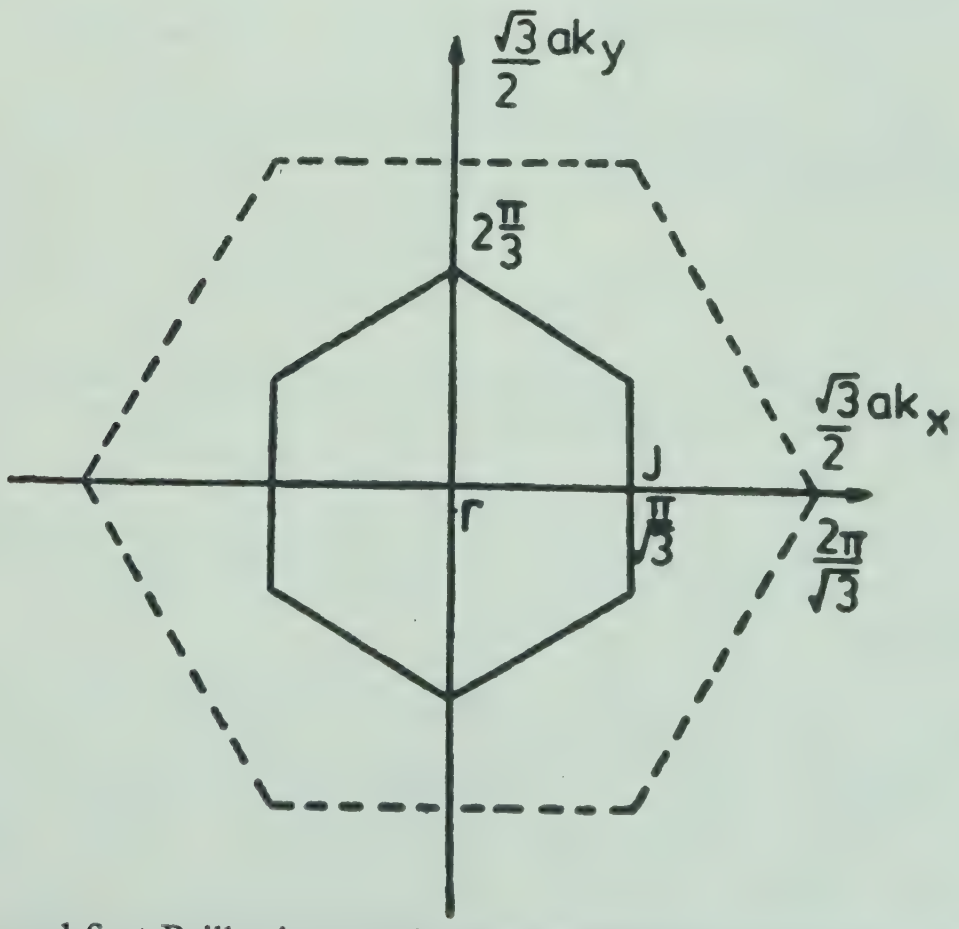

FIG. 7. Two-dimensional first Brillouin zone for the graphite basal plane. The inner small zone is for (111) surface of f.c.c. lattice like the rare-gas monolyer (in registry).

This variation of the relaxation also modifies the force constants between atoms close to the surface and then the surface vibration frequencies.

Note that the dotted lines in Fig. 6 are for vibrations polarized in the surfaces plane. These theoretically predicted peaks should be observed in forthcoming experiments, similar to the one done for H on W (001).

7. *Anharmonic Theory*

We now dis uss an anharmonic theory for treating the thermal expansion of a non-Bravais crystal. In the Taylor expansion of the potential energy (Eq. 3.3) we replace $u_\alpha(l\kappa)$ by more general atomic displacements $\xi_\alpha(l\kappa)$. The first-order atomic force constants $\Phi_\alpha(l\kappa)$ are zero in bulk but take non-vanishing values for atomic sites near the surface or for atoms of monolayer.

The atomic displacement $\xi_\alpha(l\kappa)$ arises from the three contributions as

$$\xi_\alpha(l\kappa) = u_\alpha(l\kappa) + d_\alpha(l\kappa) + s_\alpha(l\kappa),$$

where

$$s_\alpha(l\kappa) = \sum_\lambda \epsilon_{\alpha\lambda}\, x_\lambda(l\kappa) \qquad \ldots(7.1)$$

accounts for a homogeneous deformation of the crystal with $\epsilon_{\alpha\lambda}$ as thermal expansion coefficients and $x_\lambda(l\kappa)$ as the components of the position vector $\vec{x}(l\kappa)$. The quantity $d_\alpha(l\kappa)$ denotes the inhomogeneous thermal average disylacement of the atom due to the free surface and $u_\alpha(l\kappa)$ represents arbitrary time-dependent displacement of the atom from its new position in the deformed crystal.

A. Thermal Average Displacements

In our future writings we use an abbreviated notation

$$\eta_\alpha(l\kappa) = s_\alpha(l\kappa) + d_\alpha(l\kappa). \qquad \ldots(7.2)$$

It can be shown that the total free energy of a crystal has two contributions : a static part Φ_s and the vibrational part $F(T)$ as[30]

$$f(T) = \Phi_s + F(T). \qquad \ldots(7.3)$$

Here

$$\Phi_s = \Phi_0 + \sum_{l\kappa\alpha} \Phi_\alpha(l\kappa)\, \eta_\alpha(l\kappa) + \tfrac{1}{2} \sum_{l\kappa\alpha,\, l'\kappa'\beta} \Phi_{\alpha\beta}(l\kappa;\, l'\kappa')\eta_\alpha(l\kappa)\, \eta_\beta(l'\kappa')$$

$$+ \tfrac{1}{6} \sum_{l\kappa\alpha} \sum_{\text{e.c.}} \Phi_{\alpha\beta\gamma}(l\kappa;\, l'\kappa';\, l''\kappa'')\, \eta_\alpha(l\kappa)\, \eta\kappa(l'\kappa^z)\, \eta\kappa(l''\kappa'') + \ldots$$

and

$$F(T) = F^0(T) + \tfrac{1}{2} \sum_{l\kappa\alpha} \sum_{l'\kappa'\beta} \sum_{l''\kappa''\gamma} \Phi_{\alpha\beta\gamma}(l\kappa;\, l'\kappa';\, l''\kappa'')$$

$$\times < u_\alpha(l\kappa)\, u_\beta(l'\kappa') > \eta_\gamma(l''\kappa''), \qquad \ldots(7.4)$$

where $F°(T)$ describes the harmonic contribution to the vibrational free energy. $< u_\alpha(l\kappa)\, u_\beta(l'\kappa') >$ denote the correlation functions to be evaluated in harmonic approximation.

At each temperature one determines the new atomic positions by minimizing the total free energy $f(T)$ with respect to the $\{\epsilon_{\gamma\lambda}\}$ and $\{d_\alpha(l\kappa)\}$. After knowing the new positions, one calculates the renormalized harmonic force constants and then the phonons.

The minimization of $f(T)$ with respect to the $\{d_\alpha(l\kappa)\}$ gives

$$\Phi(l\kappa) + \sum_{l'\kappa'\beta} \Phi_{\alpha\beta}(l\kappa;\, l'\kappa')\, \eta_\beta(l'\kappa') + \sum_{l'\kappa'\beta}\sum_{l''\kappa''\gamma} \Phi_{\alpha\beta\gamma}(l\kappa;\, l'\kappa';\, l''\kappa'')$$

$$\times\, \eta_\beta(l'\kappa')\eta_\gamma(l''\kappa'') + F_\alpha(l\kappa;\, T) = 0 \qquad \ldots(7.5)$$

with
$$F_\alpha(l\kappa;\, T) = \tfrac{1}{2} \sum_{l'\kappa'\beta}\sum_{l''\kappa''\gamma} < u_\beta(l'\kappa')\, u_\gamma(l''\kappa'') > \Phi_{\beta\gamma\alpha}(l'\kappa';\, l''\kappa'';\, l\kappa) \qquad \ldots(7.6)$$

The expansions made above can be performed around any well-defined positions of the atoms. In our future writings, we take these positions to be the static equilibrium ones, taking due account of the static relaxation of the atomic planes near the free surface. Thus, the first term $\Phi_\alpha(l\kappa)$ in Eq. (7.5) vanishes. We also neglect here the third term which is of order 2 in $\{\eta_\alpha(l\kappa)\}$. It has earlier been checked that it is a good approximation. We are thus left with two terms and we may now easily determine the shifts in atomic positions after knowing anharmonic force constants.

B. Correlation Functions

The correlation function in harmonic approximation is determined by

$$< u_\alpha(1\kappa)\, u_\beta(1'\kappa') > = \frac{\hbar}{2\sqrt{M_\kappa M_{\kappa'}}} \left| D^{-1/2} \coth\left(\frac{\hbar \underset{\approx}{D}^{1/2}}{2k_B T}\right)\right|_{l\kappa\alpha,\, l'\kappa'\beta} \qquad \ldots (7.7)$$

where $\hbar$ is the Planck's constant, k_B is the Boltzmann constant, and the elements of the dynamical matrix $\underset{\approx}{D}$ are given by

$$D_{\alpha\beta}(1\kappa;1'\kappa') = \Phi_{\alpha\beta}(1\kappa;1'\kappa')/|\, M_\kappa\, M_{\kappa'}\,|^{1/2}. \qquad \ldots(7.8)$$

An expansion method to shorten the analytical calculation for mean square displacement is

$$< u_\alpha^2(1\kappa) > = < u_\alpha^2(1\kappa) >_E + < u_\alpha^2(1\kappa) >_1 + < u_\alpha^2(1\kappa) >_2 + \ldots, \qquad \ldots(7.9)$$

where $< u_\alpha^2(1\kappa) >_E$ is the mean square displacement in the Einstein approximation in which one considers only the diagonal part of the dynamical matrix $\underset{\approx}{D}$, and the higher order terms $< u_\alpha^2(1\kappa) >_1$, $< u_\alpha^2(1\kappa) >_2$ denote the first and second order correlations. In several systems, the first term is quite dominant.

8. Rare Gas Monolayers on Rare Gas Crystals

We have applied the theory of the last section to systems formed by the adsorption of one monolayer of He, Ne, A, Kr or Xe on (111) surface of a Ne, A, Kr or Xe solid. The interatomic interactions between the first and second neighbours are described by Lennard Jones (LJ) potential.

It is a good approximation to suppose that the relaxation changes only the distance between the plane ($1 = 0$) of the adsorbate and the substrate surface plane ($l = 1$).

Once the interatomic distances are known at each temperature, we calculate the phonon frequencies using the frozen substrate approximation. Let us recall if one has a soft mode within this approximation, it will remain in an exact diagonalization of the whole dynamical matrix.

Some adsorbate substrate systems are found unstable already at $T = 0°K$. This is in particular true when the adsorbed atoms are heavier than the substrate ones. One cannot then expect in these cases an adsorbed monolyer in epitaxy with the substrate and having the same number of atoms as the surface plane of the substrate.

There are a number of stable systems at $T = 0°K$. However, only for Xe(111) substrate containing Ne or K monolayers, soft mode appears. This mode appears first at the J point of the Brillouin zone (Fig. 7). We varied the temperature from 0°K to the melting temperature of the substrate. The transition temperatures for Xe(111) Ne and Xe(111) Kr are 15 and 69°K, respectively.

The relative variation of the interatomic distance $\Delta b/b$ with temperature is shown in Fig. 8. For details, we refer to Agrawal *et al.*[10]

When such a transition temperature T_C exists, the adsorbed monolayer may present a second order phase transition and then a superstructure above this T_C. However, the results given here must be considered only as qualitative. It may happen that before the T_C calculated here is reached, the monolayer may have a first order transition and present a new kind of order than a superstructure. The first order transition cannot be described by the soft mode concept developed here. An experimental study of the systems described here will be quite interesting.

9. Rare Gas Monolayers on Graphite

Inert-gas atoms like Xe, Kr, Ar, etc. physisorbed on the basal plane (0001) of graphite have been studied extensively, partly because of simplicity of their being monoatomic reducing thus the complexities associated with the extra intra-molecular degrees of freedom, and partly because of the commercial availability of Grafoil (a form of graphite) having larger specific areas and surfaces of exceptional uniformity and homogeneity. All three phases, i.e., gas, liquid, solid have been identified. In particular, the solid-liquid transition is interesting as it may, in principle, be second order at high converges representing a 2D analog of the usual melting process which is of first order in three-dimensional systems. Both

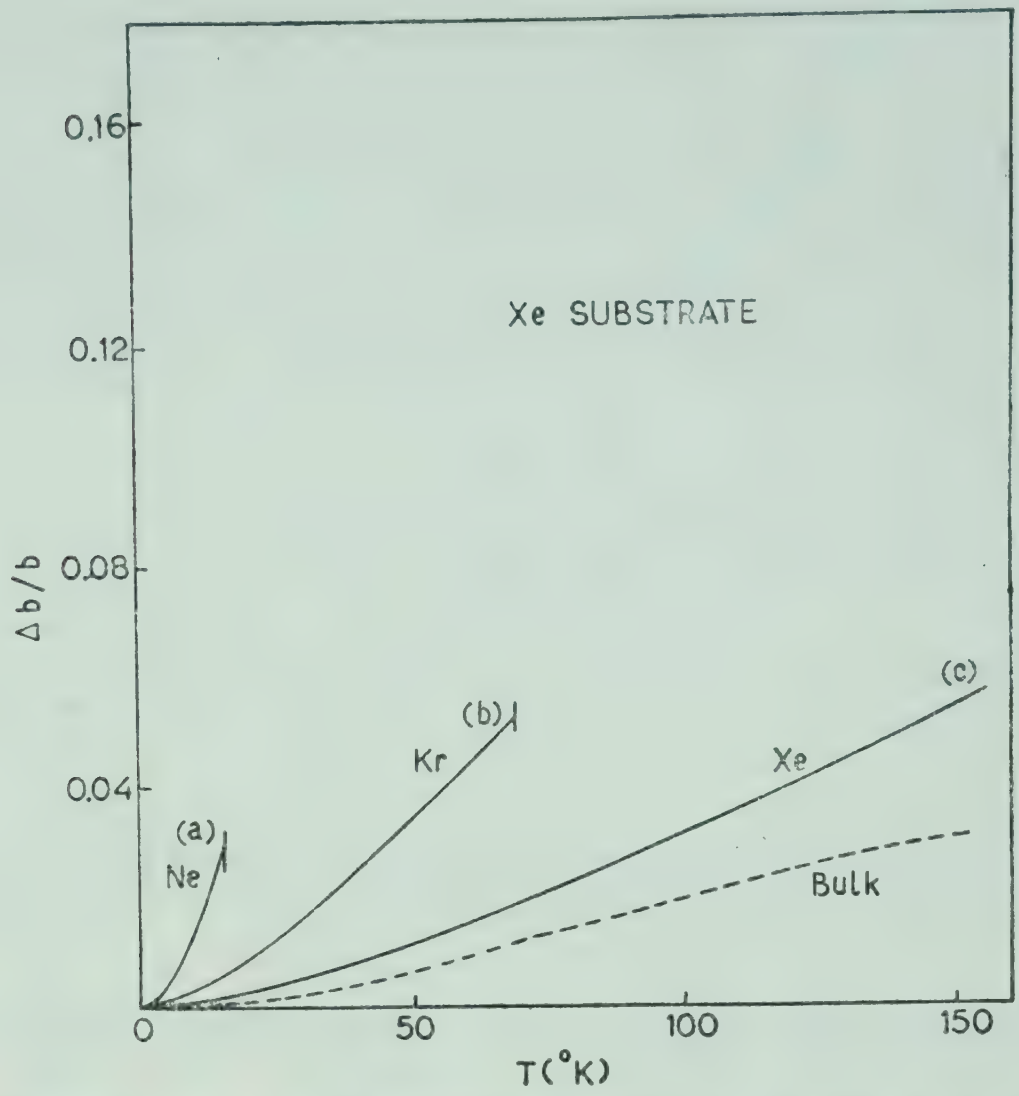

FIG. 8. Relative variation ($\Delta b/b$) of the distance between the adsorbed monolayer and Xe substrate as a function of temperature for Ne (curve a), Kr (curve b) and Xe (curve c) monolayers. When one obtains a soft phonon before the melting temperature of the substrate, the curve is stopped at this transition temperature.

commensurate and incommensurate solid phases have been detected. In some systems, by a variation of temperature and the pressure of the inert-gas, one may observe an apparently second- (or higher-) order phase transition from a commensurate (in-registry) ($\sqrt{3} \times \sqrt{3}$) 30° superstructure to an incommensurate (out-of-registry) compressed or expanded monolayer structure. Very recently, rotation of the adsorbed layer in the incommensurate phase with respect to the graphite substrate has been reported in the literature[31,32].

We make now a study of the thermal expansion and the mean square displacements of the inert-gas, Xe, Kr, Ar, and Ne monolayers in epitaxy with the (0001) graphite surface (Fig. 9), and thereafter investigate the possibility of soft phonons in these systems.

The graphite crystal possesses a hexagonal structure (Fig. 9). The unit cell contains four atoms. For a simpler calculation we use here a simple lattice-dynamical model discussed earlier by Champier *et al*[33–35]. One considers a central force constant β and the two noncentral force constants (α, γ) between the two nearest-neighbour atoms lying in a layer (0001). The interactions between the two adjacent layers are described in the same manner by the central force constant (γ') and the noncentral force constant (α').

The first two-dimensional Brillouin zone for the graphite surface (0001) has been depicted in Fig. 7 which also contains the first Brillouin zone for the inert-gas

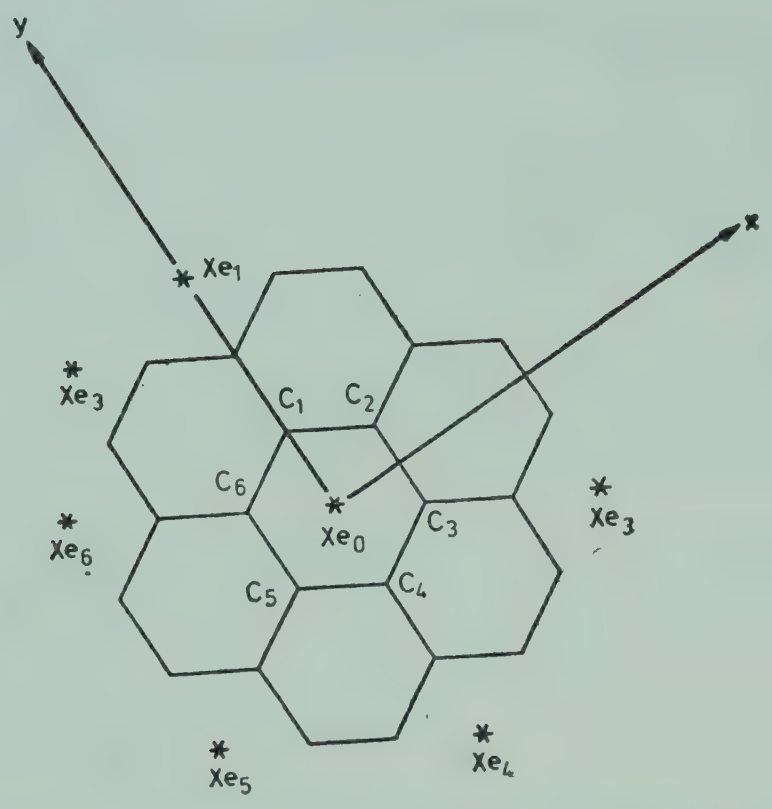

FIG. 9. Commensurate phase of rare gas atom monolayer on graphite basal (0001) plane. Xe_i and C_i denote the rare gas and carbon atoms, respectively.

monolayer in epitaxy with the substrate surface lattice. For details we refer to Agrawal[15].

A. Mie-Lennard-Jones Potential (MLJ)

The rare-gas-atom monolayer has a $\sqrt{3} \times \sqrt{3}$ structure and its Brillouin zone is rotated by an angle of 30° with respect to that of graphite surface. One describes this superstructure of the surface as $(\sqrt{3} \times \sqrt{3})\ 30°$.

Let a and c be the lattice constants of the graphite in bulk. The six nearest neighbours of inert-gas atom in the monolayer are situated at a distance of 3a. For describing the nearest-neighbor adatom-adatom interactions and also the nearest-neighbor adatom-substrate interactions we use here the Mie-Lennard-Jones (MLJ) pair potential $\Phi_{a-a}(r)$ and $\Phi_{a-s}(r)$, respectively, (a denotes adsorbed atom and s the substrate atom) given by

$$\Phi(r) = \epsilon \left| \left(\frac{\sigma}{r}\right)^{12} - 2\left(\frac{\sigma}{r}\right)^{6} \right|, \qquad \ldots(9.1)$$

where r denotes the separation of two atoms and the values of the potential parameters σ and ϵ are obtained by using the measured values of the virial coefficients of inert gases[36]. The values of the two parameters ϵ and σ for the graphite and the inert-gas atoms Xe, Kr, Ag, and Ne are contained in Table II.

For determining the values of the parameters ϵ and σ for the adatom-substrate interaction potential, we utilize the following prescription :

$$\epsilon_{as} = (\epsilon_a \epsilon_s)^{1/2} \text{ and } \sigma_{as} = \tfrac{1}{2}(\sigma_a + \sigma_s). \qquad \ldots(9.2)$$

As started earlier, the thermal expansion for graphite both parallel and perpendicular to the basal plane (0001) is quite small ($\sim 10^{-6}$/K); we therefore do not

determine any numerical values for the thermal expansion in bulk, but instead use the values given in standard tables[37].

In the absence of any experimental information about the monolayer-substrate surface separation c, the static equilibrium condition is utilized to determine it. Price[38] has determined the values of c for these systems after summing up interactions to all the neighbours. The values are reproduced in Table II.

TABLE II

Parameters of Mie-Lennard-Jones potential (MLJ 6–12) and the monolayer-substrate separation c. *The values of* ϵ *and* σ *are in K and* Å, *respectively. The melting temperature* T_M *of solid rare-gas is in K and c is in* Å.

Sample number	Atom	ϵ	σ	T_M	c
1	carbon (graphite)	27.0	3.871		(Ref. 38)
2	Xe	332.0	4.318	155	3.69
3	Kr	182.9	4.020	116	3.54
4	Ar	125.2	3.810	84	3.42
5	Ne	35.6	3.080	24.5	3.13

During the course of calculation, we find that the numerical values of the mean-square displacements for the inert-gas atom are larger compared to that of graphite atoms at all temperatures and one may work in a frozen-substrate approximation. However, we present here our results for the thermal expansion for a graphite surface where the carbon atoms are vibrating.

B. Thermal Expansion Near the Surface

The thermal expansion of the monolayer-substrate separation is defined as

$$\frac{\Delta c(T)}{c(0)} = \frac{\delta c(T) - \delta c(0)}{c(0)}, \qquad \ldots(9.3)$$

where $\delta c(T)$ is the relaxation of the monolayer at temperature T. $c(0)$ is the monolayer-substrate separation at $T = 0°K$ given in Table II. In fact, one observes a small relaxation near 0°K causing $\delta c(0)$ to be nontrivial.

The percentage relative relaxation has been calculated for all gas monolayers. As a typical example, we depict this relaxation at different temperatures for Xe in Fig. 10. For Xe, in a temperature interval of 15°K, one observes a relaxation of $\sim$ 3.5 per cent. It arises because of a comparatively large initial monolayer-substrate separation (3.69 Å). It may be recalled that the separation between the basal planes in bulk graphite is 3.35 Å. For krypton and argon, the relaxation is about 0.8 per cent in a temperature interval of $\sim$ 100 K, and for neon, the corresponding relaxation is 0.15 per cent in the temperature interval of 25°K.

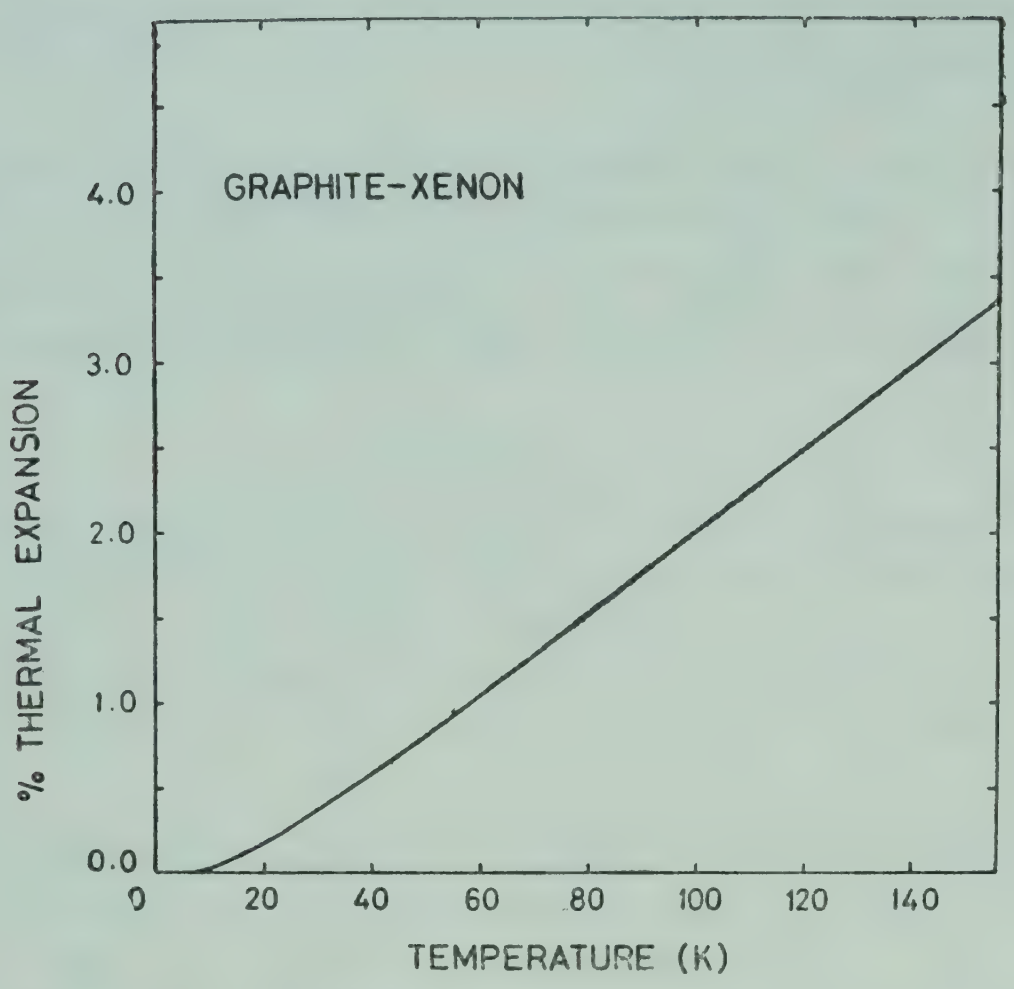

FIG. 10. Percentage relative relaxation for Xe-monolayer.

C. *Soft Phonons*

In the calculation of the temperature-dependent phonons we employ a frozen-substrarte approximation. The equation of motion for the y and z components of the displacement of an inert-gas atom in the y direction get decoupled as[39]

$$\left|-M\omega^2 + 3a_{22} + F(3 - \cos 2\Phi_y - 2\cos\Phi_y)\right| U_y^{(a)} = 0, \qquad \ldots(9.4a)$$

$$\left|-M\omega^2 + 6a_{33}\right| U_z^{(a)} = 0. \qquad \ldots(9.4b)$$

Here M is the mass of inert gas atom; F, a_{22}, and a_{33} are the nearest-neighbour central adatom-adatom and the adatom-substrate force constants, respectively. Their explicit forms are

$$F = \Phi_{aa}''(3a) + \Phi_{aa}'(3a)\,/3a; \qquad \ldots(9.5)$$

$$a_{22} = a^2 D^2 \Phi_{as}(r_0) + 2D\Phi_{as}(r_0)$$

$$a_{33} = c^2 D^2 \Phi_{as}(r_0) + D\Phi_{as}(r_0), \qquad \ldots(9.6)$$

with $D\Phi(r) = \Phi'(r)/r$, $D^2\Phi(r) = \Phi''(r)/r^2 - \Phi'(r)/r^3$ and $\Phi'(r)$ and $\Phi''(r)$ as the first and second space derivatives of the pair potential $\Phi(r)$; r_0 is the nearest-neighbour distance between the rare gas and carbon atoms.

From Eq. (9.4*a*), it is evident that a phonon may become soft if $a_{22} = 0$ at a certain temperature before the melting temperature of the inert-gas solid is reached. We look into this possibility and find that no soft phonon appears in any inert-atom monolayer physisorbed on (0001) graphite.

D. Mean-square Displacements (MSD)

The variations of the out-of-plane component u_z^2 and of in plane component u_x^2 of the mean-square displacement with temperature for monolayers of Xe, Kr, Ar, and Ne in epitaxy with the (0001) surface of graphite have been determined. Some measured values of the out-of-plane component are available in the literature. In general, the parallel component of the mean-square displacement is greater than the normal component. It is due to the fact that the adatom-adatom interactions are weaker than the adatom-substrate interactions. For details we refer to Agrawal[15].

We now discuss Xe rare-gas monolayer. For the Xe monolayer (Fig. 11) the effect of anharmonicity is apparent in the out-of-plane component. The effects are quite large due to a comparatively larger monolayer-substrate sparation (3.69Å) compared to a separation of 3.35 Å between the successive planes of the bulk graphite. Our results for $c = 3.69$ Å in harmonic approximation tally with experimental results. In fact, Coulomb *et al.*[39] have measured the variation of MSD of an Xe atom with respect to that at 48°K. A comparison of this variation has been made in Fig. 12. We observe a steeper rise in the MSD in the anharmonic theory.

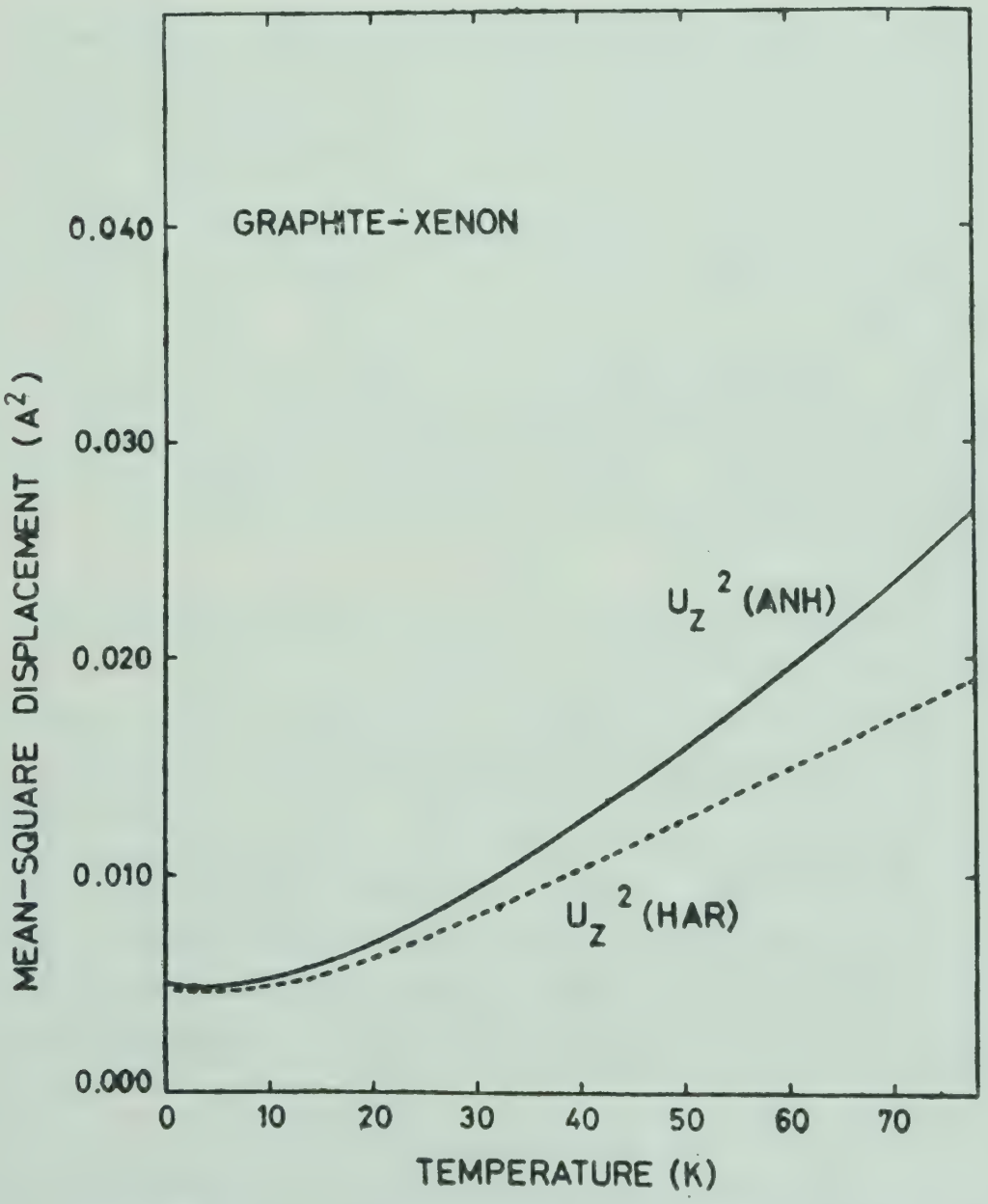

FIG. 11. Temperature variation of the out-of-plane $<U_z^2>$ mean square displacement for xenon monolayer in harmonic and anharmonic approximations.

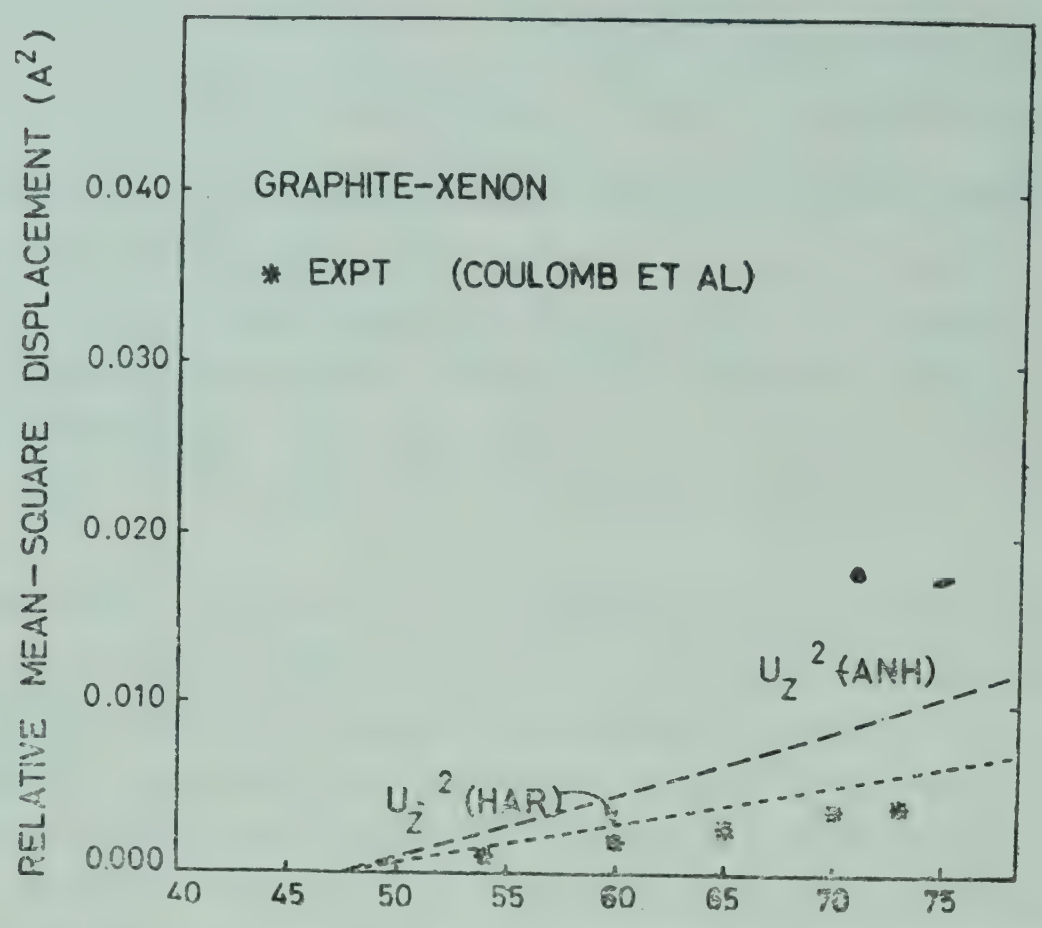

FIG. 12. Comparison of the calculated and the experimental relative out-of-plane mean-square displacement in Xe-monolayer. The experimental results of Coulomb *et al.* (Ref. 39) are shown by asterisks.

For the Kr monolayer, our values of the in-plane component are somewhat lower than the experimental values of Horn *et al.*[40] available at two temperatures $T = 30$ and 90°K. At $T = 30$ and 100°K, the calculated values are 0.04 and 0.12 Å², respectively, as compared to the experimental values 0.055 and 0.17 Å², respectively. The results seem to be reasonable as the contributions of the neglected higher-order terms in the expansion of the correlation functions may be significant for the in-plane component. Very recently deWette *et al.*[16] have calculates the harmonic values for MSD's as function of temperature for Kr and Xe monolayers on Graphite slabs. Their values are in agreement with ours except at comparatively higher temperatures.

For the Ar monolayer, the values for the in-plane component are quite high compared to those of out-of-plane component. For the Ar monolayer, some experimental and theoretical results for the phonons and the mean-square displacement for a two-dimensional lattice have recently been reported in the literature[41,42]. Taub *et al.*[41] have reported an out-of-plane Einstein oscillator frequency of ~ 5.6 meV. For this phonon mode having vibration normal to the plane of monolayer we obtain a value of 5.4 meV, quite in agreement with the neutron scattering data of these authors. Further, our value of the in-plane component of MSD is 0.043 Å² which is in very good agreement with their value of 0.04 Å² from the analysis of neutron data.

For the Ne monolayer, the in-plane component is quite large compared to the out-of-plane component. This is again indicative of a quite strong coupling of the monolayer to the substrate.

E. Conclusions

Only a small relaxation of ~ 1 per cent of the monolayer over a temperature interval of 100°K has been observed for Kr, Ar and Ne monolayers. For the Xe monolayer the corresponding relaxation is ~ 2 per cent. No soft phonon has been detected. The mean-square displacements of all the monolayers are an order of magnitude larger than those of the carbon atoms in graphite surface and one may safely work in the frozen-substrate approximation. The mean-square displacements of inert-gas atoms parallel to the surface are, in general, greater than those perpendicular to the surface. The differences in the two components increase with increased coupling with the substrate surface and decrease with the mass of the adsorbed atom. The calculated value of the mean-square displacements in Xe, Kr and Ar monolayers are in good agreement with the available experimental data. It may be noted that the present theory considers only the cubic anharmonic term to lowest order in perturbation formalism. The inclusion of higher-order terms such as the quartic anharmonic one or those in the perturbation formulation may affect the results at higher temperatures. Thus, the results at high temperatures should be taken with caution in the theory.

10. Main Conclusion

The physics of adsorbate induced optical phonons seems to be now well understood. With the increasing number of experimental results, one is faced now to propose dynamical models which can fit experimental data. The situation is similar to that of the bulk lattice dynamics when only elastic constants were measured, before the neutron scattering determinations of the phonon dispersion curves. However here we have still often a major unknown : the surface cristallography.

We believe however that thanks to many different surface experiments, he surface cristallography will be obtained for more and more systems, as well as more vibrational frequencies will be measured. Surface lattice dynamics should begin to mature.

References

1. For a review, see J G Dash, Films on solid surfaces (Academic Press, N. Y.); *J. de Physique Colloq.* **10** (1978) C4.
2. For different experimental techniques, see 'Vibrational spectroscopy of adsorbates' edited by R F Willis (Springer Verlag, Berlin) (1980).
3. See references in 'Surface Phonons and Polaritons', by A A Maradudin, R F Wallis and L Dobrzynski, Hand-book of Surfaces and Interfaces, vol. 3, edited by L Dobrzynski (Garland STPM Press, N. Y.) (1979).
4. H Kaplan, *Phys Rev.* **125** (1962) 1271.
5. T Asahi and J Hori, '*Lattice Dynamics*' edited by R F Wills (Pergamon Press, Oxford), (1965) p. 571.
6. L Dobrzynski and D L Mills, *J. Phys. Chem. Solids* **30** (1969) 1043; G Armend, P Marsi and D Dobrzynski, *J. Vac. Sci. Technol.* **9** (1972) 705; P Marsi and L Dobrzynski, *J. Phys. Chem. Solids* **34** (1973) 847.

7. G P Alldredge, R E Allen and F W deWette, *Phys. Rev.* **B4** (1971) 1682.
8. D Castiel, L Dobrzynski and D Spanjaard, *Surf. Sci.* **60** (1976) 269.
9. W R Lawrence and R E Allen, *Phys. Rev.* **B14** (1976) 2910; *Phys. Rev.* **B15** (1977) 5081.
10. Bal K Agrawal, B Djafari-Rouhani and L Dobrzynski, *Phys. Rev.* **B19** (1979) 2381.
11. L Dobrzynski, G Allan, B Djafari-Rouhani, Bal K Agrawal and J. Lopez in reference (2) p. 55.
12. V Bortolani, A Franchini, F Nizzoli and G Santero, *Solid State Commun.* **41** (1982) 369.
13. D W Bullet and M L Cohen, *J. Phys. C.* **10** (1977) 2083.
14. Bal K Agrawal, *Phys. Rev.* **B22** (1980) 3734.
15. Bal K Agrawal, *Phys. Rev.* **B23** (1981) 1778.
16. F W deWette, B Firey, E deRouffignac and G P Alldredge, *Phys. Rev.* **B28** (1983) 4744.
17. G Allan and J Lopez, *Surf. Sci.* **95** (1980) 214.
18. E Tosatti, *Solid State Commun.* **25** (1978) 637.
19. H Krakauer, M Posternak and A J Freeman, *Phys. Rev. Lett.* **43** (1979) 1885.
20. J E Inglefield, *J. Phys.* **C12** (1979) 149.
21. See for example the two review articles by L D Schmidt and by E W Plummer in Interactions on Metal Surfaces, edited by R Gomer (Springer Verlag, New York), (1975) 63 and 143.
22. R A Barker and P J Estrup, *Phys. Rev. Letters* **41** (1978) 1307; P J Estrup, *J. Vac. Sci. Tech.* **16**, (1979) 635.
23. M K Debe and D A King, *Surface Science* **81** (1979) 193.
24. A Adnot and J D Carette, *Phys. Rev. Letters* **39** (1977) 209.
25. M R Barnes and R F Willis, *Phys. Rev. Letters* **41** (1978) 1729.
26. I Stensgaard, L C Feldman and P J Silverman, *Phys. Rev. Letters* **42** (1979) 247.
27. Y J Chabal and A J Sievers, *Phys. Rev.* **B24** (1981) 2921.
28. M W Howard, U A Jayasooriya, S F A Kettle, D B Powell and N Sheppard, *J. Chem. Soc. Chem. Commun.* (1979) 18.
29. H Ibach and M Bruchmann, *Phys. Rev. Lett.* **44** (1980) 36.
30. L Dobrzynski and A A Maradudin, *Phys. Rev.* **B7** (1973) 1273.
31. A D Navaco and J P McTague, *J. Phys.* (Paris) *Colloq.* **10** (1977) C4–116.
32. C G Shaw, S C Fain, Jr. and M D Chinn, *Phys. Rev. Lett.* **41** (1978) 955.
33. G Champier, J M Genin and C Janot, *C. R. Acad. Sci.* **257** (1963) 1843.
34. G Albinet, J P Biberian and M Bienfait, *Phys. Rev.* **B3** (1971) 2015.
35. J P Coulomb and P Masri, *Solid State Commun.* **15** (1974) 1623.
36. G K Horton, *Am. J. Phys.* **36** (1968) 93.
37. American Institute of Physics Handbook 3rd ed., edited by D E Gray (McGraw-Hill, New York) (1972).
38. G L Price, *Surf. Sci.* **46** (1974) 697.
39. J P Coulomb, J Suzanne, M Bienfait and P Masri, *Solid State Commun.* **15** (1974) 1585. In the equation of motion for the y component of displacement of the Xe atom given in the Appendix of this paper the term-cos Φ_y should read as $-2\cos\Phi_y$.
40. P M Horn, R J Birgeneau, P Heiney and E M Hammonds, *Phys. Rev. Lett.* **41** (1978) 961.
41. H Taub, K Carneiro, J F Kjems and L Passell, *Phys. Rev. Lett.* **B16** (1977) 4551.
42. A D Novaco and J P McTague, *Phys. Rev.* **B20** (1979) 2469.

© *Proc. Indian natn. Sci. Acad.*, **51**, A, No. 1, 1985, pp. 57–75.
Printed in India.

SURFACE ANALYTICAL STUDIES OF OPTICALLY SELECTIVE OXIDE FILMS*

A BANERJEE *and* K L CHOPRA

Department of Physics, Indian Institute of Technology, New Delhi-110 016

Efficient optically selective surfaces/films or coatings of a variety of metal oxides have been developed in our Laboratory for a number of optical and opto-electronic applications. The understanding of the physical processes responsible for the optical selectivity of such surfaces and the possibility of precise tailoring of the optical properties have resulted from our detailed analysis of these surfaces by such analytical techniques as SEM, TEM, SAM, and ESCA. This paper presents a review of the work done in our Laboratory on structural and metallurgical aspects of oxide surfaces of technological interest.

Key Words : Surface Analysis; Optical Selectivity; Selective Surface; Oxide Films

INTRODUCTION

OPTICALLY selective surfaces/films (or coatings) can be defined as those which yield a desired and selective suppression or enhancement of the spectral dependence of reflectance, transmittance, or absorptance. A large number of oxide surfaces and coatings having appropriately graded mixed oxide or metal-oxide compositions, tandem or multilayer structures, columnar or granular microstructure, or controlled deviations from stoichiometry are known to exhibit excellent optical selectivity. The underlying surface properties which lead to optical selectivity can be tailored by controlling the surface/film fabrication parameters. Study of the surface properties, therefore, attains considerable importance both from the point of view of solid state physics as well as from applications. Solar cells, photothermal conversion, heat reflecting mirrors, transparent conductors, interference filters, integrated optics, and devices for imaging, information storage and retrieval are several hotly pursued applications on global scale. The work generated from the study of various aspects of optically selective surfaces has been crystallized in the form of several books and review articles[1–9].

Tailoring of optical selectivity required for optical and opto-electronic applications, demands a very detailed and in-depth knowledge of the surface topography and microstructure, chemical composition and its depth profile, and chemical state of the constituents of the surfaces/film. Our Laboratory has done pioneering and extensive work on the development and understanding of a wide variety of efficient and commercially viable selective surfaces/films by simple chemical techniques. This paper reviews the work of our Laboratory on the structural and metallurgical aspects of optically selective oxide coatings/surfaces of Sn, Zn, Cu, Fe, Ni, Mo, Cr, and Al, prepared primarily by chemical techniques, as studied by such analytical techniques as TEM, SEM, AES, and ESCA.

---

*Paper presented at the Symposium on Physics and Chemistry of Surfaces held at INSA, New Delhi from September 28-30, 1984.

What is Optical Selectivity ?

Though all materials exhibit a sort of intrinsic optical selectivity, from the technological viewpoint, one requires a specific type of wavelength dependence of optical properties. Which optical property is to be selectively enhanced or suppressed, and in which frequency or wavelength range and to what extent it is desired depends on the application. For example, for thermal energy applications four types of selectivities are of technical interest.

The first type is used in a "dark mirror" with absorptance (α) of unity in the wavelength range of incoming (solar) radiation and thermal emittance (ϵ) of zero (infrared reflectance of unity) in the higher wavelength region. Most of the solar energy incident on the surface of the earth is confined in the spectral region 0.3-2.5 μm. Therefore, for an ideal "dark mirror", we require

$$\alpha\ (0.3\text{-}2.5\ \mu\text{m}) = 1 \text{ and } \epsilon(\geqslant 2.5\ \mu\text{m}) = 0.$$

This type of selectivity is ideally suited for conversion of solar energy to thermal energy. The "cold mirror" utilizes the second type of selectivity in which the reflectance is unity in the visible part (0.4-0.8 μm) and transmittance is unity in the IR($> 0.8\ \mu$m). The "cold mirror" finds application in in splitting visible and the IR radiation. In the third type, transmittance is unity in the visible part of the solar spectrum and reflectance is unity in the IR region. The "heat mirror" utilizes this principle and is used for keeping out or confining in the thermal part of the solar radiation in a building. The fourth type of selectivity utilizes zero absorptance (unity reflectance) between 0.3-8.0 μm, unity absorptance between 8-13 μm and zero absorptance (unity reflectance) from 13 μm onwards. This is the underlying principle of a "radiative mirror" which undergoes emissive cooling below room temperature.

The two terms α and ϵ mentioned in the preceding section and used in the text merit a brief explanation. The absorptance α is defined as the ratio of the energy flux absorbed by the material to the incident energy flux. The emittance ϵ is the ratio of the energy radiated per unit area of the surface at a given temperature to that radiated by the unit area of a black body surface at the same temperature. All the values of emittance quoted in this article have been measured at 100°C and is denoted as ϵ_{100}. From Kirchoff's law, it is also clear that the higher the value of ϵ, the lower is the reflectance and vice versa. Thus, for an absorber surface to convert solar energy to thermal energy efficiently, the optical selectivity requirement is that the value of α must be high in the solar spectrum range (0.3-2.5 μm) and that of ϵ_{100} be low (reflectance high) beyond this range (2-2.5 μm onwards).

In the present work, the emphasis is on oxide surfaces/films which belong to the "dark mirror" and "heat mirror" categories.

Optically Selective Surfaces ("Dark Mirror" Type)

Though a single surface can give desirable characteristics, most practical selective surfaces/coatings consist of more than one layer. We will confine our discussion to only metal oxide layers which today hold the maximum potential.

Under the category of single surface metal oxides, the plasma resonance edge of the respective metals are shifted towards the IR region thereby increasing absorption in the visible region and simultaneously maintaining high reflectance in the IR region. The shifting of the plasma edge is, for example, due to localization of d band electrons of W and Re on oxidation to WO_3 and ReO_3, respectively[9].

The second category of multilayer surfaces could be further subdivided into four types, viz., (i) homogeneous semiconductor (metal oxide) film on metal, (ii) inhomogeneous semiconductor (metal oxide) on metal (iii) graded index coatings, and (iv) metal oxide on textured metal surfaces. The first type makes use of absorption in the metal oxide which is transparent to IR so that the long wavelength radiations are transmitted and are reflected by the underlying metal which is responsible for the low emittance of the entire structure. The absorption is mainly intrinsic and an example of this type is black Co (CoO) on stainless steel[10]. In the second type, the absorbing film is a composite or cermet consisting of metal particles suspended in a dielectric matrix (metal oxides). The optical absorption is mainly due to resonant scattering between particles which are small compared to the wavelength of radiation to be absorbed and are spaced far enough to act as independent scatterers. A well known example[11] of this type is black chrome which is a composite of Cr particles in a matrix of Cr_2O_3. The principle of the third type of coating is based on reducing the reflection losses of the absorber film by grading its refractive index from the bulk material value to that of air. Pigmented (with Ni or Co) anodized aluminium surface[12,13] is an example in which the gradient in the optical constants is achieved by varying the concentration of the metal particles in the pores of the Al_2O_3 film (which is created during the fabrication process) across the thickness of the oxide film. The fourth type exploits the principle of enhanced absorption in the textured surface due to multiple reflection of the incident radiation in addition to intrinsic absorption in the top oxide layer. A typical example is black Cu(CuO) on textured Cu substrate[14].

Structure of a Typical Selective Surface

An excellent example of the complexity of the surface structures necessary to bring about the desired selectivity in the optical properties is that of Ni pigmented anodized Al surface coatings. The surface coating is obtained by a two-step process. The first consists of the anodization of an Al foil. By controlling the anodization conditions it is possible to make the Al_2O_3 film porous in nature. The second step consists of filling up of the pores with Ni in a graded manner by an electrolytic technique. The embedded Ni particles in the parent Al_2O_3 matrix comprises the composite cermet type of structure. Figure 1 shows the cross-sectional view of the surface coating and composition depth profile of the constituents as measured by Auger analysis and sputter etching.

Figure 2 clearly illustrates how the optical constants n and k have been tailored across the thickness of the film to give rise to the optical selectivity shown in the inset. The low reflectivity and high absorptance in the solar spectrum region and high reflectivity (low emittance) in the IR region make this coating a candidate

for solar thermal applications. Results at two different wavelengths, namely, 0.496 μm (dashed curve) and 2 μm (solid curve) are shown in the figure. The k

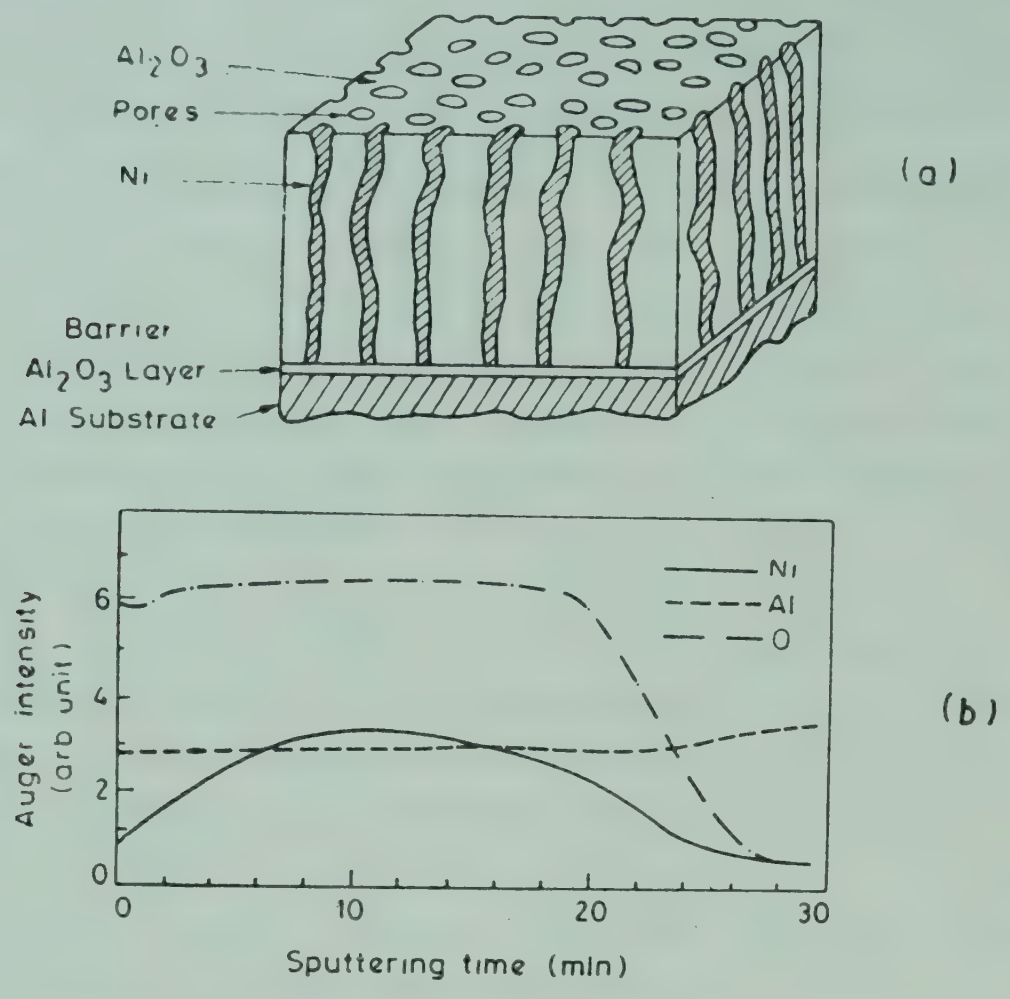

FIG. 1. Ni pigmented anodized Al : (a) structural model of the composite film and (b) Auger depth profile of the film showing the graded composition of Ni.

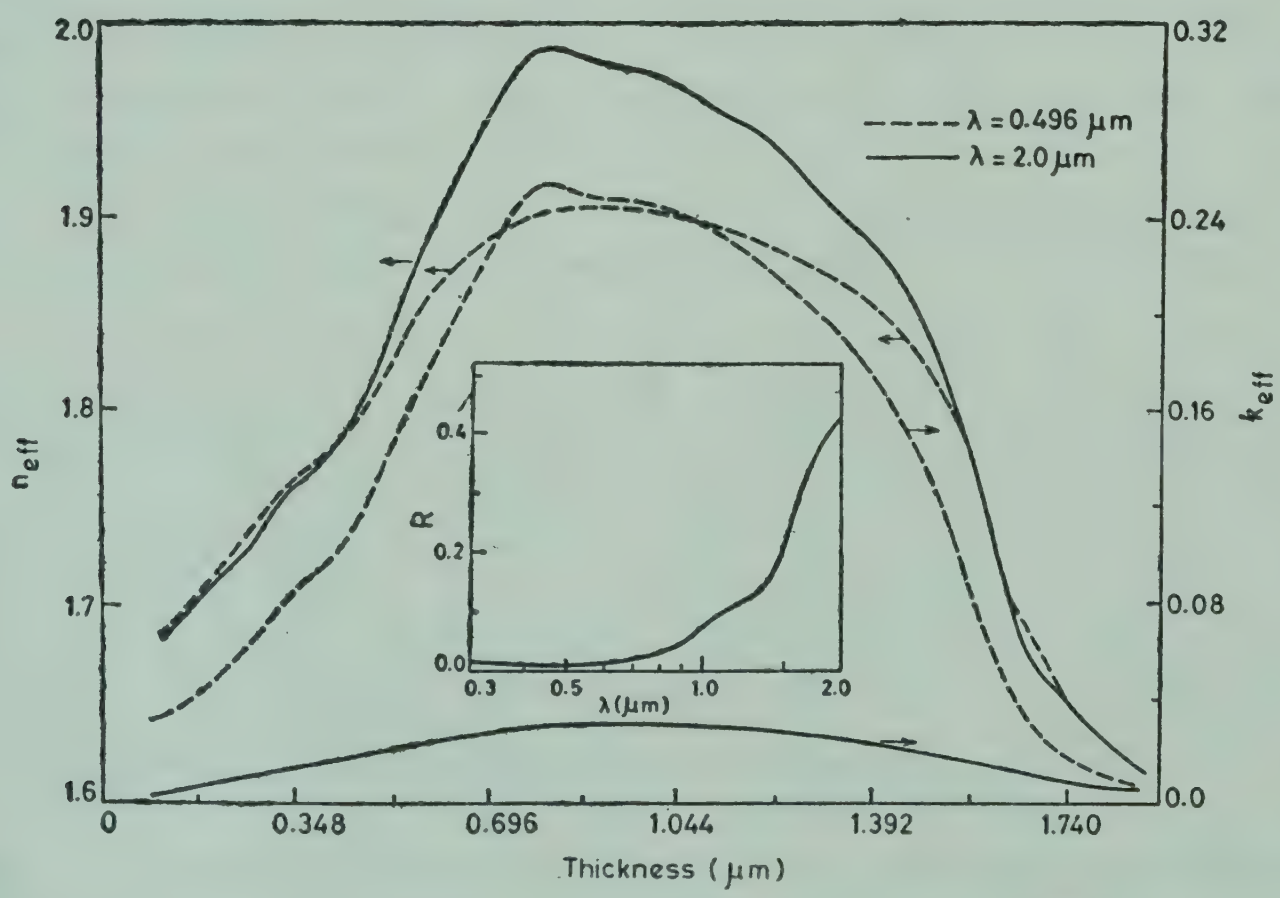

FIG. 2. Variation of optical constants n and k with thickness for two different wavelengths for Ni pigmented anodized Al coating. Inset shows the reflectance spectrum of the coating.

curve at 2 μm is significantly lower than at 0.496 μm for all the layers of the composite film and is attributed to a lowered absorption of the IR. Further, with increasing film thickness, the n and k values gradually increase, remain at a

maximum for intermediate thickness and then decreases gradually, with the k values going almost down to zero for the top layer. A very low value of k for the upper layers is desired for cutting down the reflection losses. Comparison of Figs. 1(b) and 2 very vividly brings out the important conclusion that the values of n and k and the composition of Ni are graded in an identical manner. The similarity amply demonstrates how optical selectivity has been obtained by a graded chemical composition. However, this is not the complete story as ESCA studies at various depths reveal that both Al and Ni exist in mixed elemental and corresponding oxide phases and the relative contents are also graded. More details are presented later. The complete structural model of the composite film as deduced from surface studies in addition to transmission and scanning electron microscopy studies is shown in Fig. 1(a). The figure shows the pores in the Al_2O_3 film which are partially filled by Ni particles.

The above example elucidates two significant aspects of the tailoring process for optical selectivity. The first is the unavoidable nature of complexity of the architecture of the films. The second is a result of the first and is the degree and necessity of sophisticated surface analytical techniques in understanding the construction of the entire structure. In fact, a detailed surface analysis supplemented with scanning and transmission electron microscopy result can only give complete information. Therefore, extensive use has been made of such surface analytical techniques as AES, Auger depth profiling, and ESCA, to obtain structural and metallurgical information of selective surfaces/coatings of various oxides.

Optically Selective Films ("Heat Mirror" Type)

For heat reflectors, the two main properties to be considered are high transmittance in the visible and high reflectance in the IR. The first is very conveniently obtained in the oxide films which have large optical bandgap ($\gtrsim$ 3.0 eV). Such a high bandgap leads to high resistivity (low free carrier concentration) in the intrinsic material. However, doping with appropriate materials which have shallow levels in the parent oxide lead to a degenerate behaviour with high carrier concentration. These foreign atoms tend to occupy the position of the host atom which is closest to it on the electronegativity scale. Thus, Sb in SnO_2 will tend to occupy the position of Sn while F and Cl will favour O site. The high carrier concentration of the doped oxide film exhibits plasma resonance in the IR region. The plasma resonance frequency is given by the expression

$$\omega_p = \sqrt{\frac{4\pi N e^2}{m^* \epsilon_\infty}} \qquad \ldots(1)$$

where N is the carrier concentration, e is the electronic charge, m^* is the electron effective mass and ϵ_∞ is the high frequency optical dielectric constant.

For frequencies $\omega > \omega_p$, the incoming radiation propagates through the medium and accounts for the high visible transmittance. For $\omega < \omega_p$ (IR regime), the radiation energy does not propagate through the medium and is completely reflected. Drude theory (15) is generally invoked to explain the optical behaviour in these degenerate semiconducting materials. According to this theory, the reflectance in

the IR region first goes through a minimum before it increases to its high saturation value. The position of the reflectance minimum is given by

$$\lambda_m = 2\pi c[\epsilon_0(\epsilon_\infty - 1)m^*/Ne^2]^{1/2} \quad \ldots(2)$$

where c is the velocity of light. The above expression shows that the higher the value of the carrier concentration the smaller is the value of λ_m. This means that the onset of plasma can be shifted on the wavelength scale by changing the carrier concentration. Further, the slope of the reflectance curve beyond λ_m increases with increasing mobility, as expected on the basis of the Drude theory[15]. The theory also shows that the value of the reflectivity in the plasma resonance region depends on the electronic mobility—the higher the mobility the higher is the reflectance.

Solar Selective Oxide Films

The earlier sections expose the complexity of the coatings required for practical applications. Such structures require specialized and even unique deposition techniques. Surface analytical techniques (mainly AES, depth profiling, and ESCA) provide the most powerful way of grasping the anatomy of the coatings. We have developed several oxide based optically selective films in our Laboratory for different types of photothermal applications. The following describes the coatings, their relevant properties, and results of surface analysis. Based on the characterization results, the structures obtained are discussed.

Electroless Nickel Black[16]

An electroless technique has been used to deposit Ni black on two types of substrates, namely, galvanized iron (GI) and zincated Al. In both cases, the presence of Zn on the substrate was necessary for chemical conversion process. The deposition bath was basic in nature and had zinc sulphate, sodium hypophosphite, and sodium acetate as the major constituents. The deposition temperature was optimized at 27°C which led to the best values of α and ϵ_{100} (value of ϵ measured at 100°C). These values were 0.94 and 0.10, respectively, for the coatings on GI and 0.94 and 0.36 for those on zincated Al. Both types of coatings were stable up to 250°C in air. The lower emittance in the former case is due to higher total reflectivity in IR compared to the latter case.

Auger analysis on the surface of the coatings revealed the predominant existence of Ni, Zn, and O, P and S were also detected on the surface but their concentrations decreased to zero on sputter etching. The Auger depth profiles of Ni, Zn, and O for both types of films are shown in Fig. 3. The presence of Zn throughout the thickness of film suggests the outward diffusion of Zn from the substrate during the growth of the film. The left side of the profiles in Fig. 3 corresponds to the film whereas the right side where only Zn is present corresponds to the substrate. For the coating on GI [see Fig. 3 (a)], the concentration of Zn and Ni are quite uniform throughout the thickness of the coating. The small initial increase in the Ni and Zn content is attributed to the small decrease in the O signal as well as the concentrations of P and S decreasing to zero. For the coating on zincated Al (see Fig. 3(b)), the concentration of Ni keeps increasing down to the film/substrate interface with a concomitant decrease in Zn.

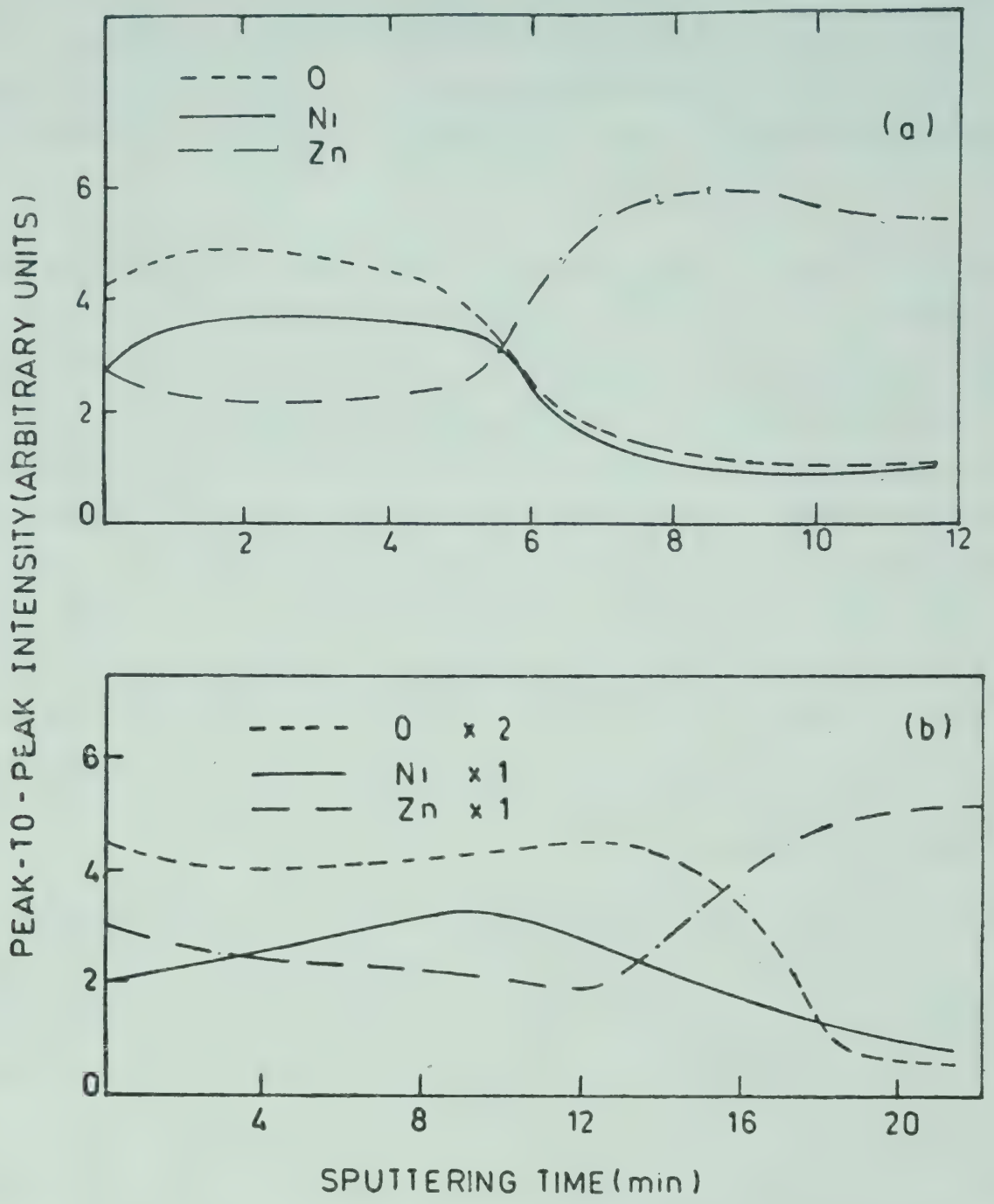

FIG. 3. Auger depth profile of electroless Ni black on (a) GI substrate and (b) zincated Al substrate. Only the Ni, Zn, and O signals are shown.

ESCA studies reveal that Ni is present as a mixture of elemental Ni and NiO. Zn is present in the elemental state throughout the thickness of the film. The coatings, therefore, consist of a homogeneous mixture of predominantly Ni, NiO, and Zn. The optical properties of this system basically corresponds to a composite of metal plus metal oxide on a metal substrate though the coatings of zincated Al also showed a graded composition. For the sake of completeness, it should be mentioned that electron diffraction studies have also revealed the existence of Ni-Zn alloy (which cannot be detected by ESCA), and traces of Ni_2O_3 and Ni_7P_3.

Electroless Molybdenum Black[17]

The electroless technique has also been used to deposit black MoO_3 coatings on GI and zincated Al substrates. The electroless bath consists of ammonia and paramolybdate ions. The properties of the MoO_3 films on both types of substrates are qualitatively similar. For an optimized deposition temperature of 32°C, the films on GI had values of α and ϵ_{100} equal to 0.91 and 0.09, respectively, whereas those on zincated Al had values of 0.91 and 0.24, respectively. Here too, the total reflectivity in the IR region was higher in the former case. It may also be

noted that coatings on GI exhibit higher specular reflectance component compared to those on zincated Al which exhibit a diffuse black appearance. This phenomenon is also valid for the earlier case of black Ni. The black MoO_3 films have been found to be quite stable up to about 200–250°C in air as monitored by the values of α and ϵ_{100}.

The results of Auger depth profiling of the MoO_3 specimens on both types of substrates are shown in Fig. 4. The behaviour is similar in nature in both cases. The composition is graded from the surface of the film to the film/substrate interface. The Mo concentration shows a maximum slightly below the interface beyond which the concentration gradually decreases to zero on reaching the interface. The Zn concentration exhibits a complementary behaviour with a minimum in the region where the Mo peak shows a maximum. Electron diffraction has been used to show that the film consists of only MoO_3. This is an example of an oxide with metal composite on a metal substrate where the composite is also graded across the thickness of the film. The presence of Zn is due to diffusion from the substrate during film formation since no Zn component was present in the deposition bath.

Ni Pigmented Anodized Aluminium[13]

The salient features of this coating has been discussed earlier. Here, a more complete work is presented. The diameter, spacing, and height of the pores in the anodically grown Al_2O_3 film can be controlled by the anodization conditions. Typical values of pore diameter, pore spacing, and height of pores obtained for

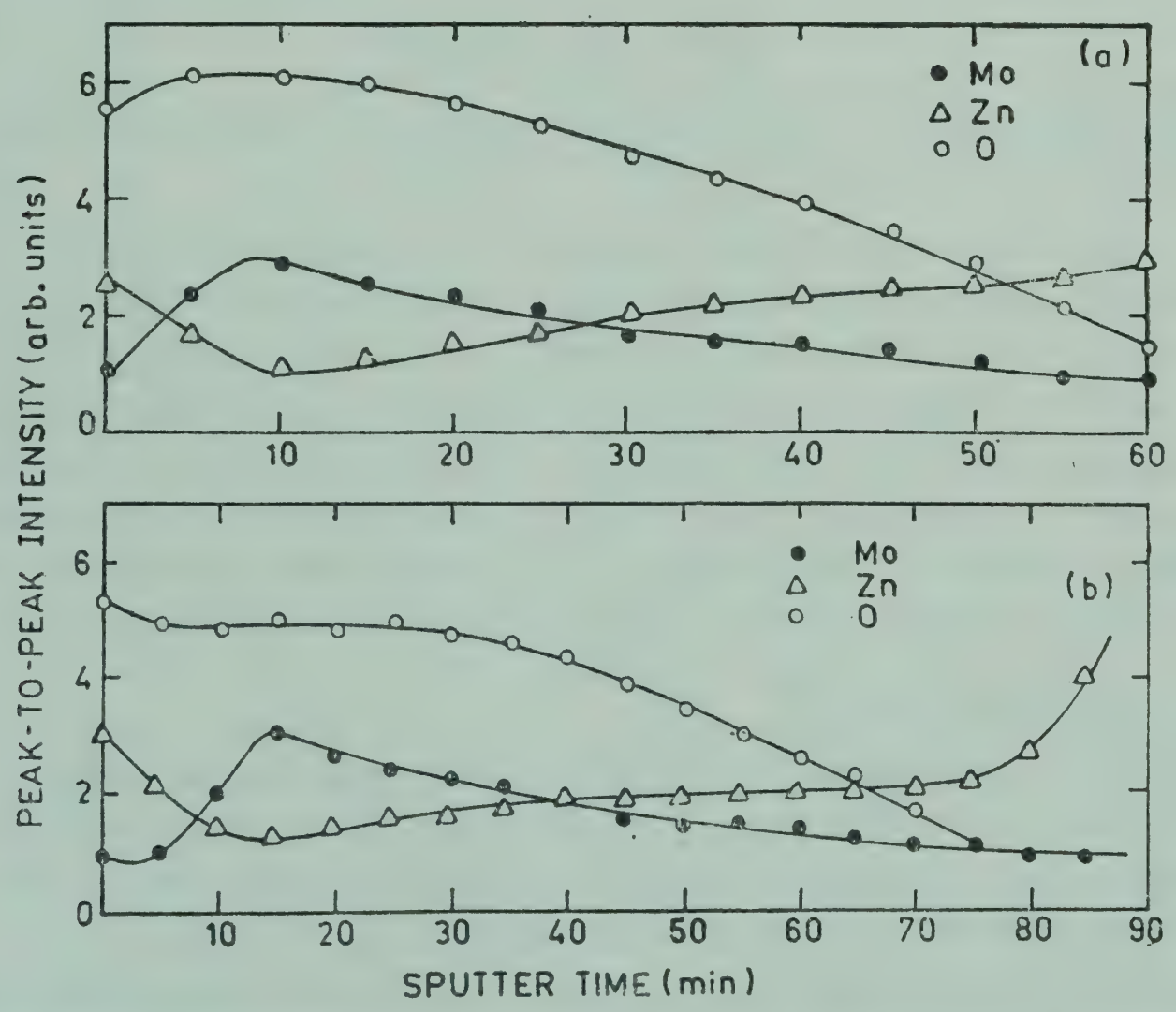

FIG. 4. Auger depth profile of electroless Mo black on (a) GI substrate and (b) zincated Al substrate. The low energy (186 eV) peak of Mo was monitored.

good quality selective coatings are ~ 300 Å, ~ 2500 Å, and ~ 5000 Å, respectively. The values of α and ϵ_{100} for three types of Ni pigmented anodized Al films (I, II and III) corresponding to three types of anodization baths are given in Table I. The three anodization baths were (i) 50 wt. per cent H_3PO_4 (coating I), (ii) 50 wt. per cent H_3PO_4 + 15 wt. per cent H_2SO_4 in a volume ratio of 1 : 1 (coating II), and (iii) 15 wt. per cent H_2SO_4 (coating III).

TABLE I

Values of α and ϵ_{100} for Ni pigmented anodized Al coatings I, II and III

Coating	α	ϵ_{100}
I	0.90	0.06
II	0.95	0.34
III	0.96	0.49

Scanning electron microscopy and replica techniques in transmission electron microscopy have provided information about the geometry of the pores and the surrounding matrix. Auger, depth profiling, and ESCA techniques have revealed the chemical composition of the films. In the Auger analysis, the scanning for the low energy Al peaks was done in the 35–95 eV range and for high energy Al peaks in the 1340–1425 eV range, so that the 55 and 1378 eV peaks of oxidized Al and 65 and 1396 eV peaks of elemental Al can be studied. The surface of all the three coatings showed both the peaks of Al corresponding to Al_2O_3. Sputter profiling revealed elemental Al peaks in addition to the oxidized Al peaks. However, the relative concentration of the elemental Al peak throughout the film was maximum in coating I and minimum in coating III. Thus, the H_3SO_4 anodized films contain larger amounts of elemental Al compared to the H_2PO_4 anodized films. The depth profiles for Al, Ni, and O for the three different coatings are shown in Fig. 5. The sputtering rates were same in all cases and, therefore, from the sputtering times required to etch the entire Al_2O_3 film, one concludes that thicknesses are very different in all the cases. Also, the Ni content is graded across the thickness though in cases II and III, it is present right from the surface downwards whereas in case I, it appears only after some sputter etching.

ESCA results of the Ni $2p_{1/2}$ and $2p_{3/2}$ peaks on the three coatings after sputter cleaning are shown in Fig 6. Coating I reveals elemental Ni 2p peaks [see Fig. 6 (a)] right across the thickness of the film. Coatings II and III exhibit an additional strong broad satellite band [see Fig. 6(b) and (c)] above the principal $2p_{3/2}$ line. This is attributed to the presence of NiO. However, in the inner layers, Ni is present only in the elemental form. Therefore, in cases II and III, the top layers consist of a mixture of elemental Ni and NiO whereas the lower layers consist of just the metal.

The Ni pigmented anodized Al films are a good example of a composite of metal and dielectric over a metal surface in which optical selectivity is obtained by

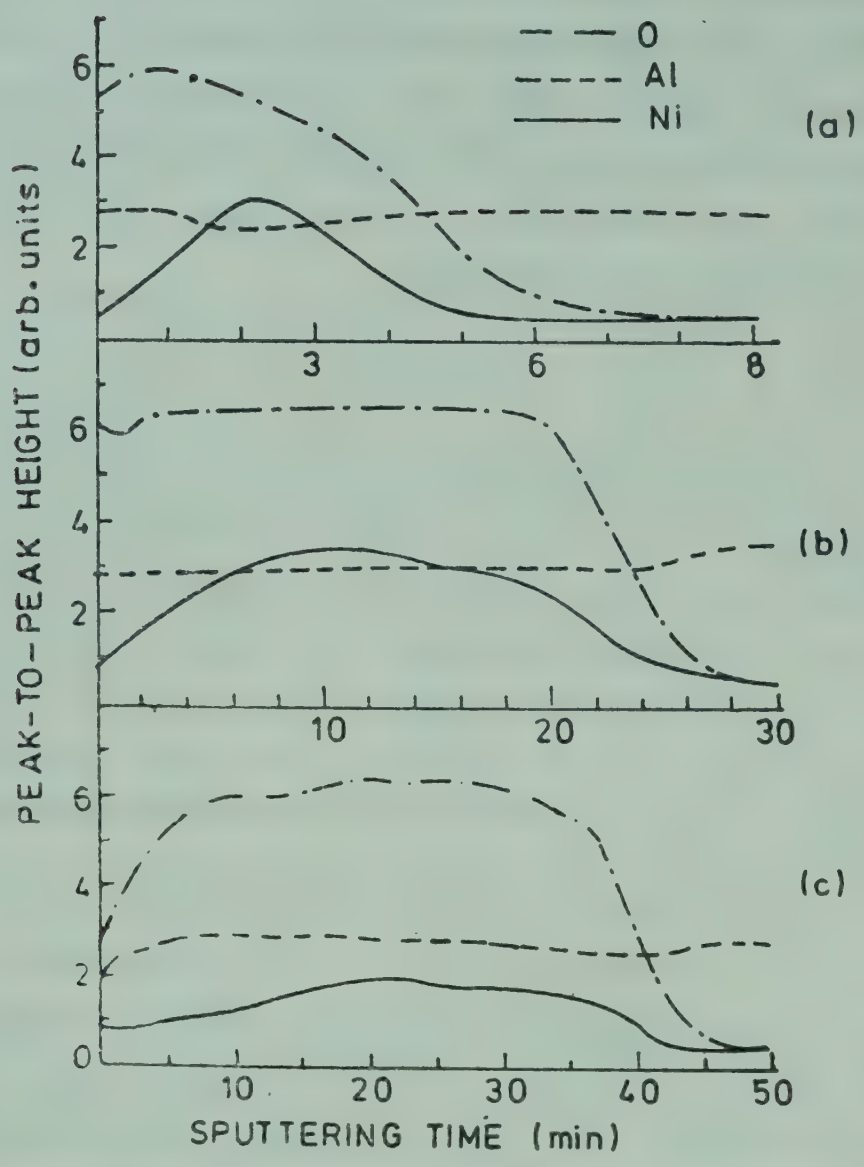

FIG. 5. Auger depth profile of Ni pigmented Al_2O_3 coatings: (a) I, (b) II, and (c) III.

grading the refractive index which in turn is achieved by grading the concentration of the Ni particles.

Cobalt Pigmented Anodized Aluminium

Here the principle of operation as well as fabrication is similar to the earlier case of Ni pigmented Al_2O_3. The Ni electrolysis step is substituted by Co electrolysis step which leads to Co deposition in the pores of the Al_2O_3 matrix. The values of α and ϵ_{100} are 0.93 and 0.42, respectively, for the Co pigmented film in which the anodization is done as coating II in the earlier case.

Auger depth profiling shows that Co is detected only after a certain amount of Al_2O_3 is sputtered off. This implies that Co is well embedded in the pores of the Al_2O_3 film. The rate of increase in the Co concentration during sputtering and the subsequent rate of decrease as one reaches the bottom of the film are relatively steeper than in the corresponding Ni pigmented films. ESCA analysis of the Co $2p_{1/2}$ and $2p_{3/2}$ levels showed that it exists in the elemental form. This coating is yet another example of graded index leading to optical selectivity.

Black Copper by Chemical Conversion[14]

These coatings have been prepared by chemical conversion of the surface of a Cu foil to black Cu. The chemical bath is alkaline in nature consisting of sodium hydroxide and peroxysulphate and serves the dual purpose of etching the Cu foil surface as well as deposition of the film. The etching leads to a textured surface

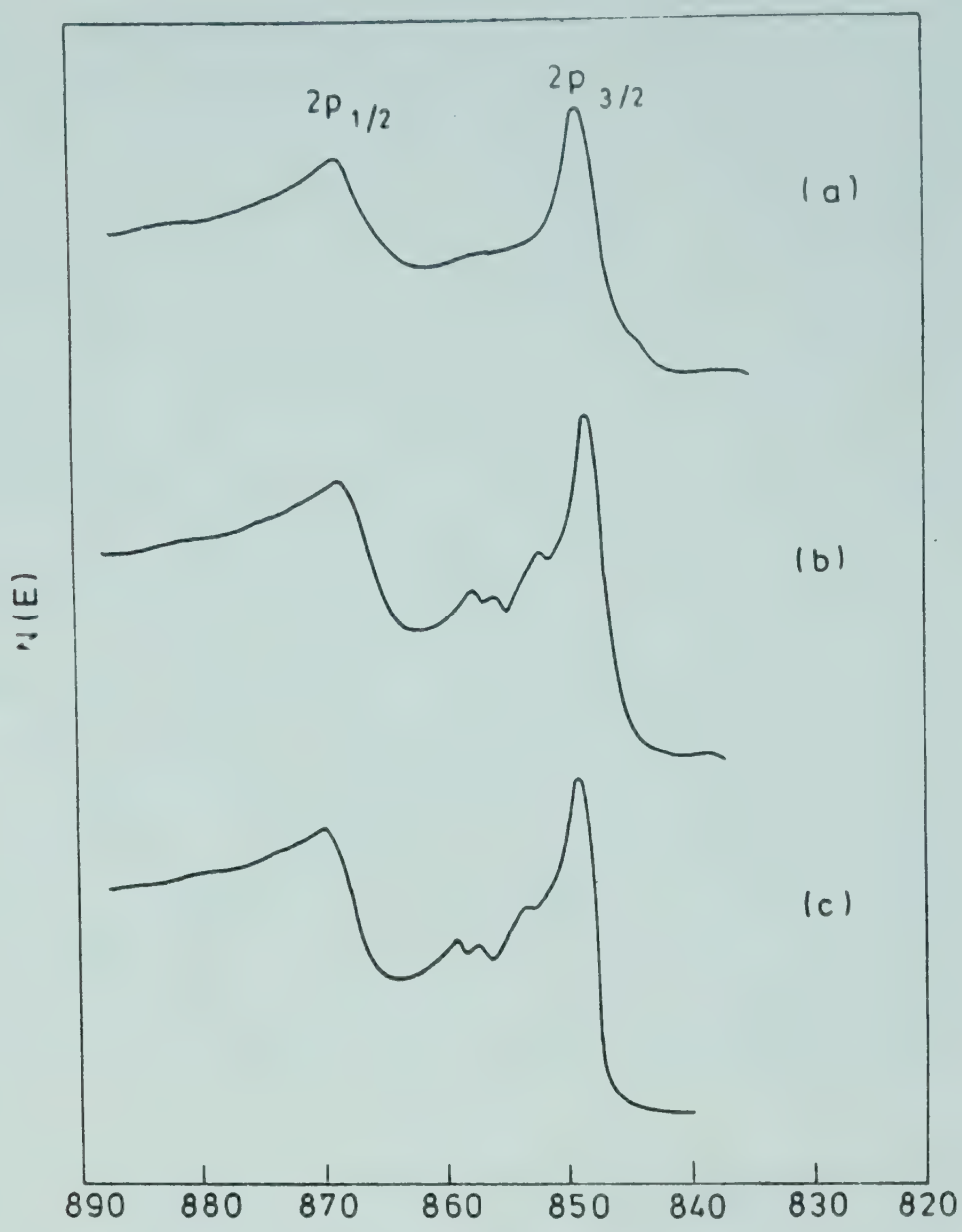

FIG. 6. ESCA spectra of Ni 2p peaks of Ni pigmented Al_2O_3 for coatings (a) I, (b) II, and (c) III after sputtering clearing.

and the film appears as a black velvet. Figure 7 shows the surface microstructure of the film as seen in the SEM. The value of α is as high as ~ 0.98 and ϵ_{100} is ~ 0.2. The high value of α is attributed to the extremely low ($\lesssim 2$ per cent) reflection losses in the solar absorption region which is shown in Fig. 8. The figure also shows high (~ 80 per cent) reflectance in the IR region which accounts for the relatively low emittance value.

Use of surface analytical techniques has established that the coating is simply a thin layer of CuO/Cu_2O on the texturized Cu substrate. The Cu $2p_{1/2}$ and $2p_{3/2}$ ESCA peaks on the surface of the black Cu film and after ~ 100 Å (equivalent thickness of Ta_2O_5) are shown in Fig. 9. The surface spectrum corresponds to CuO while the sputtered specimen shows Cu_2O. Further sputtering gives evidence of only elemental Cu corresponding to the substrate.

In this case, the absorption takes place primarily due to trapping of incoming radiation in the highly textured surface and partly due to absorption in the CuO/Cu_2O layer. Another role of the CuO layer is probably that of an anti-reflection coating. In the IR region (≥ 2.5 μm), the columnar textured structure is transparent to the incoming radiation only to be strongly reflected by the

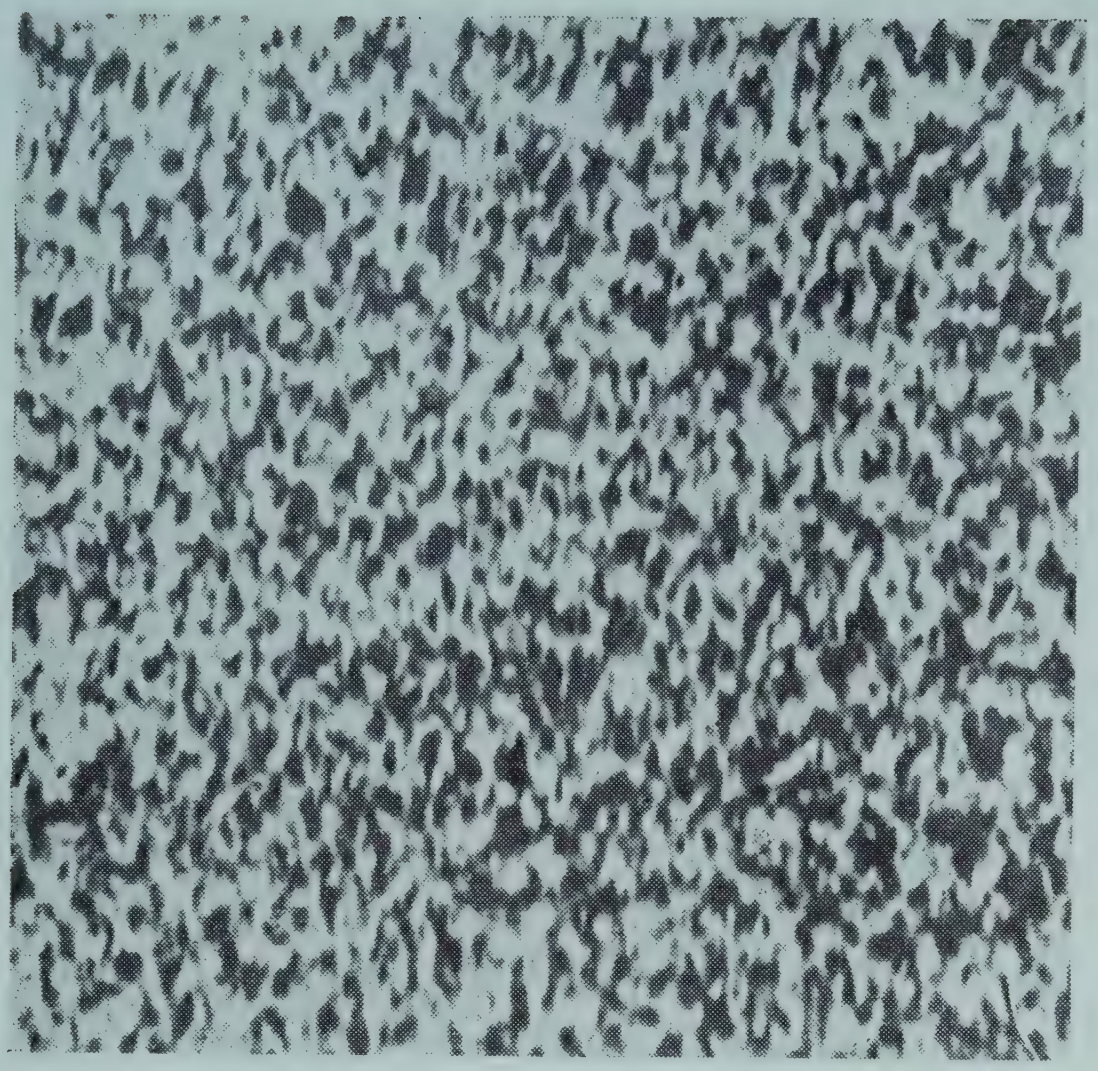

FIG. 7. SEM micrograph of black Cu prepared by chemical conversion.

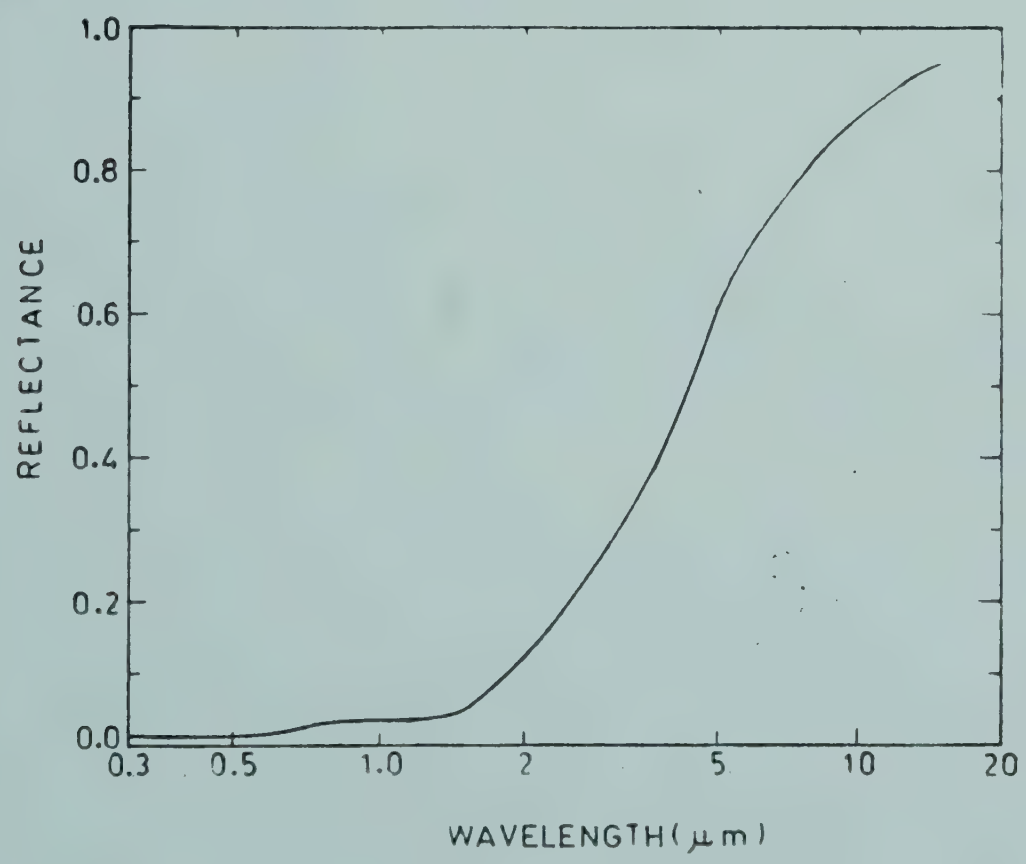

FIG. 8. Reflectance. Vs wavelength of the black Cu films.

underlying Cu surface. Thus, the absorption and reflection processes have been suitably tailored to give rise to the spectral selectivity.

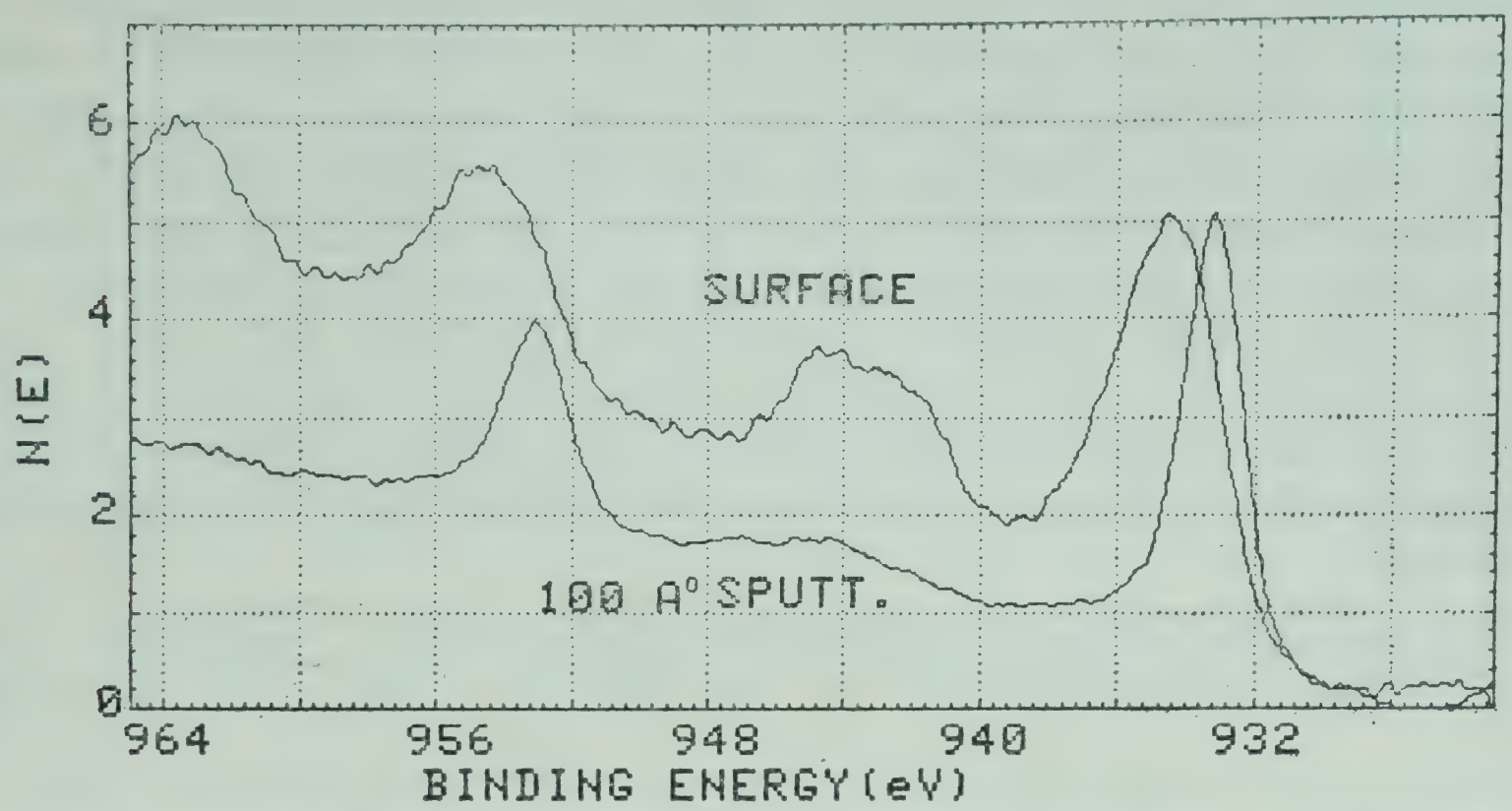

FIG. 9 . ESCA spectra of Cu $2p_{1/2}$ and $2p_{3/2}$ of black Cu films on the surface and after 100 Å of sputtering.

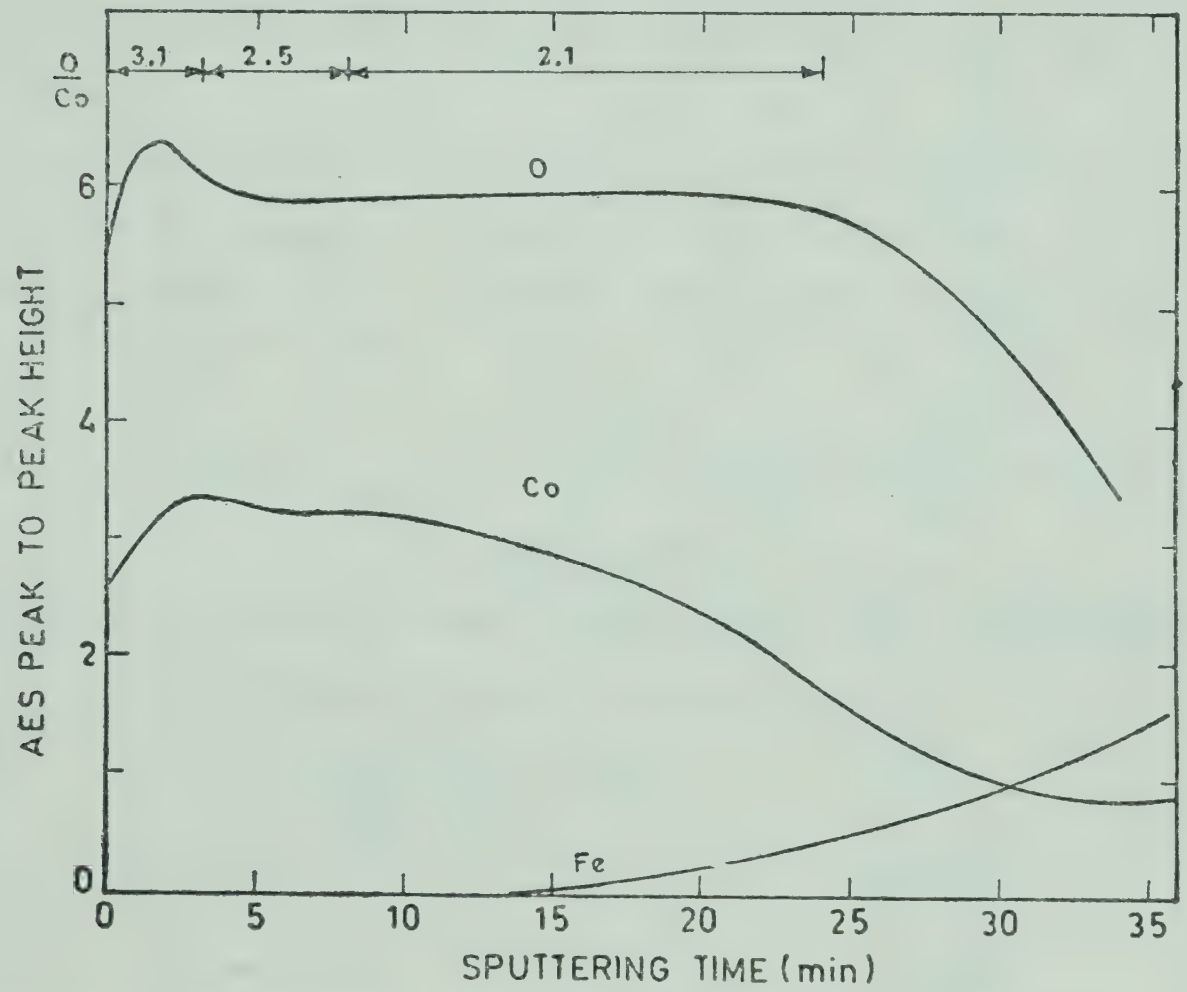

FIG. 10. Auger depth profile of black CoO films on stainless steel substrate prepared by spray pyrolysis. The O to Co ratio at various depths is also shown.

Spray Pyrolysed Black Cobalt[10]

Black Co films have been prepared on stainless steel substrates by solution spray pyrolysis technique. Typical values of α and ϵ_{100} obtained are 0.88 and 0.2, respectively.

Auger analysis showed that black Co films consist of only Co and O. The Auger depth profile is shown in Fig. 10. The onset of the Fe signal corresponds to

the substrate. The O to Co ratio is the highest (3.1) on the surface and decreases to saturate at 2.1 corresponding to the bulk of the film. These values suggest[18] that the bulk of the film exists predominantly in the CoO phase whereas the top layers contain Co_3O_4. The results have been confirmed by taking the ESCA peaks of Co $2p_{1/2}$ and $2p_{3/2}$ on the surface and in the bulk of the film. Figure 11 shows Co 2p peaks in the bulk of the film where the Auger O to Co ratio is 2.1. The strong satellite peaks suggest[19–21] the existence of CoO. ESCA scan on the surface shows the same general features. However, the Co $2p_{1/2}$ satellite peak in this case is weak. This weak satellite peak is a characteristic feature of Co_3O_4[20]. Based on the above results, it is concluded that Co_3O_4 exists only in the upper layers of the film.

An interesting feature in the reflection characteristics of the coating is a hump at $\sim$ 1.05 μm and is shown in Fig. 12. The reflectance value at this wavelength

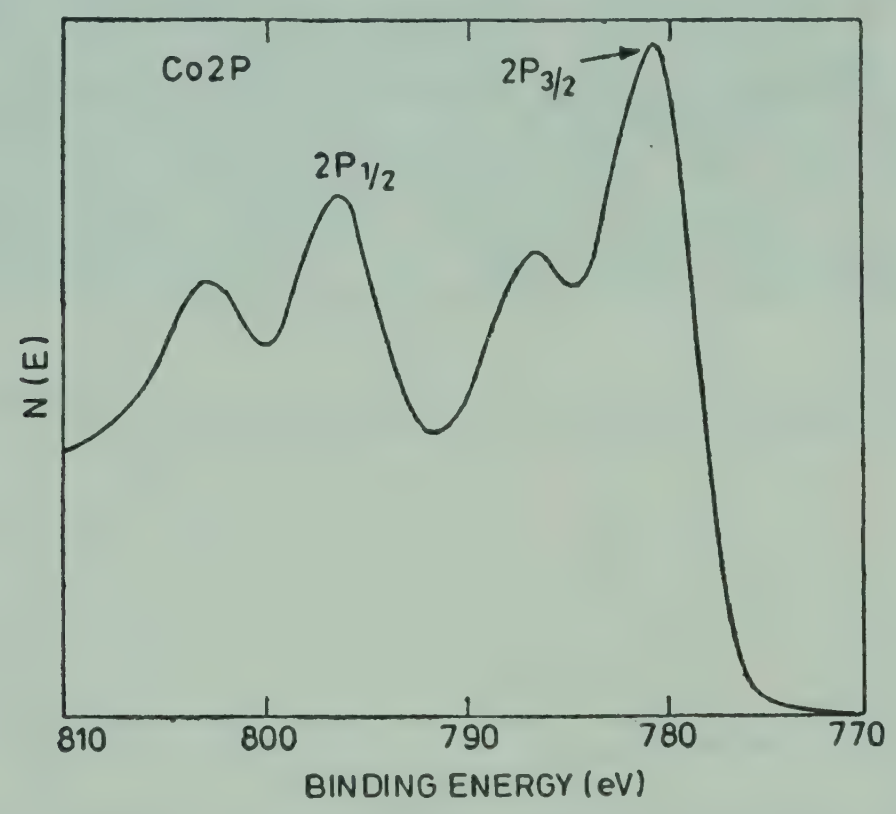

FIG. 11. ESCA spectrum of Co $2p_{1/2}$ and $2p_{3/2}$ peaks of spray pyrolysed CoO in the bulk of the film.

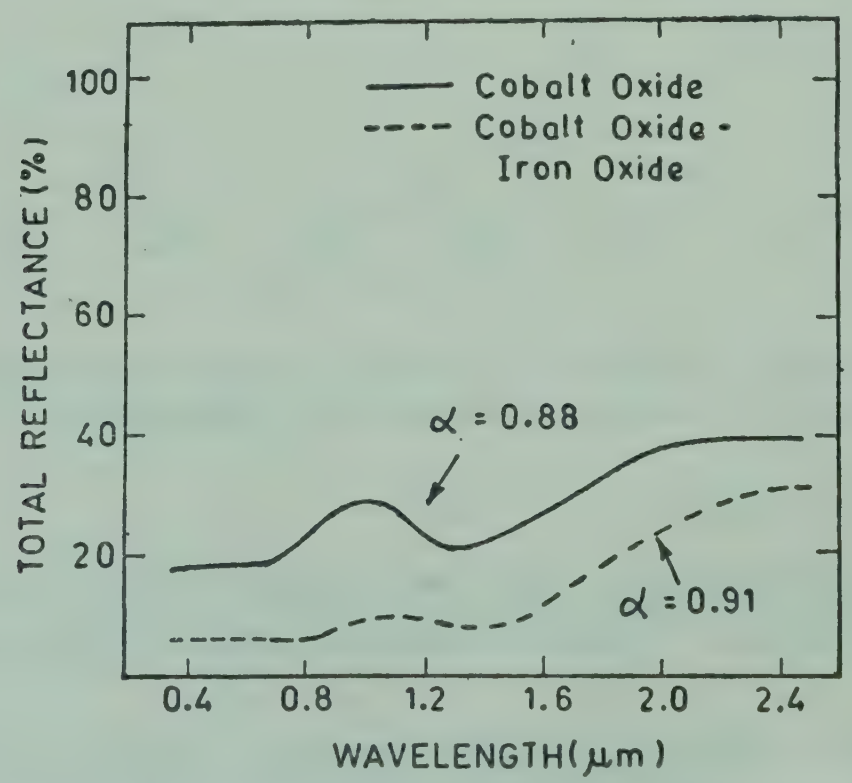

FIG. 12. Total reflectance versus wavelength of sprayed CoO and CoO + Fe_2O_3 films.

is ~ 30 per cent resulting in considerable loss of the incoming radiation. This hump is characteristic of CoO.

This coating is an example of semiconductor oxide on metal substrate. The absorption is primarily intrinsic in nature in the oxide film. The upper layers of Co_3O_4 helps in enhancing the absorptance since Co_3O_4 is known to be a better absorber than CoO. The underlying steel substrate provides the low emissivity.

Cobalt Oxide + Iron Oxide Films by Spray Pyrolysis

This work is an extension of the single component CoO on stainless steel by introducing Fe salts also in the spray solution. The motivation for mixing Fe_2O_3 with CoO is to lower the reflectance hump at 1.05 μm (see Fig. 12), since Fe_2O_3 has a lower refractive index. The lower reflectance is indeed achieved as shown in the same figure. The lowering of the reflectance leads to an increase in the value of α to 0.91 while the ϵ_{100} remains at 0.2.

Auger depth profiling shows that the concentrations of Fe, Co and O are reasonably uniform over the film thickness. ESCA analysis establishes the existence of Fe_2O_3 and CoO in the films. The surface contains some traces of Co_3O_4.

Optical selectivity in these mixed film is by the same mechanism as in the single component CoO films. However, the mixed films provide improved refractive index matching.

Chromium Oxide—Iron Oxide Mixed Films by Chemical Conversion

Mixed films of chromium oxide and iron oxide have been prepared on stainless steel substrates by a chemical conversion technique which involves the dipping of the substrates in suitable acidic baths. The best values of α and ϵ_{100} obtained are 0.91 and 0.12, respectively. A typical depth profile of the coating is shown in Fig. 13. The Fe concentration is seen to be graded increasing

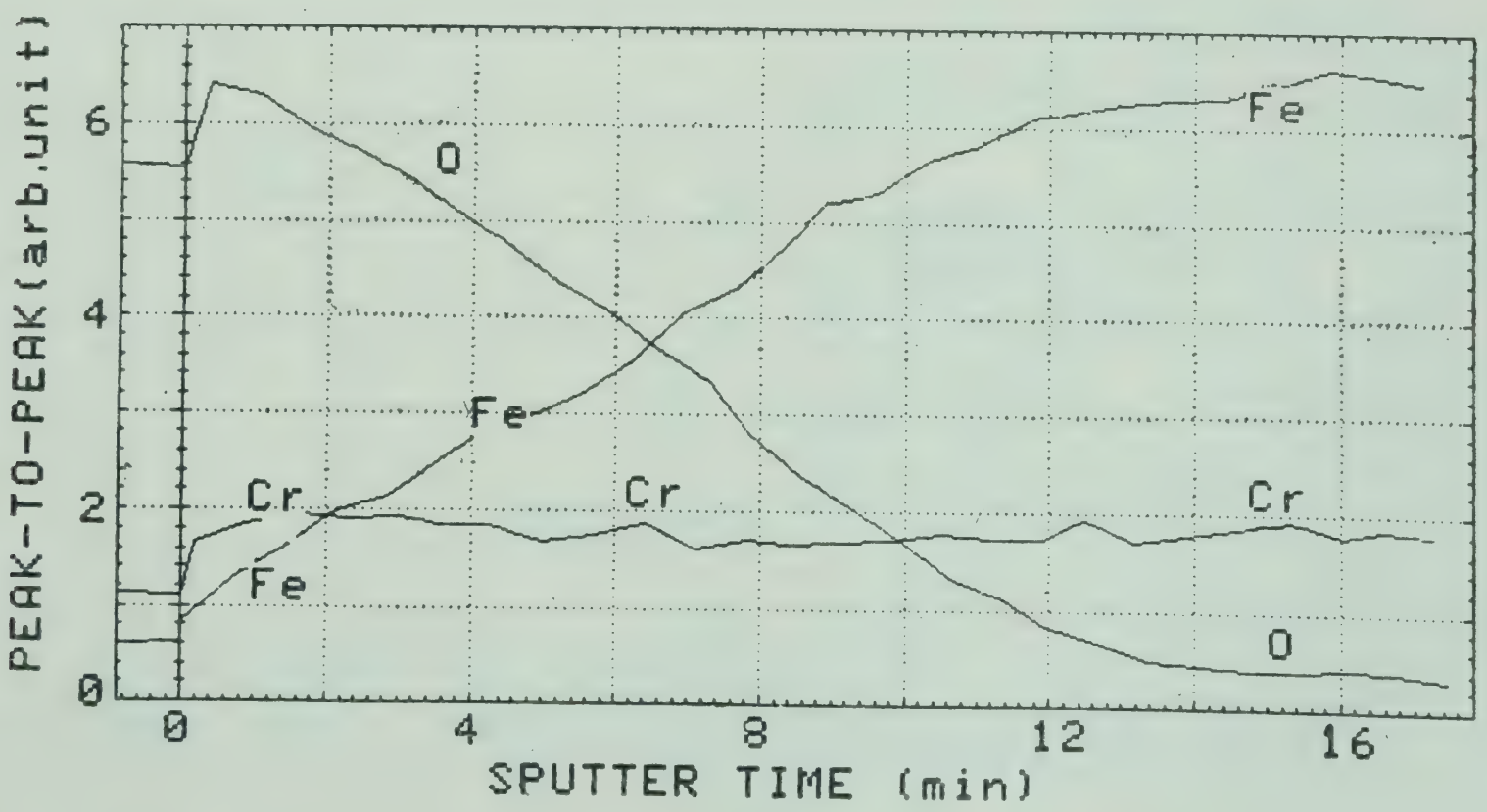

FIG. 13. Depth profile of Cr_2O_3-Fe_2O_3(Fe) prepared by chemical conversion.

towards the substrate. ESCA studies have been carried out at various depths of the film. The bulk of the film consists of Cr_2O_3, Fe_2O_3, and elemental iron. The 2p ESCA peacks of Fe at three different depths are shown in Fig. 14. The surface (after sputter cleaning) shows the presence of the Fe_2O_3 phase with a small amount of elemental Fe. At an intermediate depth, both elemental Fe and Fe_2O_3 exist with an increased concentration of elemental Fe. Near the film/substrate interface only elemental Fe is detected. This shows that the increasing Fe concentration with sputtering shown in Fig. 13 is due to an increase in the elemental Fe concentration. The optical selectivity of these films is attributed to a combination of intrinsic absorption in the oxides and interference effects amongst the various components which are suitably graded. The low emittance is due to the underlying Fe and stainless steel substrate.

Optically Selective Heat Reflectors

From Eq. (2) it is clear that the position of the plasma reflection edge can be suitably tailored by changing the carrier concentration in the films. Therefore, depending on the application, the edge is defined so that heat is reflected in a predetermined wavelength regime. Thus, if heat losses from a room are to be curtailed the windows must be coated in order to reflect at a wavelength corresponding to room temperature ($\sim$ 300 K). From Wien's law

$$\lambda_{max} = \frac{2898}{T}\,\mu m \qquad \ldots(3)$$

the wavelength at which emission is maximum for 25°C is $\sim$ 9.7 μm. Hence, the plasma edge for such coatings should be below $\sim$ 9.7 μm in order to store a large fraction of the heat. However, if heat from the sun has to be kept out of the room, the window coatings must start reflecting right from the beginning of the

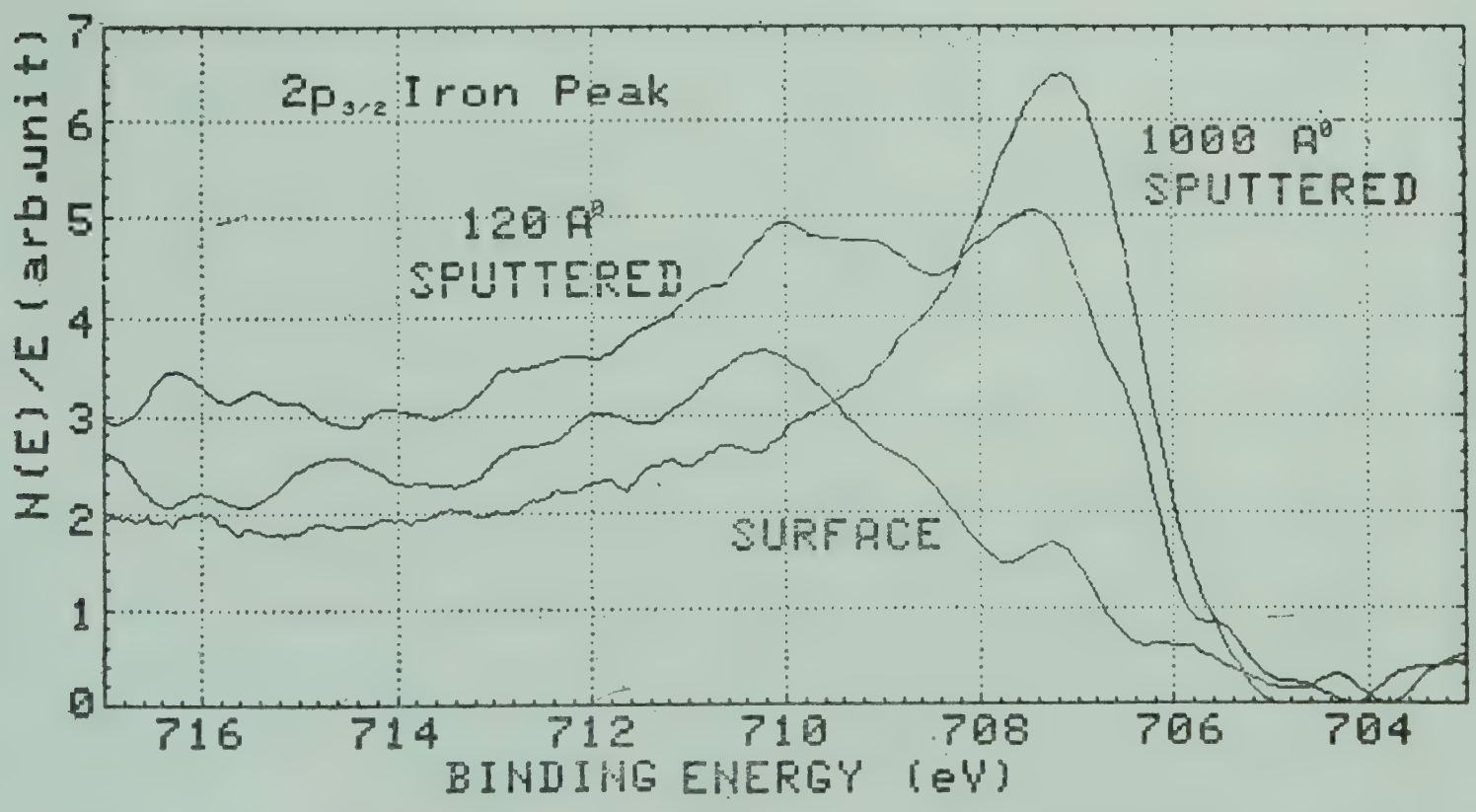

FIG. 14. ESCA peaks of Fe 2p at three different depths of Cr_2O_3-Fe_2O_3(Fe) prepared by chemical conversion.

IR (0.8 μm) onwards. Two different oxide films which have been developed are discussed in the following.

Tin Oxide Films by Spray Technique[22,23]

Spray deposited films of SnO_x doped with F or Sb are ideal materials as heat reflectors. A typical transmittance and reflectance spectrum of SnO_x films doped with different concentrations of Sb is shown in Fig. 15. A high ($\sim$ 80 per cent) transmittance is obtained in the visible region and high reflectance in the IR. The plasma edge shifts towards shorter wavelengths on increasing the Sb concentration in the films. The atomic concentration of Sb shown in the figure correspond to concentrations in the solution. A typical AES spectrum for the 65 at. per cent F (in solution) in SnO_x films is shown in Fig. 16. The concentration of F in the film as calculated from the figure is only $\sim$ 0.8 at. per cent. This low value as compared to the concentration in the solution is due to the high volatile nature of NH_4F which is used for the doping. Study of 3d ESCA peak width and position of Sn shows that it is present in the SnO_2 phase.

Zinc Oxide Films by Spray Technique[24]

Degenerate films of ZnO doped with In have been prepared by a spray technique. These films exhibit the plasma edge generally at higher wavelengths compared to the F or Sb doped SnO_x films. The edge can be shifted by changing the In concentration. Auger depth profiling has shown that the concentrations of Zn, In, and O are constant througout the thickness of the film. ESCA studies reveal that Zn and In exist in the oxidised state.

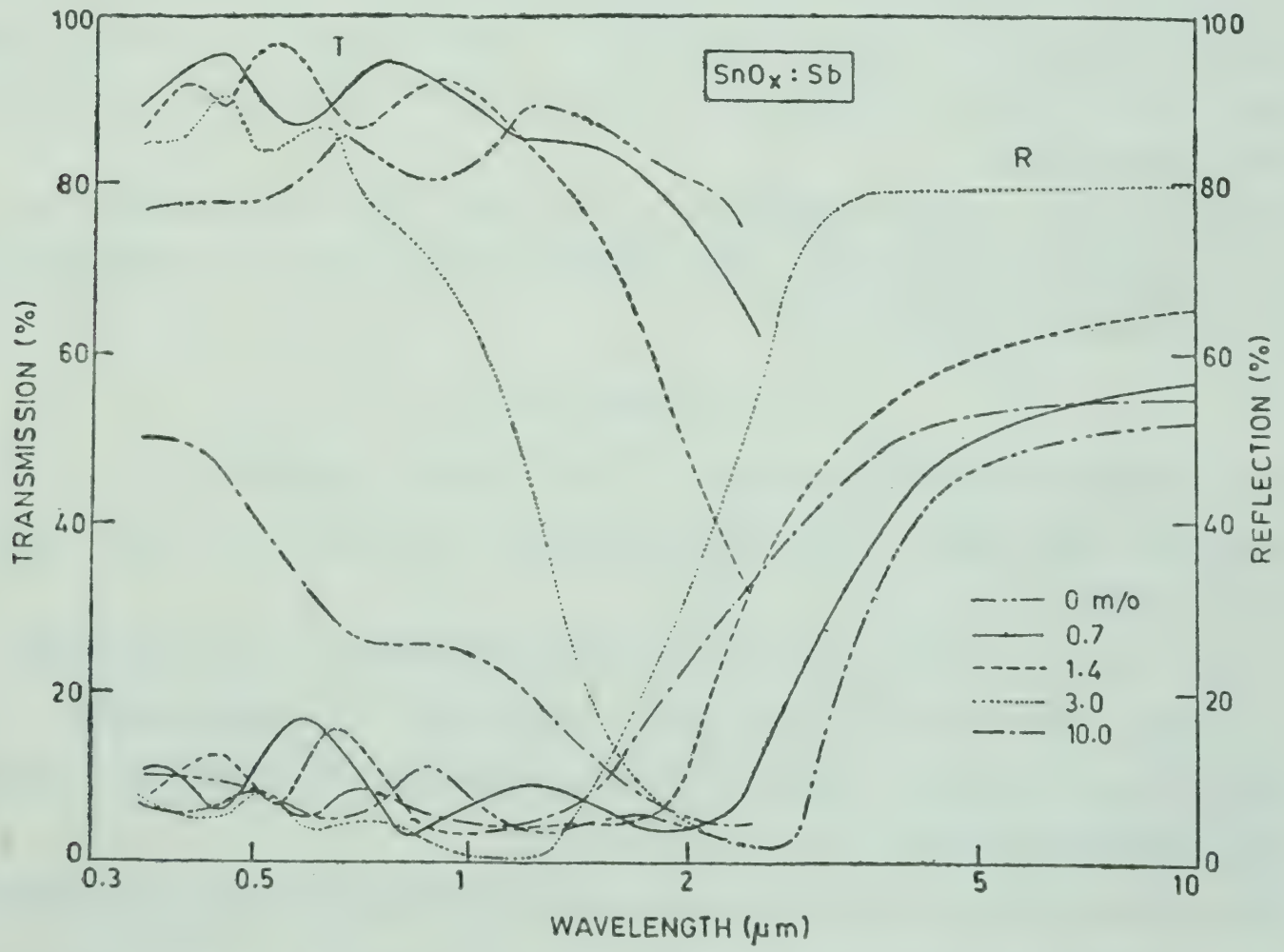

FIG. 15. Transmittance and reflectance of SnO_x : Sb films as a function of wavelength for different doping concentrations of Sb.

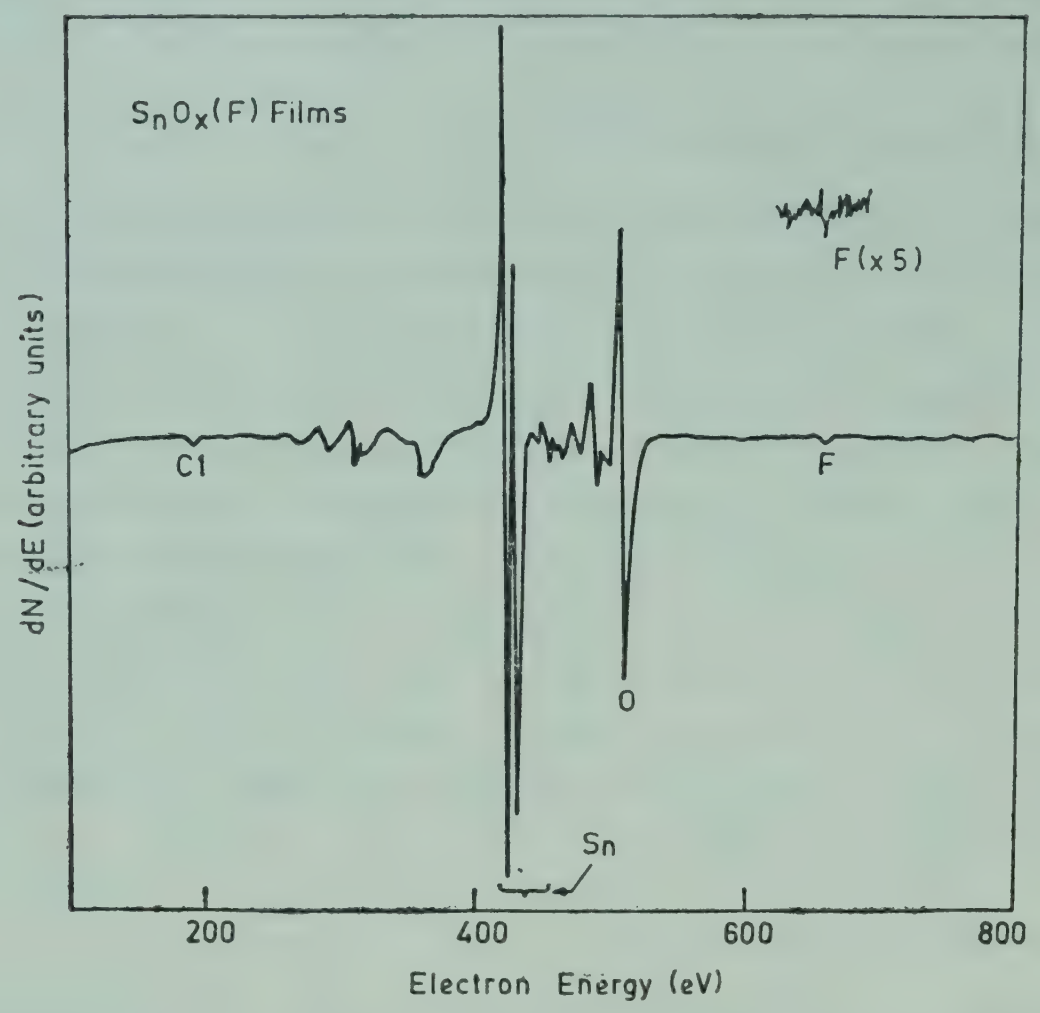

FIG. 16. AES spectrum of SnO_x : F (65 at. % in solution) films prepared by spray technique. The concentration of *F* in the films is only ~ 0.8 %.

CONCLUSIONS

Detailed understanding of the physical mechanisms responsible for optical selectivity of various oxide surfaces/coatings, and their quantitative analysis in terms of Effective Medium theories have been made possible by the application of a number of analytical techniques. Physical mechanisms prevailing in a particular case are determined by the depth profiling of the composition and microstructural details of the various components.

As a result of the surface analysis, it is now possible to tailor the optical selectivity of a surface by designing and fabricating a coating of appropriate composition profile and microstructure.

ACKNOWLEDGEMENTS

This work is based on the Ph.D. theses of our following students :

1. Selective Black Surfaces for Photothermal Conversion of Solar Energy—by P K Gogna.
2. Chemically Deposited Multilayer Selective Surfaces—by G B Reddy.
3. Spectrally Selective Black Cobalt Coatings—by K Chidambaram.
4. Electroless Deposited Blacks and Metal Pigmented Anodized Aluminium as Solar Selective Coatings—by S N Kumar.
5. Transparent Conducting Oxide Films for SIS Solar Cells—by E Shanthi.

Some of the above these have also been co-supervised by Dr L K Malhotra and Dr D K Pandya.

REFERENCES

1. H Tabor, In "*Low Temperature Engineering Applications of Solar Energy*", (Ed. R C Jordan), ASHRAE, New York (1967).
2. O S Heaven, '*Optical Properties of Thin Solar Films*', Dover Publ., New York (1965).
3. H A Macleod, In "*Thin Film Optical Filters*", Adam Hilger, London (1969).
4. K L Chopra, In "*Thin Film Phenomena*", McGraw-Hill, New York (1969).
5. B O Seraphin, *Topics in Applied Physics*, Vol. 31, Ed. B O Seraphin, Springer-Verlag, New York (1979).
6. K L Chopra and Inderjeet Kaur, In "*Thin Film Applications*", Plenum Press, New York (1982).
7. K L Khopra, D K Pandya and L K Malhotra, In "*Reviews of Renewable Sources of Energy*", Coordinators M S Sodha and S S Mathur, The UNU Fellowship Programme; Also see those in the acknowledgements (1983).
8. K L Chopra, S Major and D K Pandya, *Thin Solid Films* **102** (1983) 1.
9. J Feinbeib, W J Scouler and A Ferretti, *Phys. Rev.* **165** (1968) 765.
10. K Chidambaram, L K Malhotra and K L Chopra, *Thin Solid Films* **87** (1982) 365.
11. C M Lampert, Ph.D. Thesis Univ. of California (1979).
12. C G Granqvist, A Anderson and O Hunderi, *Appl. Phys. Lett.* **35** (1979) 268.
13. S N Kumar, L K Malhotra and K L Chopra, *Solar Energy Materials* 7 (1983) 439.
14. S N Kumar, L K Malhotra and K L Chopra, (to be published).
15. P Drude, *Z. Phys.* **1** (1900) 161.
16. S N Kumar, L K Malhotra and K L Chopra, *Solar Energy Materials* **3** (1980) 519.
17. S N Kumar, L K Malhotra and K L Chopra, *Proc. nat. Solar Energy Convention*, New Delhi pp. (1982) 8.021–8.024.
18. T Matsuama and A Ignatiev, *Surface Science* **102** (1981) 18.
19. T J Chuang, C R Brundle and D W Rice, *Surface Science* **59** (1976) 413.
20. N S Meintyre and M G Cook, *Anal. Chem.* **47** (1975) 2208.
21. C R Brundle, T J Chuang and D W Rice, *Surface Science* **60** (1976) 286.
22. E. Shanthi, V Dutta, A Banerjee and K L Chopra, *J. Appl. Phys.* **51** (1980) 6243.
23. E Shanthi, A Banerjee, V Dutta and K L Chopra, *J. Appl. Phys.* **53** (1982) 1615.
24. S Major, A Banerjee and K L Chopra, *Thin Solid Films* **108** (1983) 330.

© *Proc. Indian natn. Sci. Acad.*, **51**, A, No. 1, 1985, pp. 76-97.
Printed in India.

NEW CONCEPTS IN CATALYSIS : THE IMPACT OF SURFACE SCIENCE*

JERZY HABER

Institute of Catalysis and Surface Chemistry, Polish Academy of Sciences, Krakow, Poland

LAST year the 150th anniversary passed of the first patent for industrial application of catalysis, which stated that SO_2 in the presence of platinum transforms into sulphuric acid. Just before that Dobereiner decsribed in a letter to Goethe an experiment, in which a mixture of SO_2 and O_2 was transformed into fumes of sulphuric acid by the presence of wet platinum black and commented : "...it seems that I have discovered a new phenomenon which may prove in the future to be of great practical importance". Indeed, now after 150 years, when more than 90% of the production of chemical industry is based on catalytic processes, we can appreciate the significance of this discovery.

Catalysis is a phenomenon, in which a relatively small amount of a foreign material, called the catalyst, increases the rate of a chemical reaction. The catalyst interacts with reacting molecules, modifying their electronic and/or atomic structure and facilitating thus the rearrangement of bonds. The most important feature of catalysis is the possibility of modifying only some selected bonds in which the molecule without activating all other bonds, what makes possible to direct the reaction along certain selected pathway and formation with very high selectivity of one chosen product, which otherwise could not have been obtained. Mechanisms of catalytic reactions may be thus discussed in terms of the type of intermediate complex, formed in the course of the reaction as the result of interaction of the catalyst with reacting molecules.

Let us imagine a hydrocarbon molecule becoming bonded as a sixth ligand to a cation, coordinated octahedrally by oxygen atoms of some other ligands [Fig.1], and playing the role of an active center of the homogeneous catalyst. The modification of the electronic structure of the reacting molecule will depend on the chemical nature of the central atom of the complex and on the type of ligands surrounding this atom. Let us now suppose that we surround the central atom by ligands bonded more and more covalently. In the limiting case we shall have a metal atom surrounded by other metal atoms and forming a cluster. We pass to the situation encountered in the highly dispersed metal catalysts. The properties of the cluster depend not only on the nature of its atoms, but also on its size and on the interaction with the carrier, on which such cluster may be supported. When the size of the cluster increases, its surface properties become those of a metal surface.

The properties of an active center at the metal surface depend on the chemical composition of the surface, its geometrical structure, location of the center at

*Paper presented at the Symposium on Phyics and Chemistry of Surfaces held at INSA, New Delhi from September 28-30, 1984.

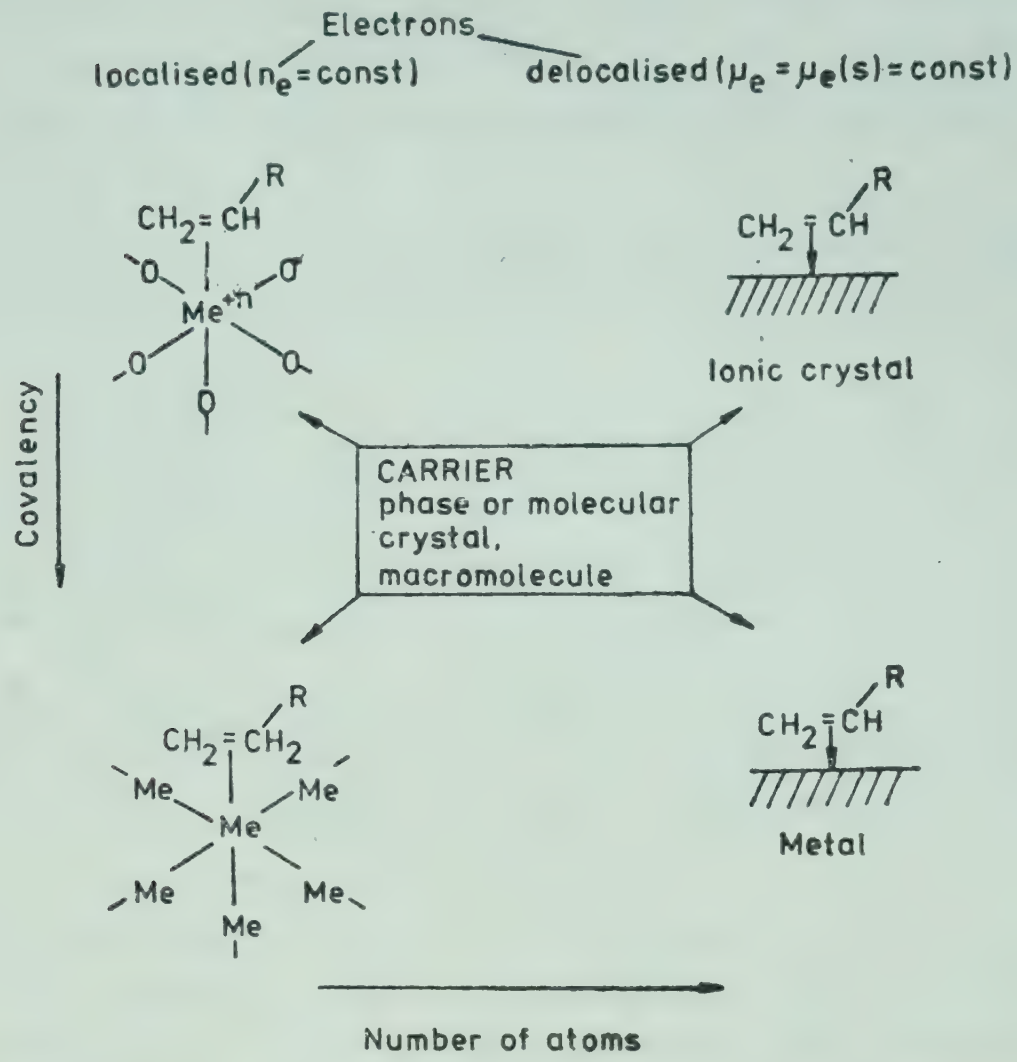

FIG. 1. Intermediate complex of the reacting molecule and the group of atoms forming the active center of the catalyst.

different structural defects [steps, edges, kinks], presence of point defects at adjacent sites, etc. Similar evolution of properties of the active center takes place when we start from the isolated coordination compound, composed of metal cation surrounded by oxygens and increase infinitely the number of such units until the system behaves as an oxide. We can cut out from the lattice of an oxide catalyst a cluster composed of the atoms directly involved in the interaction with the reacting molecule and their nearest neighbours, and consider such group of atoms of the catalyst surface as the active center for the reaction. Again its properties will depend not only its nature, but will be modified by the fact that it constitutes a part of the solid, either of the same chemical composition or being a different compound and playing the role of support as is the case in oxide-on-carrier catalysts or enzymes, in which the prosthetic group is "supported" on the protein molecule.

We may conclude that irrespective of whether it is a heterogeneous metal, oxide and sulphide catalyst or an enzyme or an organometallic complex in the homogeneous liquid phase, its catalylic properties are related to the properties of an intermediate complex composed of reacting molecules of the catalytic reaction and a group of atoms of the catalyst, constituting the active center. Development of a theory of catalysis would thus require answering of the three basic questions :

- what is the structure of the intermediate complex, composed of the reacting molecule and the active center of the catalyst;
- how this structure depends on the properties of the active center;

- how the formation of intermediate complex modifies the bonds in the reacting molecule, influencing thus its reactivity along different possible reaction pathways and determining the type of product formed and the selectivity of its formation.

Answer to the second of these questions may be very complex and in the case of heterogeneous catalytic systems would require several other questions also to be answered :

- where is intermediate complex located at the catalyst surface;
- how its properties depend on the location and on the properties of the solid;
- are there other active centers present at the catalyst surface which create other routes for parallel or consecutive transformations of the reacting molecule.

The last decade has equipped surface chemistry with a number of new techniques which yield detailed information on both atomic and electronic structures of solid surfaces and their interaction with the adsorbed species[1–5].

The fundamental basis of all surface analysis methods is to bombard the surface with a given type of input probe and collect four types of information on the emitted particles: identification of particles, their number, special distribution and energy distribution. We may consider eight basic input probes which give rise to one or more of four types of particles that leave the surface carrying information about it to a suitable detector [Fig. 2]. The input probes can be beams of particles such as electrons, ions, neutrals or photons, or non-particle probes such as thermal, electric, magnetic or sonic fields. The various surface analysis techniques can therefore be classified according to the type of input probe and the type of emitted particle, e.g. photons in-electrons out [XPS], thermal in-neutrals out [TPD], etc. From the point of view of information which they yield concerning the structure of the surface and its interaction with the adsorbed layer all methods can be devided into four groups as shown in Fig.3.[6] Such methods as low energy electron diffraction [LEED] or field electron microscopy [FEM] inform us about the geometrical arrangement of atoms at the surface of the solid (long range order) and

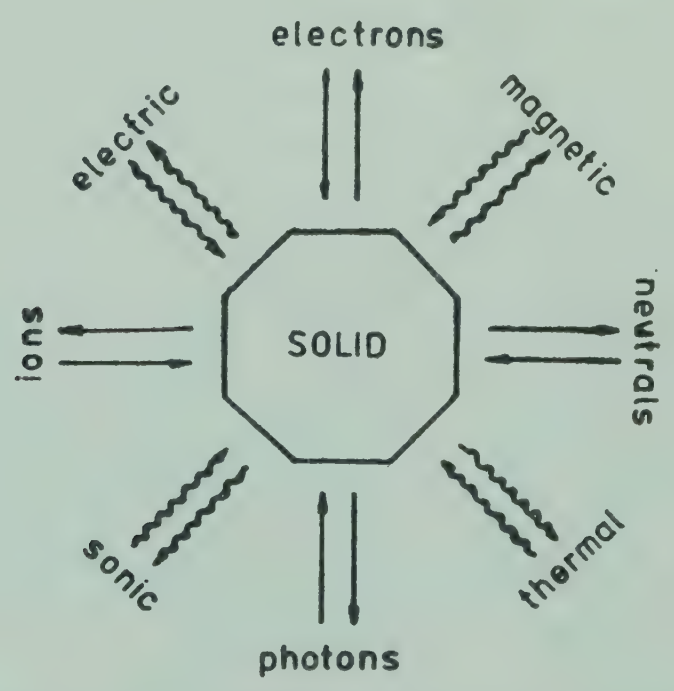

FIG. 2. Basic types of probe beams used in surface studies.

ELECTRONIC STRUTURE

Surface Potential /CPD
Electronic Conductivity
Hall Effect
Electron Spin Resonance /ESR/
Chemical Redox Titration

TYPE AND STRUCTURE OF ADSORBED SPECIES

IR Spectroscopy of Adsorbed Species
IR Reflectance Spectroscopy/ATR/
Field Ion Mass Spectrometry/FIMS/
Nuclear Magnetic Resonance/NMR/
Mössbauer Spectroscopy/MOSS/
Thermoprogrammed Desorption/TPD/
Electron Stimulated Desorption /ESD/
UV Reflectance Spectroscopy
Microcalorimetry
Photoelectron Spectroscopy/XPS, UPS/

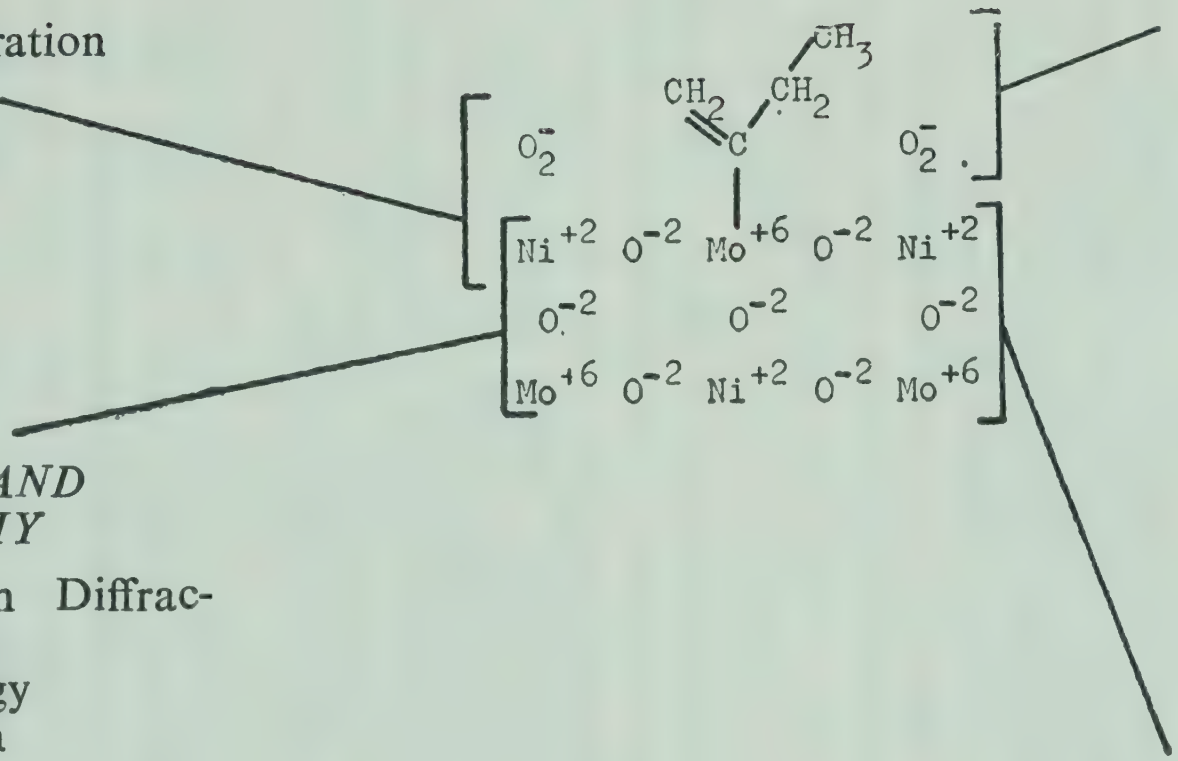

GEOMETRY AND TOPOGRAPHY

Low Energy Electron Diffraction /LEED/
Reflected High Energy Electron Diffraction /RHEED/
Field Electron Microscopy /FEM/
Field Ion Microscopy /FIM/
Electron Microscopy /TEM/
Scanning Electron Microscopy /SEM/
Extended X-Ray Absorption Fine Structure /EXAFS/
Light Microscopy

CHEMICAL COMPOSITION, COORDINATION, TYPE OF CHEMICAL BONDS

Photoelectron Spectroscopy/XPS, UPS/
Auger Electron Spectroscopy /AES/
Secondary Ion Mass Spectrometry /SIMS/
Ion Scattering Spectroscopy/ISS/
Appearance Potential Spectroscopy /APS/
Electron Energy Loss Spectroscopy/EELS/
Ellipsometry
UV Reflectance Spectroscopy
Isotopic Exchange

FIG. 3. Classification of surface techniques according to the information obtained[6].

its change under the influence of the gas phase, extended X-ray absorption fine structure [EXAFS] permits the determination of the geometry of the nearest surrounding [short range order], whereas scanning electron microscopy reveals the topography of the surface itself. Vital information on the chemical composition of the outermost atomic layer or the character of chemical bonds between surface atoms is supplied by a group of methods utilising emission caused by excitation of the energy states of surface atoms. Auger electron spectroscopy [AES] is now usually used to determine the chemical composition of the surface layer and to detect the presence of foreign atoms incorporated into the surface. Secondary ion mass spectrometry [SIMS] or ion scattering spectroscopy [ISS] enables one to limit such determination to the outermost layer, where-as photoelectron spectroscopy [ESCA] may yield the most important information on the type and energy of chemical bonds between different atoms both in the lattice of the solid and in chemisorbed molecules.

The basic requirement for the given technique to be used in surface studies is the condition that the information be collected from a very thin layer below the surface of the solid and that the depth of this layer could be varied to obtain an in-depth profile of a given property. This is the case with such methods as ESCA or AES due to a very small escape depth of eletrons from the solid and its dependence on their energy. In the case of electrons with energy of about 500 eV the probing depth is of the order of 10-20 Å i.e. a few crystal planes. Obviously, when UV radiation is used for excitation of electrons, their energy is small and the information is obtained practically only from the outermost layer, which is specially important in the case of the studies of adsorption bonds. Probing of the surface with thermal or low energy electron beams will result in the emission of ions or neutrals only from the adsorbed layer, and therefore such methods as thermoprogrammed or electron induced desorption [TPD, EID] are specially well suited for studying the type of adsorbed species, where as IR spectroscopy of admolecules yields basic information on their structure. Different kind of information concerning the collective electronic properties of the surface and the electric double layer are supplied by the group of techniques based on electrical measurements such as work function, electrical conductivity, Hall effect etc.

It should be emphasized that each of the methods mentioned above supplies a different kind of information, usually limited to only one type of questions. Therefore it is advisable to combine different techniques in one experimental apparatus. Such a combination may be particularly helpful in solving the complex problems of heterogeneous catalysis listed above. An example of a study of the mechanism of transformations of hydrocarbon molecule at the surface of a CoO-MgO solid solution is illustrated schematically in fig. 4. The LEED technique is used to obtain an information about the geometrical arrangement of atoms at the surface. Their type and concentration as well as in-depth changes of this concentration are given by the AES and ISS, their valence state and coordination by XPS whereas the presence of defects by EXAFS. The type and structure of the intermediate complexes and the routes of their transformations at the surface may be

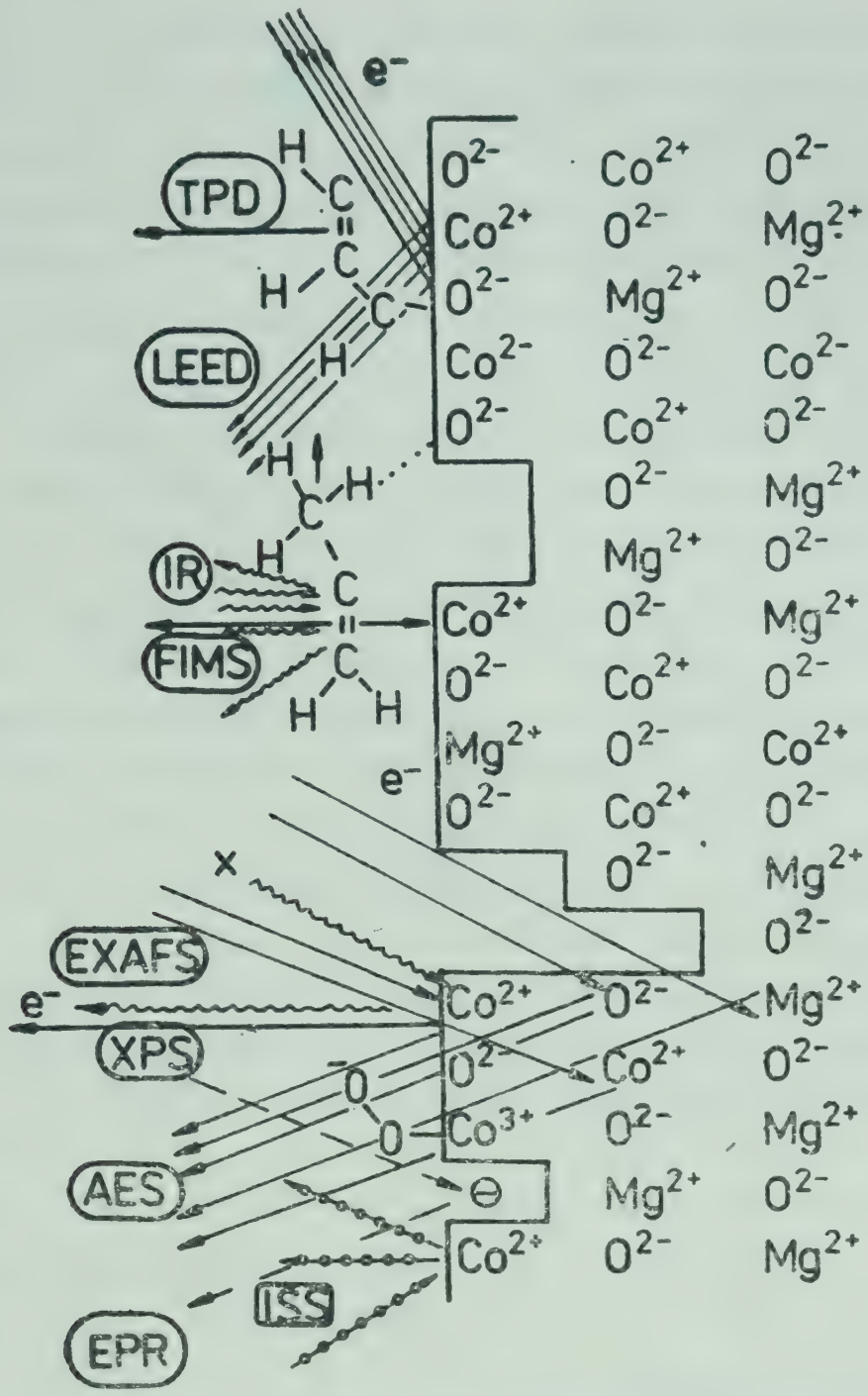

FIG. 4. Application of different techniques to study the elementary step of catalytic transformation of a hydrocarbon molecule.

studied by FIMS, TPD, and XPS, the latter technique giving informations also on the localisation of these complexes at the surface and the induced changes of the surface structure. The most vital informations on the modification of bonds in the reacting molecule and the resulting changes of their reactivity may be obtained from the IR spectroscopy of the adsorbed species, which has become the most powerful method for studying the mechanism of surface processes[7].

It will be shown latter that the catalyst surface remains in the state of dynamic interaction with the reactants of the catalytic reaction. It is therefore expedient to carry out all the measurements whenever possible in the conditions of the catalytic reaction.

To what extent did the application of these new surface physics techniques contribute to a better understanding of the properties of an active center at the catalyst surface and the mechanism of its interaction with the reacting molecule to form the intermediate complex ? How did it modify our concepts on the nature of the phenomenon of catalysis ?

The first basic question to be asked concerns the composition of the surface of a solid catalyst as compared to that of the bulk. This was a fundamental question

of all catalytic studies raised from the very beginning of the catalytic science. In all theories trying to correlate catalytic activity with other physiochemical properties some assumption had to be made as to how the measured properties of the bulk reflect the state of the surface. Application of the techniques of surface science enabled for the first time the direct answer to be obtained. As an example, Fig. 5 shows the surface concentration of copper as found by AES[8] as function of its concentration in the bulk crystallites of Cu-Ni alloy. A strong enrichment of the outermost layer in copper is observed so that the surface of a 50% Cu-Ni alloy would show the properties of practically pure copper surface. This enrichment decreases rapidly with the depth so that the fourth crystal plane below the surface already shows the composition identical to the average composition of the bulk. This phenomenon may be explained[9,10] on the basis of Gibbs adsorption equation, the alloy being a solid solution. The component, whose adsorption decreases the surface energy, i.e. which is characterized by smaller sublimation heat, will be driven to the surface. The same phenomenon is odserved in the case of oxide solid solutions, as seen from the data for the CoO-Cr_2O_3 system[11] shown in Table I XPS studies of samples of CoO containing less than 1% [at] of Cr_2O_3 showed that the surface is strongly enriched in chromium and contains more than 10% [at] of this element. When the activation energy of surface diffusion was calculated from the measurements of the changes of the work function following the exposure of

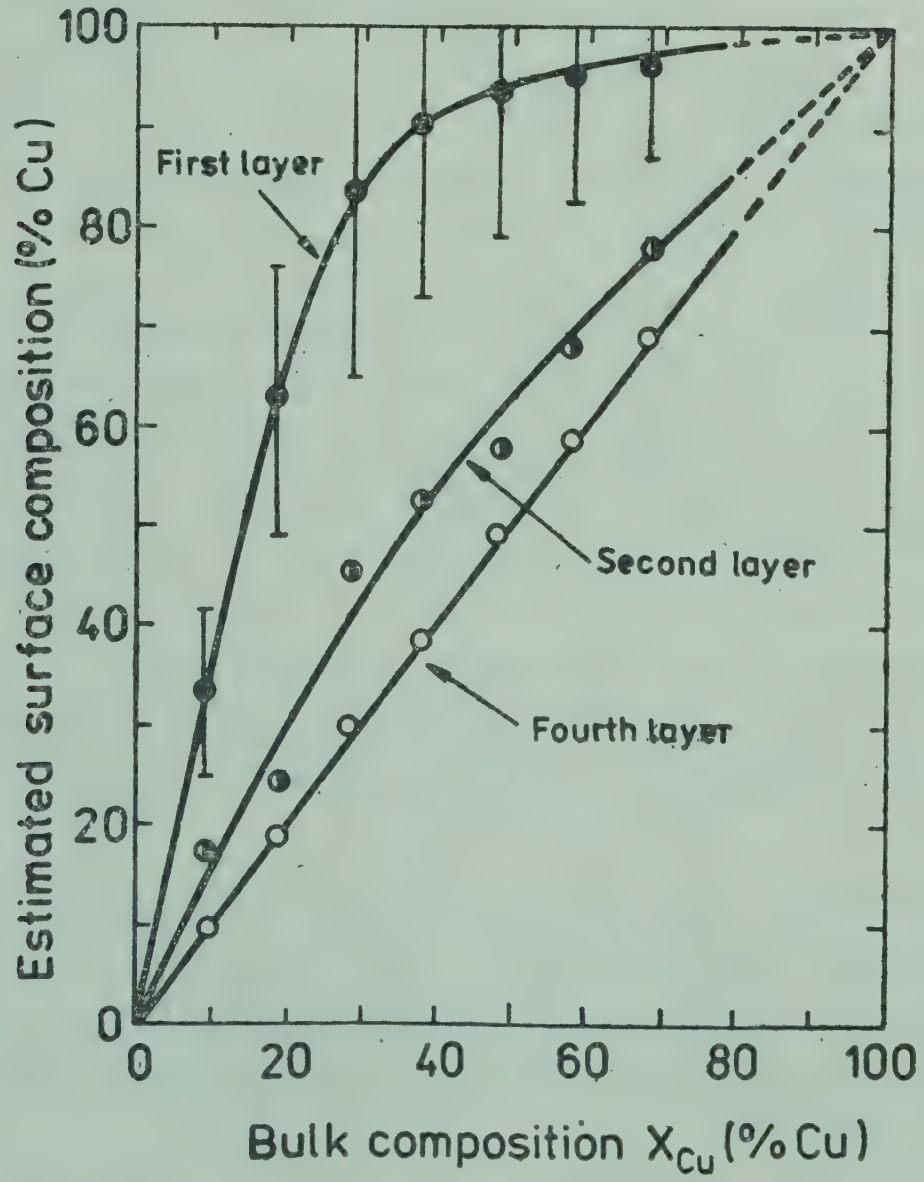

FIG. 5. Surface concentration of copper as function of its bulk concentration in the Cu-Ni alloy[8].

TABLE I

Photoelectron spectroscopic analysis of CoO-Cr_2O_3 solid solutions

No	Bulk concentration of chromium % at.	Sample	Binding energy, eV $Co2p_{3/2}$	$Cr2p_{3/2}$	01S	Surface concentration of chromium % at.
1.	0,33	solid sol. A	781,2	576,9	530,4	9,9
2.	0,90	solid sol. A	781,0	576,9	530,4	14,0
3.	0,90	solid sol. B	781,1	577,0	530,5	12,3
4.	66,6	$CoCr_2O_4$ A	781,1	576,3	530,2	65,2
5.	66,6	CoC_2rO_4 B	781,2	576,3	530,4	66,7
6.	100,0	Cr_2O_3 A	—	576,6	530,6	100,0
	Penetration depth, Å		11	13	13,5	

A — after standardization at 100°C for 1 h.
B — after standardization at 500°C for 10 h in UHV.

the sample to small doses of oxygen[12] it was found that its value remains identical to that of pure CoO phase only until the concentration of Cr_2O_3 reaches the value of about 0.4% at [Fig. 6]. At that concentration the activation energy suddenly rises to the value characteristic for the spinel phase $CoCr_2O_4$ indicating that due to the considerable enrichment in chromium the transformation of the surface layer into spinel structure must have taken place. The enrichment rapidly decreases with the depth, as illustrated by Fig. 7, in which surface concentration of chromium as determined by SIMS[13] is plotted as a function of the number of crystal planes below the surface of a NiO-Cr_2O_3 solid solution. At variance with metallic phases,

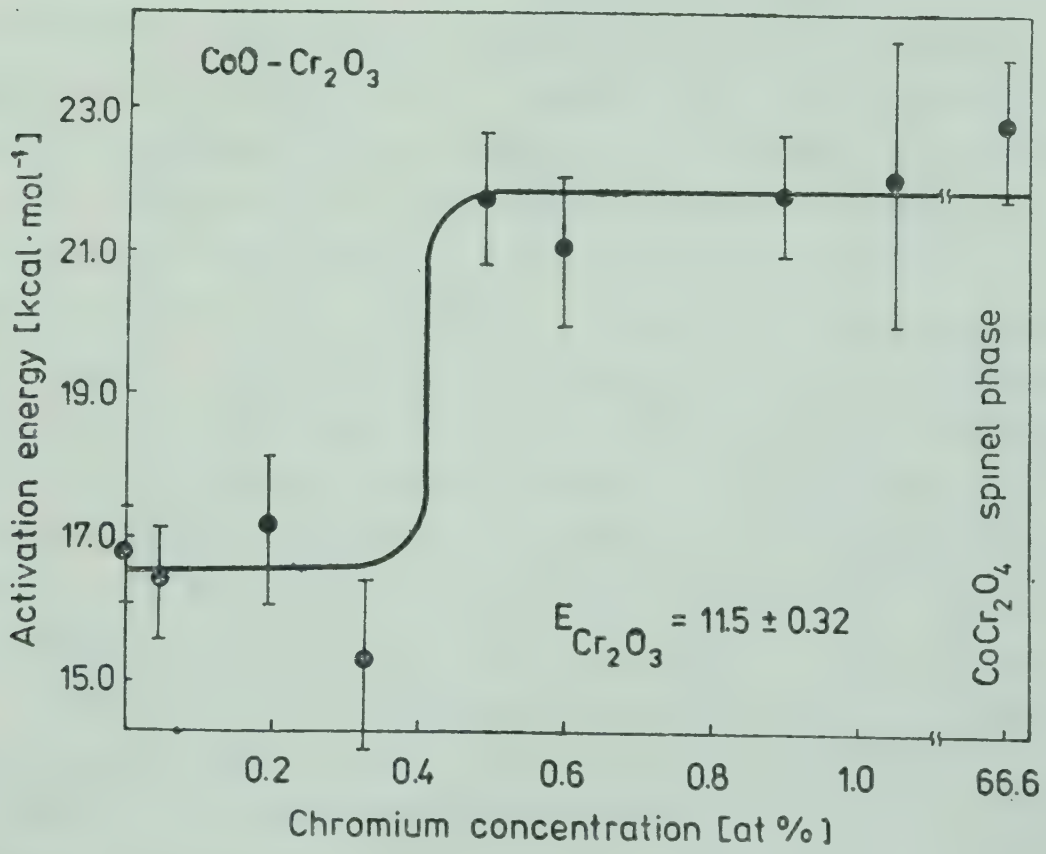

FIG. 6. Activation energy of surface diffusion of cations in CoO-Cr_2O_3 solid solutions as function of the chromium content[13].

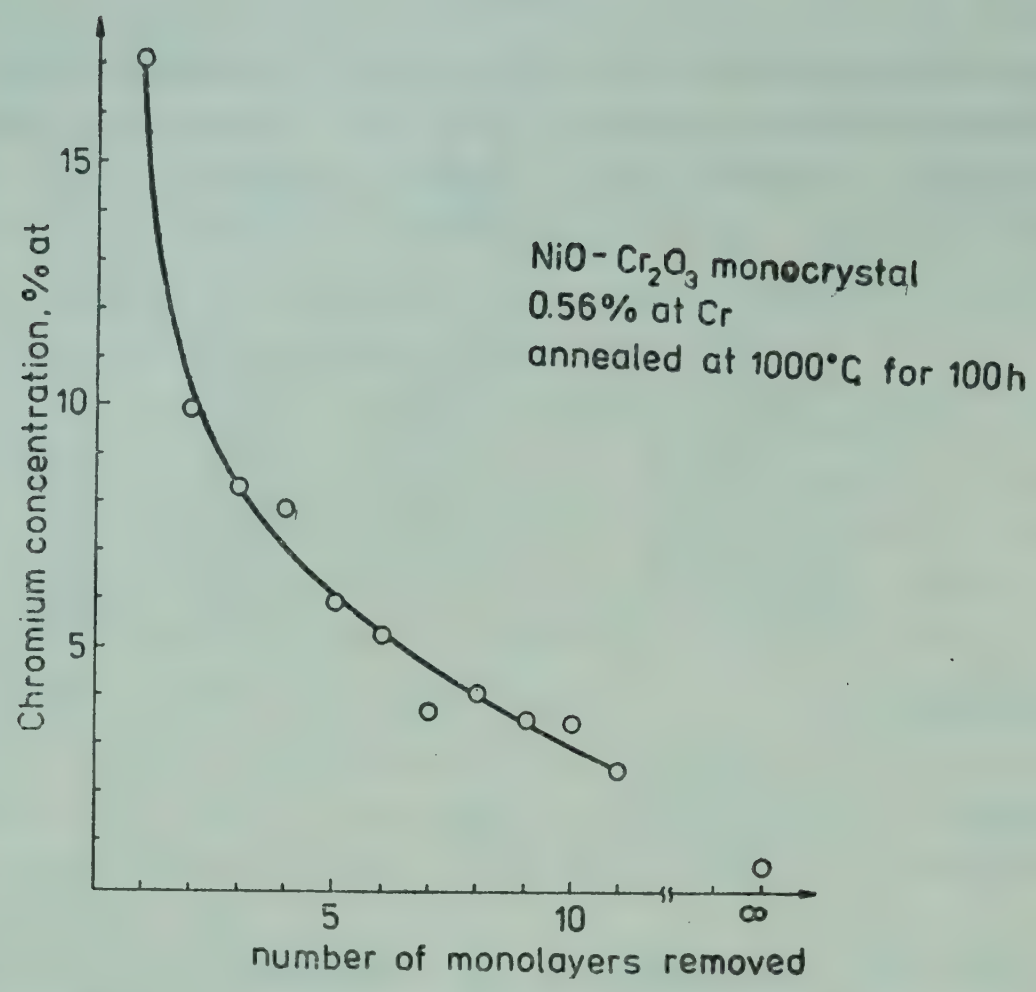

FIG. 7. In-depth profile of the concentration of chromium in $NiO-Cr_2O_3$ solid solution as determined by SIMS[13].

the surface layer in oxide solid solutions extends much deeper and may comprise several tens of crystal planes. A general conclusion of great importance for catalytic studies may be thus formulated that in the case of all solids

> composition of the surface layer is usually different from the composition of the bulk.

The next question relates to the importance of the geometrical structure of the surface for its catalytic behaviour. This question was also raised from the begining of catalytic studies and may be found in the Schwab's adlineation theory[14], Balandin's theory of ensembles[15] as well as in Rienackers studies of catalysis at different metal surfaces[16]. The first direct answer was given only few years ago by the elegant Samorjai's experiments[17] in which dehydrogenation and hydrogenolysis were studied at stepped platinum surfaces, the concentration of steps and kinks being simultaneously determined by LEED [Fig. 8]. Strong dependence of the rate of hydrogenolysis on the concentration of steps and kinks indicated that the reaction involves low coordinated platinum atoms situated at the edges of steps and kinks, whereas dehydrogenation being independent of the structure apparently takes place at terraces. Strong influence of geometry was recently demonstrated also in the case of oxide catalysts. Fig. 9 illustrates the selectivities to different products observed[18,19] when pulses of butene-1 were introduced on $Cu_2Mo_3O_{10}$ [dotted lines] and $Cu_6Mo_4O_{15}$ [full lines]. In the case of $Cu_2Mo_3O_{10}$ the majority products are trans-and cis-butene-2, considerable amount of butadiene being also formed. This indicates that allyl species are formed as intermediates by abstraction of *L*-hydrogen. As, however, isomerization of 3, 3-dimethylbutene-1 was also

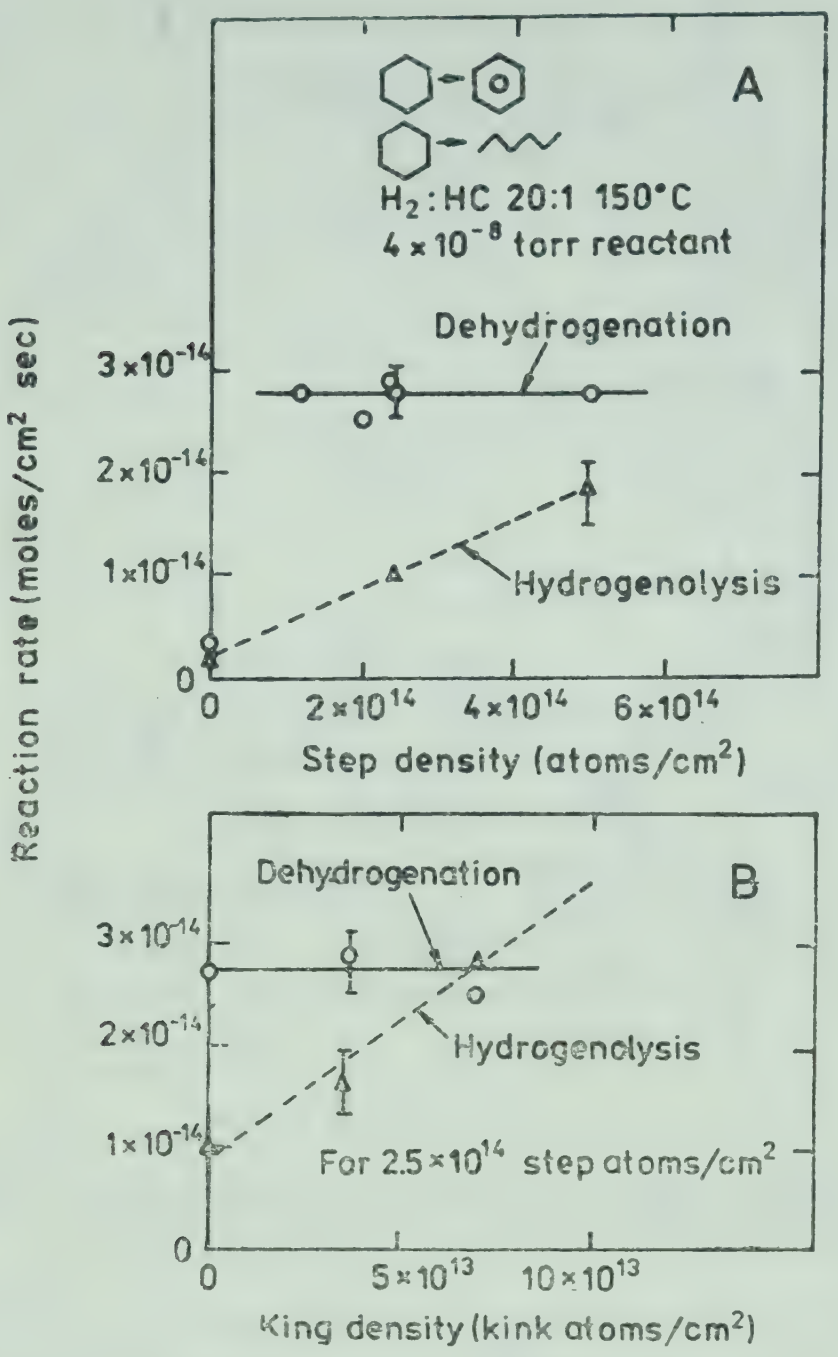

FIG. 8. Activity of platinum in dehydrogenation and hydrogenolysis as function of the concentration of steps and kinks[17].

observed, carbonium ion mechanism must also be operating. Different behaviour is observed in the case of $Cu_6Mo_4O_{15}$. Here the majority product of the reaction is crotonaldehyde, formed with the selectivity of about 70%. The most striking feature is the complete absence of isomerization. All these observations may be summarized in form of a scheme shown in Fig. 10. It should be emphasized that both $Cu_2^{I}Mo_3^{VI}O_{10}$ and $Cu_6^{I}Mo_4^{VI}O_{15}$ are composed of the same chemical elements in the same valence state and in spite of that they show completely different catalytic behaviour: $Cu_2Mo_3O_{10}$ is active in isomerization [box I of the scheme in Fig. 10], whereas $Cu_6Mo_4O_{15}$ mainly inserts oxygen into the organic molecule [box II of the scheme in fig. 10]. Equally pronounced influence of the geometry on the pathway of the catalylic reaction is visible in the case of the oxidation of o-xylene on V_2O_5 studied by Gasior and Machej[20]. Fig. 11 shows the selectivity to phthalic anhydride and the selectivity to products of total oxidation as function of the structural factor, which is expressed as the ratio of the intensity of the [110] reflection to the intensity of the [010] reflection. The arrangement of VO_6 octahedra on these crystal faces is shown in fig. 12, in which the formation of shear planes by removal of every 3rd oxygen layer perpendicular to the [110] face is also illustrated.

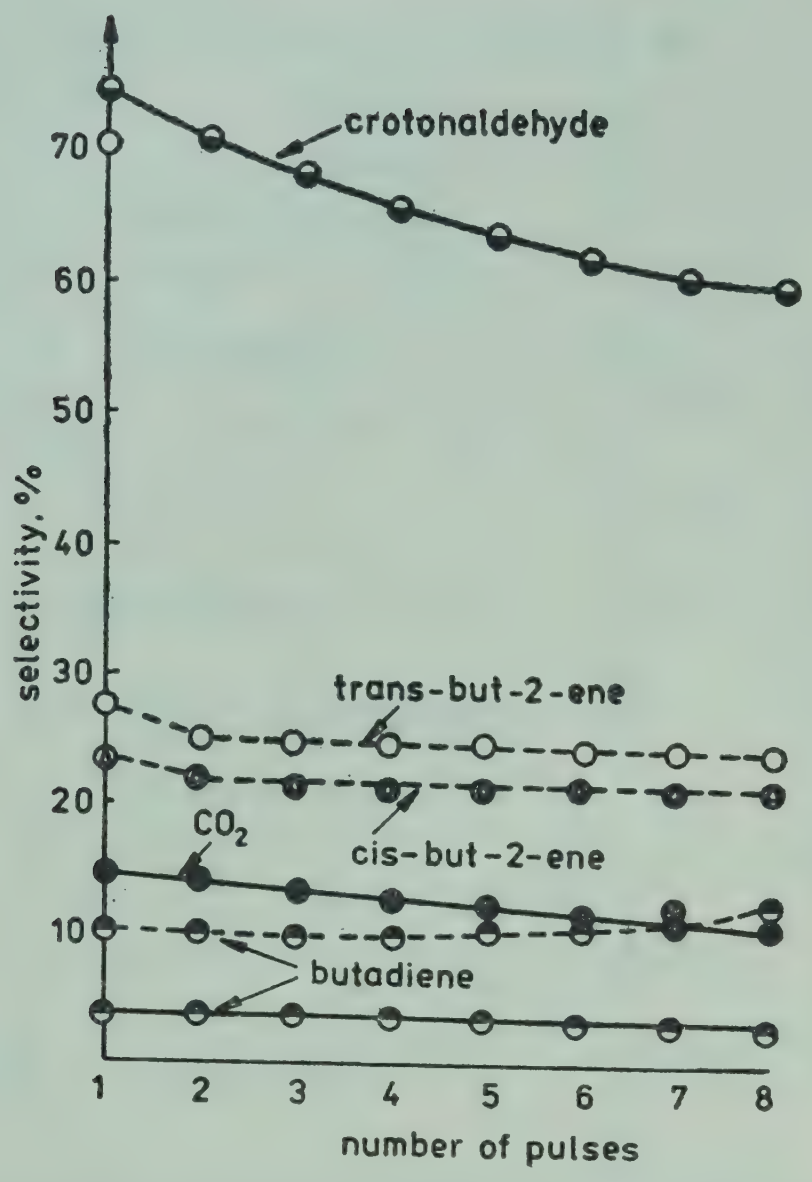

FIG. 9. Selectivities to different products as functions of the number of pulses of butene-1 on $C_2Mo_3O_{10}$ /dotted lines/ and $Cu_6Mo_4O_{15}$ /full lines/ at 370°C[18]

It may be seen that high selectivity to phthalic anhydride is observed in the case of samples with crystallites exposing mainly the [010] planes with the V = O groups sticking out of the surface. When however the crystallites expose mainly the [110] planes, at which the shear planes may be nucleated and whole perpendicular layers of oxygen extracted, total oxidation becomes the predominant reaction pathway.

Similar phenomenon of the influence of the type of crystal face exposed by MoO_3 crystallites on the selectivity of the transformation of methanol into formaldehyde or dimethylether was observed by Germain and Tatibouet[21] and on the selectivity of the oxidation of propylene to acrolein or CO_2 by Volta *et al.*[22] All these recent observations lead to an important general conclusion that:

> "Geometry of the arrangement of surface atoms may be an important factor determining the catalytic properties of the solid".

Increasing number of observations was accumulated in recent years indicating that when adsorption takes place at the surface of a solid then because the electronic structure of the near surface region of the solid is changed, so is the surface free energy and consequently many suface dependent properties. Most effects of adsorbed species arise as the result of the variation in the concentration or distribution of charge carriers in the surface layer of the solid, influencing in turn the cohesion between surface atoms[23]. One of the consequences may be the

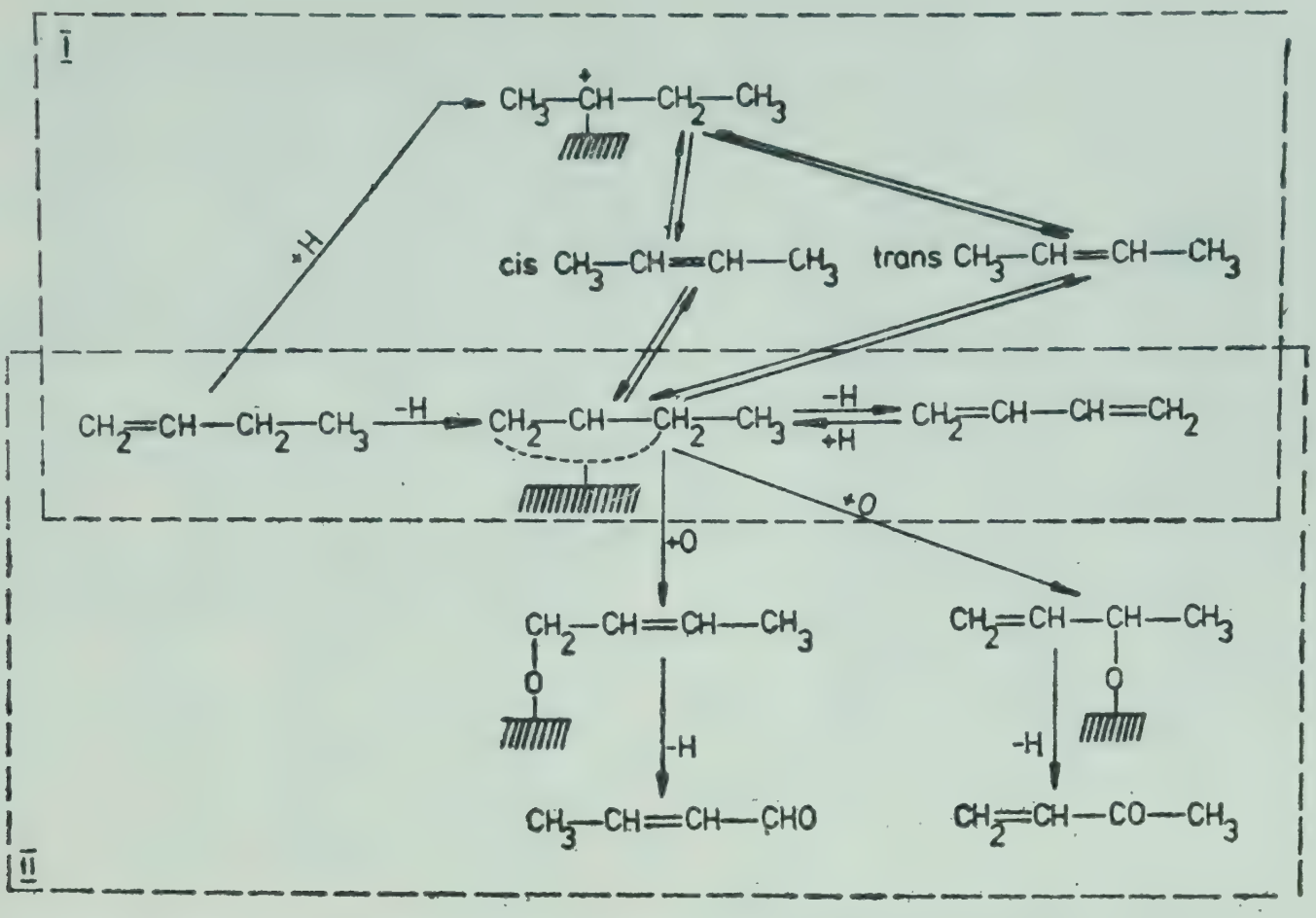

FIG. 10. Schemes of reactions of butene-1 on $Cu_2Mo_3O_{10}$ /1/ and $Cu_6Mo_4O_{15}$ /II/.

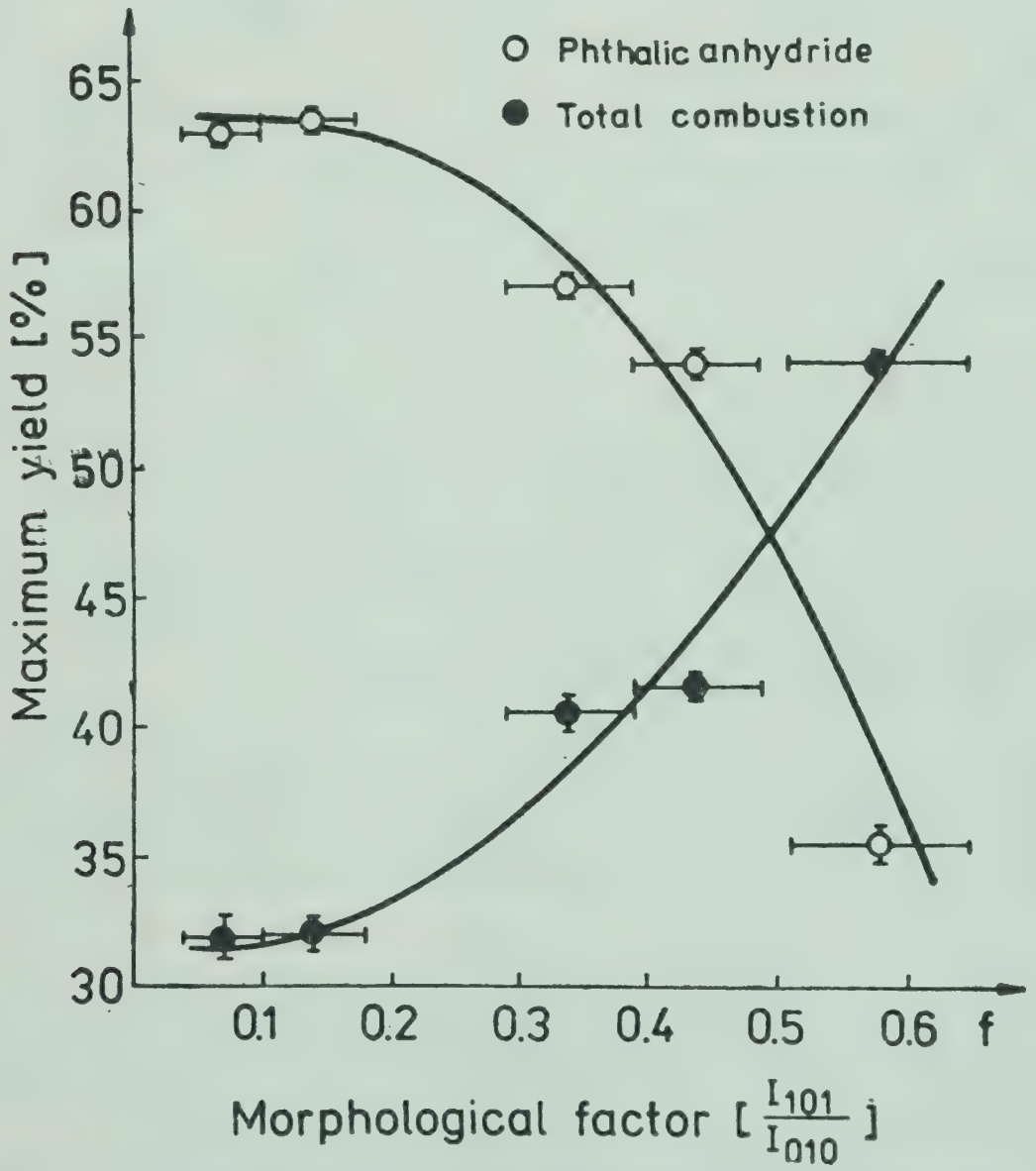

FIG. 11. Selectivities in oxidation of o-xylene on V_2O_5 of function of the structural factor[20].

displacement of the surface atoms from the lattice sites resulting in the reconstruction of the surface. One of the examples is the displacement of atoms at [100] and [110]

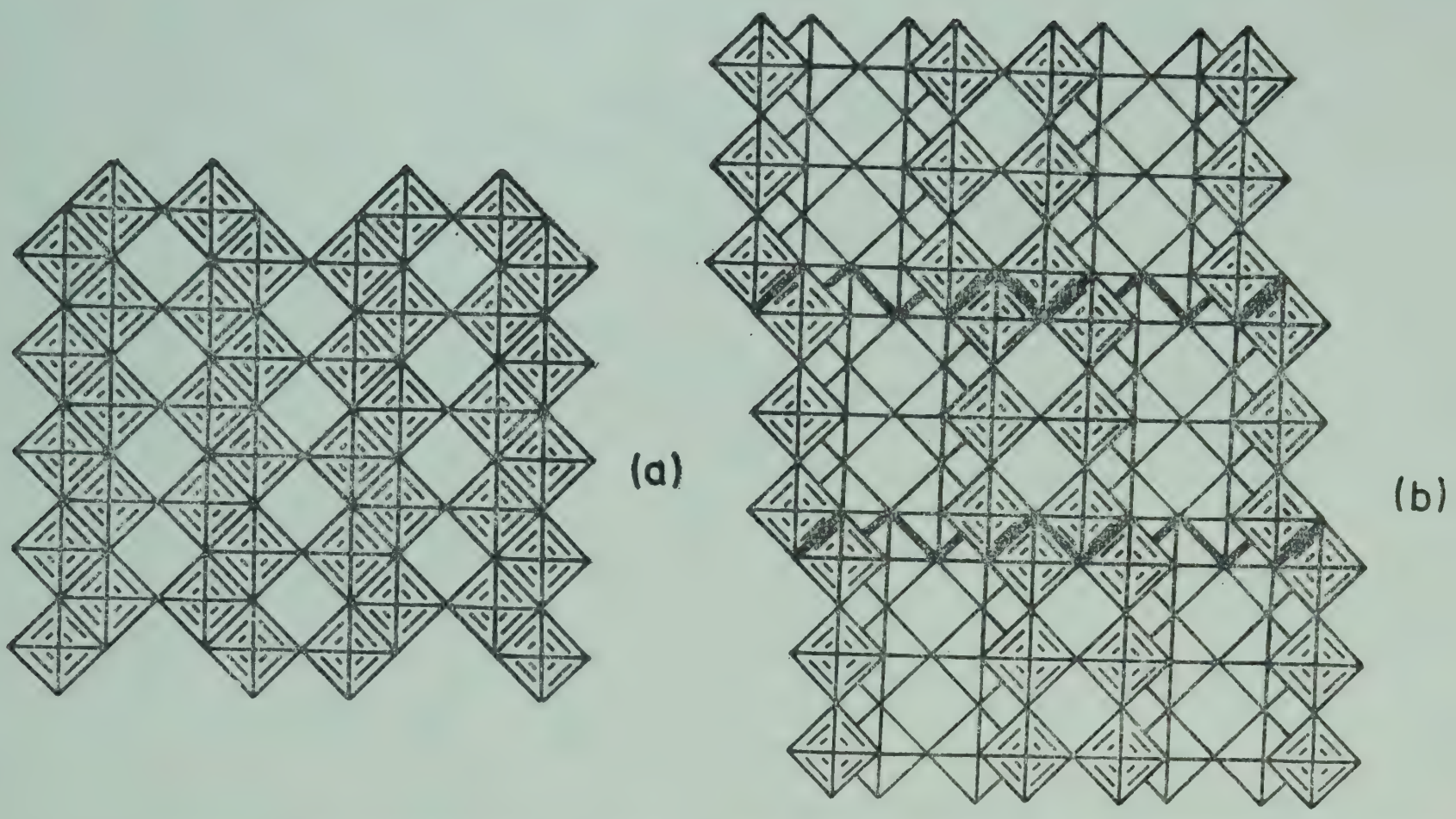

FIG. 12. Structure of V_2O_5, a—sheet formed by ribbons of edge-sharing idealized VO_6 octahedra linked through corners, b—three dimensional network formed by corner sharing of sheets. Sheer plane formed by removal of a layer of oxygens perpendicular to 110 plane is shown by bold line.

planes of group VIII metals such as nickel or iridium, which under the influence of oxygen become microfaceted exposing elements of more densely packed [111] faces[24], showed in [Fig.13]. When such reconstruction is induced at the surface of an alloy, segregation may take place resulting in dramatic change of catalytic properties. As an example Fig. 14 shows the reconstruction of silica supported small Pt-Rh crystallites under the influence of oxidation and reduction cycles[25]. When these crystallites were exposed to oxygen at 600°C, rhodium was extracted to their surface and oxidized to Rh_2O_3, which diffused over the surface of SiO_2 forming a thin layer around the remaining platinum particles. This layer, when exposed to hydrogen at low temperature, was reduced to metallic rhodium forming small particles dispersed around platinum crystallites.

On increasing the temperature in reducing atmosphere they coalesce with platinum, covering at first the surface of platinum crystallites and then diffusing at still higher temperatures into the bulk of these crystallites restoring the original structure.

This example illustrates the possibility of aggregation and redispersion of metal particles at the surface of a carrier under the influence of the gas phase. Similar phenomena are observed in the case of oxide systems. Studies of the kinetics and mechanism of the oxidation of $Cu_2Mo_3O_{10}$ have shown[26,27] that on exposing to oxygen at low pressure its surface becomes covered with clusters of $CuMoO_4$. When again reduced it shows much higher catalytic activity. This is illustrated by an experiment shown in Fig. 15. At first a mixture of butene-1 and oxygen of the

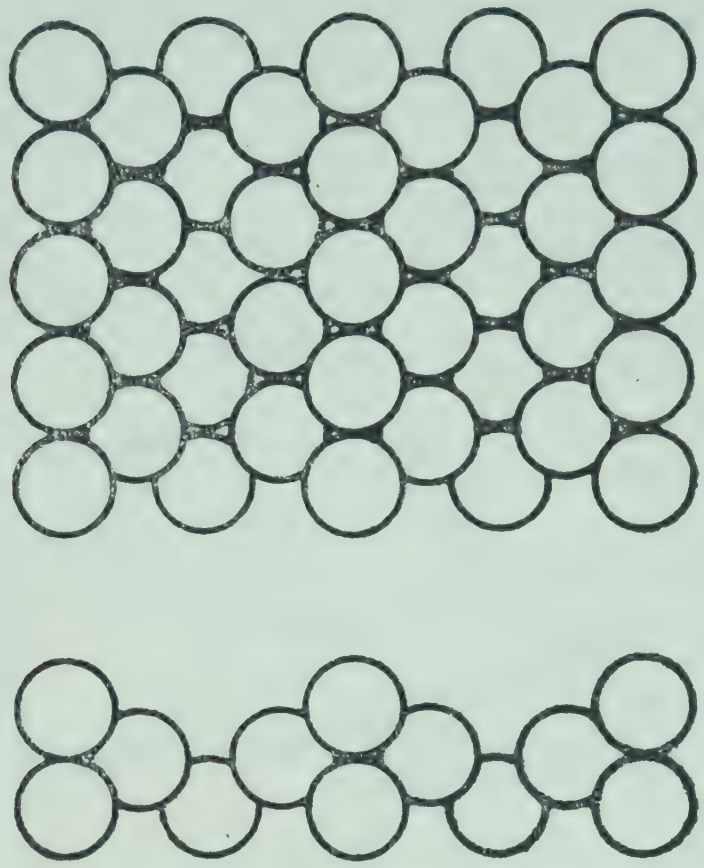

FIG. 13. Microfaceting of [110] plane with formation of elements of [111] plane 24.

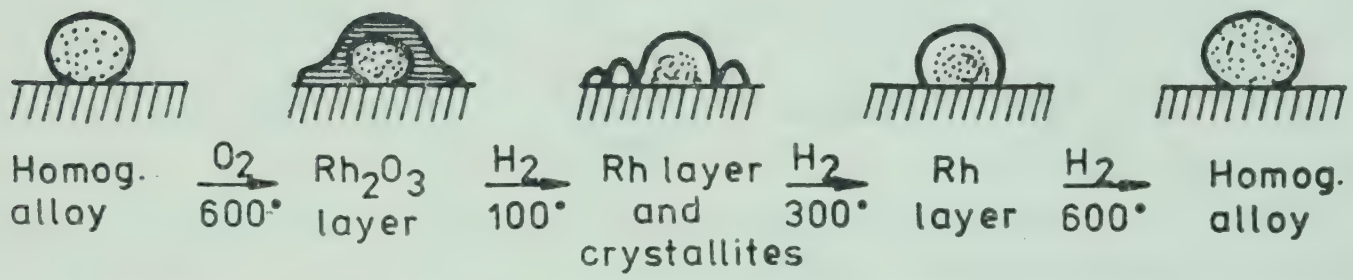

FIG. 14. Changes of the dispersion and composition of Pt-Rh crystallites supported on Al_2O_3 as function of the pretreatment[25].

composition 1 :1 was pulsed over the $Cu_2Mo_3O_{10}$ catalyst, the main products being butadiene and CO + CO_2. Then pulses of oxygen started to be introduced between pulses of the reacting mixture. This resulted in a strong increase of the conversion until it attained a new much higher level. Simultaneously a strong increase of the amount of CO + CO_2 was observed. However, when now additional pulses of oxygen were stopped, selectivity to butadiene started to increase considerably and after few pulses of the reacting mixture reached a new high plateau. Apparently, the reacting mixture reduces the surface clusters of $CuMoO_4$ back to $Cu_2Mo_3O_{10}$ but the surface generated in this way is characterized by a much higher selectivity to butadiene than the initial surface. A general conclusion may be thus drawn that :

> chemisorption may result in the reconstruction of the arrangement of atoms in the surface layer of the solid, generating new surface of much higher activity.

As already mentioned, when the chemical environment of a solid is changed and adsorption at its surface takes place, the surface free energy may be considerably influenced. This is accompanied by a change of mechanical properties[28] what may manifest itself in form of the embrittlement of the solid [Rebinder effect]. Such

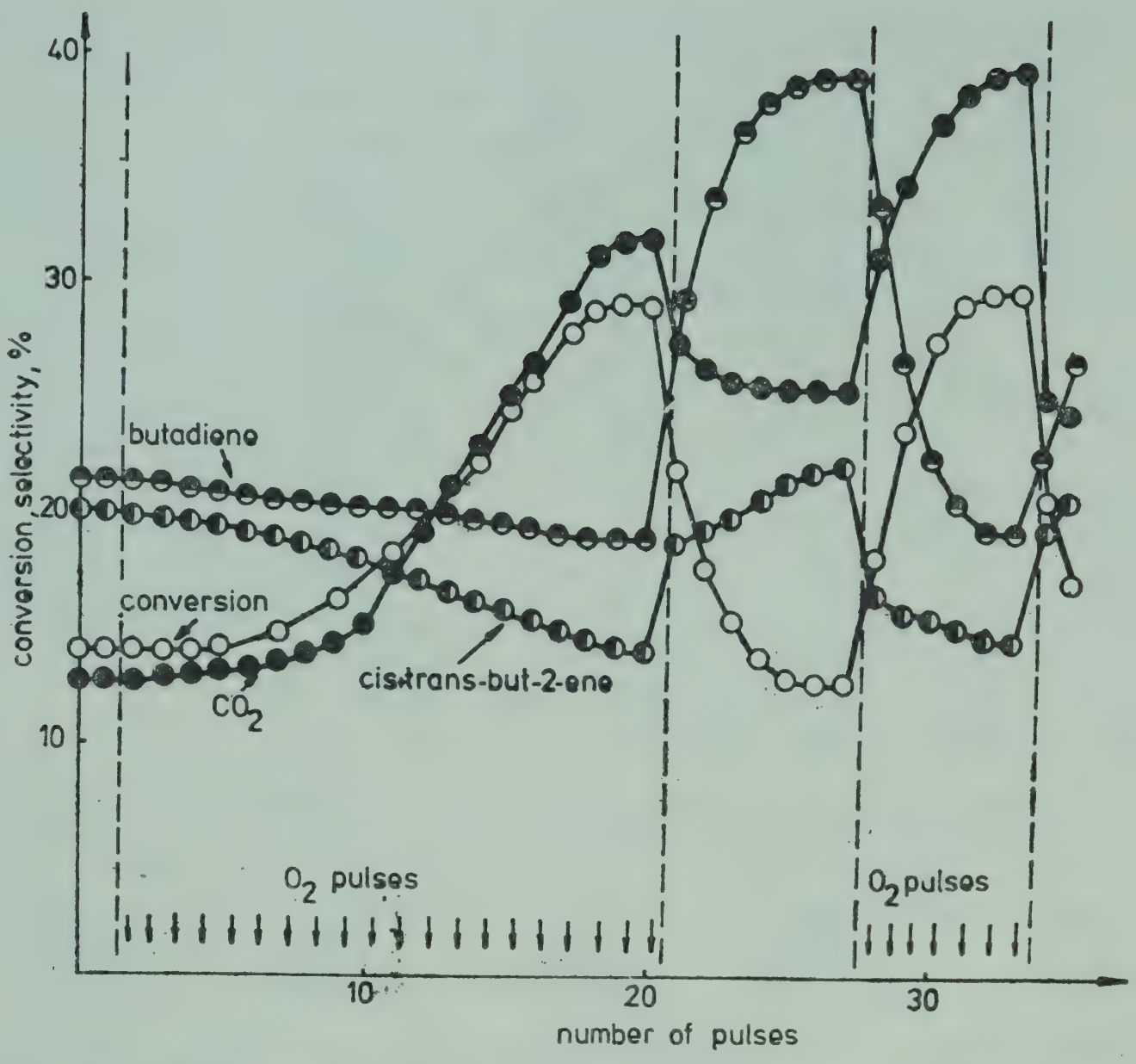

FIG. 15. Conversion and selectivities to different products as function of the number of $C_4H_8 + O_2$ and O_2 puleses on $Cu_2Mo_3O_{10}$ at 360°C[18].

effect may have far-reaching consequences for the technology of catalyst application. We may thus formulate a general conclusion that :

> chemisorption may induce a decrease of the strength of bonding between structural elements of the solid, resulting in the deterioration of mechanical strength of the catalyst and the desintegration of catalyst particles.

One of the broad fields of research, opened by the development of highly sophisticated surface science techniques is the dependence of physical and chemical properties of solids on the size of very small crystallites and the question, to what extent catalytic properties of individual atoms are retained, when collective properties of a solid appear due to the interaction of increasing number of atoms. One of the most spectacular observations in this field is the discovery that very small metallic clusters assume the fivefold symmetry unknown in crystallography[29,30]. The optimization of the lattice energy, achieved when atoms are arranged into a close-packed structure, would require that a cluster of 13 metal atoms assumes an arrangement of a cubooctahedron with 6 fold symmetry. The surface of such polyhedron is however built of a number of [100] planes, charactrized by much lower surface energy than the [111] planes, prevailing when the 13 atoms assume the structure of an icosahedron of 5 fold symmetry [Fig. 16]. The gain in surface energy compensates the loss of lattice energy due to less-close

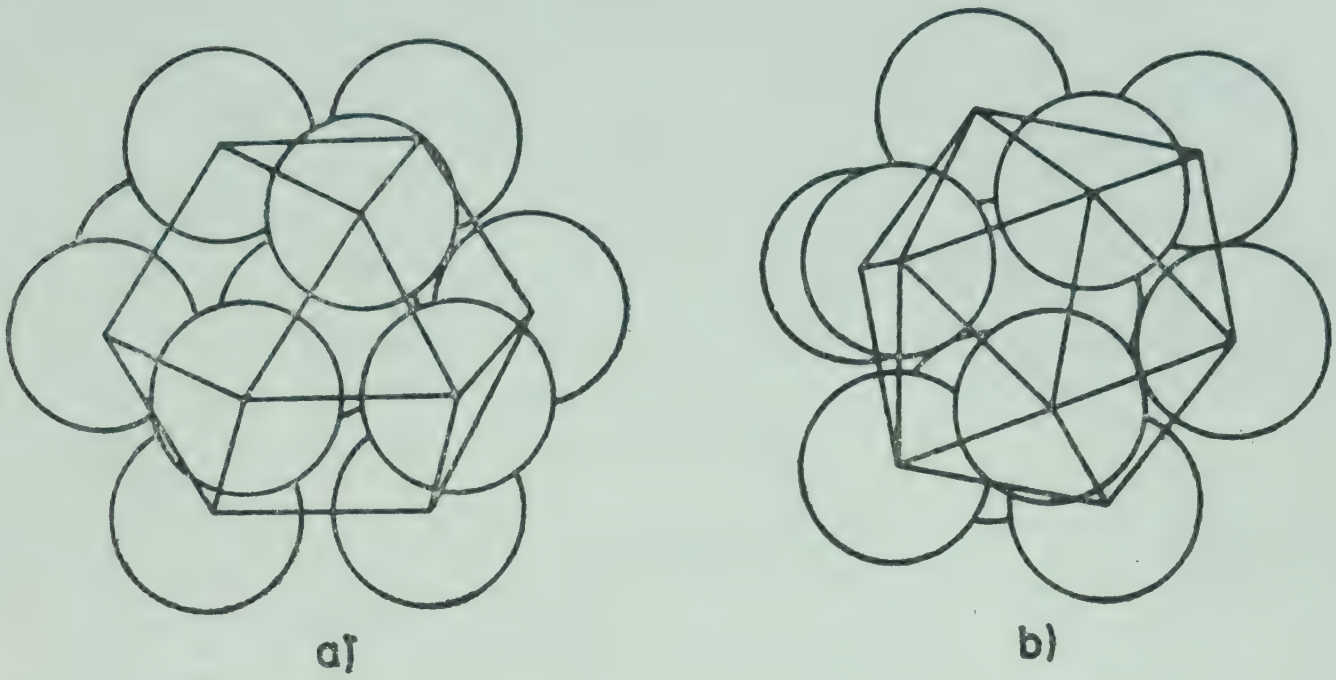

FIG. 16. Cubooctahedron(a) and Icosahedron(b).

packing and the very small clusters crystallize in form of icosahedrons. When the number of atoms in the cluster increases, the surface-to-bulk ratio decreases, the lattice energy becomes the main factor determining the stability and the transformation of the icosahedron into a cubooctahedron takes place. It may be estimated that the limiting number of atoms is of the order of 60.

It may be expected that in the range of sizes, in which the surface energy plays the dominant role, the properties of clusters will differ from those of the bulk phase. Indeed, a very interesting example was observed by Palczewska[31] in the case of Pd-H_2 system. Namely, the dissociation pressure of palladium hydride was found to depend strongly on the size of Palladium clusters. Therefore, catalysts composed of palladium highly dispersed on the carrier remain unchanged at hydrogen pressures, whereas larger palladium crystallites become transformed into palladium hydride. This observation is of paramount importance for catalytic hydrogenation, because palladium metal and hydride differ considerably in their selectivity of hydrogenation of acetylene to ethylene and ethane [Fig. 17]. Dependence of the properties on the size of crystallites was found in recent years also in the oxide systems. As an example, Table II shows the rate of reduction in hydrogen of V_2O_5 crystallites supported on TiO_2 as carrier[32]. The data clearly indicate that the rate of reduction increases by more than two orders of magnitude when massive V_2O_5 becomes highly dispersed at the surface of TiO_2. As the specific surface area increases to a much smaller degree than the rate, the acceleration of the reduction must be ascribed to the change of properties due to dispersion and the increasing influence of the carrier. We may thus formulate a general conclusion that :

> small clusters of the active phase supported on the carrier may have properties different from those of the bulk crystallites and may show different behaviour under the influence of gas phase reactants and the carrier.

It has been shown that due to the contribution from the surface free energy the composition of the surface of a solid differs from that of the bulk. As however the surface free energy depends also on the composition of the gas phase, it may be

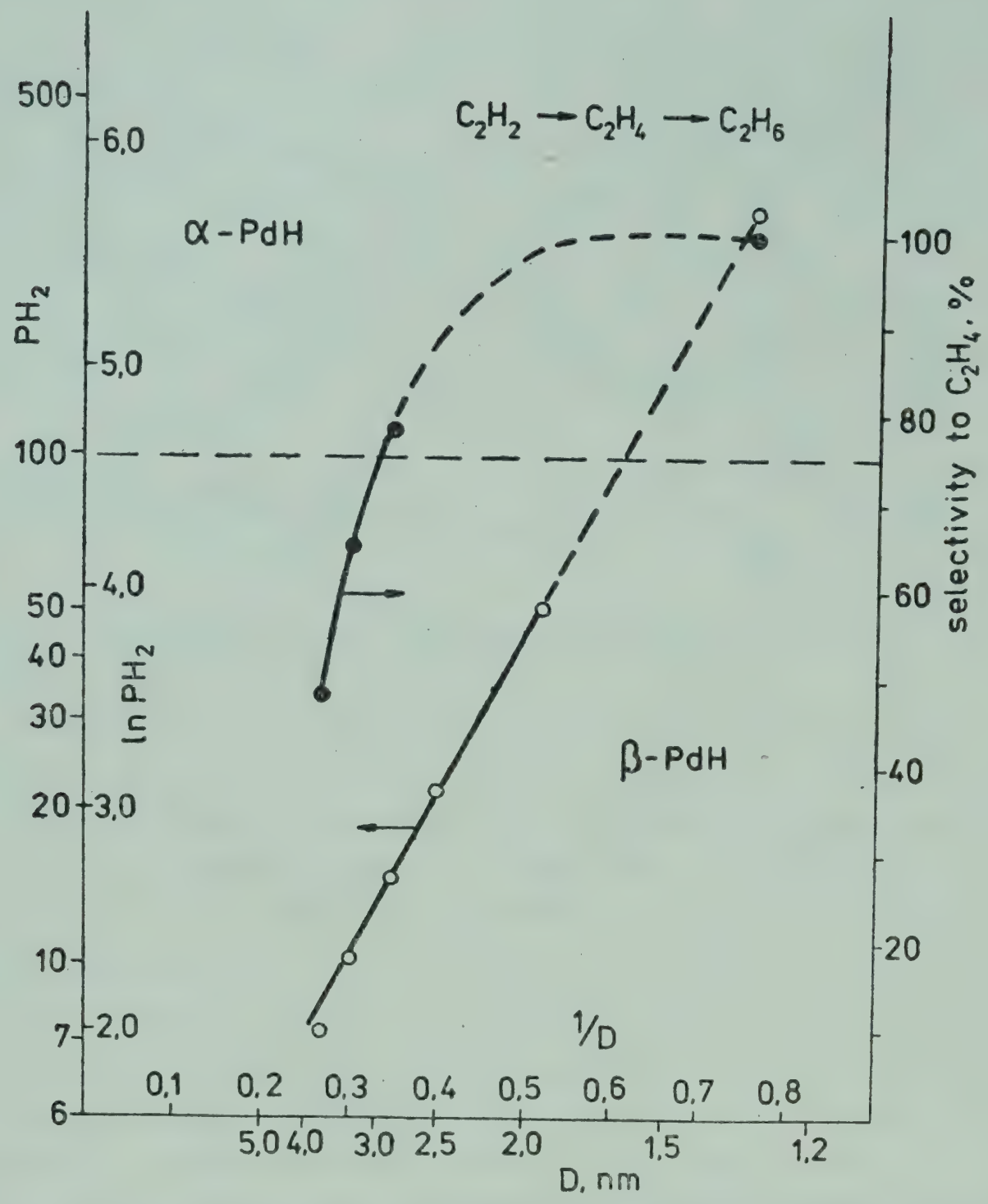

FIG. 17. Dissociation hydrogen pressure over PdH and selectivity in hydrogenation as function of the dispersion[31].

TABLE II

Reduction of the $V_2O_5 - TiO_2$ *System.*

Sample	V_2O_5 mole %	E, kcal/mol	K_s/K_r
TiO_2	0	—	—
$V_2O_5 - TiO_2$	2	25,8	139
$V_2O_5 - TiO_2$	5		66
$V_2O_5 - TiO_2$	8	26,3	37
$V_2O_5 - TiO_2$	10		23
$V_2O_5 - TiO_2$	12	26,1	18,5
$V_2O_5 - TiO_2$	20	25,6	17
V_2O_5	100	25,4	1

expected that variation of the latter will cause the changes of the surface composition. Indeed, experiments carried in recent years have shown that the surface of

alloy crystallites is enriched in this component which is characterized by higher heat of adsorption of molecules present in the gas phase.

When considering transition metal oxides the majority of which belong to nonstoichiometric compounds, the equilibria between the lattices and its constituents in the gas phase must also be taken into account. As nonstoichiometry may be described in terms of the solid solution of appropriate defects in the perfect crystal lattice, changes of composition of the gas phase entail the change of concentration of these defects considered as the solute, and this in turn is reflected in the corresponding variation of the surface composition.

Changes of surface composition due to the variation in the composition of the gas phase may have a profound influence on catalyticx properties of the surface[39,40]. Such effect is clearly manifested in the case of the oxidation of benzene to maleic anhydride on V_2O_3-MoO_3 catalysts studied by Bielanski *et al.*[33] The increase of the ratio of benzene to oxygen in the gas phase is followed by an appropriate increase of the degree of reduction of the catalyst, expressed in terms of the concentration of V^{+4} ions, which in turn causes an increase of selectivity of the reaction to maleic anhydride [Fig. 18]. These observations may be summarized by concluding that :

> composition of the gas phase determines the composition of the catalyst surface, which in turn may define the catalytic activity and selectivity.
>
> The degree of reduction attained by the catalyst at the steady state conditions of the catalytic reaction depends on the rate of reduction of the catalyst and the rate of its reoxidation. Many observations made in recent years indicate that these

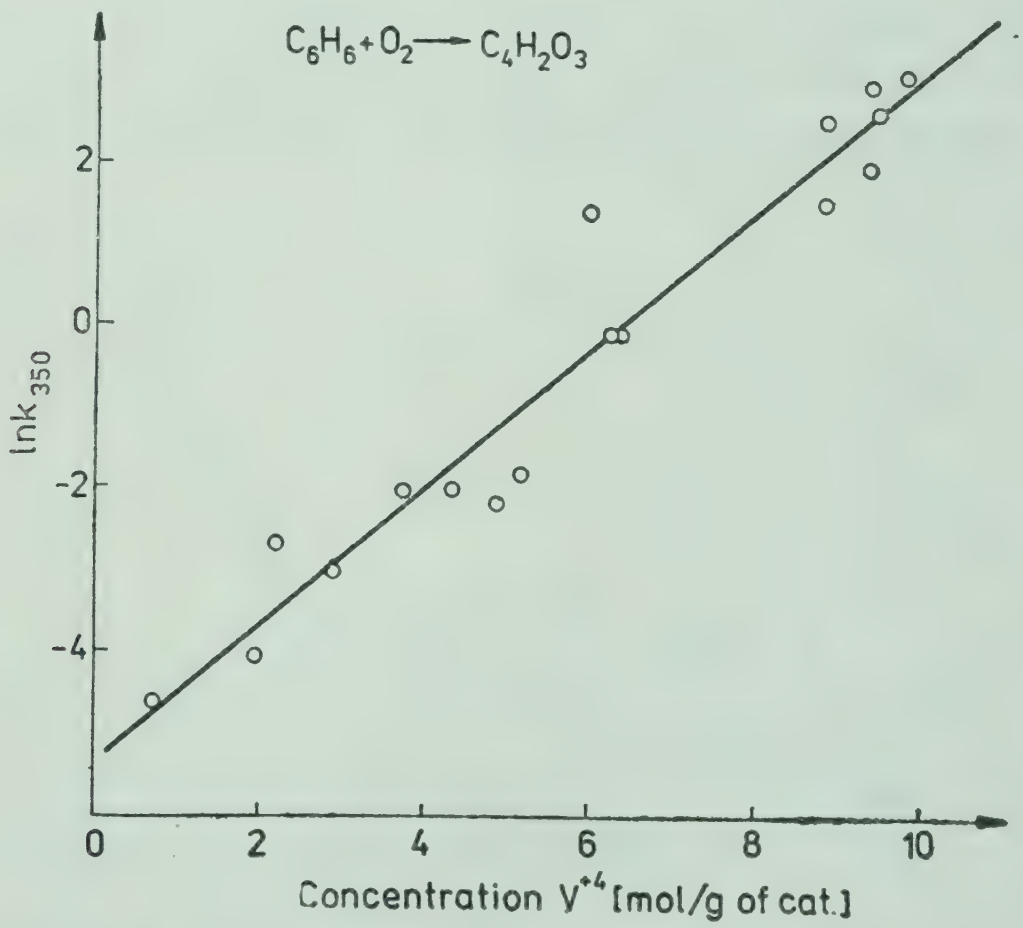

FIG. 18. Rate constant of the oxidation of benzene to maleic anhydride on V_2O_5-MoO_3 catalysts as function of the concentration of V^{+4} ions.[33]

rates may be strongly influenced by the presence of foreign additives even in very small amounts. A most spectacular phenomenon of this type is illustrated in Fig. 19[34]. Curve 1 in this figure shows the kinetics of the reduction of $CuMoO_4$ in hydrogen at 420°C. Reduction proceeds in two steps: in the first slow one $CuMoO_4$ is reduced to the intermediate products, consisting of the two monovalent copper molybdates $Cu_2Mo_3O_{10}$ and $Cu_6Mo_4O_{15}$, which then in the second very rapid step are reduced to metallic copper and MoO_2. When however 0.05% mole of MoO_3 is deposited at the surface, reduction becomes accelerated so dramatically that the first step is completed in few minutes as compared to 200 min for pure $CoMoO_4$ and becomes indistinguishable from the second step [curve 2].

As the result of the change of the ratio of rates of reduction to that of oxidation the virtual oxygen pressure at the surface may be changed to such extent that new bidimensional phases appear at the surface of the oxide.[35,36] Such behaviour was e.g. observed[18] when the $CuMoO_4 + 0.05\ MoO_3$ was used as catalyst in the oxidation of butene-1 [Fig. 20]. The fresh catalyst when exposed to pulses of pure butene-1 showed high selectivity in isomerization and the only other products were CO and CO_2 formed as the result of the surface reduction of the catalyst. Progressively more and more oxygenated products : crotonaldehyde and methylvinylketone appeared and after 20 pulses of butene the selectivity of the formation of crotonaldehyde reached a high level of about 30 %. The photoelectron spectra registered at this stage showed [Table 3] that the surface of the catalyst is covered by a surface phase of $Cu_6Mo_4O_{15}$. [It could be reversibly oxidized to $CuMoO_4$ which indicates that it has not yet the properties of a bulk phase, $Cu_6M_4oO_{15}$ being probably present in form of a bidimensional surface phase]. When now pulses of butene-1 + oxygen mixture in the 1:2 ratio were introduced the selectivity to crotonaldehyde dropped back to a low value, whereas that to CO_2 increased drastically indicating that under the influence of the reacting mixture at this composition the surface became reoxidized to $CuMoO_4$. However, when pulses of the butene + oxygen mixture in the ratio 1 :1 were injected after the pulses of

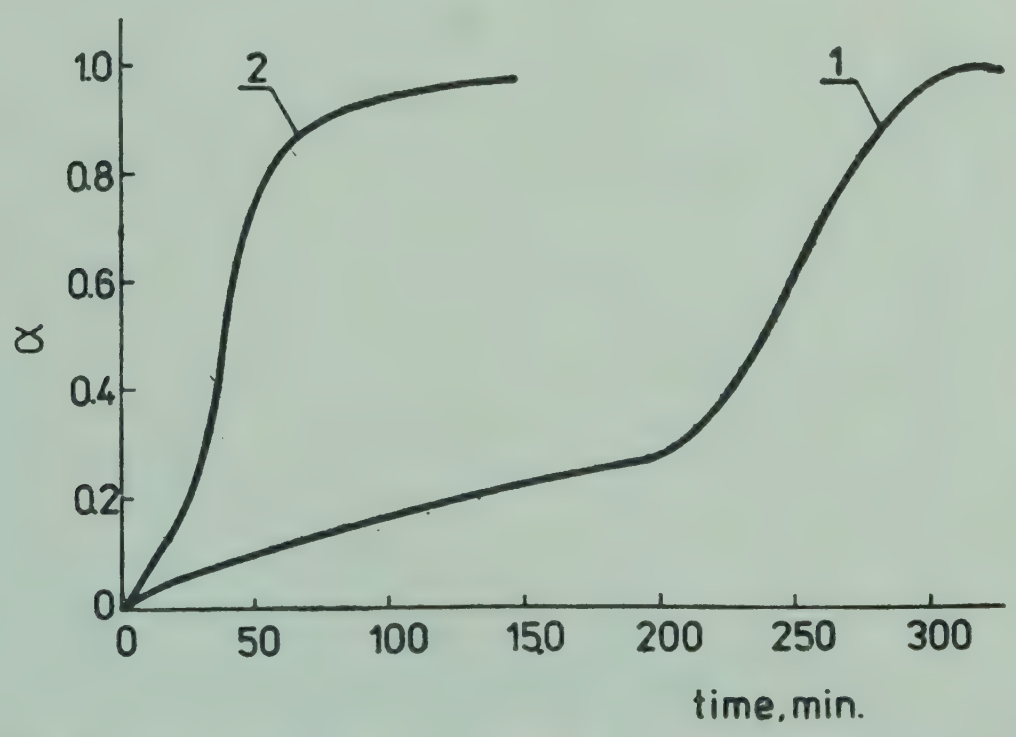

FIG. 19. Degree of reduction in 21.5 Torr of hydrogen at 418°C as function of time for :1-pure $CuMoO_4$, 2-$CuMoO_4$ + 0.05 % MoO_3[34].

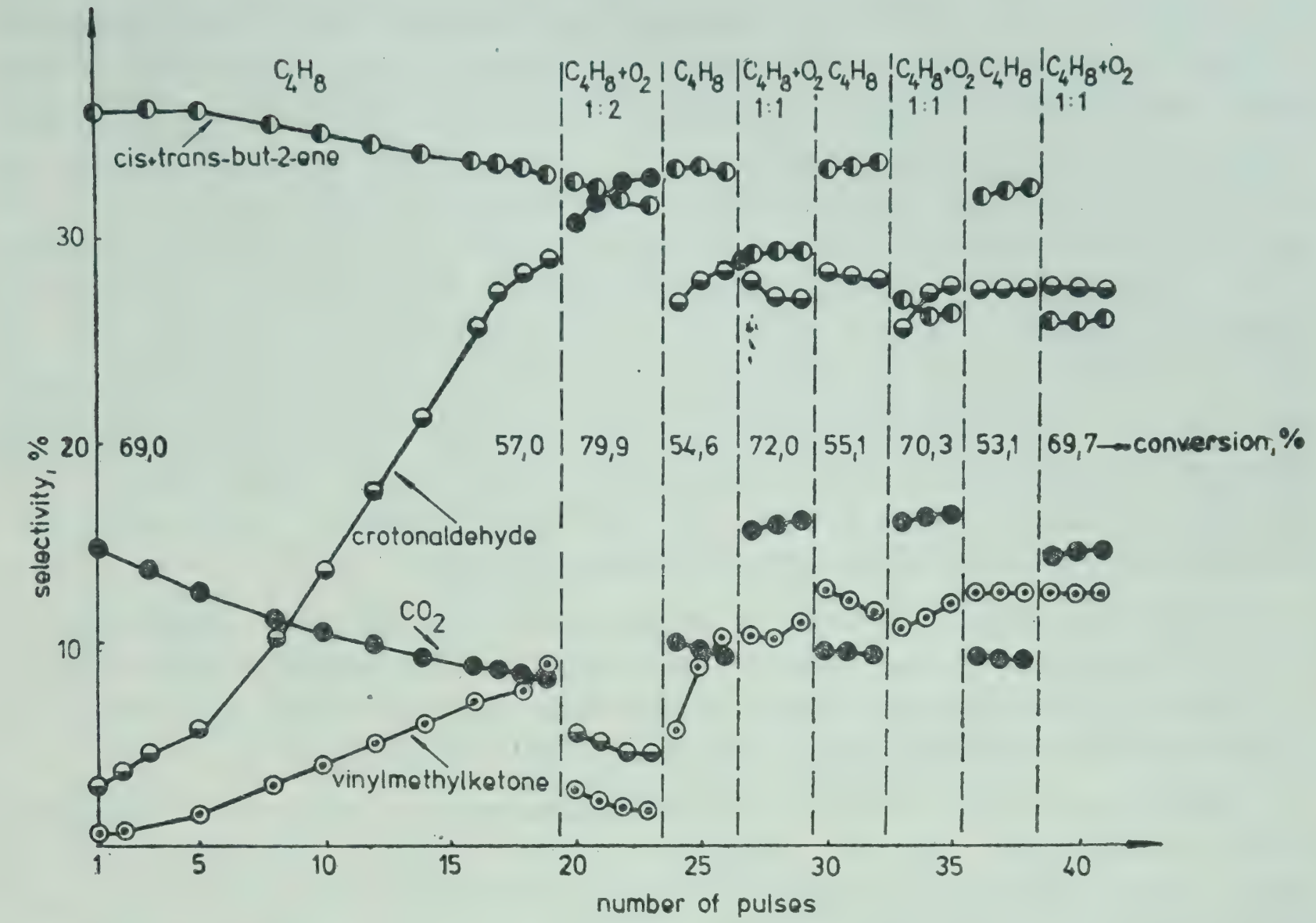

FIG. 20. Conversion and selectivities to different products of the interaction of butene-1 with $CuMoO_4$ + 0.05 MoO_3 as function of the number of pulses. Composition of pulses is indicated at the top of the figure[18].

TABLE III

Cu2p and Mo3d photoelectron binding energies and CuLMM Auger electron kinetic energy for reduced $CuMoO_4$ catalysts

Sample	Photoelectron binding energy, eV				CuLMM Auger electron kinetic energies, eV	
	Cu2p		Mo3d			
Cu_{met}	933,1					918,2
$Cu^{I}_{2}\ Mo_3O_{10}$	932,2		232,6	916,3		
$Cu^{I}_{6}\ Mo_4O_{15}$	932,2		232,3		916,4	
CuO						917,6
MoO_2		934,0	230,1			
$Cu^{II}\ MoO_4$		934,7	232,9		916,4	
fresh catalyst after reduction with butene pulses		934,6	232,9		916,4	
	932,2		232,2	916,2		
after reduction in butene flow	932,2		229,7			917,2

pure butene, the selectivity to crotonaldehyde remained high at high conversion of about 70 %. Apparently, at this composition of the reacting mixture the surface phase characterized by high selectivity of the formation of crotonaldehyde could be generated and maintained stable in the course of the catalytic reaction by periodically varying the composition of the reacting mixture from 1 :1 to 1 : 0. Similar phenomena of the formation of surface phases were observed in the case of the oxidation of propylene on $Cu_2Mo_3O_{10}$[27,37]. When such surface phase is allowed to grow into a new bulk phase, non-equilibrium phase transitions are observed, which can be accompanied by a histeresis of the change of catalytic properties as function of the variation of the composition of reacting mixture. Such phenomenon was discussed quite recently by Rieckert *et al.*[38] in the case of the oxidation of propylene on copper oxide catalysts. This part of our discussion may be summarized by formulating a general conclusion that :

> the catalyst surface is in dynamic interaction with the gas phase. Depending on the properties and composition of the reactants of the catalytic reaction different surface phases may be formed at the surface of the catalyst, generating new active centers, directing the reaction along different reaction paths.

Let us now return to the fundamental question as to what is the structure of the intermediate complex composed of the reacting molecule and the active center of the catalyst, and how this structure determines the reaction path. In recent years increasing number of attempts is being made to answer these questions on the basis of quantum chemical calculations[41–43]. Results already obtained are very encouraging and show that the quantum chemical description of intermediate complexes formed in the course of catalytic reactions may supply valuable information concerning the mechanism of elementary transformations of the reacting molecule. At present exact discussion of the interaction of an adsorbed molecule with the group of atoms of the solid, forming the active center is not yet possible and many approximations must be used. The most vital problem is the proper choice of the model of the intermediate complex which should represent as closely as possible the physical reality. As already mentioned the cluster model proved to be very useful, and results of the application of a variety of sophisticated surface techniques enable at present the quantitative determination of its parameters. The quantum-chemical method used depends on the particular problem to be solved. Discussion of the advantages and limitations of various quantum chemical methods usually applied to solve catalylic problems can be found in[44]. It may be hoped that with the development of quantum chemistry on one hand, and with further improvement in the knowledge of the molecular mechanism of the catalytic transformation on the other hand it will be possible to give a full quantum-chemical description of the interaction between the reacting molecules and the catalyst as a basis of the theory of catalysis.

References

1. *Methods of Surface Analysis*, A W Czanderna ed. Elsevier, Amsterdam, (1975).
2. *Surface Properties of Materials*, L L Levenson ed. North Holland Publ. Co. Amsterdam, (1975).

3. Characterization of Solid Surfaces, P F Kane, G B Larrabee, ed. Plenum Press, New York, (1974).
4. "*Electron Spectroscopy for Surface Analysis*, H Ibach, ed. Springer Verlag, Berlin (1977).
5. *Electron and Ions Spectroscopy of Solids*, L Fiermans, J Vennik, W Dekeyser, ed. Plenum Press, (1978).
6. J Haber, in "*Chemical and Physical Aspects of Catalytic Oxidation*, ed. J Portefaix, F Figueras CNRS Paris, (1980) 336.
7. L H Little, *Infrared Spectra of Adsorbed Species*, Academic Press (1966).
8. R Watanabe, M Hashiba, T Yamashina, *Surface Sci.* **61** (1976) 483.
9. W M H Sachtler, R A Van Santen, *Adv. Catal.* **26** (1977) 69.
10. P G Menon, T S R Prasad and S Rao, *Catal. Rev.* **20** (1979) 97.
11. J Haber, J Nowotny, I Sikora, and J Stoch, *Appl. Surf. Chem.* **17** (1984) 324.
12. J Nowotny, I Sikora, J B Wanger, Jr., *J. A. Ceram. Soc.* **65** (1982) 192.
13. W Hirschwald, B Loechel, J Nowotny, J Oblakowski, I Sikora F and Stolze, *Bull. Acad Polon. Sci., ser. sci. chim.* **29** (1981) 369.
14. G M Schwab, *Katalyze vom Standpunkt der chemichen Kinetik*, Springer Verlag (1931).
15. A A Balandin, *Adv. Catal.* **19** (1969) 1.
16. G Rienacker, *Anqew. Chem.* **69** (1957) 545.
17. G Samorjai, *Catal. Rev.* **18** (1978) 173.
18. J Haber, T Wiltowski, *Bull. Acad. Polon. Sci. ser. sci. chim.* **29** (1983) 563.
19. J Haber, Proc. IV Intern. Conf. on Chemistry and Uses of Molybdenum, Golden, Colorado 1982, H.F.Barry, P.C.H Mitchell ed., Climax, Ann Arbor (1982) 395.
20. M Gasior, T Machej, *J. Catal.* **83** (1983) 472.
21. J M Germain, J M Tatibouet, *J.Catal.* **72** (1981) 375.
22. J C Volta, M Foriossier, F Theoblad, T P Pham, *Disc. Faraday Soc.* **72** (1981) 275.
23. A R C Westwood, J S Ahearn, in *Physical Chemistry of the Solid State: "Application to Metals and their Compound"*, Elsevier 1984, 65.
24. G K Boreskov, *Kinet. Catal. (in russian)* **21** (1980) 5.
25. T Wang, L D Schmidt, *J. Catal.* **70** (1981) 187.
26. J Haber, E Jamroz, *J.Solid State Chem.* **44** (1982) 291.
27. J Haber, J Stoch, T Wiltowski, *Proc. 7th Intern. Conger. Catal.* Tokyo 1980, Elesvier (1981).
28. E D Shchukin, L J Morgolis, *Povierhnost* **1** (1982) 1.
29. Y Takasu, A M Branhshaw. *The Characterization and Properties of Small Metal Particles* in *Chemical Physics of Solids and Their Surfaces*. Specialist Periodical Report vol. 7. The Chemical Soc., London (1978).
30. J J Burton, R L Gartner, in *Advanced Materials in Catalysis*, Academic Press, New York, (1977) 33.
31. R Frak, *Institute of Physical Chemistry Polish Academy of Sciences*, Ph.D. Thesis Warsaw (1977)
32. B Dyakova, B Mehandziev, B Grzybowska, T Gasior and J Haber, *Appl. Catal.* 3 (1982) 255.
33. A Bielanski and A Inglot, *Bull. Acad. Polan. Sci. ser. sci. chim.* **22** (1974) 773.
34. J Haber and E Jamroz, *Rev. Chim. Minerale* **20** (1983) 712.
35. J Haber, *Proc. 3rd Intern. Conf. Chemistry and Uses of Molybdenum, Ann Arbor*, ed. H F Barry, P C H Mitchell, Climax Ann Arbor (1979) 114.
36. J Haberin, "*Surface Properties and Catalysis by Non-metals* ed. J P Bonnelle, B Delmon, E Derouane, Reidel Publ. Co Dordreckt, (1983) p. 1.
37. J Haber, T Wiltowski, *Bull. Acad. Polon. Sci. ser. sci. chim.* **27** (1979) 785.
38. M Greger, B Ihme, M Kotter and L Rieckert, *Ber. Bunsen gas Phys. Chem.* **88** (1984) 427.
39. J Haber, *Kinet. Katal. (russian)* **21** (1980) 1.
40. G K Boreskov, *Kinet. Katal. (russian)* **21** (1980) 5.
41. J Haber, M Sochacka and A Golebiewski, *J. Molecular Catal.* **3** (1977) 213.
42. J Haber and M Witko, *J. Molecular Catal.* **9** (1980) 399.
43. E Broclawik, J Haber and M Witko, *J. Molecular Catal.* **26** (1984) 249.
44. J Haber and M Witko, *Acc. Chem. Res.* **14** (1981) 1.

© *Proc. Indian natn. Sci. Acad.*, **51**, A, No. 1, 1985, pp. 98–123.
Printed in India.

THEORETICAL ASPECTS OF CHEMISORPTION BY METALS*+

T B GRIMLEY

Donnan Laboratories, University of Liverpool
P O Box 147, Liverpool L69 3BX, England

1. INTRODUCTION

THE clean surfaces of many solids are very reactive. Even in a good vacuum (10^{-6} torr+), most metals will become covered with a layer of *adsorbed* gas (oxygen or nitrogen) in less than a minute, and this is because nearly every gas molecule which hits the metal surface, sticks to it. In other words, the sticking coefficient is nearly unity.

Molecules may be *physisorbed* or *chemisorbed*. The former is shorthand for physically adsorbed, the latter for chemically adsorbed. Rare gases (He, Ne,... Xe) are physisorbed by metals. No chemical bond is formed, but the atom is attracted to the surface by the Van der Waals force varying with distance from the surface like $(\text{distance})^{-4}$. At short distances when the electron clouds of the gas atom and the metal begin to overlap, a strong repulsive force develops. This repulsion is due essentially to the operation of the Pauli Exclusion Principle; the metal electrons must avoid the electrons in the doubly occupied orbitals of the rare gas atom, and this raises their kinetic energy. The addition of the long-range attractive, and the short-range repulsive forces leads to a potential energy curve with a shallow minimum of depth about 1 kJ mol^{-1}, (Fig. 1).

In *chemisorption*, a chemical bond is formed between the solid (the substrate), and the adsorbed species (the adsorbate). We call this bond the surface bond, or

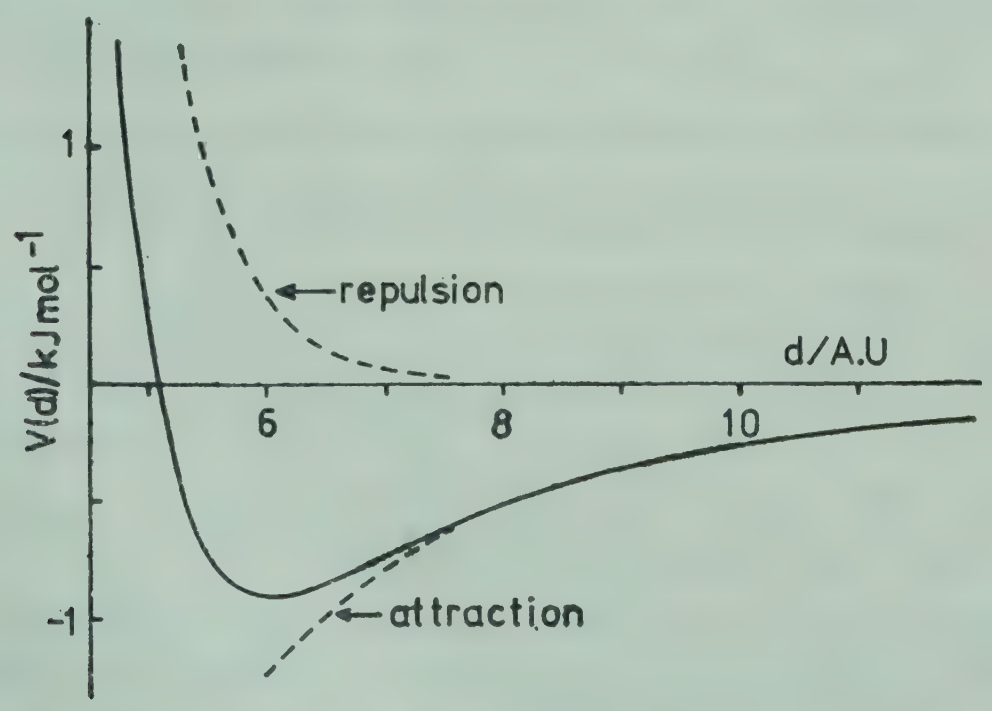

FIG. 1. The potential energy curve for a rare gas atom near a metal showing the attractive, and repulsive contributions.

---

* Paper presented at the Symposium on Physics and Chemistry of Surfaces held at INSA, New Delhi from September 28-30, 1984.

+ 760 torr ≡ 1 atmosphere pressure

the chemisorption bond. Existing chemical bonds in the gas molecule may be strongly perturbed when the surface bond is formed, and in many cases they are actually broken so that the adsorbed species are fragments of the original molecule. Thus, we speak of non-dissociative chemisorption if the gas molecule retains its integrity on the surface, and dissociative chemisorption if it does not. Examples of non-dissociative chemisorption are :

CO on (111) Ni [see (I) and (II) below]

C_2H_4 on Fe and Cu

C_6H_6 on Ni

It is not however easy to know the adsorption geometry, For CO on Ni, linear (I), and bridged (II) forms are possible.

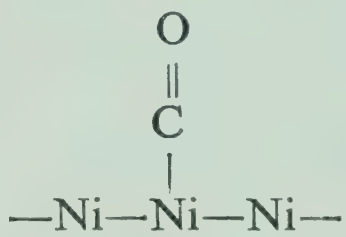

(I)

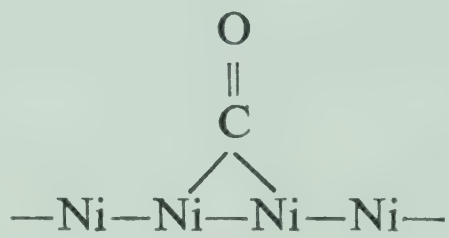

(II)

Examples of dissociative chemisorption are :

H_2 on (100) W [see (III) below]

CO on Mo

O_2 on most transition metals

N_2 on V

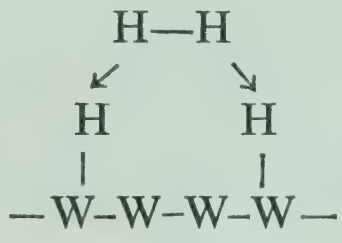

(III)

Chemisorption forces are quite different from those causing physisorption, and the Van der Waals attraction is insgnificant in determining the minimum in the potential energy curve. This minimum, and therefore the surface bond length, and the chemisorption binding energy, are determined by factors similar to those determining bond lengths, and bond dissociation energies in simple molecules. only the fact that the surface bond is formed between a macroscopic system (the solid), and a microscopic system (the adsorbed species), and can involve a very large number of electrons, might obscure this essential similarity.

Chemisorption binding energies, i.e., surface bond dissociation energies, like those of other chemical bonds, span a wide range, and include* :

*Binding energies depend on the crystal face, and on the adsorption site and geometry. The latter is not often known experimentally. Experiments with films yield an average over several crystal faces.

D (nickel-CO) 176 kJ mol^{-1}
D (vanadium-N) 795 kJ mol^{-1}
D (iron-N) 545 kJ mol^{-1}
} Films
D ((110) Fe-H) 268 kJ mol^{-1}

Chemisorption is important in many areas of Chemical Physics; in heterogeneous, catalysis, corrosion, and electrochemistry for example. In catalysis, chemisorption of at least one of the reactants is an essential step by which the solid surface provides new reaction paths not available in the homogeneous gas phase. The rate of the slowest step in the reaction by such a new path may be faster than that of the slowest step in the homogeneous reaction. If it is, the solid catalyzes the reaction.

Some important catalyzed reactions are :

$$N_2 + 3H_2 \xrightarrow{\text{Fe (450°C)}} 2NH_3 \text{ (ammonia synthesis)}$$

$$nCo + (2n+1)\,H_2 \xrightarrow{\text{Co (200°C)}} C_nH_{2n+2} + nH_2O \text{ (water gas reaction)}$$

$$C_nH_{2n} + H_3 \xrightarrow{\text{Pt (200°C)}} C_nH_{2n+2} \text{ (hydrogenation of olefins)}$$

The synthesis of ammonia in the homogeneous gas phase does not proceed at an appreciable rate because of the large activation barrier due to the need to dissociate the N_2 molecule [$D(N_2) = 941$ kJ mol^{-1}]. On an iron catalyst, the iron-N surface bond is strong enough to dissociate N_2, and this activation barrier is absent. But the iron-N surface bond is not so strong as to remove the nitrogen from further reaction with hydrogen (hydrogenation), and therefore to replace one large activation barrier by another. On the other hand, this is exactly the situation on vanadium, and with this metal there is no worthwhile catalysis of the ammonia synthesis.

There are two parts to theoretical studies of chemisorption :

(a) Statics. This is the determination of the equilibrium situation; bond lengths and energies, the adsorption geometry etc. I call this chemisorption theory.

(b) Dynamics. This is the study of molecular rate processes on solid surfaces, and of probe dynamics ; the rates of adsorption, chemical reactions, particle scattering, etc.

Dynamics is by far the larger part, but of course, by studying statics, we acquire an essential input into dynamical calculations.

Chemisorption theory proceeds at quantitative, semi-empirical, and qualitative levels. At the quantitative level, the first goal is to develop theoretical models of adsorbate/substrate systems which are suitable for the calculation of the equilibrium positions of all the nuclei, the ground-state energy, and the elementary

excitations. This goal is difficult to attain. It is a large-scale computing task, and the *a priori* geometry prediction is particularly hard to achieve over the wide range of chemisorption systems of practical importance. Because of this, many investigations determine the electronic structure, and some elementary excitations, for a single assumed nuclear geometry. But there are some notable exceptions which I shall mention in § 4.

Work at the semi-empirical level seeks to avoid the huge computer task of the fully quantitative approach by judicious use of numerical approximations, and experimental data. But semi-empirical theories are intended to be useful, and valid approximations to specific quantitative models, and because of this, I shall confine myself to the *primary* theoretical models in chemisorption theory.

Qualitative work in chemisorption theory is directed towards "understanding" the chemisorption bond, to developing useful concepts in quantum chemistry at solid surfaces, and to correlating and explaining experimental data. It is at this level that Anderson's[1] Hamiltonian has been valuable[2].

We are concerned in chemisorption theory to a large extent with molecular orbital (MO) schemes, and I mention here the more important MO schemes in use in the quantum chemistry of molecules and solids. The Hartree-Fock (HF) theory in its single configuration form is a well-known approximation, but there exist two *exact* MO schemes too. First there is the Kohn-Sham[11] scheme giving the exact ground-state energy, and the electron density by formulae involving sums on "occupied orbitals" rather like those of the HF model. On the other hand, the exact ionization, and affinity levels are the "orbital energies" of a completely different potential from that in the Kohn-Sham (KS) equations; they are the energies of *Dyson orbitals* of a non-Hermitian eigenvalue problem, and an energy-dependent potential. This is the dynamic Hartree-Fock (DHF) scheme, and in this scheme, the formulae for the ground-state energy, and the electron density involve sums on Dyson orbitals with however, non-integral occupation numbers. I give more details in § 3.

Although there are difficult problems still to be overcome in the theory of the equilibrium properties of chemisorption systems, firstly kinetics, and secondly, reaction dynamics are at the heart of Surface Chemistry. In kinetics we are concerned with macroscopic quantities like the rate of a reaction per unit area of the catalyst, the dependence of this rate on the temperature, on the pressures of the reactants, and so on. In reaction dynamics, we are concerned with the behaviour of single reactant molecules in their encounters with the catalyst, with adsorbed species, and so on. Because they are so heavy, it is usually possible to treat the translational motions of the reactants classically, but the other degrees of freedom, and of course the electronic motion, have to be treated by quantum mechanics. Among the simplest dynamical processes on solid surfaces we note :

(a) Sticking. For example the rate of adsorption of a reactive species like H atoms by a solid metal :

$$\text{Solid} + \text{H} \longrightarrow (\text{Solid-H})^*$$

the star (*) indicating an excited state.

(b) Flash desorption. For example the rate of desorption of a rare gas atom like He from a solid when the solid is suddenly heated :

$$(\text{Solid-He})^* \longrightarrow \text{Solid} + \text{He}.$$

If it is to stick on a solid, a gas atom must lose at least its kinetic energy, otherwise it will bounce back (inelastically perhaps) into the gas phase (Fig. 2). The required energy may be lost by exciting the vibrations of the solid (loss to phonons) or by exciting the electron system (loss to electrons), or by both. A light atom like hydrogen connot easily lose its kinetic energy to phonons in a collision with the surface of metal composed of much heavier atoms (think of the fairground coconut shy), and in this example, energy loss to the electrons is the likely mechanism for sticking. The fact that the H atom is a reactive species forming a strong chemisorption bond under equilibrium conditions also helps the electron loss mechanism: very profound changes in the electron distribution between the atom and the solid must occur during the collision *if the electronic motion is to remain unexcited.* By contrast, the flash desorption (Fig. 3) of a physically adsorbed rare gas atom like He is likely to be driven by energy transfer from the thermally excited phonon system; physisorption involves only small changes in the distribution of electrons between the atom and the solid.

I shall give some details of the *full quantum mechanical approach* to these dynamical processes later, but I mention here an even simpler dynamical process on a solid surface, namely the electron transfer between the solid and a fast (500 eV) atom or ion reflected from it. The translational motion of the fast gas particle can be treated classically, and this determines a time-dependent perturbation of the electron system whose quantum state therefore evolves in time through the collision. By following this time evolution with Schrödinger's

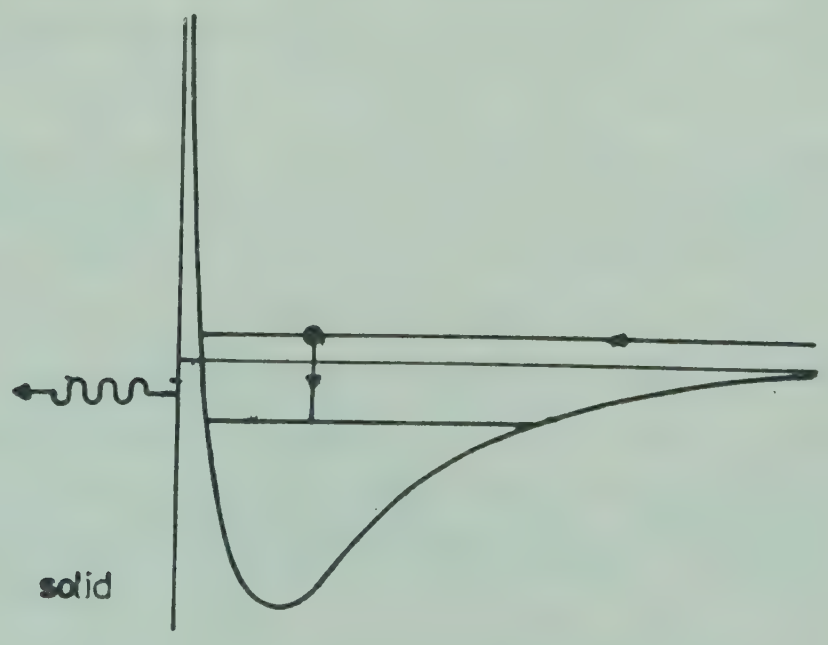

FIG. 2. Sticking. The gas atom leses energy to the solid and falls into a bound state.

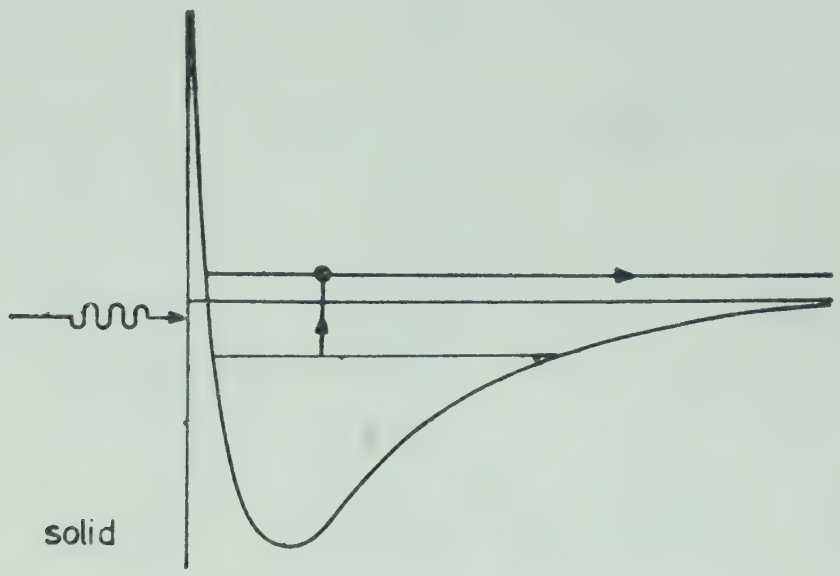

FIG. 3. Thermal desorption. The adsorbed atom gains energy from the hot solid and is excited into an unbound state.

time equation, the probability of electron transfer can be computed[3–5]. The probability of excitation of the gas atom in the process can also be obtained[6].

2. UNDERSTANDING THE CHEMISORPTION BOND

The traditional attitude in chemistry is that chemical bonds can be understood at the level of simple orbital approximations, and a knowledge of the electronic structures of atoms at this level is sufficient to understand how stable molecules can be formed, and a similar knowledge of the electronic structures of molecules can tell us how molecules can react. More recently the role of "*frontier orbitals*" has been emphasized in making predictions about reaction mechanisms[7]. I now show how the concepts of frontier orbital theory are generalized in chemisorption theory where one of the partners in the bond (the solid) is a macroscopic system with a nearly continuous spectrum of MO's and energy levels[2,8].

2.1. Generalized frontier orbital theory

I consider the interaction of ethene with the (001) surface of aluminium, and ask the question : Knowing the electronic structures (MO's and energy levels) of ethene and (001) Al, can we decide if ethene will chemisorb on (001) Al ?

First we compare the orbital energies of electrons in ethene and aluminium (Fig. 4). The Fermi level of Al which separates occupied and unoccupied levels for electrons in the metal, lies between the Highest Occupied Molecular Orbital (HOMO), and the Lowest Unoccupied Molecular Orbital (LUMO) of ethene. A chemical bond between ethene and the metal can be formed by an electron in the ethene HOMO hopping to the metal into a normally unoccupied MO of aluminium above the Fermi level, ϵ_F, or by an electron hopping from an MO of aluminium below ϵ_F into the ethene LUMO. Consequently we write an approximete many-electron wavefunction ψ for the system by mixing the above *Charge-transfer states* with the neutral ground state of the non-interacting system;

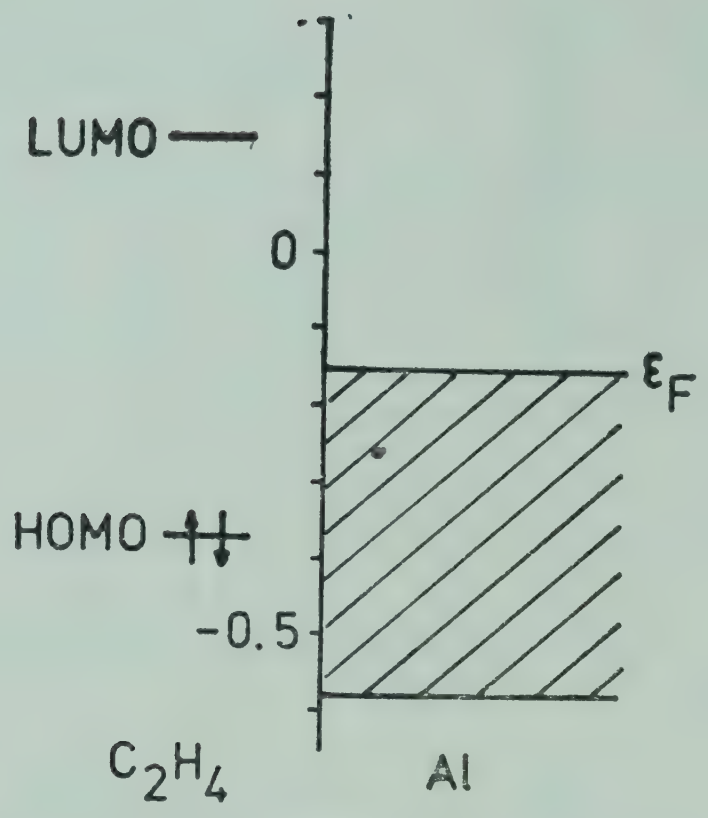

FIG. 4. The energy levels of ethene and aluminium metal.

$$\psi = N_0\psi_0 + \sum_{K = \text{occupied}} A_K\psi_k \ (C_2H_4^-, Al^+)$$

$$+ \sum_{K = \text{vacant}} C_K\psi_K \ (C_2H_4^+, Al^-)$$

We then use the variation theorem to estimate the ground-state energy. This leads to an expression for the chemisorption binding energy D (positive for stability) which through second-order terms is

$$D = 2\int_{-\infty}^{\epsilon_F} d\epsilon \frac{w_{LUMO}(\epsilon)}{\epsilon_{LUMO} - \epsilon} + 2\int_{\epsilon_F}^{0} d\epsilon \frac{w_{HOMO}(\epsilon)}{\epsilon - \epsilon_{HOMO}} \qquad \ldots (2.2)$$

Here w_{HOMO} and w_{LUMO} are the *spectral densities* of the interactions of the ethene frontier orbitals with the Mo's of the metal. I assume that w_{HOMO} and w_{LUMO} are proportional to the spectral densities of the overlaps of the respective frontier orbitals with the metal Mo's :

$$w_{HOMO}(\epsilon) \propto \rho_{HOMO}(\epsilon) = \sum_K |\langle \text{HOMO} | K \rangle|^2 \delta(\epsilon - \epsilon K)$$

$$w_{LUMO}(\epsilon) \propto \rho_{LUMO}(\epsilon) = \sum_K |\langle \text{LUMO} | K \rangle|^2 \delta(\epsilon - \epsilon K) \qquad \ldots (2.3)$$

Both integrals on the right in (2.2) are positive, and both therefore contribute to stabilize the chemisorbed state. However the first term would contribute little if ρ_{LUMO} had little of its density in the occupied states of the metal (i.e., below ϵ_F), and the second term would contribute little if ρ_{HOMO} had little of its density in the unoccupied metal states. If both conditions were to hold, ethene would not chemisorb. Detailed computer calculations[2] using the Huckel MO theory (the tight binding approximation of solid state physics) show that for C_2H_4 on (001)Al in the adsorption geometry of Fig. 5, ρ_{LUMO} and ρ_{HOMO} have significant

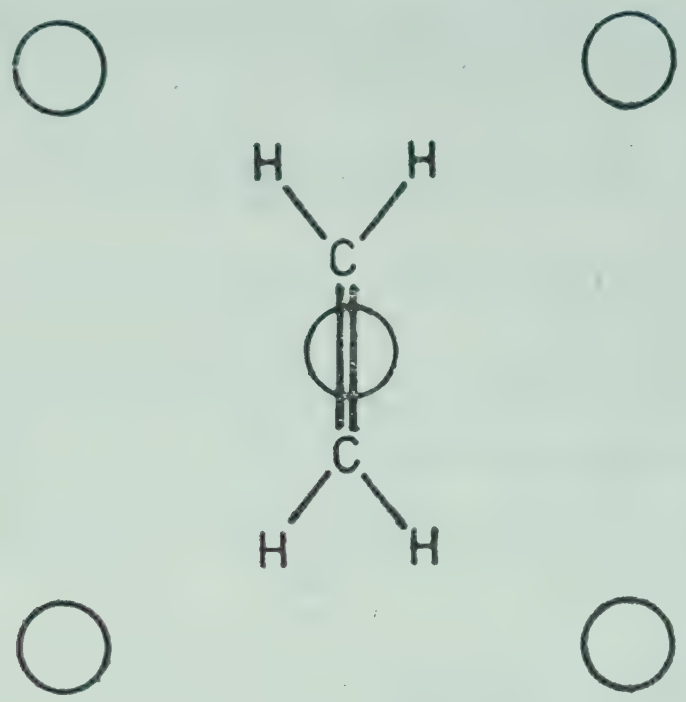

FIG. 5. C_2H_4 on (001) Al.

portions of their densities below and above ϵ_F respectively. Consequently both terms in (2.2) contribute significantly to D (A1 (100) — C_2H_4), and we expect ethene to be chemisorbed, which it is in practice.

The above argument using ρ_{LUMO} and ρ_{HOMO} is essentially a symmetry argument like those introduced into organic reaction machanisms by Woodward and Hoffman[9], and Fukui[10]. Indeed, the argument I have given here applies as much to the cyclo-addition of ethene to a diene as to its chemisorption by aluminium. But for the cyclo-addition reaction we have a discrete, not a continuous spectrum of substrate MO's, and therefore ρ_{LUMO} and ρ_{HOMO} consist simply of δ-functions of various strengths, betweed 0 and 1, at the MO energies of the diene. If we calculate using Huckel MO theory we find that ρ_{LUMO} has only 11 per cent of its density in the occupied diene MO's and similarly ρ_{HOMO} has only 11 per cent of its density in the unoccupied diene MO's. Thus both integrals in (2.2) are small, and because of symmetry factors essentially, the cyclo-addition to form vinylcylobutane is not expected. In fact, according to Woodward and Hoffmann[9] the reaction is symmetry forbidden. By contrast, the symmetry factors for the chemisorption of C_2H_4 by (001) A1 are not unfavourable because there exist in Al large numbers of MO's with energies near ϵ_F, and large amplitudes in the (001) surface, *and* with the right symmetries to interact with the C_2H_4 frontier orbitals.

3. EXACT MOLECULAR ORBITAL SCHEMES

As I have already mentioned, there are two exact, but very different MO schemes, the density functional (DF), and the dynamic Hartree-Fock (DHF) schemes.

The DF scheme gives the ground-state energy E_0, and the electron density n(r) by solving self-consistently, the one-particle Kohu-Sham[11] equations which

have a *local* potential v_{eff} [n; **r**] which is, as indicated, a functional of the electron density. The equations are, in atomic units*

$$(-\tfrac{1}{2}\nabla^2 + v_{eff}[n;\mathbf{r}]\,\psi_\alpha(\mathbf{r}) = \epsilon_\alpha\,\psi_\alpha(\mathbf{r}) \qquad \ldots 3.1)$$

$$n(\mathbf{r}) = \sum_{\alpha=1}^{N} |\psi_\alpha(\mathbf{r})|^2$$

the sum being on the N lowest energy states for N electrons in the system. The difficulty is of course that v_{eff} is not known because all the complications of the N-electron problem are contained in it. The most commonly used approximation is the *local density approximation* (LDA) where

$$v_{eff}[n;\mathbf{r}] \simeq v_H(\mathbf{r}) + \frac{d}{dn}\epsilon_{xc}(n)\,n \qquad \ldots(3.2)$$

where v_H is the electrostatic or Hartree, potential, and $\epsilon_{xc}(n)$ is the exchange-correlation energy per electron of a homogeneous electron gas of density n. Separating the exchange energy

$$\epsilon_{xc}(n) = -\tfrac{3}{4}(3n/\pi)^{1/3} + \epsilon_c(n) \qquad \ldots(3.3)$$

where ϵ_c, the correlation energy, is some interpolation of the known high- and low-density results, for example Wigner's[12] interpolation

$$\epsilon_c(n) = -\frac{0.056\,n^{1/3}}{0.079 + n^{1/3}} \qquad \ldots(3.4)$$

although more recent interpolations do not give significantly different results. The formula for the ground-state energy E_0 in the LDA is

$$E_0 = N\sum_{\alpha=1}^{N}\epsilon_\alpha - \tfrac{1}{2}\int d\mathbf{r}d\mathbf{r}'\frac{n(\mathbf{r})\,n(\mathbf{r}')}{\mathbf{r}-\mathbf{r}'} - \int d\mathbf{r}n(\mathbf{r})\,\{v_{xc}(\mathbf{r}) - \epsilon_{XC}(\mathbf{r})\} \qquad \ldots(3.5)$$

The *DF* scheme gives exact formulae for the ground-state energy E_0 and electron density $n(\mathbf{r})$, but it tells us nothing exactly about the elementary excitations or the ionization or affinity levels of the system. The *DHF* scheme does.

The dynamic Hartee-Fock theory (*DHF*) starts from the equation of motion of the single particle Green function

$$G(\mathbf{r},t;\mathbf{r}',t') = -i\langle N|\,T\psi(\mathbf{r},t)\,\psi^+(\mathbf{r}',t')\,|N\rangle \qquad \ldots(3.6)$$

where ψ^+ and ψ are creation and destruction Fermion field operators in the Heisenberg representation, T is Wick's time-ordering operator, and $|N>$ is the exact N-electron ground state. The Fourier time transform of G is

$$G(\mathbf{r},\mathbf{r}';\epsilon) = \int_{-\infty}^{+\infty} d\tau e^{i\epsilon\tau}\,G(\mathbf{r},t;\mathbf{r}',t') \qquad \ldots(3.7)$$

*The energy unit is the Hartree; 1 Hartree = 27.21 eV = 2625 KJ mol^{-1}

where $\tau = t - t'$. There exists at every ϵ, a bi-orthogonal set of function $u_\alpha(\mathbf{r}; \epsilon)$, $\bar{u}_\alpha(\mathbf{r}; \epsilon)$ which diagonalize G;

$$G(\mathbf{r}, \mathbf{r}'; \epsilon) = \sum_\alpha u_\alpha(\mathbf{r}; \epsilon)\, \bar{u}_\alpha(\mathbf{r}';\epsilon)/[\epsilon - E_\alpha(\epsilon)]$$

$$< \bar{u}_\alpha(\mathbf{r}; \epsilon) \mid G(\mathbf{r}, \mathbf{r}'; \epsilon) \mid u_\alpha(\mathbf{r}'; \epsilon) > = \delta_{\alpha\beta}/[\epsilon - E_\alpha(\epsilon)] \qquad \ldots(3.8)$$

These functions satisfy the non-Hermitian eigenvalue problem

$$[E_\alpha(\epsilon) - h(\mathbf{r})]\, u_\alpha(\mathbf{r}; \epsilon) - \int d\mathbf{r}' M(\mathbf{r}, \mathbf{r}'; \epsilon)\, u_\alpha(\mathbf{r}'; \epsilon) = 0$$

$$[E^*_\alpha(\epsilon) - h(\mathbf{r})]\, \bar{u}_\alpha(\mathbf{r}; \epsilon) - \int d\mathbf{r}' \bar{u}_\alpha(\mathbf{r}; \epsilon)\, M(\mathbf{r}', \mathbf{r}; \epsilon) = 0 \qquad \ldots(3.9)$$

where $h(\mathbf{r})$ is the Schrödinger operator for an electron moving in the field of ions, and M is the self-energy containing all the complications of the N-electron problem. *M is non-local.*

G has poles at energies ϵ_α satisfying

$$\epsilon_\alpha = E_\alpha(\epsilon_\alpha) \qquad \ldots(3.10)$$

with residues η_α, and the functions $u_\alpha(\mathbf{r}; \epsilon_\alpha)$ which satisfy equations (3.9) at these energies are known as *Dyson orbitals*. In terms of these orbitals, the electron density is

$$n(\mathbf{r}) = \sum_\alpha \eta_\alpha u_\alpha(\mathbf{r}; \epsilon_\alpha)\, \bar{u}_\alpha(\mathbf{r}; \epsilon_\alpha)$$

$$(\epsilon_\alpha < \epsilon_F) \qquad \ldots(3.11)$$

and the ground-state energy is

$$E_0 = \sum_\alpha \eta_\alpha[\epsilon_\alpha + h(\alpha, \alpha)]$$

$$(\epsilon_\alpha < \epsilon_F) \qquad \ldots(3.12)$$

where $h(\alpha, \alpha)$ is the diagonal element of $h(\mathbf{r})$ in the Dyson orbital representation. The poles ϵ_α of G are the exact ionization, and affinity levels of the N-electron system.

Equations (3.9) – (3.12) provide an exact *MO* scheme. The most commonly used approximation to it is the ordinary *HY* model in which M is energy-independent (but still non-local), and consequently the residues η_α are all unity, and also the Dyson orbitals degenerate to the *HF* orbitals. The self-energy has the well-known form

$$M_{HF}(\mathbf{r}, \mathbf{r}') = v_H(\mathbf{r})\, \delta(\mathbf{r} - \mathbf{r}') + v_X(\mathbf{r}, \mathbf{r}') \qquad \ldots(3.13)$$

where v_X is the non-local exchange potential

$$v_X(\mathbf{r}, \mathbf{r}') = - \sum_\alpha u_\alpha(\mathbf{r})\, u^*_\alpha(\mathbf{r}')/ \mid \mathbf{r} - \mathbf{r}' \mid$$

$$(\epsilon_\alpha < \epsilon_F) \qquad \ldots(3.14)$$

4. Practical Computations

Computations are performed using either :

4.1. Cluster models

Here the solid with a given exposed surface is modelled by a few atoms (perhaps as few as 5 for the (100) surface of a face-centred cubic metal), and this cluster, plus the adsorbed species is computed as a problem in ordinary quantum chemistry. As an example of this approach I mention Upton and Goddard[13] who used 20 Ni atoms to investigate *H* atom chemisorption by nickel in the *HF* approximation. A cluster as large as this contains the more important sites on (100), (110), (111) and (112) surfaces. The chemisorption binding energies, equilibrium surface bond lengths, and frequencies computed.

4.2. Embedded clusters

In small clusters, very few (one in Ni_{10}, two in Ni_{20}) atoms have even the nearest-neighbour environment of the real solid, and we must therefore receive computations on small clusters with caution. But chemisorption is often a spatially well-localized phenomenon, and we know that binding energies, together with bond lengths and vibration frequencies of adsorbed species can be computed accurately with small clusters; Ni_{20} is adequate for *H* atom chemisorption. Now quite generally, if one tries to describe the properties of a large system (*H* plus 10^{15} *Ni* atoms) by focussing on a small part of it (H-Ni_{10}), the fact that the small part is in communication with the rest of the system can be accounted for exactly in quantum mechanics by using an *effective* Hamiltonian to describe the small part, and ignoring the rest of the system completely. Examples of this procedure are widespread in Chemical Physics.

In chemisorption theory we *embed* a cluster calculation into the semi-infinite substrate by adding an *embedding self-enetgy* $M^E(\mathbf{r}, \mathbf{r}'; \epsilon)$ to the cluster Hamiltonian H^C to define the effective Hamiltonian for electrons in the cluster

$$H_{eff} = H^C + M^E(\mathbf{r}, \mathbf{r}'; \epsilon) \qquad \ldots(4.1)$$

As indicated, M^E non-local, and energy-dependent, the same as H^C will be if we used the DHF theory for the cluster calculation. For a large cluster, M^E becomes a property of the semi-infinite substrate, and ceases to depend on the adsorbed species. In this limit its calculation is simplified, and its role is to bring the electronic structure of the bare cluster (no adsorbed species) to that of the same cluster of atoms in the surface of the semi-infinite substrate, i.e., to embed the substrate cluster, *without the adsorbed species*, exactly. Chemisorption disturbs this exact embedding of course, but the disturbance is small if chemisorption is spatially localized, and in any case it goes to zero with increasing cluster size.

There are some technical problems still to be overcome (e.g., dealing with possible poles in $(\epsilon - H_{eff})^{-1}$ close to ϵ_F) before this embedding scheme can be generally used, but simple chemisorption systems have been successfully handled

this way[14-16], and many studies of single atoms, and diatomic molecules on "jellium" adopt this approach.

4.3. Slabs

For many chemisorption systems, the adsorbed species can form an ordered overlayer, with or without reconstruction of the solid surface, so that there is still a 2-dimensional translational symmetry specified by the *unit mesh* of the *surface net*. In this case, it is advantageous to consider a slab of the solid with ordered overlayers of the adsorbate on both surfaces, because this gives a 2-dimensional crystal with however a large unit cell since it extends right through the slab (Fig. 6). The large number of electrons in the unit cell limits the number of layers of the solid which can be included in the computation, but the method of proceeding is well-known whether one uses basis sets which are (i) atomic orbitals, (ii) plane waves, (iii) mixtures of both, and whether one uses the LD or the HF approximation, and an atomic orbital (AO) basis set. I mention some details of the approach using the HF approximation and an atomic orbital (AO) basis set[17,18] since I have some experience with it.

The MO's for a periodic system are expressed as linear combinations of tight-binding basis functions

$$\psi_\mu(\mathbf{k};\mathbf{r}) = \sum_i \phi_i(\mathbf{k};\mathbf{r})\, C_{i\mu}(\mathbf{k})$$

$$\phi_i(\mathbf{k};\mathbf{r}) = N^{-1/2} \sum_l \exp i\mathbf{k}.(\mathbf{l})\, u_i\,(\mathbf{r} - \mathbf{l} - s_i) \qquad \ldots(4.2)$$

where u_i is the ith AO on the atom at s_i in the unit cell at $\mathbf{l}$, and $\mathbf{k}$ is a wavevector in the 2-dimensional Brillouin zone of the surface net. ϕ_i is a Bloch sum. The coefficients $C_{i\mu}(\mathbf{k})$ in (4.2) are obtained by solving the matrix eigenvalue problem

$$\mathbf{F}(\mathbf{k})\,\mathbf{C}(\mathbf{k}) = \mathbf{S}(\mathbf{k})\,\mathbf{C}(\mathbf{k})\,\epsilon(\mathbf{k}) \qquad \ldots(4.3)$$

for every $\mathbf{k}$. For closed-shell systems in the HF approximation

$$F_{ij}(\mathbf{k}) = h_{ij}(\mathbf{k}) + \sum_{m,n} B^{-1} \int_B \mathbf{dk}\, \{J_{ijmn}(\mathbf{k},\mathbf{k})$$

$$- \tfrac{1}{2}K_{ijmn}(\mathbf{k},\mathbf{k}')\}\, P_{mn}(\mathbf{k}') \qquad \ldots(4.4)$$

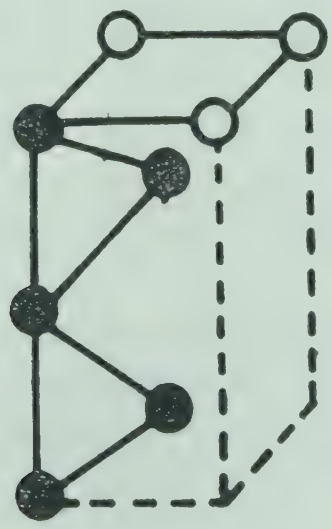

FIG. 6. The unit cell (0 atoms) and surface unit mesh of a 5-layer slab of a body-centred cubic metal with the (001) surfaces exposed.

Here h, J and k refer to the core Hamiltonian, the coulomb, and the exchange terms respectively, B is the area of the surface Brillouin zone, and $P(\mathbf{k})$ is the density matrix with elements defined on the basis set $\{\phi_i\}$ by

$$P_{ij}(\mathbf{k}) = 2 \sum_{\mu=occ} C^*_{i\mu}(\mathbf{k})\, C_{j\mu}(\mathbf{k}) \qquad \ldots(4.5)$$

the sum on μ being on the occupied orbitals ψ_μ. We note the usual *HF* self-consistency problem because we have to solve (4.3) to calculate $P(\mathbf{k})$ from (4.5), and we need $P(\mathbf{k})$ *for all* $\mathbf{k}$ to define $F(\mathbf{k})$. The total energy is given by

$$E_0 = \tfrac{1}{2}B^{-1} \int d\mathbf{k}\ \text{Trace}\ \mathbf{P}(\mathbf{k})\ \{\mathbf{F}(\mathbf{k}) + \mathbf{h}(\mathbf{k})\} \qquad \ldots(4.6)$$

Because of the long range of the Coulomb potential, there are important numerical problems connected both with the construction of F and with the evaluation of the total energy[19], but these need not concern us here, I simply remark that a comprehensive, well-documented and flexible computer program exists in the *UK* for large-scale *HF* computations on periodic systems. It is called CRYSTAL, and it began life at Turin (Italy) with the quantum chemistry group there. Results for *H*-(0001) Be using a 3-layer slab of Be (H—Be_3—H) have recently appeared in the literature[20], but tests have been made for several other systems. The results indicate that the *HF* model with small basis set of Gussian orbitals on each atom gives reliable *a priori* predictions of the adsorption geometry, with bond lenghts accurate to 0.005 *nm*, on non-metals certainly, and probably on metals too.

Many slab calculations using the *LD* approximation have been published which make various approximations to ease the computational task so that transition-metal substrates can be investigated. Much of this work concentrates on the spectrum of Kohn-Sham eigenvalues, and on the charge density, but neglects the total energy, and with it, the geometry optimization problem because total energies are unreliable due to the approximations made over and above the LD approximation. Among recent calculations of this sort I mention two :

(i) $c(2 \times 2)$ Cl on a 3-layer slab of (001) Ag using a Gaussian orbital basis, a Gaussian basis set for fitting $n(\mathbf{r})$ and $v_{\text{eff}}(\mathbf{r})$, and Wigner's[12] formula for ϵ_C[21].

(ii) monolayer Au on a 5-layer slab of (001) Pt using LAPW's (linearized augmented plane waves), touching muffin tins for the potential and Hedin and Lundqvist's[22] formula for ϵ_C[23].

My experience with the density functional scheme for small molecules[24] is that the 3-dimensional numerical integrations required to calculate the matrix elements of v_{eff} are difficult to perform with high numerical accuracy because of the rapid spatial variations of the Kohn-Sham wavefunctions both for the core electrons themselves, and for the valence electrons in the core region. This is why the total energy is difficult to compute with sufficient accuracy for *a priori*

geometry predictions. To avoid this difficulty (which is not present in the HF model because there, the integrals can be reduced analytically to 1-dimensional numerical integrations), there has been a move recently towards the use of *accurate* pseudopotentials, and pseudo-wavefunctions so that there are no core wavefunctions, and no rapid spatial variations of the valence (pseudo) wavefunctions in the core region. As an example of this approach I, mention the *ab initio* computations of the ground-state properties of Cl overlayers on (111) *Si* and (111) *Ge* using 6-layer slabs of substrate (*Cl-Si*$_6$-*Cl*, and *Cl-Ge*$_6$-*Cl*), the LD approximation in conjunction with accurate pseudopotentials, and a Gaussian orbital basis[25]. Surface bond lengths agree with experimental SEXAFS results to 0.002 A.U.

4.4. Jelliums

The jellium (Je) is a well-defined theoretical model. The positive ions of the solid are smeared out into a uniform charge distribution terminating abruptly at the surface. The electrons move in the electrostatic potential of this uniform background, and it is customory to treat their mutual interactions in the *LD* approximation. This material is a useful model for real solids if band structure effects (i.e., crystallinity), and core electrons are of secondary importance in chemisorption. It is therefore an adequate starting point for simple metals where band gaps are small (e.g., Na, Mg, Al), but is quite inadequate for surface chemistry which is intimately concerned with the adsorption geometry, and with local details rather than broad features, of the electron distribution. I remark however, that these important points can be taken into account by embedding a cluster as described in § 4.2. The great advantage of the jellium substrate is that the chemisorption of simple atoms, and molecules (*H*, *O*, *H*,) can be computed essentially exactly in the *LD* approximation[26],[27]. It has also been used with considerable success to begin the study of some dynamical processes[28].

5. Approximate Theories

The accurate computation of theoretical models which are adequate for the *ab initio* study of chemisorption poses a computing task which lies beyond the reach of most Institutions even for atomic adsorbates. Very few adsorbed molecules can be handled anywhere. Consequently, to begin to study systems of interest in catalysis, approximate methods have to be used. Among the most successful is the "Effective-medium Theory of Chemical Binding[29,30], "but I must remark that in its simplest form, which I give here, a given atom chemisorbs with the *same binding energy on all metals*.

The basic idea is to approximate $D(\mathbf{R})$, the binding energy of an atom to a substrate (another atom, or in our case a solid surface) when the atom is at $\mathbf{R}$, by the heat of solution H^{homo} of the atom in a jellium of (uniform) electron density $n_0(\mathbf{R})$, the electron density of the bare unperturbed substrate at the atom's position $\mathbf{R}$, i.e.

$$D(\mathbf{R}) \simeq H^{\text{homo}}(n_0(\mathbf{R})).$$

Systematic refinement of this idea leads to

$$D(\mathbf{R}) \simeq H^{\text{homo}}(\bar{n}_0(\mathbf{R})) \qquad \ldots (5.1)$$

where $\bar{n}_0(\mathbf{R})$ is an average of the unperturbed substrate electron density, namely

$$\bar{n}_0(\mathbf{R}) = \int d\mathbf{r} n_0(\mathbf{r} - \mathbf{R})\, \Delta\phi(\mathbf{r} - \mathbf{R}) \qquad \ldots (5.2)$$

Equation (5.1) is the zero-order result. The first-order correction to it is

$$D^{(1)}(\mathbf{R}) = -\int d\mathbf{r}\phi_0(\mathbf{r})\, \Delta\rho(\mathbf{r} - \mathbf{R}) - \int d\mathbf{r}[n_0(\mathbf{r} - \mathbf{R}) - \bar{n}_0(\mathbf{R})]\, \Delta v(\mathbf{r} - \mathbf{R}) \qquad \ldots (5.3)$$

where $\phi 0$ is the substrate electrostatic potential, and $\Delta\phi(\mathbf{r})$, $\Delta\rho(\mathbf{r})$ and $\Delta v(\mathbf{R})$ have the following meanings :

For a homogeneous jellium with uniform electron density $n_0(\mathrm{R})$, the atom placed at $\mathbf{r} = 0$ induces an electrostatic potential $\Delta\phi(\mathbf{r})$, a charge denisty $\Delta\rho(\mathbf{r})$, and a one-electron potential $\Delta v(\mathbf{r})$.

This first-order correction can be approximated by a term proportional to $\bar{n}_0(\mathbf{R})$

$$D^{(1)}(\mathbf{R}) \simeq \alpha\bar{n}_0(\mathbf{R})$$

so that

$$D(\mathbf{R}) \simeq H^{\text{homo}}(\bar{n}_0(\mathbf{R})) + \alpha\bar{n}_0(\mathbf{R}) = D[\bar{n}_0] \qquad \ldots (5.4)$$

$H^{\text{homo}}(n_0)$, the heat of solution of the atom in the homogeneous jellium has been calculated within the LD approximation for the atoms H to Ar by several authors[31], and from the details of these results, the function on the right in equation (5.4) can be obtained. I show it for the oxygen atom in Fig. 7[32]. It

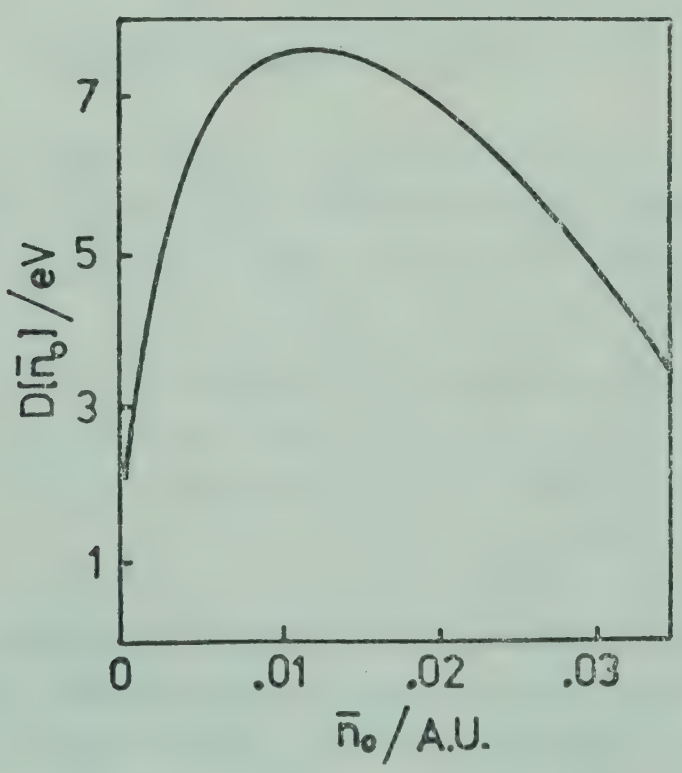

FIG. 7. The interaction energy of an oxygen atom with jellium according to equation (5.4). [Reference 32].

shows a maximum of 7.3 eV at 0.013 A.U. Outside a metal surface, an oxygen atom can always find this optimum electron density, and the corresponding position $\mathbf{R}_{eq}$ defined by

$$\bar{n}_0(\mathbf{R}_{eq}) = 0.013 \qquad \ldots(5.5)$$

gives the adsorption geometry. The chemisorption binding energy is simply the maximum value of $D[n_0]$, namely 7.3 eV. According to this simple theory, it is the same for all metals only the adsorption geometry determined by solving equation (5.5) can be different.

Experimental values of the binding energy of oxygen atoms to metals of the first transition series Ti to Cu apparently lie between 4.9 and 7.9 eV but they are not well-established quantities.

Refinements to the above scheme to differentiate one metal from another have recently been published[33], but I do not have space to discuss them here. I only remark that theoretical schemes which produce numbers for chemisorption systems of practical importance *must* produce reliable numbeas, otherwise they are useless.

6. Model Hamiltonians

Theoretical models designed to yield numbers, either to compare with experiment, or to be predictive, are at the core of chemisorption theory. But it is, in addition, very useful, particularly in the early stages of the development of the subject, and whenever new adsorption/desorption phenomena are being examined, to have a theoretical model which contains the essential features of the problem in by the simplest possible way. Anderson's model Hamiltonian[1] proposed originally to deal with a different problem, provides such a model because it can describe the formation of a chemical bond between a semi-infinite substrate with a continuum of itinerant electron states, and an atom with discrete localized ones in a simple way. Since its introduction into chemisorption theory by Grimley[34], Edwards and Newns[35], and Newns[36], it has been used very widely to exhibit many aspects of chemisorption by metals. I simply set down the Hamiltonian here for a one-electron atom interacting with a metal.

Let $\{\phi_A, \phi_K\}$ be a basis set consisting of the adatom orbital ϕ_A, and the set $\{\phi_K\}$ of metal orbitals. It is convenient to use the formalism of second quantization where the Hamiltonian is a function of Heisenberg operators $a_{i\sigma}, a^+_{i\sigma}$ $(i = A,K)$, where $a_{i\sigma}$ destroys an electron with spin σ ($\sigma = \uparrow$ or $\downarrow$) in the orbital ϕ_i. $a^+_{i\sigma}$ is the Hermitian adjoint, and is the corresponding destruction operator if the basis is orthogonal which is what is assumed in the Anderson model. Then

$$H = \sum_{\sigma} E_A n_{A\sigma} + J_A n_{A\uparrow} n_{A\downarrow} + \sum_{k,\sigma} \epsilon_k n_{k\sigma} + \sum_{k,\sigma} (V_{Ak} a^+_{A\sigma} a_{k\sigma} + V_{kA} a^+_{k\sigma} a_{A\sigma}) \qquad \ldots(6.1)$$

where $n_{A\sigma} = a^{+}_{A\sigma}\, a_{A\sigma}$ is the number operator for spin σ electrons in the orbital ϕ_A. The first term describes non-interacting electrons in the atom with energy E_A, the second is the Coulomb interaction between them, and together these two terms describe interacting electrons in the atomic orbital ϕ_A. The third term describes non-interacting electrons in the semi-infinite metal in orbitals ϕ_K with energies ϵ_K, and the fourth term couples the adsorbed atom, and the metal together by allowing them to share all the electrons. This sharing is described by $a^{+}_{K\sigma}\, a_{A\sigma}$ which takes a spin σ electron from the metal to the adsorbed atom, and by $a^{+}_{K\sigma} a_{A\sigma}$ which does the opposite. V_{AK} and V_{KA} moderate these charge transfers, and so govern the contributions of different metal orbitals ϕ_K to the surface bond.

The absence in Anderson's Hamiltonian (6.1) of any terms describing Coulomb interactions between electrons in the metal brings some unrealistic features to the model[2], which are partly removed in a different model introduced by Grimley and Pisani[14]. In this model, the states $|K>$ are tight-binding states constructed from a single atomic orbital per atom of the substrate, and such a model solid is called "cubium" if it has a cubic lattice. The atomic orbital basis set $\{\phi_A, \phi_M\ (M = \text{metal})\}$ is introduced to allow electron interactions to be extended from the adsorbed atom (A) in Anderson's model, to cover also its first shell of neighbours (B) in the substrate. Overlap among the atomic orbitals of the set $\{A + B\}$ is explicitly treated. The Hamiltonian is

$$H = \sum_{i,j,\sigma} a^{+}_{i\sigma} h_{ij} a_{j\sigma} + \tfrac{1}{2} \sum_{i,j,\sigma} a^{+}_{i} W^{\sigma}_{ij} a_{j\sigma}$$

$$(j \epsilon i,\ dbi) \qquad (i, j \epsilon A + B) \qquad \ldots(6.2)$$

where, as indicated, in the first term, j goes over i, and over the atoms directly bonded to i (dbi), and in the second, i and j go only over A and its first shell neighbours in the substrate (B). In equation (6.2)

$$h_{ij} = < i \mid \hat{h} \mid j > \qquad \ldots (6.3)$$

where $\hat{h}$ is the Schrödinger operator for an electron in the field of the ion cores, and

$$W_{ij} = \sum_{i',j',\sigma'} a^{+}_{i'\ \sigma'} < ii' \left| \frac{1}{r_{12}} \right| jj' > a_{j'\sigma'}$$

$$< ii' \left| \frac{1}{r_{12}} \right| jj' > = \int d\mathbf{r}_1 d\mathbf{r}_2\, \phi^{*}_{i}(\mathbf{r}_1)\, \phi^{*}_{i},(\mathbf{r}_2)\, \phi_j(\mathbf{r}_1)\, \phi_{j'}(\mathbf{r}_2) / \mid \mathbf{r}_1 - \mathbf{r}_2 \mid$$

$$\ldots(6.4)$$

If i belongs to the non-orthogonal set $\{A + B\}$, the operator $a^{+}_{i\sigma}$ is not the creation operator for spin σ electrons in ϕ_i, it is simply the Hermitian adjoint of the destruction operator $a_{i\sigma}$.

Extending electron-electron interactions into the substrate like this, allows a more realistic charge distribution to develop near the chemisorbed atom. This is particularly important when ionic species form on the surface, for example with *H* atoms in *Li* metal[37].

7. Dynamics

Of course we are not able to give a proper microscopic discussion of any heterogeneous reaction, but the general way of proceeding is clear. What we need to do is to calculate R_{FI}, the rate of reactive transitions out of an initial state $|I>$ to a final state $|F>$. If the Hamiltonian is written

$$H = H_0 + V \qquad \ldots(7.1)$$

where H_0 describes the non-interacting reactants (the catalyst is a reactant in a state-to-state transition), V is the interaction between them, and $|I>$ and $|F>$ are eigenstates of H_0, then by Lippmann's generalization[38] of Ehrenfest's theorem

$$R_{FI} = \frac{2\pi}{\hbar} |<F|T|I>|^2 \, \delta(E_F - E_I) \qquad \ldots(7.2)$$

where the T-matrix is defined by

$$T = V + VG^+V \qquad G^+ = (E + i0 - H)^{-1}$$
$$= V + VG_0^+T \quad , \quad G_0^+ = (E + i0 - H_0)^{-1} \qquad \ldots(7.3)$$

In a general chemical reaction, specifying the reactants specifies the *entrance channel* i, and specifying the products specifies the *exit channel* f ($A + BC \rightarrow AB + C$, and $A + BC \rightarrow AC + B$ have the same entrance channel but different f's). If the initial state is drawn from the canonical ensemble at temperature T, the transition rate from i to f can be written

$$R_{if} = \frac{kT}{\hbar} \int_0^\infty dE \exp(-E/kT) \frac{dY_{if}}{DE} Z_i(T) \qquad \ldots(7.4)$$

where $Y_{If}(E)$ is the probability of a transition to f from all states of energy E in i, and $Z_I(T)$ is the caniconal partition function for the reactants. We can write equation (7.4) in the form

$$R_F = \frac{kT}{h} \exp(-\Delta F^{\neq}/kT) \qquad \ldots(7.5)$$

and this defines $\Delta F^{\neq}$ the "free energy of activation from the entrance channel".

These equations are formal. To go beyond formalities, I consider the two simple processes which are fundamental to catalysis by solids; the rate of adsorption (sticking), and the rate of desorption of atoms at solid surfaces.

7.1. Sticking

If an atom or molecule is to stick, it must lose at least its kinetic energy in a collision with the surface. I assume that the energy is lost by exciting the electrons in the system. Whether or not this is the mechanism in any particular case it not easy to decide, but it is the most likely mechanism for H, H_2 and D_2 on transition metals. A feature of the electron-loss mechanism is that the fall in the sticking coefficient with increasing substrate temperature is expected to be very small, for the same reason, essentially, as the electronic contribution to the heat capacity of a metal is very small, namely Fermi statistics.

Consider a vessel of length b, one wall of which is the metal (Fig. 8), the other walls inert, and containing one gas atom. If we fix the gas atom at $\mathbf{R}$, and solve Schrödinger's equation for the electronic motion, we obtain the quasi-continuous sequence of adiabatic potential energy curves $E_n(\mathbf{R})$, where $n = 0,1,2,\ldots$ labels the electronic state; is the ground state, the others are excited states. By solving Schrödinger's equation for the motion of the gas atom nucleus on $E_n(\mathbf{R})$, we obtain states for the nuclear motion tabelled by α say, so that $|\, n,\alpha>$ and $E_{n\alpha}$ are the adiabatic states, and energies for the motion of the gas atom on the nth potential energy curve. If, in the course of a collision with the metal, the gas atom stays on the same potential energy curve, it can not stick, it can only reflect elastically. To stick, the atom must O move onto another potential energy curve with more energy in the electron system, and less in the nuclear motion.

I consider a situation in which the atom is initially in the state $|\, 0\alpha>$ with no electronic excitation, and with energy $E_{0\alpha}$ which is therefore the kinetic energy of the atom in the vessel. Because the electronic, and nuclear motions are not actually separable[39], the initial state $|\, 0,\alpha>$ is coupled to all other adiabatic states $|\, n, \beta>$, and therefore decays in time. From this decay, the sticking coefficient can be calculated.

The Hamiltonian has the form (7.1), and V causes the decay. The exact state at time t is $\Psi(t)$ satisfying

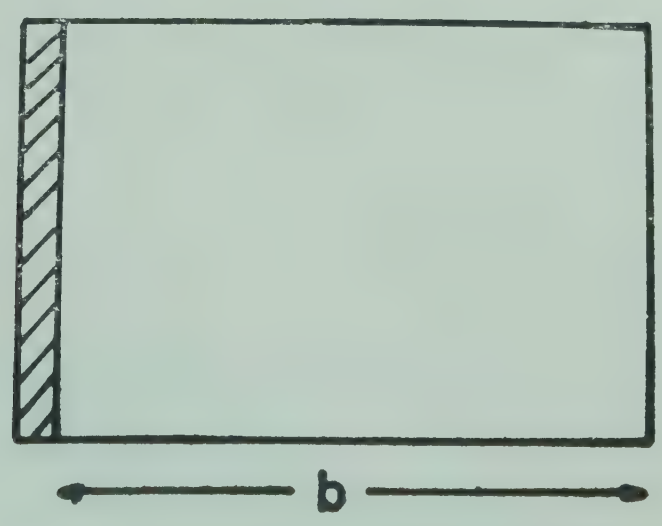

FIG 8. The gas vessel for calculating the sticking coefficient.

$$i\hbar \frac{\partial \psi}{\partial t} = H\psi \ (t > 0) \qquad \ldots(7.6)$$

and

$$\Psi(t) = \ | \ 0,\alpha> \text{ at } t = 0.$$

The probability to observe the initial state at time t is

$$| <\alpha, 0 \mid \Psi(t)> |^2 \text{ and}$$

$$<\alpha, 0 \mid \psi(t)> = <\alpha, 0 \mid U(t) \mid 0, \alpha>$$

where $U(t)$ is the evolution operator equal to $\exp(-iHt/\hbar)$ in our case. Hence

$$< \alpha,0 \mid \psi(t) > = -\frac{1}{\pi} \int_{-\infty}^{+\infty} d\epsilon \exp(-i\epsilon t) \, Im < \alpha,0 \mid G \mid 0,\alpha > \qquad \ldots(7.7)$$

where G is the Green operator

$$G(\epsilon) = (\epsilon + i0 - H)^{-1} \qquad \ldots(7.8)$$

These equations give the decay of the initial state; in general it decays through sticking, and through inelastic scattering. I now write down a simple model Hamiltonian describing sticking :

$$H_0 = \mid 0, \alpha > E_{0\alpha} < \alpha, 0 \mid + \sum_{\beta,n} \mid n, \beta > E_{n\beta} < \beta, n \mid$$

$$V = \sum_{\beta,n} (\mid 0, \alpha > W(0, \alpha; \beta, n) < \beta, n \mid + \mid n, \beta > W(n, \beta; \alpha, 0) < 0, \alpha \mid \qquad \ldots(7.9)$$

where $\mid n, \beta >$ specifies a *bound* state (β = bound) on the nth electronically excited potential energy curve, the electronic excitation consisting of *one* electron-hole pair (e-hp) (see Fig. 9).

From the Born-Oppenheimer system of linear equations[39] we identify

$$W(0, \alpha; \beta, n) = (\hbar^2/M) < \alpha \mid < \mu \mid \nabla_R \mid \nu > \Delta_R \mid \beta > \qquad \ldots(7.10)$$

where M is the mass of the gas atom, and $\mid \mu >$ and $\mid \nu >$ are one-electron states of the system with the gas atom at **R**. μ is the electron, ν is the hole (Fig. 9), and together they define the e-hp of the excited state $\mid n >$. Since the Hamiltonian (7.9) does not allow inelastic scattering (because β is confined to the bound states),

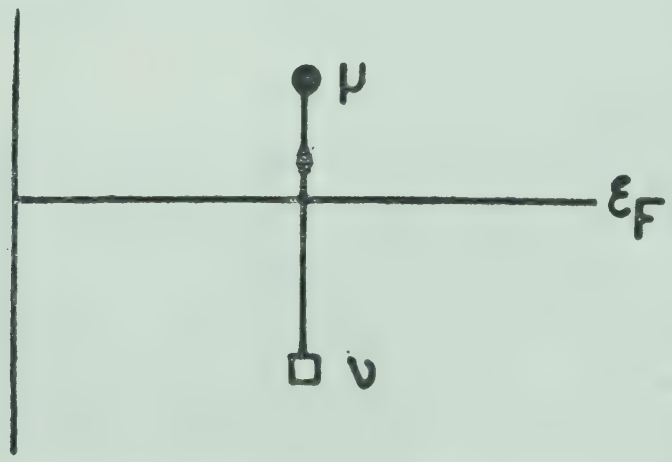

FIG. 9. One electron-hole pair. μ is the electron, ν is the hole.

the decay (7.7) is due entirely to sticking. Forming G from its definition in equation (7.8) we find

$$< \alpha, 0 \mid G \mid 0, \alpha > = (\epsilon + i0 - E_{0\alpha} - q_{0\alpha})^{-1} \qquad ...(7.11)$$

where

$$q_{0\alpha} = \sum_{\beta,n} \frac{|W(0, \alpha; \beta, n)|^2}{\epsilon + i0 - E_{n\beta}} = \alpha(\epsilon) - i\Gamma(\epsilon) \qquad ...(7.12)$$

is the self-energy of the state $\mid 0, \alpha >$ due to sticking.

Brivio and Grimley[40] have calculated the scalar product (7.7) in the quasi-particle approximation for a simple model of hydrogen chemisorption by a metal. The quasi-particle approximation consists of assuming that $< \alpha, 0 \mid G(z) \mid 0, \alpha >$ has a single pole in the lower-plane at $z_p = E_{0\alpha} - i\Gamma(E_{0\alpha})$, and in this case (7.7) reduces to

$$< \alpha, 0 \mid \Psi(t) > = \exp(-\Gamma(E_{0\alpha})\ t/\hbar \qquad ...(7.13)$$

The lifetime of the initial state is therefore

$$\tau = \hbar/2\Gamma(E_{0\alpha}) \qquad ...(7.14)$$

From the gas atom's kinetic energy $E_{0\alpha}$ we obtain τ_{coll}, the time between successive collisions of the gas atom with the metal

$$\tau_{\text{coll}} = (Mb^2/E_{0\alpha})^{1/2} \qquad ...(7.15)$$

and from (7.14) and (7.15), the sticking coefficient s is

$$s = \tau_{\text{coll}}/\tau \qquad ...(7.16)$$

Figure 10 shows some of the results[40]. The peak near 21 meV is due to a quantum mechanical transmission resonance of the hydrogen atom into the chemisorption well. I remark also that in the quasi-particle approximation $s \sim (E_{0\alpha})^{1/2}$ as $E_{0\alpha} \to 0$ as Fig. 10 shows, but the actual behaviour of s in this low energy limit requires a more accurate solution than this.

7.2. Thermal desorption

I assume that thermal desorption is driven by the substrate phonons not by the electrons, and examine the one-phonon desorption rate in the Golden Rule approximation for a simple theoretical model. The angle-resolved desorption flux $d\dot{N}/d\omega$, where ω is the solid angle, is an interesting quantity which is now being measured.

The essential features of the model are :

(i) The static gas-solid interaction potential describes a flat surface with a hard wall repulsion.

(ii) The movement of a surface atom of the substrate due to lattice vibrations causes a small area s of the hard wall round the atom to move with it.

(iii) Initial (bound), and final (unbound) states of the gas atom are described by WKB wavefunctions.

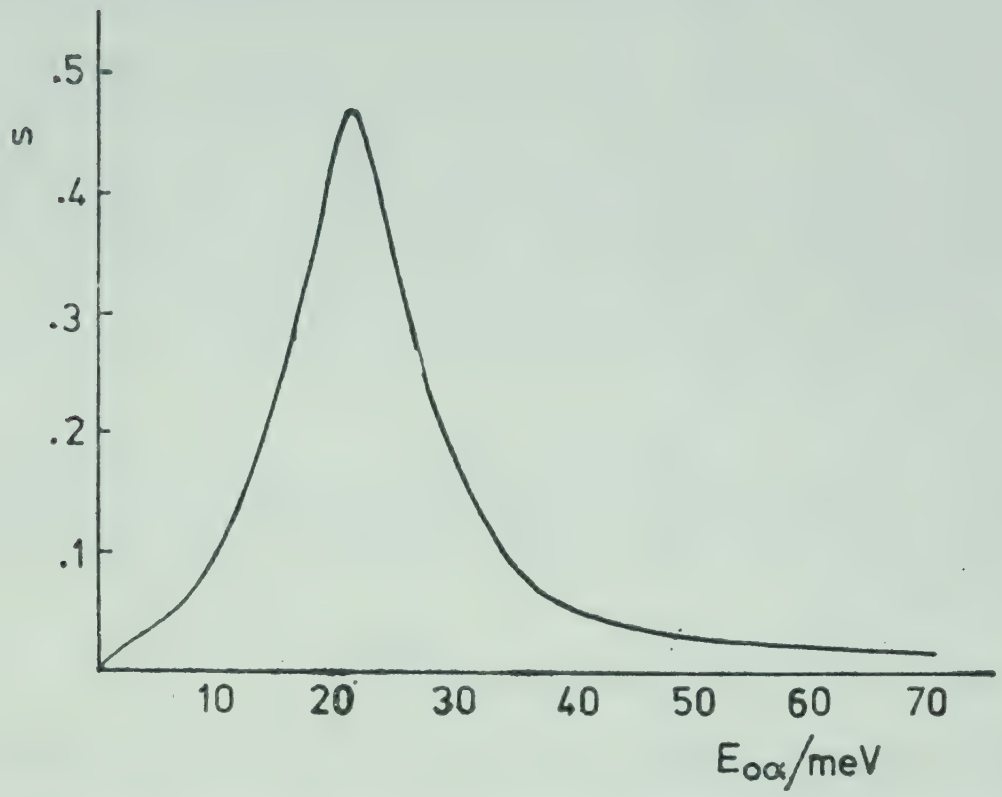

FIG. 10. Energy dependence of the sticking coefficient calculated for H atoms on a metal. $E_{0\alpha}$ is the kinetic energy.

(iv) The initial state of the system is drawn from the canonical ensemble at temperature T.

(v) Umklapp processes are neglected.
The Hamiltonian is

$$H = K_A + K_L + V(\mathbf{x}, \mathbf{u}_L) \qquad \ldots(7.17)$$

where K_A and K_L are kinetic energies of the gas atom A, and of the substrate lattice L, and V is the potential energy of the system when the gas atom is at $\mathbf{x}$, and the lattice atoms are displaced from their equilibrium positions. $\mathbf{u}_L$ is a multidimensional vector standing for the set $\{\mathbf{u}_L\}$ where $\mathbf{u}_L$ is the displacement of the atom at $\mathbf{l}$. I write (7.17) in the form

$$H = H_{\text{rigid}} + H_{\text{ph}} + V_{\text{A-ph}} \qquad \ldots(7.18)$$

where

$$H_{\text{rigid}} = K_A + V(\mathbf{x}, 0) \qquad (7.19)$$

is the Hamiltonian for the gas atom moving on the static atom-solid potential $V(\mathbf{x}, 0)$, i.e., the potential when the substrate atoms are clamped in their equilibrium positions,

$$H_{ph} = K_L + V(\infty, \mathbf{u}_L) \qquad \ldots(7.20)$$

is the Hamiltonian for the substrate lattice with the gas atom infinitely far from it, and V_{A-ph} is the atom-lattice interaction. In the harmonic approximation (7.20) is written

$$H_{ph} = \sum_{q,\sigma} \hbar\Omega_{q\sigma} b^{+}_{q\sigma} b_{q\sigma} \qquad \ldots(7.21)$$

where $(\mathbf{q},\sigma)$ are quantum numbers labelling the normal modes of frequencies $\Omega_{q\sigma}$. In a semi-infinite, crystal, $\mathbf{q} = (\mathbf{Q}, q_z)$ where $\mathbf{Q}$ is a 2-dimensional wavevector, and (q_z,σ) are the other labels which in simple cases we expect to be a perpendicular wavevector q_z, which may be complex if surface modes exist, and a mode index σ with three values. We expand $V(\mathbf{x}, \mathbf{u}_L)$ in a Taylor's series in $\mathbf{u}_L$ to find the first non-zero term in V_{A-ph}. It is the linear term

$$V_{A-ph} = \sum_{\mathbf{l}} \mathbf{u}_\mathbf{l} \cdot \nabla_\mathbf{l} V(\mathbf{x}, 0) \qquad \ldots(7.22)$$

Next we write $\mathbf{u}_\mathbf{l}$ in terms of the Boson operators. For a lattice with one atom per unit cell, N_Z layers parallel to the surface, and periodic boundary conditions over N meshes of the surface net

$$\mathbf{u}_\mathbf{l} = (NN_ZM_L)^{-1/2}\, \mathbf{e}_\sigma(l_z; \mathbf{q}) \exp(i\mathbf{Q}\cdot\mathbf{L}) \qquad \ldots(7.23)$$

where M_L is the mass of the lattice atoms, positions $\mathbf{l} = (\mathbf{L}, l_z)$ where l_z labels the layers from $l_z = 0$ at the surface, and $\mathbf{e}_\sigma$ is a unit vector specifying the direction of polarization of the mode $(\mathbf{q}, \sigma)$. In a semi-infinite crystal, the polarization depends on the l_z, the distance from the surface. Using (7.23) in (7.22), and introducing the Boson operators we can write

$$V_{A-ph} = \sum_{q,\sigma} g_{q\sigma}(\mathbf{x})\ (b^{+}_{q\sigma} + b_{q\sigma})$$

$$q_{q\sigma} = \left(\frac{\hbar}{2NN_zM_L\Omega_{q\sigma}}\right)^{1/2} \sum_{\mathbf{l}} \mathbf{e}_\sigma(l_z; \mathbf{q}) \cdot \nabla_\mathbf{l} V(\mathbf{x}, 0) \exp(i\mathbf{Q}\cdot\mathbf{L}) \qquad \ldots(7.24)$$

Equations (7.18)-(7.24) specify the problem.

Initial, and final states $|\, I>$ and $|\, F>$ are eigenstates of H_0 where

$$H_0 = H_{\text{rigid}} + H_{\text{ph}}$$

and V_{A-ph} causes desorption. $|\, I>$ describes a bond state $|\, \alpha>$ of H_{rigid} with energy $\tilde{\epsilon}_\alpha$, and with n_i phonons in the solid. $|\, F>$ describes an unbound state $|\, f>$ of H_{rigid} with energy $\tilde{\epsilon}_f$, and with n_f phonons :

$$|\, I> = |\, \alpha>\, |\, n_i>\ ,\quad |\, F> = |\, f>\, |\, n_f>$$

From Lippmann's[38] generalization of Ehrenfest's theorem, the transition rate from $|\, I>$ to $|\, F>$ is

$$R_{FI} = 2\pi/\hbar\ |\, <F\,|\, T_{A-ph}\,|\, I>\,|^2\, \delta(E_F - E_I)$$

where the T-matrix is

$$T = V_{A-ph} + V_{A-ph}\, G^{+}(E_I)\, V_{A-ph}$$

$$G^{+}(E) = (E + i0 - H)^{-1}$$

The Golden-Rule formula which I use is obtained with $T_{A-ph} \simeq V_{A-ph}$. If the initial state is drawn from the canonical ensemble at temperature T, the rate to $|\, F>$ is

$$R_F = (2\pi/\hbar) \sum_I \exp(-E_I/kT) \mid < F \mid T_{A-ph} \mid I > \mid^2 \delta(E_F - E_I) /$$

$$\sum_I \exp(-E_I/kT)$$

and we recognize the denominator as the partition function. Summing on the final phonon state (which is not measured) gives the rate to the gas atom state $\mid f >$ irrespective of the final phonon state. This is the measured desorption rate R_f;

$$R_f = \sum_{n_f} R_F,$$

which determines the angle- and energy-resolved desorption flux

$$\frac{d^2\dot{N}}{d\omega d\tilde{\epsilon}_f} = \frac{\mathcal{C}V}{(2\pi)^3} \cdot \frac{M}{\hbar^3} 2M\tilde{\epsilon}_f \cdot R_f \qquad \ldots(7.25)$$

at energy $\tilde{\epsilon}_f$ into unit solid angle at angle θ_f to the surface normal. In equation (7.25), $\mathcal{C}V$ is the normalization volume for $\mid f >$, and M is the gas atom mass. The angle-resolved flux is

$$\frac{d\dot{N}}{d\omega} = \int_0^\infty d\tilde{\epsilon}_f \frac{d^2\dot{N}}{d\omega d\tilde{\epsilon}_f}$$

Skipping all further methematical details we find with assumptions (i) - (v)

$$R_f \sim \exp(-(\tilde{\epsilon}_f + V_0)/kT) \sum_\alpha \frac{[\tilde{\epsilon}_f \cos^2\theta_f (\tilde{\epsilon}_f \cos^2\theta_f + V_0)]^{1/2}}{\hbar\Omega_{f\alpha}}$$

$$\times \rho_z(\Omega_{f\alpha}) \left(\frac{\alpha\epsilon}{a_\alpha}\right) \qquad \ldots(7.26)$$

where $\rho_z(\Omega)$ is a projection onto a surface atom of the solid of the phonon density of states :

$$\rho_z(\Omega) = \sum_{q,\sigma} \mid (e_{\sigma z}(0, \mathbf{q}) \mid^2 \delta(\Omega - \Omega_{q\sigma}) \qquad \ldots(7.27)$$

where $e_{\sigma z}(0, \mathbf{q})$ is the z-component (perpendicular to the surface) of the polarization vector of the mode $(\mathbf{q}, \sigma)$ on a surface atom. In equation (7.26), V_0 is the depth of the 1-dimensional static atom-solid potential $V(z, 0)$, ϵ_α are its bound state energies, a_α is the length of the classical trajectory of the state $\mid \alpha >$, and

$$\hbar\Omega_{f\alpha} = \tilde{\epsilon}_f \cos^2\theta_f + V_0 - \epsilon_\alpha \qquad \ldots(7.28)$$

is the energy increase of the adsorbed atom due to the adsorption of a phonon of frequency $\Omega_{f\alpha}$.

I note that it is impossible for (7.26) to lead to a $\cos\theta_f$ angular dependence such as is given by Kundsen's[41] arguments. Of course this is expected; I am dealing here with a completely non-equilibrium situation.

As an example of (7.26), suppose that thermal desorption is driven by surface phonos with

$$\rho_z(\Omega) \propto \Omega \quad , \quad 0 < \Omega < \Omega_{max} \qquad \ldots(7.29)$$

that $V(z, 0)$ has one bound state with $\epsilon_\alpha = \frac{1}{2}\hbar\Omega_{max}$, and that $V_0 = \hbar\Omega_{max}$. Then, for the angular dependence we find

$$R_f \sim [Y\cos^2\theta_f(Y\cos^2\theta_f + 1)]^{1/2}, Y = \tilde{\epsilon}_f/\hbar\Omega_{max}$$

$$\frac{dN}{d\omega} \sim \int_0^{Y_m} \cdot dY\,[Y\cos^2\theta_f(Y\cos^2\theta_f + 1)]^{1/2}\exp(-Y\hbar\Omega_{max}/kT) \qquad \ldots(7.30)$$

$$Y_m = 1/2\cos^2\theta_f$$

In Fig. 11. I show the angle-dependence of the desorption flux normalized to unity at $\theta_f = 0$ (normal emission) for two temperatures; $T_2 = \hbar\Omega_{max}/k$ and $T_1 = \hbar\Omega_{max}/3k$. The flux goes through a maximum as θ_f increases because the upper limit of integration Y_m increases with θ_f, although the integrand itself decreases. Physically, this is due to the conservation of parallel momentum in desorption from the non-localized state on a flat surface. To eliminate this maximum, and therefore to get something looking more like $\cos\theta_f$, we need the bound state $|\alpha>$ to be near the top of the well, and the desorption temperature T to be rather low. However, I emphasize that the conditions I am considering here are special, a one-phonon mechanism, and an adsorbed layer so dilute that interactions between the adsorbed atoms are insignificant. The latter condition is so special as not to be attained easily in practice. Fortunately, it is possible to re-formulate the theory without it. This reformulation has similarities with the many-body theory of the photomission of electrons from adsorbate layers[42], but I do not have space to present it here. In any case no numerical results for the new theory are available yet.

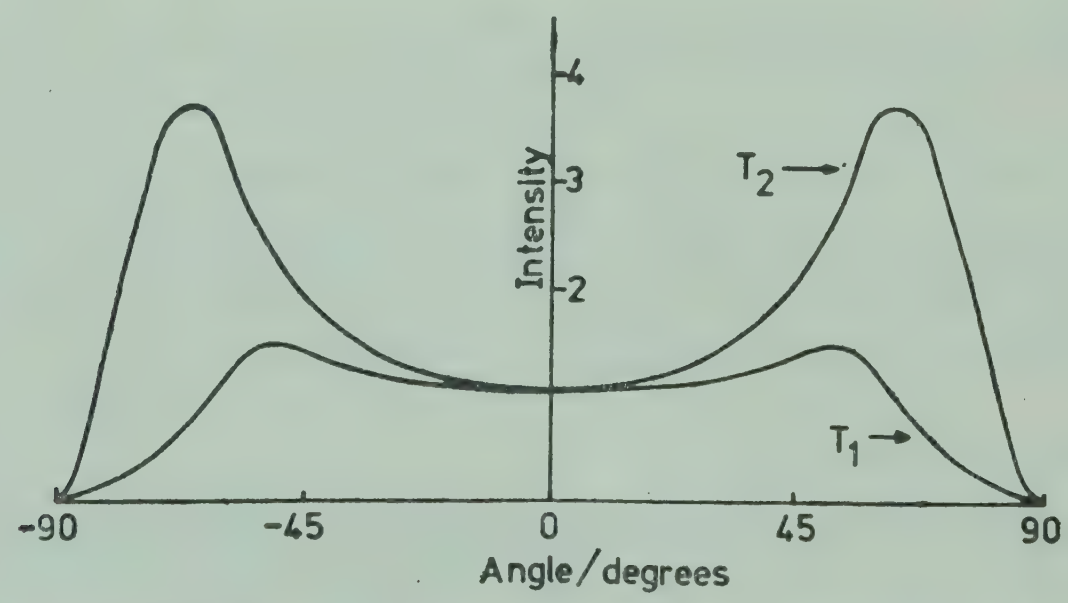

FIG. 11. The thermal desorption flux for the surface phonon mechanism as a function of angle to the surface normal for a flat adsorption potential with one bound state at $\epsilon_\alpha = \frac{1}{2}\hbar\Omega_{max}$. The well depth is $\hbar\Omega_{max}$, and the two temperatures are
$T_1 = \frac{1}{3}\hbar\Omega_{max}/k$, $T_2 = \hbar\Omega_{max}/k$.

References

1. P W Anderson, *Phys. Rev.* **124** (1961) 41.
2. T B Grimley, in *The Chemical Physics of Solid Surfaces and Hetero geneous Catalysis Vol.* **2** D A King and D P Woodruff (Eds.), Elsevier (1983).
3. K L Sebastian, V C Jyothi Bhasu and T B Grimley, *Surface Sci.* **110** (1981) L571.
4. T B Grimley, V C Jyothi Bhasu and K L Sebastian, *Surface Sci.* **124** (1983) 305.
5. K L Sebastian, to be published (1984).
6. J Hermann, B Wells, J Gehring, H Scholl and V Kempter, *Surface Sci.* **138** (1984) 570.
7. I, Fleming, *Frontier Orbitals and Organic Chemical Reaction*, Wiley-Interscience (1976).
8. T B Grimley, in *Molecular Processes on Solid Surfaces*, E Drauglis R D Gretz and R I Jaffee (Eds.), McGraw-Hill (1969).
9. R B Woodward and R Hoffmann, *The Conservation of Orbital Symmetry*, Academic Press (1970).
10. K Fukui, T Yonezawa and H Shingu, *J. Chem. Phys.* **20** (1952) 722; K Fukui, T Yonezawa, C Nagata and H Shingu, *J. Chem. Phys.* **22** (1954) 1433.
11. W Kohn and L J Sham, *Phys. Rev.* **140** (1965) A1133.
12. E P Wigner, *Phys. Rev.* **46** (1934) 1002.
13 T H Upton and W A Goddard, *Phys. Rev. Letters* **42** (1979) 472.
14. T B Grimley and C Pisani, *J. Phys. C* **7** (1974) 2831.
15. C Pisani and F Ricca, *Surface Sci.* **92** (1980) 481.
16. O Gunnarsson, H Hjelmberg and B I Lundqvist, *Surface Sci.* **63** (1977) 384.
17. J M André, *J. Chem. Phys.* **50** (1969) 1536.
18. C Pisani and R Dovesi, *Int. J. Quantum Chem.* **17** (1980) 501.
19. R Dovesi, C Pisani, C Roetti and V R Saunders, *Phys. Rev.* **B28** (1983) 5781.
20. G Angonoa, J Koutecky, A N Ermoskkin and C Pisani, *Surface Sci.* **138** (1984) 51.
21. H S Greenside and D R Hamann, *Phys. Rev.* **B23** (1981) 4879.
22. L Hedin and B I Lundqvist, *J. Phys. C* **4** (1971) 2064.
23. D S Wang, A J Freeman and H Krakauer, *Phys. Rev.* **B29** (1984) 1665.
24. T B Grimley and V C Jyothi Bhasu, *J. Phys.* **B16** (1983) 1125.
25. G B Bachelet and M Schluter, *Phys. Rev.* **B28** (1983) 2302.
26. O Gunnarsson, H Hjelmberg and B I Lundqvist, *Phys. Rev. Letters* **37** (1976) 292.
27. J K Nϕrskov, A Houmϕller, P K Johansson and B I Lundqvist, *Phys. Rev. Letters* **46 257** (1981).
28. M Person and B Hellsing, *Phys. Rev. Letters* **49** (1982) 662.
29. J K Nϕrkov and N D Lang, *Phys. Rev.* **B21** (1980) 2131.
30. J K Nϕrskov, *Phys. Rev.* **B26** (1982) 2875.
31. M Puska, R M Nieminen and M Manninen, *Phys. Rev.* **B24** (1980) 3037.
32. B Chakraborty, S Holloway and J K Nϕrskov to be published (1984).
33. P Nordlander, S Holloway and K J Nϕrskov, *Surface Sci.* **136** (1984) 59.
34. T B Grimley, *Proc. Phys. London* **90** (1967) 751.
35. D M Edwards and D M Newns, *Phys. Lett.* **A24** (1967) 346.
36. D M Newns, *Phys. Rev.* **178** (1969) 1123.
37. T B Grimley, in *The Physical Basis for Heterogeneous Catalysis*, E Drauglis and R I. Jaffee (Eds.), Plenum Press (1975).
38. B A Lippmann, *Phys. Rev. Letters* **15**, (1965)11; *Phys. Rev. Letters* **16** (1966) 135.
39. M Born and J R Oppenheimer, *Ann. Physik* **84** (1927) 457.
40. G P Brivio and T B Grimley, *Surface Sci.* **131** (1983) 745.
41. M Knudsen, *Ann. Physik* **48** (1915) 1113.
42. G Doyen and T B Grimley, in *Photoemission and the Electronic Properties of Surfaces*, B Feuerbacher, B Fitton and R F Willis (Eds.), J Wiley (1978).

© *Proc. Indian natn. Sci. Acad.*, 51, A, No. 1, 1985, pp. 124–164.
Printed in India.

AUGER ELECTRON SPECTROSCOPY AND SECONDARY ION MASS SPECTROMETRY*

ARUN S NIGAVEKAR
Department of Physics, University of Poona, Pune-411 007

Processes occurring at solid surfaces are of importance from basic research as well as from practical application angle. The knowledge of surface properties and their understanding, therefore, assumes greater significance. The meteoric resurgence of theoretical and experimental interest in surface understanding during the past two decades has, in no small way, been spared on by the development of accurated experimentation facilities to investigate the chemical and physical properties of surface.

The rate of growth of surface techniques, in last two decades, has been absolutely breathtaking. Auger Electron Spectroscopy (AES) was one of the first few techniques, to be used for elemental identification and trace analysis at the surface of solids. Indeed over these years AES has become a widely available and almost indispensible tool for determining sarface cleanliness, surface coverage, and depth profiling. More recently, the Auger line shape has been recognized as a source of chemical and electronic structure information.

One other surface technique, which also has been in use for long, is Secondary Ion Mass Spectrometry (SIMS). The possibility of surface layer analysis by measurement of secondary ion emitted after bombardment of a sample with energetic primary ions was known for some time and the recent experiments done at low primary ion currents and total doses have shown that SIMS can become powerful probe for studying the uppermost surface layer.

The major objective of this article is to give introductory information on AES and SIMS techniques. We have covered the necessary theoretical and experimental development and indicated by taking large number of examples, the potential applications of these techniques individually as well as when used in combination.

Key Words : Electron spectroscopy; Mass spectroscopy; Auger spectrometer; Scattered electrons

I. AUGER ELECTRON SPECTROSCOPY (AES)

1. INTRODUCTION

AUGER spectroscopy explores the electronic energy levels in atoms and solids. As an analytical technique, it has been applied to investigations of the first few atom layers of surface. The term "Auger process" has come to denote any electron de-excitation in which the de-excitation energy is transferred to a second electron, the "Auger electron". Because of the discrete nature of most electronic energy levels, Auger electrons are best characterized by their energies. Therefore, the Auger process can be analyzed by measuring the energy distribution N(E) of Auger electrons, where E

*Paper presented at the Symposium on Physics and Chemistry of Surfaces held at INSA, New Delhi from September 28-30, 1984.

is the electron energy. Experimental N(E) curves contain much more information than just those concerning the Auger process, and this extra information adds greatly to the usefulness of the data. Low-energy Auger electrons ($\lesssim$ 1 keV) can escape from only the first several atom layers of a surface because they are strongly absorbed by even a monolayer of atoms. This property gives Auger spectroscopy its high surface sensitivity.

2. The Aguer Process

2.1 Mechanism of Auger Ejection

Auger electrons were first discovered in 1925 by Pierre Auger[1] who observed their tracks in a Wilson cloud chamber and correctly explained their origin. These electrons are produced by the process depicted in Fig. 1, shown for silicon. The electronic energy levels of the singly ionized atom are listed on the left, taking the Fermi level E_f as the zero of energy: these are the x-ray levels K, L, M, ... as labeled on the right. When atoms are brought together to form a solid, the valence level V broadens into an effectively continuous band[2] and the calculated[3] density of states (shaded area) has been drawn in this band. Fig. 1 shows the atom immediately after K-shell ionization by a primary electron; the Auger process initiates when an outer electron fills this "hole", as shown for an L_1 electron. The energy released by this transition is either emitted as a photon or given to

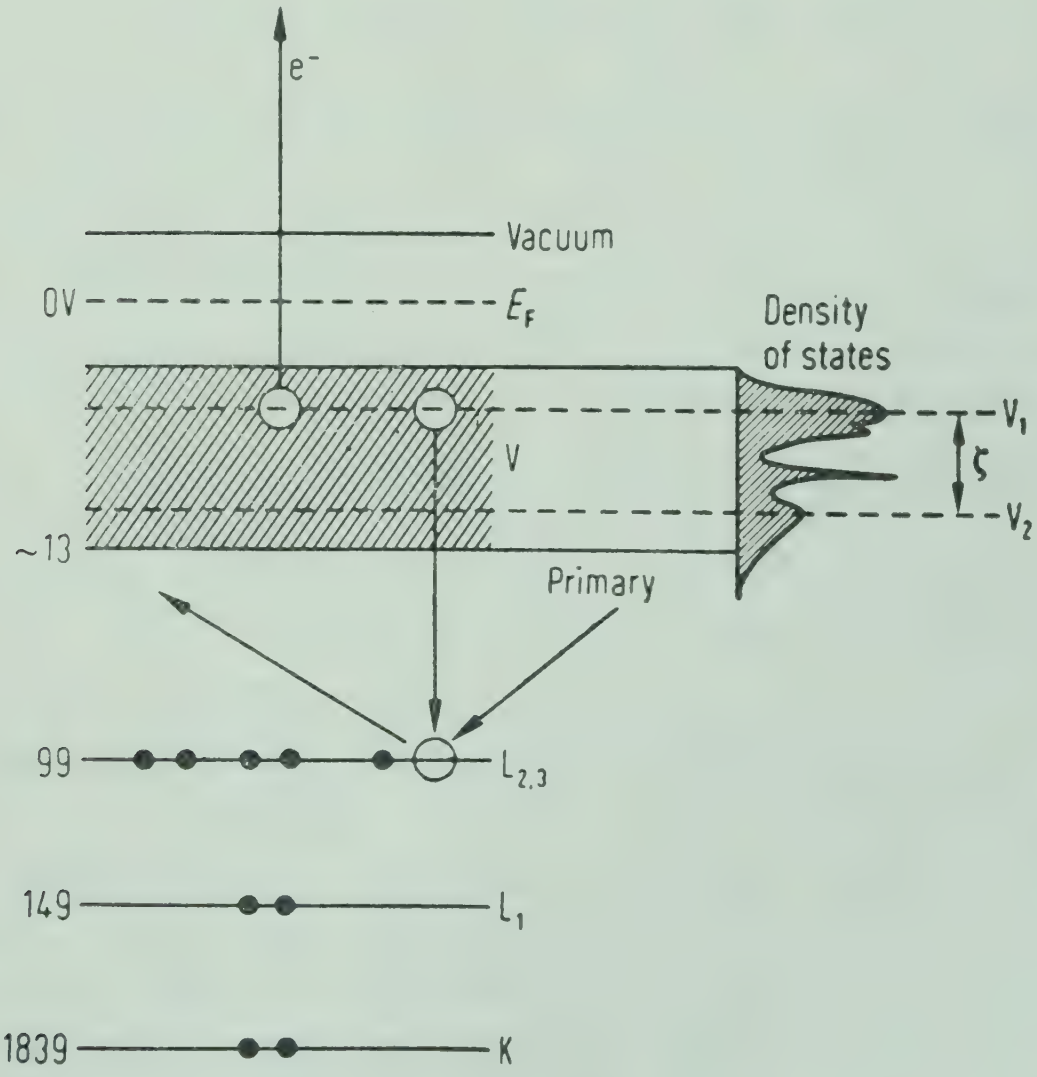

FIG. 1. The singly ionized Si atom. The electron energy levels are listed on the left (in eV) with zero of energy at the Fermi level E_f, E_c is the bottom of the conduction band. The x-ray nomenclature is given on right, and the density of states has been drawn into the valence band. A $KL_1L_{2,3}$ Auger process is depicted, after primary electron ionization[46].

another electron. If this energy is sufficient, an electron can be ejected from the atom, as illustrated for another electron at $L_{2,3}$. The process just described is called the $KL_1L_{2,3}$ Auger transition. Unfortunately, after Auger ejection, the atom is doubly ionized and the energy level diagram in general changes so that Fig. 1 cannot be used for estimating the energy of the Auger electron. We return to this point in Section 1.2.2 but will first describe a very useful semiempirical method for estimating the energy of the Auger electron.

2.2 Energies of Auger Electrons

2.2.1 Semiempirical Method

The energy E of the ejected electron can be estimated by assuming the diagram of Fig. 1 to be approximately valid. The energy released is $E_K - E_{L_1}$ (exactly), but the ejected electron must expend the energy $(E'_{L_{2,3}} + \phi)$ to escape the atom, where ϕ is the work function and $E'_{L_{2,3}} \neq E_{L_{2,3}}$ due to the extra positive charge of the atom.

Because of this positive charge $E'_{L_{2,3}}$ should be approximately equal to the $L_{2,3}$ ionization energy of the next heavier element, or $E'_{L_{2,3}}(Z) = E_{L_{2,3}}(Z + \Delta)$ where Z is the atomic number and $\Delta \approx 1$ to account for the extra charge. We, therefore, have

$$E(Z) = E_K(Z) - E_{L_1}(Z) - E_{L_{2,3}}(Z + \Delta) - \phi \qquad \ldots(1)$$

Equation (1) is useful because E is expressed in terms of signle ionizarion energy levels which can be found in the x-ray[4] and photoelectron energy tables[5]. Equation (1) can be generalised to any Auger event involving the levels $W_oX_pY_q$; also, the actual measured energy will have an additional term $-(\phi_A - \phi)$, which is the difference between the work functions of the energy analyzer ϕ_A and the meterial under investigation. This gives

$$E_{WXY}(Z) = E_W(Z) - E_X(Z) - E_Y(Z + \Delta) - \phi_A \qquad \ldots(2)$$

Note that ϕ drops out, and therefore cannot be measured using Auger energies. Experimental values of Δ are generally between 1/2 and 3/2[6–8].

Equation (2) is not self consistent if experimental values from x-ray tables are inserted, since it does not give $E_{WXY} = E_{WXY}$ although we know this must be so because the initial and final states for both transitions are identical. This discrepancy arises because Equation 2 neglects quantum mechanical exchange effects. Methods of accounting for such effects are well known, and have led to refinements of Eqution (2) which gives values of E_{WXY} that agree with experiment within $\lesssim 1$ per cent for the simpler families of Auger transitions, such as *KLL*, *LMM* and *MNN* families. The strongest transitions observed experimentally are of the type *WXY* with $X, Y = W$ or $(W + 1)$ where $(W + 1)$ is the next higher level; e.g. $K + 1 = L$. This "selection rule" follows from the fact electron interactions are strongest between electrons whose orbitals are closest together.

Since for Auger process three electrons are needed, lithium appears to be the first detectable element. However, a Li atom has only one electron in the L shell and cannot undergo an Auger transition. Therefore, for isolated atoms, Be is the lightest element that gives Auger electrons. In a solid the valence electrons are shared, so that lithium gives Auger electrons of the type KVV, where V is the valence level of the solid. Similarly, He embedded in a solid should also produce Auger electrons.

2.2 2 Theoretical Calculations

The WXY notation is almost universally used for designations of Auger energies in analytical work. However Eq. (2) was not derived from first principles and therefore exhibits numerous inadequacies in detailed analyses. For example, the WXY method does not even give the correct number of Auger transitions. To illustrate this, consider the simplest family of transitions, the KLL group. There are four x-ray levels : K, L_1, L_2, L_3 giving a maximum of six distinct transitions.

KL_1L_1 KL_2L_2

KL_1L_2 KL_2L_3

KL_1L_3 KL_3L_3

The actual number of transitions is shown in Fig. 2. There are six transitions in the limits of high and low atomic numbers; however, there are nine in between, and this is confirmed by experiment [1,12]. Clearly, from the point of view of basic physics, the WXY notation is inadequate and one must examine the theoretical approach. However, we shall not go into details of this and readers are referred to various research articles [13–15].

2.3 Intensities of Auger Transitions

For a given incident primary beam current, the observed current in an Auger peak will depend upon the Auger yield and the ionization cross-section of the W shell. The Auger yield is simply the probability that an atom excited by removal of an inner electron de-excites by the radiationless Auger process. The alternative mode of de-excitation is by emission of a photon. The Auger yield is essentially unity for the light elements, where the incident beam ejects an electron from the K or L shell. A plot of the Auger yield for the K shell versus atomic number, based on a relationship due to Hagedoorn and Wapstra[16], is given in Fig. 3. The L-shell Auger yield is more complex, but is also large for low-Z elements[6].

An expression for the ionization cross section as a function of incident beam energy has been given by Worthington and Tomlin[17]. The ionization cross section rises rapidly from zero with the beam energy at or below the binding energy to a maximum when the beam energy is two to three times the level binding energy. With higher beam energies the cross section decreases rather gradually.

Another factor in the Auger intensity is the amount of secondary ionization in the surface layers of the specimen produced by backscattered electrons.

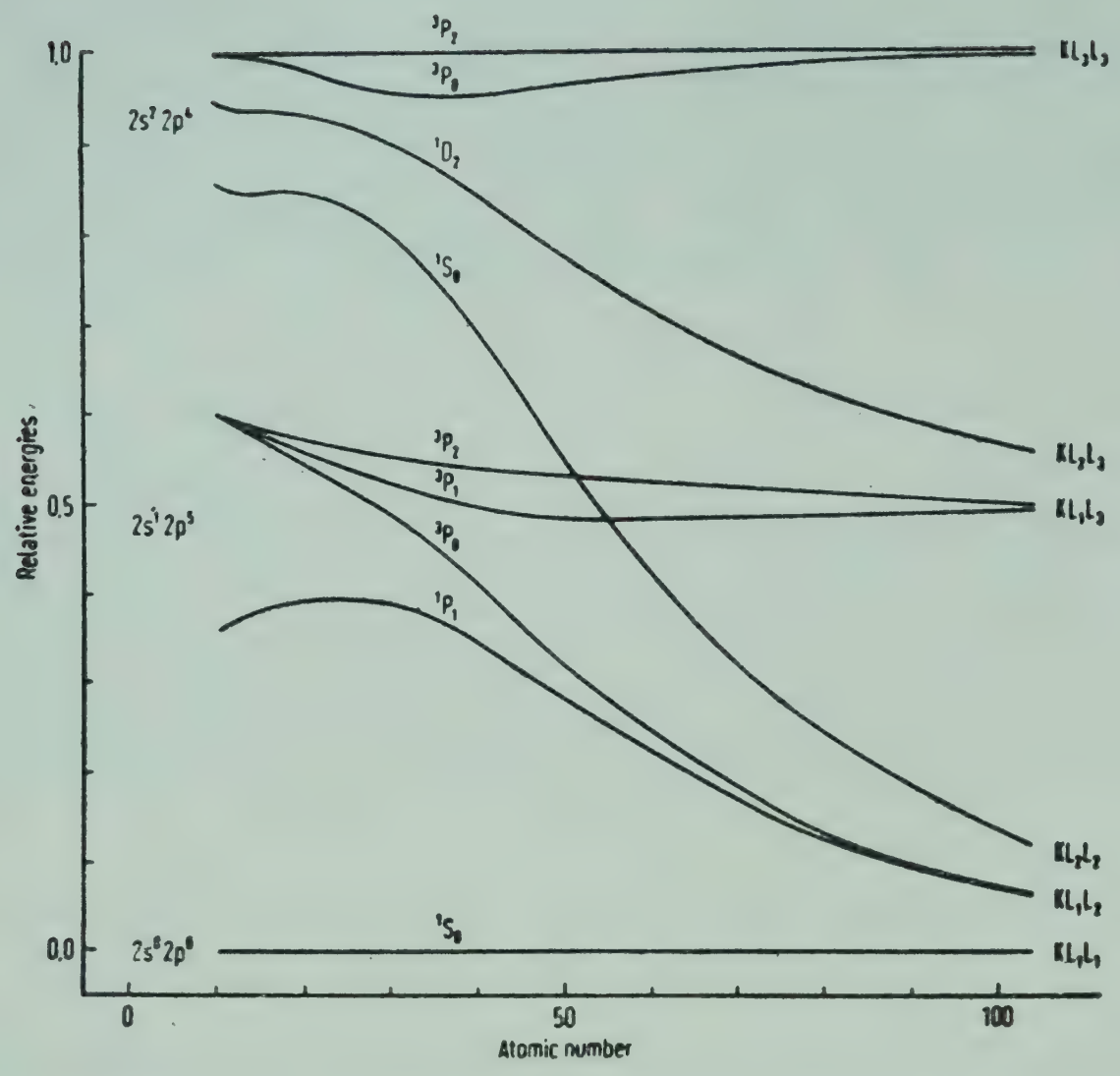

FIG. 2. Relative positions of *KLL* Auger energies, normalized to the $KL_1L(^1S_0)$-$KL_2L_3(^3P_2)$ interval. The doubly ionized atomic configurations (2s° 2P°, etc) and the spectroscopic terms are indicated. There are six transitions in the limits of low and high Z, but nine in between. The *KLL* designation is valid only for heavy atoms ($Z > 80$), when *j-j* coupling dominates. (From *K.* Siegbahn *et al.*[5])

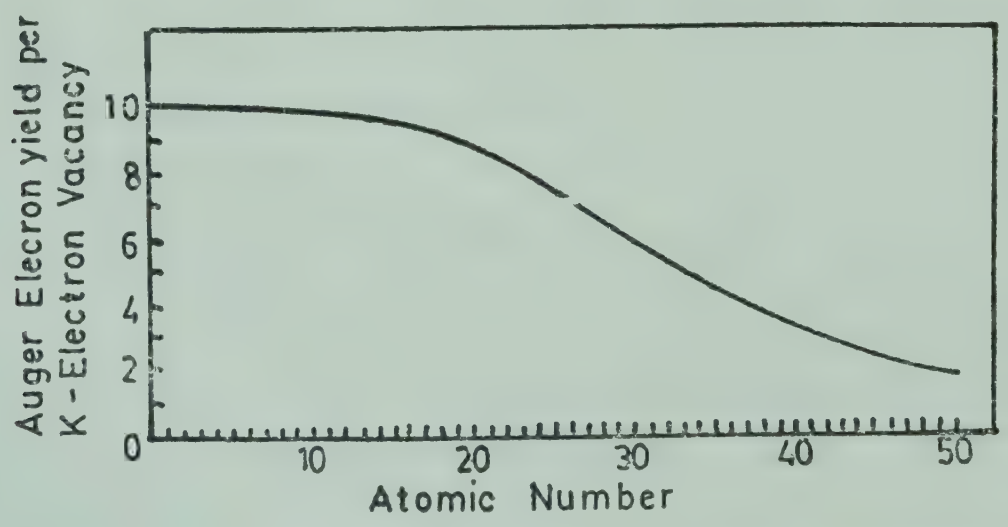

FIG. 3. Auger yield versus atomic number for the *K* shell (using the expression of Hagedoorn and Wapstra[16]).

The problem of Auger intensities has been considered by Bishop and Riviere[18]. One of their essential results, obtained by considering the combined energy dependence of the ionization cross section and ionization by backscattered electrons, is that intensity of an Auger transition is maximum when the beam energy is 3–3.5 times the binding energy of the *W* level. This prediction has been verified experimentally, see for example, a subsequent paper by Bishop *et al*[19].

2.4 Widths of Auger Peaks

Auger peaks are typically 10 eV in width (full width at half maximum). An Auger peak should have a width of about 10 eV for a transition time of 10^{-16} sec because of the uncertainty principle. This lifetime broadening is greater for faster processes of type $W_aW_bY_c$ (termed Coster-Kronig transition). Some peak broadening will also occur because of energy losses of electron escaping from the specimen.

Auger peak widths will of course depend upon the widths of the energy levels involved in the Auger transition. The widths of atomic energy levels decrease with atomic number. For transitions of the form WXV and WVV, however, where V denotes the valence band, the peak width will reflect the band structure of the solid. In the case of WVV transitions, the Auger peak will be twice the width of the valence band. Information on the band structure of a solid may be extracted from Auger spectra[20].

2.5 Escape Depth of Auger Electrons

The escape depth of Auger electrons emitted by atoms in solids is of primary importance in assessing the capabilities of Auger spectroscopy as an analytical technique. An expression for the range of low-energy (1-10-keV) electrons in solids has been given by Feldman[21].

$$R = 250\,(A/\,\rho\,Z^{n/2})\,E^n \qquad \ldots(3a)$$

where $$n = 1.2/1\,(-\,0.29\,\log_{10} Z) \qquad \ldots(3b)$$

and R is the (maximum detectable) range in Angstroms, E is the kinetic energy in kiloelectron volts, Z is the atomic number, A is the atomic weight, δ is the density in grams per centimeter cubed. In silver, for example, electrons with a kinetic energy of 3 keV will have a range of $\sim$ 370 A° according to Equation (3). Electrons with an energy of 362 eV (an observed Auger energy) will have a range of $\sim$ 3A° in silver, assuming Equation (3) is valid below 1 keV. Thus, 362 eV Auger electrons should be able to penetrate only one or two monolayers of silver. Although, the exciting beam can cause ejection of Auger electrons from greater depths, these electrons will undergo subsequent scattering and will not contribute to the Auger peaks. The limitation of Auger spectroscopy to analysis of only the first three or four monolayers of silver and other metals has been confirmed experimentally by measurement of peak heights as one metal is desposited on another[22].

2.6 Energy Spectrum of Scattered Electrons

Suppose a monoenergetic beam af electrons with an energy of several kiloelectron volts is incident upon a solid. Auger electrons will constitute only a small fraction ($\sim 10^{-5}$) of the electrons scattered back from the specimen surface. The Auger electrons which we wish to observe will have to be separated from a large electron background, and some knowledge of the various features of the complete

electron energy distribution is necessary for proper understanding of the problem. Figure 4a shows a typical energy distribution $N(E)\,dE$. The various features discussed below are labeled in the figure.

2.6.1 Elastic Peak

There is a prominent peak in the energy distribution at the energy of the incident beam. This sharp peak represents the electrons scattered elastically, i.e., without loss of energy. These elastically scattered electrons will form a diffraction pattern if the specimen happens to be a single crystal, and this fact is the basis of low-energy electron diffraction.

2.6.2 Low-Energy Maximum

The function $N(E)$ is seen to increase rapidly at low energies as a consequence of the rapid multiplication of low-energy secondary electrons by multiple scattering. The function $N(E)$ does not increase indefinitely, however, because secondary electrons must have sufficient energy to overcome the work function of the specimen if they are to be observed.

2.6.3 Plasma Loss Peaks

About 10-20 V below the elastic peak in metallic specimens, 'wiggles' in $N(E)$ are observed. These wiggles represent electrons which have lost discrete amounts of energy by interaction with the plasma modes of the electrons of the metal[23].

2.6.4 Characteristic Loss Peaks

If the incident beam has an energy E_p, then one would expect to see peaks in the energy distribution at energies $E_p - E_b$ where E_b is the binding energy of an

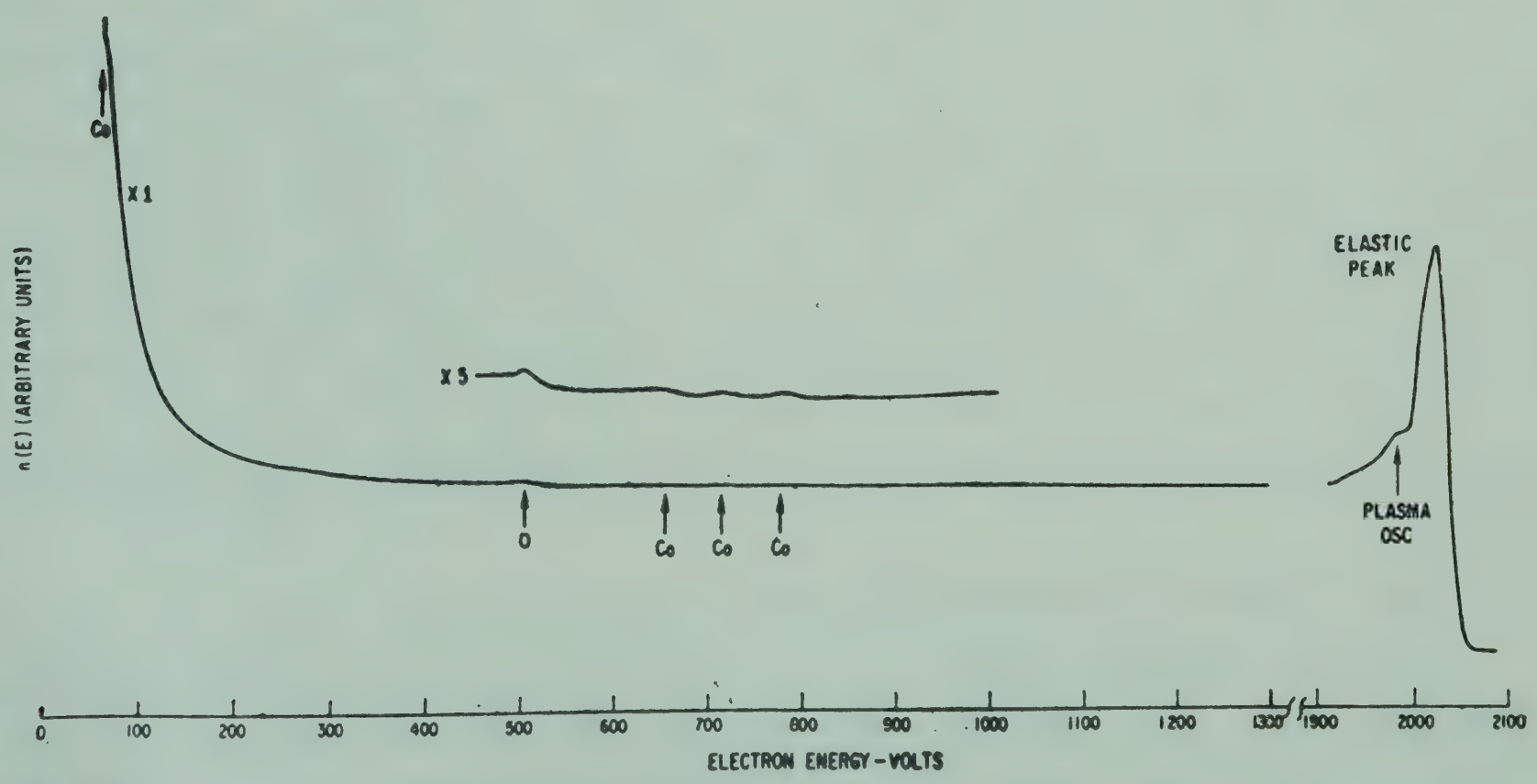

FIG. 4a. The electron energy distribution $N(E)$ obtained from a cobalt specimen[60]. The energy of the incident electron beam was 2 KeV. Auger peaks from oxygen and cobalt are barely discernible.

atomic electron. Such peaks are indeed observed in Auger analysis and can provide useful information since the characteristic loss spectra are less complex than the Auger spectra[24]. Loss peaks may be distinguished from Auger peaks since the position of the latter is independent of the incident beam energy, whereas the former always appear at a fixed energy interval below the energy of the incident beam and change their absolute position as the beam energy is varied. The characteristic loss peaks are typically of about the same amplitude as some of the less intense Auger transitions, however, and it is possible to confuse the two if precautions are not taken.

2.6.5 Auger Peaks

Finally, we note that the electron spectrum does indeed contain Auger peaks. Auger peaks are superimposed on the secondary electron background, as are the other features of interest, and are rather hard to discern in the $N(E)$ curve of Figure 4 a. The standard method for signal enhancement will be discussed in the next section. Because of various energy loss processes, Auger peaks have a 'tail' on their low-energy side and appear to fall off relatively more rapidly on their high-energy side.

3. Experimental Apparatus

We have seen that in the typical energy distribution $N(E)$, as presented in Figure 4 a, the Auger peaks are difficult to detect. Harris[25] was able to enhance greatly the signal to noise ratio of Auger spectra by electronic differentiation of the energy distribution. The differentiation technique serves to reduce the effect of the background electrons since their energy distribution has a relatively constant slope, and hence the background contribution to the derivative signal, as compared to the much more rapidly varying Auger peaks, is ralatively small. Electronic differentiation of the electron spectrum is easily accomplished by modulating the signal at an audio frequency and synchronously detecting the component of the spectrometer output at the modulating frequeny (or a multiple thereof). This is known as phase sensitive detection techniques, and Figure 4 b shows the derivative of the electron distribution of Fig. 4 a.

A variety of electron energy analyzers has been developed which can in principle be used in Auger spectroscopy. At present time, however, only two types of instrument, the retarding field analyzer and the cylindrical mirror analyzer, are in common use and we shall discuss them in this section.

3.1 Retarding Field Analyzer

Auger spectra can be recorded with *LEED* optics used as retarding field analyzer[26],[27]. The normal setup is shown in Figure 5. The *LEED* gun produces the necessary energetic primary beam. The secondary electrons are collected by the flourescent screen, after passing the grid system. The retarding potential is applied to the two central grids. A small modulating voltage is applied to the same grids. The outer and inner grids are at ground potential. The modulated collector current

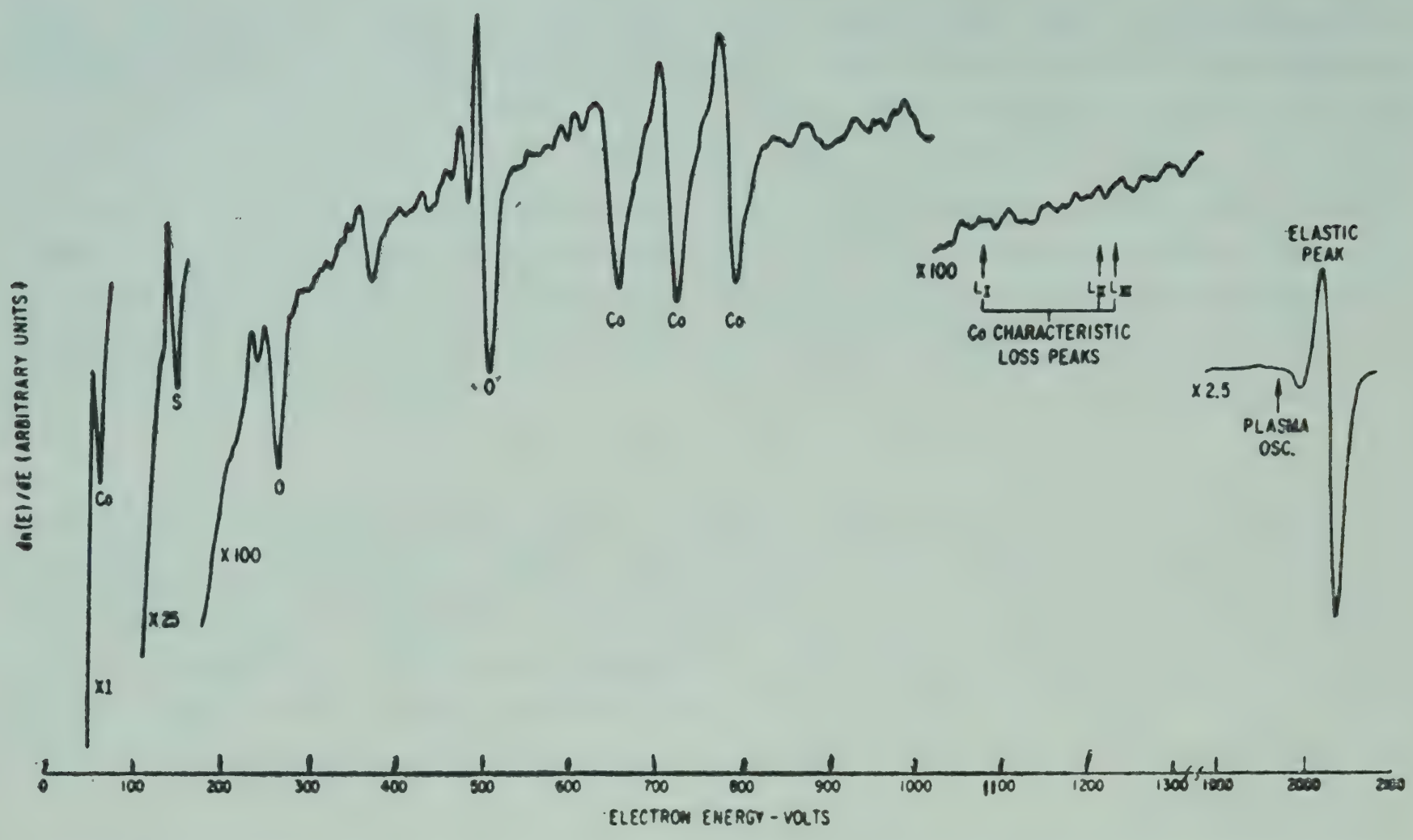

FIG. 4b. The derivative of the electron energy distribution of Fig. 4a[60]. The Auger peaks are plainly distinguished. The specimen is rather dirty, as is evident by the carbon, sulphur and oxygen peaks shown. The elastic peak, plasma oscillations are also apparent. The location of the L_I, L_{II} and L_{III} characteristic loss peaks from cobalt are marked, although they are not evident in this particular spectrum. These curves were taken with a three-grid retarding field analyzer.

that contains the information is amplified and demodulated using well established phase sensitive detection techniques.

The collector current is given by Tracy[28]:

$$I_{\text{coll}}(E) = I_p \int_{E}^{E_p} N(E)\, dE \qquad \ldots(4)$$

where $N(E)$ is the secondary emission distribution; E_p,E are the primary energy and the retarding potential; and I_p is the primary current. It can easily be shown that for a small modulating voltage

$$E - E_o = K \sin \text{wt} \qquad \ldots(5)$$

the first harmonics coefficient in the Taylor expansion of the current, is proportional to $N(E)$, the second harmonics coefficient to $dN(E)/dE$, etc.

In the second harmonics mode, the background is greatly reduced and electronic amplification can be considerably increased[25]. The limitations and extensions of this modulation technique have been discussed in detail by Hanisch *et al*[29].

Figure 6 represents a typical $dN(E)/dE$ Auger spectrum, recorded on a tungsten sample. The peaks observed are due to tungsten, carbon, sulphur and

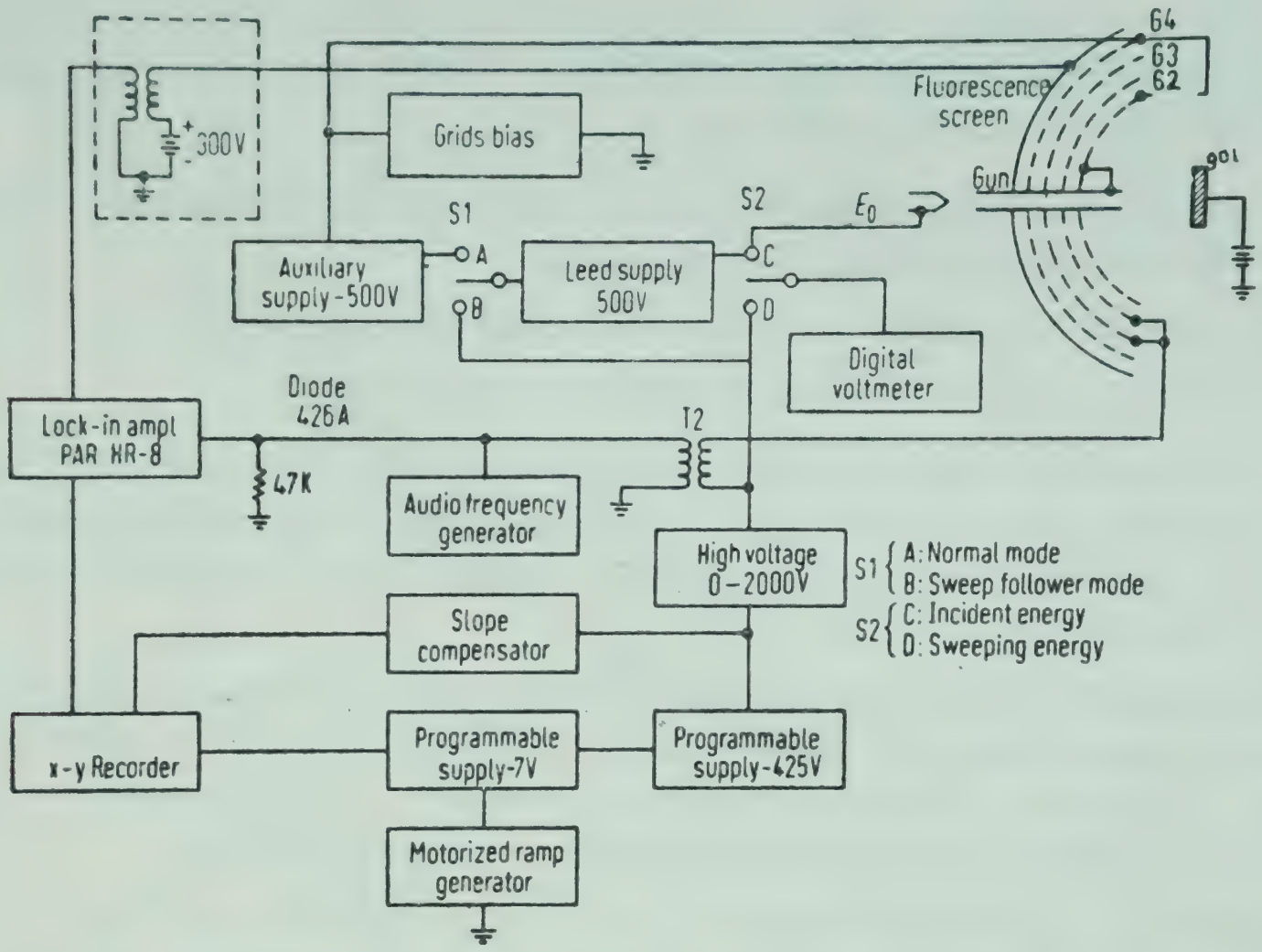

FIG. 5. Schematic representation of Auger spectrometer : 1. Specimen, 2. Oscillator 3. Amplifier 4. Sweep generator 5. Digital voltmeter 6. Averager 7. Frequency—dependent amplifier 8. Lock-in amplifier 9. Computer/X-Y recorder.

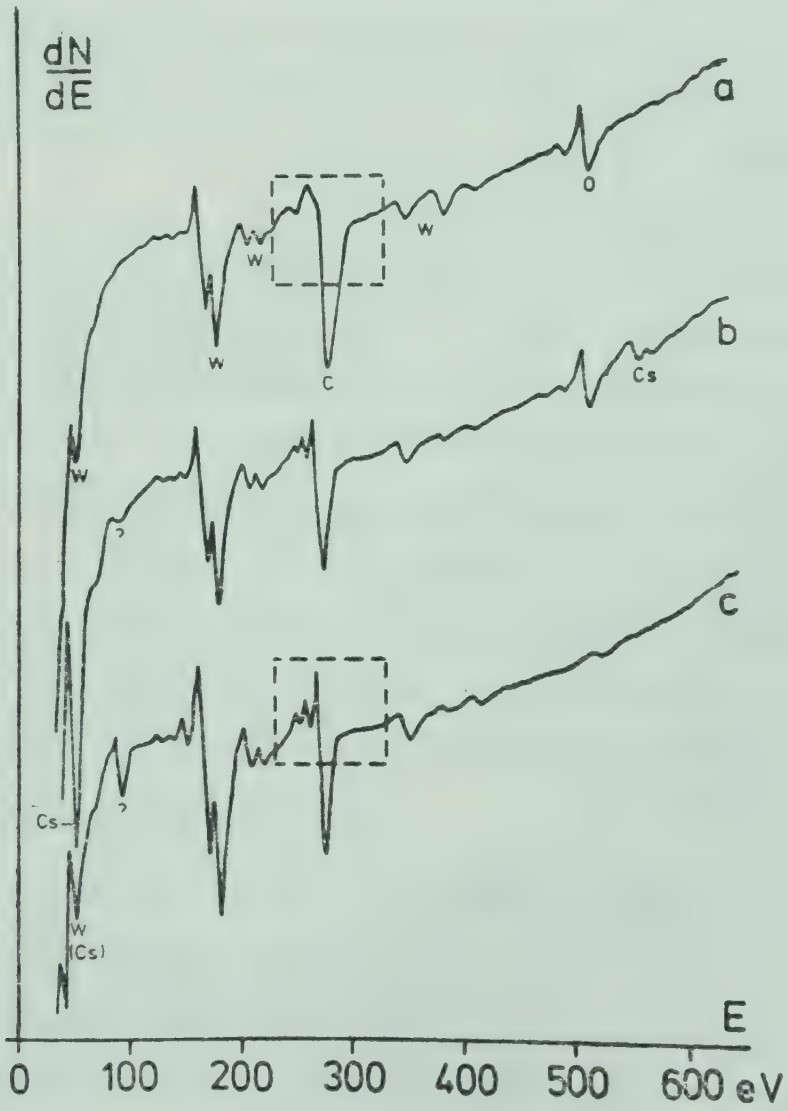

FIG. 6. Auger spectra of a tungsten sample : (a) during a cleaning procedure, contaminants carbon, sulpher, oxygen, (b) with cesium condendate, (c) after heat treatment to 1000K[109].

oxygen Auger transitions and to carbon contamination. The high signal/onise values in this manner are the major advantage of this mode of operation which however also has certain drawbacks namely:

(i) when the Auger peak is asymmetrical, it is often difficult to recognize the original shape in the derivative peak,

(ii) exact peak positions are not always easily determined, and

(iii) amplitude ratios of different peaks are ambiguous.

In practice it has been agreed upon to determine the peak position at the high energy minimum of the double wing-shaped peaks. The peak width is usually given as an energy difference between high and low energy extreme. Amplitudes are given as peak-to-peak values.

An alternative method to reduce the background consists of a computer-aided background substraction, after noise reduction through averaging of directly recorded $N(E)$ curves (first harmonics mode of operation)[30]. In this manner, the primary electron dose and hence the damage due to the beam can be reduced.

Sickafus[31], Musket and Ferrante[35], and more recently Houston[33] have discussed different methods of background substraction to retrieve optimized Auger spectra. The latter method, called dynamic background substraction, involves multiple differentiation followed by integration of the same order. The multi derivative scheme usually results in low S/N values, as demonstrated by Fig. 7, representing the $N(E)$, $N'(E)$, and $N''(E)$ spectra of minute amounts of oxygen on Ta. This can, however, be overcome by performing first and second-order background substraction, as shown in Fig. 8 where R_1 represents the integral of the data shown in Fig. 7*b* and R_2 the double integral of that given in Fig. 7*c*. In this manner the oxygen Auger spectrum is retrieved from the experimental data.

A different approach has been proposed by Mularie and Peria[34]. These authors retrieve high-resolution Auger spectra from normally recorded $[dN(E)/dE]$ curves, by integration and deconvolution with a suitable instrument function (also containing the undesired inelastic effects present in Auger spectra, such as plasmon losses).

A detailed analysis of resolution and sensitivity of the *LEED-AES* instrument has been given by Taylor[35] and Bishop and Riviere[18]. Resolutions of 0.5 per cent can be obtained. Sensitivity in terms of noise is also discussed by Taylor. A practical limit to sensitivity is the time needed to collect the data. A limit of 0.1 per cent of a monolayer can be reached, the limiting factor being the high background current inherent in a high-pass filter[36].

3.2 *Cylindrical Mirror Analyzer* (*CMA*)

The *CMA* was first used in *AES* by Palmberg *et al*[37] in an arrangement shown in Figure 9. It is a deflection type band-pass instrument with hign transmission (10 per cent for) moderate resolution (0.3 per cent). At approximately the same resolution the transmission of the instrument is thus still more than half that of the *LEED-AES* instrument (17 per cent). Its S/N ratio is 100 times larger than for a

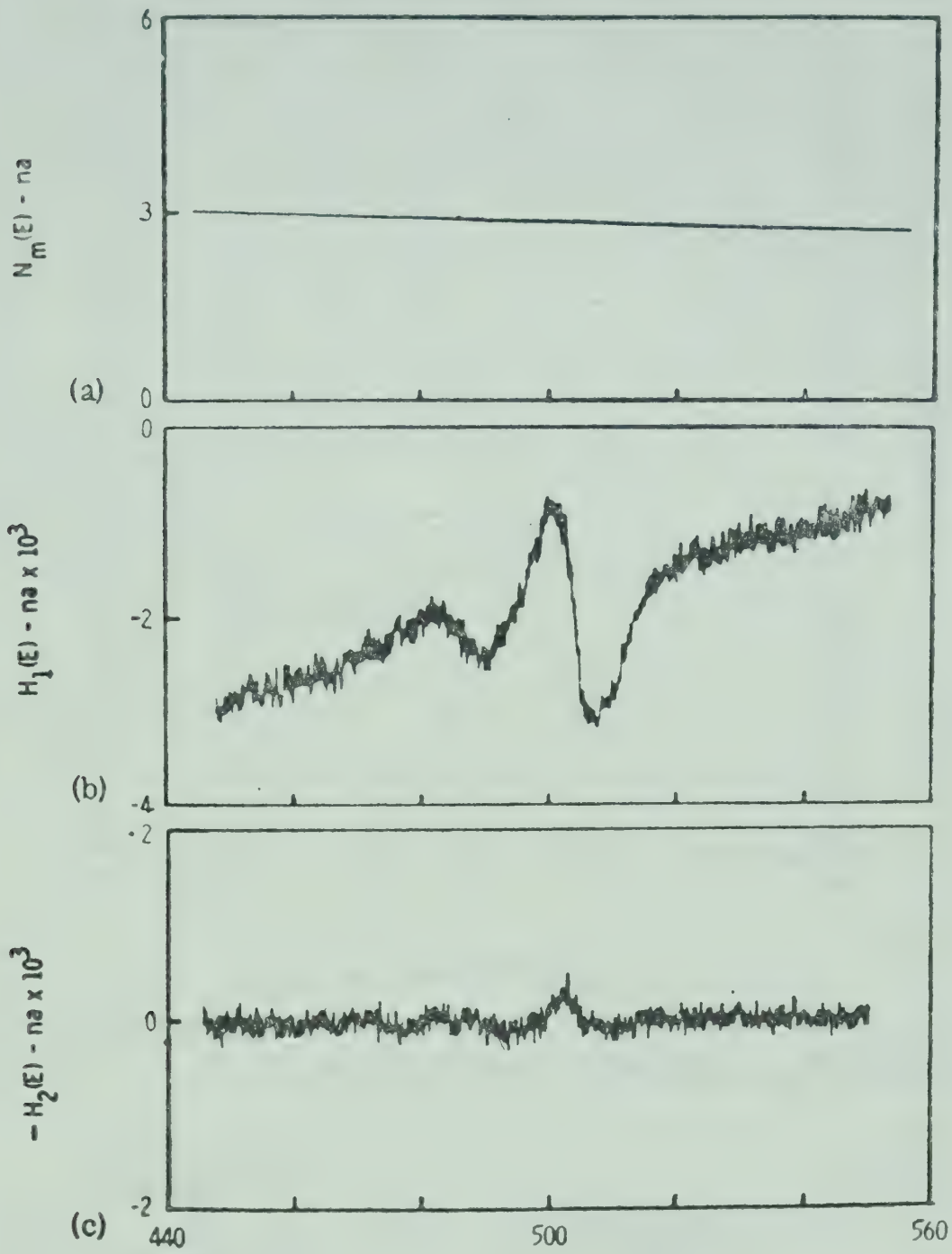

FIG. 7. Auger spectra from minute amounts of oxygen on tantalum[33] :
(a) measured electron energy distribution
(b) first derivative (first harmonic)
(c) negative second derivative (second harmonic)

retarding field instrument, enabling a direct display of the Auger spectrum on an oscilloscope screen.

The current collected in a *CMA* can be written as[28]

where $$I(E) = CE\,N(E) \qquad \ldots(6)$$

C is a constant, containing I_p.

It is easy to show that in this case the first harmonics coefficient is proportional to $E\,dN(E)/dE$, for sufficiently small K values (modulating voltage). If true distribution curves are desired, an integration has to be performed.

Figure 10 shows a typical *AES* curve, recorded on a metglass specimen prior to cleaning. In such spectra the true secondary peak at low energy is drastically reduced as a consequence of the energy-dependent transmission (factor E in Equation (6)).

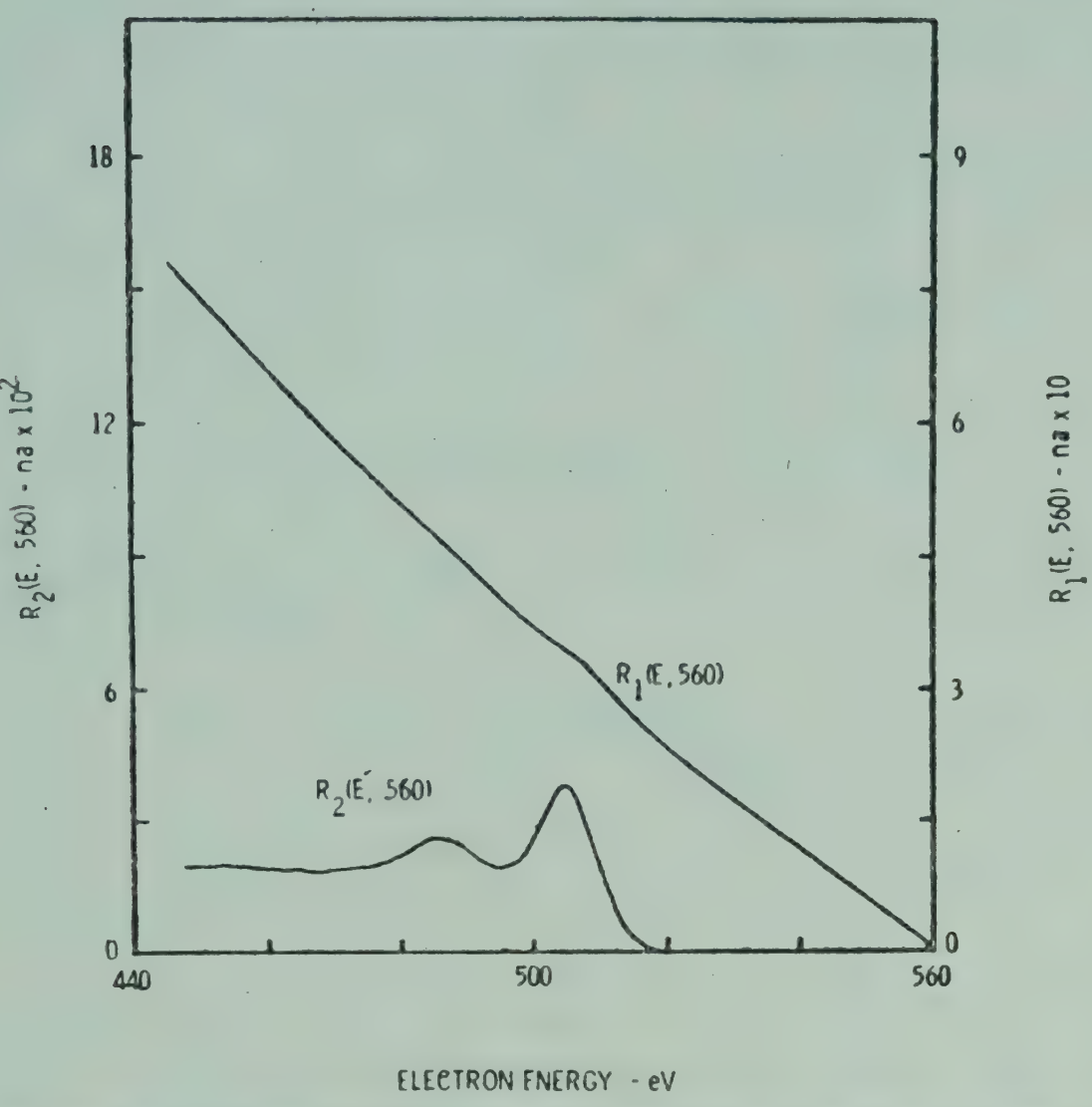

FIG. 8. Results of first-and second-order dynamic background substraction[33]. R_1 represents the integral of figure 7b, R_2 the double integral of figure 7c.

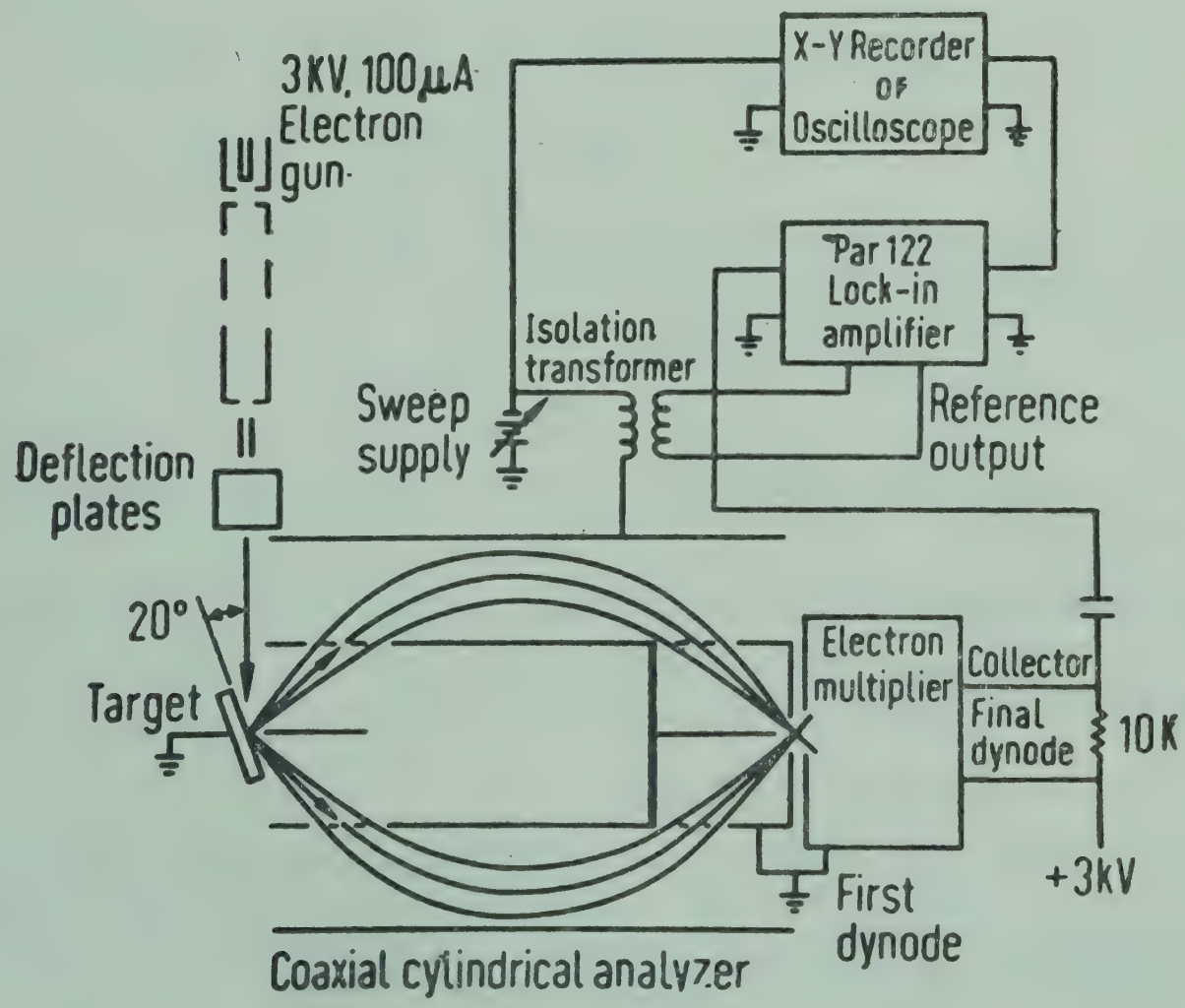

FIG. 9. The cylindrical mirror aualyzer for AES[46].

High modulation frequencies are normally used to decrease the $1/f$ noise. High gain electron multipliers allow for counting or synchronous detection with

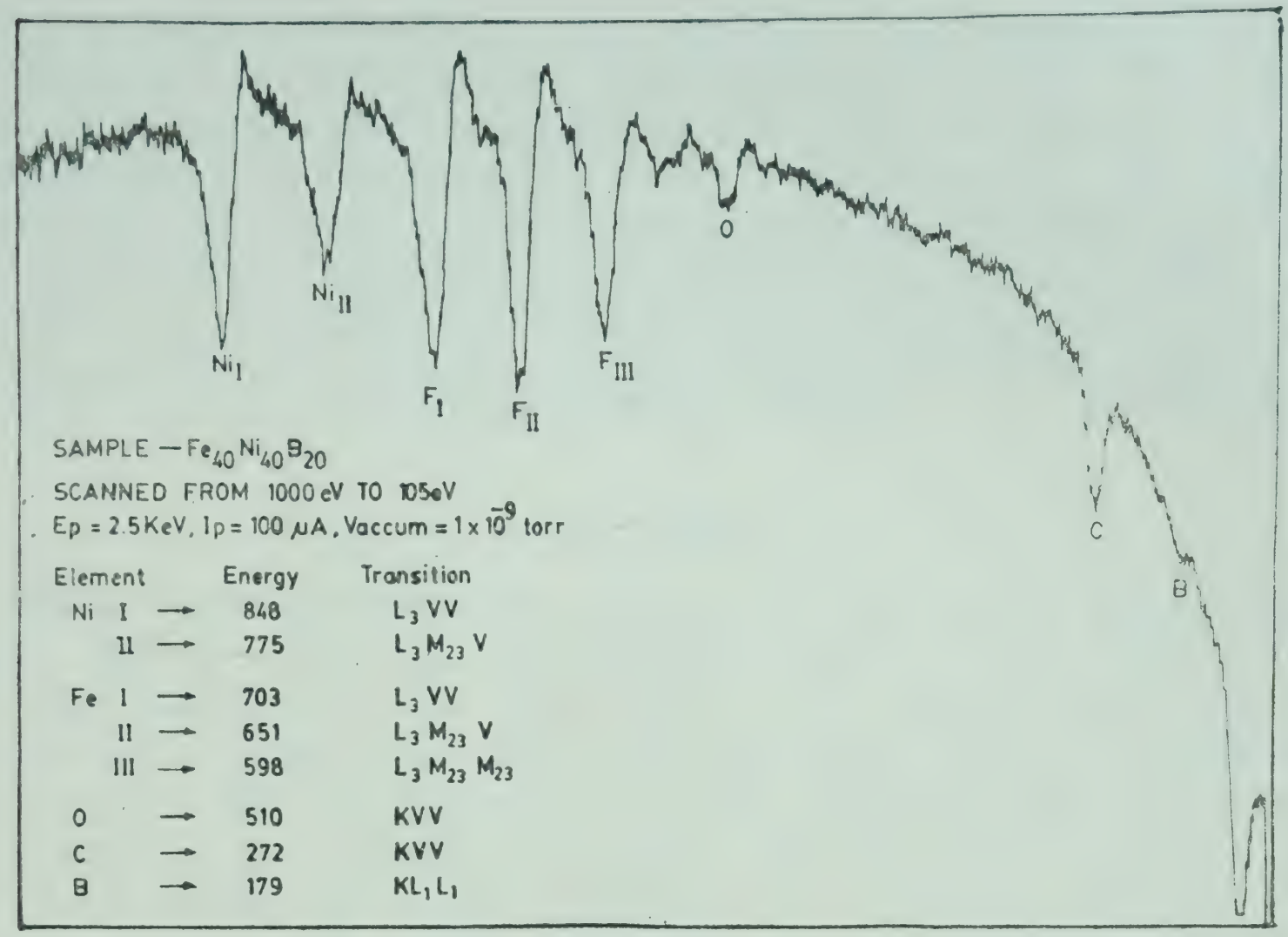

FIG. 10. Auger spectrum of $Fe_{40}Ni_{40}B_{20}$ metglass.

modulation to be used. High scan rates are possible and Auger spectrum can continuously be monitored. If on the other hand the sample is beam sensitive, low primary beam currents can be used. Optimal values for modulation amplitude and primary beam energy are mentioned in the literature[18,28,35]. High primary excitation energies are advised for the *CMA* (~ 3 keV). This has the additional advantage of flattening $N(E)$; the same amplifier gain can consequently be used throughout the spectrum. Modulation amplitudes are chosen as a function of the problem. The effect of the modulation amplitude has been studied by Grant *et al*[38], which one needs to consider while interpreting Auger spectrum.

3.3 Accessories and Modifications

Auger spectrometers usually incorporate a number of 'accessories'. An ion bombardment gun and some provision for heating the sample, either resistively or by electron bombardment, are incorporated in most instruments. Since *in situ* specimen cleaning is almost always required, these two accessories may be regarded as necessities. One may of course provide an Auger spectrometer with any sort of additional instrumentation one desires, such as a kelvin probe for work function measurements, a mass spectrometer, etc.

A number of clever modifications which may be made to the spectrometer system itself have been described in the literature. Many of those modifications are of interest only to those already working in the field, but some are of sufficient interest to warrant mention here. By applying the audio modulation voltage to (1) the retarding grid alone in a *LEED*/Auger instrument (the usual method), (2) to

both the retarding grid and the electron gun, or (3) to the electron gun alone. Gerlach *et al*[39] show that one can obtain both the Auger and characteristic loss peaks, the Auger peaks alone, or the characteristic loss peaks alone. Interpretation of spectra may thus be greatly simplified. Sickafus and Colvin[40] have described a circuit which permits the scanning of preselected Auger peaks only and generates output voltage proportional to the peak-to-peak heights of the derivative signals. This device is convenient in studies of reaction kinetics. Finally, a circuit is available which provides automatic background correction for a retarding field analyzer[41].

4. Applications

Auger emission spectroscopy has proved out extremely useful method for surface analysis. It is a useful complement to *LEED* (Low Energy Electron Diffraction) because it can tell us which atoms are in the surface layer, while *LEED* hopefully can tell us where they are located with respect to one another. The fact, that *AES* is sensitive only to elements in the first few layers of the specimen surface, is the basis of the strength and usefulness of the method, but it also constitutes limitation. It is, therefore, for questions involving the composition of bulk, the variation of the composition of thin layers as a function of depth is studied by simultaenous ion-sputtering of the specimen-surface and Auger analysis.

We shall discuss in this section the qualitative and quantitative use of *AES*. We will take up specific examples which throw light on the applications of Auger analysis.

4.1 Qualitative Analysis

Auger spectroscopy has been employed mainly as a qualitative technique to date. In qualitative analysis selectivity, sensitivity and size of the sample become the important parameters. In addition sample preparation also plays an important role. We shall discuss below all these parameters.

4.1.1 Selectivity

Auger spectra, especially of the heavier elements, can be quite complicated, as may be seen by reference to the chart of Strausser and Uebbing[42]. Since Auger peaks are of the order of 10 eV wide, it is clear that interference between the Auger peaks of the various elements present in a specimen may be a problem. However, even if certain Auger peaks do overlap, there may well be other peaks which do not. Although interpreting the Auger spectrum of a specimen of completely unknown and exotic composition could be a hopeless task, user of technique interested in solid surface is not usually confronted with such a problem. One often knows the approximate composition of a specimen and can frequently rule out the presence of certain elements (naturally such a procedure required caution). More important, one is often interested in detecting the lighter elements, such as carbon, oxygen, sulphur, phosphorus, and chlorine, which may be present

as surface contaminants. These elements give rise to fairly uncomplicated Auger spectra. Some feeling for the selectivity of Auger spectroscopy may be acquired by examination of typical experimental data. Fig. 11a shows the spectrum of molybdenum[62]. The sulphur peak is subject to interference from the molybdenum peaks, some idea of sulphur concentration can still be obtained, however, if present in sufficient quantity, by comparison with a 'clean' molybdenum surface (Fig. 11*b*). The carbon and oxygen peaks are in energy regions where interference is not a problem for this particular specimen. In the cobalt spectrum shown in Fig. 4*b* the sulphur peak is not subject to interference[62].

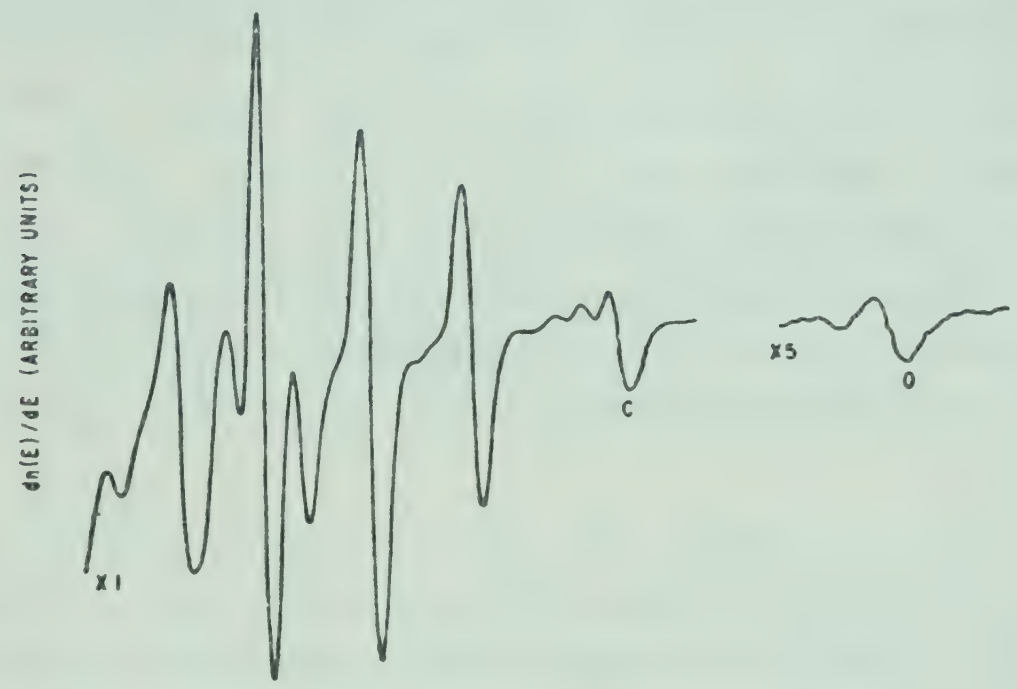

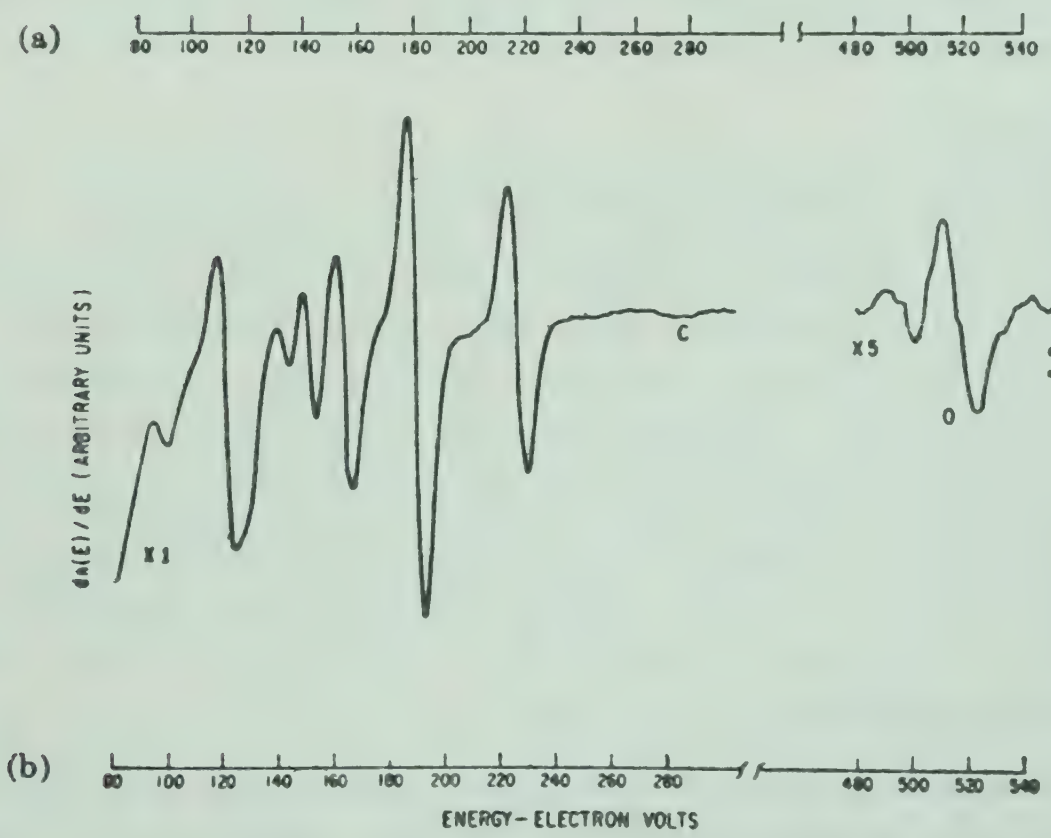

FIG. 11a. Auger spectrum of molybdenum with surface sulphure present[62]. The sulphur peak at 150 V is subject to interference from the molybdenum peaks. Carbon and sulphur are also detected.

FIG. 11b. Auger spectrum of a molybdenum surface from which sulphur has been at least partially removed. Carbon is also much reduced compared to the spectrum of Figure 11a. Oxygen is still in evidence (RFA spectra).

Although these examples are concerned with impurities, we shall discuss other applications of Auger spectroscopy in which the composition of the substrate surface itself is of primary interest.

4.1.2 Sensitivity

An analysis of the sensitivity to be expected from retarding field and cylindrical analyzers has been presented in Section 2. The calculated sensitivities have been obtained experimentally. A number of authors have reported detecting about 0.01 monolayer of a surface species with the retarding field instrument. Weber and Johnson[43] reported a sensitivity for cesium on silicon and potassium on germanium of 0.02 monolayer. For potassium on silicon, 0.02 monolayer represents about 10^{-9} g/cm^2. Less than 0.01 monolayer of nickel has been detected on silicon[44].

4.1.3 Size and Kind of Specimen

Specimen size limits are set primarily by the physical size of the instrument vacuum chamber. Naturally only that portion of the specimen illuminated by the electron beam will be observed. The illuminated portion of the specimen must be at focus of the analyzers, thus there are some geometrical limitations on sample configuration.

Auger specimens are almost invariably solids, although it would be possible to analyze conducting liquids having sufficiently low vapour pressure if surface cleaning could be accomplished. Gases also have been studied by *AES* techniques. Both metals and semiconductors are amenable to study by *AES*. Insulators, however, will give rise to spectra with energy shifts because of charging of the surface, and 'glancing incidence' techniques are generally employed.

4.1.4 Sample Preparation

For Auger analysis 'reasonably clean' surfaces are required and hence sample cleaning techniques are of great importance. If one simply inserts a specimen into an Auger spectrometer, it is likely that only the contaminant carbon will be detected. Carbon monoxide is a common residual gas in vacuum systems and can also be decomposed to elemental carbon by the electron beam. The vacuum pumps used on an Auger spectrometer are of the oil-free sorption, sputter-ion, or titanium sublimation types, but carbon contamination can still be very troublesome. Specimens are usually cleaned before being placed in the spectrometer. In addition, most spectrometers have provisions for *in situ* specimen cleaning as described in Section 3.3.

(a) *Preliminary Sample Cleaning Technique* : Specimens may be cleaned with the various chemical etches and solvents customarily employed for such purposes Residues of these cleaning agents are often readily detectable provided no further cleaning has been undertaken. The detection of such residues is a major area of application of *AES*.

(b) *In Situ Cleaning Techniques* : Samples may be heated, either in vacuum or in oxygen, or hydrogen, to remove contaminants. Heating a metallic specimen

in vacuum is often effective in removing surface carbon since the caabon will diffuse into the bulk. Unfortunately other substances, such as sulphur, may diffuse from the bulk to the surface along grain boundaries during heating.

Ion bombardment is the other commonly employed method of *in situ* specimen cleaning. Ion bombardment may be carried out either by establishing a gaseous discharge to the sample or by employing an auziliary ion gun. With an ion gun ion current densities are typically $1\mu\ A/cm^2$ at the specimen. Assuming that one surface atom is removed by every incident ion, this current density corresponds to removal of about one third of an atomic layer of the surface every minute. Removal rates are much greater with a glow discharge.

Recently ion guns which provide current densities of the order of $100\mu A/cm^2$ have become available. Typical sputtering rates on the order of 50Å/*min*. Simultaneous Auger analysis and ion sputtering are possible resulting in a depth profile of specimen composition. Under such circumstances one need not be as concerned about cleaning and preparing the specimen surface since layers of the specimen are continuously being removed during the analysis.

4.2 Quantitative Analysis

The use of *AES* as a quantitative analytical method is increasing. The remarks made in the foregoing concerning sensitivity, selectivity, sample preparation etc. in connection with qualitative analysis also apply to quantitative analysis. Complications in interpreting Auger spectra which arise in quantitative work will be discussed below.

If Auger spectroscopy is to provide quantitative information, it is necessary to calibrate the spectrometer in terms of the amplitudes of observed Auger signals at known surface coverages for each species of interest. It is essential that the amplitude of the observed Auger peaks be a known function of the surface concentration of the emitting species. It is not completely obvious that a proportionality exists because backscattering of incident electrons and secondary electron production in the specimen may cause variations in the electron flux at the surface. The proportionality of the Auger signal and surface concentration has been verified experimentally in a number of cases.

Weber and Johnson[43] deposited potassium quantitatively on the (111) surface of germanium and found that the relationship between surface coverage and the peak-to-peak deflection of the derivative signal was highly linear, at least upto surface coverages of one monolayer. Incidentally, it is customary to use the peak-to-peak deflection of the derivative in quantitative work as a 'signal amplitude'. It may be demonstrated that this quantity is proportional to the surface concentration of the emitting species, assuming that the shape of the peak is independent of coverage and that the area under the (undifferentiated) peak is proportional to the coverage.

Vrakking and Mayer[45] used ellipsometry to verify the proportionality of the oxygen Auger signal and surface coverage upto 1.5 monolayer of oxygen adsorbed on silicon.

Perdereau[46] obtained a calibration curve for sulphur adsorbed on nickel. The ratio of the 150-*u* sulphur peak to the 62-*U* nickel peak was found to be a linear function of the surface concentration of sulphur. The surface sulphur concentration was independently determined by a radioactive tracer technique.

It is also possible to calibrate Auger peak height as a function of the surface coverages obtained from *LEED* data. In the last few years it has been possible to obtain accurate quantitative information from *AES* data. This has been possible because of emergence of more sound theoretical background and reader is referred to articles by A Joshi *et al*[45] and Chang[46].

4.3 Examples

A number of examples of applications of Auger spectroscopy taken from the literature will be discussed in the following. This survey is intended to be representative rather than exhaustive. New applications of Auger spectroscopy continue to appear with great frequency. The technique will likely be applied to the control of manufacturing processes as well as to problems in research and materials analysis.

4.3.1 Detection of Surface Contamination

The detection of surface contamination is certainly the area in which *AES* has found its greatest use. Surface contamination may result from adsorption of residual gases or by diffusion to the surface of impurities present in the bulk. Another possible source of specimen contamination is surface diffusion from specimen mounting holder if heating of the specimen is necessary. We have already noted that contamination may result from residues of cleaning agents used during specimen preparation[47].

Considerable work has been done on the detection of impurities on silicon and germanium because of the technological importance of these materials. Weber and Peria[48] and Weber and Johnson[43] studied deposited alkali metals. Grant and Hasa[49] studied iron, copper and gold on Si (111). Carbon and oxygen on silicon have beed studied by Chang[50]. Nickel on silicon has also been investigated by *AES*[41]. The surfaces of some solids are known to undergo a rearrangement under certain conditions, the surface structure being no longer the same as that of the bulk. These structural changes are known to be caused by impurities in some cases. Nickle has been found to be associated with the so-called *Si* (111)-$(19)^{1/2}$ surface structure[35]. Surface structural changes can have important consequences in the epitaxial growth of semiconductors.

In another area of semiconductor investigations, it has been determined that one monolayer of carbon is sufficient to greatly reduce the photoyield of GaAs photocathodes[51].

Surface segregation of impurities is also frequently observed. Sulphur is a common impurity in many metals and after heating a surface layer of sulphur is often detected. For example, Harris[25] observed surface sulphur segregation on nickel and Bishop *et al*[19] observed sulphur segregation on titanium.

The adhesion of gold-plated nickel leads to silicon wafers has been investigated[52]. Poor bonding characteristics were related to the presence of thallium on the gold surface.

4.3.2 Fracture Mechanisms

Studies of metal fractures by *AES* also in effect involve the detection of surface impurities. Antimony is found to have segregated preferentially along grain boundaries upon fracturing *AISI* 3340 steel in vacuum[53]. Nickel and chromium also segregate to grain boundaries in steel, although apparently to a lesser extent[54]. By ion bombardment of the fracture surface, it was shown that the antimony was concentrated in the immediate vicinity of the surface [53].

4.3.3 Studies of Problems Relating to Catalysis and Surface Reactions

Catalysis is a major area of interest to surface scientiais. *AES* can provide valuable information on the state of catalytic surfaces.

Catalytic reactions occurring on copper-nickel alloys have been of great interest because of changes in the d-band structure of the alloy which occur as the composition is varied[55]. Although copper and nickel form a continuous range of solid solutions, there can be regions of local inhomogeneity and phase separation which complicate interpretation of experimental data. In particular, it is difficult to insure that the surface region, at which catalytic reactions occur, has the same composition as the bulk alloy. The first examination of copper nickel alloy using *AES* was made by Harris[25]. Ion bombardment has been shown to result in an increase in nickel concentration at the alloy surface[56],[57]. Ertl and Kuppers[58] have made a *LEED*/Auger study of adsorption on *Cu-Ni* single crystals. Not only could the composition of the surface layer be determined it was also possible to deduce that the composition of the alloy was independent of depth in the first few layers of the surface by varying the angle of incidence of the electron beam. As the angle of incidence of the electron beam is increased, the relative contribution of the outermost layers of the specimen decreases relative to deeper layers. Therefore, the relative peak heights of elements at the surface will vary with beam incidence angle if the specimen is not homogeneous. The angular dependence of Auger peaks has been considered by Harris[59].

Determination of surface impurities is naturally also of importance in catalytic studies. It should be possible to use *AES* as a monitor of actual surface reactant and product concentrations during catalysis under some conditions, although interaction of the electron beam with adsorbed species and local heating of the specimen by the beam might prove troublesome.

The foregoing considerations apply not only to catalytic problems but to other problems involving reactions at solid surface as well, e.g. corrosion.

4.3.4 Impurity Concentration as a Function of Depth

It would obviously be useful to be able to determine the concentration of impurities as a function of depth beneath the surface. Depth profiles of this type have been obtained by simultaneous ion sputtering and Auger analysis, as already mentioned[52]. The vacuum system may be back-filled with argon to a pressure of 5×10^{-5} Torr to permit ion bombardment without affecting the performance of the Auger spectrometer.

In a study of an oxidized silicon surface, chlorine was detected at the SiO_2— *Si* interface[52]. The oxide layer was about 1100 Å thick. The maximum chlorine concentration was found to be 3×10^{19} atoms/cm^3. Depth resolution was 10 $A°$ and the sensitivity was 0.1 per cent.

II. SECONDARY ION MASS SPECTROMETRY (SIMS)

1. Introduction

The interaction of energetic ions with a solid results in the ejection of substrate atoms and molecules in both neutral and charged states. This moderately efficient production of charged particles (secondary ions) coupled with high sensitivity mass spectrometric techniques forms the basis of the *SIMS* method. The significant characteristics that have generated the considerable interest in *SIMS* techniques are :

- high detection sensitivity for the majority of the elements ($< 10^{-4}$ monolayer).
- depth concentration profiling of trace constituents with depth resolutions $\leqslant$ 50 Å.
- lateral characterization of the surface on a micrometer (μm) scale.
- isotopic analysis, and analysis of low atomic number elements (*H*, *Li*, *Be*, etc.).

The first experiments dealing with *SIMS* were carried out in the late 1930's by Aront and co-workers[63] and Herzog and Vichbock[64], who described sputter ion sources for mass spectrometers. This early beginning did not produce any immediate interest in *SIMS* as a useful tool. In the sixties a number of workers[65–69], who used *SIMS* mainly for bulk analysis, added more knowledge about the general features of secondary ion emission. In mid-sixties, the *SIMS* was shown useful for thin film analysis[70,71] and it was shown[70] that by measuring the ion current as a function of bombardment time, not only the concentration (number of particles per (m^3) in terms of depth (Å) could be found but diffusion coefficients could also be determined. This was a beginning of quantitative analysis of depth profiles. Since then the interest in *SIMS* has grown, which is evident from the analytical applications as are reviewed by Honig[72], Carter and Colligon[73], Werner and De Grefte[71,74] Fogel[75,76] and others[77–79]. Today *SIMS* instruments are available with a diversified programme on a commercial basis.

2. Theory of SIMS

2.1 Physical Basis

An energetic ion (Ar^+, O^+) of KeV energy impinging on a solid target is either back-scattered from a surface atom (a very low probability event) or it enters the solid and dissipates its energy to lattice atoms through a number of elastic and inelastic binary collisions. The primary ion will finally come to rest after a slowing down time at the so called penetration depth i.e. it is implanted into the solid (Fig. 12). The collision cascade process displaces the lattice atoms and if they are close enough to the surface and their velocity vectors are pointing outside the target, the process called sputtering occurs i.e. a target particale (atom) is emitted from the surface. The possibility of the primary ions sputtering target atoms by directly knocking them is relatively scarce.

The information depth (escape depth) depends on the mass m_1 and energy E_1 of the projectile ions and on the mass m_2 and Energy E_2 of the recoil matrix atoms. Obviously the greater the energy of the recoil atoms, the greater the depth at which they were originally situated. In Figure 13 we give the distribution of the original depth of sputtered atoms versus depth[80]. There are very few number of particles with escape depths in excess of 20 Å, this is due to the high energy recoil. Most of the contribution comes from mean escape depth of about 6 Å. These values are in good agreement with estimation of the projected range of low energy particles.

2.2 State of Emitted Particle

It is obvious that inside a solid when a collision cascade with many violent collisions occurs, the atoms can get excited and/or singly or multiply ionized. The

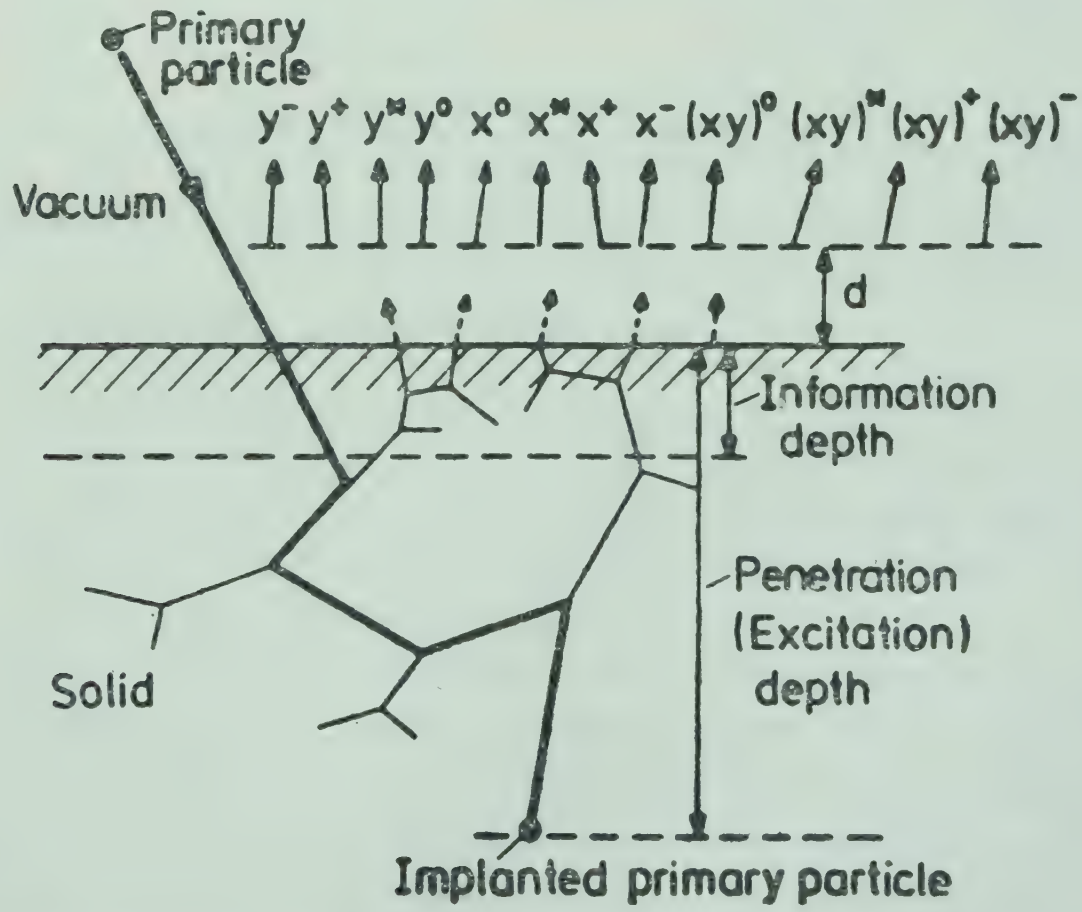

Fig. 12. Schematic representation of an ion-solid interaction, leading to the emission of neutral, excited and ionized (+ or −) target atoms (X, Y) and of molecules (XY). In surface near regions of thickness d, processes may take place which change the state of the particles as emitted (Table 1) (after H W Werner 70).

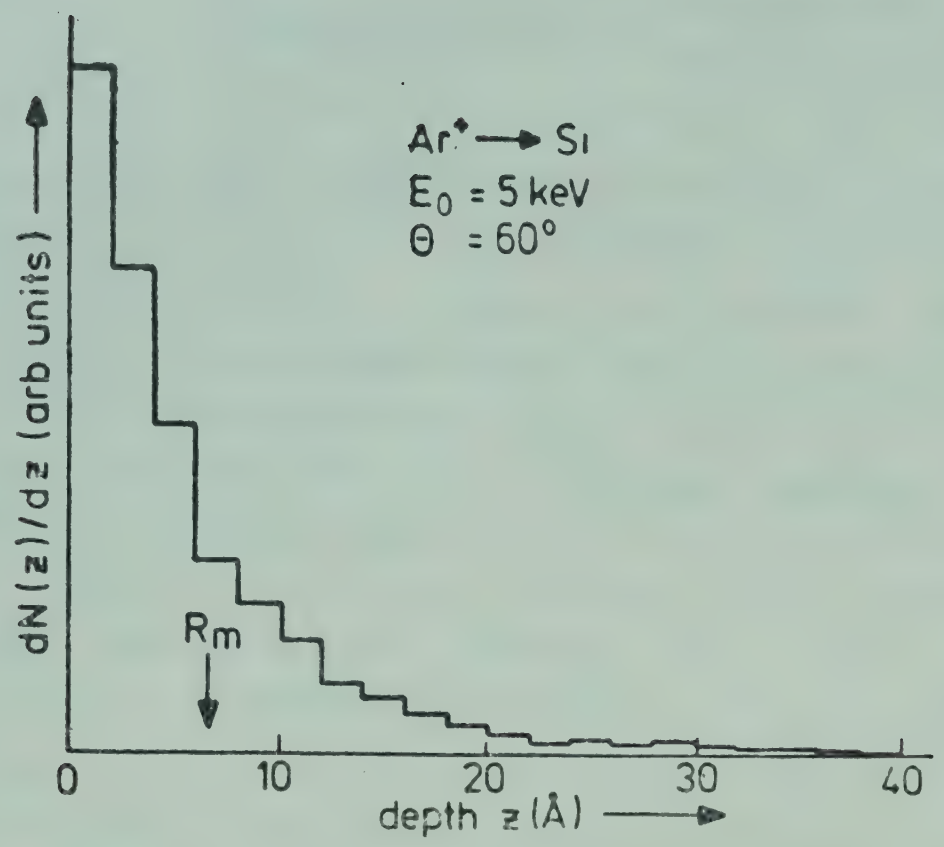

FIG. 13. Distribution of the original depth of sputtered atoms versus depth[30].

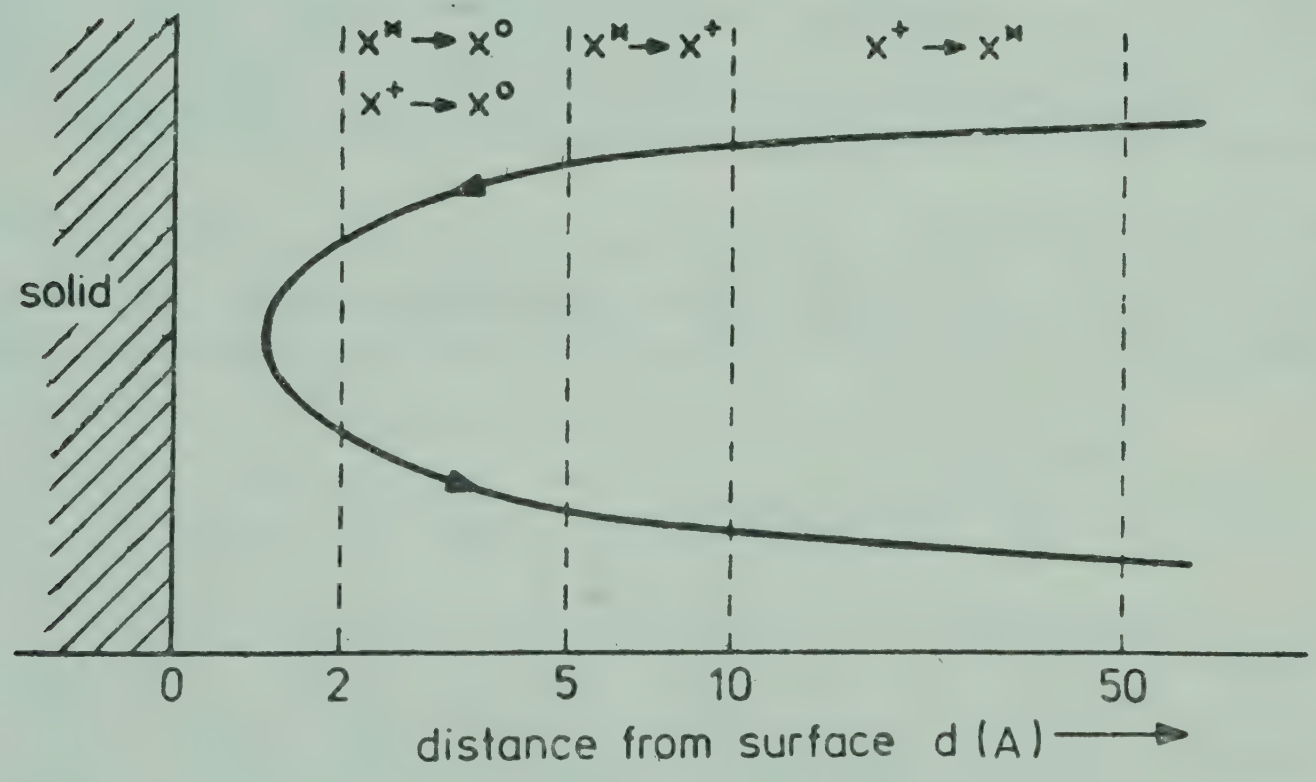

FIG. 14. Different zones infront of the target in which the original state of emitted particles may change[81]. From O-2Å violent collision between incoming ions and lattice atoms positioned at $d = O$ takes place; $d =$ Å : Auger deexcitation or neutralization may take place, $d =$ 5-10Å : resonance ionization, $d =$ 10-50Å resonance neutralization[82].

state of these particles as generated inside the target can be changed, however, by "reactions" in zones of at the most 50 Å infront of the target. Such mechanisms are indicated in Figure 14[81,82]. In Table I, a number of possible processes which the ejected particle can undergo are listed together with the final state of the particle. There is a possibility that a particle ejected from the surface region may escape without undergoing any of these transitions. It is shown[83] that such a survival probability p is dependent upon the time for which the ejected particle remains in the reaction zone.

TABLE I

Some mechanisms which may take place after particle ejection in zones close to the surface. (State of particles : X° = ground state atom, X^* = excited ; X^+, X^- = positive or negative ground state ion).

State of ejected particle	Life time (sec.)	Mechanism	Final state particle
X^*	10^{-8}	De-excitation by light emiss.	X°
	10^{-14}	Auger de-excitation	X°
	10^{-14}	Resonance ionization	X^+
X^{**}		Autoionization (Auger de-excitation)	X^+
X^+	10^{-14}	Auger-neutralization	X°
	10^{-14}	Resonance neutralization	X^*, X°
	10^{-8}	Radiative neutralization	X°
X^+, Y°		Charge-exchange	X°, X^+
$(X^+Y^-)^*$		Bernhein processes	
		Dissoc. of ionic bond	$X^+ + Y^-$
X°		Electron capture	X^-

It is clear that many complicated processes play role in the emission of secondary ions. There is no complete theory at the moment which accounts for these processes. However, a number of theories, which present models to explain the mechanisms of various processes mentioned above, have been given in last twenty years. These theories have been reviewed in detail by Rudenauer[84].

2.3 Basic Equations for SIMS Analysis

The primary objective of the very *SIMS* analysis is to determine the concentration of element A from the measured secondary ion current I_s which is corrected for the isotopic abundance of the element. The secondary ion current measured in a *SIMS* instrument is given by

$$I_{sA}^{\pm} = \eta S_A^{\pm} I_p$$

The quantity $I_{SA}^{\pm}$ is the ion current for a monoisotopic element. The ion current for a given isotopic component of a multi-isotope element, say, A, is $f_a I_{SA}^{\pm}$, where f_a is the isotopic abundance for isotope 'a' of element A. The term η is the ion collection efficiency of the *SIMS* instrument for a given isotope. It is the product of the secondary ion mass analyzer transmission efficiency and the ion detector efficiency. I_p is the total primary ion current (ion sec^{-1}) at the sample.

The positive or negative secondary ion yield $S_A^{\pm}$ (ions per incident ions) for element A in the target material is given by

$$S_A^{\pm} = \gamma_A^{\pm} C_A S$$

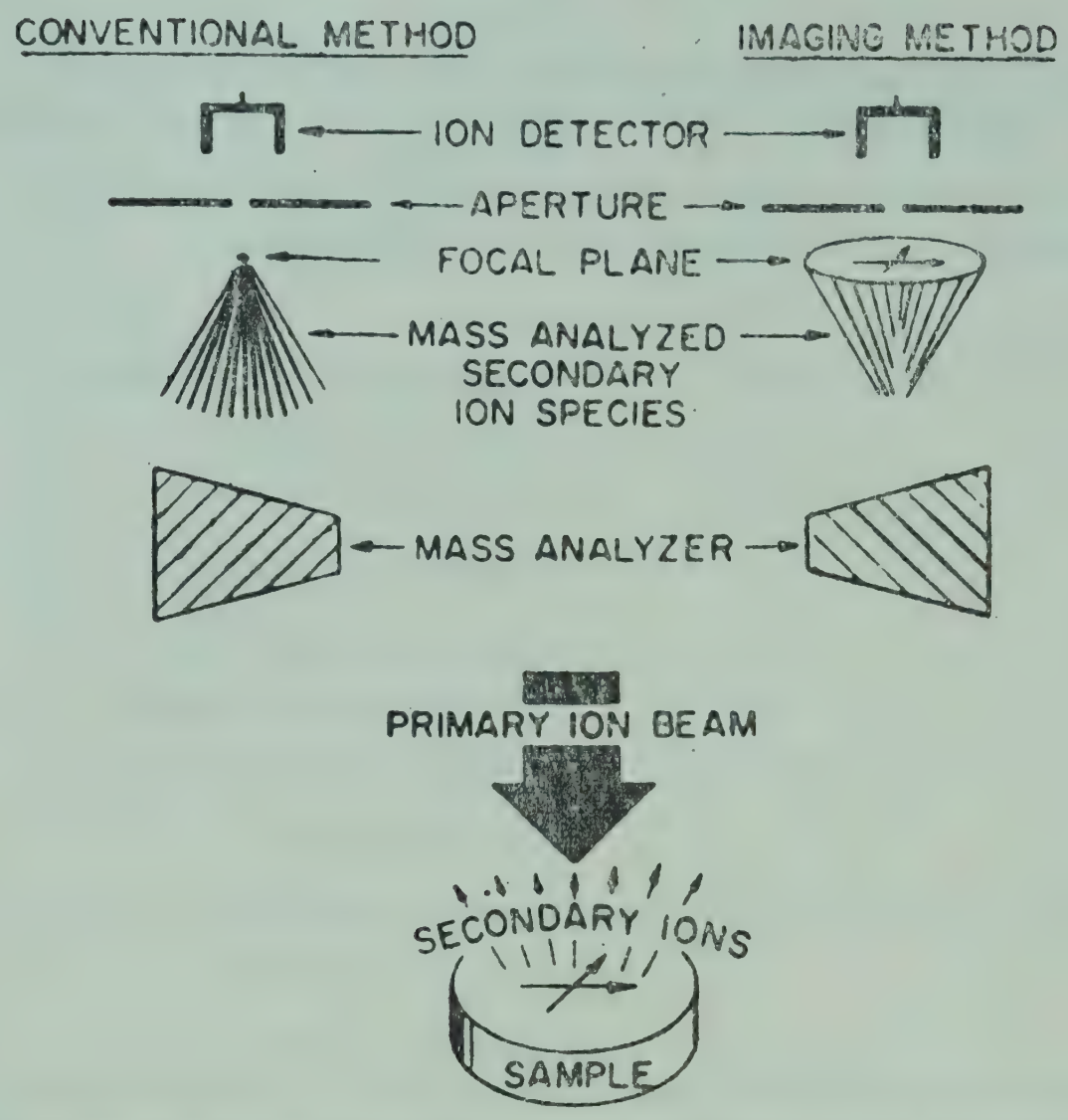

FIG. 15. Schematic representation of the conventional and direct imaging approaches to the mass spectrometric analysis of secondary ions[108].

The $\gamma_A\pm$ is the degree of ionization = number of particles which are sputtered as ...ve/negative) ions/number of particles which have been sputtered in a state 'K'

$$= N_S\pm/N_S{}^K$$

Here 'K' relates to neutral or charged particles, excited or in the ground state atoms, or clusters, respectively. C_A is the atomic concentration of element A in the target (sample). S is the total sputter atom yield of the sample = number of particles sputtered. N_{KS}/number of impining primarp ions $N_P = N_{KS}/N_P$. The quantities $\gamma_A\pm$ and S depend strongly on the composition of the sample matrix. The degree of ionization ($\gamma_A\pm$) is sensitive to the electronic properties of the surface and the sputter yield (S) is mainly controlled by the elemental binding energies.

The primay current I_P is related to the primary ion current density j_P (ions cm^{-2} sec^{-1}) and the beam diameter d_P. The ion current density $j_P = I_P/A_{eff}$ where A_{eff} is the effective bombarded area. The ion current density (j_P) is proportional to errosion rate say Z (the layer thickness sputtered per unit of time). Z is given by

$$Z\ (\mu m/h) = 3.6 \times 10^{-4}(M\ (amu/\delta\ (g/cm^3)\ )\ j_P\ (\mu A/cm^2)\ S$$

In *SIMS* experiment it is necessary to estimate S, Z, $\gamma_A\pm j_P$ for known I_P and d_P. Several researchers have published data for estimation of these quantities and we present, in Table II, the typical values for these parameters.

TABLE II

Typical values for SIMS parameters

$\gamma_A^{\pm}$	10^{-5}–10^{-1}
S	1–10
η_A	10^{-5}–10^{-2}
D_p	10^{-6}–10^{-2} mA cm^{-2}
d	10^{-4}–10^{-1} cm

3. SIMS EXPERIMENTATION

The basic components of a *SIMS* instrument are a vacuum chamber primary ion source, a sample holder, an analyser and a detector for the secondary ions. Now a days, in modern *SIMS* instruments instrument control, automatic data acquisition and processing are left to μ processor.

The primary ion sources used in the majority of instruments are gas discharge of plasma type. In most cases Ar,O_2 or N_2 are used as a source gas and the proper beam handling and focussing system allow one to have a wide range of surface removal rates, from 10^{-5} to 10^{3}Å sec^{-1}. The mass/charge analysis is done either by a magnetic or quadrupole analyser. In most of the *SIMS* instruments, which are used from an analytical and trace analysis stand point, double focussing magnetic system (energy and momentum analysis) is used because of its inherent high sensitivity. Quadrupole analysers, which are less expensive, are also used for particular application. Rudenauer[85] has compared the utility and qualities of the quadrupole and magnetic instruments for secondary ion mass analysis. For detection of secondary ions either a Faraday cup with *DC* amplifier or electron multipliers are used along with necessary electronics. The Table III lists some of the useful information about secondary ions mass spectrometers.

3.1 SIMS instruments

Evans[86,87] and Liebl[88] have done a good review on the state of *SIMS* instrumentation. Basically *SIMS* instruments are used in two modes : conventional mass spectrometric mode and the direct imaging mode. In Fig. 16 we show schematic representation for both these modes. In the conventional method a significant fraction of the energetic secondary ions from a large area of a sample ($\sim 1\ mm^2$) are brought to a single point focus at the entrance slit to the detector. One, therefore, does not know the information regarding the exact point at which a particular secondary ion was created. The direct imaging method, on the other hand, produces a stigmatic ion image in the focal plane of the analyzer, and with appropriate aperaturing information regarding the point of origin can be readilly derived for a particular m/e secondary ion species.

It is possible to obtain secondary ion image of a surface with the conventional approach. One does a sequential analysis by scanning the surface with a small-diameter primary ion beam. Electrical rastering of a focused primary ion beam and its synchronization with the electron beam in the CRT produces secondary ion

TABLE III

Some criteria used to classify the different types of secondary ion mass spectrometers

	Primary ions
Current density	: high (Dynamic SIMS) low (Static SIMS)
Beam diameter	: ~ mm (macroprobe SIMS) ~ μm (microprobe SIMS)
	Secondary ions
Mass separation	: quadrupole or sectortype (occasionally time of flight (TOF))
Energy selection	: electrostatic designs
Mass resolution	: low (300), with single focussing instruments; high (up to 10000), with double focussing instruments
Element mapping	: by scanning beam (μm diameter) : Ion Microprobe by ion optical imaging : Ion Microscope
Vacuum system	UHV (bakeable) : p = 10^{-10} Torr or HV 10^{-7}–10^{-8} Torr.
Modular design	: compatible with other thin film analytical methods

images on the CRT tube. The amplified signal from the secondary ion detector modulates the intensity of the CRT electron beam. The image magnification in this method is the ratio of the CRT horizontal trace dimension to the horizontal dimension of the area on the sample swept by the primary ion beam.

All SIMS instruments possess a capability for surface and elemental depth concentration analysis. Figure 16 shows the schematic of a SIMS instrumement used for depth profiling. The parameters that differentiate various SIMS instruments, apart from those given in Table III, are their ability to provide lateral or *xy* surface characterization through probe scanning or direct imaging.

4. SIMS APPLICATION: TYPE OF INFORMATION OBTAINABLE

The informations that can be obtained from SIMS analysis fall into three broad categories : surface analysis, depth analysis and structural analysis.

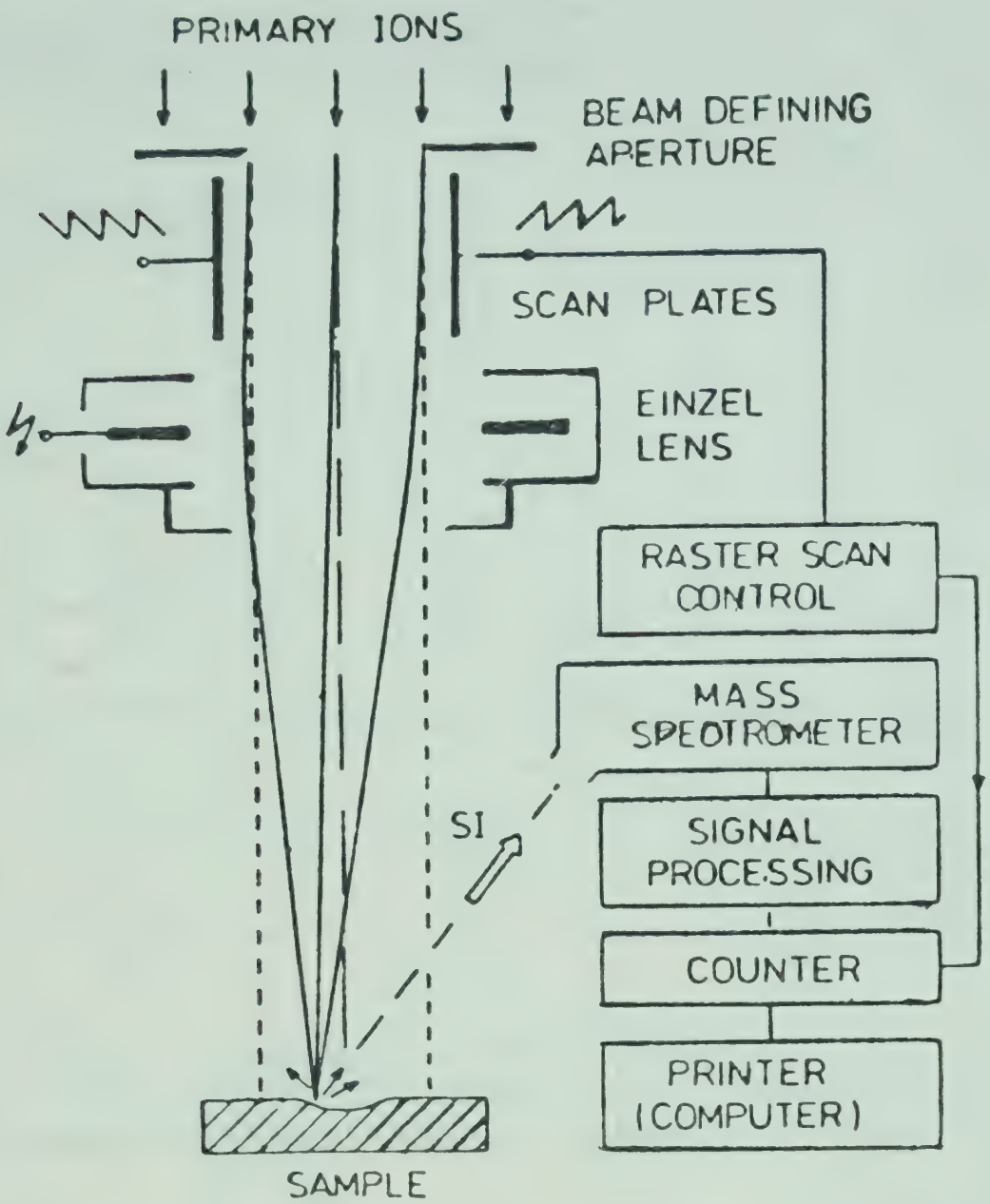

FIG. 16. Schematic of a SIMS instrument used for depth profiling[100] (SI-secondary ions).

4.1. Surface Analysis

As mentioned earlier all elements from hydrogen to uranium and combination of these elements (polyatomic ions or cluster ions) can be detected in SIMS analysis. It is also possible to analyse only the uppermost atomic layer if the current density of primary beam is kept so low that only about one monolayer per hour is sputtered away.

The study of oxygen adsorption on tungsten by Rybalko *et al.*[89] is a good example of a dynamic surface process investigated by SIMS. These authors confirmed the two stage interaction mechanism observed by others methods[90]. The secondary ion signals of O^+ and WO^+ were measured as a function of time for various surface temperatures. In Fig. 17 their results are given and it can be seen that O_2 dissociates into atomic oxygen (stage I) when adsorbed on the surface. Whereas, compound formation of W is evident, at low temperature, by the appearance of the molecular ion species (stage II).

The interaction of CO with Ni (100) has been investigated by SIMS[19] and it is shown that the SIMS yields are co-related with the changes in heats of adsorption that occur as the CO coverage is changed. Baber *et al.*[92] have successfully used the secondary ino mass spectrometry to study the adsorption of carbon monoxide on polycrystalline nickel, copper, iron, palladium and tungsten foils. The results

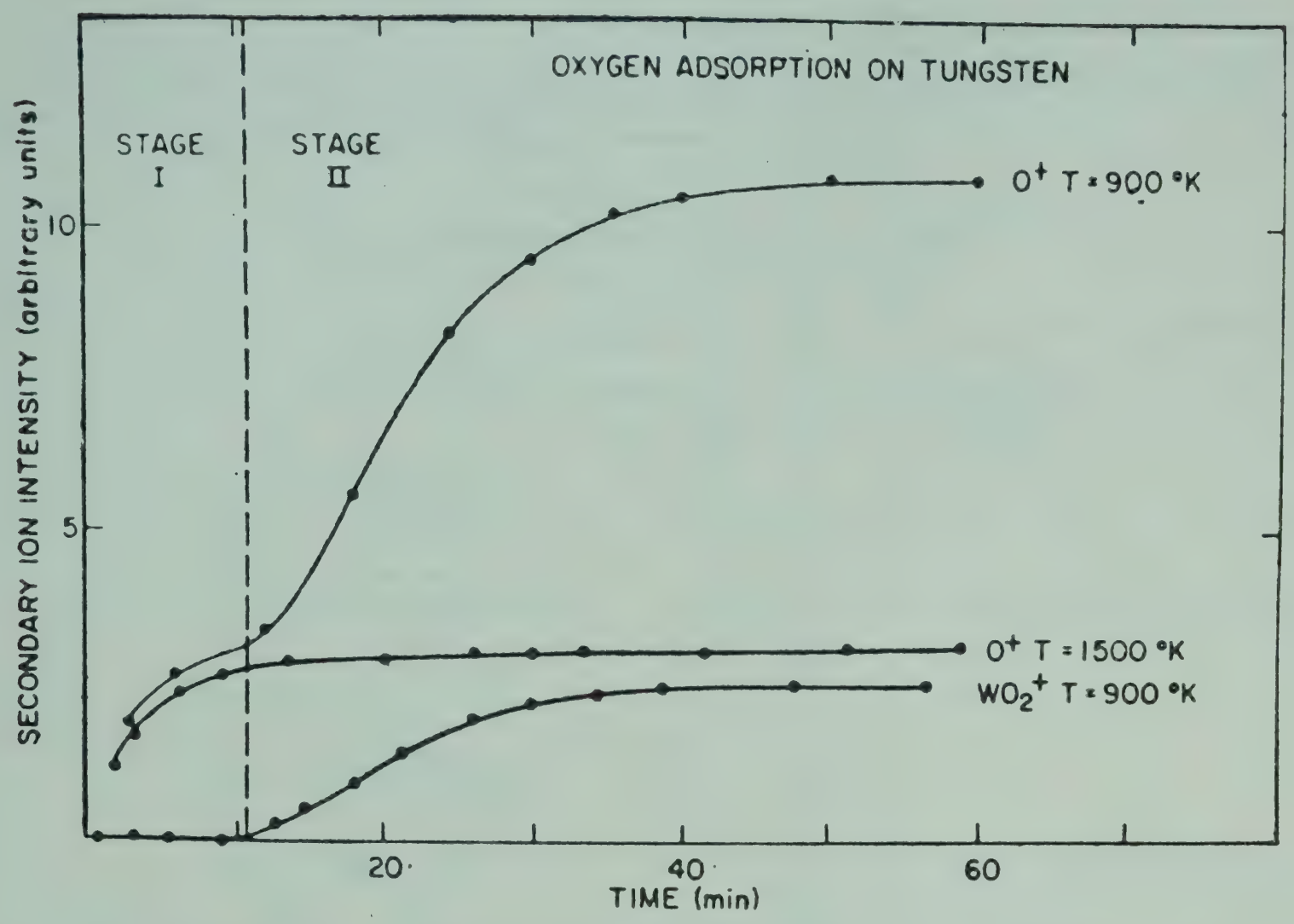

FIG. 17. The variation with time of the sedondary ion intensities of O^+ and WO^+ from a W surface at 900 and 1500°K. (At $t = O$ the surface of the W sample was free of adsorbed gases). The stage II process or compound formation is evident in the lower temperature 900°KO^+ and WO_2^+ curves [89,108].

demonstrate the ability of SIMS to distinguish, qualitatively, between molecular and dissociative adsorption. We reproduce in Fig. 18 and 19 the results for iron foil when its clean surface was exposed to 10^{-8} Torr of carbon monoxide at 195K and subsequent higher temperatures upto 315K. The Fig. 18 shows the SIMS spectrum recorded (at equilibrium) at 195K. It shows the effect of raising the temperature upon the intensities of Fe^+ and $FeCO^+$ peaks. $FeCO^+$ peak intensity decreases rapidly and, at room temperature, becomes very low. Figure 19 shows the variation of the $FeCO^+/Fe^+$ peak intensity ratios with temperature. It could be seen that the intensity of the $FeCO^+$ increases over the same temperature range as the $FeCO^+$ intensity decreases. This suggests that the two effects are connected and increase an increase in amount of dissociated carbon monoxide as the temperature is raised. Thus there is little dissociation at low temperatures, at room temperature there is some dissociative adsorption which co-exists with molecular adsorption, while at 350K there is almost complete dissociation.

4.2. Depth Analysis

The aim of a depth profiling study is to determine the concentration of one or more elements as a function of sample depth, measured with respect to the original surface. This requires a well-defined correlation between the secondary ion intensity and dopant concentration as well as between the time at which the signal is recorded and the instantaneous position of the receding surface. If the depth rate is

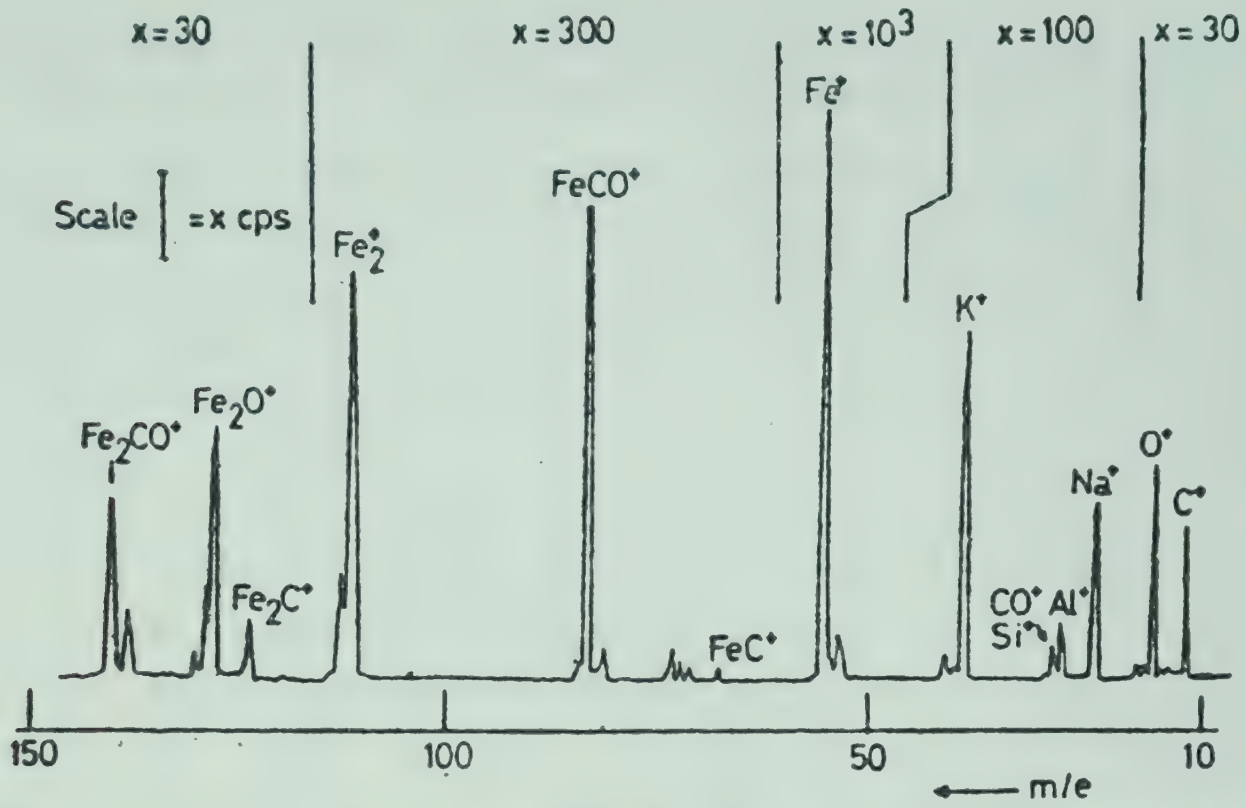

FIG. 18. SIMS spectrum recorded at equilibrium when iron is exposed to 10^{-8} Torr of carbon monoxide. Primary iron current density = 5×10^{-10} A cm^{-2}, energy = 3keV[92].

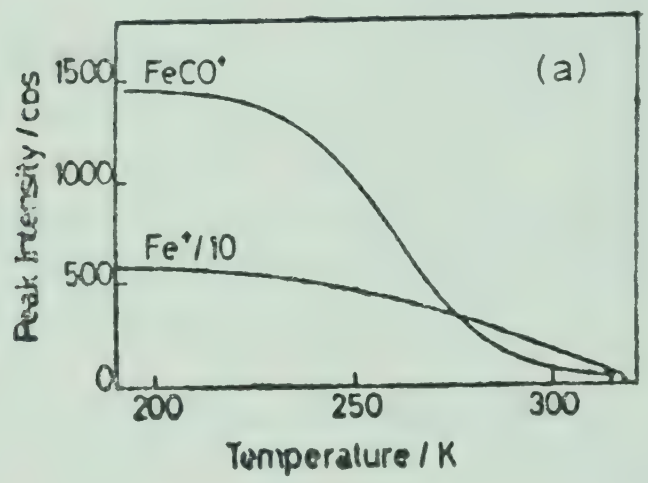

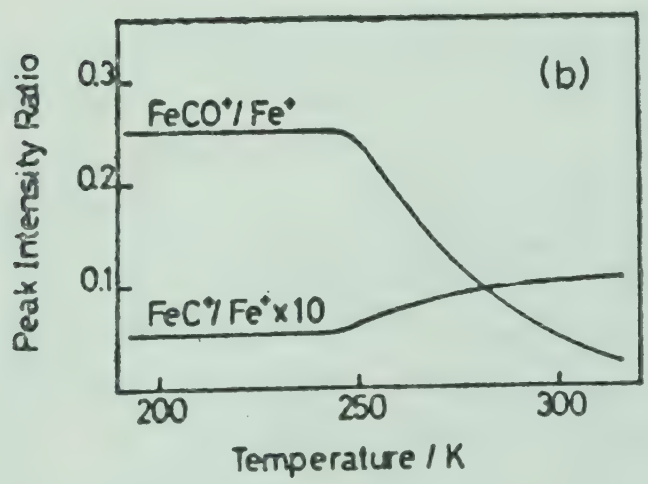

FIG. 19a. Variation of equilibrium peak intensities of Fe^+ and $FeCO^+$ with temperature, partial pressure of carbon monoxide is 10^{-8} Torr throughout.

FIG. 19b. Variation of relative peak intensities $FeCO^+$ and FeC^+ with temperature[92].

chosen high, an analysis of the distribution of element at depths between 50 Å and several μm is achieved in typical times from 20 minutes upto 1 hour. This mode is used for the investigation of diffusion processes and for the determination of diffusion coefficients[70], for the study of implantation profiles[93,94] in semiconductor industry,

for study of thin film sandwich layers[95], for the study of electrons for devices (Co, Si) as well as for a better understanding of adhesion problems, etc.

Ion bombardment continuously removes the surface of the sample "layer by layer". Simultaneously the secondary ion current of one or more elements is detected as a function of the bombardment time. At constant erosion rates the bombardment time is proportional to the depths[10]. Werner[96] has given a method to convert measured ion current vs. bombardment time obtained from implantation profiles into concentration cm^{-3} vs. depth (Å). The absolute depth resolution is that layer thickness which must be sputtered away before the signal obtained from an element, distributed in depth according to a step function, has increased by a given amount[97]. The depth resolution depends on the concentration profile in the sample and on instrument factors such as information depth, the basic sputter process, the original and final surface roughness ionic mixing and atomic transport[98,99]. In addition, there are several effects which may cause deviations of the measured profile from the original dopant distribution. These detrimental effects are due to interaction of primary ions with the residual gas, adsorption and incorporation of residual gases. Wittmack[100] has critically reviewed these effects as well as methods of minimizing them in a recent review.

The work of Maul *et al.*[101] demonstrates the capability of SIMS for measuring implant profiles. In their experiment (Fig. 20), they measured the profile of 22KeV B implanted in amorphous Si. The boron secondary ion intensity was measured as a function of time and the sputter rate was calculated from the experimentally measured crater depth. Crater edge effects were elliminated by maintaining constant ion current density over an area greater than the implanted area.

A gaussian range distribution was observed, and the measured projected range, R_p, and the standard deviation, ΔR_p, agreed quite well with theoretical values[101].

The ability of SIMS to obtain isotopic concentration information adds another dimension in depth profiling. An example[102] of this is an ^{18}O profile taken of a Ta_2O_5 sample containing an enriched ^{18}O layer (Fig. 21). A Ta sample was anodized in three stages, each designed to produce a zone 1020Å thick. The middle stage employed an electrolyte enriched in ^{18}O. The ^{18}O gradient was established by monitoring the $Ta\ ^{18}O^+$ secondary ion signal as a function of time[102]. The time was converted to depth on the basis of information that the Ta_2O_5-Ta interface is at 3050Å from the surface.

4.3 Structural analysis

The short range structural order of the atoms in surface adjacent regions or layers in crystals has been determined with SIMS. The resulting secondary ion spectrum for CaF_2 crystal was shown to be related to an atomic arrangement on cleavage plannes of crystals[103]. Similarly a low dose SIMS has been successfully used for chemical structure determination. Figure 22 shows the positive secondary ion spectrum of a Teflon i.e. arrangement of carbon with respect to F[95]. The chain

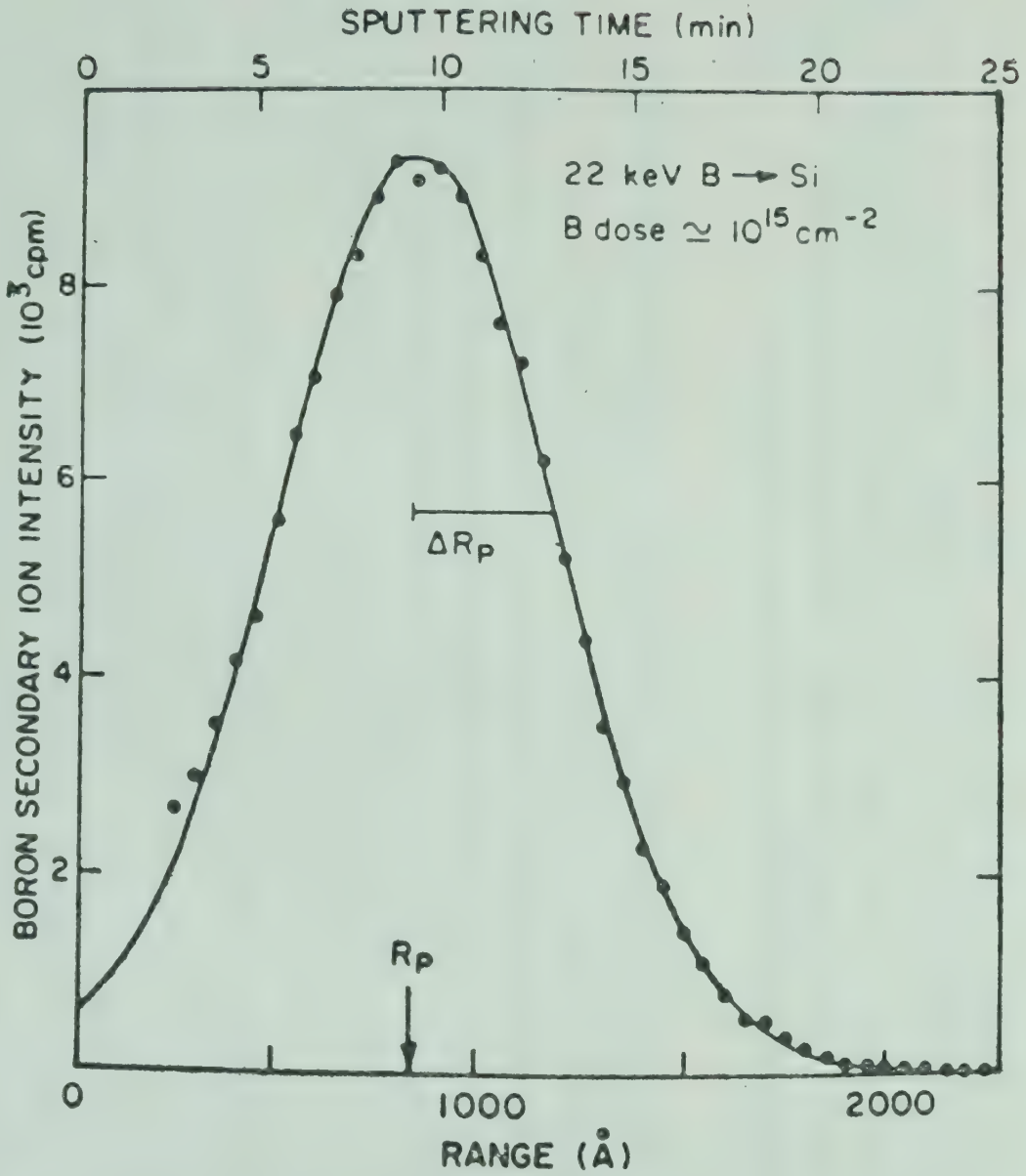

FIG. 20. Depthconcentration profile of ^{11}B implanted in amorphous Si. Each experimental point represents removal of 50Å of Si. The experimental the prints are fitted with a normal distribution where R_p and R_p are 840Å and 340Å, respectively[101,108].

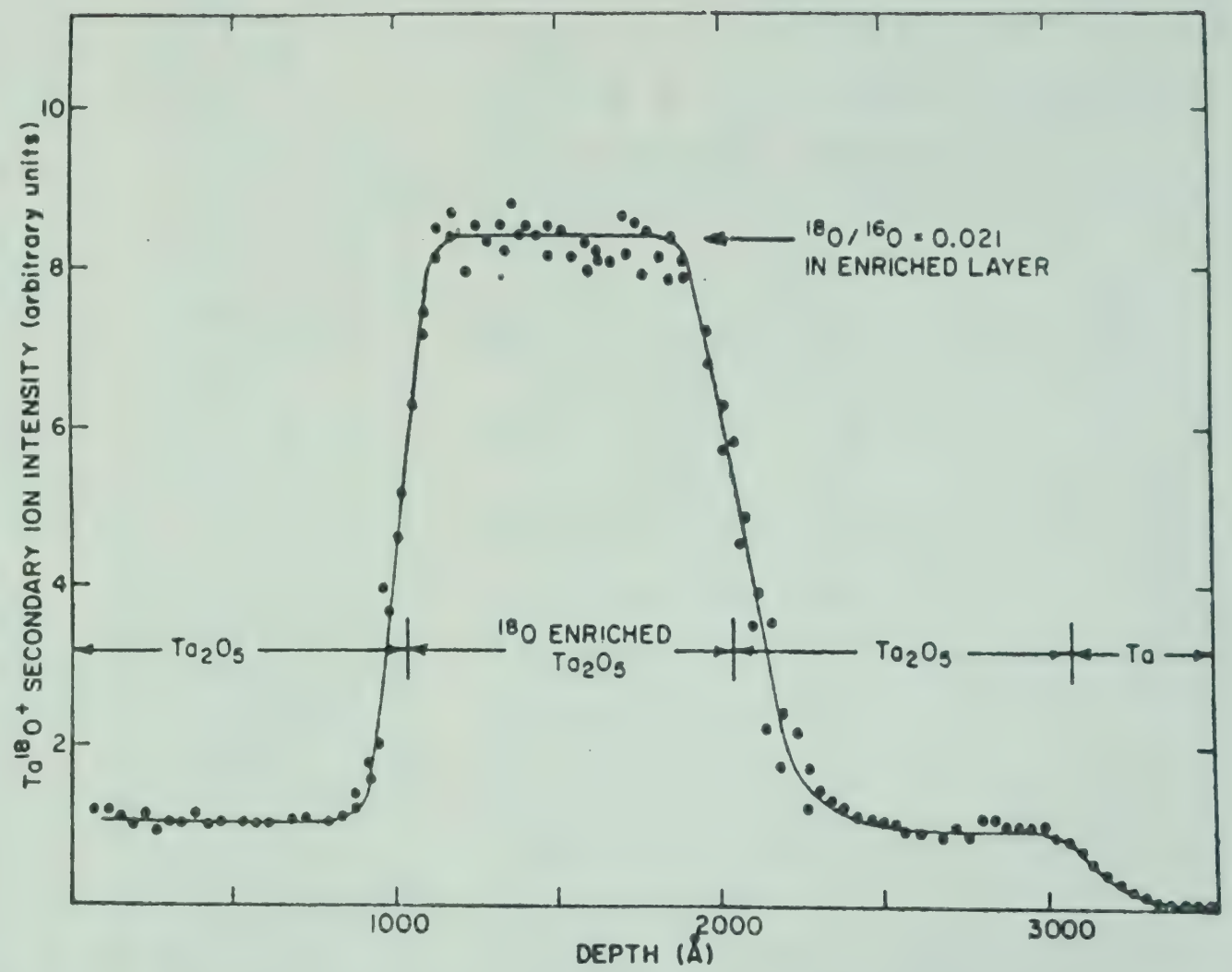

FIG. 21. The depth concentration profile of ^{18}O in a Ta_2O_5 sample containing a layer of enriched ^{18}O. The profile was performed with an ARL ion microprobe using 8.5 keV. N_2^+. and the monitor of the ^{18}O concentration was $Ta\,^{18}O^+$. The ^{18}O is 2 per cent of the oxygen in the enriched layer. The $Ta\,^{18}O^+$ signal preceding and following the enriched layer peak is due to the ^{18}O level in normal oxygen[102,108].

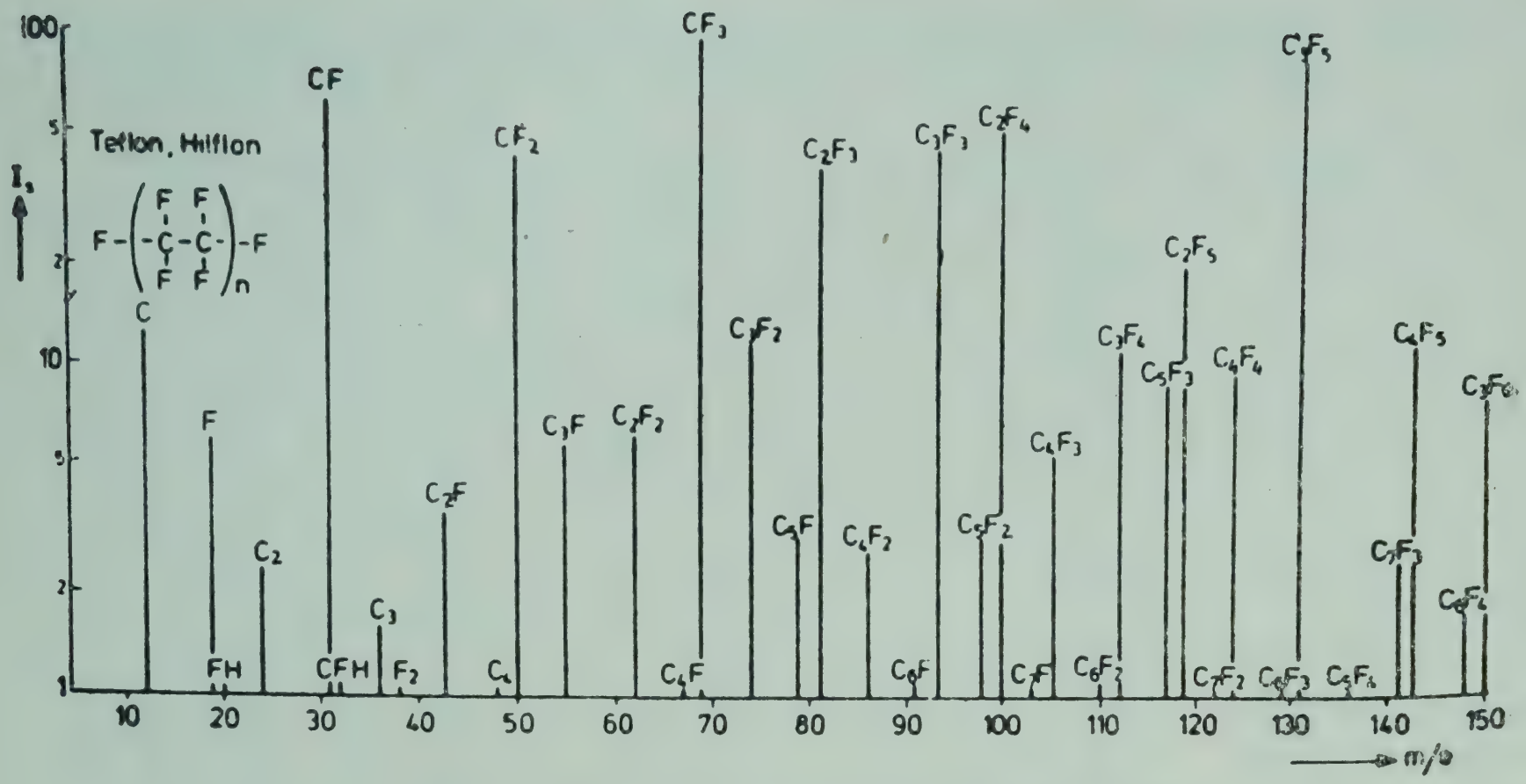

FIG. 22. Teflon : positive secondary ion spectrum[95].

character of Teflon can be derived from the presence of ions of the series CF_2, C_2F_2, C_3F_2, C_4F_2, C_5F_2. It is also shown that it is possible to determine the degree of branching in this linear chain from height of the CF_3 peaks by means of calibration standards having a known degree of branching.

III. SIMULTANEOUS AES-SIMS MEASUREMENTS

In the preceding sections we have seen how AES and SIMS could be effectively used as independent tools to study surfaces. Now-a-days the trend is to use two or more surface analysis methods in combination, so as to get as complete picture as possible of the surface processes. We shall present in this section few examples of the combination of SIMS and AES measurements.

1. In Depth Concentration Profile of 40 KeV Implanted ^{11}B in Si[104]

Figure 23 shows the SIMS determined *B* profile as obtained from 10 KeV oxygen ion beam sputtering. In the figure the AES measured intensities of the simultaneously measured oxygen are also shown. It is known that the *B* secondary ion yield depends on the oxygen concentration and hence it is essential to find out the onset of the oxygen saturation. It is then possible to evaluate the B^+ intensities quantitatively.

2. In Depth Concentration Profile of a Multilayer Metallization[104]

A simultaneous AES-SIMS in-depth profile measurement of multilayer metallization of Fe and Cr on Si as obtained from 10 KeV oxygen ion beam sputtering is shown in Fig. 24. The SIMS intensities are in good agreement with AES results. The only obvious difference is in the intensities of oxygen. The AES intensities show

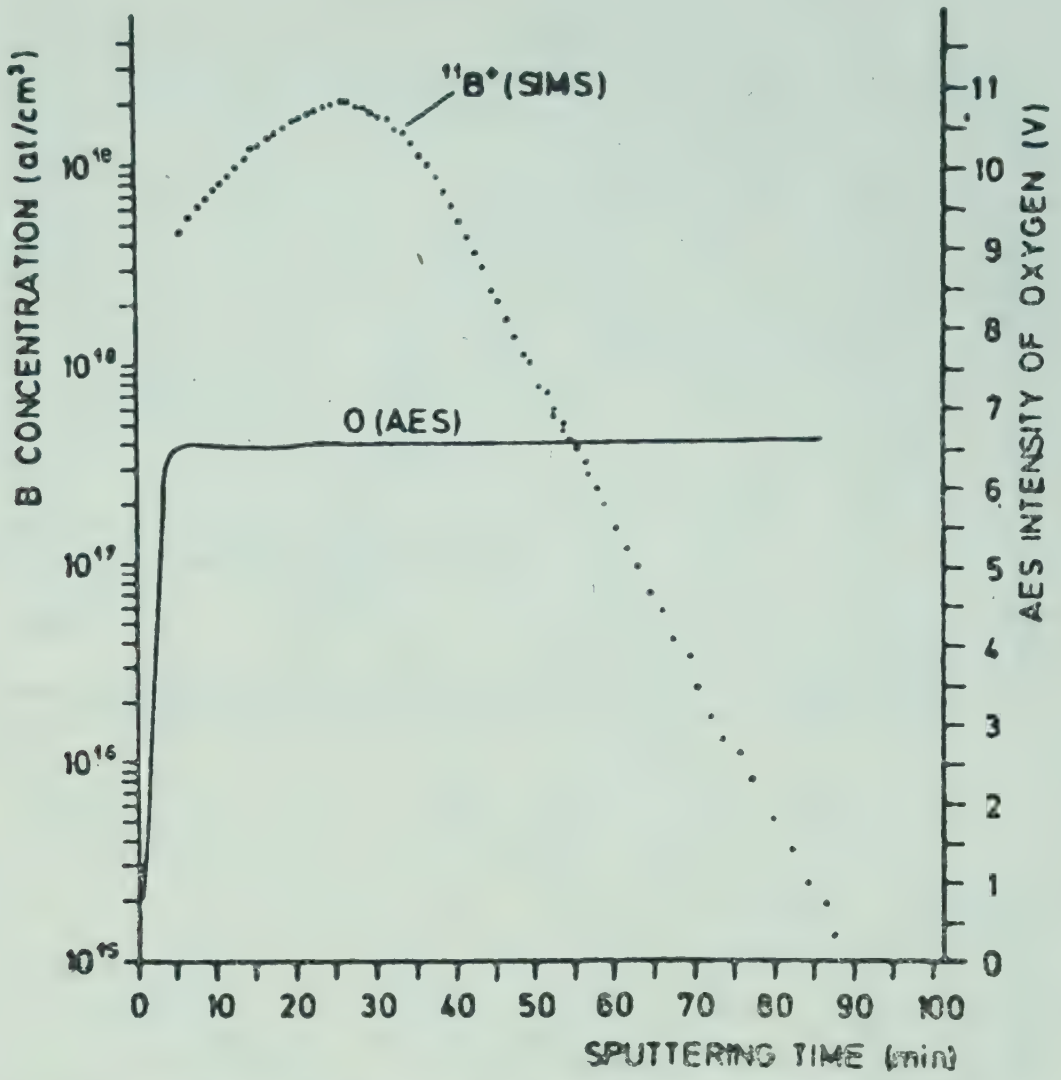

FIG. 23. SIMS in-depth profile of *B* in Si compared to the simultaneous measured AES intensity of oxygen[104].

the different oxygen saturation behaviour in the different metallization layers during sputtering whereas the SIMS intensities reflect the different secondary ion yield of oxygen.

3. SURFACE PROCESSES ON COPPER-BERYLLIUM

R Buhl *et al.*[105] have studied copper-2 per cent beryllium foil by SIMS and AES methods. Copper-berryllium foils are used for the production of secondary electron multiplier and their main interest was to understand the process on the surface due to thermal influence.

The behaviour of Auger electron and secondary ion peaks during that treatment is shown in Figs. 25 and 26 respectively. What can be concluded from AES data is that upto step 4 there is a continuous increase of the beryllium concentration in the top monolayer in form of an oxide or hydroxide at the cost of surface copper. After applying the heat treatment c.f. step 5, the intensity courses are inverted, indicating that now copper is predominent in the top layer and that the chemically bound beryllium is removed to a great part from the surface. The SIMS data indicates that the surface is containing parent structures like Be_n, BeH_2, BeO, $Be(OH)_2$, Cu_n, CuBe, CuBeO, CuO. There is general increase of all secondary ion emission yields by oxidation.

Thus upto 340°C the diffusion of beryllium to the surface and its oxidation takes place. By formation of an oxide or hydroxide the Be atoms are fixed at the surface

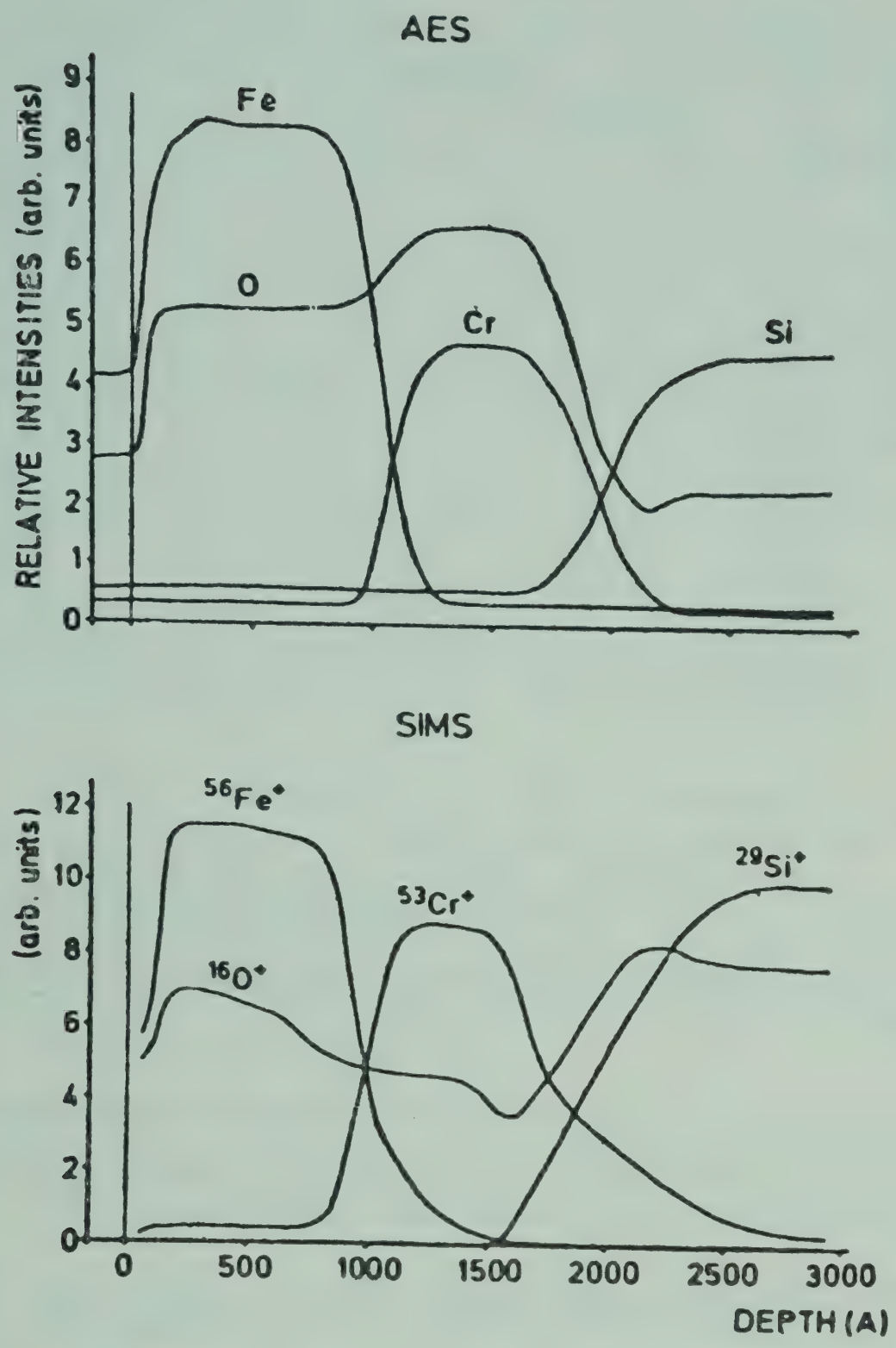

FIG. 24. Simultaneous SIMS–AES in depth concentration profile measurement of a multilayer metallization[104].

thus becoming immobile and are removed from the surface after heating step 5. The AES and SIMS data, therefore, clearly show that a major part of the surface oxygen is bound to beryllium and a smaller portion to copper.

4. INTERACTION OF OXYGEN WITH POLYCRYSTALLINE NICKEL[106]

The interaction of oxygen with polycrystalline nickel has been investigated by using AES, UPS and X-ray emission by many workers. It has been shown that at room temperature the oxygen uptake by the clean surface occurs in two distinct stages. First, there is a rapid chemisorption upto about half a monolayer of oxygen atoms. This is followed by a plateau where the sticking coefficient is very low. Oxide nucleation occurs and oxygen uptake then increases again as a lateral growth of oxide over the surface occurs to give a limiting oxide two or three layers thick. The clean separation in this system between the chemisorption stage and the oxide growth is of great interest for AES and SIMS studies.

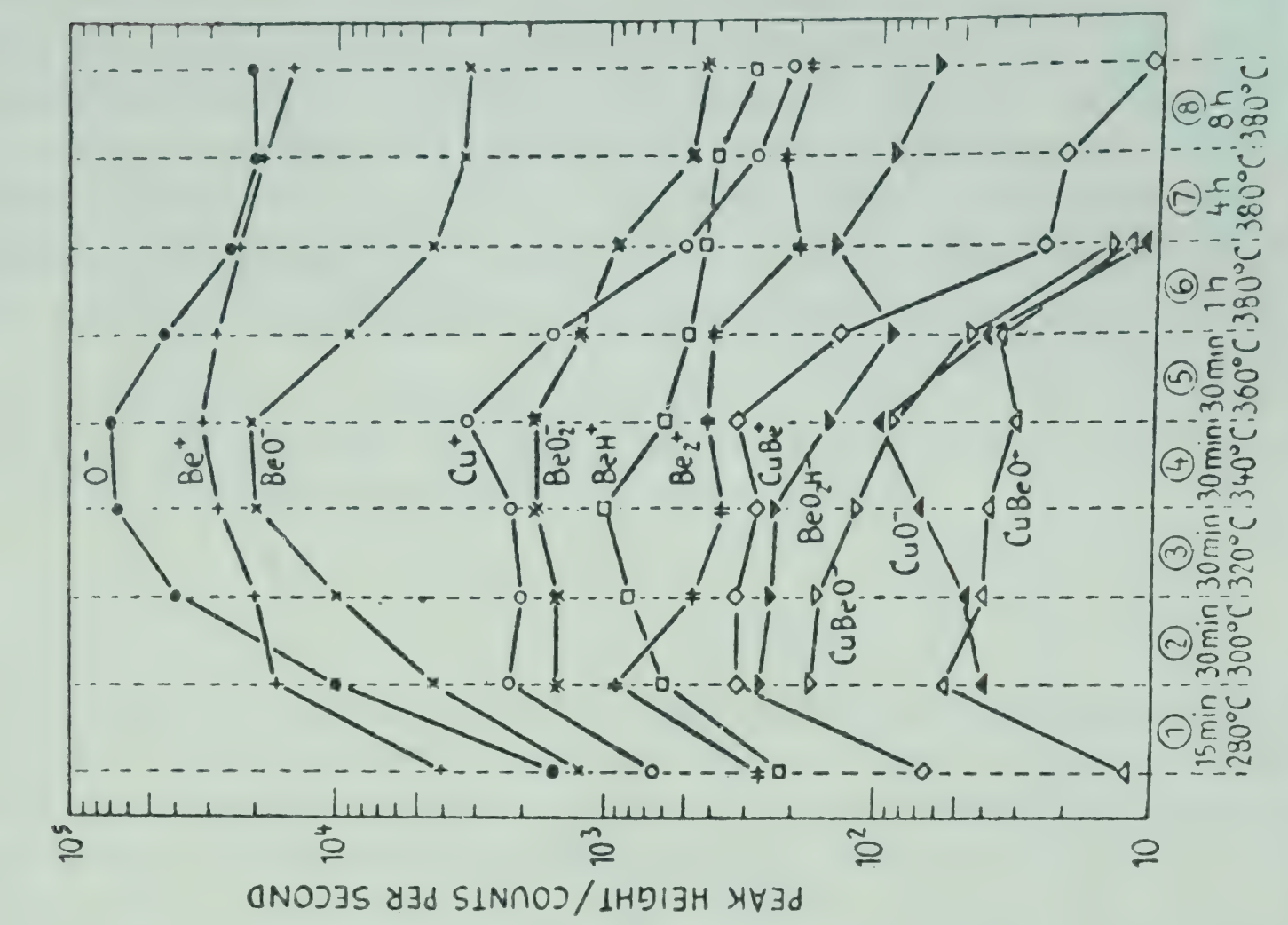

FIG. 26. Behaviour of secondary ion peaks during heat treatment
$E_p = 3\text{keV}$, $I_p = 5\mu A$, A^{+105}.

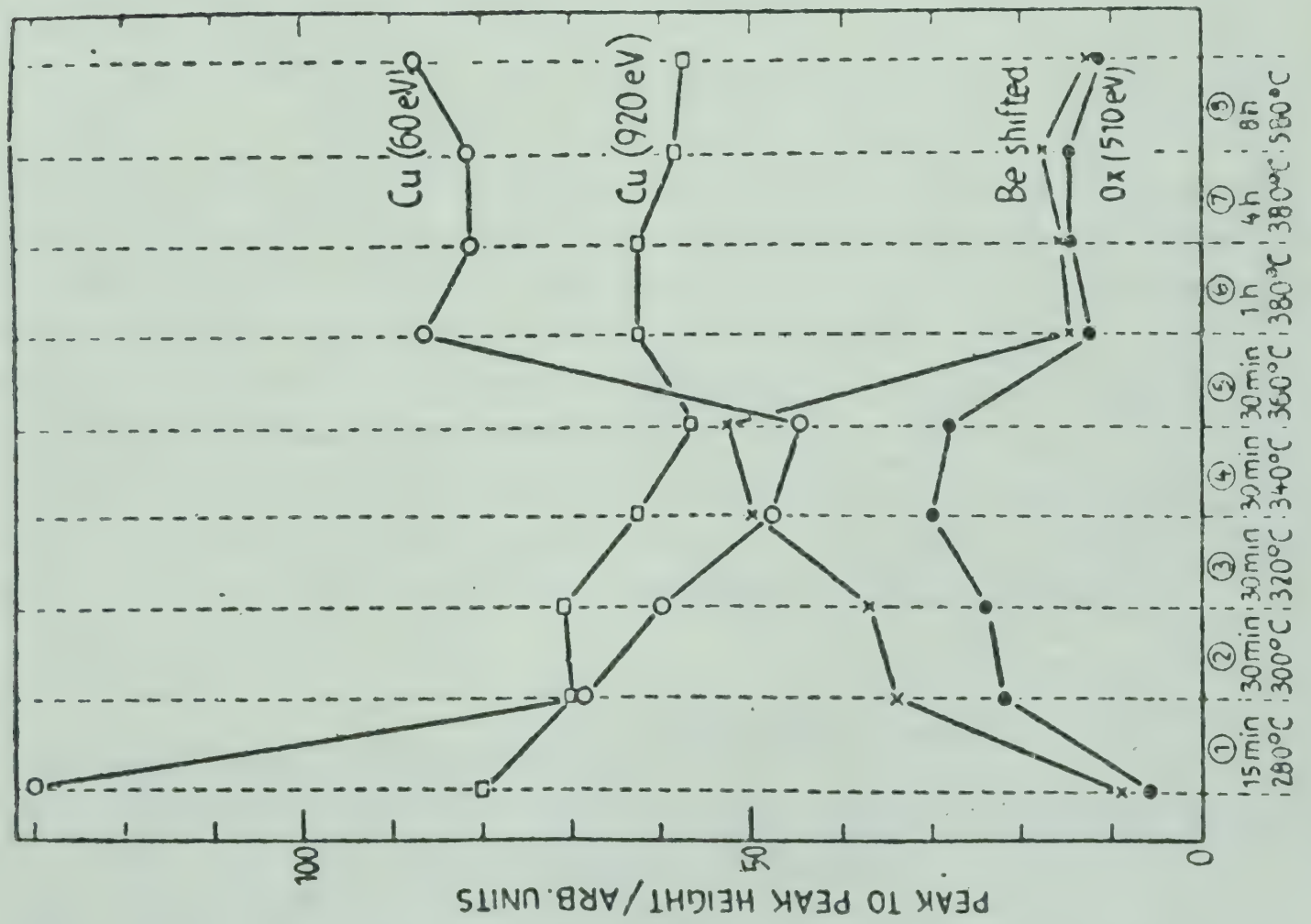

FIG. 25. Behaviour of Auger electron peaks during heat treatment.
$E_p = 3\text{keV}$, $I_p = 20\ \mu A$, $V_{pp} = 3V$, $f_M = 50\ KH_z$[106].

Dawson and Tam[106] have examined for polycrystalline nickel the changes in SIMS positive ion yields as a function of oxygen exposure at room temperature, at 480 and 750K. These are compared to AES measurements made under the same conditions. Figure 27 shows the variation in Ni (843 eV) and O(503 eV) Auger signals as a function of oxygen exposure at 300K. The SIMS peak heights as a function of oxygen exposure at 300K are shown in Fig. 28. The AES measurements indicate an initial rapid chemisorption, a plateau in oxygen uptake during which oxide nucleation occurs and the subsequent lateral growth of the oxide layer at its limiting thickness (of 2–3 monolayers).

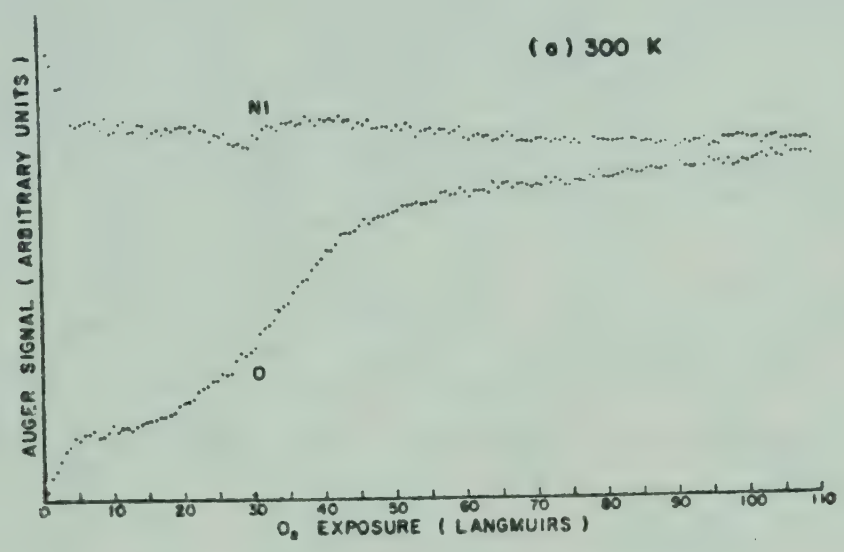

FIG. 27. The variation in Ni (843eV) and O (503eV) Auger signals as a function of oxygen exposure at 300K[106].

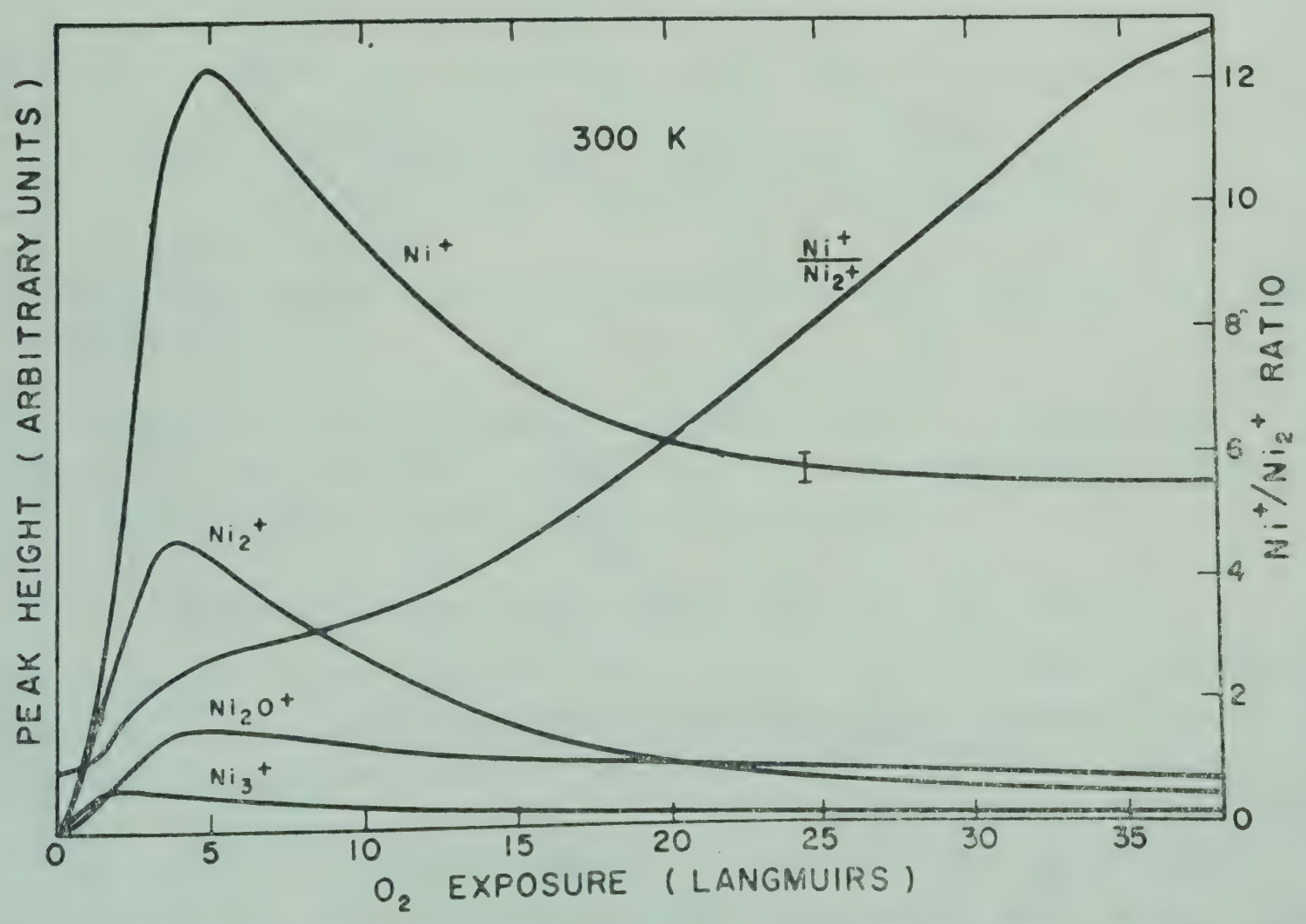

FIG. 28. SIMS peak heights as a function of oxygen exposure with the nickel at 300K when the primary energy was 500eV. The error bar indicates the scatter for Ni^+ curve. The relative scttaer for other curves are similar[106].

The SIMS data shows interesting result indicating two parts in chemisorption stage. In the preliminary stages of adsorption the Ni^+ and Ni_2^+ peaks behave in a parallel manner, and Ni_2O^+ appears. This is true upto 1L exposure. In the second stage (1-4L), there is a break in the slope of Ni^+ yield curve. The Ni^+ increases rapidly and reaches a maximum at the beginning of the first plateau of oxygen uptake. During the surface transformation as the oxide nuclei are formed, the yields of ions decrease significantly. This is particularly true for Ni_2^+. Dawson and Tam have also shown that AES and SIMS data at higher temperatures could be usefully used for clear separation of the stages of chemisorption, oxide nucleation, and lateral oxide growth in case of the oxidation of nickel.

IV. SUMMARY

Fundamental concepts, the instrumentation used, modes of operation and the general capabilities and limitations of both Auger Electron Spectroscopy and Secondary Ion Mass Spectrometry for surface studies have been discussed in previous sections. AES has moved ahead at a remarkable pace since its introduction. The major advantages of the AES are (1) the high spatial resolution in the plane of the surface attainable by using a finely focussed excitation beam of electrons, (2) the ability to observe transient effects, and (c) the ability to carry out time-efficient elemental profiles normal to the surface as the result of the relatively large Auger peak currents. In recent time, the AES is also proving to be a source of valence band information in case of metals, insulators, and molecules[107].

SIMS appears to be a method which can be used for the most diverse problems. Its high detection sensitivity for the majority of elements, analysis of low atomic number elements, isotopic analysis, high resolution depth profiling and its capability for lateral characterization of surfaces, provide a tool for three-dimensional isotopic and trace elemental characterization of solids. The SIMS possesses certain limitations, particularly in the analysis of insulators and metal insulator sandwiches. However, it should be noted that the level of perfection achieved in SIMS is unparralleled by other analytical techniques. This holds true in particular for the in-depth analysis of low concentration impurity profiles. Since many of the problems presently limiting ultimate performance of the SIMS technique are just being recognized, one might expect further progress in the near future.

REFERENCES

1. P Auger, *J. Phys. Radium* **6** (1925) 205.
2. C Kittel, *Introduction to Solid State Physics*, John Wiley and Sons, New York (1978).
3. E O Kane, *Phys. Rev.* **146** (1966) 558.
4. a. J A Bearden and A F Burr, *Rev. Mod. Phys.* **39** (1967) 125.
   b. G Wiech and E Zopf, *Z. Physik.* **244** (1971) 94.
5. K Siegbahn, C Nordling, A Fahlman *et al.*, *Atomic, Molecular and Solid State Structure Studied by Means of Electron Spectroscopy*, ESCA, Almquist and Wiksell Boktryckeri A B Uppsala (1977).

6. I Bergstrom and C Nordling, *Alpha-Beta and Gamma-ray Spectroscopy* (K Siegbahn, ed). Vol. II, North-Holland Amsterdam (1965) 1523.
7. K D Sevier, *Low Energy Electron Spectroscopy*, Interscience, New York (1972).
8. M A Listengarten, *Bull. Acad. Sci. USSR, Phys. Sci.* **26** (1962) 182.
9. M F Chung and L H Jenkens, *Surface Sci.* **22** (1970) 479.
10. T A Clark *et al., J. Chem. Soc. London, Part A, Inorg. Phys. Theor.* **9** (1971) 1156.
11. O Hornfeld, A Fahlman and C Nordling, *Arkiv Fysik* **23** (1962) 155.
12. O Hornfeld, *Arvik Fysik* **23** (1962) 235.
13. W N Asasad, *Proc. Roy. Soc.* (London) **A249** (1959) 555.
14. W N Asasad, *Nucl. Phys.* **44** (1963) 329; **44** (1963) 415; **63** (1965) 337; **66** (1965) 494.
15. E U Condon and G H Sortlyer, *The Theory of Atomic Spectra*, Cambridge Univ. Press London, (1970).
16. H L Hagedoorn and A H Wapstra, *Nucl. Phys.* **15** (1960) 146.
17. C R Worthington and S G Tomlin, *Proc. Phys. Soc.* **A69** (1956) 401.
18. H E Bishop and J C Riviere, *J. Appl. Phys.* **40** (1969) 1740.
19. H E Bishop, J C Riviere and J P Coad, *Surface Sci.* **24** (1971) 1.
20. G F Amelio, *Surface Sci.* **22** (1970) 301.
21. C Geldman, *Phys. Rev.* **117** (1960) 455.
22. P W Palmberg and T N Rhodin, *J. Appl. Phys.* **39** (1968) 2425.
23. D Pines, *Solid. State Phys.* **1** (1955) 367.
24. H E Bishop and J C Riviere, *Appl. Phys. Lett.* **16** (1970) 21.
25. L A Harrts, *J. Appl. Phys.* **39** (1968) 1419.
26. R E Weber and W T Peris, *J. Appl. Phys.* **38** (1967) 3320.
27. L N Thorp and E J Scheibner, *J. Appl. Phys.* **38** (1967) 3320.
28. J C Tray, *Electron Emission Spectroscopy* (C W Dekeyser, L Fiermans, G Vanderkelon and J Vennik, Eds). Reidel Publ. Dordrecht, Netherlands (1973) 331.
29. R S Hanisch, G P Hughes and J R Merill, *Rev. Sci. Instrum.* **46** (1975) 1262.
30. L Fierman, and J Vennik, *Surface Sci.* **38** 237 (1973).
31. E N Sickafus, *Rev. Sci. Instrum* **40** (1969) 792.
32. R G Musket and J Ferrante, *J. Vac. Sci. Technol.* **7** (1970) 14.
33. J E Houston, *Appl. Phys. Lett.* **24** (1974) 42.
34. W N Mularie and W T Peria, *Surface Sci.* **26** (1971) 125.
35. N J Taylor, *Rev. Sci. Instrum.* **40** (1969) 792.
36. C C Chang, *Surface Sci.* **25** (1971) 53.
37. P W Palmberg, G K Bohn and J C Tracay, *Appl. Phys. Lett.* **15** (1969) 254.
38. J C Grant, T W Hans and J E Houston, *Surface Sci.* **42** (1974) 1.
39. R L Gerlack, J E Houston and R L Park, *Appl. Phys. Lett.* **16** (1970) 179.
40. E N Sickafus and A D Colvin, *Rev. Sci. Instrum.* **41** (1970) 1349.
41. E N Sickafus, *Rev. Sci. Instrum.* **42** (1971) 933.
42. Y Strausser and J J Vebbing, Verians Chart of Auger Electron Energies, Varian Associates, Palo Alto, California (USA).
43. R E Weber and A L Johnson, *J. Appl. Phys.* **40** (1969) 314.
44. J M Charig and D K Skinner, *Surface Sci.* **19** (1970) 283.
45. A Joshi, L E Davis and P W Plamber, *Methods and Phenomena* 1, *Methods Surface Analysis* (A W Czanderna ed). *Elsevir Sci. Publ. Company* (1975) 159.
46. C C Chang, *Characterization of Solid Surface* (P F Kane and G B Larrabee eds). Plenum, New York (1974) 509.
47. C G Dunn and L A Harris, *J. Electrochem. Soc.* **117** (1970) 81.

48. R F Weber and W T Peria, *J. Appl. Phys.* **38** (1969) 4355.
49. J T Grant and T W Has, *Surface Sci.* **23** (1970) 347.
50. C C Chang, *Surface Sci.* **23** (1970) 283.
51. J J Webbing, *J. Appl.* **41** (1970) 802.
52. N C MacDonald and G E Riach, *Electron Packing Prod.* **13** (1973) 50.
53. H L Marcus and P W Palmberg, *Trans. Metallurg. Soc. AIME* **245** (1969) 1664.
54. D F Stein, A Joshi and R P LaForce, *Trans. ASM* **62** (1969) 776.
55. G C Bond, *Catalysis by Metals*, Academic Press, New York (1962).
56. M L Trang and G K Wehner, *J. Appl. Phys.* **42** (1971) 2449.
57. M Ono, Y Takasu, K Nakayama and T Yamashina, *Surface Sci.* **26** (1971) 313.
58. G Ertl and J Kuppers, *Surface Sci.* **24** (1971) 104.
59. L A Harris, *Surface Sci.* **15** (1969) 77.
60. G Stupian, *Systematic Materials Analysis.* Vol. 1, J H Richardson and R V Peterson eds, Academic Press, New York (1974) 57.
61. L Fiermans and J Vennik, *Surface Sci.* **24** (1971) 541; **35**, (1973) 42.
62. L Fiermans and J Vennik, *Adv. Electronics and Electron Physics* Vol. 43, L Marton Ed, Academic Press, New York (1977) 139.
63. F L Arnot and J C Milligan, *Proc. Roy. Soc. Ser A* **156** (1936) 538.
64. R F K Herzon and F P Viehbock, *Phys. Rev.* **76** (1949) 855.
65. V E Krohn, Jr., *J. Appl. Phys.* **33** (1962) 3523.
66. A Swith *et al.*, *J. Appl. Phys.* **34** (1963) 2489.
67. H E Beske, *Z. Angew. Phys.* **14** (1962) 30.
68. A Benninghoven, *Ann. Phys.* **15** (1965) 13.
69. J A McHugh and J C Sheffield, *J. Appl. Phys.* **35** (1984) 512.
70. H W Werner, *Dev. Appl. Spectroscopy*, Eds. El. Grove and A J Perkins, Plenum, New York 7A (1969) 239.
71. H W Werner and H A M deGrefte, *Vakuum Technik* **17** (1967) 37.
72. R E Honig, *Advan. Mass Spectrom* **6** (1974) 337.
73. G Larter and J S Colligon, *Ion Bombardment of Solids*, Heinemann Educational Books, London (1968).
74. H W Werner and H A M DeGrefte, *Surface Science* **35** (1973) 458.
75. Ya. M Fogel, *Sov. Phys. Usp.* **10** (1967) 17.
76. M Fogel, *Int. J. Mass Spectrom. Ion Phys.* **9** (1972) 109.
77. A J Soch, *Surface Sci.* **25** (1971) 147.
78. C A Anderson and J R Hinthorne, *Science* **175** (1972) 853.
79. R Castaing and J F Hennequin, *Advan. Mass Spectrom* **5** (1971) 419.
80. T Ishitani and R Shimizu, *Appl. Phys.* **6** (1975) 249.
81. H D Hagstrum, *Phys. Rev.* **123** (1961) 758.
82. C B W Kerkdij, Ph.D. Thesis, Leiden, the Netherlands (1975).
83. W V d Weg, Proc. NATO Summer School on Material Characterization, Corsica (Plenum Press) (1976).
84. F G Rudenaur, *Round table discussion on SIMS, 7th Intern. Mass Spectrom. Conf.* (Florence) (1976).
85. F G Rudenauer, *Vacuum* **22** (1972) 609.
86. C A Evans, Jr. *Anal. Chem.* **44** (1972) 67A.
87. C A Evans, *Jr. Proc. Tutorial Session 8th Nat. Conf. Electron Probe Anal. Soc. Amer.* New Orieans, La (1973) 29.
88. H Liebl, *Anal. Chem.* **46** (1974) 22A.
89. V F Rybalko, B Ya Kolot and Ya M Fogel, *Sov. Phys., Solid State* **14** (1970) 1290.

90. B MaCarroll, *J. Chem. Phys.* **46** (1967) 863.
91. P H Dawson and Wing-Chenug Tam, *Surface Sci.* **91** (1980) 153.
92. M Barber *et al.*, *Surface Sci.* **68** (1977) 130.
93. J M Morbito and R K Lewis, *Anal. Chem.* **45** (1973) 869.
94. W K Hofker, Ph.D. Thesis, University of Amsterdam, (1975).
95. H W Werner, *Mikrochimica Acts, Suppl.* **7** (1977) 63.
96. H W Werner, *Acta Electronics* **19** (1976) 53.
97. H W Werner, *Vacuum* **24** (1974) 493.
98. H J Mataien *et al.*, *Thin Solid Films* **38** (1976) 281.
99. S Hofanaum, *Appl. Physics* **9** (1976) 59.
100. K Wittmaack, *Radiation Effects* **6b** (1982) 205.
101. J Maul, F Schutz and K Wittmaach, *Phys. Lett. A.* **41** (1972) 177.
102. J A MacHugh, unpublished results.
103. R Bhul and A Preisinger, *Surface Sci.* **47** (1975) 344.
104. G Kaus and J Keruf, *Proc. 7th Intrn. Conf. Solid Surfaces* (Vienna) (1977) 2277.
105. R Bhul, W K Huber and E Lobach, Proc. 2nd Internl. Conf. on Solid Surfaces, Japan *J. Appl. Phys. Suppl* **2**, Pt 2, 807.
106. P H Dawson and Wing-Cheung Tam, *Surface Sci.* **81** (1979) 164.
107. D E Ramaker, *Chem. Phys. of Solid Surfaces IV*, Ed. R. Vanselow and R Howe, Springer-Verlag (1982) 19.
108. J A McHugh, *Methods of Surface Analysis.* Ed. A. W. Czandarna, Elsevier, NewYork (1975) 273.
109. K Muller, *Surface Physics, Springer Tracts in Modern Physics* Vol. 77, Springer-Verlag Berlin (1975) 97.

© *Proc Indian natn. Sci. Acad.*, **51**, A, No. 1, 1985, pp. 165-179.
Printed in India.

THE IMPACT OF PHOTOELECTRON SPECTROSCOPY ON SURFACE CHEMISTRY AND CATALYSIS*

M W ROBERTS
Department of Chemistry, University College, CARDIFF, CF1 1XL, U. K.

Photoelectron spectroscopy has been shown to be capable of providing not only information on the bonding and surface reactivity of such molecules as carbon monoxide, nitric oxide and water to metal surfaces but also on the mechanism of some catalytic reactions involving these molecules. The role that water may have in surface catalysed hydrogenation reactions is illustrated through a detailed study of the water assisted reduction of nitric oxide. Essential for the interpretation of this reaction are the conclusions from studies of water adsorption and in particular the specific role that chemisorbed oxygen can have in the activation of molecularly adsorbed water. The role that a hydrogen-bonded water-chemisorbed oxygen complex might play in directing the reaction mechanism-hydroxylation or water desorption-is discussed. The temperature stability of the surface hydroxyls, highly unstable with Cu(111)-O but relatively stable with Zn(OOO1)-O surfaces, determines the potential of such species in hydrogen-transfer reactions.

Key Words : Photoelection spectroscopy; Surface chemistry; Catalysis and Chemisorption

1. INTRODUCTION

THE Golden Jubilee Celebrations of the Indian National Science Academy of is a most appropriate occasion for reflecting on how particular specialised areas of scientific endeavour develop. This not only enables the subject to be seen in perspective but also we can judge better how the element of chance may determine the scientific path followed by research in a given field.

During the 19th century there were many attempts at defining catalysis but it was probably towards the end of that century with the emergence of thermodynamics and the idea that a catalyst could not change the position of equilibrium that mark the first scientific appreciation of the phenomenon of catalysis. The development of the subject of surface chemistry and heterogeneous catalysis during the 20th century was in three phases, the dates are approximate : (a) the classical approach, 1900–1950; (b) the "clean surface" approach, 1950–1965; (c) the emergence of surface sensitive techniques, post 1965. There is, of course, some overlap between (a) and (b) with Langmuir, J K Roberts and Beeck already pointing the way during the 30's and 40's of the role that fundamental research using clean metal surfaces was to make to future thinking in the field of the science of surfaces. The emergence of the first surface sensitive analytical technique, Auger Electron Spectroscopy (AES), was largely due to Harris who was at the General Electric Company, Schenectady—an industrial laboratory and the "home" of Irving Langmuir. He devised a simple method of electronically differentiating the secondary electron current in Low

*Paper presented at the Symposium on Physics and Chemistry of Surfaces held at INSA, New Delhi from September 28-30, 1984.

Energy Electron Diffraction (LEED) systems, of which there were about twenty installed throughout the world in 1967. Immediately, and for very little extra cost, surface analysis became feasible at the sub-monolayer level.

The emergence of photoemission, leading eventually to photoelectron spectroscopy, was, by comparison with AES, slow. Although photoemission had been studied extensively in the 30s (Fowler, Milliken, Hughes and Dubridge) it was during the period 1950–1965, when research in semiconductor surface physics was increasing rapidly, that the subject developed experimentally and theoretically[1]. Our own interest at that time was in the oxidation of metals using both kinetic and work function studies. The particular question that bothered us[2] was to find an experimental parameter that enabled a distinction to be made between chemisorbed oxygen and the electronic structure associated with an oxide overlayer ($\simeq$ 10 Å). It was the papers of Apker, Taft and Dickey and Gobeli and Allen that pointed us in the direction of photoemission (see reference 2) and in particular of studying the energy distribution of photoelectrons from metal surfaces. Elegant work by Kai Siegbahn, D W Turner and W C Price, reviewed in reference 1, showed how photoemission from gases using x-rays and uv sources could provide information on the electronic structure of molecules. With hindsight it is not difficult to appreciate that the next step was to combine the two approaches particularly since in 1965 it had been established that the photoelectron escape depth was no more than about 10Å in the nickel-oxygen system (Quinn and Roberts)[2] for low energy (uv) photons. In the early 70s Delgass[3] described x-ray photoelectron spectra obtained with metal oxides, Thomas *et al.*[4] reported O(ls) spectra of oxygen chemisorption on carbon while Roberts *et al.*[5] showed that a UHV compatible photoelectron spectrometer (incorporating both uv and x-ray sources) could provide spectra relevant to the surface chemistry of well defined 'clean' metals.

In the present paper we discuss how photoelectron spectroscopy provides information on the surface bonding and reactivity of diatomic molecules, the activation of molecules at solid surfaces and the mechanism of surface catalysed reactions with some emphasis given to the role of water vapour.

2. Photoelectron Spectroscopy : Surface Chemistry and Catalysis

Having established the sub-monolayer surface sensitivity of both XPS and UPS[5] the next stage was to explore how specific problems in surface chemistry could be resolved. The chemisorption of carbon monoxide, studied extensively by kinetic and infrared techniques, was a key system with both important fundamental and technological implications. It was the conclusion that with some metals carbon monoxide was dissociatively chemisorbed which led to the resurgence of interest in the carbide-theory for Fischer-Tropsch synthesis (Jones and McNicol[6], Smutek and Cerny[7]). Furthermore controlling the interplay between the dissociative and molecular states of adsorption, by preadsorbing sulphur, paved the way to exploring how surface additives can promote or inhibit (poison) catalysed reactions. It is not surprising that it was not long before dinitrogen chemisorption and the mechanism of ammonia synthesis was studied by PES[8], particular attention being given to the role of potassium.

A particular criticism that can be made of photoelectron spectroscopic studies of surfaces is that the maximum gas pressure at which (surface) spectra can be monitored is about 10^{-5} torr. A high-pressure photoelectron spectrometer was constructed which can take spectra at gas pressures up to a maximum of about 2 torr, the signal from the surface decreasing by only about 30 per cent compared with that observed at a pressure some 10^5 times smaller. This spectrometer has been particularly useful for unreavelling the pressure, rather than exposure, dependence of surface spectra[9]. More recently with the advent of microprocessors it has become possible to improve the quality of the spectra (signal-noise ratio) and to extend both the speed and the quantitative aspects of spectra analysis through smoothing, curve-fitting and spectral subtraction. We have found the Apple II microprocessor particularly advantageous for interfacing with our spectrometers using soft-ware developed in our laboratory.

The general strategy adopted is to obtain quantitative data on surface concentrations from XPS data, evidence for different surface species from 'chemical shifts' in core-level spectra and the nature of 'surface orbitals' from valence-level (helium induced) spectra. It is such cumulative information that provides confidence in spectral assignments. In 1971 there was no data base available of spectral assignments for surface species.

2.1 Chemisorption

Although the very facile nature of the dissociative chemisorption of carbon monoxide was recognised as early as 1973 with transition metals[10] (molybdenum and tungsten) through shifts in core-level C(ls) and O(ls) spectra, the correct assignment of the valence level spectra did not occur until later[11]. This was partly as the result of angular studies of the 5σ, 1π and 4σ orbitals leading to the conclusion that the 5σ and 1π orbitals were degenerate. The dependence of the magnitude of the shifts observed in the C(ls) and O(ls) spectra on the heat of adsorption, the relative insensitivity of the O(ls) binding energy when dissociative chemisorption occurred[10] and the absence of orbital structure in the helium-induced valence-level spectra provided good evidence for the Blyholder or Dewar-Chatt model for CO bonding at metal surfaces. Important studies of the catalytic chemistry of carbon monoxide have been carried out here in India by Rao and his colleagues[12] who gave particular attention to the dissociation and disproportionation or Boudouard ($2CO \rightarrow C + CO_2$) reactions over transition metal surfaces. These authors illustrated the particular advantage of acquiring Auger spectra in addition to XPS data.

Nitric oxide with an extra electron (compared with CO) in the antibonding orbital showed very similar behaviour to carbon monoxide in the low temperature regime (80K-300K) except that no real distinction was possible between the behaviour of transition and non-transition (or sp) metals. This was surprising and contrasted with the reactivity pattern observed with carbon monoxide[10], where a clear distinction was possible between metals like molybdenum and tungsten on the one hand and copper, zinc and magnesium on the other. In the case of nitric oxide both molecular and dissociative chemisorption was observed with copper, zinc and aluminium at 80K. We shall return and discuss the implications of these results in

the context of the mechanism of the hydrogenation of nitric oxide, a reaction of considerable technological importance for the automobile industry.

It was in the general context of surface hydrogenation that we initiated studies of the adsorption of water vapour at metal and oxide surfaces[13]. This was stimulated by observations we had made regarding the activation of S-H bonds in hydrogen sulphide by chemisorbed oxygen[14] where not only was the specificity attributed uniquely to the surface oxygen (the atomically clean metal being inert) but also activation was followed by a chemisorptive replacement reaction, the surface oxygen being replaced stoichiometrically by chemisorbed sulphur. The activation energy of the replacement process is less than 20kJ mole^{-1} since the process is facile at 100K. In general with water there are two distinct types of adsorption behaviour: (a) physical adsorption at low temperature attributable to dispersion forces followed by desorption at about 150K to give the original atomically clean surface and (b) dissociative chemisorption to generate an oxyhydroxide overlayer. In category (a) we have metals such as copper and zinc while examples where an oxyhydroxide overlayer is formed are iron and magnesium; these overlayers may well be examples of dipole-stabilised surface structures, surface hydroxy-formates being also in this category.[15] Distinction between chemisorbed oxygen, surface hydroxyls, and molecularly adsorbed water is, in the majority of cases, possible through spectroscopic studies using a combination of XPS and UPS over a wide range of temperature, 80K to 400K. Electron energy loss spectroscopy (EELS) has also made important contributions to the understanding of the surface chemistry of water[16].

One of the most significant observations to emerge, however, from photoelectron spectroscopic studies of metal surfaces was the specific role that chemisorbed oxygen can have in activating the O-H bonds in water i.e. just as was observed with the S-H bonds in hydrogen sulphide[14a]. Subsequent studies have established the oxygen activation of N-H bonds in ammonia, H-Cl bonds in HCl[14b] and C-H bonds in hydrocarbons[10]. Furthermore, the reactivity of the adsorbate bond, O-H, N-H, C-H etc is specific to the *precise* nature of the surface oxygen as emphasised recently by Haber at the 8th International Congress on Catalysis. The interplay between molecular and dissociative states of adsorbed oxygen on metals and in particular the weakening of the dioxygen bond, without fragmentation, is an are a that deserves detailed investigation in the context of selective oxidation catalysis. Studies of oxygen-promoted water interactions at metal surfaces of, for example, copper, silver, zinc, lead and nickel suggest that activation occurs through the formation of a hydrogen bonded surface complex[17]. The formation of this complex is closely related to the presence of coordinatively unsaturated chemisorbed oxygen at the surface. For example, an overlayer orthorhombic PbO at a Pb(100) surface shows no activity[17] for the activation of O-H bonds while the same overlayer in the presence of weakly adsorbed oxygen adatoms is reactiv eleading to the generation of surface hydroxyls at 150K. Studies of Ni(210) surfaces lead to the same conclusion.

We suggest that the stability of the hydrogen-bonded complex formed between coordinatively unsaturated chemisorbed oxygen and molecularly adsorbed

water is a crucial factor in determining the particular reaction pathway followed. This is best discussed in terms of Polanyi-type potential energy diagrams (fig. 1). In the case of Cu(111) surfaces, it is suggested that there is a finite activation energy barrier to complex formation, ΔE_H, which accounts for there being no experimental evidence of hydrogen bonding in the temperature range 80K–140K, followed by a second but larger barrier ΔE_B to bond cleavage and surface hydroxyl formation. Therefore, as the temperature is increased from 80K, over a very restricted range (160–170K) hydrogen-bonding is observed but at a slightly higher temperature, 220K, the complex becomes unstable with the main reaction pathway being desorption of water rather than surface hydroxylation. In the case of ZnO(0001)-O surfaces hydroxylation occurs at 200K rather than desorption of water (see below). At higher temperature (400K) using a dynamic high pressure system, and mixtures of water vapour and oxygen, Cu(111)-O surfaces hydroxylate. Presumably surface complexes form (in small concentration) which at the higher temperature cleave to generate hydroxyl species (radicals) rather than after surface interaction desorbing as $H_2O(g)$. The activation energy barrier to the cleavage of the H-OH bond induced by $O^{\delta-}$ is ΔE_B (Fig. 1). It is worth recalling here a crucial experiment[13] that established the distinct chemical identities of the two O(ls) components in the Cu(111)-O plus water system, 530 eV and 531.5 eV, since it removed any possible ambiguity regarding their interpretation. Fig. 2 shows the selective reduction of a Cu(111)-O.OH surface by carbon monoxide at 295K. The intensity of the 530 eV

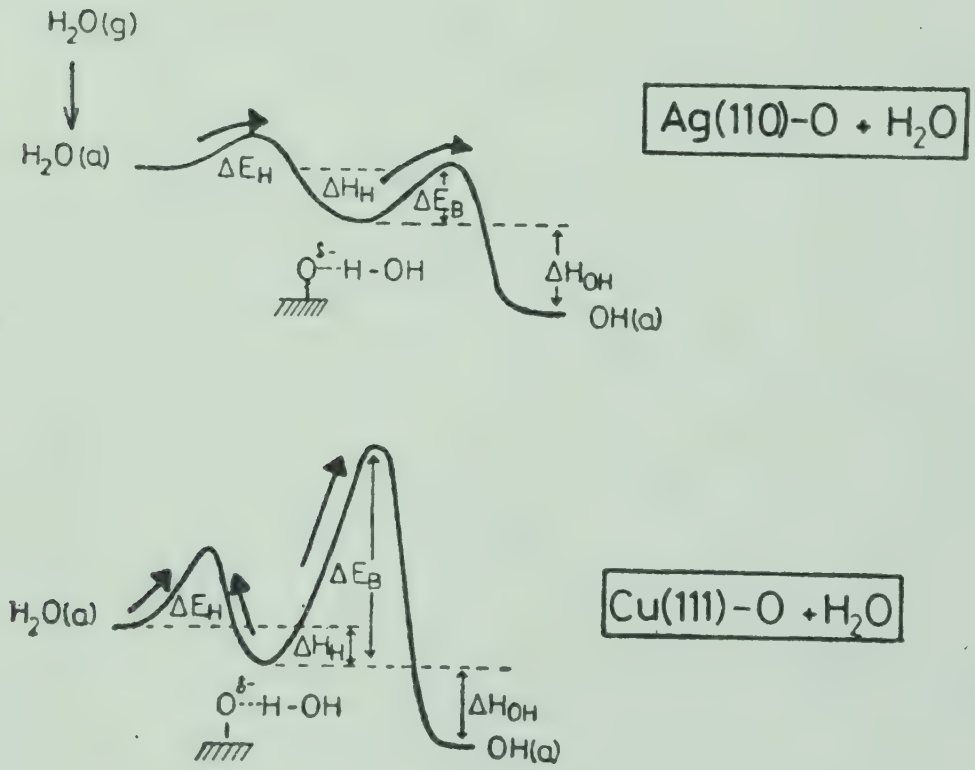

ΔE_H : formation of H-bonded complex.
ΔH_H : stability of H-bonded complex.
ΔE_B : cleovage of complex.
ΔH_{GH} : stability of surface "hydroxyls".

FIG. 1. Polanyi-type potential energy profiles of chemisorbed oxygen assisted water interaction with Ag (110) and Cu(111) surfaces.

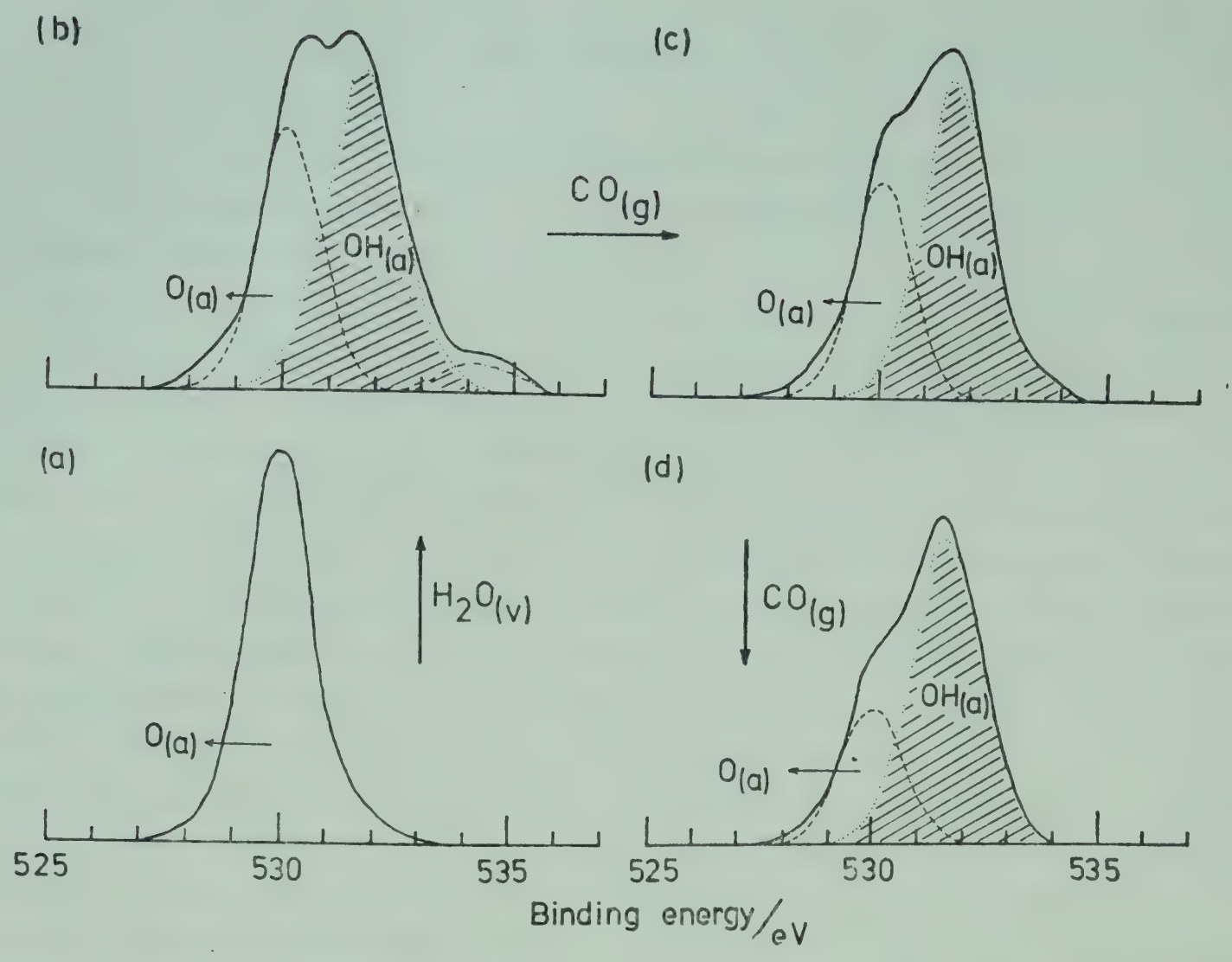

FIG. 2. Assignments of O(ls) spectra : selective reduction by carbon monoxide of the chemisorbed oxygen of a Cu(111)-O.OH adlayer.

component (chemisorbed oxygen) decreases while that at 531.5 eV (hydroxyl species) remains unchanged. The result is of general significance in the assignment of O(a), OH(a) and H_2O(a) peaks in O(ls) spectra.

In the case of Ag(110)-O surfaces, Ag(110) is inactive, the hydrogen bond complex is observed even at 80K and surface hydroxylation at 200K (fig. 3). The energy profile diagram for this highly reactive surface is suggested to have the form shown (fig. 1). In the Zn(0001)-O system, surface O^- species interact with molecularly adsorbed water to generate OH species in the temperature range 170K to 200K. The O^{2-} species of the oxide overlayer are by comparison unreactive. Above 200K the surface hydroxyls are thermally unstable and decompose to generate O^{-2}(b) as follows :

$$OH(a) \rightarrow O^-(a) + H(a)$$

$$O^-(a) \xrightarrow{e} O^{2-}(b)$$

We have therefore in the case of zinc oxide overlayers present at a Zn(0001) surface relatively stable surface hydroxyls so that rather than dehydroxylation leading to water desorption, increase in temperature leads to dehydrogenation with the transformation of O^-(a) to O^{2-}(b). We will see the relevance of this to the water assisted hydrogenation of nitric oxide below.

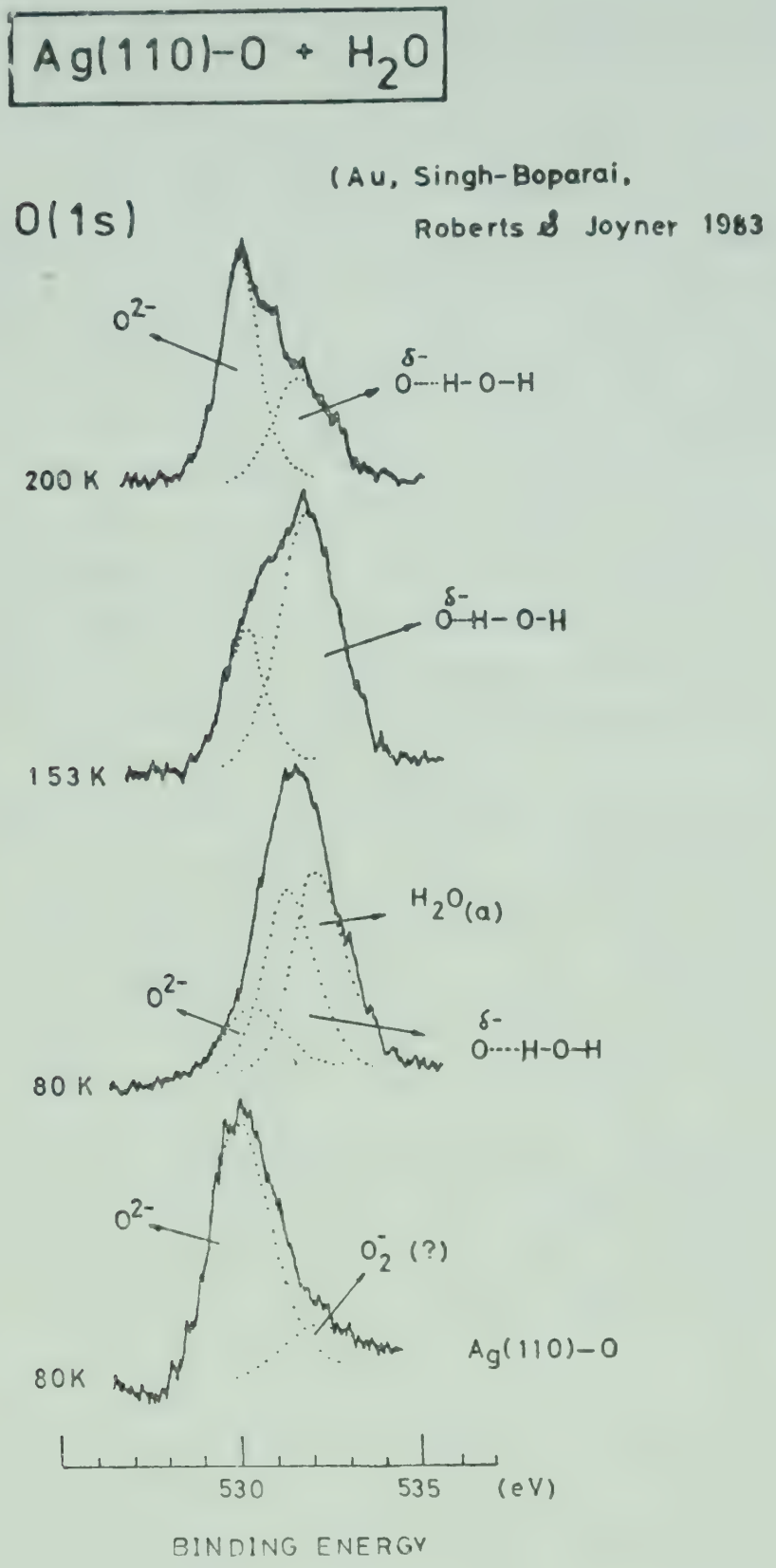

FIG. 3. O (ls) spectra for the Ag(110)-O plus water interaction in the temperature range 80K to 200K.

3. CATALYTIC HYDROGENATION OF NITRIC OXIDE AT A ZN (0001) SURFACE

Somewhere in the vast catalytic literature most (if not all!) possible mechanisms have been suggested for any one particular reaction. What is missing in virtually every case is the direct experimental evidence for the intermediate steps in the reaction. Photoelectron spectroscopy has considerable potential for the elucidation of the mechanisms of surface reactions and the particular system we have chosen to consider here is chemisorption of nitric oxide at a Zn(0001) surface with emphasis on the possible role that water vapour might have in its hydrogenation. The system was studied[18] as four quite separate problems : (a) oxygen chemisorption and oxide overlayer formation; (b) water adsorption and the role of an oxide overlayer in water

activation; (c) the chemisorption of nitric oxide and (d) the influence of water vapour on the reactivity of nitric oxide.

3.1 Oxygen Chemisorption and Oxidation

The interaction of oxygen with an atomically clean Zn(0001) surface results in the formation of two oxygen species : O^{2-}(b) and O^{-}(a) which can be distinguished by photoelectron spectroscopy (Fig. 4). The former subsurface species develops first at 300K and the 'surface' O^{-}(a) more slowly at higher exposures. By cooling to 80K the incorporation of oxygen leading to the formation of O^{2-}(b) is inhibited due to a small activation energy and the development of O^{-}(a) occurs not only at smaller oxygen exposures but also more extensively. The O(1s) binding energies of the O^{2-}(b) and O^{-}(a) species are 530 eV and 532 eV repectively making it relatively easy to quantify their concentrations and to probe their separate reactivities. The He(I) induced spectra of the two species are not so easy to distinguish, that assigned to O^{2-}(b) is at about 4.0 eV while that of O^{-}(a) is at about 5.5 eV below E_F.

3.2 Adsorption of Water Vapour and the Role of Surface Oxygen

An atomically clean single crystal Zn(0001) surface adsorbs water vapour at 77K with an O(1s) peak at 533.5 eV. The molecularly adsorbed adlayer is desorbed completely on warming to 150K. Helium induced spectra of the adlayer at 77K exhibited peaks at 7.5 eV, 11 eV and 14 eV assigned to the $1b_1$, 3a, and $1b_2$ orbitals associated with the water molecule. These are absent at 295K.

However, if the Zn(0001) surface is preoxidized and exposed to water vapour then activation of the molecular adsorbed layer occurs at about 100K leading to the formation of surface hydroxyls (Fig. 5). At 100K and above dehydroxylation occurs by a dehydrogenation-type mechanism :

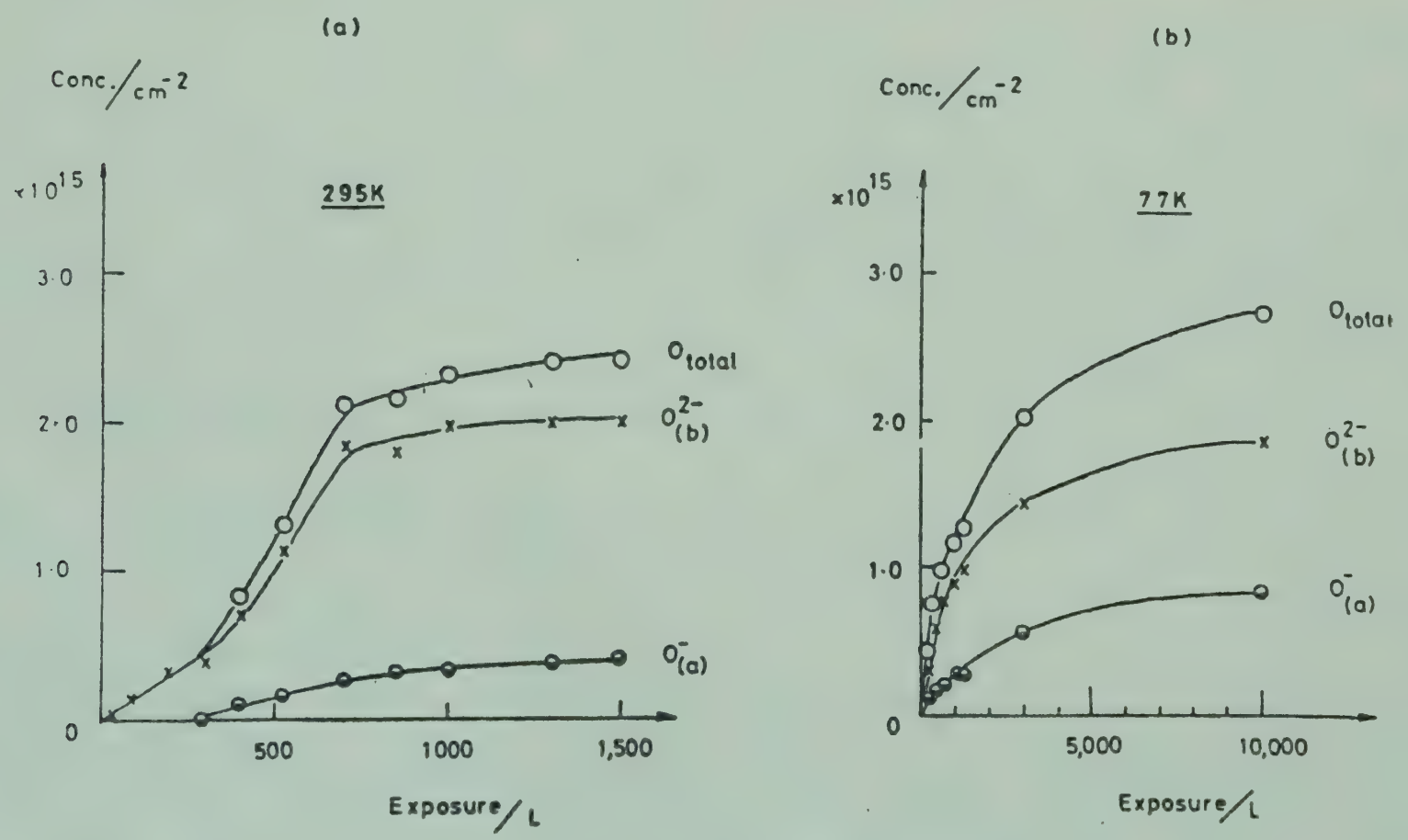

FIG. 4. Oxygen interaction with a Zn(0001) surface at 295K and O (ls) spectra provide a distinction between O^{-2}(b) and O^{-}(a).

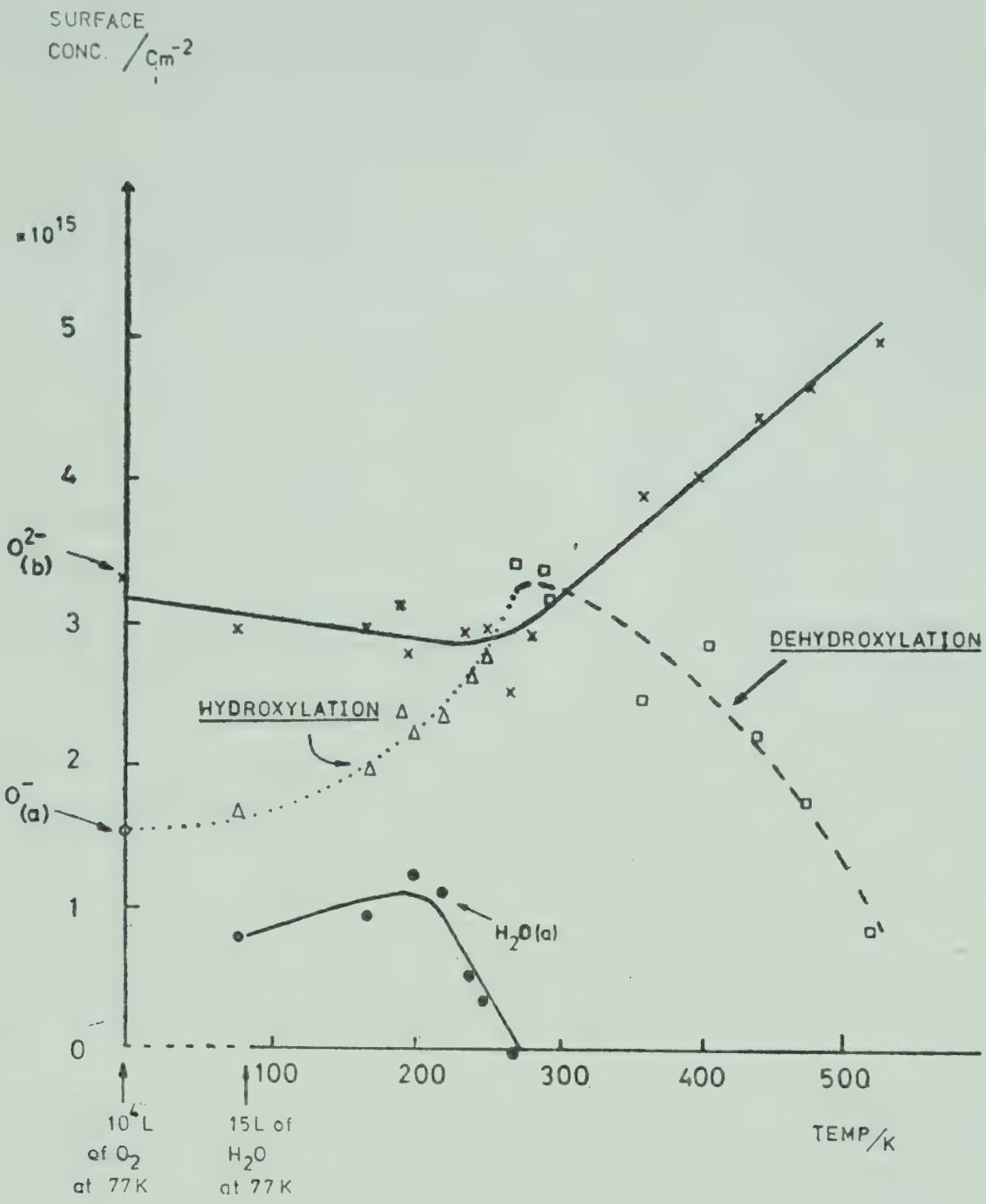

FIG. 5. Surface chemistry of the Zn(0001)-plus water system : hydroxylation, water desorption and dehydroxylation.

$$OH^-(a) \rightarrow O^-(a) + \tfrac{1}{2}H_2(g)$$

$$O^-(a) \xrightarrow{e} O^{2-}(b)$$

The stoichiometry of dehydroxylation, reflected by analysis of the O(1s) specta, establishes the mechanism of the surface reaction. Valence level difference spectra confirm that molecularly adsorbed water first hydroxylates the surface but with increasing temperature dehydrogenation followed by oxygen incorporation, as O^{2-}, occurs. It is the combination of core-level and valence-level spectra obtained over a wide range of temperature and the generation of relevant difference spectra that provides confidence for the proposed chemistry.

3.3 Chemisorption of Nitric Oxide

At 80K nitric oxide is dissociatively chemisorbed giving rise to a characteristic N(1s) peak at 396 eV (Fig. 6); the corresponding O(1s) spectra with assignments are also shown. There is no evidence for the bridge-bonded molecular state observed Cu(111) and Cu(100) surfaces and shown to be the precursor state of dissociation.

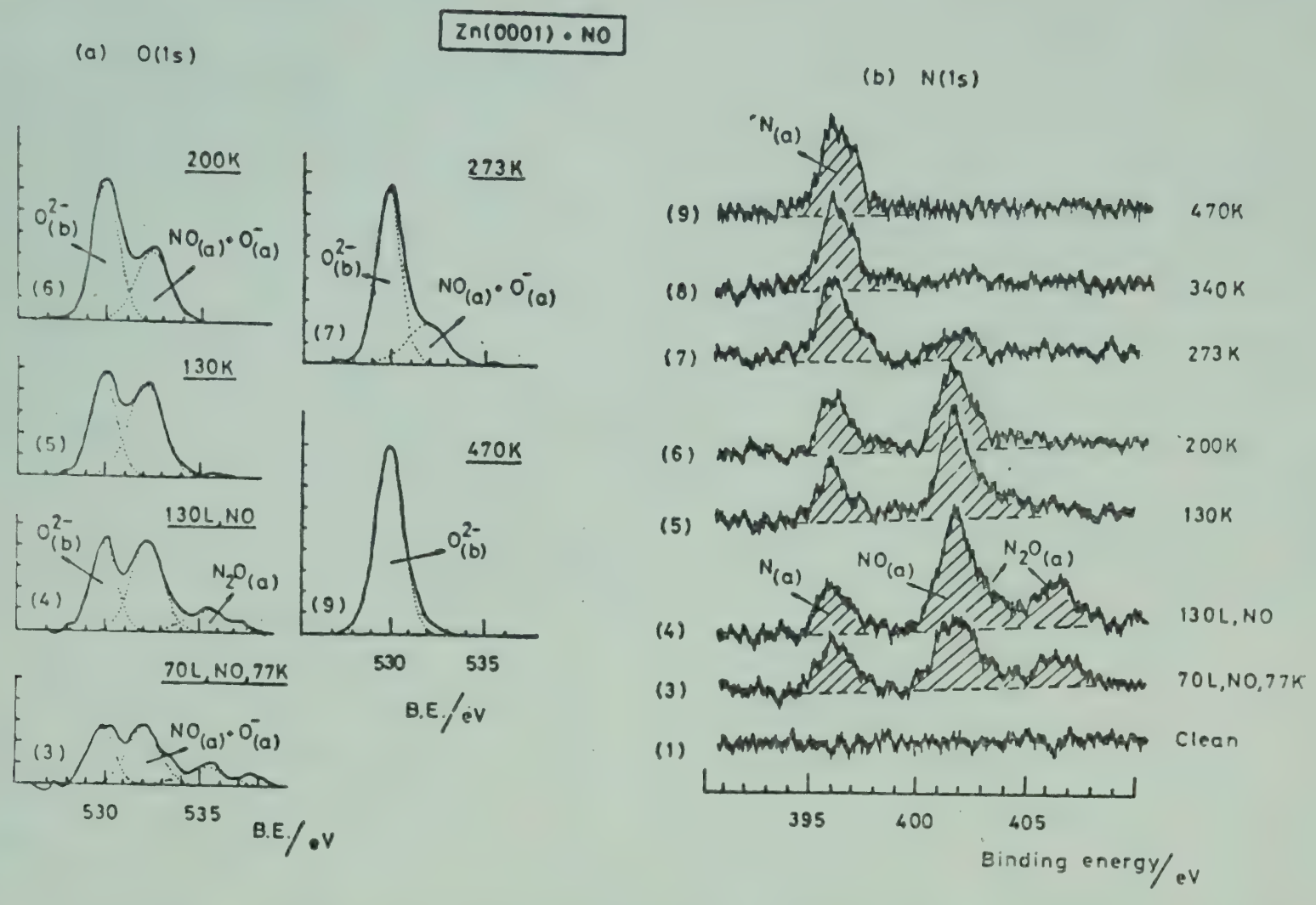

FIG. 6. Curve-fitted O (ls) and raw N(ls) spectra with assignments for the adsorption of nitric oxide by Zn(0001).

Clearly the bridge-bonded molecular state is inherently unstable even at 80K indicating that the activation energy barrier for dissociation is very small (less than a few kJ $mole^{-1}$). The linearly bonded state of nitric oxide with an N(ls) binding energy at 401 eV, and also N_2O(a) are present at 80K (fig. 6). The latter has been observed in a number of different studies of the chemisorption of nitric oxide at metal surfaces: copper, aluminium and ruthenium[19]. This would not have been anticipated since N_2O is thermodynamically less stable than NO; it is, however, the surface 'oxidation' accompanying the dissociative chemisorption that provides the thermodynamic driving force for N_2O formation. At 200K the N_2O has desorbed, the molecularly adsorbed NO, characterized by an N(ls) binding energy of 401.5 eV, desorbs at 273K while the surface nitride, N(ls) peak at 396 eV, is stable up to 470K. He(I) spectra and difference spectra (fig. 7) confirm the chemistry suggested by the core-level spectra.

The N(ls) and O(ls) spectra observed when the Zn(0001) surface was exposed to nitric oxide and water vapour at 77K and then the mixed-adlayer warmed to 295K are shown in fig. 8. The main feature to notice is the development at 200K of intensity in the N(ls) spectral region of 397 eV to 399 eV but with little evidence of any N(ls) intensity being present when the temperature was raised slowly to 360K. This is in strong contrast to what was observed with nitric oxide in the absence of water vapour. Valence level spectra (fig. 9) confirm the assignments of the peaks in the core-level spectra.

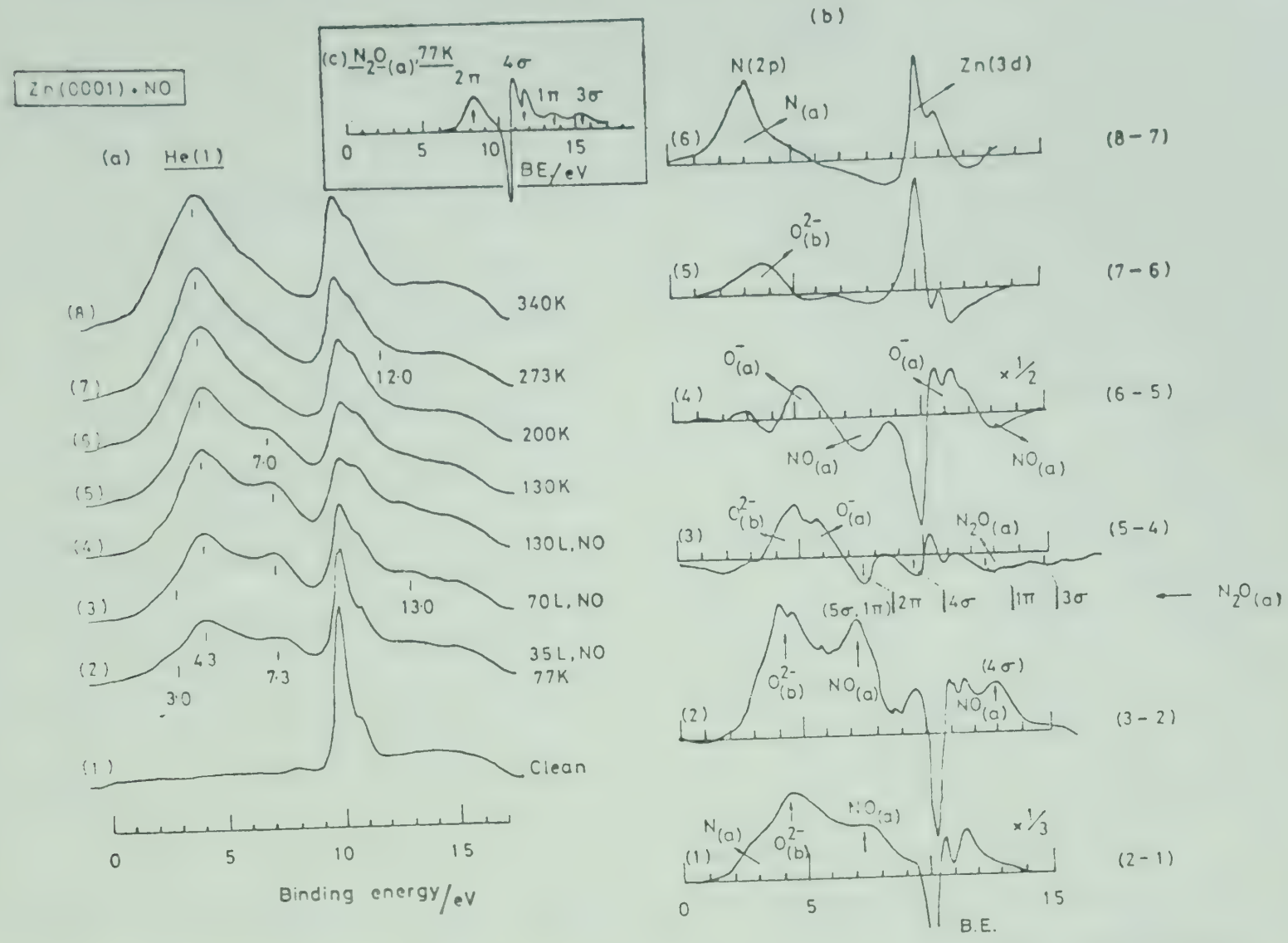

FIG. 7. He(I) and appropriate 'difference spectra' for the Zn(0001) plus NO system in the temperature range 77K to 340K.

Previous studies of both hydrazine and ammonia chemisorption have established[20] that NH_2(a) and NH(a) species have characteristic N(ls) binding energies of about 399 eV and 398 eV respectively. These assignments were particularly obvious with Cu(111)-O surfaces where the chemisorptive replacement of chemisorbed oxygen by NH(a) species was a stoichiometric process, $O(a) + NH_3(a) \rightarrow H_2O(g) + NH(a)$. The O(ls) and helium induced spectra confirm that reduction of the chemisorbed nitrogen species by surface hydroxyls is occurring above 200K. Furthermore quantitative analysis of the curve-fitted spectra has provided estimates of the concentration of all the surface species over the temperature range 80K to 470K (Fig. 10).

In summary it has therefore been established that :

(a) A "clean" Zn(0001) surface is unreactive to water vapour in the temperature range 160K–300K. At 77K water vapour is physically adsorbed and desorbs at 150K.

(b) Chemisorbed oxygen, O^-(a), present at a ZnO(0001) overlayer activates molecularly adsorbed water to generate surface hydroxyls. The surface hydroxyls dehydrogenate in the temperature range 200K to 350K.

(c) Nitric oxide is both molecularly and dissociatively chemisorbed at 80K; the surface nitride is stable up to 470K. The chemisorbed oxygen generated by NO dissociation activates the molecularly adsorbed water, thereby generating OH species.

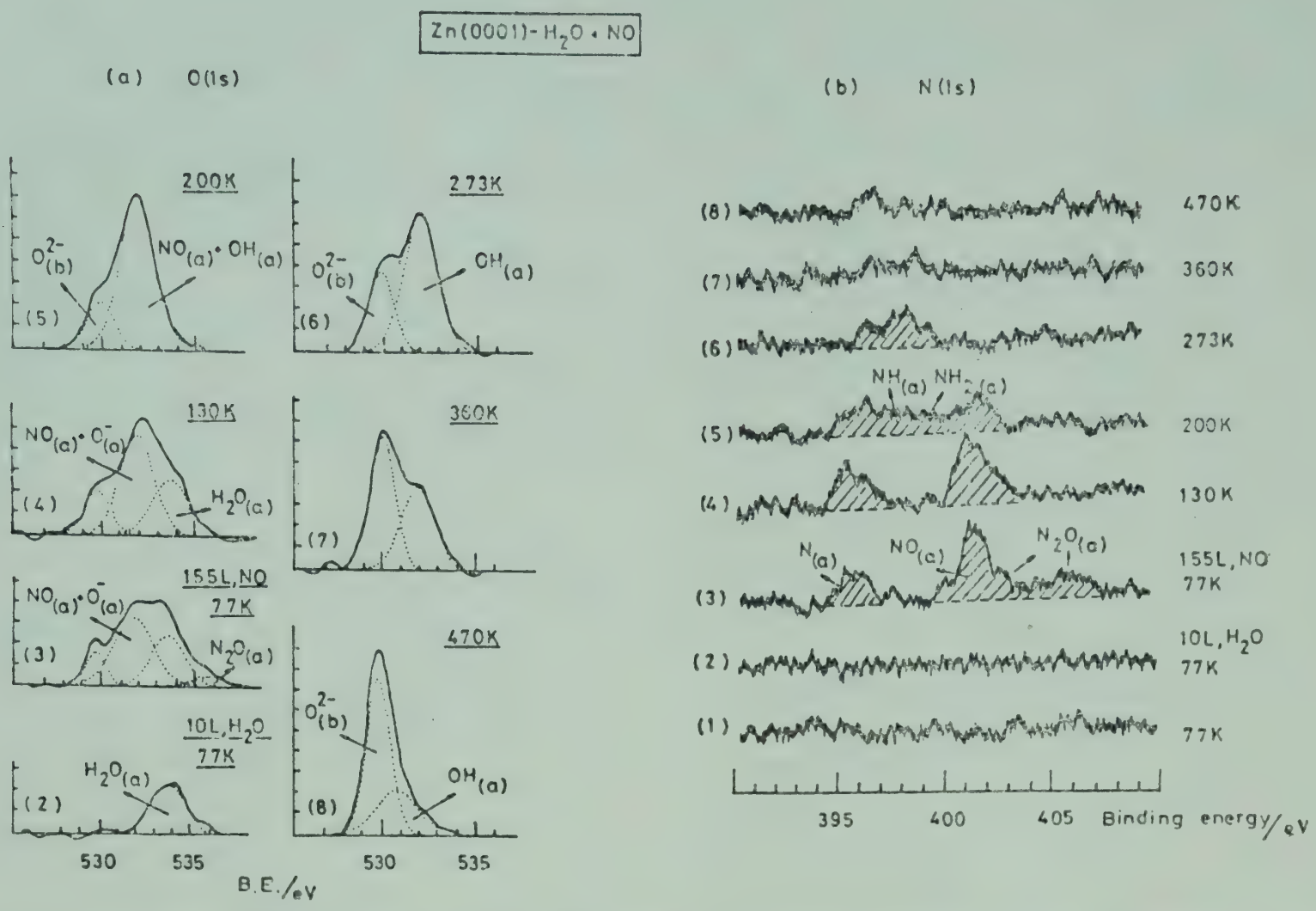

FIG. 8. Curve-fitted O(1s) and N(1s) spectra for the mixed adlayer of water plus nitric oxide in the temperature range 77K to 470K.

The mechanism of nitride hydrogenation is, therefore, likely to involve step-wise processes :

$$NO(g) \rightarrow N(a) + O^{-}(a)$$
$$O^{-}(a) + H_2O(a) \rightarrow 2OH(a)$$
$$N(a) + OH(a) \rightarrow NH(a) + O^{-}(a)$$
$$NH(a) + OH(a) \rightarrow NH_2(a) + O^{-}(a)$$
$$NH_2(a) + OH(a) \rightarrow NH_3(a) + O^{-}(a)$$
$$NH_3(a) \rightarrow NH_3(g)$$
$$O^{-}(a) \rightarrow O^{2-}(b)$$

The hydrogen transfer process is facile, occurring at low temperature, 200K to 295K, and driven by the strong nucleophilicity of the nitride species with which is associated a high negative charge. Furthermore the transfer of $O^{-}(a)$ to the sub-surface $O^{2-}(b)$ known to occur in the same temperature regime will be exothermic and therefore will facilitate the overall energetics of the reduction process. The stoichiometric calculations provide further evidence for the validity of the mechanism in that three hydroxyl species are lost for each chemisorbed nitrogen adatom hydrogenated (Fig. 10).

Equilibria involving hydrogen bonding between amines and phenols in solution have been shown recently to involve complexes which exhibit large proton polarizabilities[23]. The interesting analogy with our present studies is the observation

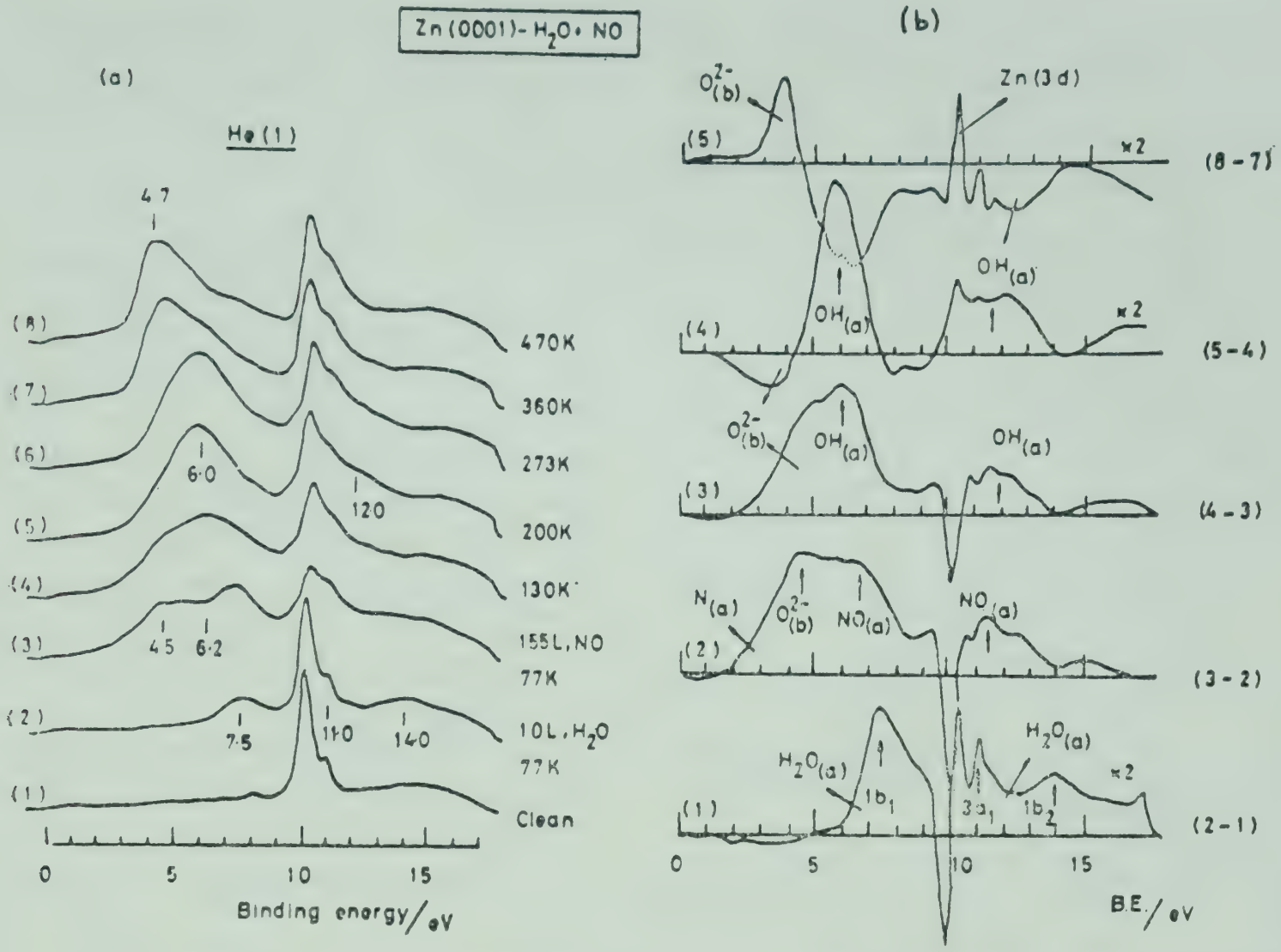

FIG. 9. He(I) and appropriate difference spectra relevant to the XPS data in Fig. 8.

that in liquids equilibria such as OH—N $\rightleftharpoons$ O^- + H^+N lie to the right, an important factor in this being the interaction of the hydrogen bond with its environment. Under certain conditions it is suggested that the proton becomes attached to the nitrogen atom. It is therefore not difficult to visualise how schematic potential energy profiles of such systems illustrate how hydrogenation of chemisorbed nitrogen might be assisted through the formation of an "intermediate complex" which involves strong hydrogen bonding between the following species : N (a), OH (a) and H_2O(a). Such complexes certainly appear to determine the precise nature of the chemistry of oxygen promoted reactions at silver, copper, zinc and nickel surfaces. What is now required is quantitative data for parameters analogous to those shown in Fig. 1, through a combination of vibrational and photoelectron spectroscopies.

4. Mechanism of Ammonia Synthesis

That hydrogenation of chemisorbed nitrogen can be effected by hydrogen transfer from the surface hydroxyls raises the important question of the role of alkali metals in ammonia synthesis, in particular the possibility of hydrogen transfer occurring between acid surface hydroxyls and chemisorbed nitrogen adatoms. Whether the role of potassium under synthesis conditions should be considered in terms of a hydrogen transfer reaction,

$$KOH + N(a) \rightarrow KO + NH(a) \text{ etc}$$

iron being responsible for the dissociation of dinitrogen, can only be ascertained by further studies. That the 'potassium' under synthesis conditions may be partly

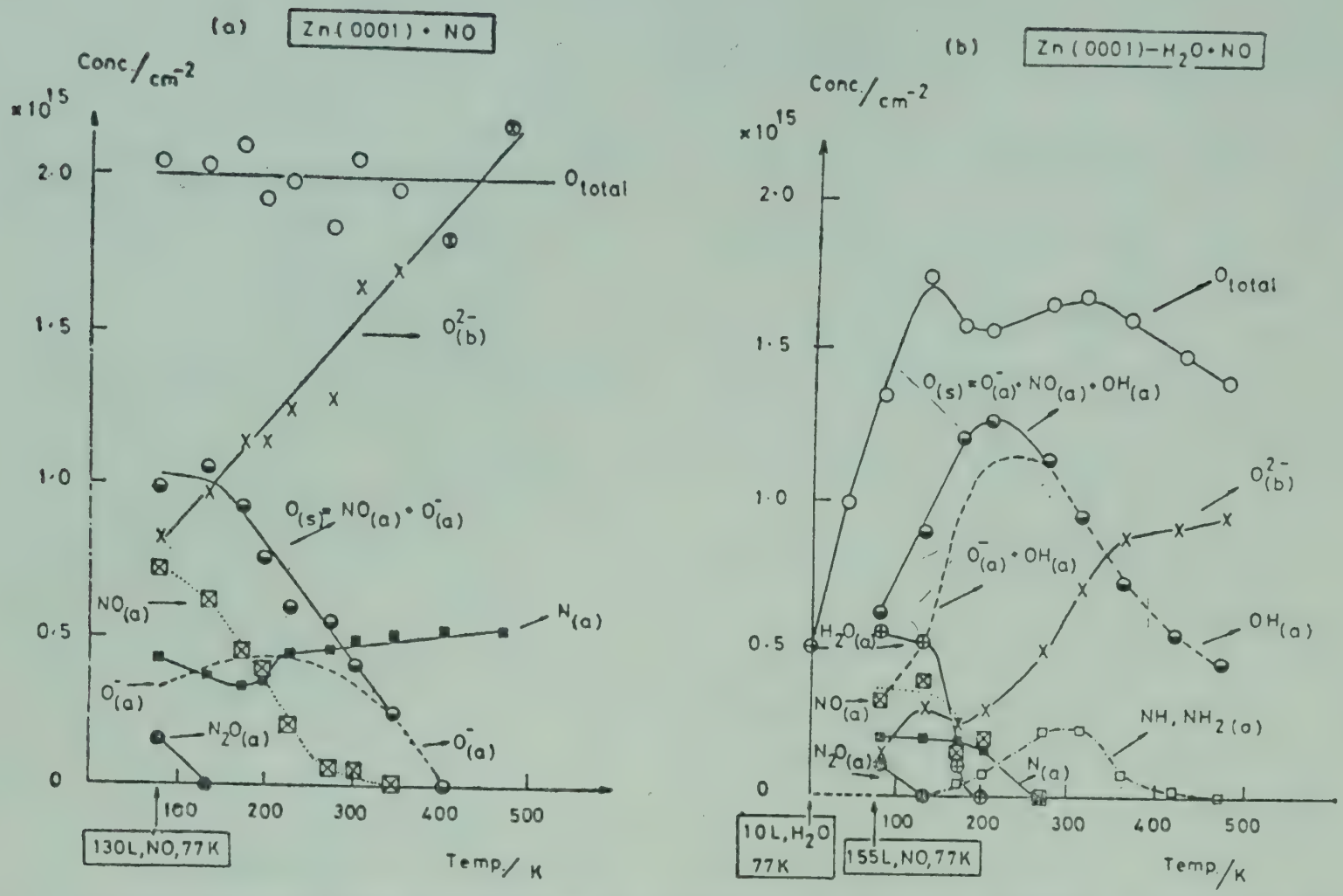

FIG. 10. Quantitative analysis of XPS data for Zn (0001) + NO and Zn(0001) + NO/H_2O systems.

present as an amide KNH_2 is controversial. Aika and Ozaki[21] having provided circumstantial evidence for its involvement in synthesis whereas Van Ommen *et al.*[22] conclude that KH, KNH, and K_2O could not be present under synthesis conditions, the most likely from being KOH.

Now—the title of my talk was 'The Impact of Photoelectron Spectroscopy on Surface Chemistry and Catalysis'. What has the impact of PES been on catalysis? If we consider first the reactivity pattern in chemisorption that was used in catalysis in the late sixties—then there is no doubt whatsoever that PES has put an entirely new complexion on the subject. I don't, for example, believe there is good chemical reactivity evidence for dividing metals into transition and non-transition—they now merge. The sp-band is as important in chemisorption as the d-band. When we consider the case of carbon monoxide and its relevance to Fischer-Tropsch synthesis the impact of PES is very clear to be seen : the molecular/dissociative chemisorption problem was resolved, kinetic, infrared and field emision data were reconciled and the carbide theory of FT synthesis resurrected. Details of the role of stepped surfaces and disproportionation reactions emerged from the work of Mason and Rao and his colleagues in Bangalore. Studies of NO chemisorption indicate the role of N (free redical?) in determining reaction pathways with implications for CO chemistry. The nitric oxide-water study also has thrown a new light on the mechanism of surface reactions relevant to motor—exhaust catalysis-kinetic studies important though they are, could not provide the details that PES has provided—in fact I would argue that it would have been virtually impossible to obtain the molecular information from any other experimental method. The proof that hydrogenation of nitric oxide occurs by surface hydroxyls has obvious implications not only in ammonia synthesis but also in CO hydrogenation.

REFERENCES

1. W E Spicer, in *Chemistry and Physics of Solid Surfaces IV* Ed : R Vaneslow and R Howe, Springer-Verlag (1982).
2. C M Quinn and M W Roberts, *Trans. Faraday Soc.* **61** (1965) 1775.
3. W N Delgass, T R Hughes and C S Fadley, *Cat. Rev.* **4** (1970) 179.
4. J M Thomas, E L Evans, M Barber and P Swift, *Trans. Faraday Soc.* **67** (1971) 1875.
5. C R Brundle and M W Roberts, *Proc. Roy. Soc. London* **A331** (1972) 383.
6. A Jones and B D McNicol, *J. Catal.* **47** (1977) 384.
7. M Smutek and S Cerny, *Int. Revs in Phys. Chem.* **3** (1983) 263.
8. I D Gay, M Textor, R. Mason and Y. Iwasawa, *Proc. Roy. Soc. London* **A356** (1977), 25.
   G Ertl, M Weiss and S B Lee, *Chem. Phys. Lett.* **60** (1979) 391.
   M Grunze, in *The Chemical Physics of Surfaces*, Elsevier (1982).
9. R W Joyner, M W Roberts and K Yates, *Surf. Sci.* **87** (1979) 501.
10. Reviewed by M W Roberts, *Adv. in Catalysis* **29** (1980) 52. Academic Press Inc.
11. D R Lloyd, *Faraday Disc. Chem. Soc.* **58** (1974) 136.
    T A, Clark, I D, Gay, B Law, and R. Mason, *Chem. Phys. Lett.* **31** (1975) 29.
    Gustafsson *et al.*, *Solid State Commun.* **17** (1975) 391.
12. K Jaganathan, A Srinivasan, M S Hegde and C N R Rao, *Sci.* **99** (1980) 309.
13. C T Au, J Breza and M W Roberts, *Chem. Phys. Lett.* **66** 340; C T Au and M W Roberts, *Chem. Phys. Lett.* (1980) **74** (1979) 472.
14. (a) K Kishi and M W Roberts, *J. Chem. Soc. Faraday Trans. I.* **71** (1975) 1721; R W Joyner, K Kishi and M W Roberts, *Proc. Roy. Soc.* **A358** (1976) 223.
14. (b) A F Carley, M S Hegde and M W Roberts, *Chem. Phys. Lett.* **90** (1982) 108.
15. S Isa, R W Joyner, M Matloob and M W Roberts, *Appl. Surf. Sci.* **5** (1980) 345.
16. G B Fisher and B A Sexton, *Phys. Rev. Lett.* **44** (1980) 683.
17. A F Carley, S Rassias and M W Roberts, *Surf. Sci.* **135** (1983) 35; L Moroney, S Rassias and M W Roberts, *Surf. Sci.* **105** (1981) L249; C T Au, S Singh-Boparai, M W Roberts and R W Joyner, *J. Chem. Soc. Faraday Trans. I*, **79** (1983) 1779.
18. C T Au and M W Roberts, *Chem. Comm.* **737**; *Proc. Roy. Soc. London.* A **396** (1984) 165.
19. D W Johnson, M Matloob and M W Roberts, *Faraday Trans. I.* **75** (1979) 2143; A F Carley and M W Roberts, *Proc. Roy. Soc. London* **A363** (1978) 403.
20. M Matloob and M W Roberts, *J. Chem. Soc. Res.* (*S*) **336** (1977) D W Johnson and M W Roberts, *J. Electron Spec. Rel. Phenom.* **19** (1980) 185.
21. K J Aika and A Ozaki, *J. Cat.* **35** (1974) 61.
22. J G Van Ommen, W J Bolink, J Prasad and P Mars, *J. Cat.* **380** (1975) 120.
23. G Albrecht and G Zundel, *J. Chem. Soc. Faraday Trans. I.* **80** (1984) 553.

© Proc. Indian natn. Sci. Acad, 50, A, No. 1, 1985, pp. 180-201.
Printed in India.

NEW POSSIBILITIES OF NMR SPECTROSCOPY IN THE STUDIES OF ADSORPTION AND CATALYSIS*

K I ZAMARAEV *and* V M MASTIKHIN

Institute of Catalysis, Novosibirsk 90, U. S. S. R.

Using modern Fourier spectrometers operating at high (about 7T) magnetic field and having special devices for magic angle spinning (MAS) one can obtain within reasonable periods of time the NMR spectra for nuclei of various elements present in heterogeneous catalysts including nuclei with small magnetic moments and low natural abundance as well as the high resolution spectra of these catalysts and of molecules adsorbed on their surfaces. The following examples of such studies are presented.

Comparison of ^{51}V, ^{17}O, ^{23}Na NMR spectra of vanadium catalysis for SO_2 oxidation to SO_3 with those of various reference compounds made it possible to identify some chemical compounds present in the active component of these catalysts as well as to elucidate the interaction between the active component and the support. Coordination of vanadium by pyrosulphate has been studied in the melt of the active component under typical conditions (500°C) at which the catalysts usually operate.

Using ^{27}Al MAS NMR it is possible to resolve the lines from aluminum ions in tetrahedral and octahedral positions for various crystalline modifications of Al_2O_3. For zeolites using ^{27}Al NMR some of the aluminum, upon certain treatments was found to escape from tetrahedral positions in the lattice and to acquire octahedral cooordination in the presence of water.

The ^{29}Si MAS spectra support this conclusion indicating simultaneous decrease of the fraction of silicon atoms of the lattice that have 4 and 3 aluminum atoms in the second coordination sphere and the increase of the fraction of silicon atoms that have 2 and 1 aluminum atoms in the second coordination sphere. In ^{1}H MAS spectra of zeolites lines from various hydroxyl groups can be resolved.

Higher sensitivity of modern spectrometers together with the use of MAS technique open novel possibilities in the study of adsorbed species.

As an example the results obtained for the adsorption of hydrogen, methane, carbon monoxide and propylene on heterogeneous catalysts are presented.

Key Words : NMR Spectroscopy; Adsorption; Catalysis and MAS techniques.

1. INTRODUCTION

As has been shown recently by investigations made in a number of laboratories, the use of modern Fourier Transform NMR spectrometers operating at high magnetic field and having special devices for magic angle spinning has provided qualitatively new possibilities in the study of heterogeneous catalysts and molecules adsorbed thereon[1-22].

A substantial increase in the sensitivity due to the high operation frequency and larger sample volume permits one to obtain within a reasonable period of time the

*Paper presented at the Symposium on Physics and Chemistry of Surfaces held at INSA, New Delhi from September 28-30, 1984.

NMR spectra of various elements present in heterogeneous catalysts including those with small nuclear magnetic moments and low natural abundance.

The use of the magic angle spinning (MAS) techniques for the narrowing of NMR lines makes it possible to observe the high resolution spectra of solid catalysts and of adsorbed molecules.

In this paper we present the data about the structure of certain chemical sites in some typical heterogeneous catalysts (including catalysts used in industry) and of the species formed upon adsorption of various molecules on these catalysts, obtained with NMR at the Institute of Catalysis in Novosibirsk.

All the NMR spectra have been obtained with the Bruker CXP-300 spectrometer. Most of the measurements were made at room temperatures using an Oxford Instruments V22463 cryomagnet. Some measurements were made at elevated temperatures (500°C) using a BM–18 iron magnet equipped with a special high temperature probe head (see 26 for more detail). ^{27}Al, ^{29}Si and ^{1}H NMR spectra of catalysts were obtained using comercial Bruker MAS rotor and sample tube. ^{1}H and ^{13}C MAS NMR spectra of adsorbed species were obtained using a rotor and a sample tube specially designed to rotate sealed samples (see Fig. 1). Our experience shows that using this rotor one can rotate carefully sealed samples with a frequency of 2–2.5 kHz without the sample exploding due to centrifugal forces. The rotor used is seen to have the shape of a mushroom. For measurements of proton spectra the "hat" of the mushroom was made of teflon and the "leg"—of the quartz tube. The sample tube was fixed in a rotor with a 0.05 millimeter thick teflon foil.

2. The Study of Chemical Sites in Catalysts

In this section the NMR data are presented that allow one to identify and study certain chemical sites in some important heterogeneous catalysts, such as vanadium

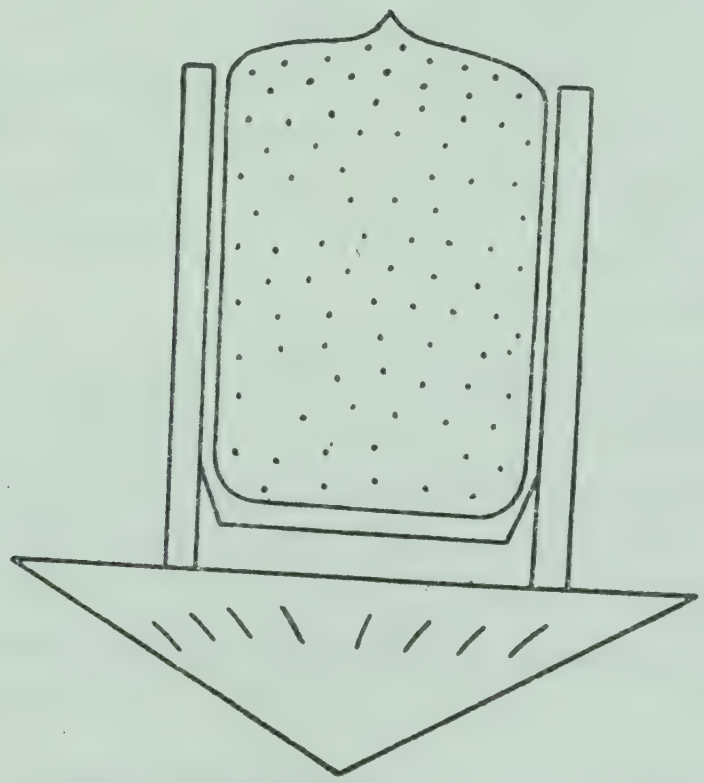

Fig. 1. Rotor and ampoule for study of ^{1}H and ^{13}C spectra of adsorbed molecules.

sites in vanadium catalysts for sulphur dioxide oxidation, aluminum and silicon sites in aluminas and zeolites as well as various OH-group on the surface of solid acid and base catalysts. For various industrial vanadium catalysts ^{51}V NMR spectra clearly indicate that the active component of vanadium catalysts for SO_2 oxidation is formed in the course of the catalysts reaction and is essentially the same for various industrial catalysts studied despite the differences in their initial composition and preparation procedures. After treatment in the reaction mixture and subsequent cooling up to room temperature the compound $K_3VO_2(SO_4)$ (S_2O_7) seems to be formed in the catalysts studied as the main component containing vanadium. A certain portion of vanadium in these catalysts is present also in a form of some other compound which is formed upon chemical interaction of the active component with the support. In this compound vanadium seems to be surrounded with a tetrahedron of oxygen atoms.

In aluminas and zeolites ^{27}Al NMR permits to detect separately aluminum in tetrahedral and octahedral oxygen environments. For zeolites ^{27}Al and ^{29}Si NMR clearly indicates that some of the aluminum, upon certain treatments escapes from tetrahedral positions in the lattice and acquires octahedral coordination in the presence of water.

In ^{1}H MAS NMR spectra of various acid and base catalysts (silicates and phosphates) signals from different surface OH-groups are often resolved. Comparison of the variations in the signals intensity with the catalysts composition can be used to assign the signals to OH-groups bound to certain elements. The concentration of more acidic OH-groups bound to aluminum is seen to be much higher in ZSM–5 zeolites than in amorphous alumosilicates with the same Si/Al ratio.

2.1 ^{51}V, ^{17}O and ^{23}Na NMR of Vanadium Catalysts for the Oxidation of Sulphur Dioxide[24–26]

These catalysts which are known to be of crucial importance for the industrial production of sulphuric acid consist of sulphate and pyrosulphate compounds of vanadium and alkali metals, usually potassium, which are supported on porous materials such as silica or silica-alumina. From the X-ray data for sulphates and pyrosulphates vanadium is known to be coordinated in these compounds to oxygen atoms being surrounded either by a regular or a distorted tetrahedron or by a distorted octahedron of these atoms.

When recorded at low frequencies ^{51}V NMR spectra of solids are usually rather complicated due to contributions from the dipole-dipole interactions, the quadrupole interactions and the anisotropy of chemical shift; all of which can be of the same order of magnitude[23,27]. However at high enough frequencies (79 MHz in our case) the effect of the quadrupole interactions of the second order is insignificant so that the spectra become much more simple and the anisotropy of ^{51}V chemical shift can be directly observed.

First, we have studied the ^{51}V NMR spectra for a variety of model vanadium compounds of known structure. In these studies for a large number of vanadium

compounds with surrounding oxygen it was demonstrated that the anisotropy of chemical shift was a characteristic of a particular vanadium environment. Fig. 2 presents some typical ^{51}V NMR spectra for vanadium in a regular tetrahedron (orthovanadates and pyrovanadates), in a distorted tetrahedron (methavanadates) and in a bipyramid environment (vanadium pentoxide and oxosulphovanadates*). For vanadium in a regular tetrahedron the spectrum is seen to be isotropic. The spectrum of vanadium, in a distorted tetrahedron, is characterized by an anisotropic chemical shift tensor (the corresponding computer simulated spectrum calculated for the best fitted parameters is shown in Fig. 2 with a dotted line). Vanadium in a distorted octahedron (bipyramid) environment demonstrates a spectrum with almost an axial symmetry[24,25].

For methavanadates of alkali metals a clear correlation between the anisotropy and the distortion of the tetrahedron of the oxygen atoms has been obse rved. Fig. 3 demonstrates the dependence of the chemical shift anisotropy on the O_3'-V-O_2 angle the deviation of which (from the value of 109°) characterizes the distortion of the tetrahedron from a regular one. At the same time the point for NH_4 $VO_3$is

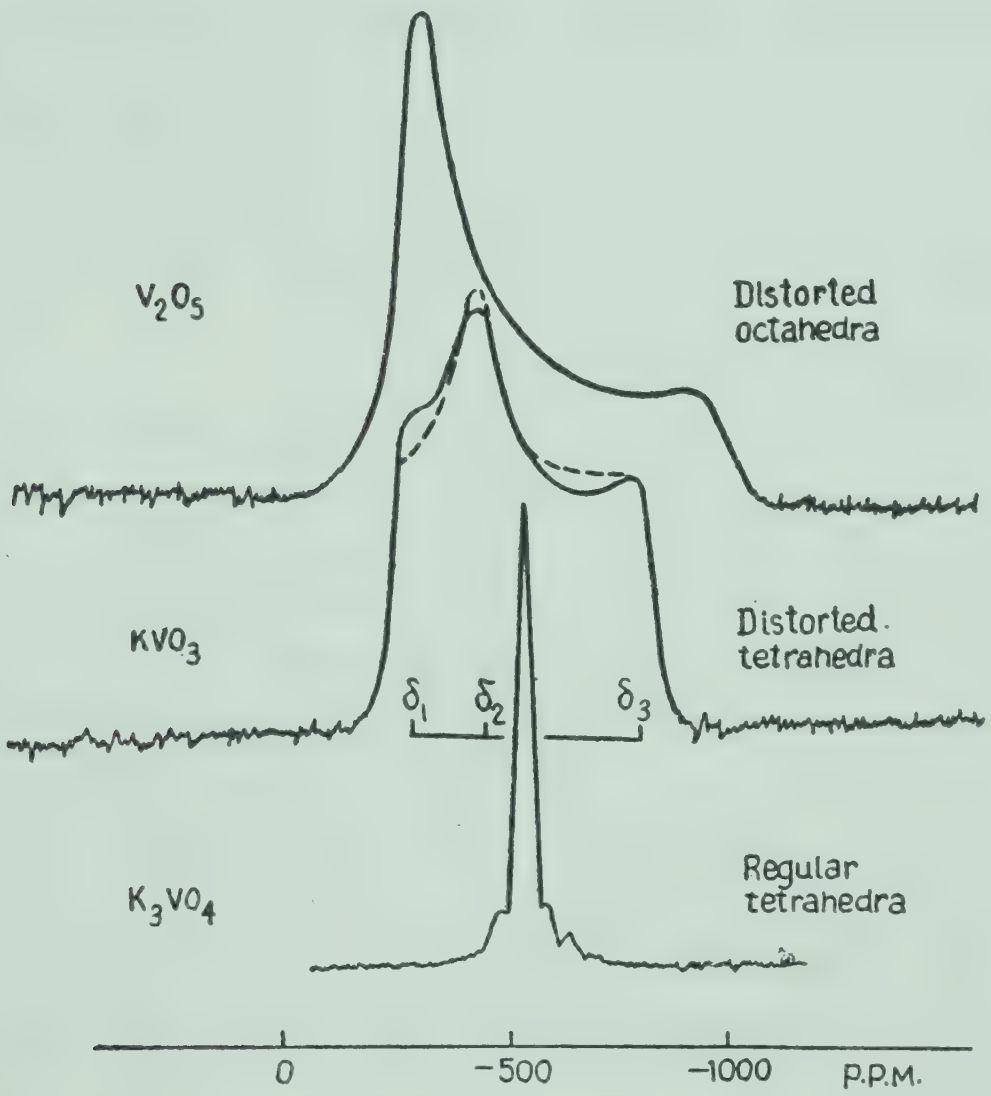

FIG. 2. The ^{51}V NMR spectra of vanadium compounds for various oxygen environments : from top to bottom :
V_2O_5-distorted octahedra,
KVO_3-distorted tetrahedra,
K_3VO_4-regular tetrahedra.

*In this and other figures ^{51}V chemical shifts are given relative to $VOCl_3$.

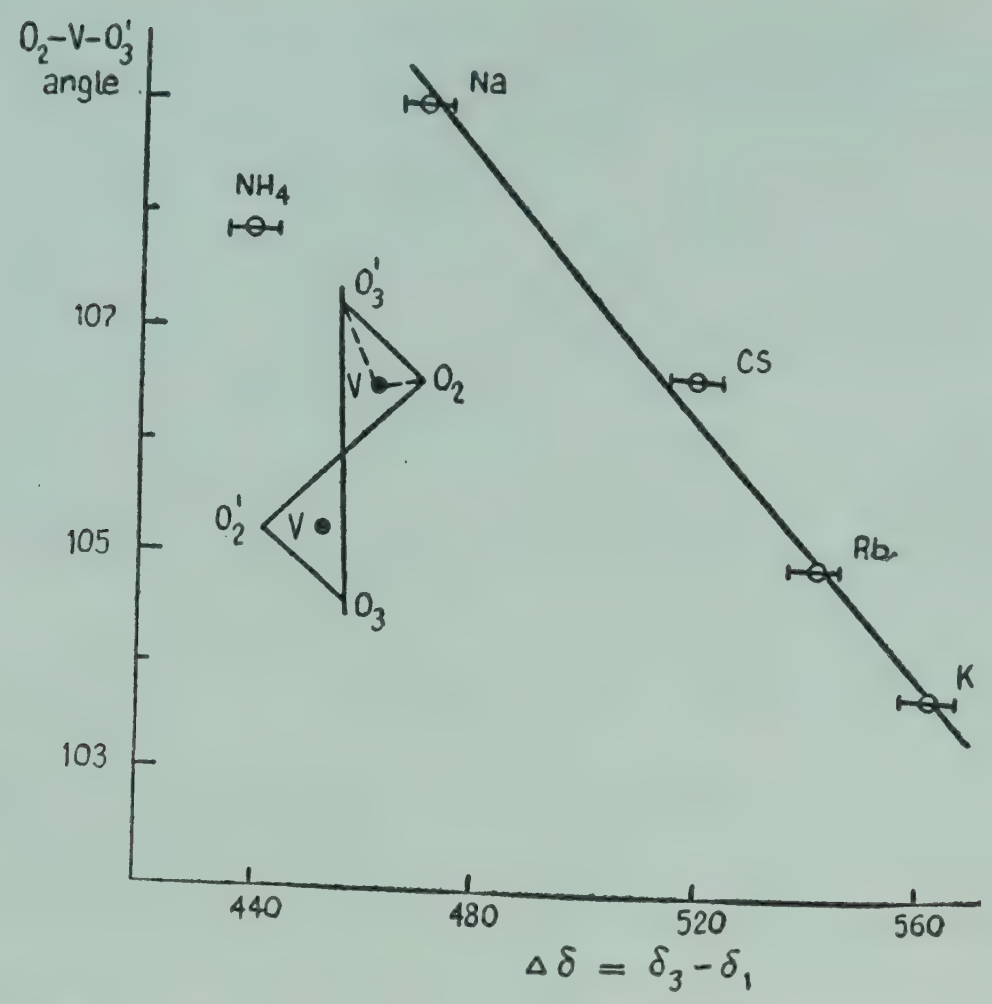

FIG. 3. Dependence of ^{51}V δ-tensor anisotropy on the tetrahedron distortion in MVO_3 compounds.

seen to notably deviate from this correlation towards a smaller value of the chemical shift anisotropy. Probably this fact reflects the decrease of the strength of the oxygen anions ligand field around vanadium cation in NH_4VO_3 as compared to that for methavanadates of alkali metals as a result of the hydrogen bond formation between the oxygen anions and NH_4^+ cations.

Consider now the ^{51}V spectra of the catalysts themselves. Before the treatment in the catalytic reaction the spectra of various industrial vanadium catalysts studied (BAV, IK-1, IK-1-6, KS) were found to be significantly different and to depend on the catalysts preparation procedure. However, the treatment of the catalysts under the catalytic reaction conditions was found to smooth these differences out[15]. This seems to indicate that an active component in all the catalysts studied is the same and is actually formed in the course of the catalytic reaction. Though the chemical nature of compounds which are responsible for the catalytic properties of vanadium catalysts is still under study it is possible to make some preliminary conclusions on this subject. First from the comparison of ^{51}V spectra of the catalysts with those for various oxosulphovanadates it seems possible to conclude that the compound $K_3VO_2(SO_4)(S_2O_7)$ is present in the industrial catalysts as the main component (see Fig. 4). The position and the shape of the line from this compound is typical for vanadium surrounded with a distorted octahedron of oxygen atoms (compare e.g. the bottom spectrum in Fig. 4 with the upper spectrum in Fig. 2).

But in the spectra of industrial catalysts there is also a line with a chemical shift of about −540 ppm which corresponds to vanadium in a regular tetrahedral coordination (see Fig. 4). We attributed this line to vanadium which interacts with the support-silica or silica-alumina[25]. Indeed, for vanadium pentoxide supported

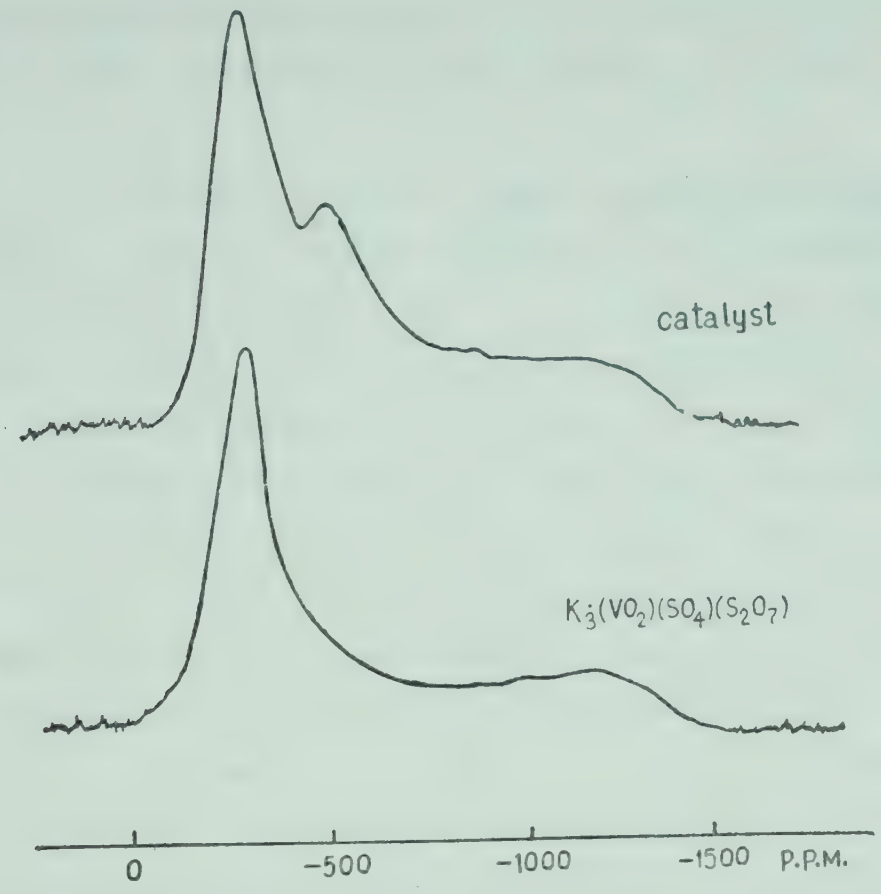

FIG. 4. Comparison of the ^{51}V spectrum of the industrial catalyst for the oxidation of SO_2 with the spectrum of oxosulphovanadate $K_3VO_2(SO_4)(S_2O_7)$.

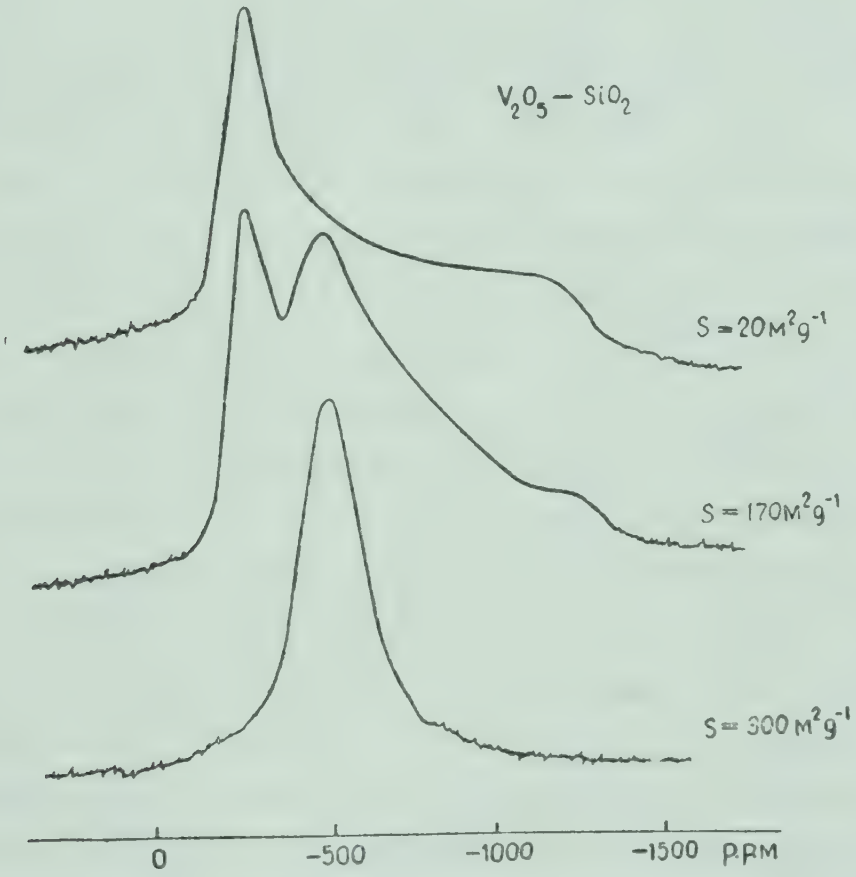

FIG. 5. Dependence of ^{51}V spectra of V_2O_5—SiO_2 on SiO_2 specific area.

on silica we observed the same line (see Fig. 5). The intensity of this line grew up dramatically when the surface of the silica support was increased, the amount of supported V_2O_5 remained the same (also see Fig. 5). The position and the shape of this line is typical for vanadium surrounded with a tetrahedron of oxygen atoms (compare e.g. the spectra in the bottoms of Figs. 2 and 5).

These data clearly show that the support is not an inert material but interacts chemically with the active component.

We assume that interactions of this type may be responsible for the well known dependence of the catalytic activity of the vanadium catalysts on the type of the support.

All the ^{51}V spectra presented above were recorded at room temperature when both the active component of the catalysts and the model vanadium compounds are in a solid state. These conditions are in fact quite different from the conditions existing at 400–500°C—the temperatures at which the catalysts for sulphur dioxide oxidation usually operate. At these high temperatures the active component exists not as a solid but as a melt forming a very thin liquid layer on the surface of the solid support. In this situation, the chemical composition of the catalysts that have been rapidly cooled from the reaction to room temperature though being dependent on their composition at the reaction temperature still perhaps can deviate from the latter due to the possible shift of the equilibrium between various states of vanadium upon cooling.

Having this in mind and utilizing the high sensitivity of modern NMR spectrometers we have recently studied vanadium catalysts for sulphur dioxide oxidation at temperatures as high as 500°C, i.e. under typical conditions at which these catalysts operate. Fig. 6 presents the ^{17}O NMR spectra of vanadium pentoxide-potassium pyrosulphate melts recorded at 500°C that were kept for a long time at this temperature under an atmosphere of the equilibrium $SO_3 \leftrightarrows SO_2 + 1/2O_2$ mixture with the initial pressure of SO_3 400 Torr. The atmosphere was generated by partial dissociation of pure SO_3 introduced into the samples at low temperature. The spectra were taken for various concentrations of vanadium in the melt. It is seen from Fig. 6 that both the chemical shift δ and the width of the ^{17}O NMR line $\Delta\nu$ are strongly dependent on the concentration of vanadium in the melt. This clearly indicates the coordination of the pyrosulphate anions present in the melt to vanadium cations. The following preliminary explanation of the data obtained can be suggested[26]. The character of the dependences on Fig. 6 can be understood if one e.g. assumes that the predominant part of the oxygen-containing anions ($S_2O_7^{2-}$ and SO_4^{2-} that perhaps are formed upon the interaction of $S_2O_7^{2-}$ with the oxygen atoms of V_2O_5) exists in the melts being either coordinated or noncoordinated to vanadium cations, the conditions for exchange of oxygen atoms between its various states being provided. A break on the curves of Fig. 6 at a vanadium concentration of about 1M seems to reflect the change in the state of vanadium complexes and can be tentatively attributed to the dimerization of the monomeric vanadium species—a process which is often assumed to exist at high vanadium concentrations on the ground of kinetic studies of the SO_2 oxidation process[28].

If one substitutes in the melts potassium for sodium it occurs possible to observed the ^{23}Na NMR of these melts as well. As a typical example Fig. 7 presents the spectra of $Na_2S_2O_7$—V_2O_5 melts obtained at 500°C and the dependence of the chemical shift of sodium-23 signal on the sodium to vanadium ratio. From these data the conclusion follows on the coordination of a part of sodium cations to pyrosulphate (or sulphate) anions that are already bound to vanadium cations, forming a sort of ionic complexes with vanadium-pyrosulphate (sulphate) compounds.

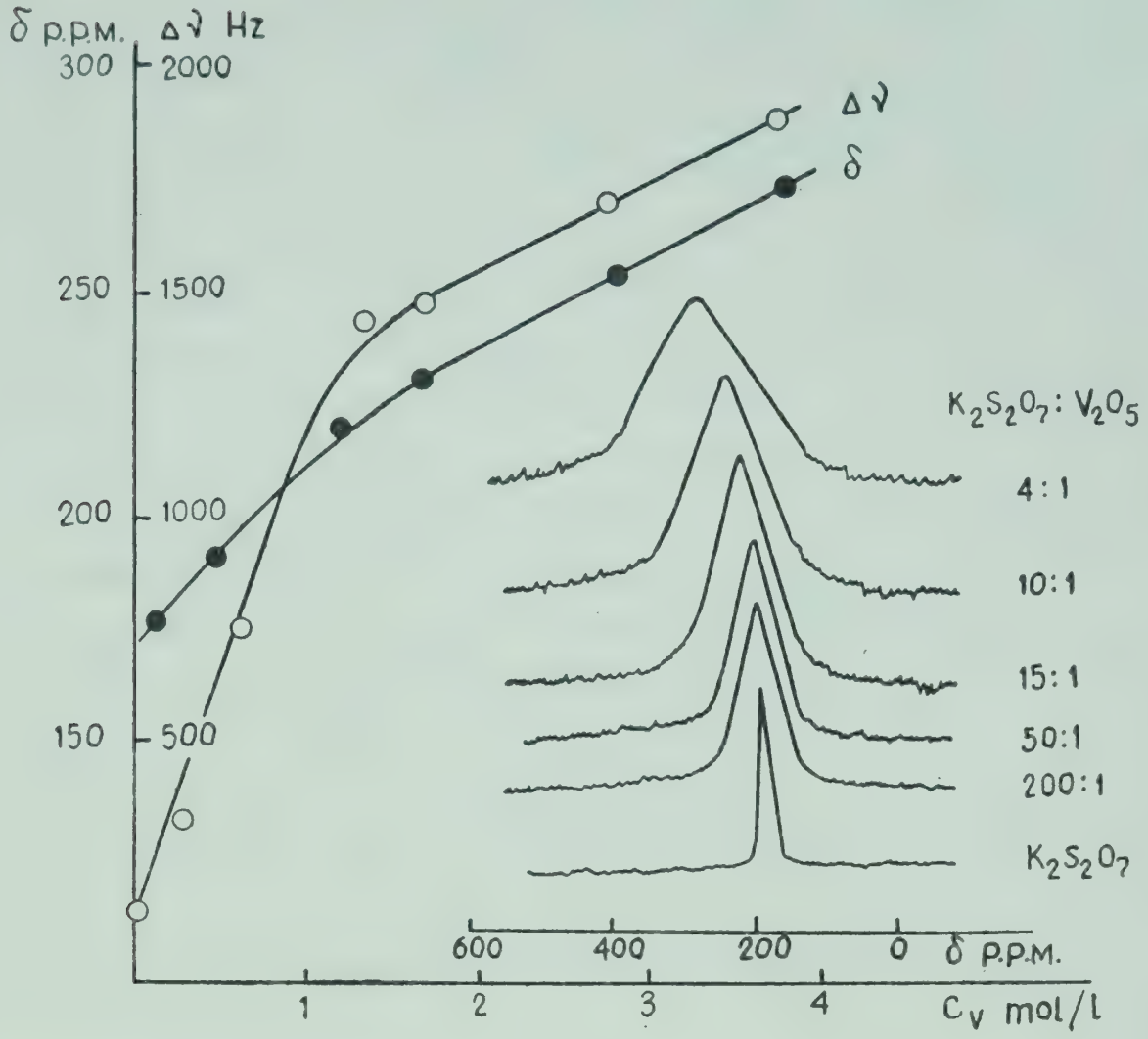

FIG. 6. Dependence of ^{17}O spectra of $K_2S_4O_7.nV_2O_5$ at 500°C in the SO_3 atmosphere (400 Torr) on vanadium concentration. δ is given relative to H_2O at 25°C.

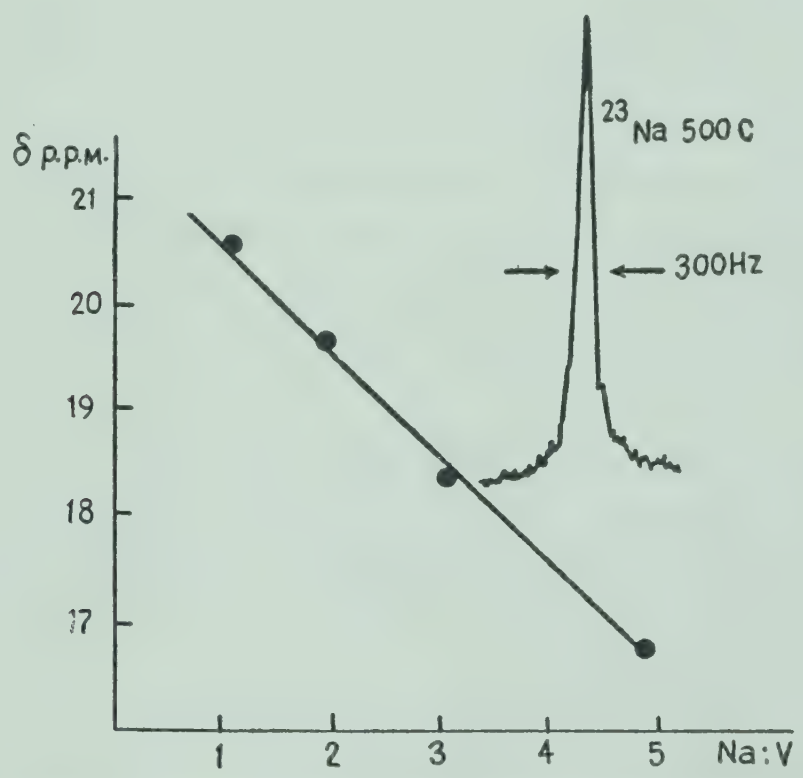

FIG. 7. ^{23}Na spectra of $Na_2S_2O_7.V_2O_5$ melt at 500°C and dependence of δ on Na: V ratio. δ is given relative to NaCl at 500°C.

The relatively small changes in the chemical shift and in the width of ^{23}Na NMR lines upon addition of vanadium agree with this model.

2.2 ^{27}Al and ^{29}Si NMR of Aluminas and Zeolites[29,14,15]

These compounds are famous for their remarkable properties in numerous catalytic transformations of hydrocarbons and of other organic compounds. Until

recently mainly ^{1}H NMR was used to study the hydroxyl groups in aluminas and zeolites. However, recently the use of ^{27}Al and ^{29}NMR at high frequencies together with magic angle spinning (MAS) was shown to open new possibilities in the study of these compounds[11,15,18–22,30]. The aluminum-27 NMR at low frequencies is strongly influenced by the second order quadrupole effects. As a result, in most cases the NMR line is extremely broad. For example, for dehydrated zeolites the linewidth is so large that it is very difficult to record it at the frequencies lower than 20 MHz. The measurements at much higher frequencies such as 78MHz allow one to suppress considerably the mentioned quadrupole effects and simultaneously provide both much higher sensitivity and much better resolution of ^{27}Al NMR spectra. Fig. 8 shows the spectrum of a dehydrated HY zeolite recorded at 78.18 MHz. The asymmetric line shape of this spectrum suggests that it probably contains two or more lines with different parameters from different aluminum sites of the zeolite. Further studies using MAS technique have earned support to this suggestion (see below). Note that elucidation of various aluminum states in catalysts is quite important for understanding of their catalytic properties.

In order to demonstrate the power of the MAS technique in improving the sensitivity and resolution of ^{27}Al NMR spectra consider first the results obtained for aluminas.

Fig. 9 presents the spectra of various aluminum oxides. It can be seen that the magic angle spinning indeed considerably sharpens the NMR lines. For example, for γ-alumina the line-width decreases by six times. This permits one to resolve the lines corresponding to tetrahedral and octahedral coordination of aluminum atoms. Indeed in the MAS spectrum of γ-alumina we observed two lines. Comparison of their positions with those for various aluminum compounds with oxygen environment in solution permits us to attribute the line in the low field to aluminum atoms in tetrahedral coordination, and the line in the high field-to aluminum atoms in octaheral coordination. Such attribution is supported by the spectrum of α-alumina which consists of a single line with the chemical shift corresponding to octahedral aluminum. Note that from X-ray data α-alumina indeed is known to contain aluminum atoms only in octahedral coordination. The relatively good resolution in the spectra of aluminas allows one in principle to find the relative content of aluminum in octahedral and tetrahedral coordinations. But it is necessary

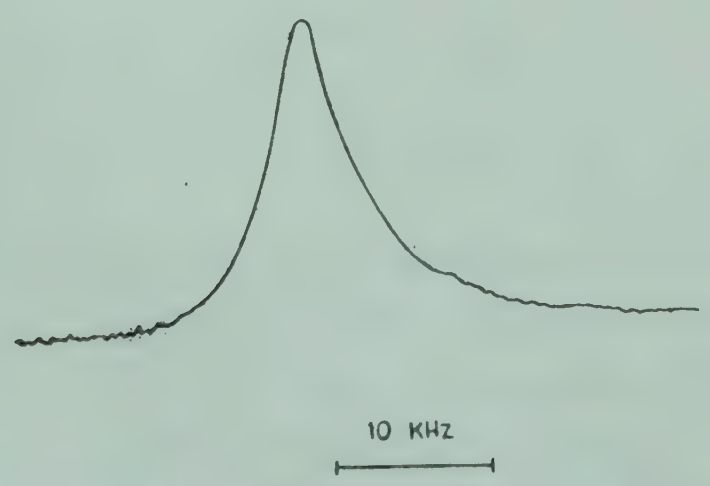

FIG. 8. The ^{27}Al NMR spectrum of a dehydrated HY-zeolite.

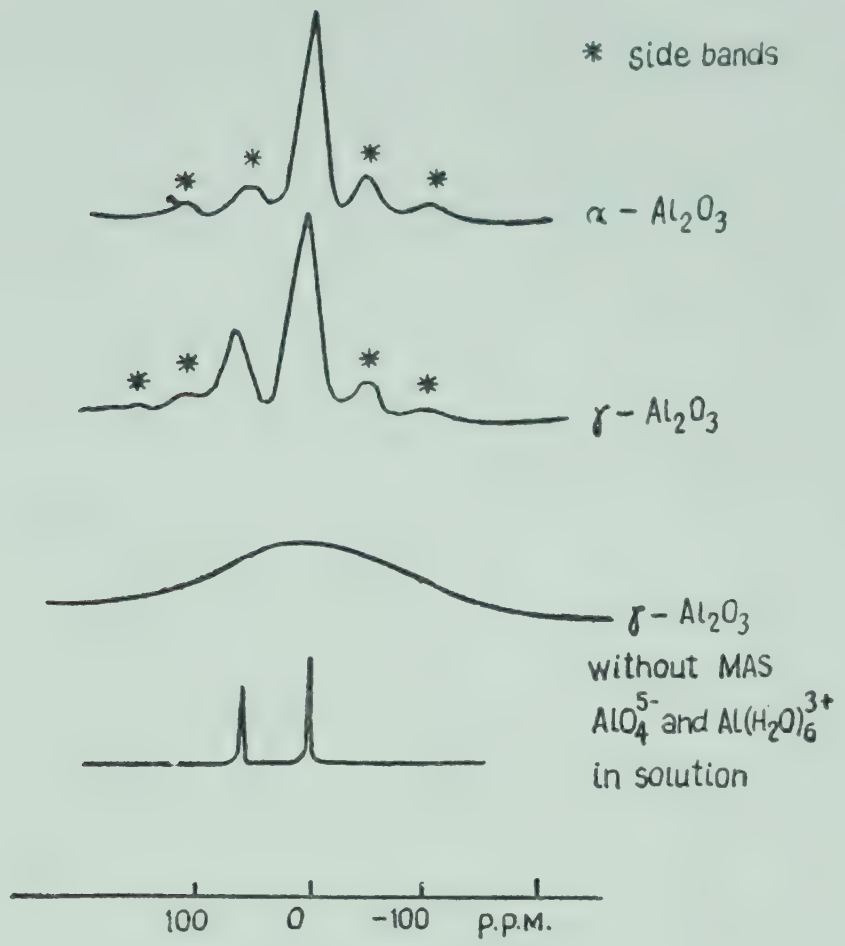

FIG. 9. ^{27}Al MAS spectra of aluminas.

to note that the quantitative calculations of this ratio are rather difficult due to the complicated line shape of ^{27}Al NMR spectra and the interference of the satelite lines.

Using ^{27}Al NMR (even without MAS) it was possible to resolve the lines from tetrahedral and octahedral sites also for aluminum atoms in zeolites. Fig. 10 shows that on the hydrothermal treatment of NH_4Y zeolite leading to ammonia elimination and formation of HY zeolite, part of aluminum content escapes from the tetrahedral position in the lattice into the zeolite cavity where they acquire an octahedral coordination in the presence of water. High temperature treatment leads to the destruction of the zeolite framework. This is reflected by the broadening of the lines.

The same processes can also be seen in ^{29}Si MAS spectra of the same zeolite samples. High resolution ^{29}Si NMR specra of these samples consist of four lines with chemical shifts from -85 ppm to -105 ppm relative to TMS (Fig. 11). These lines correspond, according to the data of[30], to silicon atoms having respectively 4, 3, 2, and 1 aluminum atoms in the second coordination sphere. The deammoniation of the zeolite is seen to redistribute the intensities of these lines in such a manner that the intensity of lines corresponding to silicon atoms with a small number of aluminum atoms in the second coordination sphere increases, while the intensity of those with a large number of aluminum atoms in the second coordination sphere decreases.

Such a behavior of ^{29}Si NMR spectra confirms the escaping of aluminum atoms from the zeolite lattice. After the high temperature treatment (above 700°C) ^{29}Si

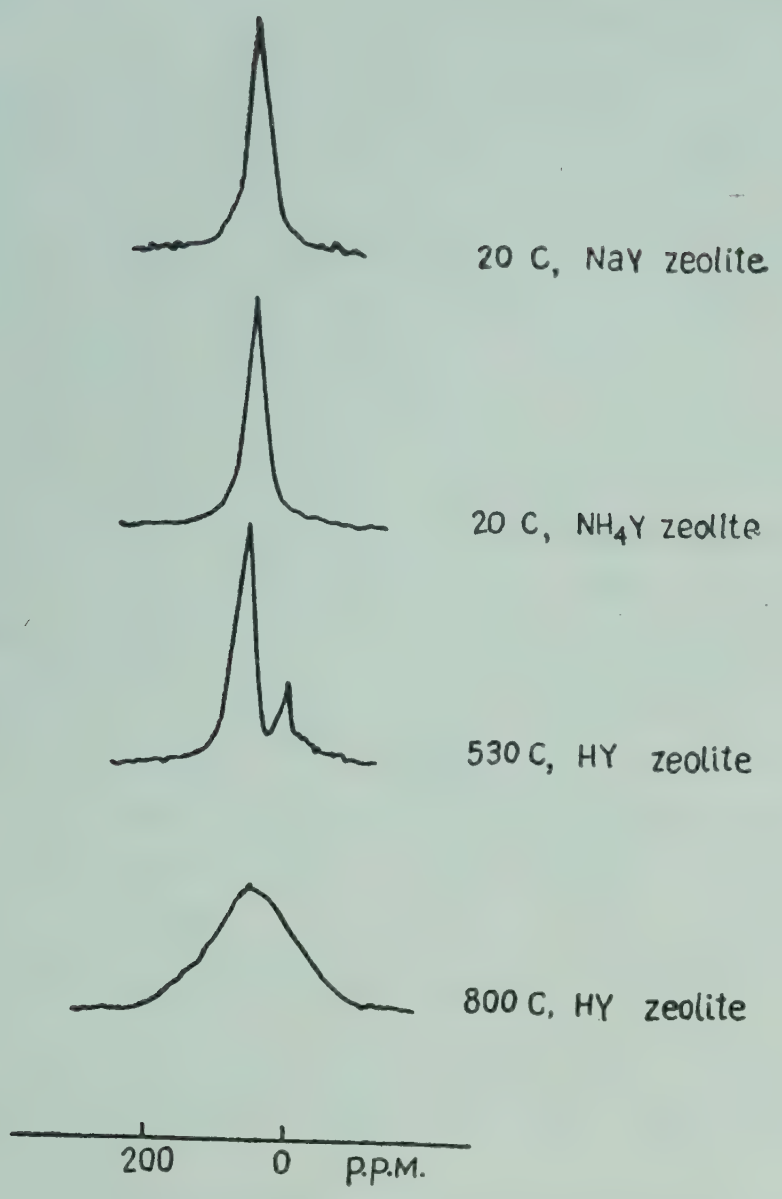

FIG. 10. ^{27}Al spectra of Y zeolites with Si/Al = 3,5 after treatment at various temperatures. δ is given relative to $Al(H_2O)_6^{3+}$ in water solution.

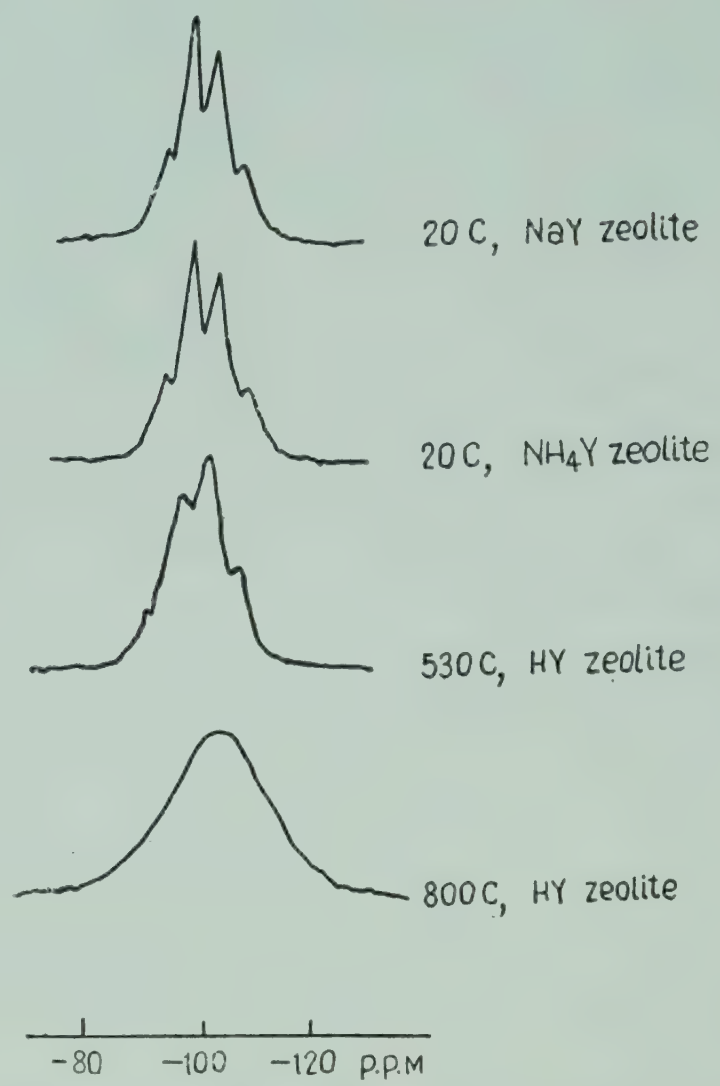

FIG. 11. ^{29}Si MAS spectra of Y zeolites with Si/Al = 3, 5 treated at various temperatures. δ is given relative to $Si(CH_3)_4$.

lines became broader due to the destruction of zeolite frame work just as it had been observed for ^{27}Al lines.

Note that the amount of aluminum escaping from the lattice into the cavity depends strongly upon the conditions of thermal treatment of the zeolites[14,15].

Other interesting results on ^{27}Al and ^{29}Si NMR of aluminas and zeolites have been recently presented in refs[18–22]. The main conclusions made in these works concerning the nature of various aluminum and silicon sites in these compounds seem to be similar to ours.

2.3 MAS ^{1}H NMR of Surface Hydroxyl Groups

The magic angle spinning permits one to resolve the lines from various hydroxyl protons on the surface of catalysts having acidic and basic properties[32].

Fig. 12 shows the spectra of ZSM zeolites with various aluminum-to-silicon ratio. Without spinning the spectra have a line width of about 4 kHz with no structure. The magic angle spinning decreases the line width six times. This permits one to resolve the spectra into two lines with the chemical shifts equal to 1.4 ppm and 4.5 ppm. The intensity of the line at 4.5 ppm increases with the increase of the alumiunm content in the zeolite and on this basis can be attributed to hydroxyls having the chemical bond with an aluminum atom. The line at 1.4 ppm belongs to

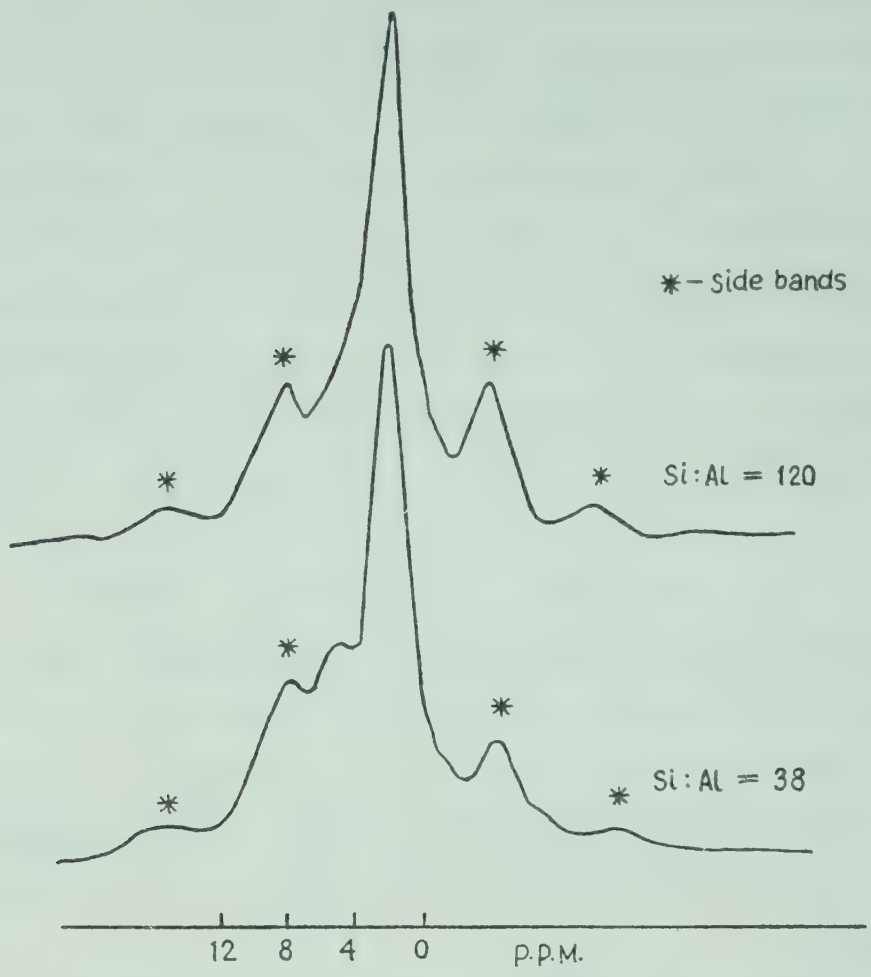

FIG. 12. ^1H MAS spectra of ZSM-5 zeolites with various Si-Al ratio.

Si-OH hydroxyls. This conclusion agrees with our observation that for the OH-groups in silica the ^1H NMR line has almost the same chemical shift of about 1.7 ppm. The position of a line attributed to OH-groups bound to aluminum atom in a low field can be naturally explained by lower electron density around the proton of this more acidic group. The chemical shifts of protons for various OH-groups of these and other oxide catalysts that we have studied are summarized in Table 1.

It is interesting that for all the amorphous silicates studied, including silica-alumina with the same aluminum content as in ZMS-5 catalysts of Fig. 12 no line with a chemical shift 4.5 ppm corresponding to hydroxyls having a bond with an

TABLE I

Chemical shifts of OH protons for silicate and phosphate catalysts

Catalyst	Chemical shift ppm relative to T. M. S. (± 0.1 ppm)
SiO_2	1.7
Al-Si (10% Al_2O_3)	1.5
Zr-Si (10% ZrO_2)	1.7
Ga-Si (20% Ga_2O_3)	1.7
Be-Si (20% BeO)	1.7
$AlPO_4$	1.2; 3.8
64% ZrO_2, 36% P_2O_5	2.9; 5.6
$Ca_3(PO_4)_2$	−0.3; 3.8
53% SnO_2, 47% P_2O_5	0.9; 4.4; 5.8
BPO_4	0.7; 5.6; 8.1

aluminum atom was observed in the ^1H NMR spectra. This seems to indicate a much higher concentration of such hydroxyls in ZSM-5 zeolites than in amorphous silicates of the same chemical composition. Also note that the phosphate catalysts are seen to have several different hydroxyl groups. It seems reasonable to attribute the lines with chemical shifts 3.5–8 ppm to acidic P-OH hydroxyls of various types.

The lines at around 1 ppm can be attributed to OH-groups having a bond to elements other than phosphorus. Note that for calcium phosphate the shielding of the hydroxyl protons at -0.3 ppm is the largest observed for the catalysts studied. This seems to reflect a high basicity of Ca-OH hydroxyls.

3. The Study of Adsorbed Species

Spectra of adsorbed molecules are usually very broad, due to the low mobility of these species. This often leads to the loss of information on chemical shifts and spin-spin coupling constants and to a very poor signal to noise ratio. Such techniques as the use of multipulse sequences, magic angle spinning and the use of carbon-13 and nitrogen-15 rather than of ^1H NMR often makes it possible to overcome these difficulties.

In this section the results are presented showing the efficiency of MAS ^1H NMR and ^{13}C NMR in the study of some adsorbed species, that are typical for heterogeneous catalysis. NMR data are used to study the mechanisms of propylene chemisorption on γ-Al_2O_3, methane adsorption on modified H-ZSM-5 zeolite. H_2 and CO adsorption and reaction on supported Rh/La_2O_3 catalyst.

A model for C_3H_6 adsorption is proposed that explains the variations of ^1H and ^{13}C chemical shifts for C_3H_6 upon the change of surface coverage and the conditions of pretreatment of γ-Al_2O_3 in terms of fast equilibrium between physisorbed and chemisorbed propylene and its chemisorption on aluminum sites rather than on hydroxyl or oxygen sites. A notable decrease $J_{^{13}C-^1H}$ coupling constants for various groups of C_3H_6 seems to indicate a weakening of C-H bonds upon chemisorption.

A notable change of ^{13}C chemical shift and $J_{^{13}C-^1H}$ coupling constant for methane are observed upon its adsorption on modified H-ZSM-5 zeolite. This seems to indicate a notable perturbation of CH_4 molecule upon its adsorption on this zeolite.

For the reaction between H_2 and CO over Rh/La_2O_3 catalyst several species, such as physisorbed H_2, a hydride, water, alcohols, hydrocarbons etc, that are formed upon adsorption of the reagents as well as of intermediate and final reaction products on the catalyst surface are observed and some of them are identified.

3.1 MAS ^1H NMR and ^{13}C NMR of Propylene Adsorbed on γ-Al_2O_3

The ^1H and ^{13}C spectra of propylene adsorbed on γ-alumina are presented in Fig. 13 and Fig. 14. The upper spectrum in Fig. 13 is obtained without rotation, the spectrum below-upon rotation at a frequency of about 2 kHz. Without rotation each line has a width of about 500 Hz. This does not permit to resolve the

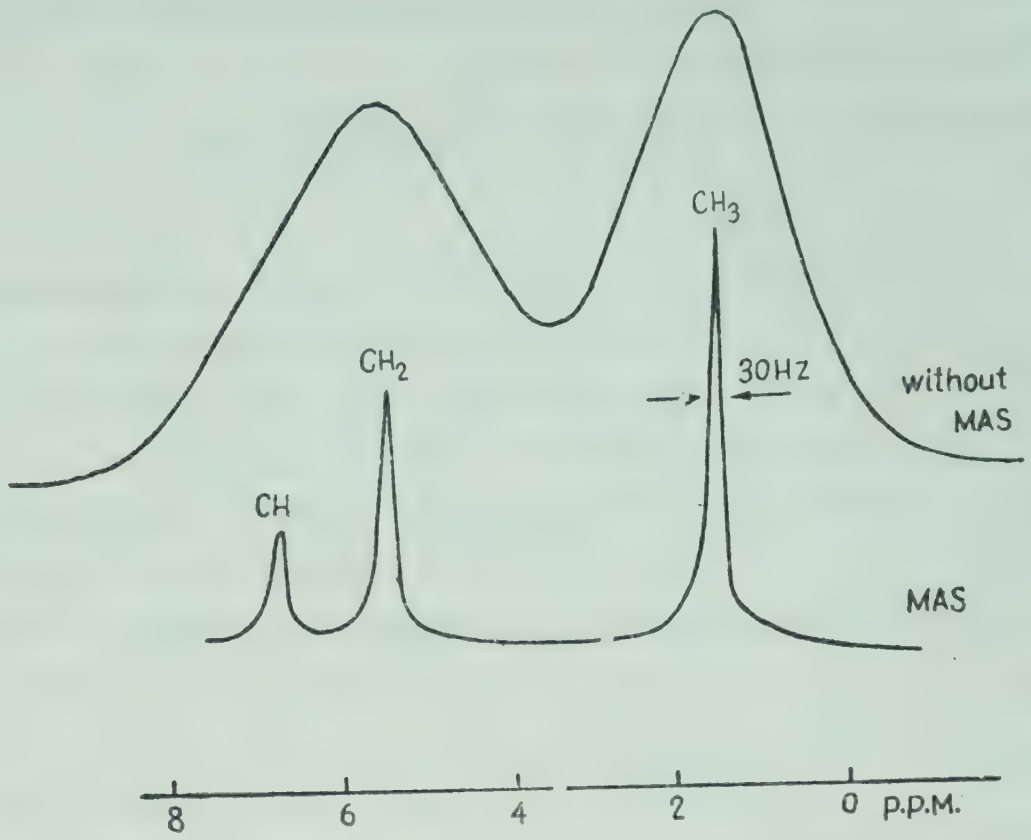

FIG. 13. Effect of MAS on ^{1}H spectra of propylene adsorbed on γ-alumina.

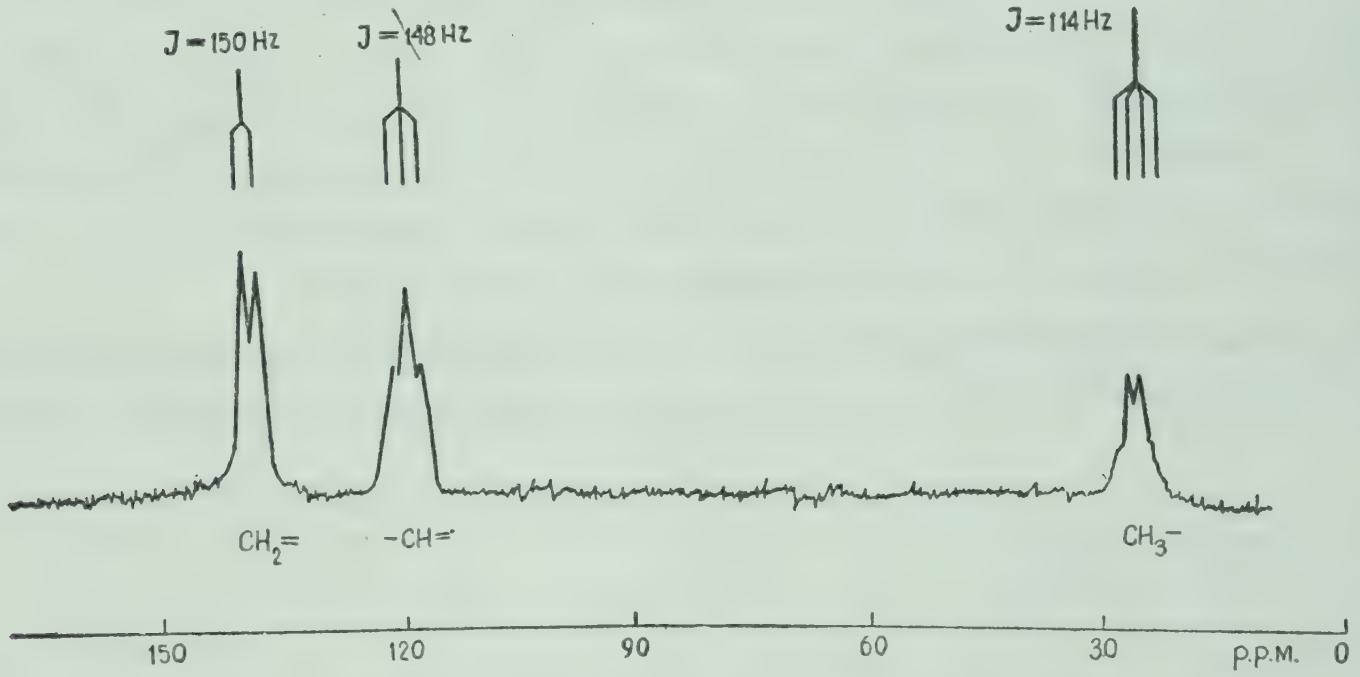

FIG. 14. ^{13}C NMR spectrum of propylene adsorbed on γ-alumina ($A_0 = 0.9 \times 10^{14}$ cm^{-2}), obtained without ^{1}H-^{13}C decoupling.

lines from $-CH =$ and CH_2—protons. On rotation, the line width decreases about 20 times. All the lines are seen now separately; the accuracy of chemical shift determination being upto ± 0.02 ppm at high surface coverage. For this system we observed the shift of all resonance lines towards the low field as compared to the spectrum of gaseous propylene. The largest shift in both proton and carbon-13 spectra is observed for $-CH =$ -group.

The dependences of the chemical shift on the γ-Al_2O_3 surface coverage with propylene are similar for all the three lines in both ^{1}H and ^{13}C spectra and have a

character typical for the situation of fast exchange between the physisorbed and chemisorbed states of propylene.

These dependences are well described with the formula

$$\delta = \delta_0 nK/(1 + KA_0) \qquad ...(1)$$

which corresponds to a chemisorption of C_3H_6 on active sites with the formation of complexes with a 1 : 1 composition (see e.g. the dependences of Fig. 15 for the ^{13}C chemical shifts of the $-CH=$ group). In this formula δ is the observed chemical shift of a given nucleus relative to the line of C_3H_6 in the gas phase, δ_0- the chemical shift of the same nucleus in the chemisorbed C_3H_6 molecule relative to the gaseous C_3H_6 molecule, K—the equilibrium constant for the propylene transition from the physisorbed to the chemisorbed state upon the reaction with the chemisorption sites Z :

$$(C_3H_6)_{phys} + Z \rightleftarrows (C_3H_6)_{chem},$$

n—the concentration of the chemisorption sites,

A_0—the total concentration of adsorbed molecules.

Formula (1) is valid for $n \ll A_0$ (see references[14,15] for more detail).

From the dependences of the chemical shift on the coverage we have found the equilibrium constant K (which, as was expected, occured to be the same for all the six lines in ^1H and ^{13}C spectra) and the product $\delta_0 n$ of the chemical shift in the chemisorbed state by the number of the surface chemisorption sites. The equilibrium constant K was found to be independent of the temperature of the preliminary thermovacuum treatment of γ-Al_2O_3 but the product $\delta_0 n$ for all the lines was found to increase as the temperature of the treatment was increased.

This seems to indicate that the sites of the propylene chemisorption are unsaturated aluminum ions (the concentration of these ions is expected to be the more

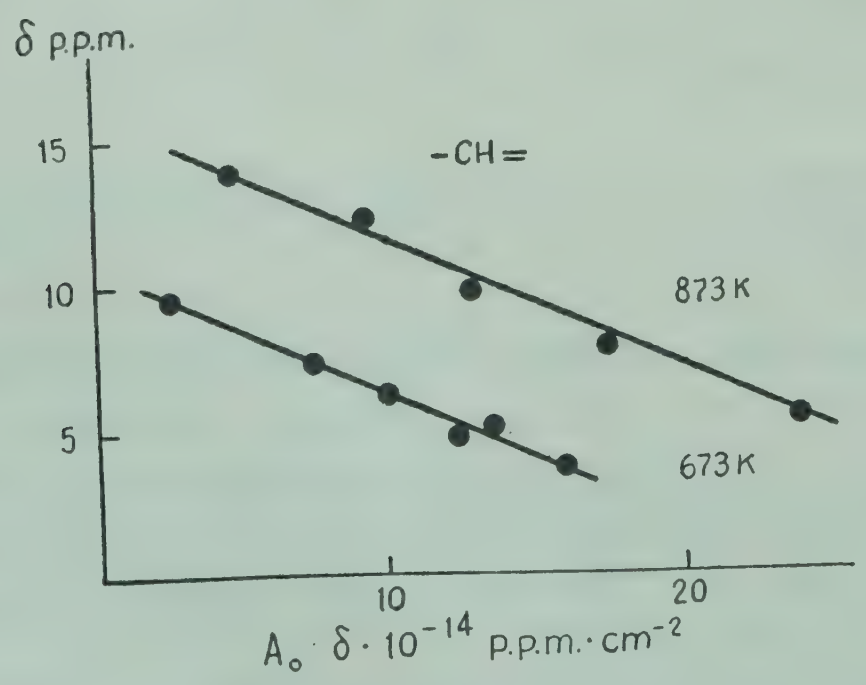

FIG. 15. Dependence of ^{13}C chemical shift of adsorbed propylene on $A_0.\delta$ for various pretreatment temperatures.

the higher is the temperature of the treatment) rather than the surface OH-groups or oxygen atoms (the concentration of which is expected to go down with the increase of the temperature of the treatment). We have also observed a notable decrease of carbon-13- proton coupling constants $J_{^{13}C-^{1}H}$ for all the groups of the chemisorbed propylene compared with the gaseous propylene, the largest decrease being observed for the methyl group (see Table 2). Note that for hydrocarbons the decrease of the J_{C-H} coupling constant is known usually to reflect the increase of the C-H interatomic distance and the corresponding weakening of the C-H bond[33]. These experimental data on the chemical shifts and the spin-spin coupling constants variation upon C_3H_6 chemisorption when compared with the MINDO/3 calculations of various adsorption structures[34] (see also Table 3) permit one to suggest a probable model for propylene chemisorption on γ-Al_2O_3. According to this model propylene is bound to the surface via two types of interaction : the interaction of the π-electrons of the double bond with the aluminum atom and the hydrogen-bond-type interaction of the methyl group hydrogen atoms with surface oxygen atoms.

TABLE II

Variation of $^{1}H - ^{13}C$ coupling constants with the coverage for adsorbed propylene

	Coverage $A_0 \times 10^{-14}$ cm^{-2}	$J_{^{13}C-^{1}H}$, Hz		
		CH_3-	$CH_2=$	$-CH=$
GAS		125	156	152
Propylene on	2.5	122	153	150
γ-Al_2O_3	1.5	118	151	148
	0.9	114	150	148

TABLE III

*MINDO/3 calculation of adsorbed propylene**

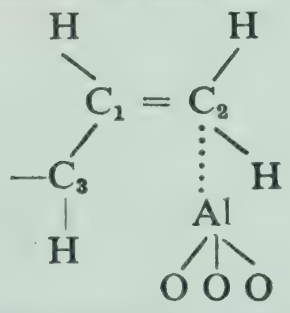
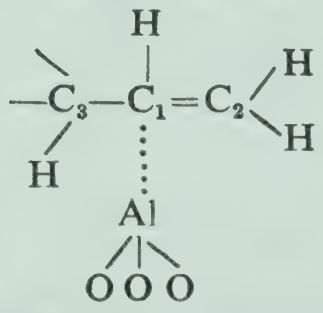
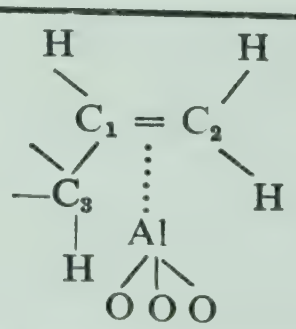

Heat of adsorb. kJ mol^{-1}	46	29	55
$\rho_\delta(C_1)$	1.234	1.276	1.245
$\rho_\delta(C_2)$	1.247	1.206	1.219
$\rho_\pi(C_1)$	1.033	0.831	0.935
$\rho_\pi(C_2)$	0.772	0.987	0.872
$\delta C_1/\delta C_2$	0.13	—24	1.6**

* ρ_δ and ρ_π are charge densities on δ- and π-orbitals respectively.
** best fitted to experimental value $\delta C_1/\delta C_2 = 2.0$.

3.2 MAS ^{13}C NMR of Methane Adsorbed on Modified H-ESM-5 Zeolite[35]

The ^{13}C spectra of methane adsorbed on modified H-ZSM-5 zeolite with the ratio Si/Al = 36 are presented in Fig. 16. The upper spectrum was obtained without rotation, the lower one with a rotation frequency of about 2.5 kHz. It can be seen from these spectra that the rotation sharpens the lines considerably. An interesting feature of the MAS ^{13}C spectrum is the possibility to observe simultaneously the lines for the adsorbed methane and those for the gaseous methane. In this case it is convenient to use the signal of the gaseous methane as a reference for the determination of the chemical shift for the adsorbed methane. It is seen that the signal from the adsorbed state is shifted to the low field. The carbonhydrogen coupling constant was found to decrease upon adsorption by approximately 10 Hz. This seems to indicate the formation of a bond between methane and some surface centers, which makes the C-H bonds in adsorbed CH_4 molecules longer than in free CH_4 molecules. Note that modified H-ZSM-5 zeolites were recently found to serve as catalysts for methane oxidative coupling reactions leading to formation of more heavy hydrocarbons[36].

Further studies are expected to provide more information on the structure of the observed methane surface complex and its role in methane activation on H-ZSM-5 catalysts.

3.3 ^{1}H and ^{13}C NMR Study of the Reaction Between H_2 and CO over a Rh/La_2O_3 Catalyst[37,38]

Fig. 17 presents the proton NMR spectrum which is observed when molecular hydrogen is adsorbed on Rh/La_2O_3 catalyst. The spectrum consists of three lines—

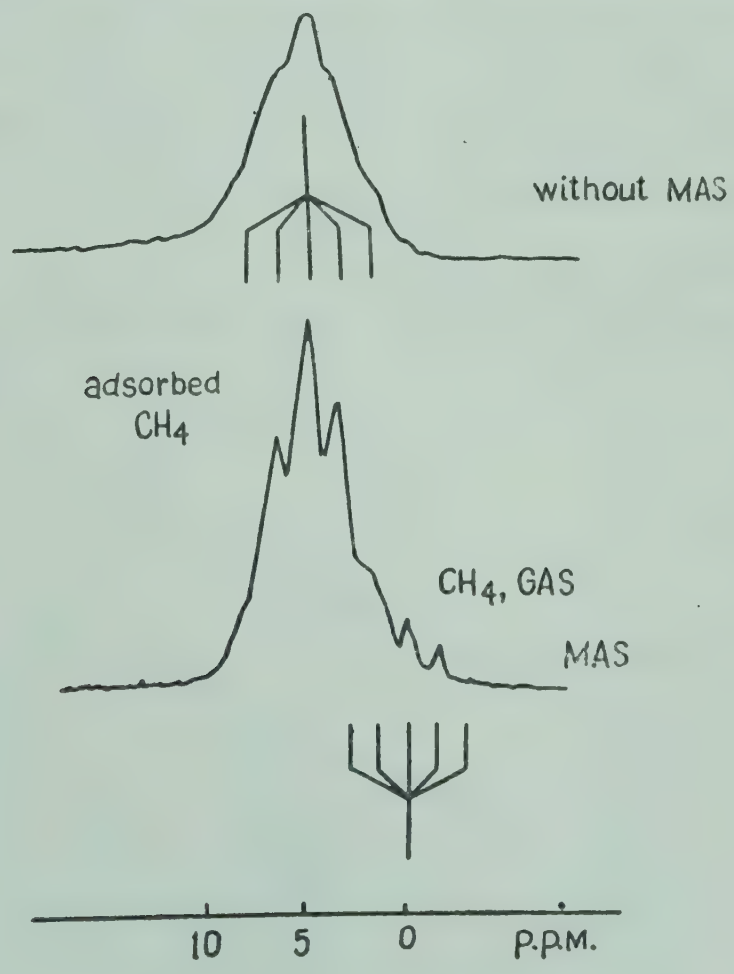

FIG. 16. Effect of MAS on ^{13}C spectra of CH_4 adsorbed on modified H-ZSM-5-zeolite with Si/Al = 36. Spectra are obtained without ^{1}H-^{13}C decoupling.
The lines at high field belong to gaseous methane.

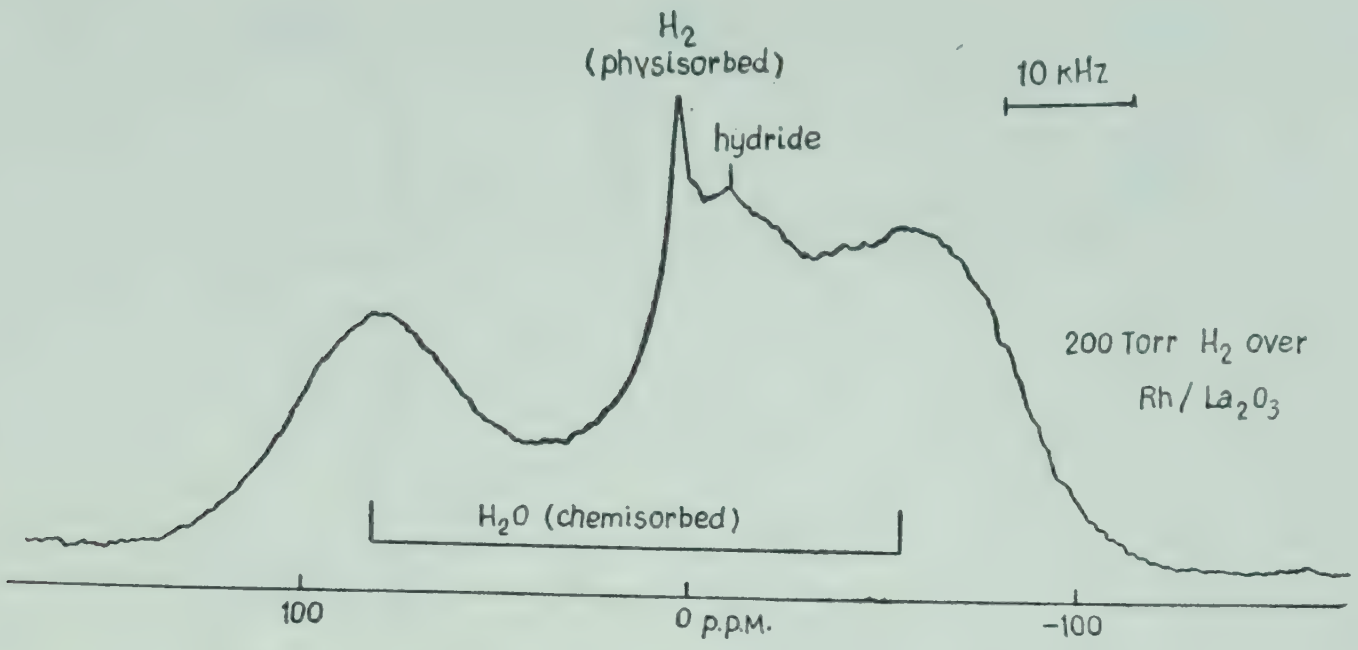

FIG. 17. ^1H spectra of hydrogen adsorbed on Rh/La_2O_3.

a line with a chemical shift $-10 + -15$ ppm from the surface hydride, a Pake doublet (i.e. a doublet resulting from the dipole-dipole interaction of the nuclear spins of two protons) line with the splitting of 44 kHz from water molecules which are formed as a result of the reaction between hydrogen and the support La_2O_3 and a narrow line from physically adsorbed molecular hydrogen. The spectrum clearly indicates that on Rh/La_2O_3 catalyst the activation of dihydrogen takes place with the formation of a hydride. Subsequent spillover of the activated hydrogen to the support leads to the reduction of its surface. The water molecules formed in this process are strongly bound to metallic rhodium (see reference[37] for more detail). Thus ^1H NMR spectrum allows one to observe directly the processes of dihydrogen activation and of the spillover of the activated hydrogen to the support in supported metal catalysts.

Using carbon monoxide enriched with ^{13}C isotope it was possible to elucidate also the species that are formed when pure CO or $CO + H_2$ mixtures of various compositions are adsorbed on the Rh/La_2O_3 catalyst.

Fig. 18 presents the spectra that are observed when CO enriched by 90 per cent with the ^{13}C isotope is adsorbed on La_2O_3, Rh/La_2O_3 and Rh/SiO_2 surfaces. Note first that for carbon monoxide adsorbed at room temperature on clean SiO_2 only a single and rather narrow line (with the chemical shift of 184 ppm and the linewidth of 600 Hz) of a weakly adsorbed CO was observed. This line was easily removed upon evacuation of the sample. In contrast to this adsorption of CO on La_2O_3 at 293 K resulted in the appearance of a much broader line from much stronger bound species. With time, the width of this line increased (see the two lower spectra in the left side of Fig. 18). Heating of the sample up to 423 K resulted in a further broadening of the line and its shift towards low field. Note that the values of chemical shift in the region 180–250 ppm observed for CO adsorbed on La_2O_3 are characteristics for carbon atoms of metal carbonyls or in aldehyde groups. Thus, in the species formed upon their adsorption on La_2O_3 the CO molecules seem to retain a carbonyl-type structure.

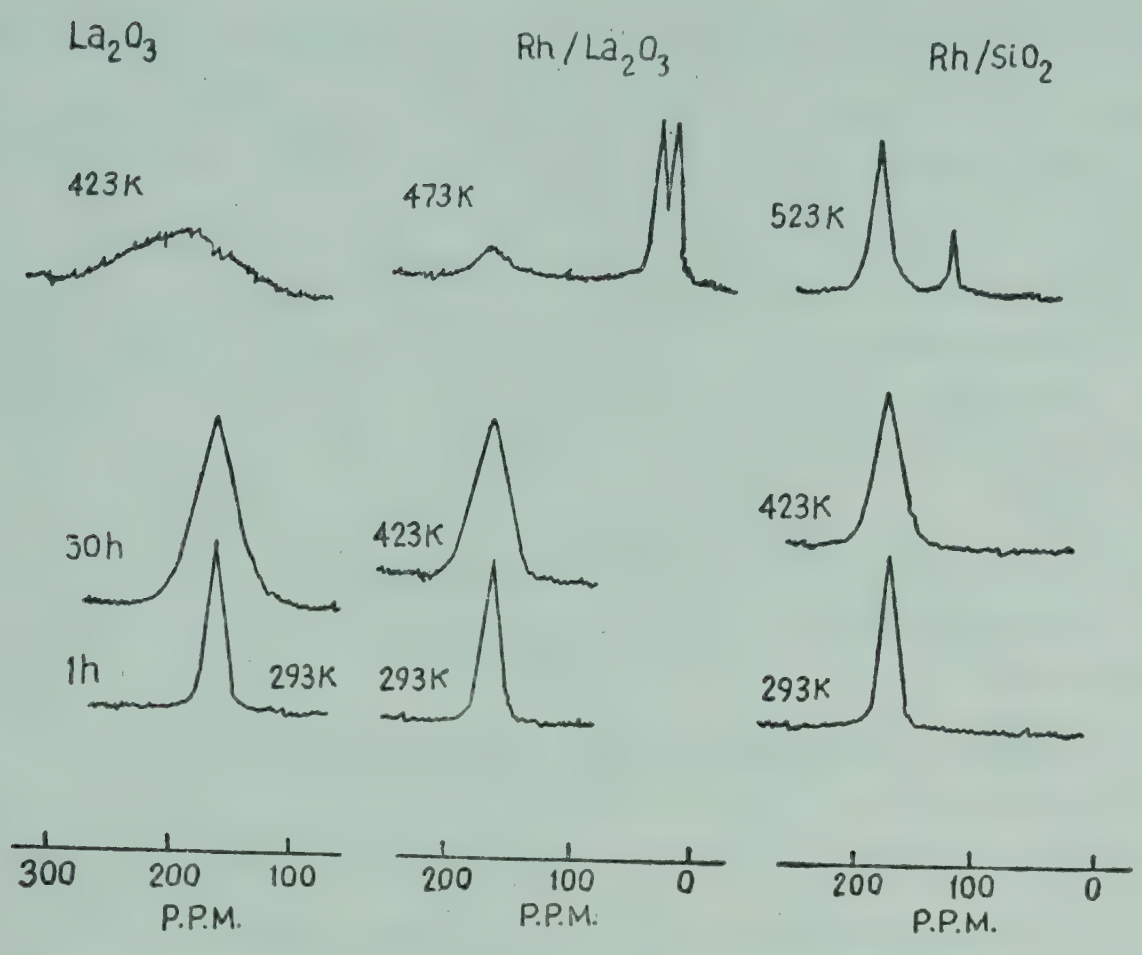

FIG. 18. ^{13}C NMR spectra of CO adsorbed on La_2O_3, Rh/La_2O_3 and Rh/SiO_2.

The ^{13}C NMR spectra for CO adsorbed on Rh/La_2O_3 catalyst at 293 K and 423 K are also typical for carbonyl-type species. But further heating of these samples resulted in the formation of saturated hydrocarbons (see the lines in the high field of the corresponding spectrum in Fig. 18) presumably via the reactions of these carbonyl species with the hydroxyl groups of the surface or water molecules which are perhaps present in the catalyst.

In a similar experiment with Rh/SiO_2 ethylene rather than alkanes was the main reaction product, the extent of transformation of carbonyl species to hydrocarbon species being much less than for Rh/La_2O_3 catalyst.

Fig. 19 presents the ^{13}C NMR spectra observed during the reaction of CO with H_2 over the Rh/La_2O_3 catalyst. As is seen from this figure the interaction of carbon monoxide with hydrogen for both $CO : H_2 = 1 : 3$ and $CO : H_2 = 1 : 1$ mixtures is seen to start from the formation of carbonyl type species having ^{13}C NMR lines at 180–200 ppm.

These species are the only ones observed with NMR up to temperature as high as 353 K. The hydrogenation of these species in a hydrogen excess (mixture $CO : H_2 = 1 : 3$) at 473 K leads to the formation of alcohols (broad lines in the region 20–100 ppm). At 513 K the alcohols are seen to be dehydrated to produce hydrocarbons (lines at 10–50 ppm) which, in turn, undergo further hydrogenolysis to methane at 533 K.

At a lower partial pressure of hydrogen ($CO : H_2 = 1 : 1$) at temperatures above 473 K we observed the formation of a large amount of oxygen-containing

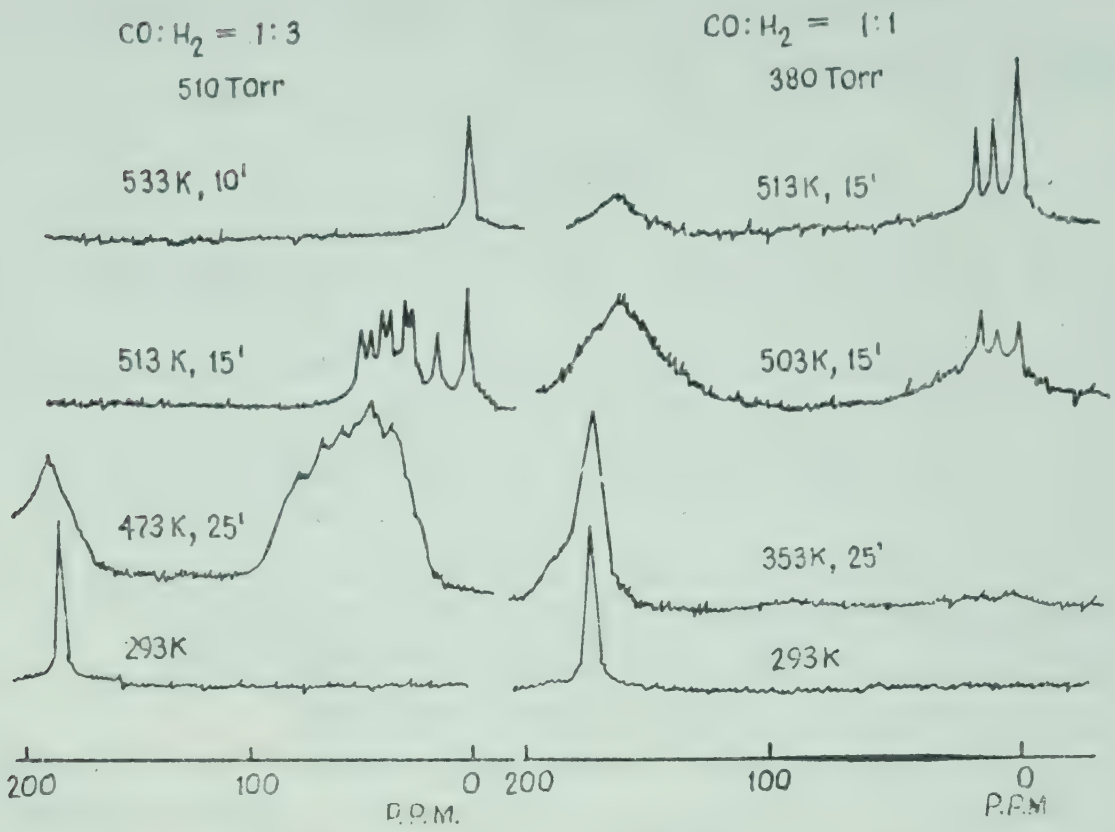

FIG. 19. ^{13}C NMR spectra of CO + H_2 reaction products on Rh/La_2O_3.

compounds which seem to contain carbonyl-type fragments (lines at 180–220 ppm), formiate-type fragments (lines at 150–180 ppm) and alkyl groups (lines at 5–30 ppm). The formation of these compounds is most probably, related to the condensation of the carbonyl-containing compounds at a hydrogen deficiency. However, as the temperature was raised, the final products observed with NMR were again predominantly the saturated hydrocarbons.

Assignments of the signals presented in Fig. 17–19 to adsorbed water, alcohols and hydrocarbons have been confirmed by observing these compounds in the products of the catalytic reaction at the same temperatures. |————————————| |————————————| Assignments of the signals from H_2O, alcohols and CH_4 have been also directly confirmed by observing the same NMR signals upon adsorption of these compounds on Rh/La_2O_3 catalyst in the absence of CO and H_2.

These examples demonstrate the possibility of the study of intermediate products of heterogeneous catalytic reactions using NMR. Other very interesting examples of such studies can be found also in references[12,39,40].

Thus, the use of modern Fourier Transform NMR Spectrometers operating at high frequencies and having special devices for magic angle spinning indeed open up qualitatively new possibilities both for the study of the structure of solid catalysts and for investigation of adsorption and surface reactions.

ACKNOWLEDGEMENTS

The authors are expressing their deep thanks to the coworkers from the Laboratory of the Mechanisms of the Catalytic Reactions : Drs O B Lapina, I L Mudrakovsky, V M Nekipelov and AA Shubin, as well ast o the colleagues from other laboratories of the Institute of Catalysis : Professors. Yu I Yermakov, K G Ione, Drs V B Fenelonov, V L Kunetsov, V S Kotsarenko, L G Karaktchiev, A V Romanenko, S V Shepelev,

L G Simonova, V G Stepanov for the most valuable contributions made to the studies reviewed in this paper.

References

1. D Deininger and D Michel, *Wiss. Z. Karl Marks Uni. Leipzig, Math. Naturwiss. Reihe,* **22** (1973) 551.
2. R W Vaughan, L B Schreiber and J A Schwarz, *International Symposium on Magnetic Resonance in Colloid and Interface Science,* San Francisco, reprint (1976) N 34.
3. T M Duncan and R W Vaughan, *Journal of Catalysis* **67** (1981) p. 975.
4. T M Duncan, J T Yates and R W Vaughan, *J. Chem. Phys.* **73** (1980) p. 49.
5. C Slichter, *Surface Sci.* **106** (1981) 382.
6. D Freude, McHunger and H Pfeifer, *Chem. Phys. Lett.* **91** (1982) 307.
7. G E Maciel and D W Sindorf, *Jour. Am. Chem. Soc.* **102** (1980) 7606.
8. W H Dawson and S W Kaiser, *J. Phys. Chem.* **86** (1982) 867.
9. D Michel, A Germanus and H Pfeifer, *J. Fan. Soc., Faraday Trans.* 1 **78** (1982) 237.
10. M D Sefcik, J Shaffer and E O Steijskal, *Symposium* on *Magnetic Resonance in Colloid and Interface Science,* San Francisco (1976).
11. I D Gay and S Liang, *Journ. of Catalysis* **44** (1976) 306.
12. E G Derouane, I B Nagy and C Naccache, *Journ. of Catalysis* **53** (1978) 40.
13. D Derney, V M Mastikhin, S Namba and J Turkevich, *J. Phys. Chem.* **82** (1978) 1752.
14. V M Mastikhin, A A Shubin, V M Nekipelov and K I Zamaraev, *Kinetika i Kataliz,* **24** (1983) 756.
15. V M Mastikhin, V M Nekipelpelov and K I Zamaraev, *Kinetika i Kataliz* **23** (1982) 1323.
16. S Schramm, R J Kirkpatrick and E Oldfield, *Journ. Am. Chem. Soc.* **105** (1983) 2483.
17. M A Fedotov and G F Gerasimova, *React. Kinet. Catal. Lett.* **22** (1983) 113.
18. J Klinowski, I M Thomas, C A Eyfe and G C Gobby, *Nature* **296** (1982) 533.
19. I M Thomas, L A Bursill, E A Lodge, A K Cheetham and C A Fyfe, *J. Chem. Soc., Chem. Comm.* (1981) 276.
20. J Klinowski, A M Thomas, C A Fyfe and J S Hartmann, *F. Phys. Chem.* **85** (1981) 2590.
21. T M Melchior, D E Vaughan and A J Jacobson, *Journ. Amer. Chem. Soc.* **104** (1982) 4859.
22. G Engelhardt, U Lohse, E. M. Lippmaa, M Tarmak and Mägi, *Z. anorg. allg. Chem.* **482** (1981) 49.
23. W H Johnes, T P Graham and R G Barnes, *Phys. Rev.* **132** (1963) 1898.
24. V M Mastikhin, O B Lapina, V N Krasilnikov and A A Ivakin, *Reaction Kinetics and Catal. Letters* **24** (1984) 119.
25. V M Mastikhin, O B Lapina and L G Simonova, *React. Kiuet. Catal. Lett.* **24** (1984) 127.
26. V M Mastikhin, O B Lapina and L G Simonova, *React. Kinet. Catal. Lett.* (in press).
27. R N Pletnyov, V A Gubanov and A A Fotiev, *NMR in Oxide Vanadium Compounds,* Moscow, Nauka (1979).
28. G K Boreskov, G M Polyakova, A A Ivanov and V M Mastikhin, *Doklady AN SSSR,* **210,** (1973) 626.
29. V M Mastikhin, O P Krivorutchko, B P Zolotovsky and R A Bupanov, *React. Kinet. Catal. Lett.* **18** (1981) 117.
30. E T Lippmaa, M Mägi, A Samoson, E Engelhardt and A R Grimmer, *J. Am. Chem. Soc.* **102** (1980) 4889.
31. V M Mastikhin and I L Mudrakovski, *React. Kinet. Catal. Lett.* **20** (1982) p. 351.
32. I L Mudrakovskii, N S Kotsarenko, V M Mastikhin, L G Karakchiev and K I Zamaraev, *React. Kinet. Catal. Lett.* (in press).

33. J W Emsley, J. Feeney and L H Sutcliffe, *High Resolution Nuclear Magnetic Resonance Spectroscopy*, Pergamon Press (1966).

34. V M Mastikhin, I L Mudrakovskii, A G Pelmentschikov and G. M. Zhidomirov, *Surface Sci.* (in press).

35. I L Mudrakovskii, S S Shepelev, V M Mastikhin, K G Ione and K I Zamaraev, *Kinetika i Kataliz* **25** (1984) 766.

36. S S Shepelev and K G Ione, *React. Kinet. Catal. Lett.* (in press).

37. V L Kuznetsov, A V Romanenko, I L Mudrakovskii, V M Mastikhin and Yu I Yermakov, *React. Kinet. Catal. Lett.* **25** (1984) 137.

38. V L Kuznetsov, A V Romanenko, I L Mudrakovskii, V M Mastikhin and Yu I Yermakov, *React. Kinet. Catal. Lett.* **25** (1984) 147.

39. M A Enriquez and J P Fraissard, *Journ. of Catalysis* **74** (1982) 89.

40. J P von den Berg, J P Welthuitzen, A D H Clague, G R Hays, R Huis and J H C Van Hooff, *Journ. of Catalysis* **80** (1983) 130.

© *Proc. Indian natn. Sci. Acad.*, **51**, A, No. 1, 1985, pp. 202–210.

Printed in India.

CATALYTIC CHEMISTRY AT THE ZEOLITE SURFACE*

PAUL RATNASAMY

National Chemical Laboratory, Pune-8. India

INTRODUCTION

ZEOLITES are crystalline silicates with a framework structure enclosing cavities, channels and intersections which are occupied by large cations, complexes and water molecules. Most of the zeolites are aluminosilicates whose framework structure consists of crosslinked tetrahedra in which small atoms (such as aluminium, silicon, boron or iron, collectively denoted as T atoms) lie at the centres of tetrahedra and oxygen atoms lie at the corners[1]. The T sites of all natural zeolites consist of aluminium and silicon. There are more than 35 naturally occurring zeolites known at present. Most of them have been prepared synthetically. In addition, zeolites like Linde type A, X, Y, and Mobil's ZSM5 have been synthesized which do not have natural analogues.

The composition of zeolites can be expressed by the empirical formula $M_{2/n}O.Y_2O_3.xSiO_2.zH_2O$ where M is a cation of valence n and Y is usually Al^{3+} but can also be other trivalent cations like Fe^{3+}, Ga^{3+} or B^{3+}. While the value of x is usually below 10 for naturally occurring zeolites, it can approach or even equal infinity for some of the synthetic zeolites like ZSM5 or silicalite. The cation-exchange ability and the consequent catalytic activity of zeolites arises from the feasibility of substitution of trivalent ions like Al^{3+} for tetravalent Si^{4+} in the crystalline framework of SiO_2. This generates an anionic site in the environs of aluminium atoms. To preserve electroneutrality, a cation is required. The cation can be an alkali metal cation, like Na^+, which can easily be exchanged for other ions like NH_4^+, H_3O^+, etc. Zeolites, active in acid-catalysed reactions are obtained when the NH_4^+ or H_3O^+-exchanged forms are decomposed to generate the Bronsted acid centres active in many of the reactions catalysed by zeolites.

The pattern of usage of zeolite catalysts in the fuel and chemical industries is shown in Table I. Catalytic cracking and hydrocracking, both reactions, wherein acid-catalysed cleavage and isomerisation of carbon-carbon bonds are key steps, account for more than 98% of consumption of zeolite catalysts. Some of the main milestones in the development of zeolite catalysis are shown in Table II. The present paper deals with the catalytic chemistry of zeolites obtained by substitution of Al^{3+} in the zeolite lattice framework by other trivalent ions like gallium, boron and iron. The major emphasis would be on the zeolites obtained by the substitution of aluminium by iron and boron.

---

*Paper presented at the Symposium on Physics and Chemistry of Surface held at INSA, New Delhi from September 28-30, 1984.

Synthesis of Zeolites

A preliminary consideration in the isomorphous replacement of cations in silicate structures is the number of stably occupiable cation sites. The total number of

Table I

Zeolite usage in the fuel and chemical industries

(Annual consumption 350,000 tons)

Process	WT %	Catalyst
(1) Catalytic cracking	88	REY, HY
(2) Hydrocracking	10	CO, MO, Ni, W, HY mordenite, erionite
(3) Organics	1	ZSM–5, REY
(4) Inorganics	1	Mordenite

Table II

Milestones in Zeolite Catalysis[2]

Milestone	Reference	Date
(1) Shape selectivity in chemical reactions	Weisz et al[3]	1962
(2) Organic cations used as templates for zeolite synthesis	Barrer[4]	1961
(3) Zeolites used in commercial cat cracking	Plank and Rosinski[5]	1964
(4) Synthesis of ALPO zeolites	Flanigan[6]	1982

cations can never exceed the total number of cation sites available for stable occupation. Thus, in the feldspar amorthrite $CaAl_2Si_2O_8$ all stable cation sites are occupied by Ca^{2+} ions. It is, therefore, impossible to replace one Ca^{2+} by two Na^+ to give $NA_2Al_2Si_2O_8$ because there would then be twice as many cations as there were sites for them to occupy. Hence, only substitutions of the type Ca, Al $\rightleftharpoons$ Na, Si can occur.

The situation is different in the case of zeolites : There are many more cation sites available than the number of cations needed for neutralising the negative charge on the anionic framework so that isomorphous substitution can occur in ways that allow the total number of cations to vary. Hence, both type of substitutions, namely replacement of two cations by two others (e.g., Ca, Al$\rightleftharpoons$ Na, Si) as well as replacement of one cation by two others (e.g. Si $\rightleftharpoons$ Na, Al) can occur. As a result, one can have large variations in the relative proportions of Al to Si according to the conditions of formation of a particular zeolite. Examples of variations in ratio of $SiO_2 \rightleftharpoons Al_2O_3$ in some zeolites is given in Table III[7]. It may be noticed in Table III that the lower limit is around 2.0 which is what one would expect is linking of two AlO_4 tetrahedra was energetically unfavourable since adjacent negative charges on the paired AlO_4 tetrahedra render the groupings [Al-O-Al] + [Si-O-Si] less stable than 2[Al-O-Si]. The above statement constitutes the Lovenstein's rule(8) which is found to be usually valid in aluminosilicates.

It is feasible to synthesise zeolites with SiO_2/Al_2O_3 rations much higher than those given in Table III. Examples of some very siliceous synthetic zeolites are given

TABLE III

Variations in SiO_2/Al_2O_3 ratios in some zeolites SiO_2/Al_2O_3

Zeolite	Lower limit	Upper limit
Chabazite	2.16	7.8
Faujasite	2.2	6.8
Linde — A	2.0	6.8
Linde — L	2.08	7.0
Sadalite	2.0	10.0

TABLE IV

SiO_2/Al_2O_3 ratios of some Silicious Synthetic Zeolites[7]

Zeolite	SiO_2/A_2lO_3
Beta	30 – 75
ZSM 5	25 – ∞
ZSM 11	78 – 1000
ZSM 12	45 – 160
ZSM 23	55 – 217
ZSM 48	870 – 1340
Nu-1	40 – 120
Fu-1	20 – 40
Zeta-1	25 – 32
Zeta -3	60 – 74

in Table IV. Highly siliceous zeolites such as those given in Table IV are usually synthesised by replacing some or all of the alkalimetal cations in the reaction mixtures by large oganic ammonium cations such as tetramethyl or tetrapropyl ammonium cations. During the synthesis, the organic cations replace the alkali ion in the intracrystalline pore space of the zeolite framework. However, due to the larger size of the organic cation, there is not sufficient space in the intracrystalline viod to accommodate as many organic cations as the alkali ions and hence the cationic charge density in the pore space is less. Hence, when the zeolite forms, the anionic lattice framework will have lower negative charge to be compatible with the lower balancing cationic charge in the intracrystalline void space. The resulting material is a silica-rich zeolite. For example, in the 14-hedral cavities of sodalite there is room for just one tetramethylammonium ion per cavity and in accordance with this steric requirement, the sodalite grown from Na-free alkaline tetramethyl ammonium aluminosilicate hydrogel had $SiO_2/Al_2O_3 = 10$ compared to 2 for samples obtained in the absence of the organic cation (Table III). Similarly, it is possible to enhance the Al content of zeolites by using polyvalent cations instead of the alkali ions. For example, when zeolite L is synthesized in the presence of Ba^{2+}, $SiO_2/A1_2O_3 = 2\ 08$ compared to a value of 7.0 obtained in the presence of alkali ions. Again, the

double charge on Ba^{2+} allows the L structure to form with a larger anionic framework charge and hence a higher Al conent.

Isomorphous Replacement in the Framework of Zeolites

Elements other than silicon and aluminium can also form tetrahedrally coordinated oxide networks. Gallium and germanium are next to Al and Si in their respective groups of the periodic table and could therefore be expected to replace these two elements in aluminosilicates. Similarly, phosphorus, at the right of silicon in the periodic table, frequently assumes tetrahedral coordination with oxygen. With phosphorus in the pentavalent cationic state as phosphate, aluminium phosphate possesses many structural similarities to silica.

One of the early examples of isomorphous replacement in the zeolite framework was the synthesis by Goldsmith[9] in 1952 of a germanium containing thomsonite wherein Ge replaced Si in the lattice. It was synthesised hydrothermally at 245°C from a glass of composition $Ca_4Ga_3Al_5Si_8O_{32}$. Barıer *et al*[10]. reported a number of Ga- and Ge-bearing zeolites. They reported a Ga thomsonite, faujasite, zeolite A and a harmatome type zeolite each containing Ge, and faujasite, zeolite A and thomsonite containing both Ca and Ge. In 1961, Selbin and Mason[11] reported the synthesis of Ga-faujasite and Ga-sodalite from reaction mixtures which were alkaline aqueous hydrogel s at reflux around 100°C. They also reported a number of mixed (A1, Ga) faulasites. All the samples had good sorption capacities comparable to Linde Na-X. A Ge-faujasite having the composition $Na_2O.Al_2O_3.2GeO_2.xH_2O$ was next reported by Lerot *et al*[12] in 1974. It was synthesized from aqeous alkaline mixtures of $NaAlO_2$ and GeO_2.Due to the larger size of germanium compared to silicon, the unit cell of aluminogermanate zeolites is slightly larger than aluminosilicate analogs. The Ge-faujastite zeolite was found to be less stable thermallly[12] than the Si analog. Severe structural damage was observed at 400°C. The NH_4/Ni and Cu-forms were structurally even less stable than the Na-form.

Borosilicate zeolites designated as 'boralites' containing framework boron were reported to be synthesized first by Taramasso *et al.*[13] in 1980. The syntheses were carried out in the range 140–175°C for 5–15 days. $B(OC_2H_5)_3$ or H_3BO_3 were the sources of B_2O_3 and $Si(OC_2H_5)_4$ was the normal source of silica. Zeolites in the following composition range were crystallized :

SiO_2/B_2O_3	1 – 5
OH/SiO_2	0.2 – 0.5
H_2O/SiO_2	25 – 40
M^+/SiO_2	0.1
R^+/SiO_2	1 – 10

wherein M^+ denotes an alkali metal cation, and R^+ a tetra-alkylammonium cation. Borosilicate analogs of the aluminosilicate zeolites ZSM5, ZSM11, NU–1 and Beta were reported to be synthesized. The evidence for framework substitution of Si by B came from the determination of unit cell dimensions which decreased as the boron

TABLE V

Dependence of frame work B content on base used in Synthesis

Base	B/(B + Si)	
	In reaction mixture	In crystalline product
$N(C_3H_7)_4OH$	0	0
$N(C_5H_{11})_4OH$	0.5	0.022
$N(C_2H_5)_4OH$	0.5	0.049
$NH_2(CH_2)_2NH_2$	0.5	0.102
$N(C_3H_7)_4OH$	0.5	0.041
$N(C_3H_7)_4OH$	0.074	0.016
$N(C_3H_7)_4OH$	0.02	0.007

content, as is to be expected. A rather unexpected finding[13] was that the framework boron content in the zeolite was a function not only of B/(B + Si) in the parent misture, but also depends on the base used in synthesis for a fixed B/(B + Si) in the parent mixtures (Table V). Recently, workers at BASF reported the synthesis of borosilicate zeolites using hexamethylene diamine as the organic template[14]. The synthesis and application of borosilicates with the pentasilzeolite structures in the conversion of methanol to olefins had also been reported from laboratories in India[15] and USSR[16]. Solid state NMR spectroscopic evidence that boron was indeed present in the zeolite lattice framework was also presented[15]. However, boron present in framework positions in the as-synthesized form, tended to move out of such positions into non-framework locations during catalytic reaction/regeneration operations. Apparently, trivalent boron is not as stable as aluminium in tetrahedral positions in the zeolite lattice.

The synthesis of ferrisilicates belonging to the pentasil group of zeolites was reported by workers at BASF[17,18] and NCL[19] wherein Fe^{3+} had replaced Al^{3+} in the zeolitic framework. They were synthesized from reaction mixtures containing sources of silica, ferric oxide [17,18] or sulphate[19], NaOH and organic bases like hexamethylenediammine [17,18] or tetrapropylammonium hydroxide[19]. In the iron zeolite in the as-synthesized form, part of the iron was in non-framework positions[19]. After extraction with 0.1 HNO_3, these were removed and the resulting material contained iron mainly (more than 90%) in the tetrahedral lattice framework. X-ray diffraction, Mossbauer, ESCA and ESR spectroscopy were used to confirm that the samples did indeed contain Fe^{3+} in tetrahedral lattice positions. Due to the lower value of the ratio of ionic charge to radius of Fe^{3+} compared to Al^{3+}, these iron-containing zeolites were less acidic than their Al analogs andwere hence found to possess superior catalytic properties in those reactions which do not need very, strong acid sites like alkylation of aromatics, conversion, of methanol to light olefins etc.

Catalytic Reactions over Zeolites

An outstanding feature of zeolite catalysis is their shape selectivity. Zeolites work by using intracrystalline spaces as catalytic sites and simultaneously using the closely controlled pore structure to augument reaction control. This collectively constitutes the phenomenon of shape selectivity. If the large majority of catalytic sites are contained in the porous structure, the fate of the reactant molecules will be determined by the size and shape of the porous channels and cavities. Their are several different types of shape selectivity : reactant selectivity, product selectivity, restricted transition-state selectivity and effects.

Reactant selectivity arises in cases where only certain molecules in a reactant mixture are of a shape and size suitable for admission into the catalyst pores. An example is the selective dehydration of n-butanol, in its admixture with isobutanol to n-butene over Linde type 5A zeolite. Isobutanol with a larger cross-section is unable to enter the pores of Type 5A zeolite and hence cannot be dehydrated. Zeolites with larger pores (e.g. type X, Y or mordenite) dehydrate both isomers.

Product selectivity arises in those cases where some of the products formed in a reaction are too large to exit the pores and either block the catalyst pores or undergo subsequent reactions to produce molecules small enough to leave the pores. The selective production of para xylene (rather than an equilibrium mixture of ortho, meta and para isomers) by the alkylation of toluene with methanol over modified pentasil zeolites is a typical example of product selectivity. Due to its smaller cross-section the para-isomer diffuses out of the pores very fast The bulkier ortho and meta isomers, having relative diffusivities (compared to the para isomer) lower by a factor of 10^4, undergo subsequent isomerisation to the para-isomer before exiting from the zeolite crystal.

Restricted transition state selectivty occurs in those reactions which are prevented because the corresponding transition state (for example, a bimolecular complex) would require more space than is available in the catalyst cavity. Neither reactant nor potential product molecules are prevented from diffusing through the pores and reactions requiring smaller transition states proceed normally. This is the cause of the high selectivity observed in the xylene isomerisation process over ZSM5 zeolites. In the presence of acid catalysts, xylene molecules can undergo either monomolecular isomerisation (to an equilibrium composition of the 3 isomers) or bimolecular disproportionation to benzene and trimethylbenzene. Table VI shows this[20] in terms of the ratio of the rate constants for the unwanted bimolecular disproportionation reaction to that of the desired monomolecular xylene isomerisation for four zeolite catalysts of varying intracrystalline channel dimensions (HY) ZSM4 > mordenite > ZSM5).

A special case of shape selectivity, the cage effect, is manifested in the reactions of n-paraffins over zeolites. Usually, the properties of a homologous series vary continuously with molecular weight. However, there are exceptions in the intactions of n-paraffins with zeolites. The three most important features are unexpected maxima and minima in the diffusion coefficients, the absence of certain products

from cracking of larger molecules and unusually high rates of cracking. For the faujasite zeolites, for example, the diffusivity rates exhibit a minimum for the C_8 and a maximum for the C_{12} members of the series. The rate for octane is several orders of magnitude lower than for either of the neighbouring homologs. This behaviour persists over a wide range of temperatures. The explanation is that a cage effect occurs because some molecular dimensions are about the same as dimensions of the zeolite cavity. Smaller molecules pass through unhindered. Larger molecules literally extend through the cages. Closer fitting molecules (like octane in faujaite cages, for example) may have to reorient themselves within the cages before exiting, thereby experiencing a holdup and decreased diffusion rate.

Table VII illustrates some industrial processes based on shape selective zeolites.

TABLE VI

Restricted transition state selectivity in xylene isomerization

Zeolite	$(K_d/K_i) \times 10^3$
HY	50
Mordenite	13
ZSM–4	10
ZSM–5	1

TABLE VII

Industrial processes based on shape selective zeolites[21]

Process	Objective	Major Chemical/Process Characteristics
Selecto-forming	Octane increase in gasoline : LPG production	Selective n-paraffin cracking.
M-forming	High yield; octane increase in gasoline	Cracking depending on degree of branching; aromatics alkylation by cracked fragments.
Dewaxing	Light fuel from heavy fuel oil; lube oils with low temperature pour point	Cracking of high mol wt. n- and mono methyl paraffins.
Xylene isomerisation	High yield *p*-xylene production	High thruput; long cycle life; suppression of side reactions.
Ethyl benzene	High yield; No $AlCl_3$ handling	-do-
Toluene disproportionation	Benzene and xylenes from toluene	-do-
Methanol to gasoline	Methanol (from coal or natural gas) conversion to high grade gasoline.	Synthesis of C_4-C_{10} hydrocarbons including aromatics.

TABLE VIII

Comparison of Al and B-silicate zeolites for methylation of toluene

Feed	Toluene + methanol (8:1)	
Temperature	673 K	
WHSV	40	
Zeolite	A1	B
Toluene conversion %	46	37
Selectivity to xylenes %	88	85
p-Xylene selectivity	65	81

TABLE IX

Alkylation of Toluene with ethanol—comparison of alumino-, boro-and ferrisilicates

TEMP : 623 K; WHSV = 2.5; TOLUENE/ETHANOL = 2; $SiO_2/M_2O_3 = 80$

Catalyst Products (% wt.)	Al*	B	Fe
Aliphatics	0.7	1.2	1.7
Benzene	2.8	0.3	0.3
Toluene	69.8	50.4	53.6
C_8 aromatics	5.0	0.8	0.5
p-Ethyl toluene	4.4	9.7	11.9
m-Ethyl toluene	13.6	36.6	31.6
o-Ethyl toluene	—	—	
C_{10} aromatics	3.8	0.3	0.3
Toluene conversion %	25.1	46.0	44.0
Selectivity to ET % (toluene basis)	59	90	96.8
ET isomer distribution %			
Para	76	79	72.6
Meta	24	21	27.4
Ortho	—	—	—

The selectivity of zeolite catalysts in hydrocarbon conversion reactions can also be modified by isomorphous replacement of Al^{3+}, the site of catalytic action by other cations like B^{3+} or Fe^{3+}. This is illustrated in Tables VIII and IX for the alkylation[22] of toluene with methanol and ethanol, respectively. The thermodynamic equilibrium concentrations of xylenes are : ortho-23, meta–53 and para–24, respectively. Studies of the acidity of the Al and B-zeolites by temperature programmed desorption of NH_3 reveal that[23] the concentration of strong acid sites decreases in the order Al > B > Fe. In accordance with the acidity data, the toluene conversion also decreases from Al^-, B^- to Fe^- zeolites.

CONCLUSION

The greatest single aid to the current wave of advances in catalyst design has been the development of shape selective, zeolite catalysts with controllable type and

concentration of active sites. Zeolite catalysis has already transformed refinery processes and may well be the key to synfuels and other industrial process breakthroughs.

References

1. J V Smith, In *Zeolite Chemistry and Catalysis,* ACS, 171, Ed. J.A. Rabo (1947).
2. T E Whyte Jr., and R A Dalla Betta, *Catal. Rev. Sci. Eng.* **24** (1982) 567.
3. V J Frilette, P B Weisz, and R L Golden, *J. Catal.* **1** (1962) 301.
4. R M Barrer, and P J Denny, *JCS* 971 (1961).
5. C J Plank, E J Rosinski, and W P Hawthorne, *IEC Prud. Res. Dev.* **3** (1964) 165.
6. S T Wilson, B M Lok, C A Messina, T R Canon, and E M Flanigen, *JACS* **104** (1982) 1146.
7. R M Barrer, '*Hydrothermal Chemistry of Zeolites*', AP (1982).
8. W Lovenstein, *Amer. Mineral.* **39** (1954) 92.
9. J R Goldsmith, *Min. Mag.* **29** (1952) 952.
10. R M Barrer, J W Baynham, F W Bultitude, and W M Meier, *J. Chem. Soc.* (1959) 195.
11. J Sellun, and R B Mason, *J. Inorg. Nucl. Chem.* **20** (1961) 222.
12. L Lerot, G Poucelet, and J J Fripiat, *Mat. Res. Bull.* **9** (1974) 979.
13. M Taramasso, G Perego, and B Notori, In *Proc. of the 5th International Conference on Zeolites* (Ed.L.V.C. Rees), Heydon, London (1980) p. 40.
14. L Marosi, *Proc. 6th Natl. Symp. Catal.* Pune, India (1983).
15. A J Chandwadkar, S B Kulkarni, Rajiv Kumar, I Balakrishnan, and P Ratnasamy, *Proc. First Indo-Soviet Seminar on Catalysis,* Novosibirsk, (1984) p. 14.
16. V N Romannikov, L S Chumachenko, and K G Ione, *Proc. First Indo-Soviet Seminar on Catalysis,* Novosibirsk (1984) p. 127.
17. L Marosi, J Stabenow, and M Schwarzman, *Ger. Pat.* **2** (1980) 831, 611.
18. L Marosi, J Stabenow, and M Schwarzman, *Ger. Pat.* **2** (1980) 831, 630.
19. P Ratnasamy, R B Borade, S B Kulkarni, S G Hegde, A N Kotasthane, and V P Shrialkar, 275/DEL/83 (1983).
20. W O Haag, and F G Dwyer, *Aromatics Processing with Intermediate powere size Zeolite Catalysts, Am. Inst. Chem. Eng.—Ann. Mtg* (1979).
21. P B Weisz, *Pure L & Appl. Chem.* **52** (1980) 2091.
22. K H Chandawar, A N Kotasthane, and P Ratnasamy, *Proc. First Indo-Soviet Seminar on Catalysis* (1984) p. 9.
23. S G Hegde, unpublished results.

© *Proc. Indian natn. Sci. Acad.*, 51, A, No. 1, 1985, pp. 211–255.
Printed in India.

RADIATION PROCESSING OF SURFACES : APPLICATIONS OF CONVERSION ELECTRON MÖSSBAUER SPECTROSCOPY*

S B Ögale, S V Ghaisas, S M Kanetkar

Department of Physics, University of Poona, Pune 411 007

and

V. G. Bhide

School of Energy Studies, University of Poona, Pune 411 007

Recent advances in the modification of surface layers using techniques such as ion implantation, ion beam mixing, laser annealing and alloying, electron beam annealing are discussed. These techniques have distinct advantages over conventional methods such as thermal diffusion, tinning, boriding etc, inasmuch as, with these techniques it is possible to modify surface layers to the required specifications without affecting the bulk in any way. All these techniques are non-equilibrium in nature and can give rise to exotic metastable phases, in which Hume Rothery rules are considerably relaxed. Some of the applications of the surfaces modified using these techniques are also described.

Various attempts made to characterise the modified surface layers using techniques such as Rutherford Backscattering, low angle X-ray diffraction, resistivity measurements are mentioned. With these methods, it is not possible to characterise the modified surfaces to the atomistic details and to obtain information on the mechanism of the process of surface modification. In this context, the utility of Mössbauer spectroscopy in scattering mode is brought out and the use of the technique of conversion electron Mössbauer spectroscopy in characterising the surface layers is described in details.

Some of the recent experiments on the application of Conversion Electron Mössbauer Spectroscopy for the characterization of surfaces modified using directed energy processing techniques are discussed. A few other applications of Conversion Electron Mössbauer Spectroscopy for the study of surface reactions, interfaces etc. are also described.

Key Words : Radiation Process; Mössbauer Spectroscopy; XRD and CEMS

1. Introduction

In recent years, there has been an enormous growth of research activity in the field of material science. The major attention of this activity is focussed on the question of obtaining material surfaces tailored to the required specifications[1–4]. The conventional technique of equilibrium thermal treatment either for alloying, annealing or impurity diffusion can not offer a useful solution to this problem because of three reasons[4]; (i) In the thermal case there are no parameters to control except the temperature and treatment—time, (ii) the equilibrium thermal treat-

*Paper presented at the Symposium on Physics and Chemistry of Surfaces held at INSA, New Delhi from September 28–30, 1984.

ment can only yield stable phases of materials and, metastable phases having newer features can not be synthesized (By using non-equlibrium thermal methods such as splat-quenching[5], one can obtain metastable phases of different materials and composites; but these methods are not useful in modifying the properties of a given material); and (iii) the thermal treatment cannot be region selective within a small volume of the sample and as such, by using this method it is not possible to modify the properties of a given material differently in different distributed regions within a small volume. Hence, during the past decade there has been a considerable growth of interest in the use of the radiation processing methods to tailor the properties of solid surfaces to the desired specifications[6–11].

Considerable experimental work has already been done in this research area so as to understand the physical processes which can occur when radiation of a specific type is incident on the material surface. In most of these studies the techniques of Rutherford Backscattering (RBS), X-ray diffraction (XRD) resistivity measurements etc. have been employed and valuable information regarding the structural and chemical properties of processed layers has been obtained. Yet a need is felt for additional data[9], especially on the atomistic aspects of the beam induced processes, so as to reveal the finer details regarding the nature and properties of the new materials which can be synthesized by using the beam processing techniques. Amongst the characterization techniques which can directly address to the atomic level details, the technique of Mössbauer spectroscopy[12,13] has a special place because, this technique can, in a single measurement, bring out an information regarding the structural, chemical, electrical a well as magnetic properties of materials along with a valuable data on the defect complexes and their symmetries. Also, this technique being non-destructive in nature, it does not forbid the use of the other characterization concepts for studying the same material; thus a coherent picture regarding state of the solid can be obtained without difficulty. Mössbauer spectroscopy provides a number of windows such as isomer shift, quadrupole splitting, magnetic dipole interaction, Lamb Mössbauer factor etc. through which one can obtain an extremely useful information about the nature of chemical environment, symmetry of the neighbours, magnetic field at the nuclear site, dynamics of the Mössbauer atom etc. Yet, the use of this technique requires presence of suitable isotopes of elements which can serve as source and absorber nuclei in a Mössbauer experiment, and as such this technique can not be conveniently applied to the studies of arbitrarily chosen material system. However, by making an appropriate choice of a representative Mössbauer system, the physics of the non-Mössbauer accessible materials can also be studied by this method.

In the following section (Section II) we have briefly discussed some important radiation processing techniques which are of current interest, and in Section III, the elements of the theory of Mössbauer effect have been discussed, alongwith the information regarding the experimental systems used for Mössbauer measurements in transmission, scattering and conversion electron modes[14]. In Section IV, a number of examples of the use of Mössbauer spectroscopy in characterizing radiation processed surfaces have been given.

2. Radiation Processing of Surface Layers

As mentioned earlier several radiation processing techniques have been developed over the past decade to tailor the properties of material surfaces to the desired specifications. The prominent ones among these are the techniques of ion implantation[6–8], ion beam mixing[9], laser treatment[10], electron beam treatment[3,11] etc. In the following, these techniques have been briefly introduced and their potentialities for rendering a desired surface modification have been brought out.

2.1. *Ion Implantation*

This method of surface modification is based on the bombardment of solid surfaces with selected ionic species having energy in the range of a few tens to a few hundreds of KeV[6–8]. This is a high vacuum (10^{-6} Torr) process which offers a possibiliy of obtaining a specific dopant distribution in the submicron region below the solid surface by controlling the ion energy, target temperature, orientation of the target structure with reference to the ion direction etc. Various physical processes can occur when an energetic ion hits the solid surface. Since the implantation energies used in most experiments are in the KeV range, the atoms of the solid which are displaced from their sites by the incoming ions also possess substantial energy to atomically displace other atoms on their track, leading to the formation of a 'Collision Cascade Region' which generally has a high concentration of vacancies[15]. This region is often surrounded by distributed interstitials. The cascade formation occurs over a time scale of only 10^{-13}—10^{-10} secs which renders a high non-equilibrium nature to the implantation process. The depth distribution of implanted ion concentration generally has a semi-Gaussian nature as shown in Fig. 2.1 (a). Under special circumstances wherein the ions are incident on a crystalline solid along one of its low index crystallographic directions however, anamolous range distributions can result due to ion-channelling effects (See Fig. 2.1 (b)). In the normal situations (no channelling case) the projected ion ranges (or typical penetration depths) are of the order of a few hundreds of Angstroms; while under channelled conditions the ions can penetrate as deep as a few microns.

Since ion implantation leads to a forced and transient introduction of dopants into solids, this highly non-equilibrium process can be used to surpass the limits of solid solubility allowed by the Home-Rothery rules[16] and to synthesize extended solid solutions. This aspect is especially important in the context of metals, wherein one desires to obtain newer metastable alloys with novel application potentials. In order to obtain high concentration alloys however, the process of direct implantation is not suitable because, to obtain high concentration alloys the requirement of ion dose is as high as 10^{17} — 10^{18} ions/cm^2, and at such dose values the sputtering effect[17] erodes the pre-synthesized alloy layers. Very recently it was shown by Tsaur *et al.*[18] that a simple but interesting variation of the implantation method itself can be used to synthesize concentrated metastable alloys on the surfaces of any material without the intrinsic limitation imposed by the sputtering effect in the direct implantation case. This innovation is referred to as ion beam mixing.

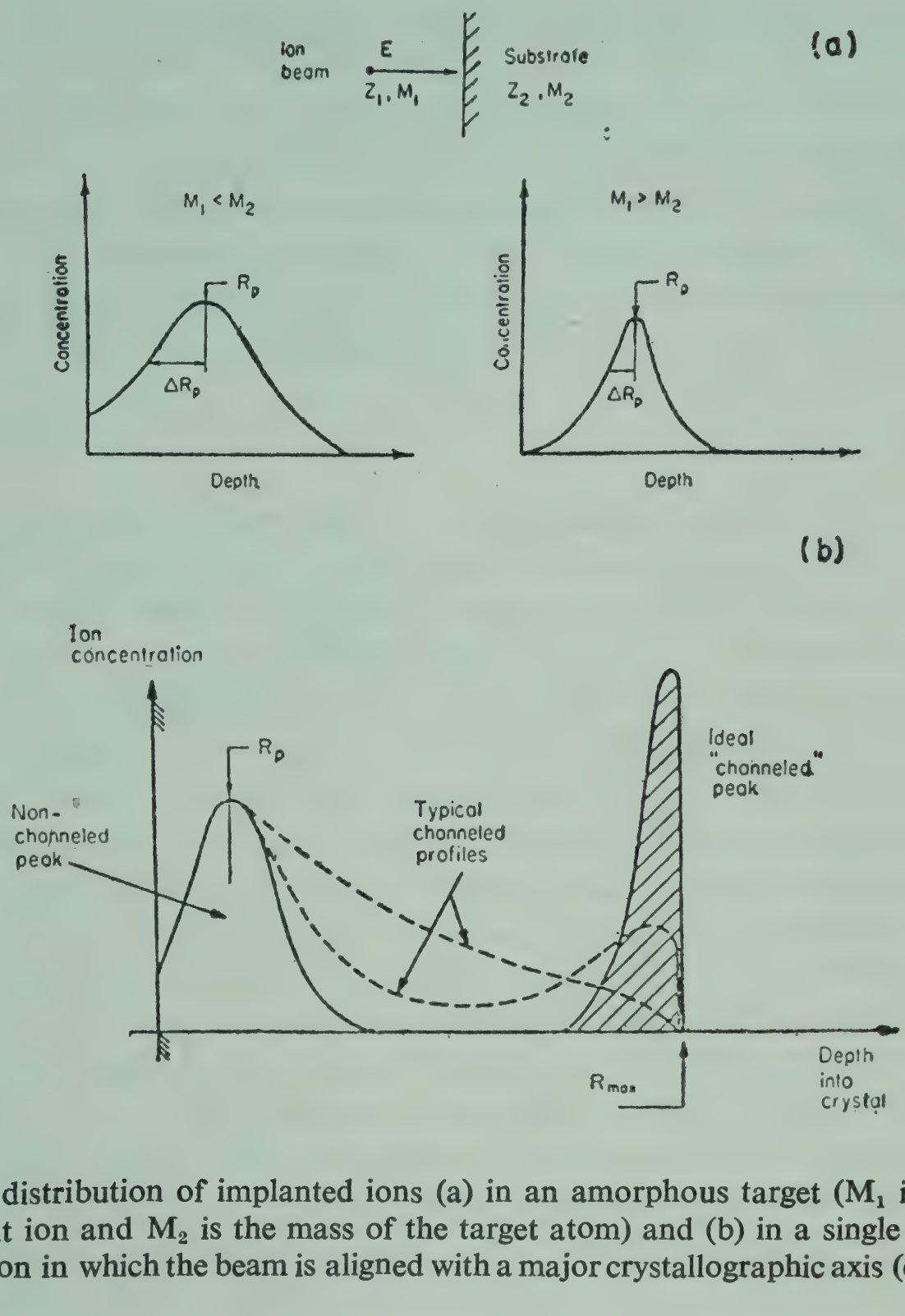

FIG. 2.1 Depth distribution of implanted ions (a) in an amorphous target (M_1 is the mass of the incident ion and M_2 is the mass of the target atom) and (b) in a single crystal under the condition in which the beam is aligned with a major crystallographic axis (channelling case).

2.2. *Ion Beam Mixing*

The principle of ion beam mixing[9,18,19] has been depicted in Fig. 2.2(a). This technique is based on the fact that one energetic ion incident on a solid surface can dynamically move nearly hundred or more of the atoms of the surface layers over many lattice distances. Hence, an ion dose of 5×10^{15} ions/cm^2 can lead to a dynamical mixing of 10^{17} to 10^{18} atoms in the surface layers of a solid. If these layers are composed of successively deposited thin films, an atomic mixing of these films can take place yielding a homogeneous high concentration alloy. Of course, for alloy formation, the energy of ions should be such that the ions cross the interface where the process of mixing begins. Generally, the energy of ions is so chosen as to yield a projected range R_p equal to the depth of the interface below the solid surface. Clearly, if one wants to synthesize thicker layers of metastable materials, then higher ion energy has to be employed. The energy can not however be far greater than a few hundred KeV because, beyond this typical energy regime (50–400 KeV) the ion-nuclear cross-section diminishes at the cost of an enhancement of the electronic excitation cross-section and efficient dynamical mixing can not take place.

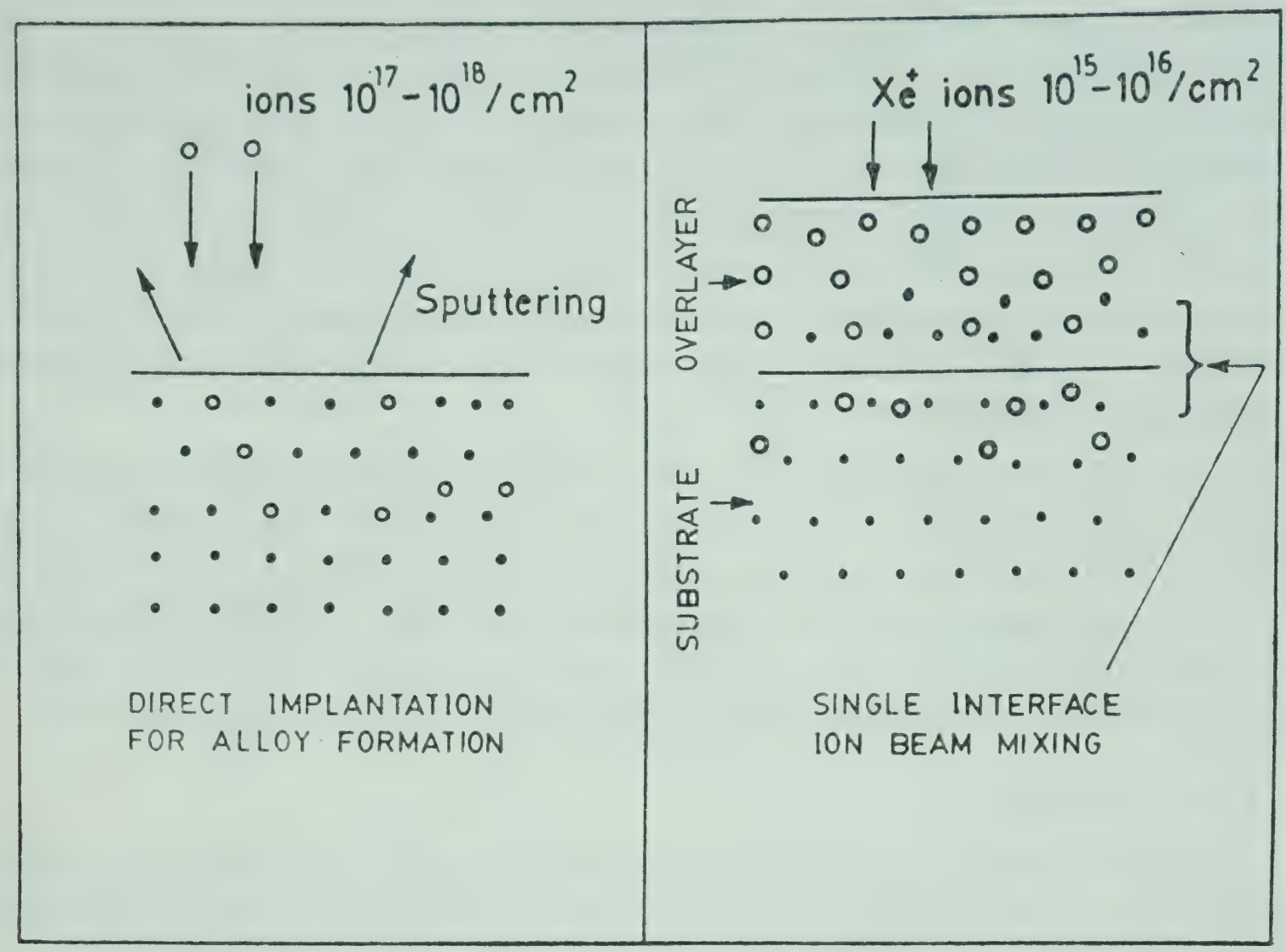

FIG. 2.2 (a) Schematic representation of ion beam mixing process when an energetic ion is incident on a thin film couple.

(b) Ion beam mixing process in the case of a multilayered structure.

It may be noted that the ion dose required to form a concentrated alloy is almost two orders of magnitude lower in the case of the ion beam mixing than that required in the direct implantation method. Hence, the sputtering limitation of the latter method is almost completely eliminate[9]. Also, in view of the small dose, the percentage of the implanted ions in the composition of the mixed alloy is extremely

small and thus, beam mixing can be carried out by using any suitable ions of chemically inert gaseous species such as Ar^+, Kr^+, Xe^+, etc, with little risk of influencing the physical properties of the alloy. This avoids the requirement of solid ion production and acceleration, intrinsic of the direct implantation method and relatively simple implantation machines can be used to carry out the alloying process. It may also be observed that since the basic process used in ion beam mixing in ion implantation itself, it preserves the most important advantage of the implantation method, viz. its highly non-equilibrium nature which can lead to novel metastable structures and compositions.

It may further be pointed out that the technique of ion beam mixing can be used effectively to tailor the composition of the mixed layer [see Fig. 2.2(b)]. This can be achieved by preparing a layered structure of alloying elements having thickness suitable to yield specific final composition and subsequently, mixing the deposited multilayered sandwich by energetic inert gas ions. In this multi-interface case, the energy of ions used to achieve mixing may be varied over a chosen range.

2.3. *Laser Treatment*

The laser treatment of materials which was initially developed to anneal the implantation induced damage can be performed by using high power lasers operating either in a 'Pulsed' mode[10,20-22] (Q-switched Ruby, Nd-YAG lasers etc.) or CW mode[23–25] (Co_2, Ar, CW Nd-YAG laser etc.). The power requirements for imparting a certain modification to the surface differ in the two cases for obvious reasons. Also, the mechanism of the modification process is substantially different in the pulsed and CW cases; and hence one may not be able to attain a specific state of the material surface by both the methods. In particular, when one uses pulsed Laser having pulse width of a few tens of nanoseconds or smaller, highly non-linear processes occur in the submicron region near the sample surface; and, structurally and compositionally metastable layers can be synthesized[11]. In view of its highly non-equilibrium nature, the pulsed laser treatment has emerged as an area of immense scientific interest in the recent years and as such, in the following discussion we have mainly concentrated upon the pulsed laser technique of material processing.

The technique of pulsed laser treatment has been found to be extremely useful in achieving the following objectives[10] : (i) Annealing of implantation induced damage; (ii) redistribution of implantation profiles; (iii) epitaxial growth of amorphous layers deposited on crystalline surfaces; and (iv) alloying of the layers of different materials[11] so as to obtain novel metastable phases of materials. The experimental process of impurity redistribution and surface annealing has been depicted in Fig. 2.3(a); while in Fig. 2.3 (b) the process of pulsed layer induced alloying has been shown. A laser pulse having a pulse width of a few nanoseconds and an energy density of a few Joules/cm^2 is generally employed in such experiments. In specific applications, such as in the formation of a glassy metal metalloid alloy, even picosecond laser pulses have been employed[24].

The pulsed laser treatment has a number of interesting and useful features which cannot be realised by using other procesing methods : (i) This technique being

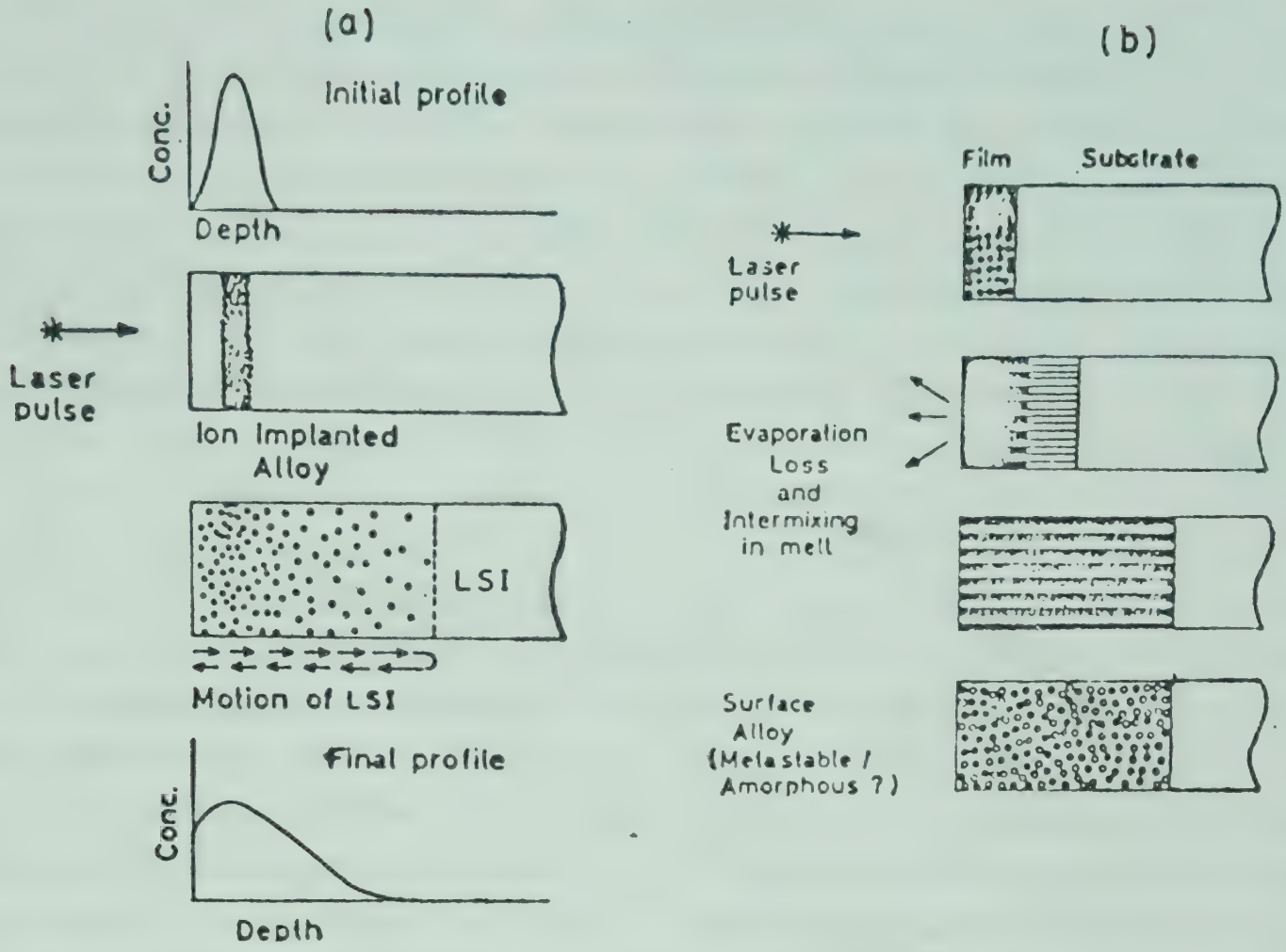

FIG. 2.3 Schematic of (a) the redistribution of implanted impurities due to the pulsed laser treatment and (b) mechanism of pulsed laser induced mixing of an overlay solute film on a substrate.

an optical processing method, it does not leave its mark on the solid-state, subsequent to the completion of the transient modification process; (ii) by focussing the optical radiation, this method can be easily rendered to be highly area selective; (iii) since the pulse duration is generally less than a few tens of nanoseconds, this process can be carried out in air without any risk of oxidizing the submicron layers (In fact, it has been shown that not more than a few monolyarers are oxidized during the extremely fast transient surface processing); (iv) this method is far more simple and quicker as compared to any other surface modification technique and as such it is easy for automation; (v) this method allows an easy control of the depth of the annealed region and also the extent of impurity redistribution by an appropriate control of the pulse parameters; (vi) since this is a highly non-equilibrium process (quenching rate 10^8–10^{10} °K/s) metastable phases can be synthesized; and (vii) the thickness of the surface layer which can be effectively modified is considerably larger (in microns) as compared to that by the other techniques such as ion implantation, ion beam mixing etc. In view of these tremendous advantages it is not surprising that the method of pulsed-laser treatment has acquired a prominent position amongst the newer and unconventional methods of material modification.

Although the experimental aspects regarding the results of the laser treatment seem to have been understood reasonably well, the physical processes occurring over the short processing time-scale appear to have many complexities which have not been clearly understood[26–28]. When the laser radiation is incident on a solid it can be absorbed by various processes; the primary channel of absorption being via the excitation of the electronic system. Thus, the pulsed laser can instantly pro-

duce a very large concentration of electrons and holes in the region of optical absorption and this electron-hole plasma can then loose energy to the lattice by generation of phonons, leading to the melting of the solid. The structural and compositional transformations may then be expected to occur in the molten phase, whose spatial and temporal development is dependent upon the absorbed laser power as well as the parameters of the meterial itself such as its specific heat, thermal diffusivity, solubility conditions in the case of the composite system etc. This model which is popularly known as the 'melting model' has been found to be adequate to explain most of the observations.

2.4. *Electron Beam Treatment*

Electron beam can also be used for processing materials both through thermal effects and through non-thermal or chemical, effects[29]. In the annealing or alloying applications, the thermal aspects of the electron beam treatment of surfaces is exploited. The electron beam processing method has certain specific advantages over the laser annealing technique : (i) In the process of laser annealing the sample undergoes significant changes in reflectivity, and as such there is a considerable uncertainty regarding the amount of energy actually absorbed by the sample. The electron beam treatment does not suffer from this drawback; (ii) Very high, steady-state values of power per unit area can be maintained in the case of electron beams by adequate emission control and the control of the focussing conditions. Also, the value of the incident power can be measured precisely bya ppropriately compensated Faraday-cup assemblies. In the case of laser beams, especially the pulsed-lasers, the determination of absolute power is an extremely complicated process. Moreover, it is difficult to obtain an areal uniformity of better than a few percent without the use of beam homogenizers which leads to considerable loss of beam energy; (iii) in the case of electron beams (used in continuous mode) a controlled scanning of the beam across the area can be performed easily by electrostatic and/or magnetic deflection methods; while in the case of the laser beams, the scanning in most cases involves mechanical motion of the target. The electron treatment, however, has a major drawback as compared to the pulsed laser treatment viz. the electron treatment systems necessarily require vacuum operation, which is not the case with pulsed-laser treatment as mentioned earlier. Yet, for its specific advantages the electron beam treatment stands out as an independent and useful alternative for material processing. The typical parameters of the electron beam, which can yield a suitable surface modification are :

Pulse duration	:	40–400 ns
Electron energy	:	5–50 KeV
Total current	:	1–50 KA
Beam diameter	:	8–10 cm
Pulse energy	:	upto 20 Joules/cm^2

Such a continuous high current electron beam can be generated by hot cathode assemblies and such beams in the scanning mode can be used for lithography, welding, annealing etc.

Apart from the techniques of ion implantation, ion beam mixing, laser treatment and electron beam treatment which have been discussed in the above paragraph, there exist a host of other techniques which are capable of modifying the material surfaces in a variety of ways. These include pulsed ion beam treatment, flash-lamp (incoherent light source) annealing, transient heat pulse treatment via resistive heating, plasma treatment etc. These techniques are still in the stage of development and we shall omit a detailed discussion concerning them in the present article. Since this article refers to the applications of Mössbauer spectroscopic technique to the study of radiation processed surfaces, we now turn our attention to some basic concepts concerning Mössbauer spectroscopy and different experimental channels available to observe this nuclear resonance absorption.

3. Mössbauer Spectroscopy

3.1 *Mössbauer Effect (Basic Considerations)*

Mössbauer effect[12–13] refers to the recoilless emission and absorption of gamma rays by atomic nuclei. In view of the high energy and hence momentum transfers associated with a gamma transition, the energy required to be spent in compensating for the recoil motion of the emitting or absorbing nuclei is high enough to disallow the realisation of any resonant exchange of gamma photons between free atomic and molecular systems. However, when a gamma-emitting or absorbing atom is strongly bonded into a solid, the recoil can be taken up by the entire solid; thus diminishing the recoil energy to a negligibly small value and making a recoilless exchange of gamma photons possible. Since the gamma rays involved in the Mössbauer effect emerge in a recoilless mode, they are characterised by a spread of energy corresponding only to the natural linewidths of the nuclear levels and hence, even minute perturbations caused to the environment experienced by the nucleus can be very sensitively reflected in the results of a Mössbauer experiment. This is especially important in the context of the studies of material systems, wherein extremely small perturbations are caused to the nuclear levels via hyperfine interactions, which represent the interactions between a nuclear property such as electric quadrupole or magnetic dipole moment and appropriate electronic and atomic properties. Since the variations in the nuclear energies caused by the changes in the structural, chemical, magnetic and electrical state of the environment of a Mössbauer nucleus can be measured with an accuracy of 1 eV in 10^{13} eV or better (e.g. in the case of Fe^{57}) by using the Mössbauer technique, this method of material characterization has found a central place in the field of material science. In a typical Mössbauer experiment [see Fig. 3.1(a)] one uses a source, which is in the form of a crystalline medium embedded with atoms having Mössbauer active gamma emitting nuclei and an absorber (which is the sample under study) containing atoms of the isotope which represents the ground state of the gamma emitting nuclei in the source medium. If the source is moved in a constant acceleration mode (so as to obtain a Doppler spread of frequencies) then the various possibilities of excitation of absorber nuclei appear as sharp dips on the scale of source velocity. By deconveluting such spectra,the nature, strength and symmetry properties of the different hyperfine interactions can be studied.

There are three main hyperfine interactions which are of great importance in the context of Mössbauer spectroscopy. These are :

i. Electric monopole interaction (e0)
ii. Magnetic dipole interaction (ml) and
iii. Electric quadrupole interaction (e2)

The first type of interaction emerges as a result of the Coulomb interaction of the nuclear charge and the S-electron density at the nucleus, and leads to a shift of the centre of gravity of the Mössbauer spectrum with reference to the zero velocity position. This interaction is referred to as 'isomer shift'. The second and third type of interactions lead to the occurrence of multiplets in the Mössbauer spectrum and such multiplets correspond to the Zeeman and quadrupole splitting of the nuclear levels. In addition to these parameters, recoilless fraction and linewidth corresponding to Mössbauer spectrum also provide very useful information regarding the

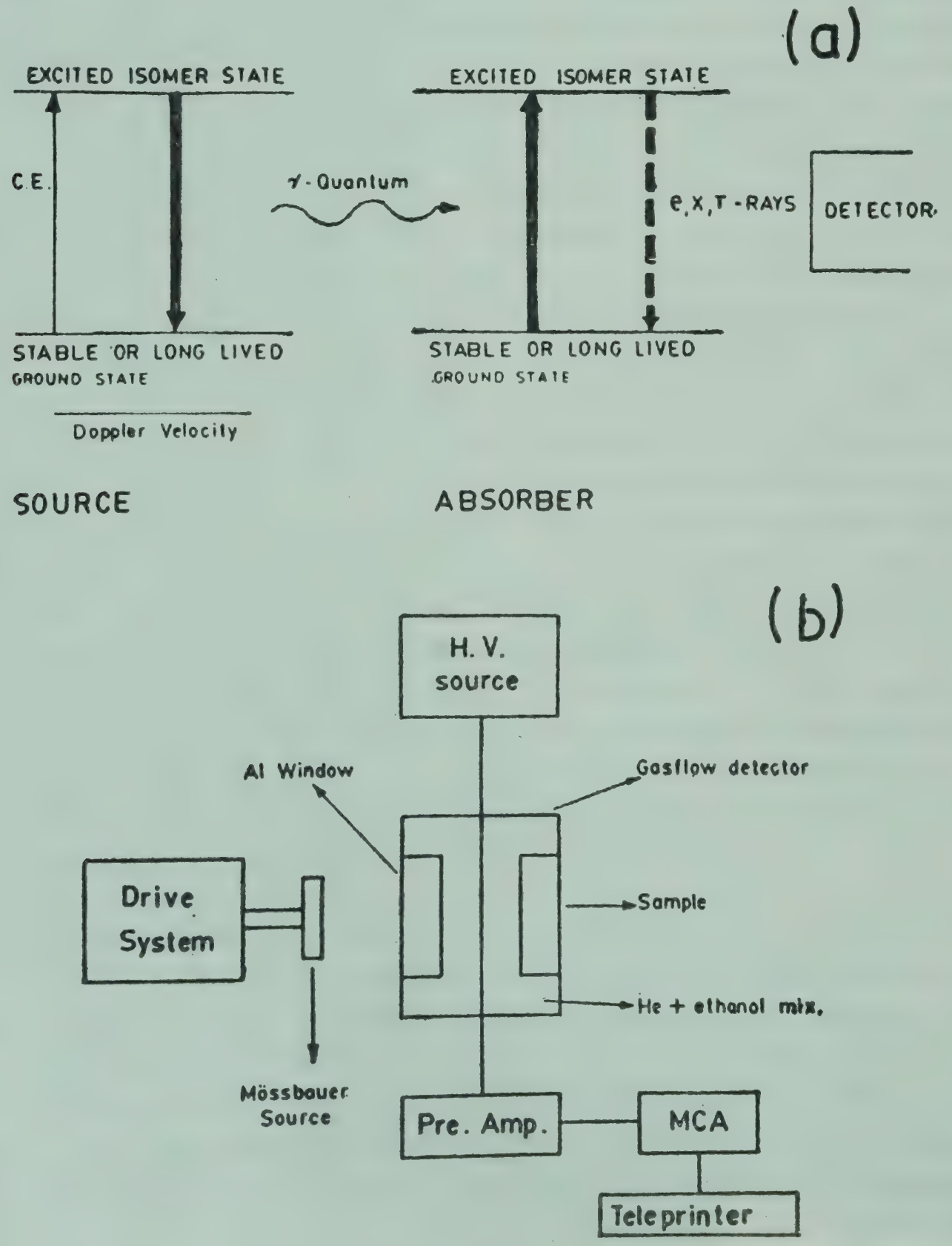

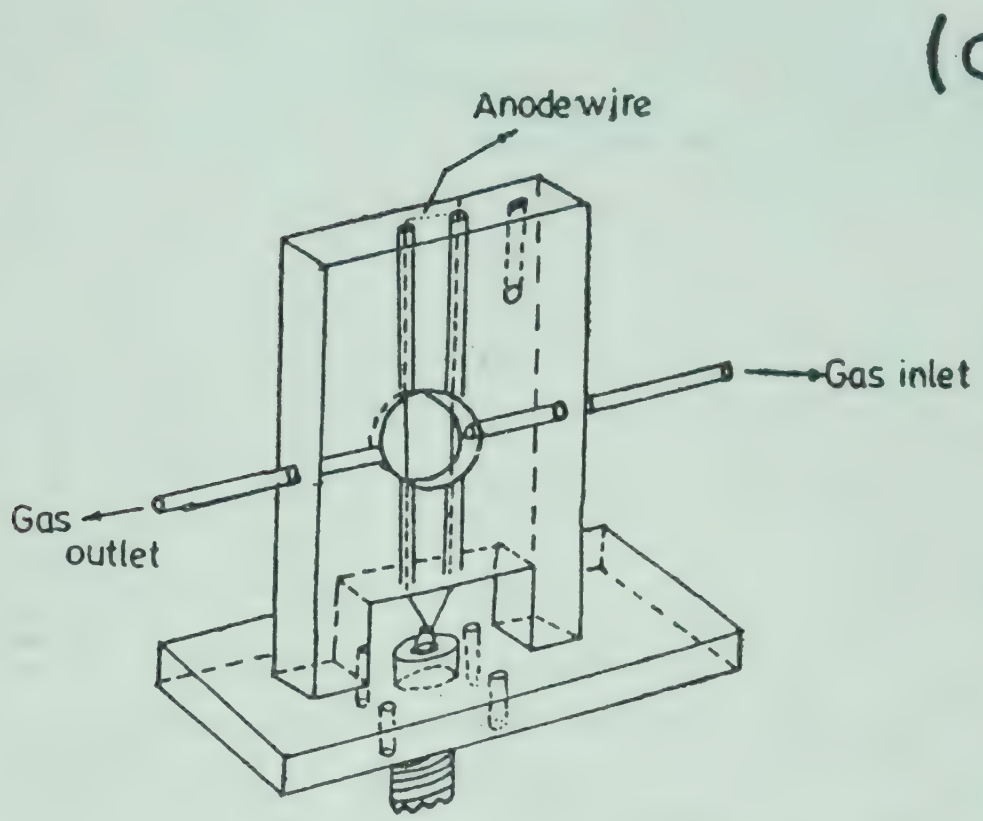

FIG. 3.1(a) Schematic representation of nuclear γ-ray resonance fluoroscence, (b) A block diagram of the experimental set-up for the Conversion Electron Mössbauer Spectroscopic studies, (c) A typical gas flow conversion electron detector.

diffusion processes of atoms, disorder in the lattice, distribution of hyperfine para meters etc. Especially, in the case of amorphous alloys, it is of interest to study the collapse of linewidth with the thermal annealing treatment so as to infer about the ensuance of atomic order, nucleation and growth of alloy phases etc.

3.2. *Scattering Mössbauer Spectroscopy*

When a γ-photon interacts with a nucleus of an atom bound in a solid matrix, a variety of phenomena can take place. In the earlier paragraphs we have discussed only the nuclear absorption process which can be studied in the Mössbauer transmission mode. Other possibilities include gamma ray scattering, de-excitation of the nuclear state formed by gamma absorption via emission of gammas, β-particles X-ray etc. or by other complex decay schemes involving the composite nuclear and electronic system. All these possibilities can be exploited to carry out some immensely interesting experiments of both the basic as well as applied nature, and a host of new information can be generated. These studies are classified under the category of 'scattering Mössbauer Spectroscopy'.

Amongst the radiations which are emitted by the absorber nucleus (Table I) subsequent to the γ-absorption, the K-shell conversion electrons have been found to be particularly suitable to perform Mössbauer studies on surfaces, interfaces and thin films; and this technique is popularly known as Conversion Electron Mössbauer Spectroscopy (CEMS)[14,30].

In the case of Iron, which is an element of considerable interest in the context of Mössbauer spectroscopy, the K-conversion electrons have an energy of 7.3 KeV, and their intensity is 79% of the total deexcitation radiation. The typical distance

TABLE 1

Type of emitted radiation	E (KeV)	Intensity	Range 'r' in Fe metal
Gamma rays	14.4	0.11	$r \sim 20\ \mu m$
K X-rays	6.3	0.28	$r \sim 20\ \mu m$
L X-rays	0.7	0.002	
K-shell conversion electrons	7.3	0.79	$10\ nm \lesssim r \lesssim 400\ nm$
L-shell conversion electrons	11.6	0.08	$20\ nm \lesssim r \lesssim 1.3\ \mu m$
M-shell conversion electrons	14.3	0.01	$20\ nm \lesssim r \lesssim 1.5\ \mu m$
K-LL Auger electrons	5.5	0.6	$7\ nm \lesssim r \lesssim 200\ nm$
L-MM Auger electrons	0.5	0.6	$1\ nm \lesssim r \lesssim 2\ nm$

Energies, intensities and ranges of photons and electrons emitted after resonant excitation of the 14.4 KeV state of ^{57} Fe (electron con0ersion coefficient $\gamma = 8.2$). Radiations emitted with energies lower than 0.5 KeV are not included.

over which these electrons loose their energy in solids is 0.25 μm. Thus, conversion electrons emitted within this distance below the surface of a solid alone can be ejected out of it, conveying the Mössbauer information. Moreover, if these electrons are detected in a proportional mode, the pulse height selection can allow a further control on spatial selectivity of the Mössbauer signal. Thus, in a sense the technique of conversion electron Mössbauer spectroscopy [Fig. 3.1(b)] is a superior mode of operation than other scattering modes so far as the surface layer characterization is concerned. Also, this method is very sensitive because of the high signal to noise ratio attainable in this case. Since internal conversion coefficient depends inversely on the excitation energy, and since the most viable Mössbauer sources (like Fe) have reasonably small γ-ray energy, the differential cross-section for γ-e scattering is comparable to and often larger than that of the γ-γ scattering. This enables one to carry out an efficient Mössbauer characterization of submicron layers below material surfaces. The CEMS technique has been considerably exploited in the studies of a variety of phenomena such as corrosion[31–33], oxidation[34–35], surface magnetism[36] ion-implantation[30–35], etc.

In a typical CEMS detector the conversion electrons emitted from the sample are detected in a gas filled proportional counter or with a channelltron, depending upon the type of information one desires to obtain. In a gas filled detector, in most cases, the entry of the conversion electron is registered irrespective of it's energy; and all the electrons with varying energies at 'on and off ' resonance conditions are counted in integral manner. On the other hand, in the arrangement using channeltron, not only the entry of electron is registered but it's energy is also measured, leading to a degree of depth selectivity. This is called a Differential Conversion Electron Mössbauer Spectroscopic technique (DCEMS).

The simplest possible design of a CEMS detector is the one which makes use of an 'Anode wire between parallel plate' type of a geometry[14] [See Fig. 3.1(c)]. In

such a detector more gas multiplication occurs only in a very small region around the wire and the pulse height is independent of the direction of travel of the electron as well as the site of the primary ionisation. This leads to a reasonable energy resolution and proportionality. We have developed such a detector and an associated experimental system in our laboratory to perform CEMS studies on radiation processed surfaces.

Figure 3.2 shows a typical spectrum of an Iron foil (containing 2.2% of Fe^{57} Mössbauer isotope) obtained by using our system under the following choice of the different operating parameters :

1.	Anode voltage	=	900 volts
2.	Rate of gas flow	=	10 cc/min
3.	Distance between anode and the sample	=	0.3 cm
4.	Distance between two anode wires	=	0.5 cm
5.	Average pulse height	=	0.2 volts
6.	Ethanol temperature	=	0°C
7.	Sample and ambient temp.	=	300°K

The percentage effect exhibited by this spectrum is 12%. Recalling that this spectrum is due to the Fe^{57} atoms within a distance of 0.25 μm below the surface, this result demonstrates that a simple gas filled detector can yield a performance which is quite satisfactory for most of the room temperature Mössbauer studies on material surfaces, interfaces and thin films. In order to perform CEMS studies at low (LN_2 or Liquid He) and high (600°C) temperatures, different detector designs have to be used.

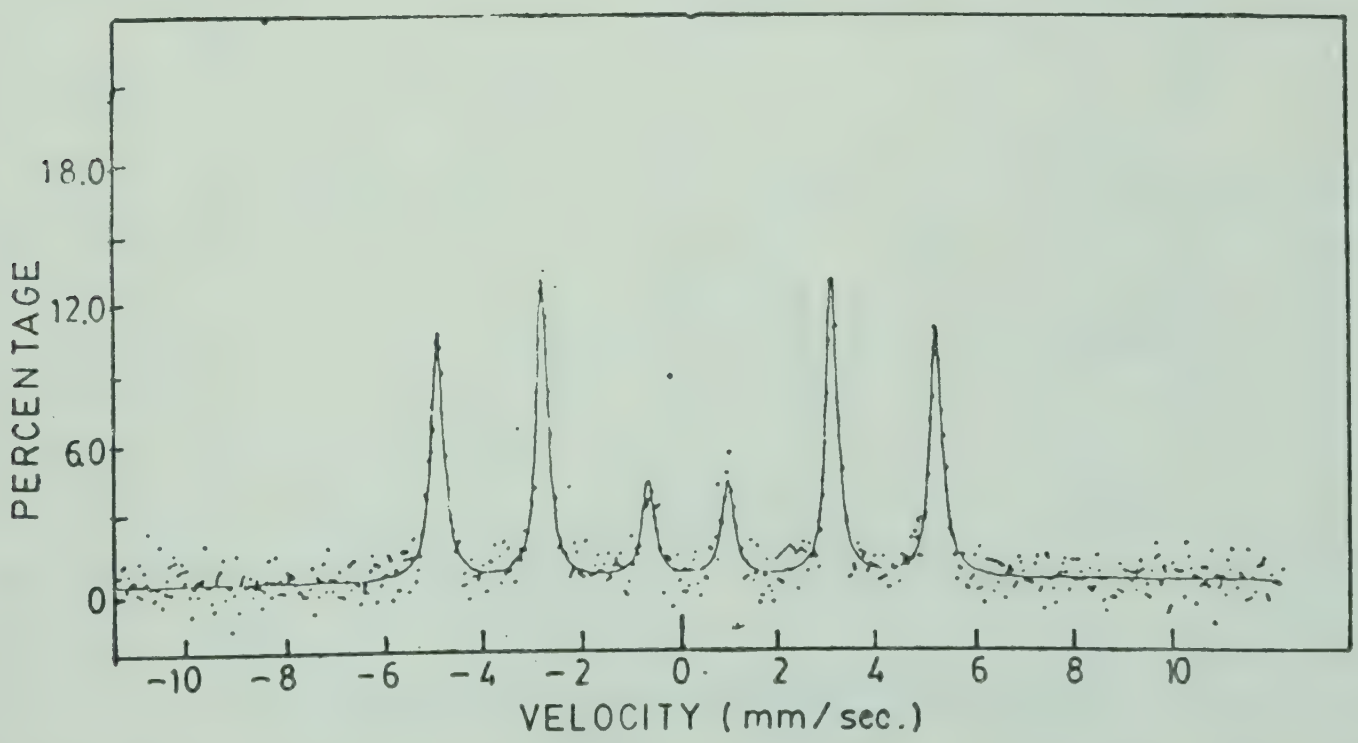

FIG. 3.2 Typical Mössbauer spectrum of iron foil surface obtained by conversion electron Mössbauer spectroscopic technique.

3.3. *Other Advances in CEMS Technique*

In all the earlier considerations we have restricted ourselves only to the absorber experiments in Mössbauer spectroscopy. Another interesting possibility of carrying out Mössbauer studies on material systems is afforded by the source experiments, which can bring out very useful information concerning dynamical processes such as diffusion. In order to carry out source experiments on surface layers a novel design concept has been suggested by Mullen *et al.*[37] His CEMS detector, which is referred to as a MICE (Micro-foil Conversion Electron) detector, consists of a series of 1 mil. diameter tungsten wire anodes alternated with cathodes of Fe^{57} enriched stainless steel foils having a thickness of ~ 3000Å. The counter is operated as a flow counter using a premixed-helium and 8% methane as the gas mixture. The operating voltage of one counter is typically 800V. The signal to noise ratio of such a detector can be enhanced by either applying upper and lower discriminators or by utilizing thin sheets of lucite to selectively filter the 6.3 KeV X-rays. In order to bring out the advantages offered by the MICE detector, we have reproduced in Fig. 3.3 the results of Mullen *et al.* on the comparison of the MICE and the proportional

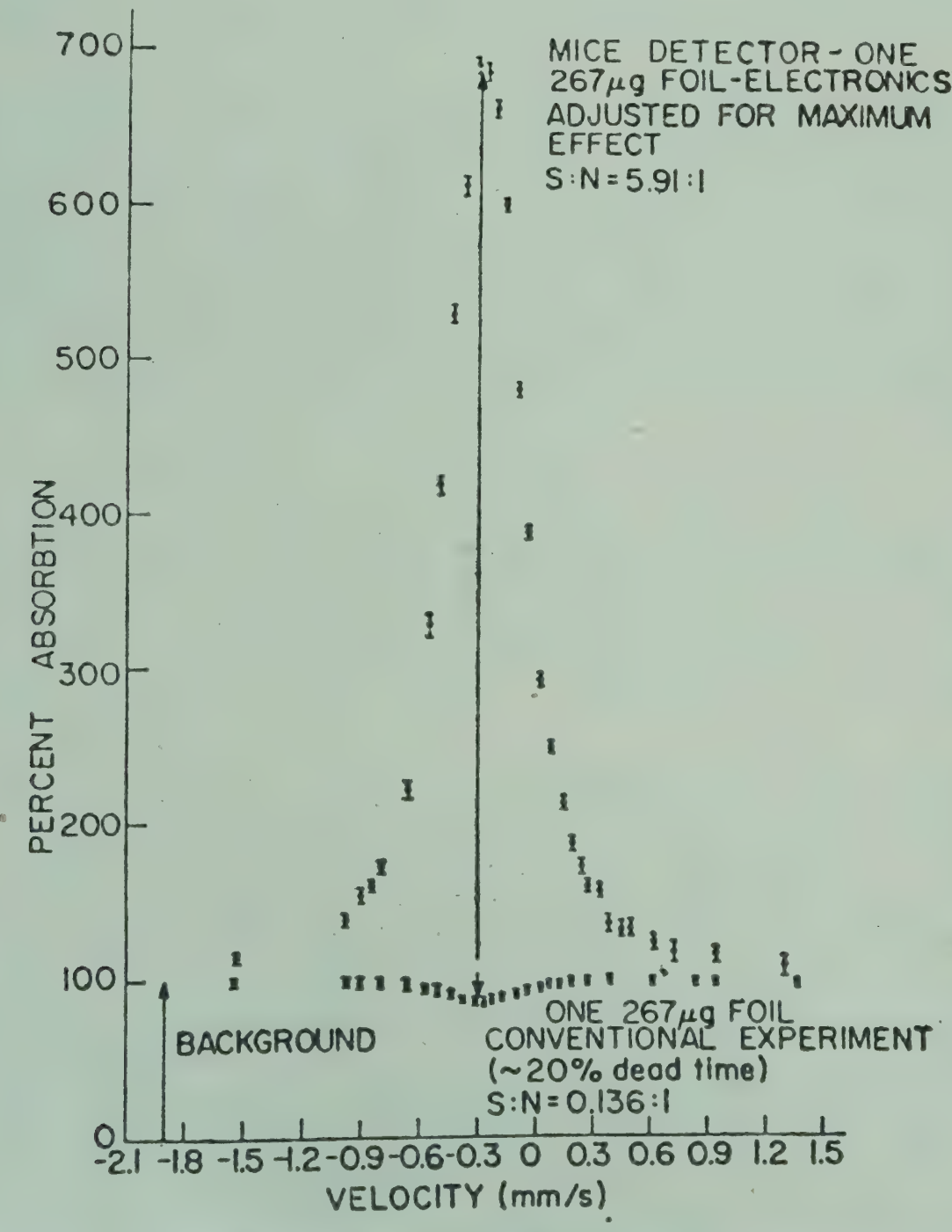

FIG. 3.3 A large 'f' experiment, illustrating the signal to noise enhancement of the MICE detector compared to a proportional counter used in transmission experiment.

detectors. It is clearly seen that the MICE detector enhances the signal to noise ratio by a factor of over 40 in this case, while the differences between the on-resonance and off-resonance count rates is only a factor of 2 less for the MICE detector as compared to the proportional detector. Thus, the MICE detector offers newer possibilities of performing Mössbauer characterization of materials.

Another important aspect of the surface Mössbauer Spectroscopy on which work is presently in progress is the depth selective CEMS technique. Depth selective CEMS requires analysis of electron spectra with a good energy resolution. These experiments have to be performed using electron spectrometers with high luminosity and high transmission. In spite of many serious attempts made to achieve these aims however, it has not been possible to enhance the depth resolution of the CEMS technique to such a value as to allow a reasonably good determination of interface composition profiles, distribution of implanted ions in solids etc. Thus, further progress in this direction is necessary.

Finally, a reference may be made to an interesting work by Tyliszczak *et al*[38], who have demonstrated that good quality Mössbauer spectra can be recorded even with resonant electrons at an energy as low as 10 eV or below. With improvement of such a technique interesting new possibilities of investigations in the field of surface science can be foreseen.

4. Applications of Conversion Electron Mössbauer Spectroscopy(CEMS) to the Studies of Radiation Processed Solids

The CEMS technique was first applied to the study of ion implantation[39] in 1975 and since then, this method of Mössbauer characterization has been successfully applied to a number of useful studies on radiation processed solids. In what follows, we have given illustrative examples of the applications of the CEMS technique to the studies of ion implantation, ion beam mixing and laser treatment.

4.1 *Ion Implantation : CEMS Studies*

Sawicka *et al.*[30] have studied the Fe^{57} implanted Al, Si, Ge and diamond samples by using the CEMS technique. In the case of aluminium host these authors have studied the effects of Fe^{57} implantation[40] over an ion dose range of 10^{14} ions/cm^2 to 2×10^{17} ions/cm^2. The maximum average ion concentration in aluminium which has been attained is $\sim$30%, which is far above the solid solubility limit of iron in aluminium (0.001% at room temperature and 0.025% at 650°C). Some results of CEMS measurements on Fe^{57} implanted in aluminium are given in Fig. 4.1. At iron concentrations smaller than 5% the spectra are composed of a singlet and a quadrupole split doublet. The single line can be attributed to iron monomers, while the doublet to higher iron associations (especially dimers[41]). As the average iron concentration is raised up to 5% the contribution of the single line decreases while that of the doublet increases systematically. The values of isomer shift corresponding to the two contributions show that the S-electron density at Fe-nucleus

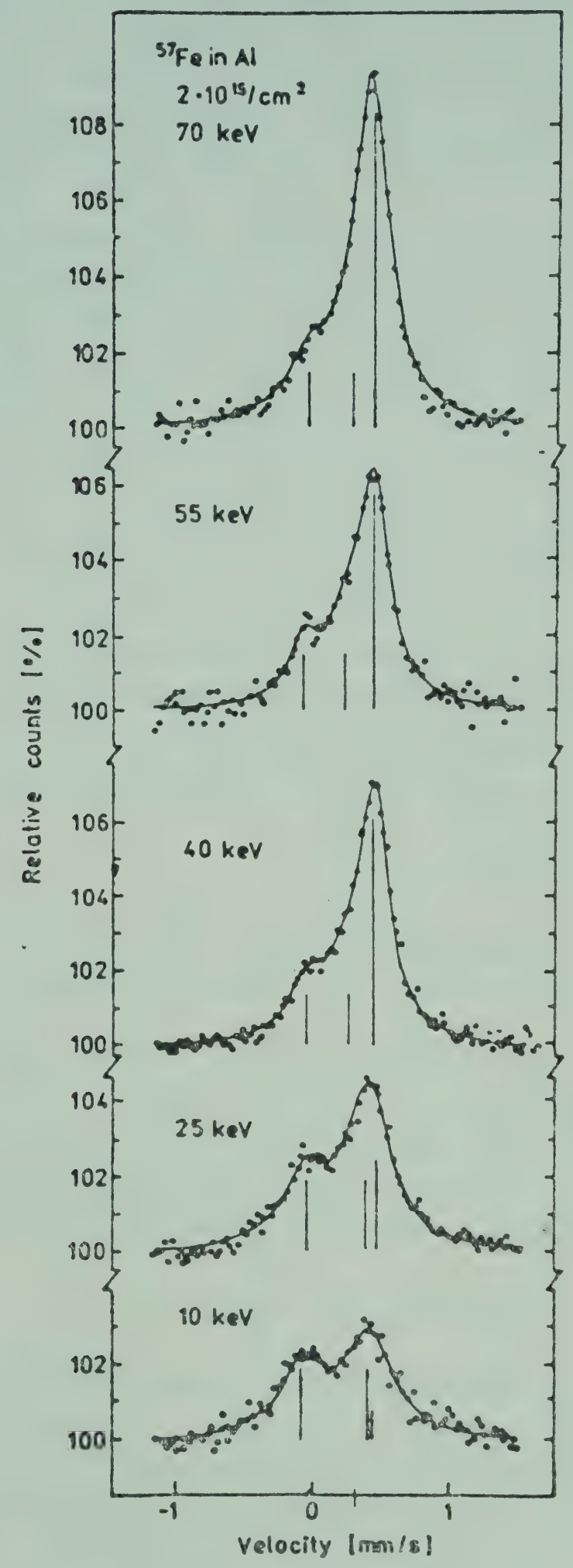

FIG. 4.1 Variation of CEM Spectra of Fe^{57} implanted in Al with ion energy and therefore, with concentration of implants ($\bar{x} = 0.5\%$, 0.6%, 0.9%, 1.1% and 2.1% respectively). A single line is due to iron monomers and a doublet is due to iron dimers.

is larger in iron dimers than in the monomers. In this case the CEMS technique has also revealed that the iron aggregation process is enhanced both by implantation at high doses (leading to high defect concentrations) and by thermal treatment. In fact, the fast quenching nature of ion implantation process has a very significant

contribution which can be seen from the fact that at dose values which are not high enough to lead to the formation of large iron clusters and yet high enough to surpass the limits of solid solubility, the contribution of iron monomers (non associations) does appear in the CEM spectra. These and other results on metallic hosts implanted with Fe^{57} ions reveal that the relative sizes of iron and the host atom play a significant role in deciding the final site of the implanted atoms in the host structure[30]. The Fe^{57} ions implanted in Fe, Co, Ni, Ru, Rh, Pd, Re, Os, Ir and Pt matrices indicate a good substitution of the host atoms and no contribution of dimers. On the other hand, Fe^{57} implantation in V, Cr, Rg, Mo and Ta (which incidently are bcc lattices) leads to the formation of a state in which monomers and dimers coexist. The Cracow group has also studied Fe^{57} implantation effects in silicon[42] and germanium[43] over a dose range between 5×10^{14} to 5×10^{16} ions/cm^2 and has obtained a very useful information about the implantation process.

Apart from the above mentioned basic studies on the physical processes associated with ion implantation, the CEMS technique has also been used to perform studies of applied nature in the same field. Baumvol has studied the influence of tin implantation on the oxidation of iron[34]. He has studied the influence of the implantation of Sn^+ ions over a does range between 5×10^{15} ions/cm^2 and 5×10^{16} ions/cm^2 on the oxidation of iron at the temperatures between 300°C to 500°C. It has been shown that the implantation of Sn^+ reduces the oxidation rate constant of iron upto a factor of ten, at all the experimental temperatures. Baumvol has used the Rutherford Backscattering, SEM (Scanning Electron Microscopy) and CEMS techniques to understand the mechanism of oxidation inhibition. His CEMS results obtained by using Sn^{119} in $CaSnO_3$ source are shown in Fig. 4.2(a); while the CEMS results obtained by using the Fe^{57} in Rh source are given in Fig. 4.2(b). The spectrum corresponding to the as-implanted sample [Fig. 4.2(a)] shows the presence of an intermetallic compound $FeSn_2$ and a solid solution of FeSn at an average concentration of 4 at % of Sn. The spectrum corresponding to oxidation at 350°C reveals the formation of SnO_2 while the spectrum corresponding to the oxidation at 500°C shows the formation of another intermetallic viz. FeSn along with SnO_2. The Fe^{57} CEMS study [Fig. 4.2(b)] reveals that, upon oxidation at 350°C the unimplanted sample forms Fe_3O_4, while the implanted sample does not indicate any oxidation within the detection limit afforded by the CEMS technique. Also, subsequent to the oxidation at 500°C, 100% of the CEM spectrum of the unimplated sample is composed of Fe_2O_3 and Fe_3O_4 lines, while the spectrum of the implanted sample mainly shows α-Fe with less than 14% contribution of Fe_2O_3. These results clearly reveal a considerable inhibition of oxidation of iron upon tin implantation.

Dorik *et al.*[35] (Poona group) have recently studied the oxidation properties of iron implanted with nitrogen ions by using the CEMS technique. In these experiments 80 KeV N_2^+ ions were implanted on iron foils at a dose of 2×10^{16} ions/cm^2 and a number of such samples in the as-implanted form or subsequent to a vacuum annealing treatment were subjected to oxidation treatment in air at the temperature in the range between 300°C and 500°C for four minutes in each case. The CEMS as well as the conventional gravimetric measurements preformed on these samples

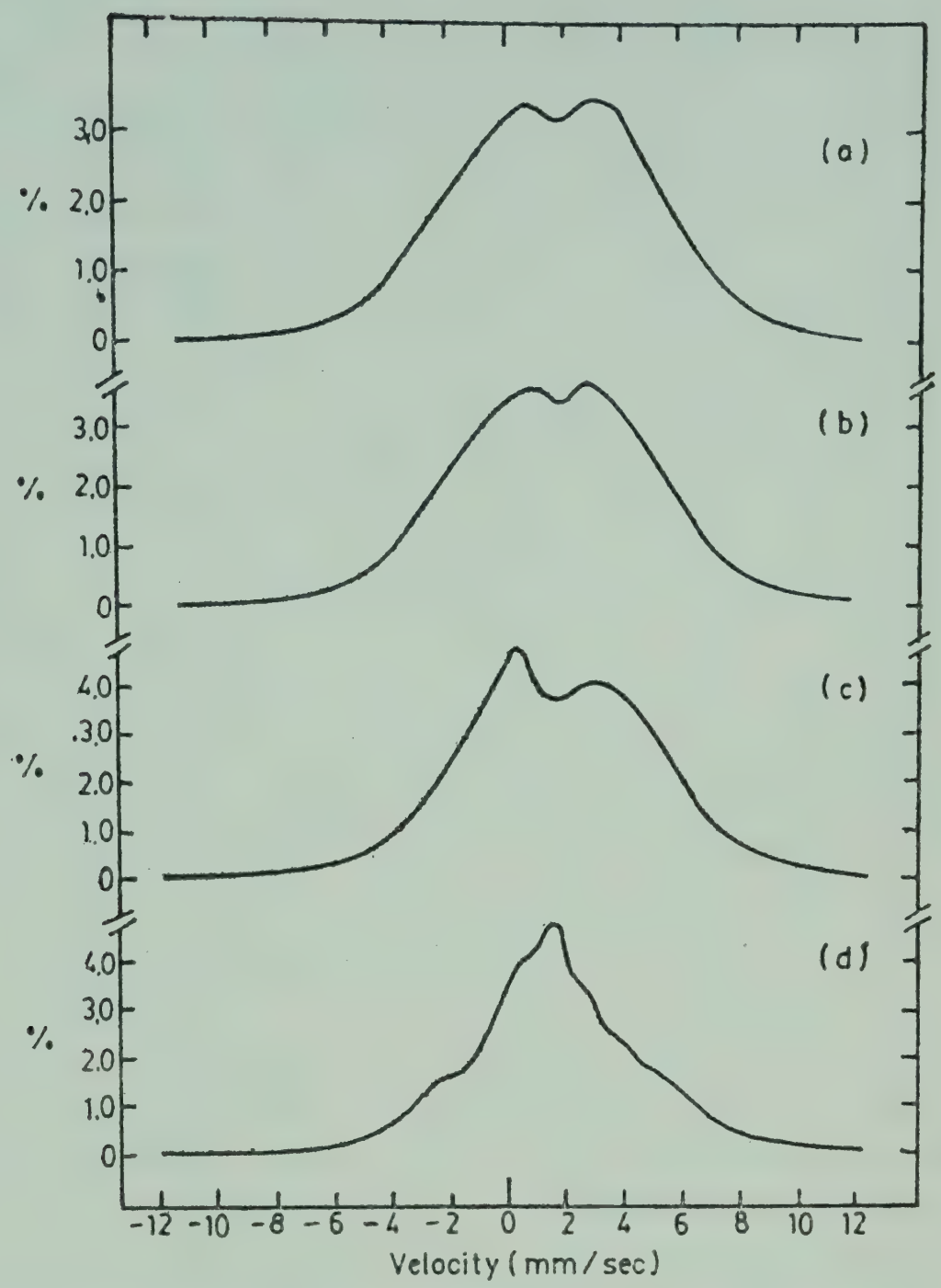

FIG. 4.2 (a) Room temperature Sn^{119} CEM spectra of iron implanted with Sn^{+} ions at a dose of 5×10^{16} ions/cm^2, oxidised at different temperatures for 20 minutes : (a′) as implanted, (b′) oxidised at 200°C, (c′) oxidised at 350°C and (d′) oxidised at 500°C.

revealed that the as-implanted samples exhibit an enhanced rate of oxidation as compared to the virgin iron foils. If one compares the spectra of Fig. 4.3 and 4.4(a) which correspond to the unimplanted and implanted samples oxidized at 300°C for 4 mins respectively, it is clear that the oxide components (Fe_2O_4 and Fe_2O_3) are dominant in the implanted case as compared to the case of the unimplanted sample. In fact, the ratio of the oxygen coordinated Fe to α-Fe has a value of 3.6 in the implanted case while a value of 0.96 in the case of the unimplanted sample. These differences in the oxidation rate were also confirmed by using gravimetric measurements. When the implanted foil which is annealed in a vacuum of 10^{-6} Torr at 300°C for 30 mins is oxidised, it shows a reduction in the oxidation rate even as compared to the rate exhibited by the virgin foil. This can be clearly seen by comparing the CEM spectra of Fig 4.3 and Fig. 4.5(a). The spectrum of Fig. 4.5(a) shows no detectable amount of the oxide fractions indicating thereby that the ion implanted and vacuum annealed foils show a significant improvement in the oxidation resistance of the virgin iron foils. This observation is once again in agreement

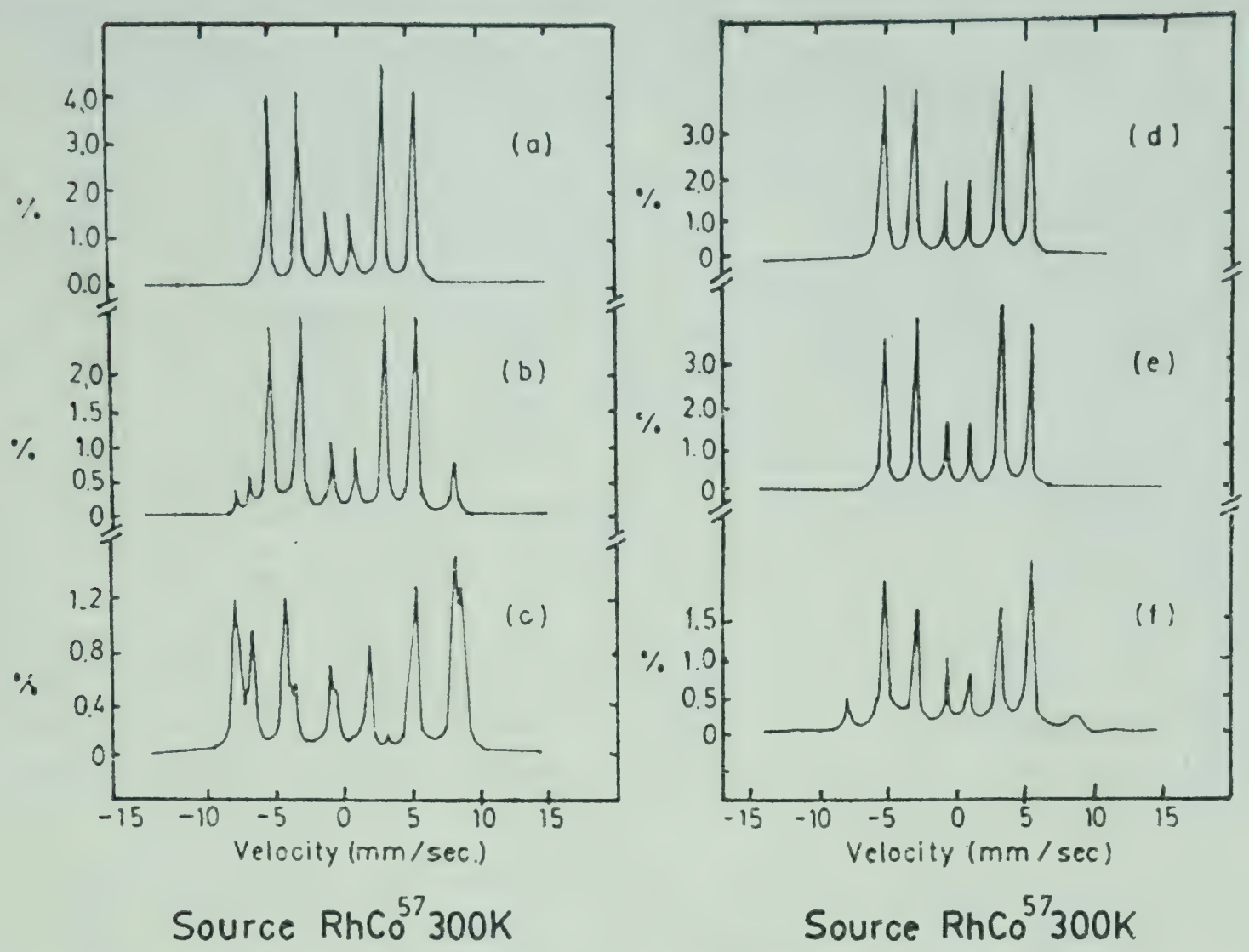

FIG. 4.2 (b) Room temperature Fe^{57} CEM spectra for unimplanted and implanted (5×10^{16} Sn^{+} ions/cm^2) iron, oxidised at different temperatures. Figures (a′), (b′) and (c′) correspond to the unimplanted iron foils oxidised at 200, 350 and 500°C respectively and (d′), (e′) and (f′) correspond to the implanted iron foils oxidised at 200, 350 and 500°C respectively.

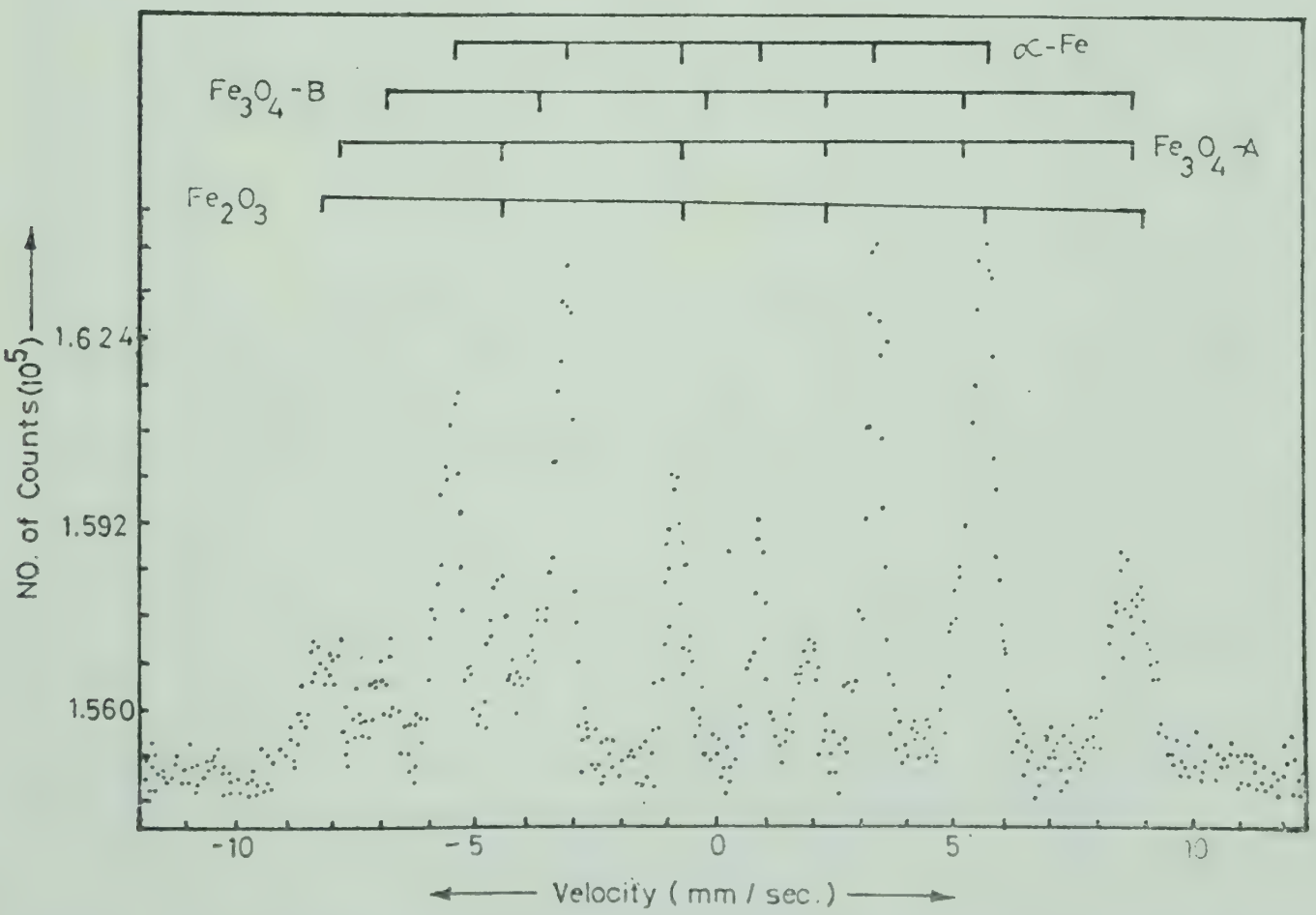

FIG. 4.3 Room temperature conversion electron Mössbauer spectrum of iron foil heated 300°C in air for 4 minutes.

of the gravimetric measurements. It may also be observed from Fig. 4.4 and 4.5 that at the oxidation temperature of 500°C both the implanted as well as the impalanted and annealed foils exhibit considerable oxidation.

It has been argued that ion implantation in iron produces defects and compressive stresses in the surface layers. Whereas the former effect enhances the oxidation rate due to defect assisted diffusion, the latter effect tends to inhibit it; the overall effect in the implanted sample being a reduction in oxidation resistance. The vacuum heat treatment (which is carried out at a temperature above the vacancy annealing temperature[44] for α-iron of 140°C but below its recovery temperature of 450°C) anneals out the point defects, stabilizes the compressive stresses and favours the magration of the implanted nitrogen atoms towards the grain boundaries and dislocation pipes leading to blockage of the short circuit paths for oxygen indifussion[18].

From the examples discussed in the above paragraphs it may be clear that the CEMS technique has a tremendous potential in investigating the properties of ion implanted metals and alloys which contain a suitable Mössbauer accessible

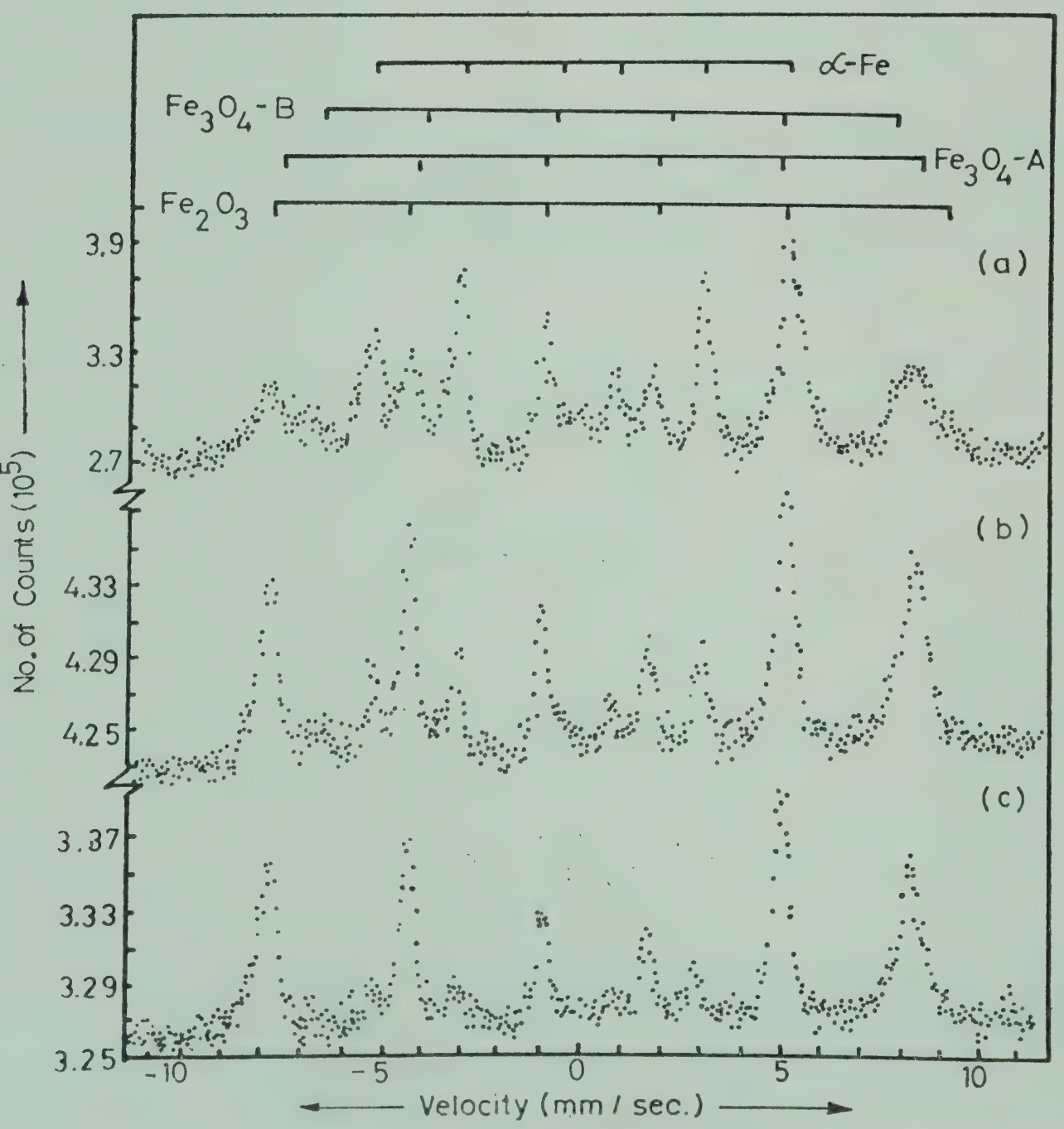

FIG. 4.4 Room temperature conversion electron Mössbauer spectra of N_2^+ implanted iron foil heated in air at (a) 300°C, (b) 400°C (c) 500°C for 4 minutes each.

element such as Fe or Sn. Very recently it has also been demonstrated that the CEMS technique is equally powerful in studying the physics of ion beam induced interface reactions, which have been a subject of considerable interest in recent years.

4.2. *Ion Beam Mixing : CEMS Studies*

The first experiments on the use of the CEMS technique for the studies of ion beam induced interface mixing and subsequent reactions were carried out very recently by the Poona University group [45–50]. The Ion beam induced interface reactions in the single interface Fe-Al (V. P. Godbole *et al.*)[45,47,50] Fe-Si (S. B. Ogale *et al.*)[44] and Fe-Ge (J. Patankar *et al.*)[44] structures have been investigated by this group, by using the Fe^{57} CEM Spectroscopy and interesting new information regarding the bombardment induced interface phenomena has been brought out. In all these studies, an iron film of a thickness of 300 Å was deposited onto the

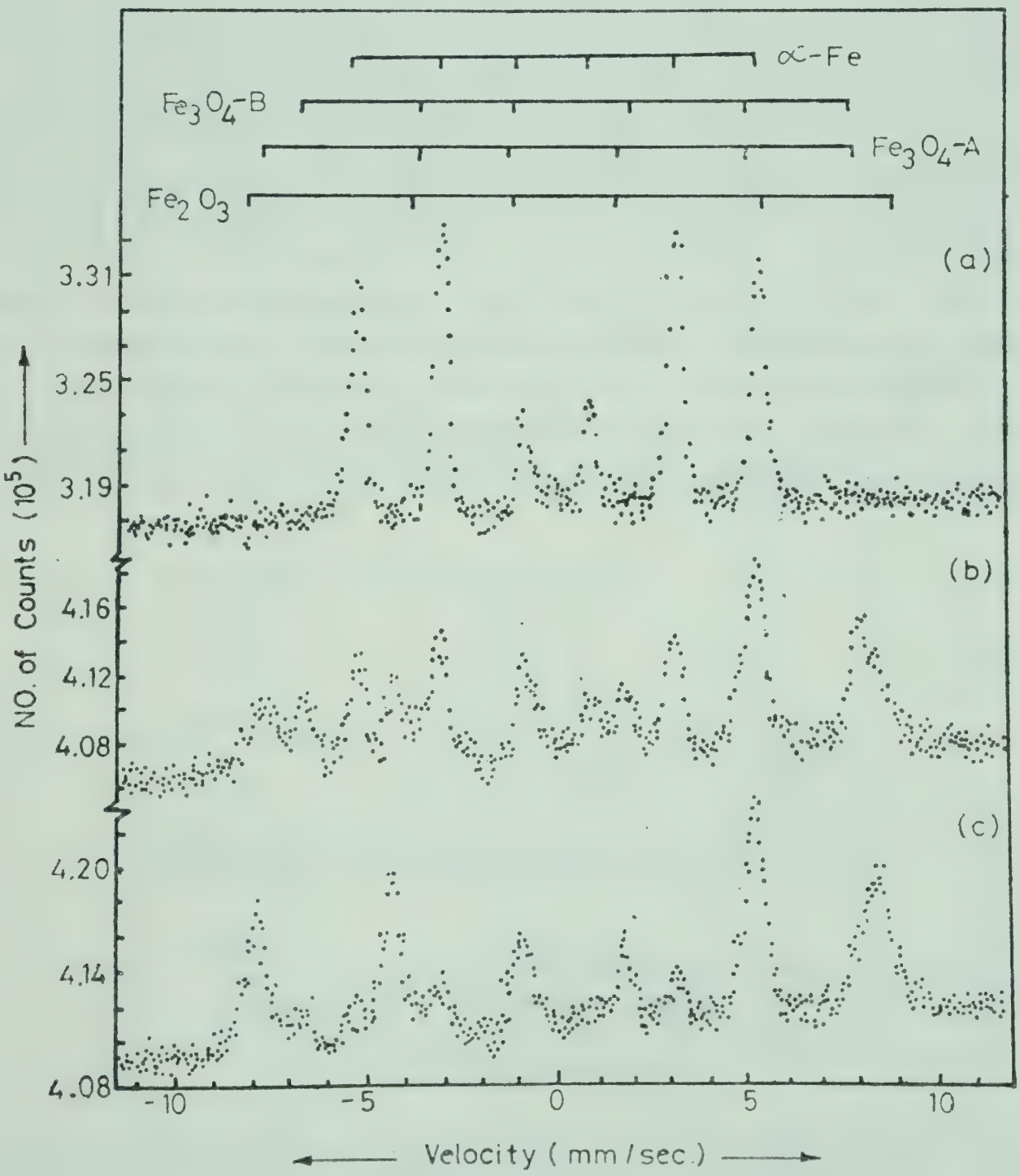

FIG. 4.5 Room temperature conversion electron Mössbauer spectra of N_2^+ implanted and vacuum annealed (300°C for 30 minutes) iron foils heated in air at (a) 300°C, (b) 400°C, (c) 500°C for 4 minutes each.

aluminium, silicon and germanium substrates conditioned by appropriate thermal and chemical treatments. Since ion beam mixing occurs at the interface and grows across it, a novel method of sample preparation was adopted to obtain the Mössbauer information predominantly from the interface region. For this purpose an ~ 50Å film of Fe^{57} Mössbauer isotope enriched to 95.45% was deposited on the substrates of Al, Si and Ge, followed by a deposition of an 250Å thick film of natural iron which contains only 2.2% of the Fe^{57} isotope (Fig. 4.6). Since the Mössbauer signal emanates only from the Fe^{57} nuclei, by using this sample preparation procedure an interface sensitive conversion electron Mössbauer spectroscopic study could be carried out and the early interface reactions in the ion beam mixed region could be revealed.

The first system in which the ion beam mixing process was characterised by the interface sensitive CEMS technique was Fe-Al. This system was chosen for the following reasons[47] : (i) Fe^{57}, a celebrated Mössbauer isotope is a constituent of one of the components of this system; (ii) the equilibrium solid solubility of Fe in Al is extremely low i.e. only 0.005 at. % even upto 450°C, with the result that the conventional thermal treatment does not lead to any substantial interface reaction in this system; which enables one to clearly identify the characteristic differences between the ion beam induced and pure thermal reactions at the interface of two elemental solids; (iii) the phase diagram of the Fe-Al system is extensively investigated and it shows the existence of a large number of phases such as Fe_4Al_{13}, FeAl, $FeAl_6$, Fe_2Al_5, Fe_3Al etc; which is a favourable situation in so far as the occurrence of mixing at the interface is concerned, as per the empirical rule established earlier; (iv) Al being a low-z material, it does not produce a high photoelectron background and thus the CEM spectra are expected to be of a good quality in the case of this system; and (v) Al being non magnetic, it does not create any complications in elucidating the magnetic hyperfine interactions at the Fe^{57} nuclei. Many Fe-Al samples,

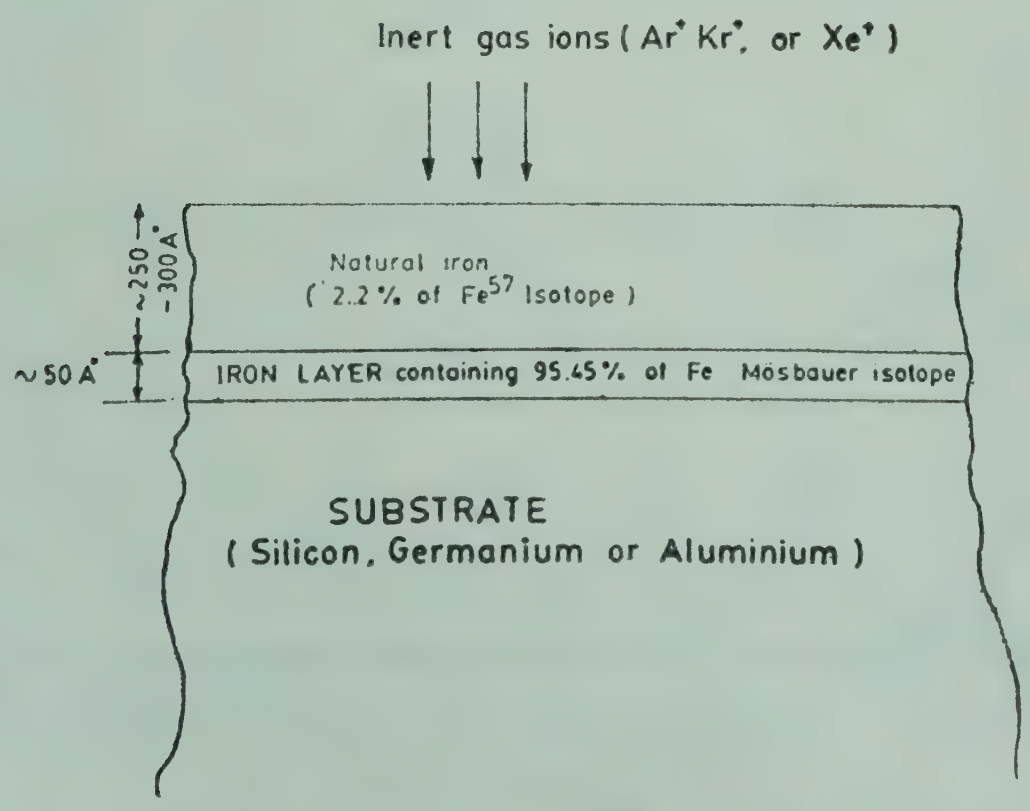
Inert gas ions (Ar⁺ Kr⁺, or Xe⁺)
~250 - 300 A°
Natural iron
(2.2 % of Fe57 Isotope)
~50 A°
IRON LAYER containing 95.45 % of Fe Mösbauer isotope
SUBSTRATE
(Silicon, Germanium or Aluminium)

FIG. 4.6 Sample for the interface sensitive Conversion Electron Mössbauer Spectroscopic Studies.

prepared by following the procedure mentioned above, were implanted with 100 KeV Ar^+ ions at a dose range between 1 × 10^{16} to 3 × 10^{16} ions/cm^2 to achieve the interface mixing. The fact that the interface mixing has occurred was confirmed by Rutherford Backscattering measurements (Fig. 4.7), which also brought out the average composition of the mixed zone to be $Fe_{55}Al_{45}$. The as-deposited as well as ion beam mixed samples were annealed at a background vacuum of 10^{-6} Torr at various temperatures up to a maximum of 600°C and the transformations in the CEM spectra were monitored. All the spectra were computer analysed by following the conventionl Mössbauer fitting procedure along with the procedure for obtaining the distribution of magnetic hyperfine fields as outlined by window.

The CEM spectra of the as-deposited sample and the corresponding hyperfine field distribution are shown in [Fig. 4.8(a) and Fig. 4.8(e)] respectively. In addition to the h.f. field of 330 KOe corresponding to α-Fe, the h.f. distribution also shows another dominant magnetic interaction corresponding to a field value of ~240 KOe, and an intense low field component which could indeed be due to the quadrupole and not the magnetic interaction. The h.f. field of 240 KOe corresponds to the presence of three aluminium neighbours at the sites of a number of Fe^{57} nuclei near the interface region. This can happen due to the deposition induced reaction. The appearent low field magnetic component could indeed be fitted with a quadrupole doublet contribution having the h.f. interaction parameters of isomer shift δ = 0.33 mm/s and quadrupole splitting Δ = 1.018 mm/s. The appearance of this

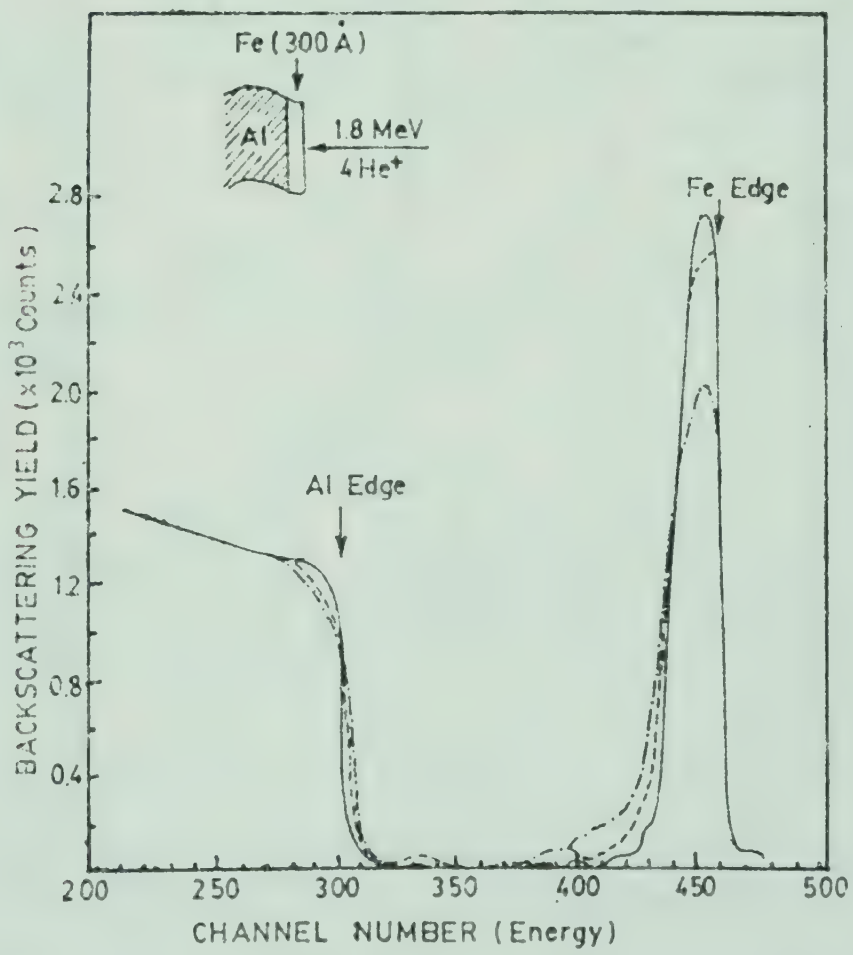

FIG. 4.7 Rutherford Backscattering Spectra (RBS) of the as-deposited and ion beam mixed composites. The————line corresponds to the as-deposited sample, the.....line corresponds to the sample bombarded with 100 KeV Ar^+ ions at a dose of 1 × 10^{16} ions/cm^2 and the–.–.–.–. line corresponds to the sample bombarded with 100 KeV Ar^+ ions at a dose of 3 × 10^{16} ions/cm^2.

doublet was attributed to the presence of Fe^{57} atoms in the γ-Al_2O_3 skin on the surface of aluminium[51] (This natural oxide of Al is always present on the surface of aluminium in the form of an ultra-thin film). When bombarded with Ar^+ ions the CEM spectrum shows a drastic change [see Fig. 4.8(b) and Fig. 4.8(f) for the field distribution [P(H) curve]. Figure 4.8(f) shows a considerable reduction of the peak at 330 KOe corresponding to α-Fe and emergence of low field components at field values of 100 KOe, 190 KOe and 252 KOe. It may be hypothesized that the local atomic coordination in the ion beam mixed region fluctuated randomly between the aluminium like (i.e. f.c.c.) and iron-like (i.e. b.c.c.) environments. The peaks at 192 koe and 252 kOe can thus be attributed to the fluctuations of atomic coordination between 8 to 12 neighbour environments. The peak at 100 KOe (lower field) can possibly be attributed to the dilute magnetic alloy of Fe in aluminium on the aluminium side of the interface.

When the ion beam mixed sample is annealed at 300°C and 400°C for twenty minutes in each case, the corresponding CEM spectra [Figs. 4.8(c) and 4.8(d)] and the field distributions [4.8 (g) and 4.8(h)] do not show any significant changes from the characteristics exhibited by the ion beam mixed sample. When annealed at

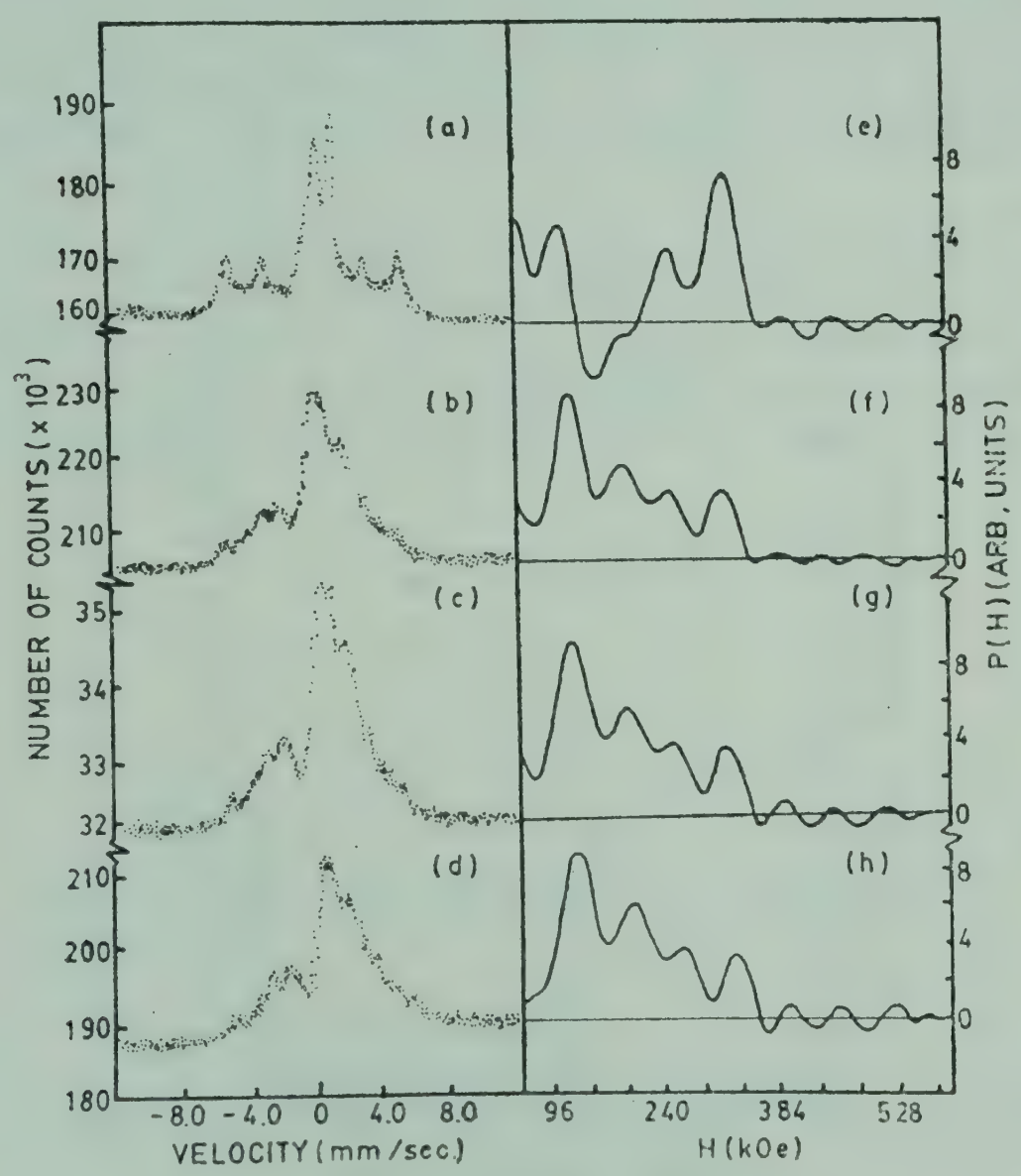

FIG. 4.8 Room temperature Conversion Electron Mössbauer Spectra of (a) as-deposited and (b) ion beam mixed Fe-Al composite. The spectra (c) and (d) represent ion beam mixed samples annealed at 300°C and 400°C respectively for 20 minutes each. The curves in figs. (e), (f), (g) and (h) are the hyperfine field distribution plots corresponding to the spectra in (a), (b), (c) and (d) respectively.

500°C for twenty minutes, however, the spectral features show a drastic change, and the standard computer fitting procedure reveals the presence of α-Fe and Fe_3Al phases[53] in the sample (Fig. 4.9). This sample when further annealed at 600°C, shows another drastic change in the CEM spectrum, which now indicates the presence of a small contribution of α-Fe and a large contribution of a central doublet component. The h.f. interaction parameters corresponding to the doublet match reasonably well with the parameters corresponding to the iron clusters in aluminium matrix[52].

When the as-deposited sample was annealed at various temperatures upto 500°C. the spectra continued to show the presence of α-Fe with an increase in the intensity of this spectral component and a gradual reduction of the central doublet corresponding to Fe^{57} in Al_2O_3 skin, which could be due to the out-diffusion of iron from the oxide. No Fe_3Al phase was observed in the case of the as-deposited sample annealed at 500°C, which showed the presence of only α-Fe. This clearly brings out the difference between the characteristics of the thermally induced interface reactions in the as-deposited and ion beam mixed samples.

The Poona group has also studied the dose dependence of ion beam mixing at the Fe-Al interface[57]. For this purpose, non-interface sensitive studies were carried out; in which the samples were prepared by depositing iron overlayer, containing~

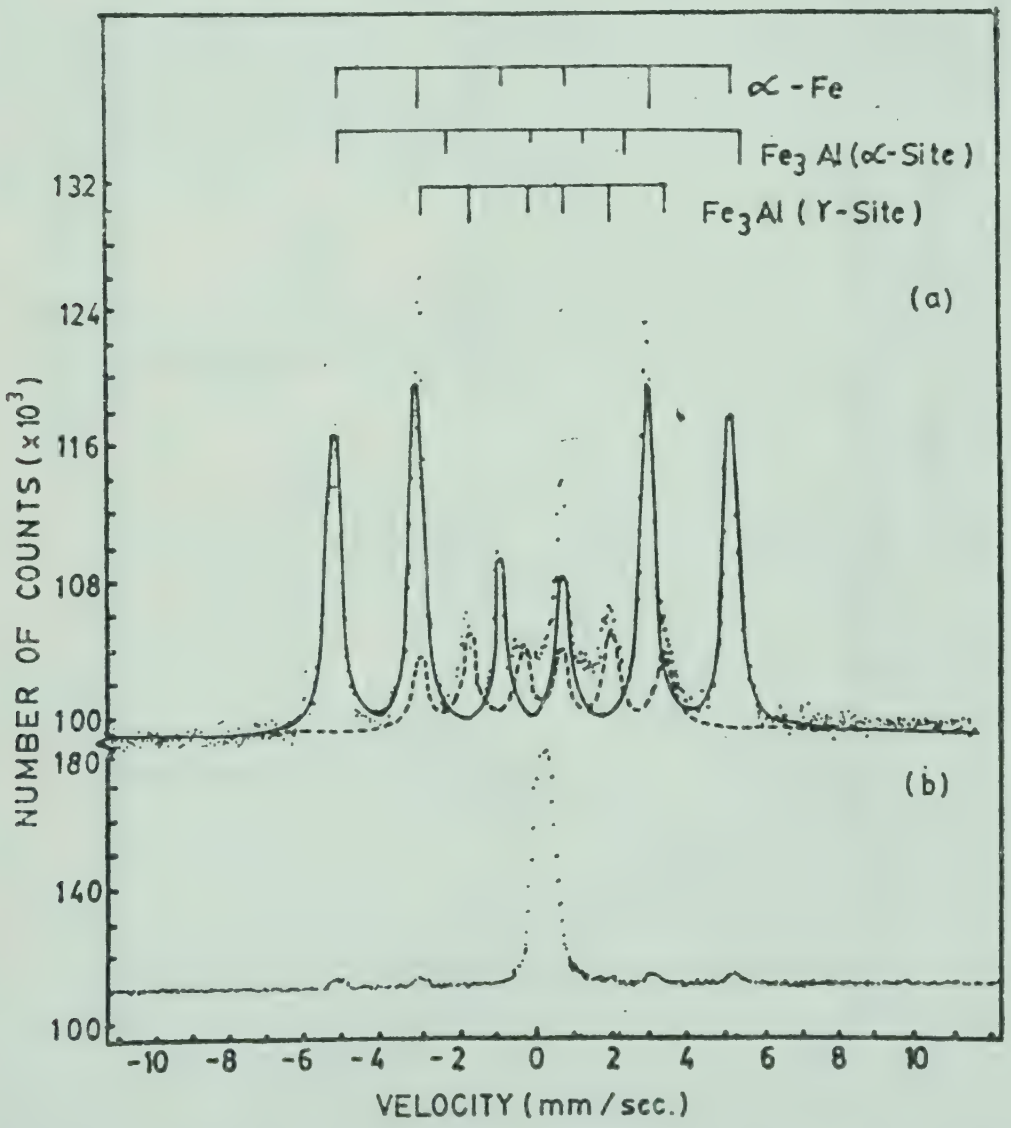

FIG. 4.9 Room temperature Conversion Electron Mössbauer Spectra of ion beam mixed samples annealed (a) at 500°C showing the precipitation of Fe and Fe_3Al phases, and (b) at 600°C showing the formation of iron clusters.

30% of the enriched Fe^{57} isotope uniformly distributed over the film region onto the aluminium substrates. Such non-interface sensitive studies were undertaken primarily to understand the nature of the change in the beam mixing process when the ion dose is raised from a low value of less than $\sim 5 \times 10^{14}$ ions/cm^2 at which individual cascade effects dominate, to the high doses at which the cascade overlap effects start playing an important role. The non-interface sensitive method was used in the place of the interface sensitive one in these studies because the interface sensitive technique defines a fixed length scale (of $\sim$ 50 Å) at the interface, which is not compatible to the growth of the mixed region as a function of the increase of the ion dose. The results of the non-interface sensitive CEMS studies are shown in Fig. 4.10.

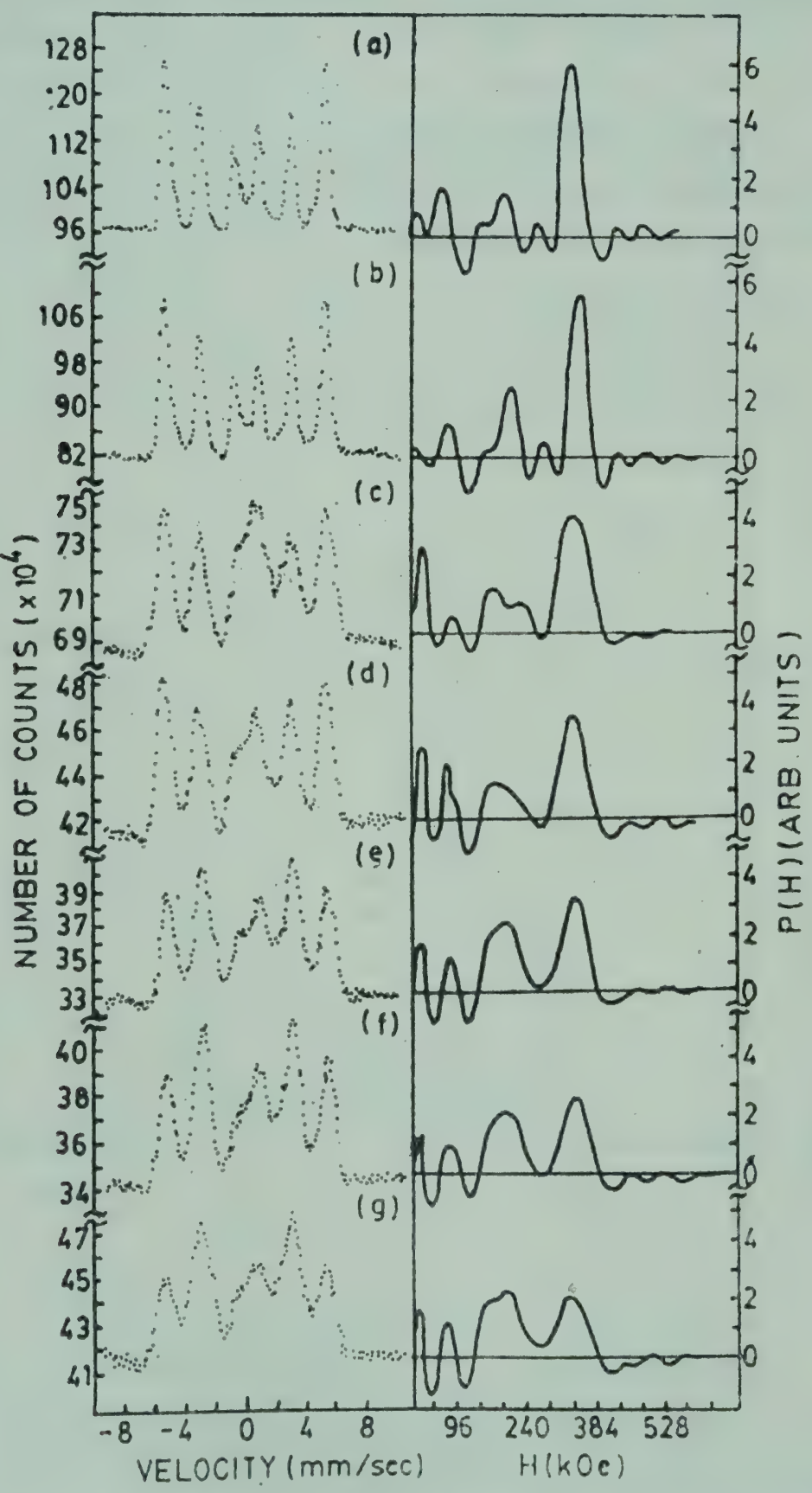

FIG. 4.10 Room temperature CEM spectra of (a) as deposited Fe-Al composite and ion beam mixed Fe-Al composite with a dose o[1] (b) 1×10^{14} ions/cm^2, (c) 5×10^{14} ions/cm^2 (d) 1×10^{15} ions/cm^2, (e) 5×10^{15} ions/cm^2, (f) 1×10^{16} ions/cm^2, (g) 3×10^{16} ions/cm^2. The corresponding hyperfine field distribution curves are represented with continuous curves.

In Figure 4.10(a) the CEM spectrum of the as-deposited sample is shown while in Fig. 4.10(b) to 4.10(g) the CEM spectra of the composites implanted with Ar^+ ions at various values of ion dose ranging between 10^{14} ions/cm^2 to 3×10^{16} ions/cm^2 are shown. The distributions of internal magnetic field have also been given for all the specta. The distribution corresponding to the as-deposited sample exhibits a peak at 330 KOe (which corresponds to α-Fe) and other small variations which can partly be attributed to the use of Fourier series in the decomposition procedure upon ion beam mixing. With increasing implantation dose the peak at 330 KOe shows a systematic decrease in intensity with emergence of peaks corresponding to lower values of hyperfine fields. Also the line widths of the Mössbauer spectral components show an increase with implantation dose, indicating the presence of disorder in the mixed zone. The emergence of peaks corresponding to lower field values is due to formation of an interface alloy in which the Fe^{57} nuclei find one or more of aluminium neighbours which contribute to the decrease of hyperfine field. When integrated over the entire range of lower field values distinguishable from the peak at 330 KOe, the total low field contribution shows an almost exponential rise with ion dose (Fig. 4.11). It may be noted however, that the rise is almost linear upto a dose of 10^{15} ions/cm^2 beyond which the nature of the curve and hence possibly the mixing process, shows a derivation[9]. It is interesting to note that the dose value of 10^{15} ions/cm^2 is typically the value at which the cascade overlap effects may be expected to dominate the mixing process.

Another binary system on which the ion mixing work has been carried out by the Poona group by employing the CEMS technique is Fe-Si (S. B. Ogale *et al.*)[18]. Apart from the fact that this system offers many advantages similar to those mentioned in the case of the Fe-Al system, the Fe-Si system can serve as a representative

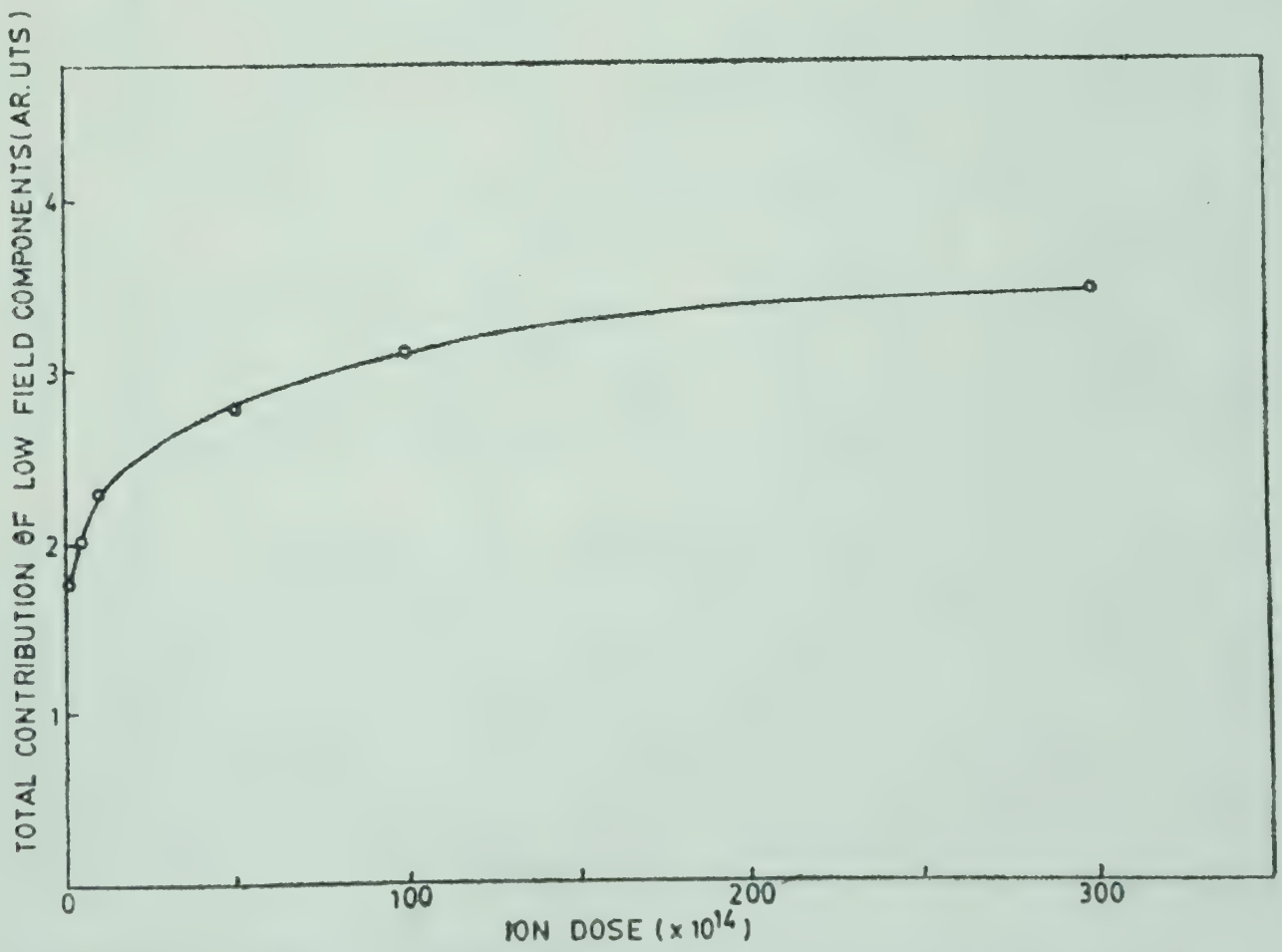

FIG. 4.11 Total contribution of low field component as a function of ion dose for Fe-Al composite.

of the 3d-transition metal silicides which are extremely useful in applications. The CEM spectra of the as deposited and ion beam mixed samples and the corresponding field distributions are shown in Fig. 4.12(a,b). It can once again be seen that ion beam mixing leads to an enhancement in the intensity of the low field components due to the incorporation of nonmagnetic silicon atoms in the iron matrix. Upon annealing at various temperatures upto a maximum of 700°C the ion beam mixed sample passes through various stages of recovery (see Fig. 4.13) leading finally to the precipitation of Fe_3Si phase. The as deposited sample on the other hand shows a diffusion limited interface reaction leading to the formation of only avery small quantity of Fe_3Si. In order to further reveal the interesting features of the interface reactions, we carried out resistance annealing measurements on the as-deposited as well as ion beam mixed samples. The results of these measurements (Fig. 4.14) are found to be in agreement with the results of CEMS measurements.

In addition to the Fe-Al and Fe-Si systems, the ion beam induced interface reactions have also been studied in the case of the Fe-Ge system by employing the CEMS technique. In these experiments the germanium substrates were prepared on

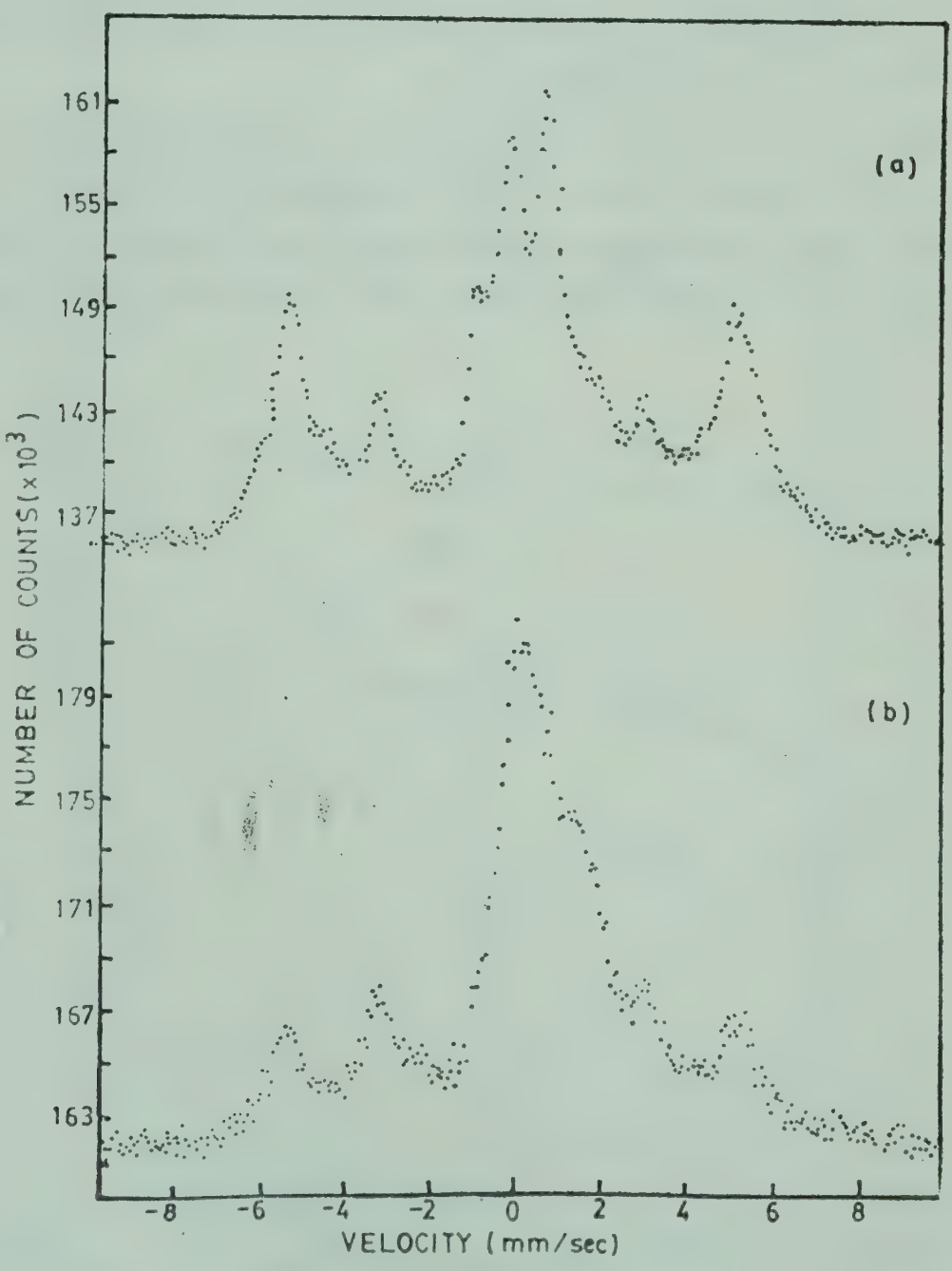

FIG. 4.12 (a) Room temperature Conversion Electron Mössbauer (CEM) spectra of (a′) as-deposited and, (b′) ion beam mixed (IBM) Fe-Si composites.

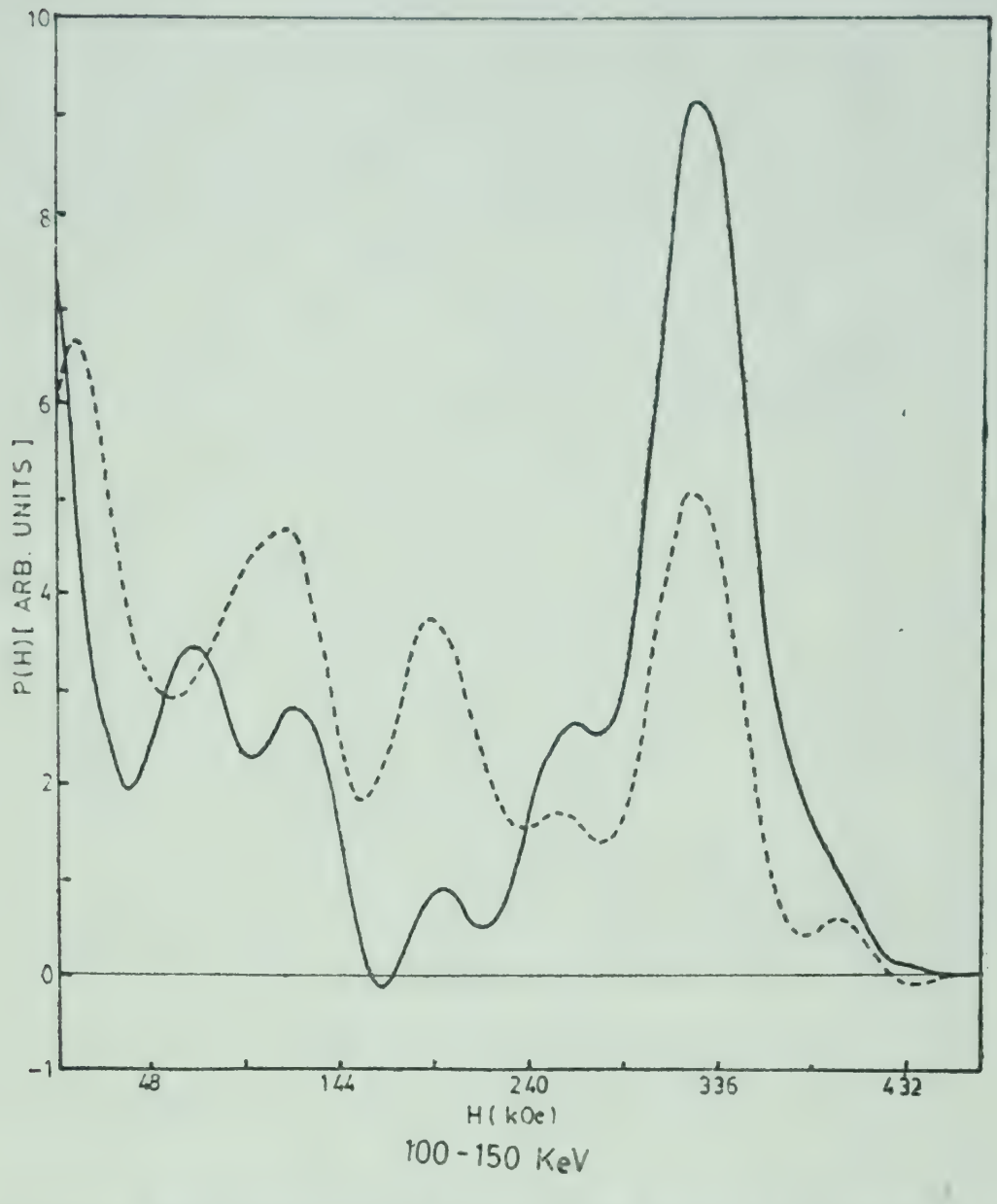

4.12 (b) The hyperfine field distribution P(H) curves for the as-deposited (solid line) and ion beam mixed (dashed line) Fe-Si composites.

the SiO_2 layers thermally grown on single crystal silicon surface; by vacuum evaporation method. Such substrates were then deposited with an ~ 50Å thick layer of Fe^{57} isotope enriched to 95.45% and subsequently with a 250A° thick layer of natural iron, as in the case of the interface sensitive studies on Fe-Al and Fe-Si systems. The CEM spectra corresponding to the as-deposited and ion beam mixed samples in the as-prepared form and subsequent to thermal annealing treatments at various temperatures upto a maximum of 625°C are shown in Fig. 4.15. These results once again clearly bring out the differences between the ion beam induced and purely thermal interface reactions. For detailed discussion regarding these spectra the reader is referred to the publication.

In the earlier paragraphs we discussed the work of basic nature concerning the ion beam mixing process which has been carried out by employing the CEMS technique. Using the same techniques the Poona group has also carried out an investigation of applied nature on the ion beam mixed state of Fe-Al alloy, in which the electro-chemical corrosive properties of this alloyhave been studied[47]. In these experiments the as-deposited as well as ion beam mixed Fe-Al samples prepared for interface sensitive CEMS measurements were subjected to electro-chemical corrosion by employing the three-sweep potentio-kinetic polarization technique at a sweep rate of 10 mv/s.

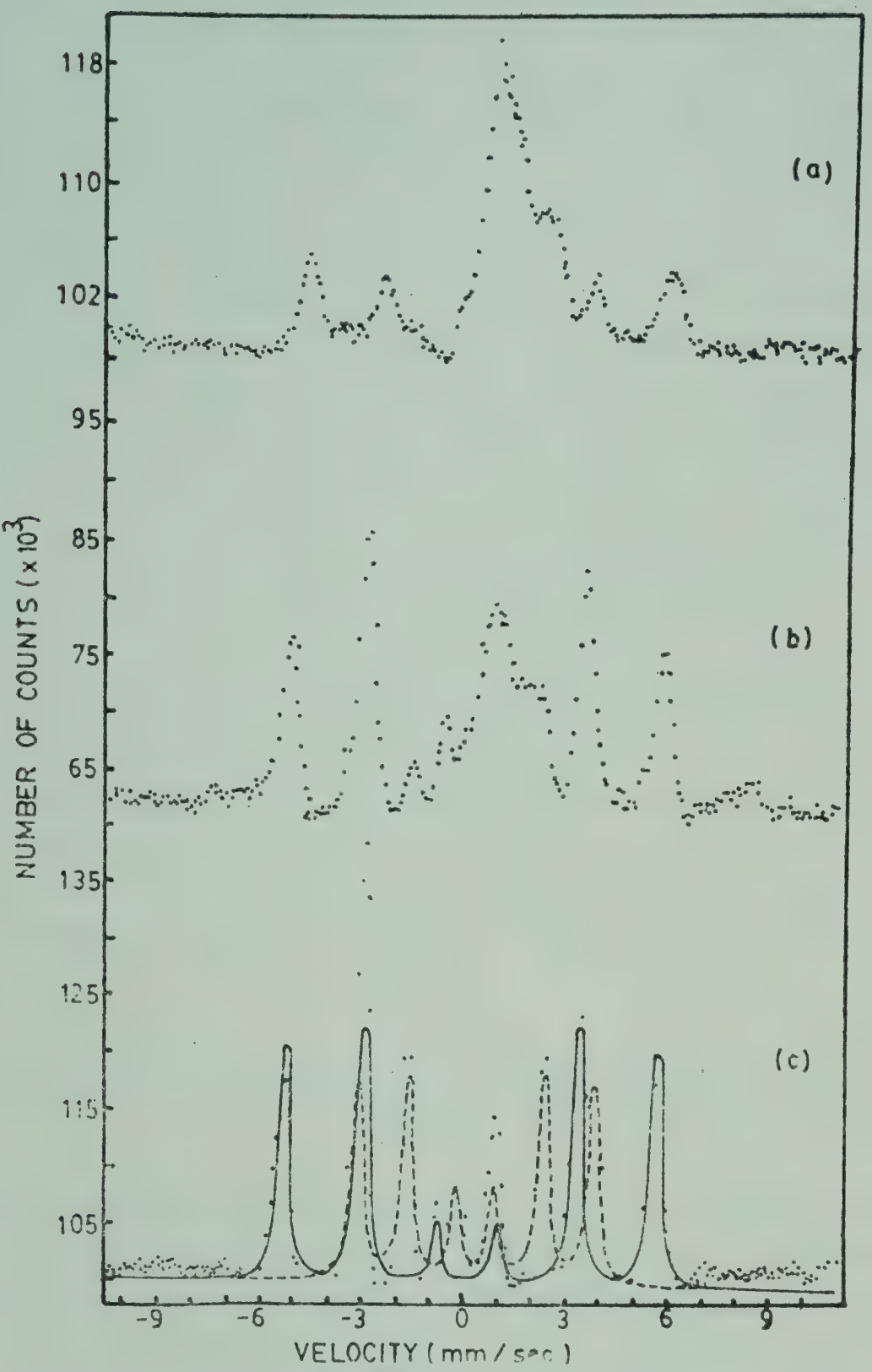

FIG. 4.13 Room temperature Conversion Electron Mössbauer Spectra of ion beam mixed Fe-Si composite vacuum annealed at (a) 240°C, (b) 450°C, (c) 700°C for one hour in each case. Subspectrum shown with dashed line in Fig. (c) shows the sextet corresponding to the Fe_{II} site! of the Fe_3Si phase while the other subspectrum (solid line) shows the sextet corresponding to α-Fe with an overlap of the contribution of site of Fe_3Si.

From Fig. 4.16(a), it is observed that the Fe foil clearly shows active to passive transition. In the case of aluminium, no active to passive transition is observed [Fig. 4.16(b)] because, subsequent to an initial dissolution, the passivation ensues almost immediately due to the formation of an aluminium oxide coating in the aqueous medium.

When the as-deposited sample was subjected to electrochemical corrosion, the iron layers deposited on the aluminium substrates dissolved completely [Fig. 4.17(a)]. On the other hand, the ion beam mixed Fe-Al sample exhibited distinctly different features as compared to as-deposited Fe-Al sample [Fig. 4.17(b)]. An examination of [Fig. 4.17(a) and Fig. 4.17(b)] clearly shows that the dissolution of iron is

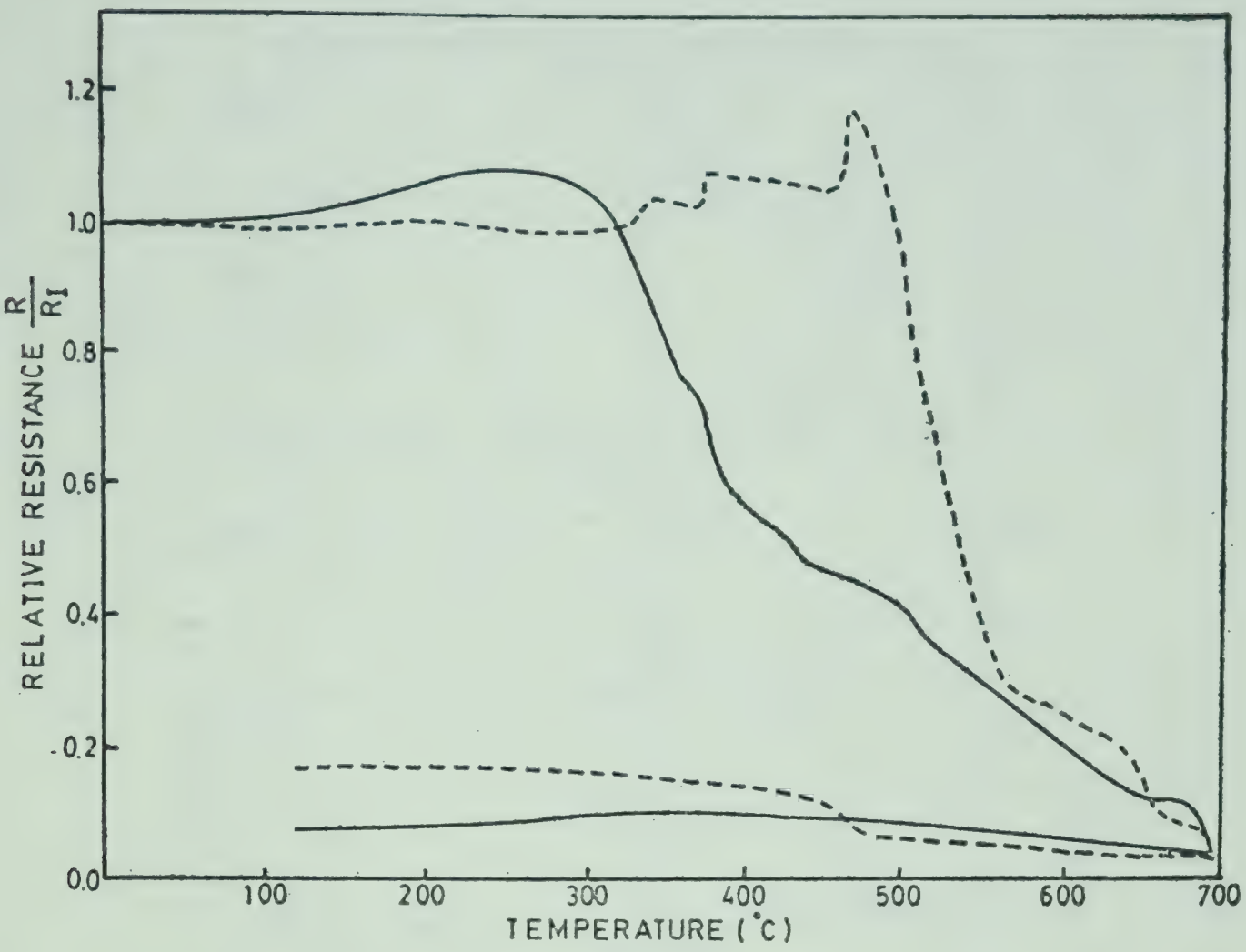

FIG. 4.14 Resistance-annealing curve for the as-deposited (solid line) and ion beam mixed (dashed line) Fe-Si composites.

considerably higher in the as-deposited sample as compared to the ion beam mixed the curve sample. This is indicated by the current density corresponding to the point G on of the first negative going sweep. It is also observed that the as-deposited sample does not show any active-passive transition and indicates a dissolution similar to that of pure aluminium.

In order to reveal the physics of the corrosive properties exhibited by the ion beam mixed sample we characterised this sample before and after the corrosive action by using the CEMS technique. The CEM spectrum of the ion beam mixed sample [Fig. 4.18(b)] is significantly different as compared to that of the as-deposited sample [Fig. 4.18(a)] and the corresponding magnetic field distribution [Fig. 4.18(e)] shows four peaks at 100 KOe, 192 KOe, 252 KOe and 330 KOe. On comparing [Fig. 4.18(d)] with [Fig. 4.18(e)], it is clearly seen that the peak at 330 koe which corresponds to α-Fe is considerably reduced and low field components are increased upon ion bombardment. This means that significant atomic mixing has occuried at the interface. The average composition of the mixed layers obtained by RBS technique turns out to be $Fe_{55}Al_{45}$. The details of this CEM spectrum and the corresponding field distribution have already been discussed earlier in this report. In the present context it may only be mentioned that the ion beam mixed interface is a disordered alloy with significant fluctuations in local alloy structure and composition.

When subjected to corrosion the ion beam mixed sample leads to CEM spectrum as shown in Fig. 4.18(c). When decomposed, this spectrum gives magnetichy perfine

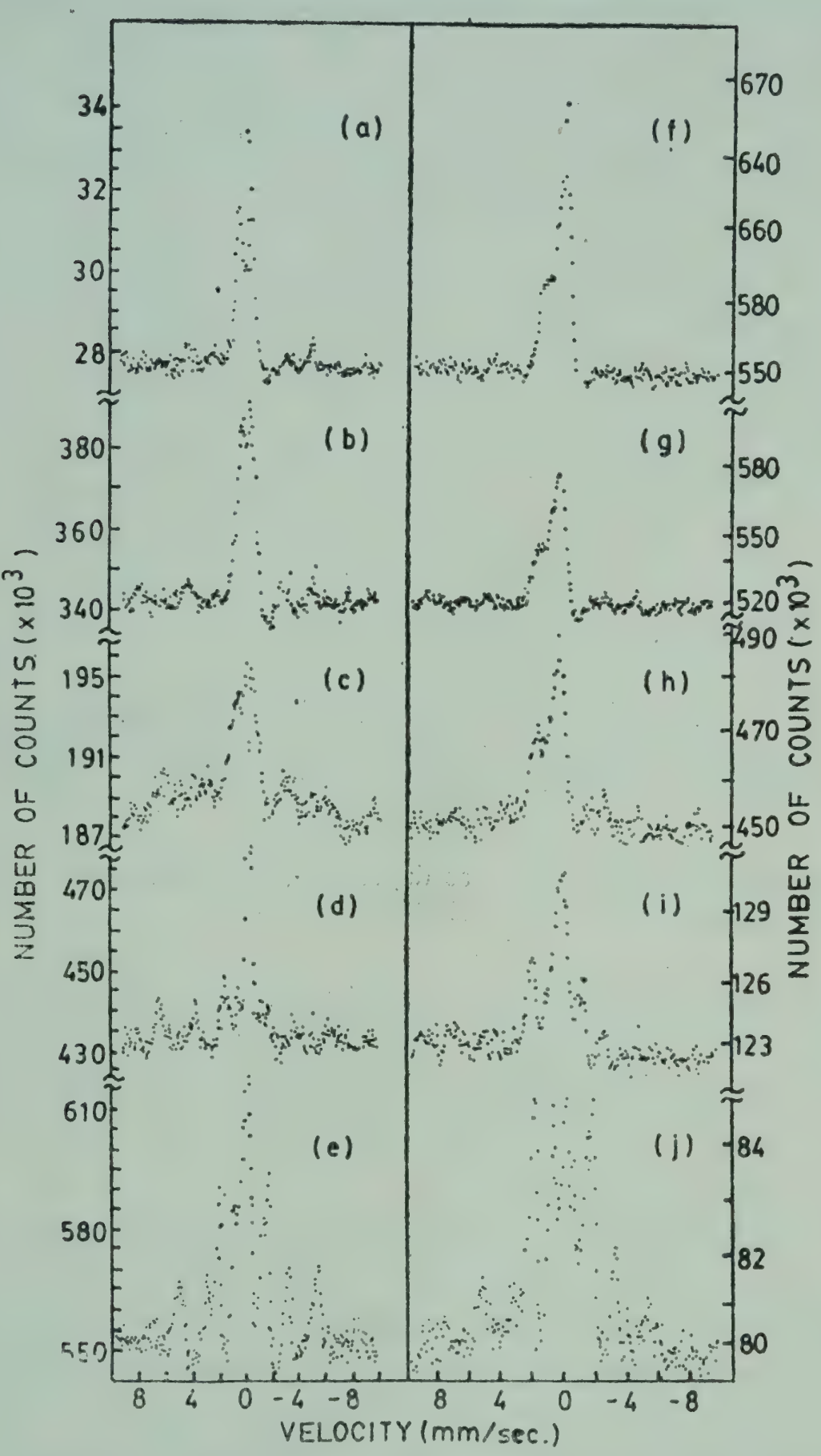

FIG. 4.15 Conversion Electron Mössbauer (CEM) spectra of (a) as-deposited and (f) ion beam mixed Fe-Ge composites. CEM spectra in figures b(g), c(h), d(i) and e(j) correspond to the as-deposited (ion beam mixed) sample annealed at 200°C), 350°C, 500°C and 625°C respectively, for one hour each.

field distribution as given in Fig. 4.18(f). It can be readily seen that the peaks at 192 KOe and 252 KOe, in the field distribution corresponding to the ion beam mixed sample are decreased substantially upon corrosion while the peak at ~ 100 KOe is shifted to a lower field value of ~ 90 KOe. It is also observed that the peak at 330 koe is decreased to a certain extent. In addition to these changes in the magnetic components we could fit the total spectrum of Fig. 4.18(c) with two quadrupole-split doublets. One of the doublets has an isomer shift of 0.40 mm/sec and a quadrupole splitting of 0.63 mm/sec, while other doublet has an isomer shift of 0.89 mm/

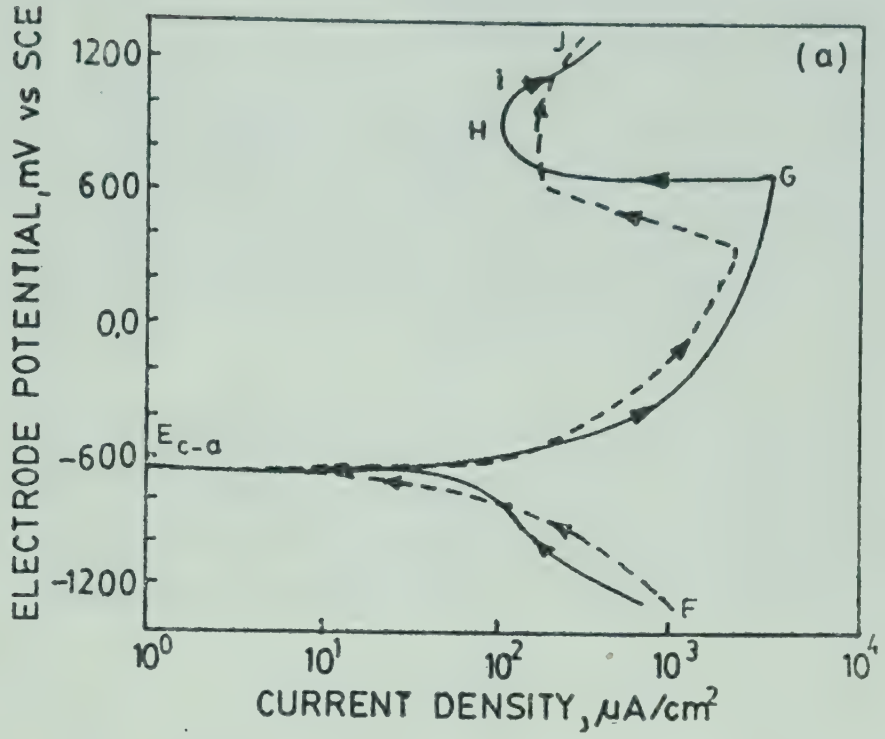

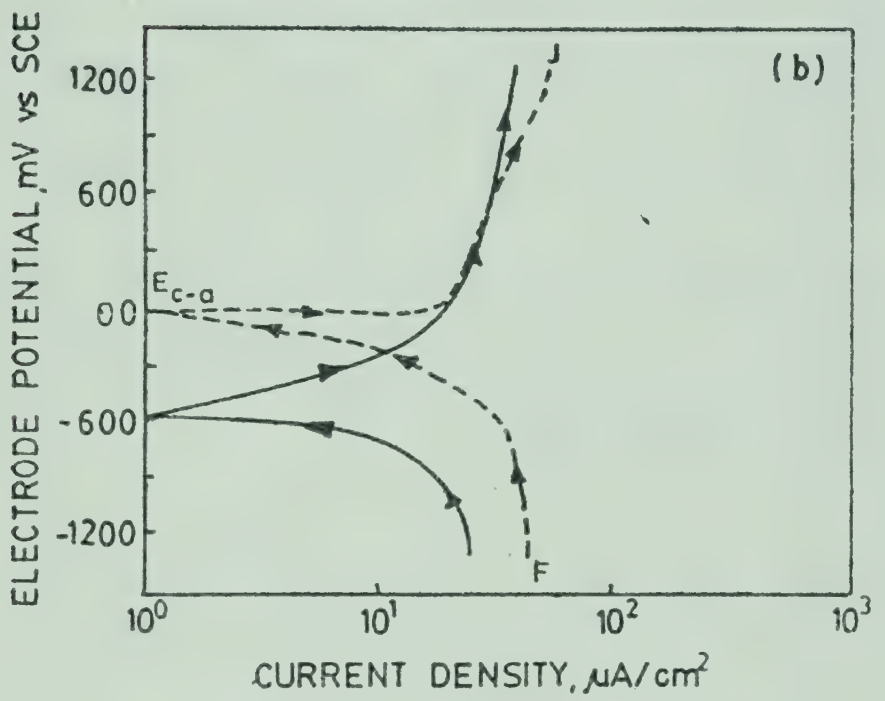

FIG. 4.16 Second positive going sweeps in the three sweep potentio-kinetic polarization curves for (a) pure iron foil and (b) pure aluminium foil. The full line (———) and dashed (- - -) curves correspond to sweep rates of 1.33 mV/sec and 10 mV/sec respectively.

sec and a quadrupole splitting of 1.27 mm/sec. The hyperfine parameters of the latter doublet match resonably well with those of FeO[54–56] (I. S. = 0.91 mm/sec.; Q. S. = 0.80 mm/sec) except for a higher value of the quadrupole splitting which may be attributed to the thinness of the ion beam mixed film and to the damage imparted to the interface structure due to the ion bombardment. The hyperfine parameters of the other doublet can be favourably compared to those of hydrated nonmagnetic oxides of Fe[53–56] such as, γ-FeOOH (I. S. = 0.38 mm/sec. Q. S. = 0.59 mm/sec), β-FeOOH, (I. S. = 0.37 mm/sec., Q. S. = 0.71 mm/sec. and also α-Fe_2O_3 clusters[57] (I.S. = 0.31 mm/sec. and Q. S. = 0.98 mm/s). As indicated earlier, the local atomic coordinations in the ion beam mixed alloy fluctuate within the mixed region and hence formation of two or more phases of the above type is indeed possible.

4.3. *Laser Treatment : CEMS Studies*

As mentioned earlier the laser treatment has emerged as a powerful material processing technique in recent years. Applications of CEMS technique to the study of the physics of laser-solid interactions have begun to appear in literature only very recently and in what follows, as have discussed a few such cases to serve as illustrations.

Petrikin *et al.*[58] carried out very interesting experiments by using laser irradiation as an alternative to diffusion and ion implantation, to incorporate iron dopants from a deposited layer into the bulk of silicon. A typical spectrum of a sample with an iron layer (30 μg/cm^2) deposited on silicon and irradiated with 2.6 J/cm^2 is shown

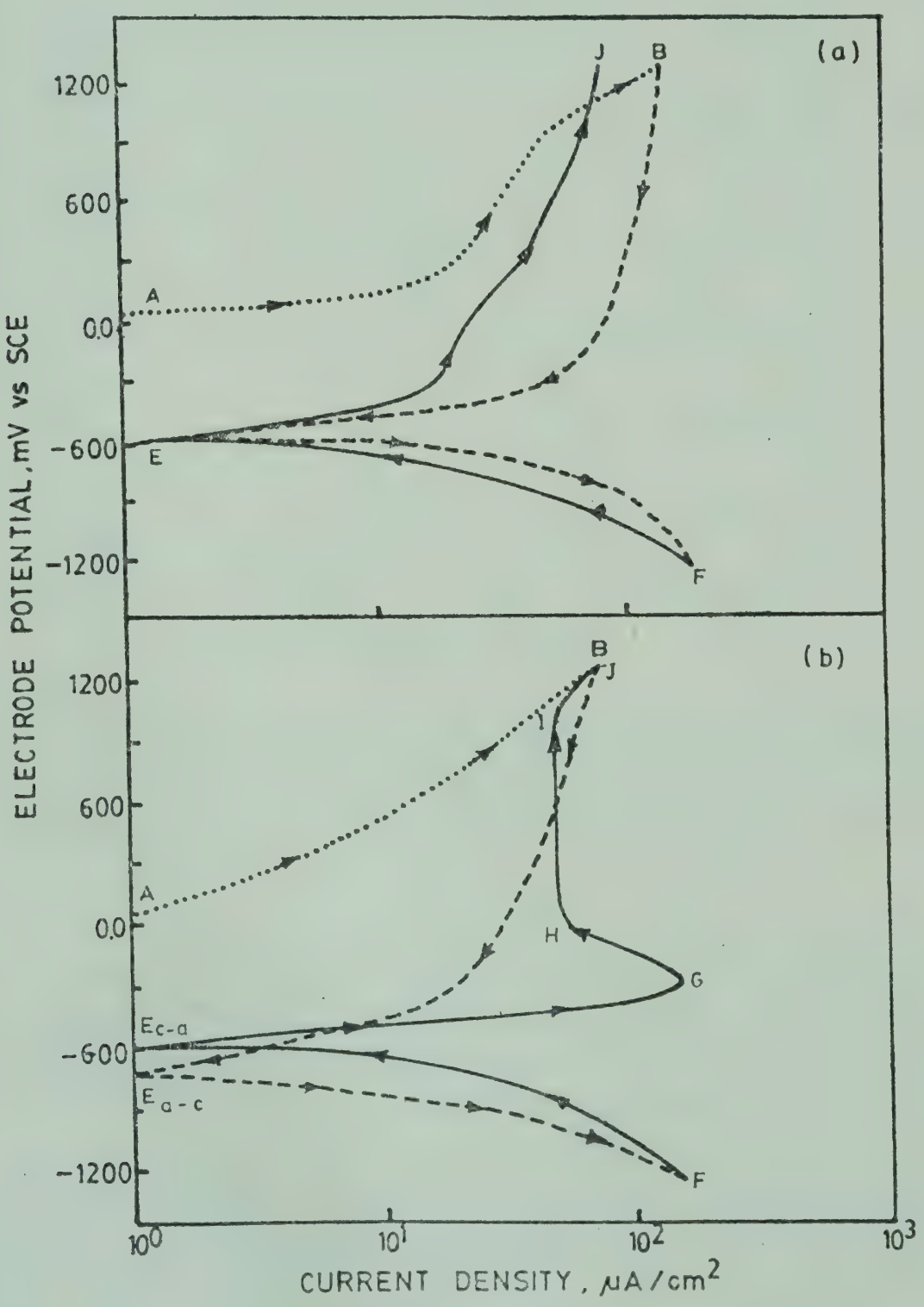

FIG. 4.17 Three sweep potentio-kinetic polarization curves for (a) as-deposited and (b) ion beam mixed, Fe-Al composite. The dotted (.....) curve corresponds to 1st positive going sweep, the dashed (– – – –) curve corresponds to 1st negative going sweep and the full line (————) curve corresponds to 2nd positive going sweep at the sweep rate of 10 mV/sec.

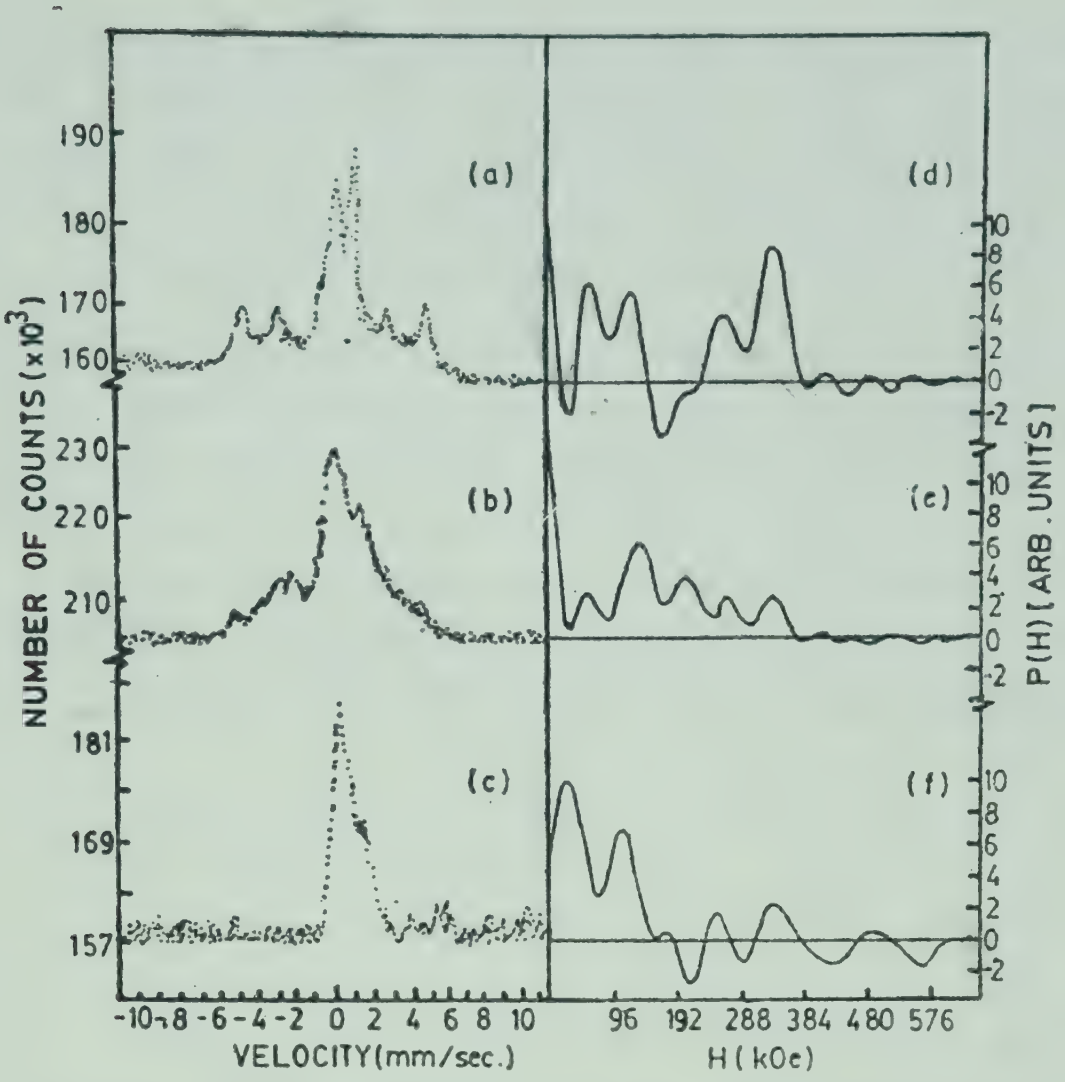

FIG. 4.18 Room temperature conversion electron Mössbauer spectra of Fe-Al composite : (a) as-deposited (b) ion beam mixed and (c) ion beam mixed composite subjected to aqueous corrosion. Hyperfine field distributions corresponding to the spectra in (a), (b) and (c) are shown in (d), (e) and (f) respectively.

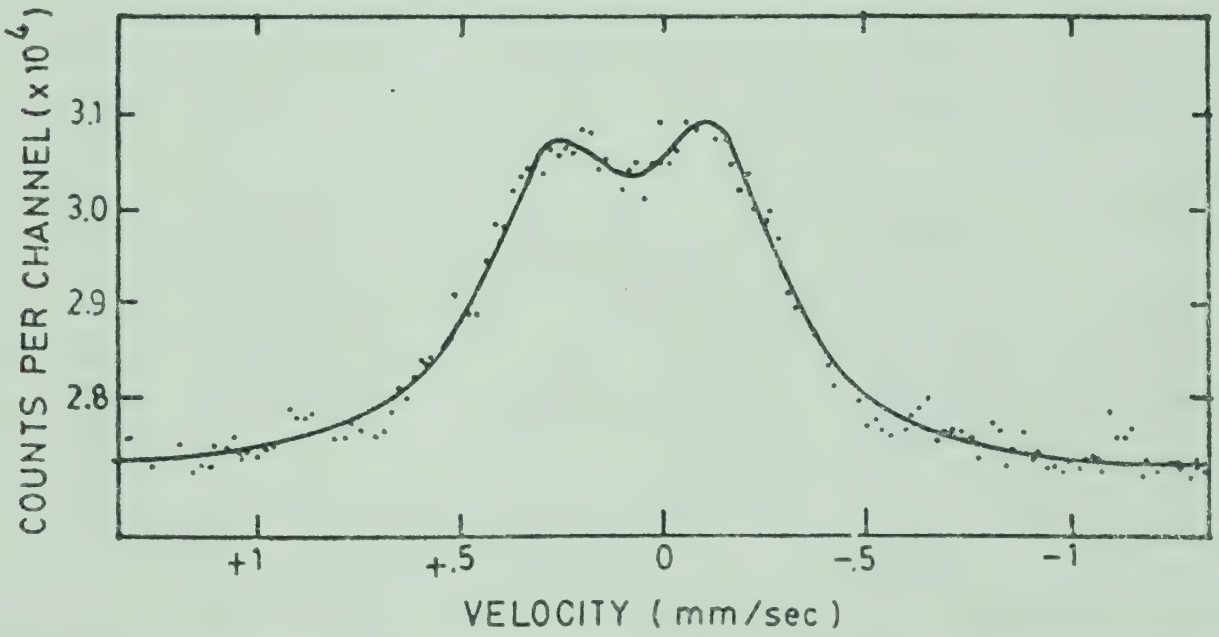

FIG. 4.19 Room temperature CEM spectrum of a sample (Fe^- implanted in Si) irradiated with 2.6 J/cm² laser pulse.

in Fig. 4.19. The Mössbauer lines in the spectra are interpreted as components of a quadrupole-split doublet (I.S. = 0.2 mm/sec relative to α-Fe and Q. S. = 0.40 mm/sec) due to $FeSi_2$[59]. The nature of this spectrum did not exhibit any change upon the stripping up of surface layers upto a depth of 3500Å, except for a decrease in intensity. This laser induced diffusion of iron atoms can be explained on the basis of the liquid phase model. It was also observed that with the use of a low power

density (1—0.6 J/cm²) of laser irradiation, iron atoms could not be incorporated below 100Å from the surface. Though the concentration of iron atoms diffused inside silicon was very high, the penetration was observed to be only in shallow surface layers. This can be due to the solid phase nature of the interface reaction induced by the laser irradiation at a low power density.

Experiments of the type discussed above have also been reported by Prasad[60]. In this investigations, an iron film (100Å) of enriched Fe^{57} isotope was deposited on polycrystalline Al foil and such samples were irradiated with a pulsed ruby laser ($\lambda = 0.693\ \mu m$) having a pulse width of 25 ns and an energy density in the range of 0–4 J/cm². Figure 4.20 shows CEM spectrum of the Fe-Al sample irradiated with a single 3.6 J/cm² laser pulse, alongwith the CEM spectra of the laser treated samples which were thermally annealed at 300°C, 500°C, 600°C and 630°C for 20 minutes

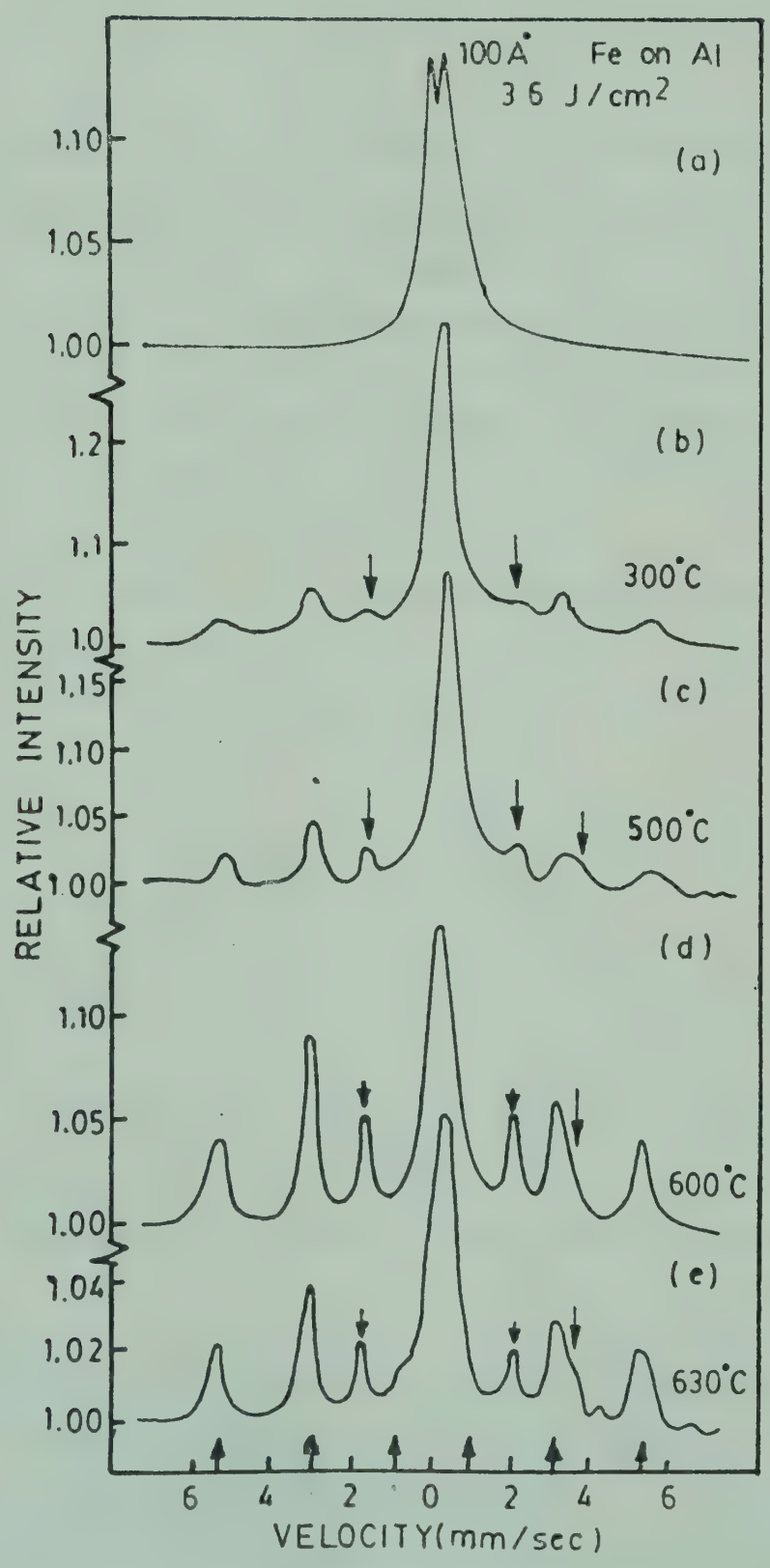

FIG. 4.20 Room temperature CEM spectra of Fe-Al composite irradiated with 3.6 J/cm² laser pulse (top) and subsequent thermal annealing.

in each case. The spectrum of Fig. 4.20(b) shows the presence of a quadrupole doublet (I.S. = 0.19 mm/sec, Q. S. = 0.4 mm/sec) and a singlet (I.S. = 0.43 mm/sec) having a small intensity. These Mössbauer parameters correspond to Fe dimers and monomers in Fe-Al system[52]. The CEM spectra of the vacuum annealed samples show development of resonance lines characteristic of α-Fe, Fe rich clusters, Fe_3Al and $Al_{13}Fe_4$[52]. This brings out the nonequilibrium nature of the pulsed laser irradiation process. The spectra shown in the work of Prasad also bring out that laser induced amorphasization is quite insignificant in the case of nanosecond pulsed laser treatment.

Recently, Dektiyar *et al.*[61] have reported CEMS studies on Laser irradiated Nb-Fe binary systems. They have basically investigated the redistribution of elements and formation of intermetallic compounds near the Nb-Fe boundary subsequent to laser irradiation. The CEM spectrum of a sample having niobium layer deposited on Fe^{57} layer shows no resonant absorption due to the attenuation of conversion electrons in the niobium over layer. When irradiated with the laser beam ($\lambda = 1.06\ \mu m$) the sample yields a CEM spectrum which shows the presence of distorted α-Fe lines [Fig. 4.21(a)] and this observation can be explained on the basis of the directed diffusion of iron atoms across the Nb-Fe interface which is connected with the directed defect generation by the laser action. Dektiyar *et al.*[61] also observed that the change in the sequence of layer deposition i.e. deposition of Fe^{57} on Niobium results in completely different laser induced reactions (Fig. 4.21(b)). In this case, the spectrum of the as-deposited sample shows a six finger pattern corresponding to α-Fe; however, upon laser irradiation the magnetic spectrum is found to transform into a quadrupole doublet (I.S. = 0.05 mm/sec. Q. S. = 0.28 mm/sec) which can be attributed to the formation of the $NbFe_2$ Phase[61]. These studies once again bring out the potentialities of the CEMS technique in the studies on laser treated materials.

5. Applications of Conversion Electron Mössbauer Spectroscopic (CEMS) Technique in Other Fields

In view of its simplicity and potentiality in bringing out the Mössbauer information regarding the submicron layers on solid surfaces the CEMS technique has found

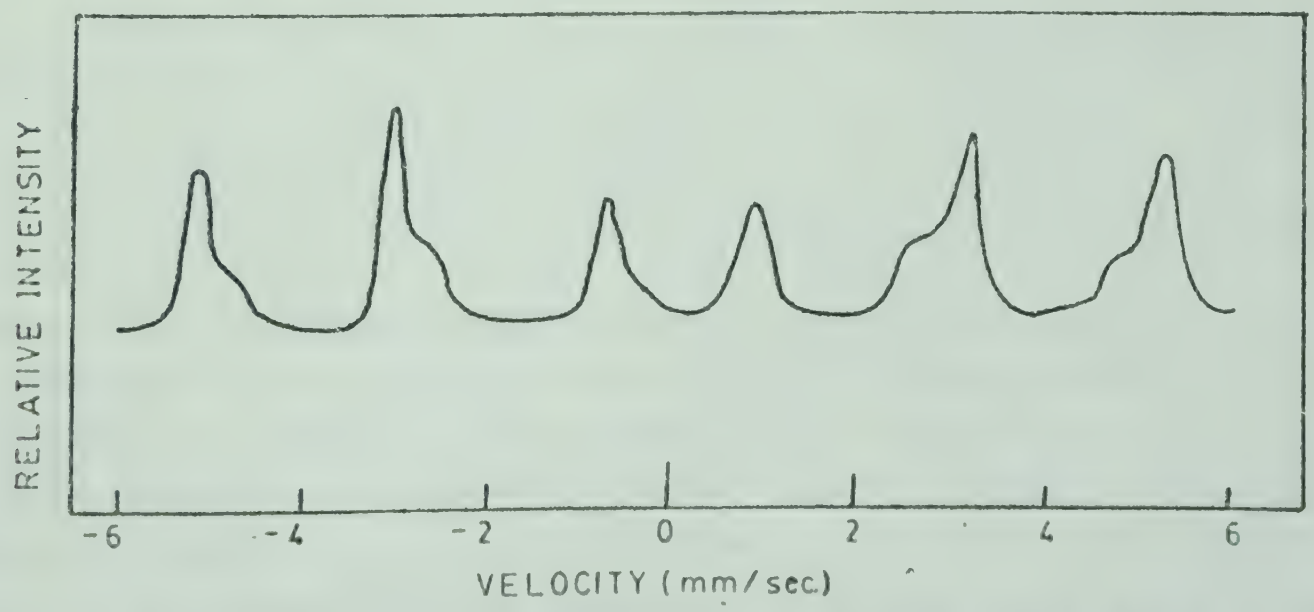

Fig. 4.21 (a) Room temperature CEM spectrum of Laser treated Nb-Fe couple.

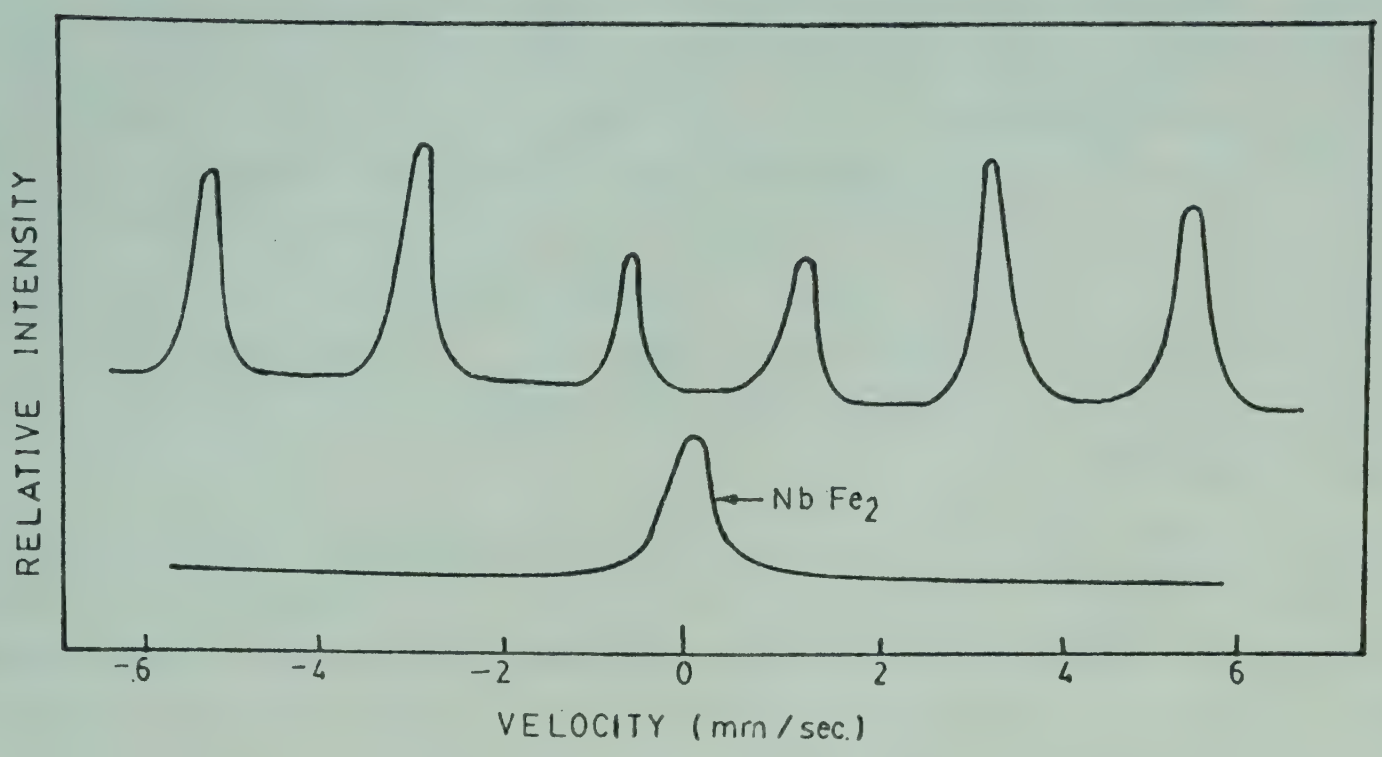

FIG 4.21 (b) Room temperature CEM spectra of Laser treated Fe-Nb composite.

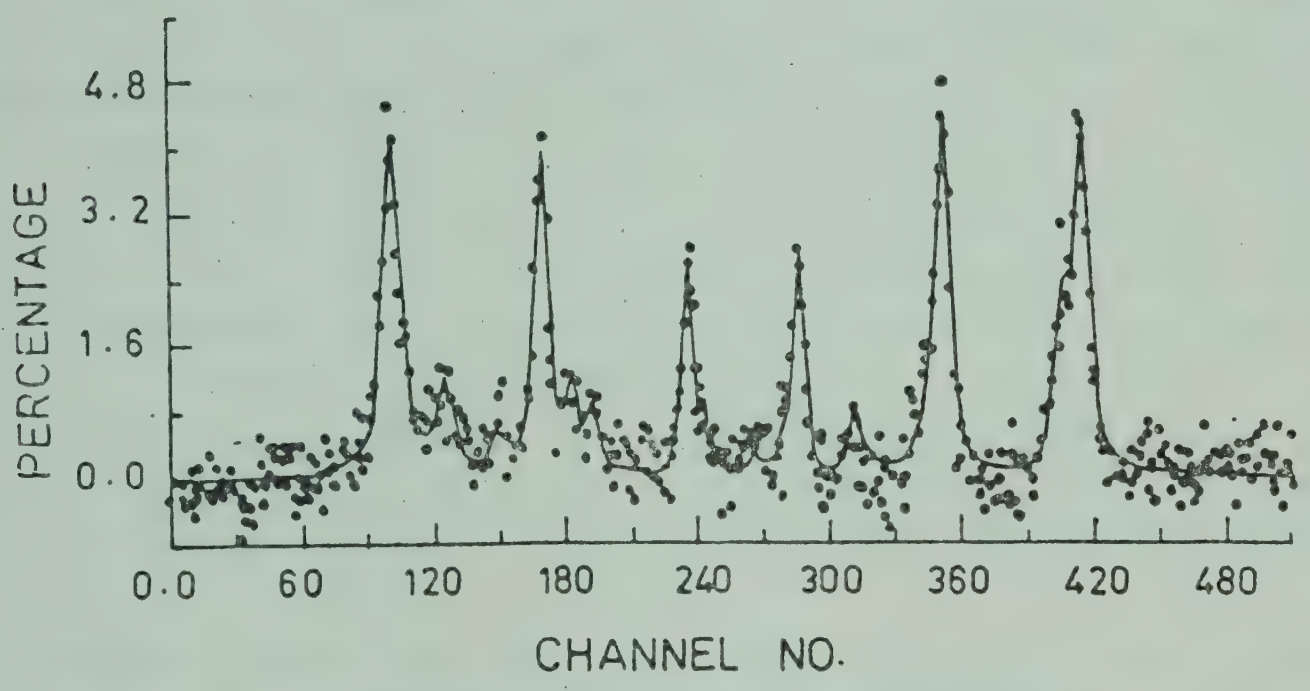

FIG. 5.1 (a) Room temperature CEM spectrum of steel sample corroded at 310°C for 1 day (10.5 pH, oxygen low).

numerous applications in other fields of Material Science. These applications include diversified areas such as oxidation and corrosion phenomena, magnetism in thin films, thermal reactions near surfaces and interfaces, structural and magnetic relaxations near the surfaces of amorphous metallic alloys etc. In the following paragraphs, we have briefly discussed some such applications, meant only to serve as illustrations and not to indicate the entire scope of the subject.

Jaggi *et al.*[14] have used the CEMS technique to study the high temperature corrosion of plain carbon steels in alkaline water which is an important investigation in the context of nuclear pressurized water reactors (PWR). Two typical spectra obtained by these authors for steel samples corroded in a solution of 10.5 *p*H at 310°C but corresponding to one and seven days of corrosion time, have been reproduced in Fig. 5.1(a) and Fig. 5.1(b) respectively. The differences in the spectral features clearly bring out the sensitivity of CEMS technique to the corrosive reactions

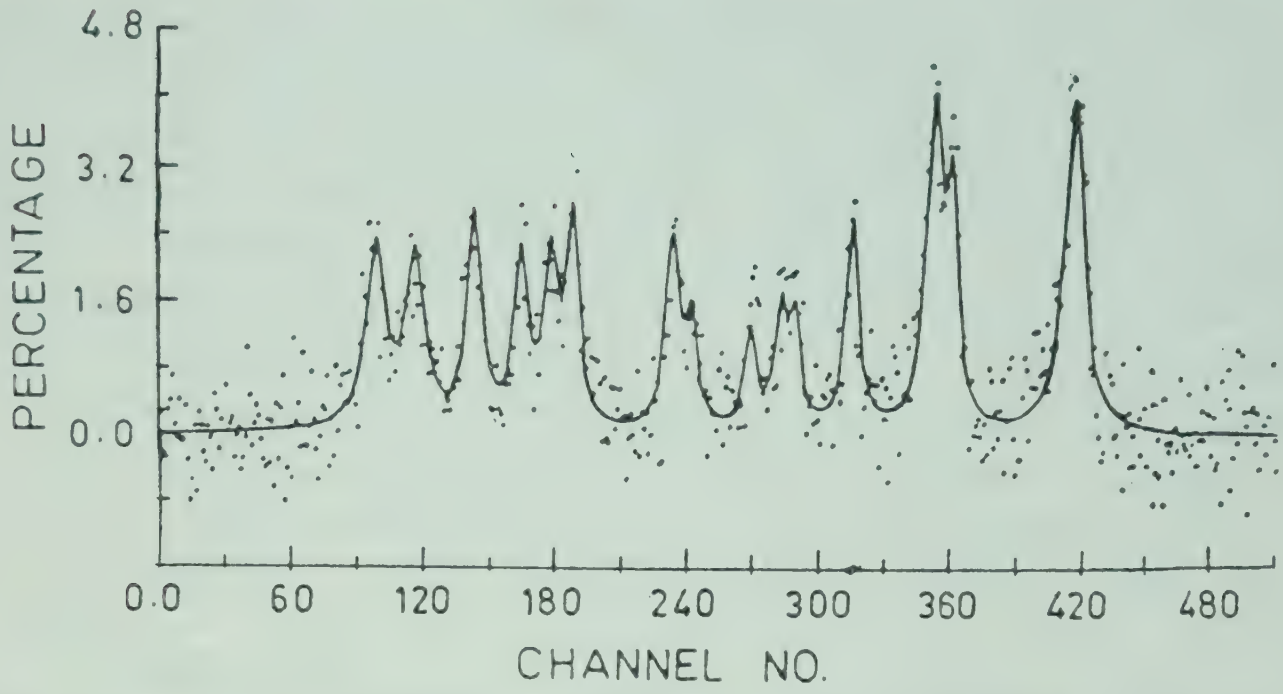

FIG. 5.1 (b) Room temperature CEM spectrum of steel sample corroded at 310°C for 7 days (10.5 pH, oxygen high).

occurring near surfaces. Through a series of systematic studies of corrosion products formed under differing conditions of the ambient, these authors have brought out the formation of non-stoichiometric $Fe_{3-v}O_4$ oxide in the initial phase, its growth at the oxide-electrolyte interface, as well as the approach of its composition to Fe_3O_4. With the increase in the oxygen content of the ambient to a value of .3 ppm the corrosion has been shown to be inhomogeneous, with the formation of an initial film which contains both α-Fe_2O_3 and spinel $Fe_{3-v}O_4$.

Another interesting application of CEMS technique in the studies of oxidation is the Mössbauer depth profiling method demonstrated by Bayreuther[36]. This method uses a special sample preparation technique which employs the use of a thin probe layer of enriched Fe^{57} isotope at a given depth below the iron surface. By changing the depth of the position of this probe layer below the surface, it has been shown that a resolution of $\sim$ 5Å can be obtained in ascertaining the location of the oxide-metal interface. This method is especially useful in the context of early oxidation studies, since it can yield an information regarding composition, stoichiometry and chemical nature of oxide films having thickness of less than $\sim$ 100Å.

Metallic glasses have emerged as scientifically interesting and technologically important materials in recent years. Since many of these materials involve iron as a component, Mössbauer spectroscopic techniques have found a central role in the studies on these systems. A considerable work on the bulk properties of met-glasses has already been carried out by using the Mössbauer transmission technique, and work employing the scattering Mössbauer techniques has just begun to appear. Nasu and Gonser[62] have reported results of simultaneous transmission and scattering measurements on $Fe_{40}Ni_{40}P_{14}B_6$ metallic glass. It has been shown by these authors that the surface atoms have 10% higher average hyperfine field as compared to the bulk atoms; the line-width obtained in the case of the scattering Mössbauer spectrum are larger than those in the transmission spectrum and the intensities of 2nd and 5th lines in the surface spectrum are 27% larger in area as compared to the

case of the bulk spectrum. Ok and Morrish[63] have reported on observation of magnetic an isotropy in the surface and bulk regions of a thermally annealed $Fe_{82}B_{12}Si_6$ metglass sample by carrying out CEMS and transmission measurements. These authors have shown that the surface region recrystallizes at a temperature lower than the glass transition temperature (T_g) leading to generation of stresses and hence anisotropy of magnetization. The fact that the dull surface of the metglass crystallizes faster than the shiny surface at a given temperature below T_g has also been demonstrated in these studies. Recently, we (Poona group) have performed systematic studies of structural relaxation and diffusive transport near the surface of $Fe_{67}Co_{18}Si_1B_{14}$ metglass by employing the CEMS technique[64]. It has been shown that annealing of this metglass in vacuum at 300°C for 10 hrs. does not show significant changes in the hyperfine field distributions; however, annealing at 390°C (i.e. 40°C below $T_g = 430$°C) leads to atomic transformation leading to Fe_3B-like atomic order. On annealing at 440°C (i.e. above T_g) for ten hours, three phases viz. Iron with substitutionally dissolved cobalt[65]. Fe_2B[66] and Fe_5SiB_2[66] are seen to precipitate (see Fig. 5.2). We have also carried out CEMS studies on the thermally induced transformations in the samples of the same metglass coated with a 300Å over layer of iron enriched to 33% with Fe^{57} atoms. It has been shown that a deposition induced reaction leads to the formation of an interface phase close in

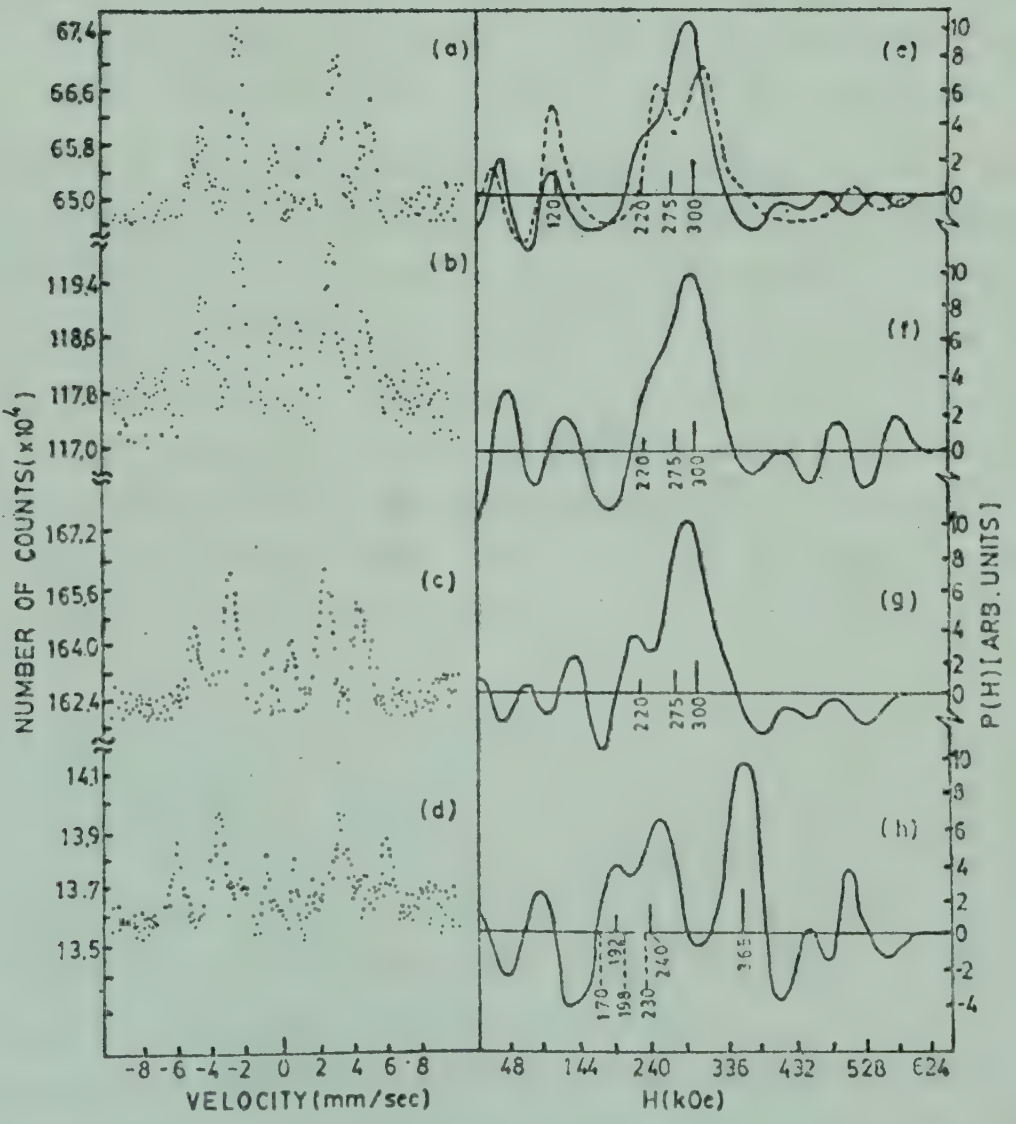

FIG. 5.2 Conversion electron Mössbauer spectra of the front (Shiny) surface of the as-received metglass (a), and metglass annealed at 300°C (b), 390°C (c), and 440°C (d), for ten hours each. The hyperfine field distributins [P(H)] curves corresponding to the CEM spectra in (a), (b), (c) and (d) are shown in (e), (f), (g) and (h) respectively. The dashed line in (e) shows the P(H) curve corresponding to the CEM spectrum of the back (dull) surface.

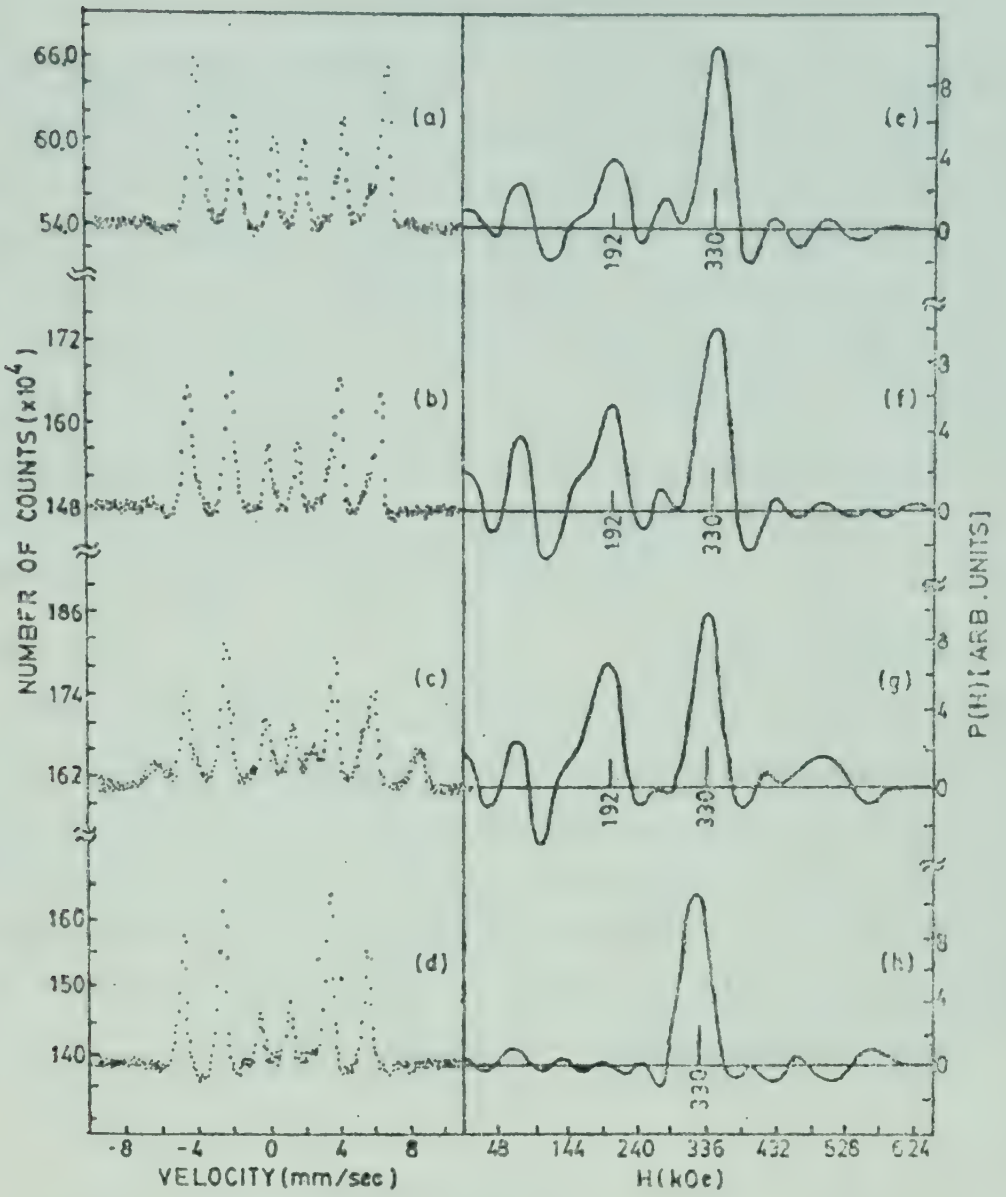

FIG. 5.3 Conversion electron Mössbauer spectra of the metglass deposited with 3 00Å iron overlayer in the as-deposited form (a); and subsequent to annealing of the composite at 300°C (b) 390°C; (c) and 440°C; (d) for ten hours each. The hyperfine field distribution (P(H) curves) corresponding to the CEM spectra in (a), (b), (c) and (d) are shown in (e), (f), (g) and (h) respectively.

composition to Fe_5SiB_2 (peak at h.f. field of 192 koe, see Fig. 5.3) and it grows upon thermal annealing at 300°C and 390°C for ten hours. This has been attributed to the (out) diffusion of Si and B (metalloid) atoms and the corresponding diffusion coefficients have been estimated to have values of 6.3×10^{-19}cm²/sec. and 1.4×10^{-18} cm²/sec. at 300°C and 390°C respectively. These are indeed in the range of values expected in the case of glassy metals[67]. The differences in the surface (back and front) and bulk atomic arrangements even in the as-quenched glass and their thermal transformation behaviour have also been brought out in these studies for the first time. Figures 5.2 and 5.4 demonstrate the differences in the field distributions near the shiny (front) surface, dull (back) surface and the bulk region in the case of the as-quenched glass. Comparison Fig. 5.2 and 5.4 also brings out the differences in the thermally induced transformations near the shiny surface and the bulk.

From the examples discussed in this subsection it is clear that the technique of Conversion Electron Mössbauer Spectroscopy (CEMS) has a major role to play in the field of material science, especially in the context of submicron physics.

Conclusions

In view of the important role played by surfaces and interfaces in a variety of physical and chemical processess, there is a growing interest in both the modification of surfaces to the required specifications and characterization of surfaces at the atomic level. Recently developed techniques of directed energy processing of surfaces such as ion implantation, ion beam mixing, electron and laser annealing have very many advantages in the modification of surfaces without altering the bulk characteristics. Some of the recent experiments show that all these techniques are highly non-equilibrium in nature and have characteristic time scales of the order of $10^{-10} - 10^{-13}$ sec. Thus, these methods can yield exotic and novel metastable phases and stable compositions in which limits of solid solubility and Hume Rothery rules are relaxed considerably.

In the characterization of surface layers and interfaces, Conversion Electron Mössbauer Spectroscopy has a number of advantages. The technique not only helps in characterizing the surface layers and bringing out details of interface reactions, but also helps in elucidating the very process of the modification of surfaces. Besides, Conversion Electron Mössbauer Spectroscopy finds applications in the study of thin films, phenomena of catalysis and chemisorption as also in under standing of the atomic arrangements in glassy metals.

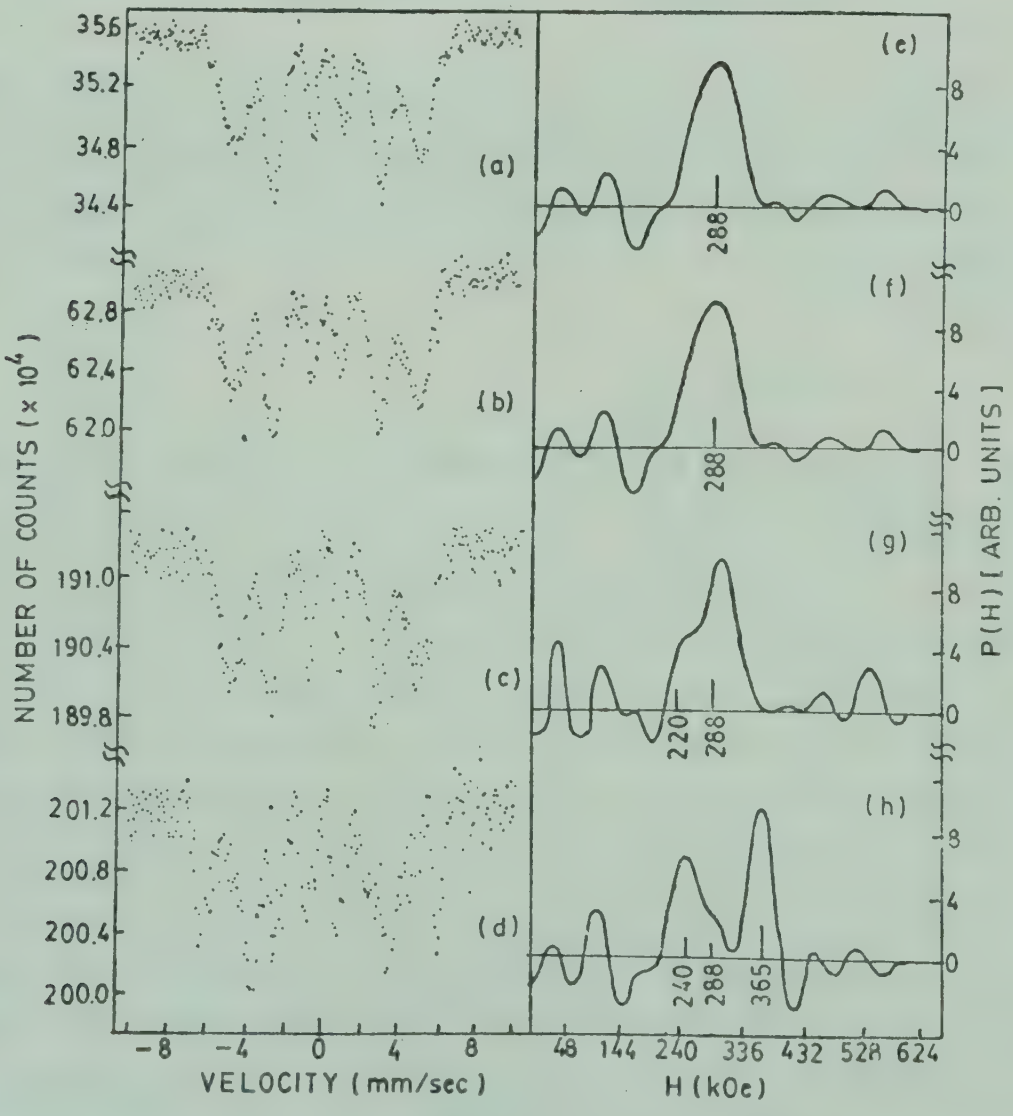

FIG. 5.4 Transmission Mössbauer spectra of as-received metglass (a), and metglass annealed at 300°C (b), 390°C (c), and 440°C (d); for ten hour each. The hyperfine field distributions [P(H) curves] corresponding to the transmission spectra in (a), (b), (c) and (d) are shown in (e), (f), (g) and (h) respectively.

Acknowledgements

The authors gratefully acknowledge the help and cooperation of the members of the 'Submicron-Physics Group' of the Department of Physics, University of Poona in carrying out the work which has been included in the present article as the contribution of the 'Poona Group'. These members include Dr S. M. Chaudhari, Mr. V. P. Godbole, Mr. S. A. Kulkarni, Mr. Y. S. Dorik, Mrs. Rekha Joshee, Mr. P. P. Patil, Mr. Y. V. Bhandarkar, Mr. D. M. Phase, Mrs. Jayashree Patankar and Mr. D. B. Shinde. Three of us (SBO, SVG, SMK) are also thankful to Professor M. R. Bhiday. Professor A. S. Nigavekar, Professor P. S. Damle and Dr. V. N. Bhoraskar for their help and encouragement and for making the appropriate Institutional facilities available to us.

The research programmes undertaken by the 'Submicron Physics Group' in the field of 'radiation processing of surfaces interfaces and thin films' have been funded by the Department of Science and Technology (DST) Defence Research and Development Organisation (DRDO), Department of electronics (DOE), Department of Atomic Energy (DAE) and Counil of Scientific and Industrial Research (CSIR), India. The authors gratefully acknowledge the support of these funding agencies.

The authors are also grateful to the scientists who have kindly permitted the reproduction of their results in the present article.

Refrences

1. *Surface Modification and Alloying by Laser,* Ion and Electron Beams, (Ed : J. M. Poate, G. Foti, D C Jacobson), Plenum Press, New York, London, 1981.
2. *Thin Films—Interdiffusion and Reactions,* (Ed : J M Poate, K N Tu, J W Mayer, A Wiley—Interscience Publication, New York, 1978).
3. *Laser and Electron Beam Solid interactions and Materials* Processing, (Ed : J F Gibbson, L D Hess, T W Sigmon, Elsevier North Holland, New York, 1981).
4. *Laser and Electron-beam Processing of Materials,* (Ed : C W White, PS Peercy, Academic Press, New York, 1980).
5. Duwez, Paul *J. Vac. Sci. Tech.*, **B1(2)**, (1983) 218.
6. J W, Erikson, L and Davies, J A *Ion implantation in Semiconductors*, Plenum Press, Mayer, New York, London, (1970).
7. Crowder B L (Ed) *Ion Implantation in Semiconductors and other materials*, Plenum Press, New York, London, (1973).
8. Carter, G and Colligon, J S (1968) *Ion bombardment of solids,* (Gresham Press, England.)
9. *Surface Modification and Alloying by Laser, Ion and Electron Beams,* (Ed : J M Poate, G Foti, D C Jacobson, Plenum Press, New York, London, 1981), Chapter 9.
10. Hoonhout, D Ph.D. Thesis, Fom Institute, The Netherlands (1981).
11. Sood, D K (1982) *Rad. Eff.*, **63**, 141.
12. Bhide, V G *Mössbauer Effect and its Applications,* Tata McGraw Hill Publishing Co. Ltd. New Delhi, (1973).
13. Gonser, U (Ed.) *Mössbauer Spectroscopy-II,* (Springer Verlag Berlin, Heidelberg, New York, (1981).
14. Jaggi, N K Ph.D. Thesis, Bombay University, Bombay, India, (1982).
15. *Surface Modification and Alloying by Laser, Ion and Electron Beams,* (Ed: J M Poate, G Foti, D C Jacobson, Plenum Press, New York, London, 1981), Chapter 7.

16. Sood, D K *Phys. Lett.* **68A,** (1978) 469.
17. Dearnaley, G *Nucl. Instr. and Meth.,* **182/183,** (1981) 899.
18. Tsaur, B Y, Liau, Z L and Mayer, J W *Appl. Phys. Lett.,* **A71,** (1979) 270.
19. Lau, S S, Tsaur, B Y, Von Allmen, M, Mayer, J W, Strizker, B, White, C W and Appleton, B *Nucl. Instr. and Meth.,* **182/183,** (1981) 97.
20. Tsaur, B Y and Hung L S *Appl. Phys. Lett.,* **37**(10), (1980) 922.
21. Hung, L S, Nastasi, M, Gyulai, J and Mayer, J W *Appl. Phys. Lett.,* **42**(8), (1983) 672.
22. Mazoldi, P, Dona, Dalle L F, Rose, and Sood, D K *Rad. Eff.,* **63,** (1982) 105.
23. Tsou, S C, Tsien, P H, Takai, M., Roschenthaler, D, Ramin, M, Ryssel, H and Ruge, I *Appl. Phys.,* **23,** (1980) 163.
24. Gat, A, Gerzberg, L, Gibbson, J F, Magee, T J, Peng, J and Hong, J D, *Appl. Phys. Lett.,* **33,** (1978) 775.
25. Bamchil, G, Bensahel, D, Goldanskii, A, Ferrieu, F, Auvert, G, Perio, A and Pfister, J C *Appl. Phys. Lett.,* **41**(1), (1982) 46.
26. Wang, J C, Wood, R F and Pronko, P P *Appl. Phys. Lett.,* **33,** (1978) 455.
27. Von, J A, Vechten, Tsu, R and Saris, F W *Phys. Lett.,* **A74**(6), (1979) 422.
28. Baeri, P, Compisano, S V, Foti, G and Rimini, E *Phys. Rev. Lett.,* **41,** (1978) 1246.
29. *Laser and Electron Beam Solid Interactions and Material Processing,* (Ed: J F Gibbsons, L D Hebs, T W Sigmon, Elsevier North Holland Inc. New York, 1981), pp. 45–47, 511–524.
30. Sawicka, B D and Sawicki, J A In *Mossbauer Spectroscopy-II,* (Ed: U Gonser, Springer Verlag Berlin, Heidelberg, New York), (1981) .
31. Hussey, R J, Coplan, D and Graham, M J *Oxidation of Metals,* **15**(5/6), (1981) 421.
32. Longworth, G and Hartley, N E W *Thin Solid Films,* **48**(1), (1978) 95.
33. Kanetkar, S M, Dorik, Y S, Chaudhari, S M, Ogale, S B and Bhide V G *Thin Solid Films* (Submitted).
34. Baumvol, I J R *J. Appl. Phys.,* **52**(7), (1981) 4583.
35. Dorik, Y S, Bhide, V G, Kanetkar, S M, Ghaisas, S V, Chaudhari, S M and Ogale, S B *J. Appl. Phys.* August 1984 issue, (in press).
36. Bayreuther, G *J. Vac. Sci. Tech.,* A **1**(1), (1983) 19.
37. Mullen, J G and Stevenson, J *Nucl. Instr. and Meth.,* **153,** (1978) 77.
38. Tyliszczak, T, Sawicki, J A, Stanek, J, and Sawicka, B D *Journal de Physique,* **C-1,** (1980) 117.
39. Sprouse, G D, Kalvius, G M and Hanna, S S *Phys. Rev. Lett.,* **18,** (1965) 1041.
40. Sawicka, B D, Drwiega, M, Sawicki, J A and Stanek, J *Hyperfine Interactions,* **5,** (1978) 147.
41. Nasu, S, Gonser, U and Preston, R S *Journal de Physique,* **C-1,** (1980) 385.
42. Sawicka, B D and Sawicki, J A *Phys. Lett.,* **A64,** (1977) 311.
43. Sawicki, J A and Sawicka, B D *Phys. Stat. Sol.'* **B88,** (1977) K 41.
44. Jastrzebski, Z D *The Nature and properties of Engineering materials,* (John Wiley and Sons, Inc. New York, U.S.A.), (1976).
45. Godbole, V P, Bhide, V G, Ghaisas, S V, Kanetkar, S M, Chaudhari, S M and Ogale, S B (1984) *Mat. Res. Soc. Symp.* Proc. (Thin Films and Interfaces-II, Eds. Baglin, Campbell, Chu; Elsevier Science Publishing Co. Inc.), **25,** 247.
46. Godbole, V P, Bhide, V G, Ghaisas, S V, Kanetkar, S M, Joshee, R S and Ogale, S B (1984) *Mat. Res. Soc. Symp. Proc.* (Thin Films and Interfaces-II, Eds. Baglin, Compbell, Chu; Elsevier Science Publishing Co. Inc.), **25.**
47. Godbole, V P, Chaudhari, S M, Ghaisas, S V, Kanetkar, S M, Ogale, S B and Bhide, V G *Phys. Rev.* **B** (Submitted).
48. Ogale, S B, Joshee, Rekha, Godbole, V P, Kanetkar, S M and Bhide, V G *J. Appl. Phys.* (U.S.A) (in Press).
49. Patankar, Jayashree, Bhandarkar, Y V, Kanetkar, S M, Ogale, S B and Bhide, V G, *Nucl. Instr. and Meth.* (in Press).
50. Ogale, S B, Godbole, V P, Kanetkar, S M and Bhide, V G *Appl. Phys. Lett.* (Submitted).

51. Preston, R S (1972) *Met. Trans.*, **3,** 1831.
52. Hirvonen, H and Raisanen J *J. Appl. Phys.*, **53**(4), (1982) 3314.
53. Gonser, U and Ron, M In *Applications of Mössbauer Spectroscopy* ol. II, ((Ed: R L Cohen, Academic Press, New York, 1980).
54. Terrell, J H and Spijkerman, J J *Appl. Phys. Lett.*, **13,** (1968) 11.
77. O'Grady, W E *J. Electrochem. Soc.*, **127,** (1980) 555.
56. Eldridge, J, Kordesch, M E and Hoffman, R W *J. Vac. Sci. Tech.*, **20,** (1982) 934.
57. Kundig, W, Bommel, H, Constabaris, G and Lindquist, R H *Phys. Rev.*, **142,** (1966). 327.
58. Petrikin, Yu V, Damgaard, S, Oron, M, Petersen J W and Weyer, G *Journal de Physique,* **C—11,** (1980) 423.
59. Blaauw, C, Woude, Van, der and Sawatzky, G A (1973) *J. Phy. C.* (*Solid State*), **6,** 2371.
60. Prasad, K G. *Proc. of the International Conference on the Applications of the Mössbauer Effect,* Jaipur, India (Dec. 1981).
61. Dektiyar, I Y, Nomoshkalenko, V V, Nishchenko, M M, Razumov, O N and Tomashevasky, N A (1983) *Proc. of International Conference on the Applications of the Mossbauer Effect* (Alma Ata, USSR).
62. Nasu, S and Gonser, U. *Journal de Physique. Coll.*, **B.20,** (1979) 476.
63. Ok, N H and Morrish, A H *Phy. Rev. B.*, **23**(5), (1981) 2257.
64. Ogale, S B, Bhandarkar, Y V, Patil, P P, Kanetkar, S M and Bhide, V G *Phy. Rev. B.* (Submitted).
65. Johnson, C E, Ridout, M S and Cranshow, T E (1963) *Proc. Phys. Soc.*, **81,** 1079.
66. Ok, H N and Morrish, H *Phy. Rev. B.*, **22**(7), (1980) 3471.
67. Gupta, D, Tu, K N and Asai, K W *Phy. Rev. Lett.*, **35**(12), (1975) 796.

© *Proc. Indian natn. Sci. Acad.*, **51**, A, No. 1, 1985, pp. 256-285
Printed in India.

SURFACE CHEMISTRY OF ALKALI—COVERED METALS*+

M S HEGDE *and* M AYYOOB

Solid State and Structural Chemistry Unit, Indian Institute of Science
Bangalore-560 012

Alkali and Alkaline earth metals are known to promote the catalytic activity of many transition metals in several important surface reactions. Electron spectroscopic techniques have made a great impact on modern surface science and these have now been used to understand the role of alkali metals on the catalyst surfaces. In this article, the adsorption of reactive molecules such as $O_{,2}$ N_2, CO and NH_3 on metals dosed with alkali and alkaline earths has been examined. The reactivity of alkali promoted surfaces has been highlighted. The phenomena of charge transfer and oxygen spill over, the thermal stability of adsorbed species and the effect of chlorine on inhibiting atomic oxygen adsorption have been discussed.

Key Words : XPS; AES; UPS; Adsorption; Reactivity; Alkali Covered Surfaces

INTRODUCTION

Adsorption of oxygen, nitrogen, nitric oxide, hydrogen and carbon monoxide on transition metal surfaces form the basis of most of the catalytically important reactions such as oxidation, synthesis of ammonia, Fischer-Tropsch reaction and so on. Alkali metals on transition metal surfaces are known to increase the sticking probability of molecules. Adsorbed potassium on Fe has been found to accelerate the rate of nitrogen adsorption markedly[1] and the dissociation probability of N_2 is found to be greatly enhanced[2]. Alkalis such as potassium oxide are routinely added to Ag catalysts to promote epoxidation[3]. Thermal desorption studies using isotope mixing and CO titrations have shown the presence of molecular dioxygen species on potassium and rubidium dosed Ag surfaces[4]. The promoting action of potassium and calcium oxides in Fe catalyst in the synthesis of ammonia is well known. Presence of potassium on Ni catalyst is known to enhance the production of higher homologues of carbon in Fisher-Tropsch reaction[5]. Barium and Thorium oxide coated cathodes increase the emissivity of electrons in thermionic emitters[6]. Thus small quantities of alkali and alkaline earth metal oxides play a major role either individually or in combination in altering the reactivity and surface properties of metal surfaces. Due to the advent of surface sensitive techniques such as X-ray and UV photoelectron spectroscopy (XPS, UPS) Auger electron spectroscopy (AES), Electron energy Loss Spectroscopy (EELS) and Thermal desorption studies (TDS), it is now possible to understand the role of alkali metals in altering the adsorption and reactivity of metal surface.

While extensive surface studies on the adsorption of molecules on clean metal surfaces employing the above techniques are available in the literature[7], relatively

---

*Paper presented at the Symposium on Physics and Chemistry of Surfaces held at INSA New Delhi from September 28–30, 1984.

+Contribution No. 269 from the Solid State and Structural Chemistry Unit.

less attention has been paid to the study of alkali promoted surfaces. The physics of metal adsorption on metals has been reviewed by Roberts and McKee[8]. Recent studies on the adsorption of molecules on alkali covered metal surfaces have been done by using mainly temperature programmed desorption and by studying change in the work function[4]. We have been working on the adsorption of oxygen and other molecules on alkali-dosed metals such as Ag, Cu and Pt. We find that XPS and UPS can be very useful in isolating reactive adsorbed species on the surface. It has been possible to characterize different types of adsorbed oxygen species on alkali-dosed metal surfaces. Also, for the first time, we have made use of quantitative estimations of surface concentrations to determine the surface stoichiometry[9]. The quantitative assessment of adsorbates has shown a new way of understanding reaction pathways[10].

In this article, adsorption of oxygen, carbon monoxide, hydrogen, nitrogen, ammonia and chlorine on alikali and barium covered transition metal surfaces has been presented. Reactivity of adsorbed oxygen towards CO, and NH_3 has been highlighted. The role of chlorine in enhancing the stability of molecular dioxygen on alkali dosed Ag has been examined. Charge transfer from alkali metal to the transition metal substrate has been shown to be one of the important factors in altering the surface properties of alkali dosed catalyst surfaces.

Experimental Techniques

The adsorption studies on alkali covered metal surfaces presented here have been carried out in UHV conditions with several probes. Combinations of two or more techniques are employed at a time. In XPS, core level photolines give information on the binding energies of adsorbed species. Recently, surface concentrations of adsorbates have been determined from the core level X-ray photolines[9,10]. Auger electron spectroscopy has been primarily used to characterize the surface and peak to peak heights of O(KLL), N(KLL), K(LVV), Ba(MNN) have been used to get quantitative information about adsorbates. UPS has been employed mainly to characterize the molecular nature of CO, O_2 etc. and to see any dissociated products. Electron energy loss spectroscopy has not been used to any significant extent to study the adsorption of molecules on alkali dosed surfaces. Temperature programmed desorption is a powerful technique, now employed extensively to study desorption kinetics of adsorbed N_2, O_2, CO and so on[2].

The alkali metals, Na, K, Rb and Cs are dosed on the metal surfaces by (a) heating respective Zeolites on Mo or Ta wire[11], (b) heating gold-alkali alloys in the form of a wire and (c) by directly evaporating the alkali metals. Barium is dosed by heating a Ba-Ti getter. In the Zeolite method, it is difficult to avoid oxygen contamination. This, however, is not a serious problem in oxidation catalyst studies.

Studies of adsorption on alkali covered metal surfaces have been carried out in this laboratory in ESCA–3 Mark II spectrometer of V. G. Scientific Ltd., U. K. equipped with XPS, UPS and AES facilities. The substrate metals are cleaned by

repetitive heating and argon ion etching. A photograph of the spectrometer is given in Fig. 1. The alkali metals have been dosed by the zeolite method and barium from a getter. The temperature of the substrate is generally measured using a Chromel-Alumel thermocouple. Surface concentrations of oxygen, carbon, chlorine and alkali or alkaline earth metal adsorbates are obtained from the intensities of the core level photolines such as O(1s), K(2p), etc. following the method of Carley and Roberts[12].

Work function measurement is a very useful tool in these surface studies. Generally diode method is employed, wherein changes in the work function on alkali coverage and after subsequent adsorption of molecules can be determined. For details on surface science instrumentation, the reader is referred to a recent publication by Briggs and Seah[13].

Charge Transfer from Alkali Metal to the Substrate

On dosing alkali or alkaline earth metal on transition metals, decrease in work function has been observed[14]. Variation in the work function of Ag when dosed with cesium is shown in Fig. 2. With increasing initial cesium coverage, drastic decrease in work function occurs and by about 0.4 to 0.5 monolayer alkali coverage, the minimum work function is reached. This variation is typical of any alkali dosed transition metal system. Decrease in work function is a manifestation of charge transfer from alkali metal to the substrate[8]. From simple electronegativity considerations, electron transfer and effective charge on the substrate atom has been estimated by Albano[15].

Charge states of transition metal atoms in their oxides and other compounds were determined in this laboratory employing metal Auger intensity ratios[16]. Occupancy of the valence band of first row transition metals was shown to decrease with decrease in the $I(L_3VV)/I(L_3M_{23}M_{23})$ Auger intensity ratio[17]. The Auger ratio technique was employed extensively to study the surface oxidation of metals such as Fe, Ni, Cu[18]. We considered it worthwhile to examine the ratio after deposition of barium on the Cu surface with a view to see whether the charge transfer from barium to Cu could be seen by this new method[19].

Fig. 3 shows the Auger spectra of Cu before and after oxygen adsorption at 300K. Also shown is the Auger spectrum seen after the Cu surface was exposed to oxygen at 500K. The electron beam energy and other spectrometer condition were maintained identical during the study. Very little oxygen is adsorbed on copper at 300K even after 2000L O_2 exposure. The $Cu(L_3VV)/L_3M_{23}M_{23})$ Auger ratio for clean and oxygen-exposed Cu at 300K measured from the peak to peak heights remains essentially the same with a value of 5.3 ± 0.1 However, on oxidation at 500K, there is a significant increase in the O(KLL) intensity and the Cu Auger ratio decreases to 4.3, a value close to that for Cu_2O[18].

In Fig. 4 are shown the Auger spectra of Cu + Ba and after subsequent oxygen exposure. The Cu Auger ratio is about 5.9 on the barium covered surface and after oxygen exposure to this surface, the value comes down to 4.8 only, although

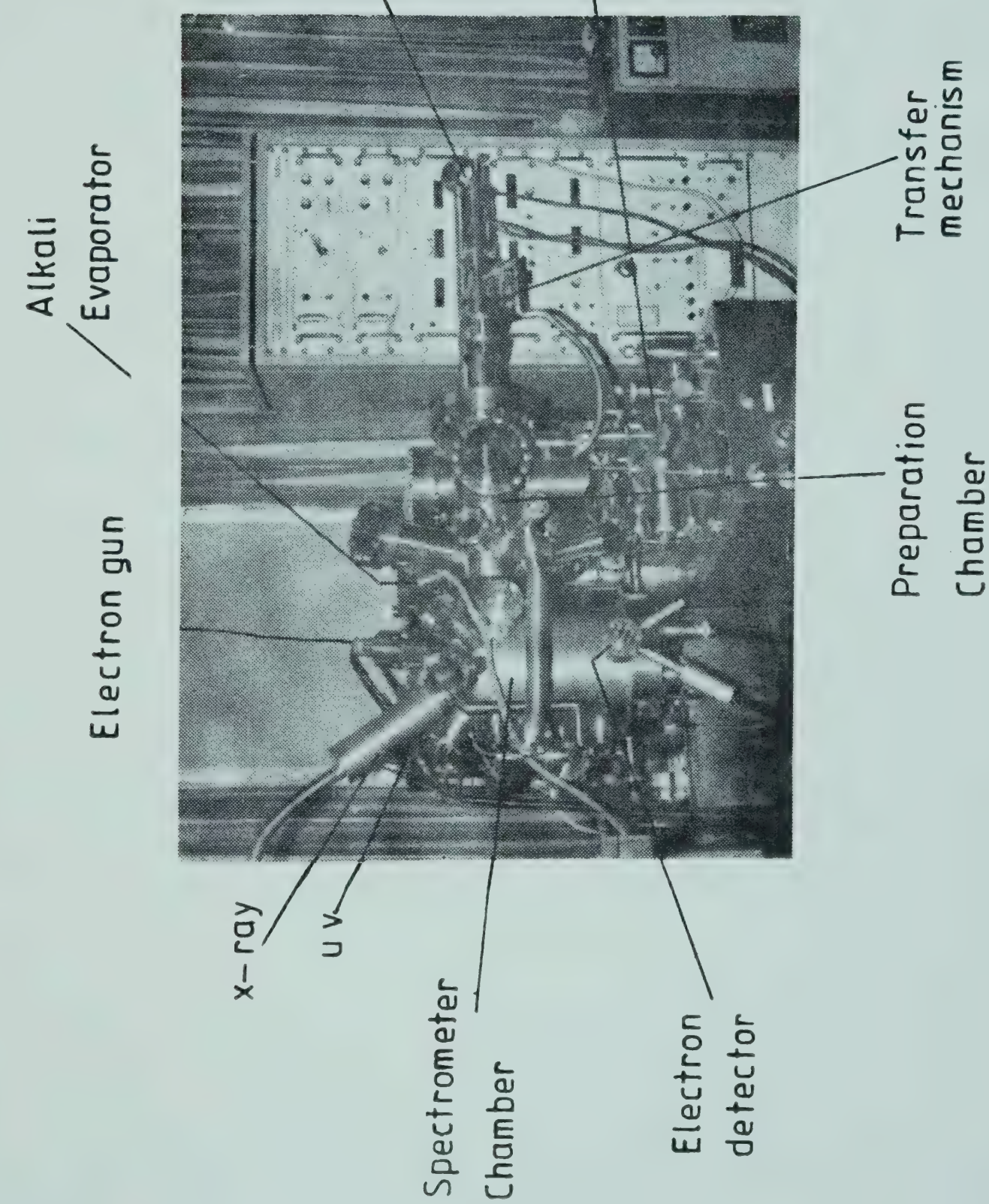

FIG. 1. Photoelectron spectrometer used in our study.

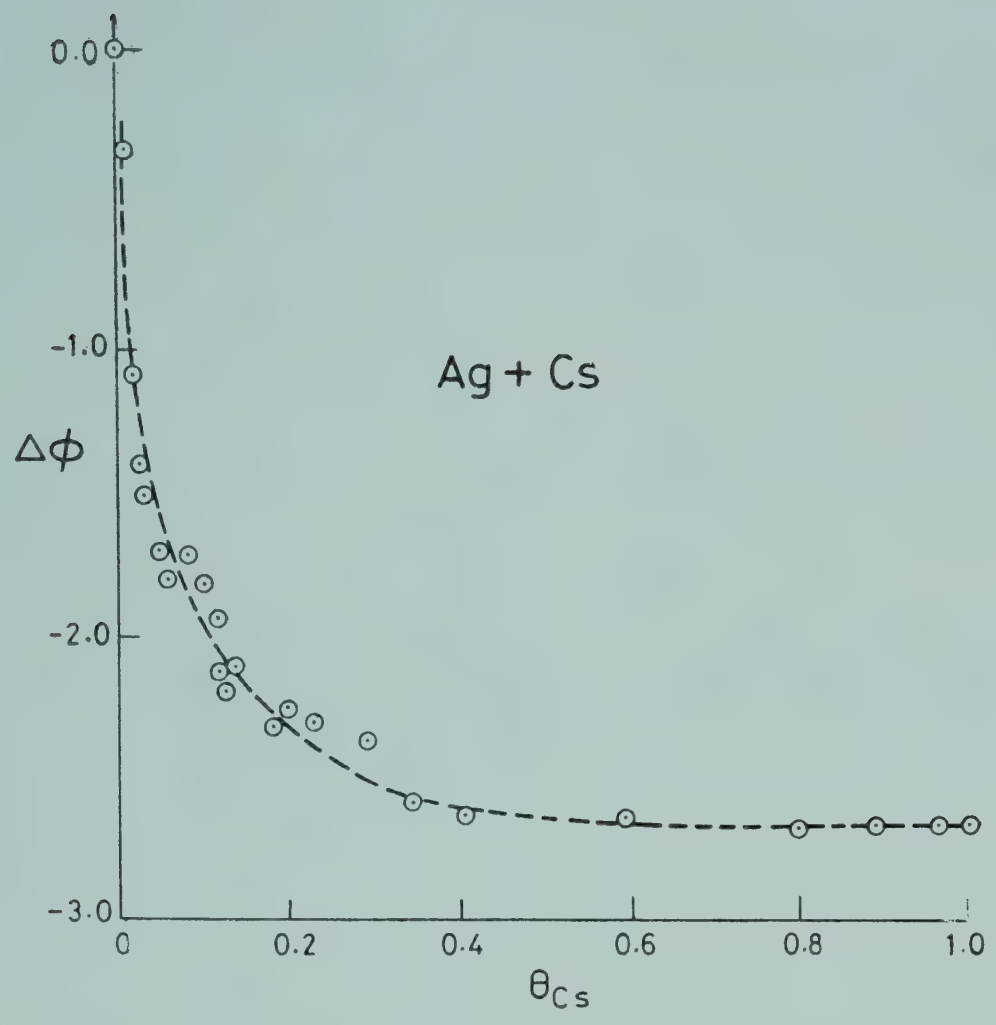

FIG. 2. The variation of work function with cesium coverage on silver.

the oxygen concentration is found to be higher on the barium covered surface compared to that on oxidized Cu surface.

Having seen the change in the $Cu(L_3VV)/L_3M_{23}M_{23})$ ratio on barium coverage, we have measured the Auger ratio as a function of barium concentration [Fig. 5(a)]. Barium concentration is obtained from the $Ba(3d_{5/2})$ peak in these experiments. For a typical barium concentration, the increase after barium deposition and subsequent decrease in the ratio with increasing oxygen exposure is shown in Fig. 5(b).

The role of barium in activating the surface is manifest in the variation of the $Cu(L_3VV)/(L_3M_{23}M_{23})$ ratio. It has been shown in an earlier paper by Yashonath *et al.*[16,18], that this ratio (R) is given by an equation of the type :

$$R = k\frac{N(N-1)}{n(n-1)} \qquad \ldots(1)$$

where N is the total number of valence electrons in copper and n is the occupancy of the M_{23} level; k is the Auger transition probability ratio. It is clear that with n remaining constant (equal to 6), any change in the occupancy in the valence band alters the magnitude of R. This is schematically shown in Fig. 5(c). Thus on barium deposition, charge transfer from barium to the copper valence band should result in an increase in the value of N to say, $N + q$ and the Auger ratio can be given by :

$$R' = k\frac{(N+q)(N+q-1)}{n(n-1)} \qquad \ldots(2)$$

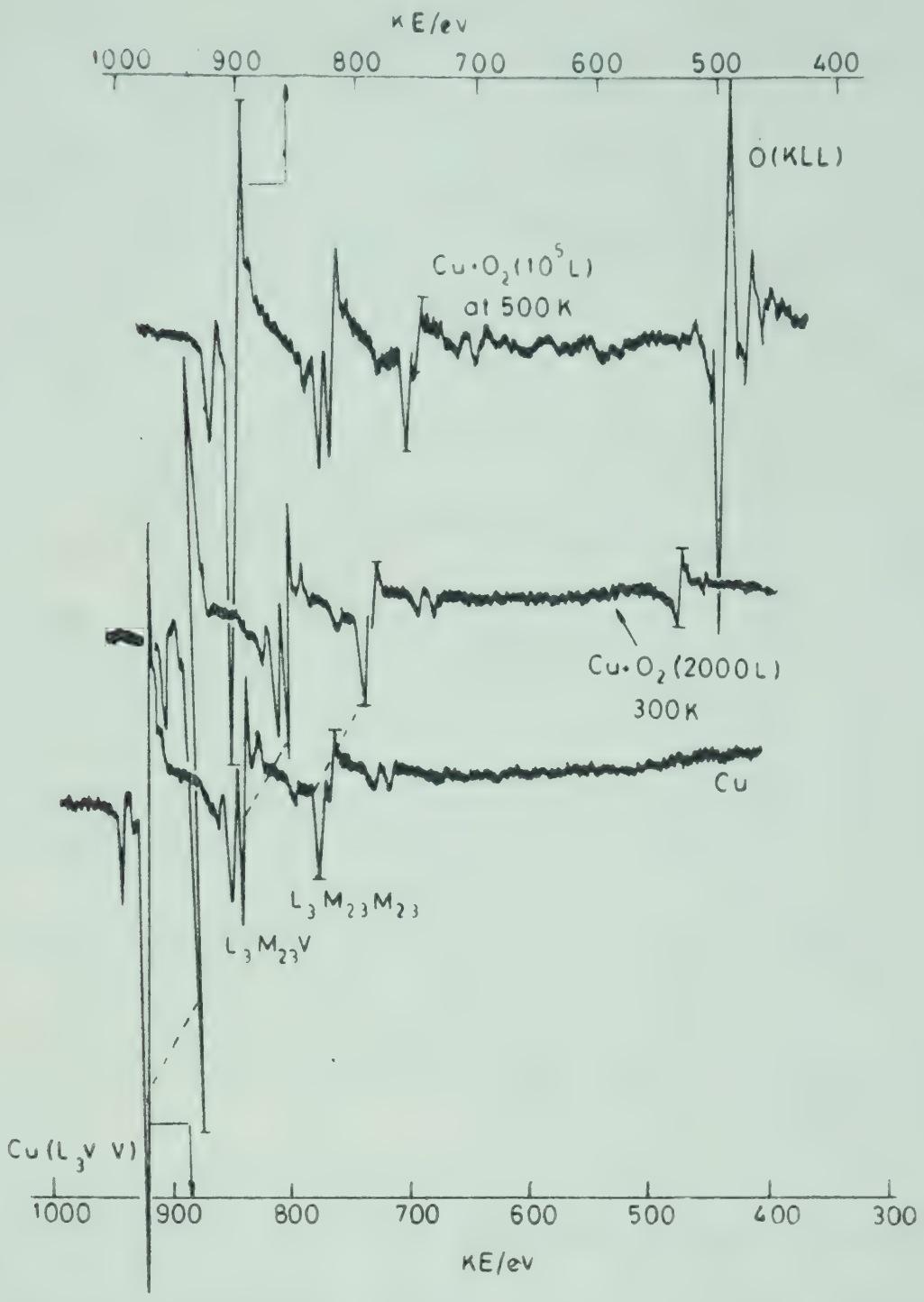

FIG. 3. Augar spectra of clean Cu, after oxygen adsorption at 300K and 500K

Further, on oxygen adsorption on the barium covered surface, charge transfer to the O(2p) level from Cu should result in a decrease in the occupancy of Cu valence band to a value, say $N + q - r$. This in turn, alters the value of R' to a different value R'' given by :

$$R'' = k.\frac{(N+q-r)\,(N+q-r-1)}{n(n-1)} \qquad \ldots(3)$$

Obviously $R'' < R'$. Increase in R' with σ_{Ba} shown in Fig. 5(a) supports the above argument. Also, the decrease in R'' with oxygen exposure [Fig. 5(b)] further supports eq. (3).

This experiment, therefore, clearly demonstrates that there is charge transfer from the alkali metal to the substrate Cu. The ratio does not decrease significantly even after the adsorption of a large quantity of oxygen on the surface. This indicates that only the excess charge received by Cu from barium may be back transferred to oxygen for chemisorption to occur[20]. This type of behaviour seems to be a general phenomenon occurring when an alkali is adsorbed on a transition metal.

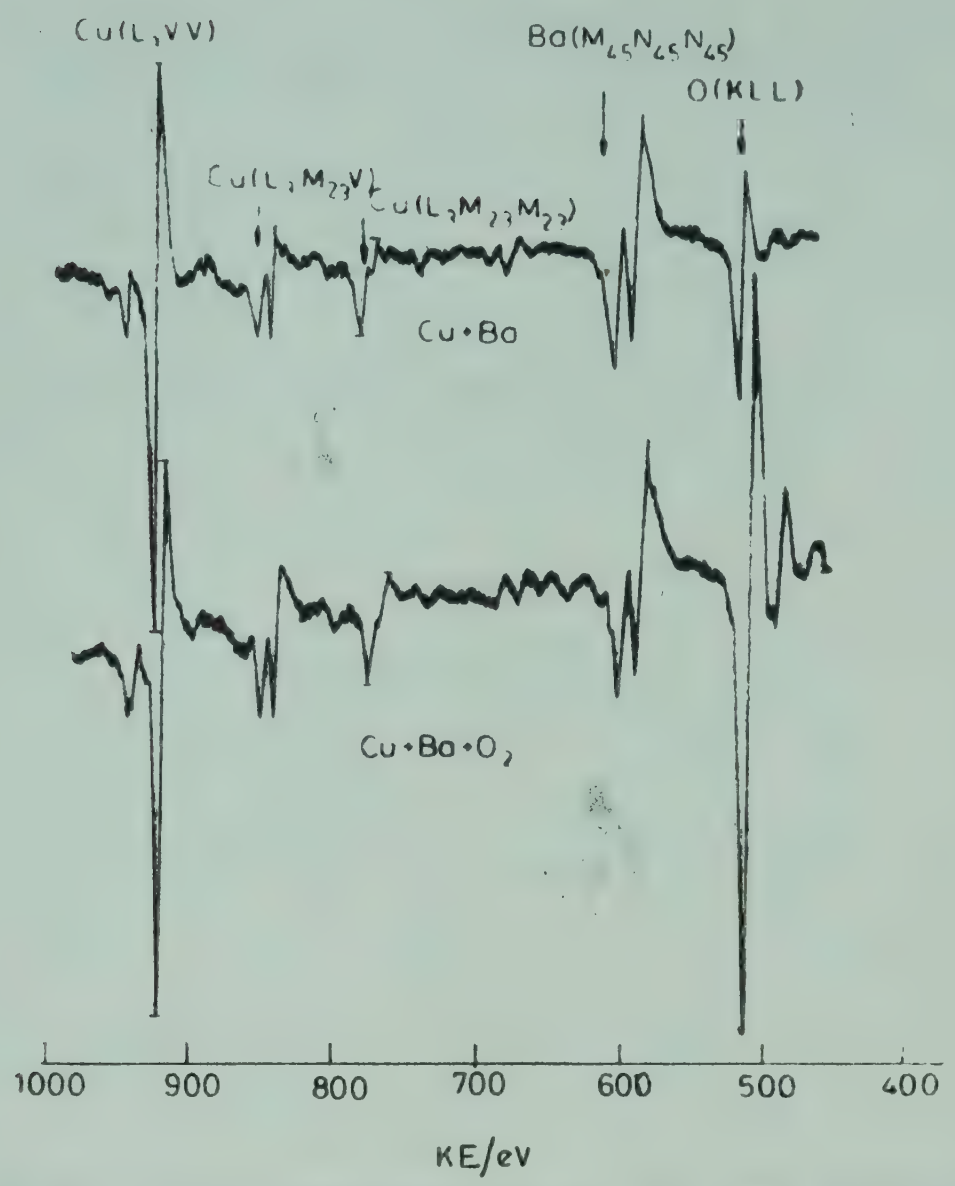

FIG. 4. Auger spectra after barium adsorption on Cu and after subsequent oxygen exposure ($\sigma_{Ba} = 3.7 \times 10^{14}$ atoms/cm^2)

Oxygen on Na, K, Rb, Cs, and Ba dosed Ag

The study of adsorbed oxygen on silver has aroused major interest in the past due to the high selectivity of silver catalyst in the epoxidation of ethylene to ethylene oxide[3]. Adsorbed molecular oxygen is believed to be involved in the oxidation mechanism in presence of K_2O on Ag catalysts. Molecularly adsorbed oxygen on silver has been observed at high oxygen pressures by XPS and UPS techniques[21]. Adsorption of molecular oxygen has been shown to occur on silver and platinum surfaces at 80K[22]. At such low temperatures, the presence of both atomic and molecular oxygen on silver[23] has been shown. However, on clean Ag at 300, after O_2 exposures of even upto 10^4L, almost no oxygen adsorption is observed by any of the surface sensitive techniques including thermal desorption studies[4]. We have examined the nature of oxygen species on silver dosed with potassium, cesium and barium by XPS and UPS[9].

The X-ray photoelectron spectra in the O(1s) and K(2p) regions were recorded at 300K before and after exposure of the potassium covered Ag surface to oxygen. Typical spectra of the O(1s) and K(2p) core levels are given in fig. 6 for different potassium coverages after the surface was saturated with oxygen (> 200L O_2). For comparison, the O(1s) spectrum on clean Ag after 1000L O_2 exposure is also given. Oxygen adsorption on clean silver at 300K was found to be insignificant even upto 1000 L O_2 exposure. However, a large O(1s) peak was observed on the

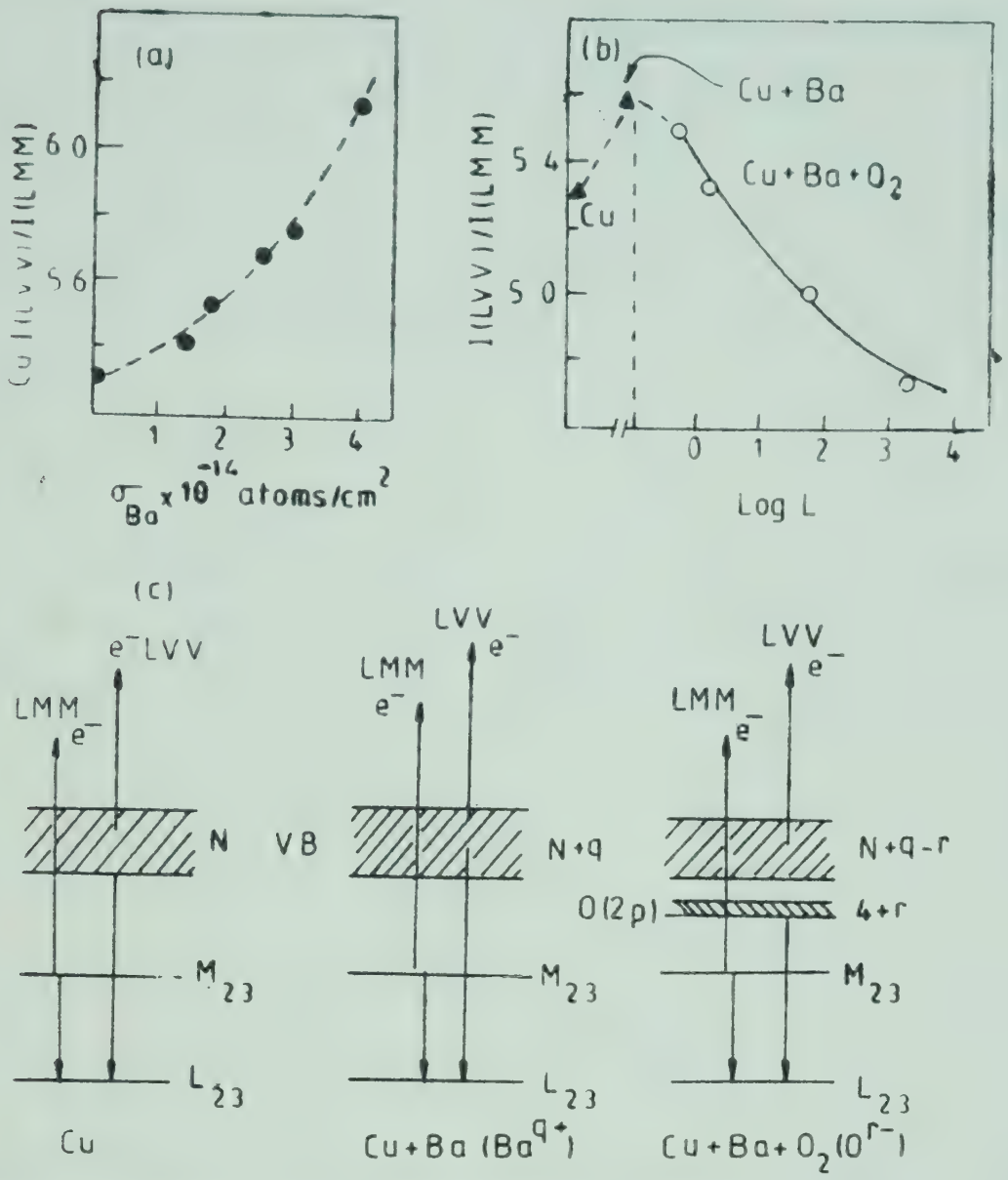

FIG. 5. (a) Variation in Cu $I(L_3VV)/I(L_3M_{23}M_{23})$ ratio with barium coverage.
(b) Effect of a typical barium dosage and subsequent oxygen exposure on the Cu $I(L_3VV)/I(L_3M_{23}M_{23})$ ratio.
(c) Schematic diagram showing changes in the occupancy of the Cu valence band with barium adsorption and subsequent oxygen exposure.

potassium covered Ag surface at 0.1 LO_2 exposure, indicating a high sticking probability on this surface. Furthermore, the surface becomes saturated even at 10 LO_2 exposure. At low potassium coverages, we see two distinct peaks at 528.2 (O(α)) and 530.2 eV, (O(β)) (curves A and B of fig. 6). As the potassium concentration increases, a distinct peak at 533.2 eV (O(γ)), is seen. K(2p) peaks shift to lower values by about 1 eV after the potassium covered surface was exposed to oxygen[9].

Similar O(1s) peaks are seen on the cesium and barium covered Ag surfaces. At higher cesium coverages, a peak at 533 eV clearly develops. The O(1s) binding energies in all the three cases are summarized in table 1.

The O(α) and O(β) species attributable to O(1s) peaks at around 528–529 and 530–531 eV can be identified as the dissociatively chemisorbed oxygen entities, O^{2-} and O^{x-}, $x < 2$ while the O(γ) peak observed around 533 eV can be assigned to molecular oxygen $O_2^{\delta-}$ ($\delta < 2$). The intensity of the O(α) species is found to be independent of the initial alkali coverage, while the saturated O(β) peak intensity increases consistently with σ_M. This suggests that the O(α) species is associated with silver.

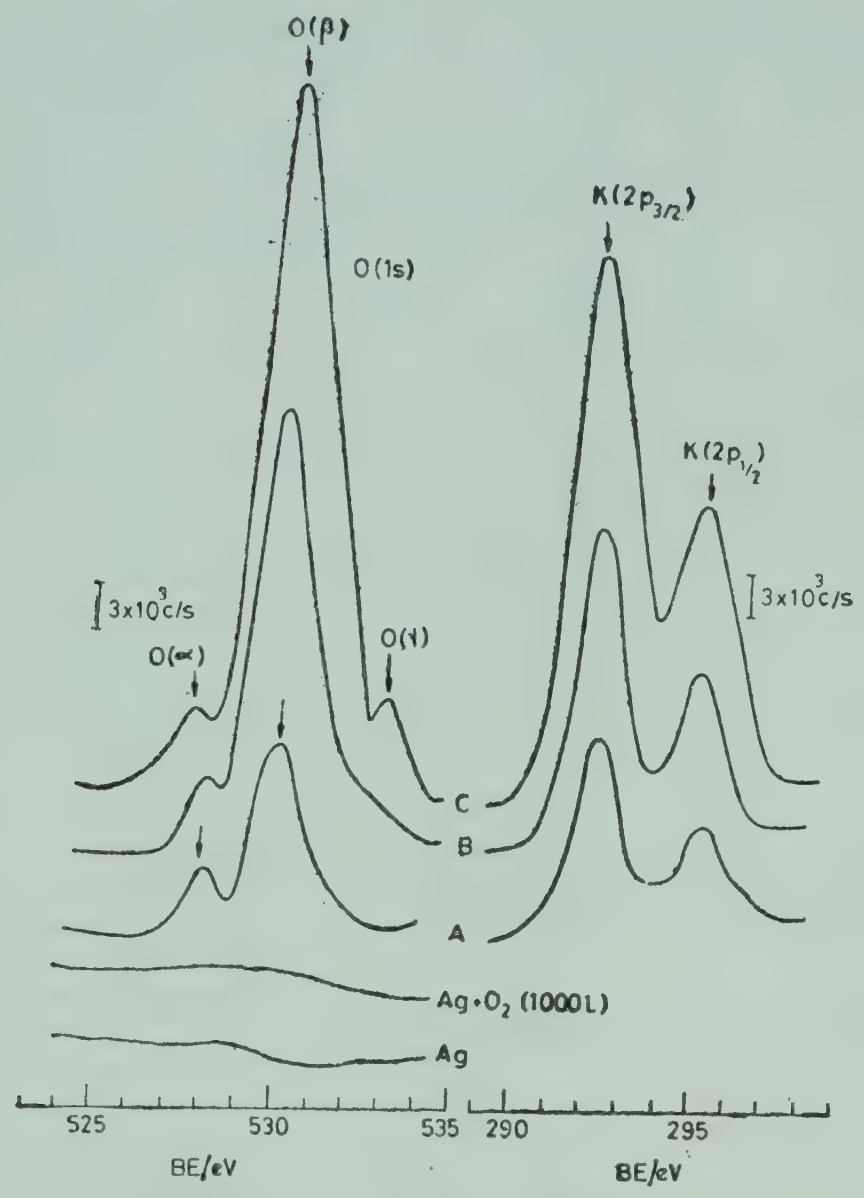

FIG. 6. O(1s) and K(2p) spectra on Ag at 300K for different potassium concentrations after the surface was saturated with oxygen (exposure > 200 L O_2; σ_K for curve C corresponds to 9.4×10^{14} atoms/cm²). For comparison, the O(1s) spectrum on clean Ag after 1000 L O_2 exposure is also given.

TABLE I

O(1s) binding energies of adsorbed oxygen on alkali dosed Ag, Cu, Pt

System	$\sigma_M \times 10^{-14}$ atoms/cm²	0(α) eV	0(β) eV	0(γ) eV
Ag — K	8.0	528.0	530.7	533.2
Ag — Cs	8.0	528.5	531.1	533.0
Ag — Ba	5.0	528.9	530.8	533.0
Cu — K	5.0	529.8	530.8	—
Cu — Ba	5.0	529.6	531.0	—
Pt — K	5.0	530.0	531.1	
Pt — Cs	5.0	529.6	530.8	

The study of adsorption of oxygen on sodium dosed Ag(110) has shown that sodium-oxygen stoichiometry of the oxygen saturated surface remains essentially constant and it is found to be independent of the initial sodium dose[24]. Diffusion of sodium into bulk Ag is thought to be the reason for such a behaviour. No molecular dioxygen species was, however, detected on the Na dosed surface.

On the potassium dosed Ag surface, however, three distinct oxygen species were detected for $\theta_K < 0.5$ by TDS studies: O(ad), O_2(a) and dissolved O. The rubidium dosed Ag (111) surface also showed the presence of dioxygen[11]. Typical desorption studies for the Ag(100)/K system are given in Fig. 7.

With increasing alkali coverage, the saturated oxygen concentration was found to increase appreciably in our study. The relative variation of σ_0 with σ_M is shown in Fig. 8 for potassium, cesium and barium covered Ag surfaces. The solid line is a fit to the equation:

$$\sigma_0 = a_M [1 - \exp(-b_M \sigma_M)] \qquad \ldots(4)$$

where σ_0 is the saturated oxygen concentration for a given alkali concentration σ_M; a and b are empirical constants for a given alkalisubstrate system. This variation implies that the oxygen uptake co-efficient $d\sigma_0/d\sigma_M$ decreases exponentially with σ_M:

$$\frac{d\sigma_0}{d\sigma_M} \alpha \exp(-b_M \sigma_M) \qquad \ldots(5)$$

This clearly shows that the adsorption of oxygen takes place on sites in the vicinity of adsorbed alkali adatoms. As the initial alkali coverage increases, these sites decrease in number and σ_0/σ_M ratio decreases. From Eq. (4) it can be shown that the $_0\sigma/\sigma_M$ ratio is close to the product p_M of the two constants a_M and b_M:

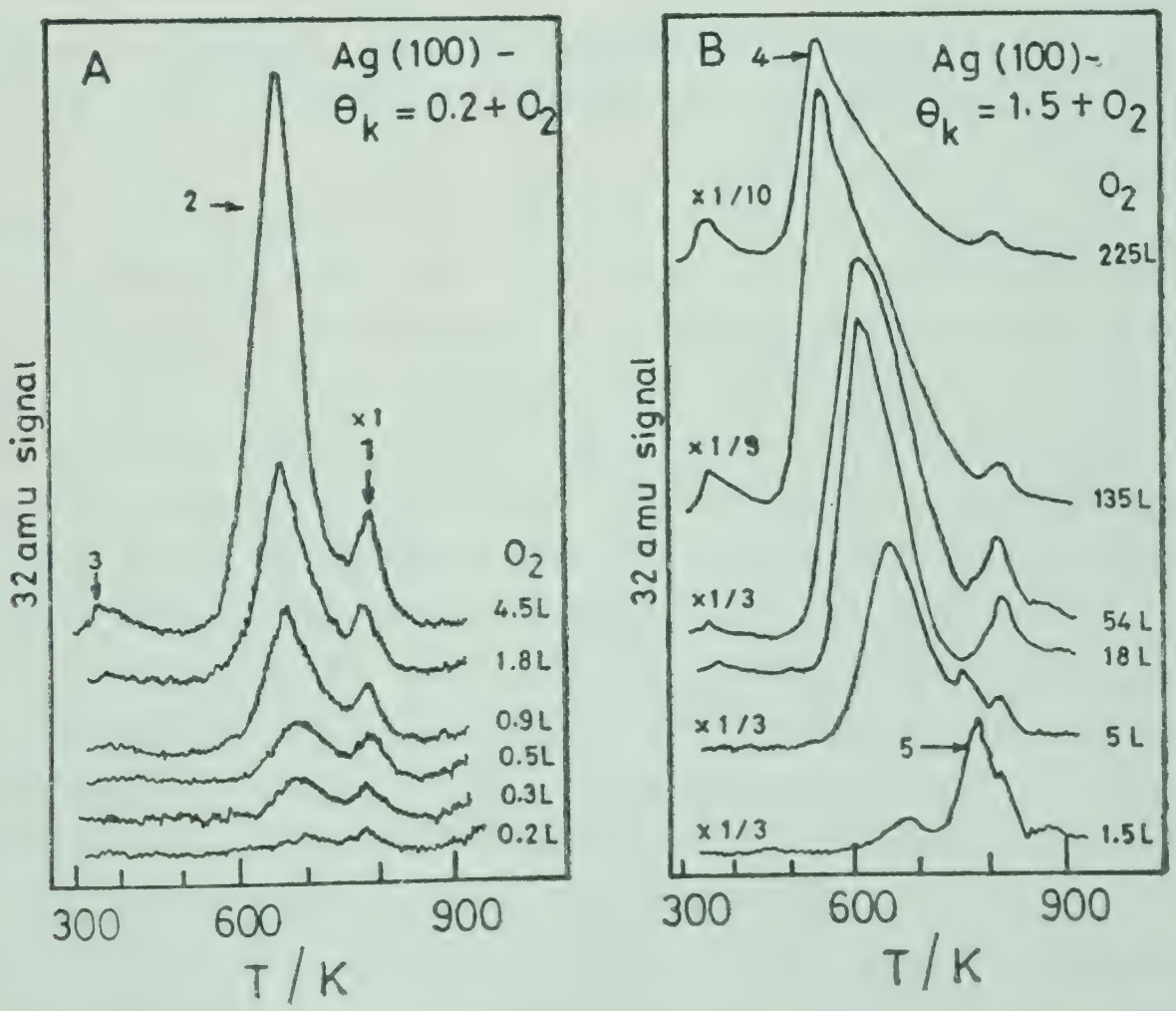

FIG. 7. 32 amu (O_2^+) thermal desorption spectra as a function of O_2 exposure for two different values of θ_K. Heating rate 10 K s^{-1} (from Ref. 4).

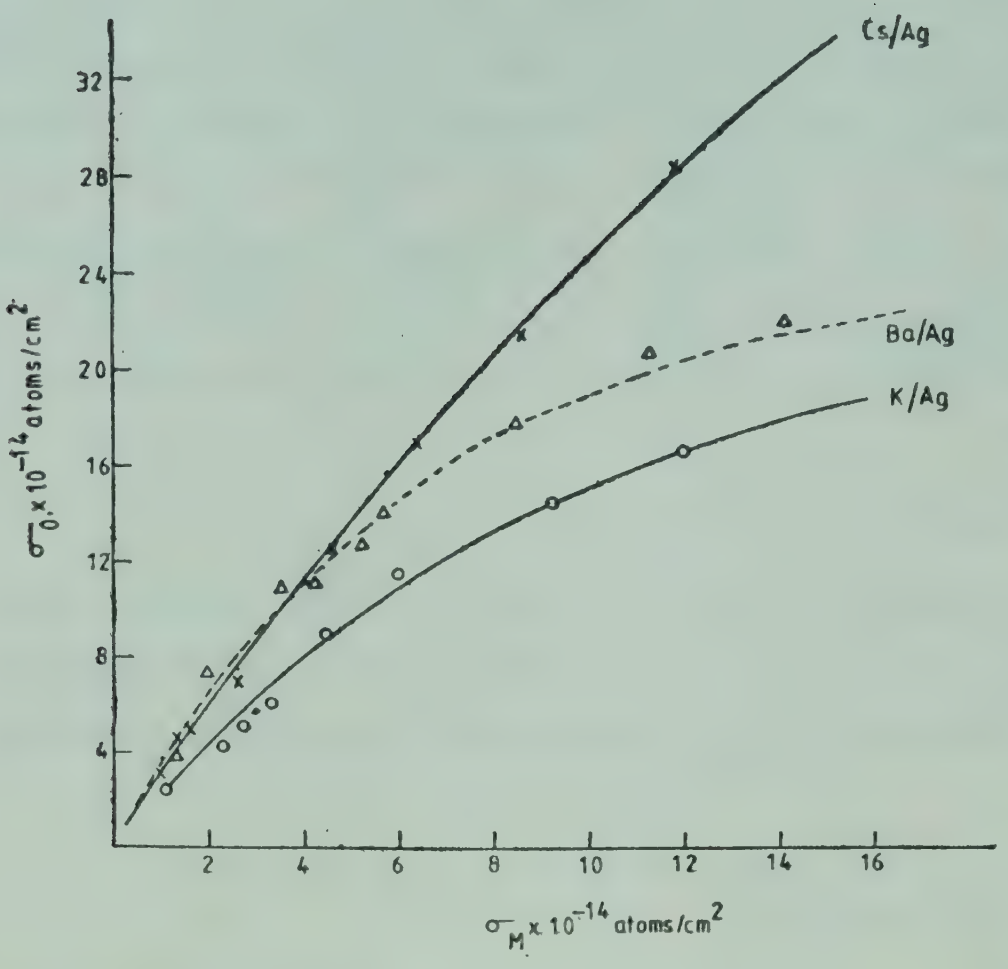

FIG. 8. Variation in the saturated oxygen concentration (σ_o) with surface alkali concentration (σ_M) at 300K (see eqs. 4–6 in the text).

$$\lim_{\sigma_{M\to 0}} \frac{d\sigma_0}{d\sigma_M} = a_M b_M = p_M \qquad \ldots(6)$$

The values of p_M and hence the number of oxygen atoms for every alkali metal atom on the surface at low alkali coverages are thus found to be 2.3, 3.0 and 3.8 for potassium, cesium and barium respectively on Ag. At low alkali coverages, the σ_o/σ_M ratio, therefore varies in the order K < Cs < Ba while at higher coverages ($\sigma_M > 5 \times 10^{14}$ atoms/cm^2), the ratio is in the order K < Ba < Cs (See fig. 8). In the case of K and Ba, there is a steady decrease in the σ_o/σ_M ratio with increasing σ_M. In contrast to this, cesium shows appreciably large values of σ_o/σ_M even at high coverages of cesium, thereby the σ_o vs. σ_{o_s} curve tends close to linearity. This behaviour of oxygen uptake can be interpreted in terms of the ionic size, electron transfer and surface to bulk diffusion of the alkali metal atoms. The large ionic radius (1.67Å) and the very high electropositive nature of cesium seem to facilitate greater oxygen adsorption. On the other hand, potassium and barium having nearly the same ionic raddii (1.33 and 1.34Å) show similar trends in the $\sigma_o - \sigma_M$ variation. At low coverages, oxygen to barium concentration ratio is appreciably higher compared to the corresponding ratio in the case of potassium. This could possibly be due to greater charge transfer to Ag in the case of barium. In Ag, mixed adlayers of potassium and oxygen have been shown to induce surface to bulk transport of both potassium and oxygen[4]. This could also be one of the reasons why σ_o/σ_K ratio is smaller than σ_o/σ_{Ba} on Ag. This would mean that the diffusion of barium into the bulk is comparatively lesser than that of potassium.

Oxygen on Potassium and Barium Dosed Cu

Interaction of oxygen with the copper surface has been of considerable interest in heterogeneous catalysis due to its selectivity in methanol oxidation to formaldehyde[25]. Several electron spectroscopic studies of oxygen on Cu are reported in the literature[26]. While dissociative chemisorption of oxygen on Cu is seen at 300K, the formation of Cu_2O, however, is identified only after very high oxygen exposures (10^9L) as shown in a recent EELS study[27]. Rao *et al.*[18] have shown that at 500K, oxidation of Cu to Cu_2O proceeds via an intermediate stage of incorporation of oxygen into the octahedral voids of Cu. Au and Roberts[28] have shown that dissociatively chemisorbed oxygen on Cu at 295 K is reactive with molecules such as H_2O, NH_3 and HCOOH through a hydrogen abstraction mechanism. However, it was observed that only a certain part of the adsorbed oxygen could take part in the hydroxylation process, while the rest of the oxygen remained unreacted even at 373K.

We were interested in knowing whether sub-monolayer coverages of alkali or alkaline earth metal could effect a change in the nature of adsorbed oxygen and its reactivity on Cu[19]. Fig. 9 shows O(1s) and Ba($3d_{5/2}$) spectra as a function of oxygen exposure at 300K. O(1s) spectrum on clean Cu is also shown. On clean Cu, the O(1s) region shows a single peak at 529.9 eV after 2000 L O_2 exposure (curva a). However, on the barium covered surface ($\sigma_{Ba} = 2 \times 10^{14}$ atoms/cm^2), at low exposure (0.1 L O_2), a broad peak at 531.6 eV is seen and with increasing exposure, peaks a 529.6 eV, O(α). and 531.0 eV, O(β) develop. The surface saturates with oxygen for exposures less than 200 L O_2. The Ba(3d) peaks shift to lower binding energy by 1.0 eV on exposure of oxygen (see fig. 9). Shown in Fig. 10(b) are some typical Ba($3d_{5/2}$) spectra for different barium coverages on Cu at 300K and

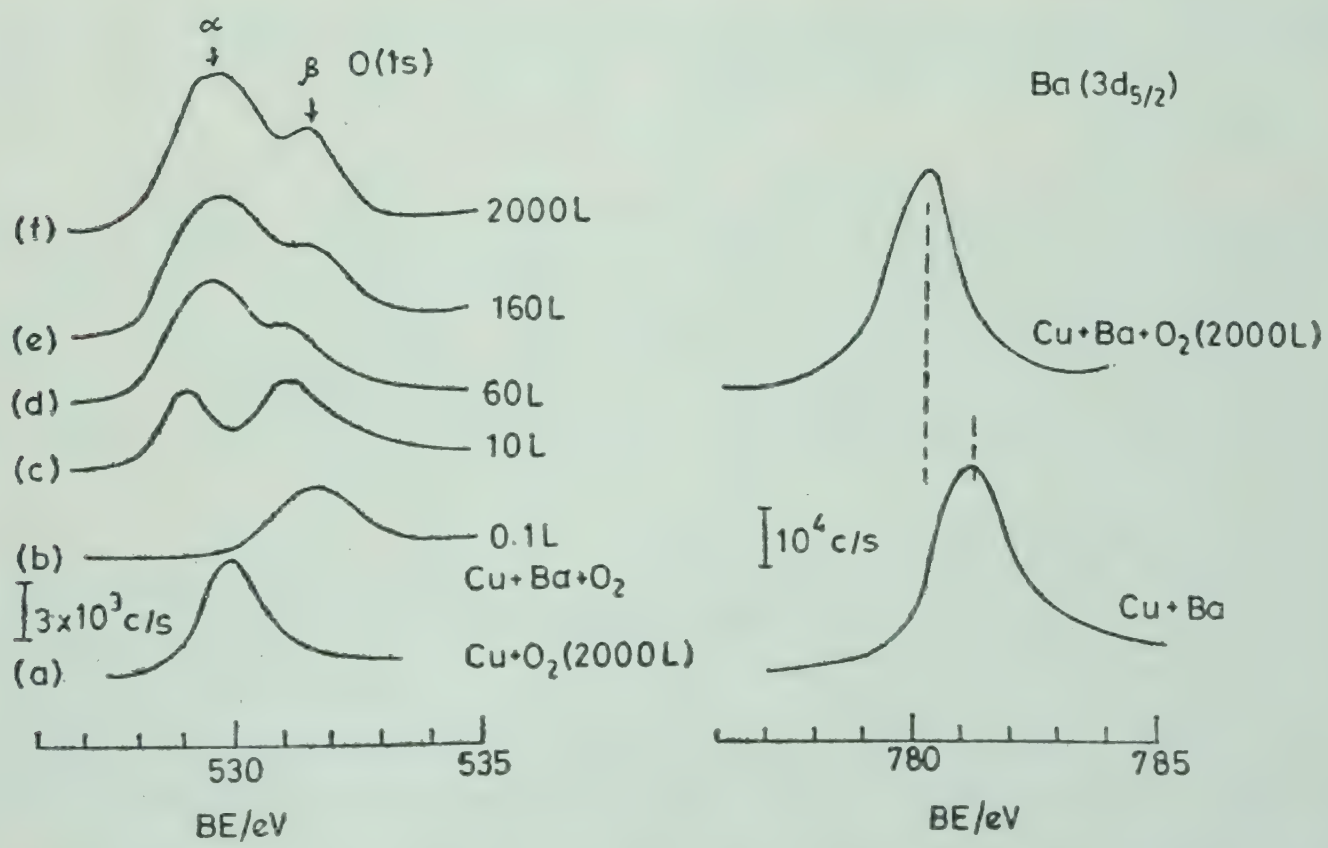

FIG. 9. O(1s) and Ba($3d_{5/2}$) spectra at 300K on barium covered Cu as a function of oxygen exposure ($\sigma_{Ba} = 2 \times 10^{14}$ atoms/cm^2). O(1s) on clean Cu at 300K is also shown.

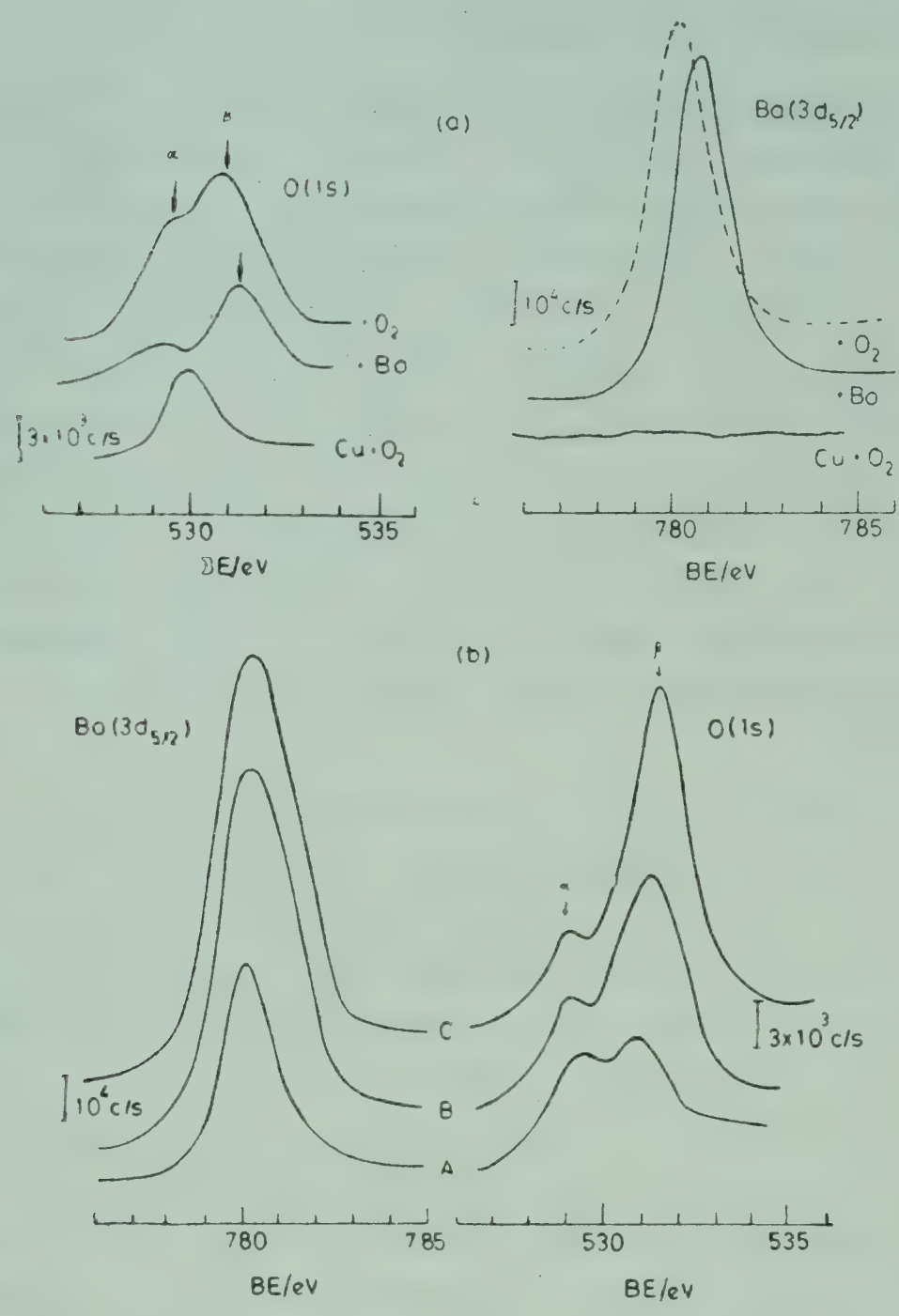

FIG. 10. (a) O(1s) and Ba ($3d_{5/2}$) spectra on Cu + O_2, Cu + O_2 + Ba and Cu + O_2 + Ba + O_2 at 300K.

(b) Ba($3d_{5/2}$) and O(1s) spectra at 300K for different barium coverages after the surface is saturated with oxygen (exposure 1000L O_2; σ_{Ba} for curve A = 2.5×10^{14} atoms/cm^2)

the corresponding O(1s) spectra after saturation (exposure 500 L O_2). As the barium coverage increases, the intensity as well as the binding energy of the 531 eV peak increases. Intensity of the 529.6 eV peak essentially remains the same. There is no significant variation in the binding energy of Ba(3d) peaks with increase in concentration. O(1s) peak at 533eV attributable to molecular oxygen is not seen in the case of barium on Cu.

To characterize the oxygen peaks further, the oxygen covered Cu surface was dosed with barium. The changes observed in the O(1s) spectra are shown in Fig. 10(a). After barium coverage, the 529.9 eV O(1s) peak on Cu decreased considerably in intensity and a new peak around 531 eV was found to increase. On oxygen exposure to this surface, increase in the intensity of the low binding energy O(1s) peak at 529.6 eV was indicated.

The O(1s) position on clean Cu in the absence of barium is close to that of O(α) at 529.6 eV. Also the intensity of O(α) is independent of the alkali coverage, while

there is selective increase in the O(β) intensity with increasing σ_{Ba}. The binding energy and the relative intensity together suggest that the oxygen species O(α) is associated with Cu and O(β) with barium. On the barium covered surface, even after small exposures of oxygen (0.1 L), the peak at 531 eV emerges owing to O(β). This clearly shows that oxygen is preferentially adsorbed with barium. For subsequent O_2 exposures (above 5L), the O(α) is observed to grow. After barium dosage to the oxygen covered Cu surface (Fig. 10(a)) the shift of the O(1s) peak at 529.9 eV to 531 eV clearly demonstrates the transformation of the O(α) species associated with Cu to the O(β) associated with barium. In other words, barium can reduce the adsorbed oxygen on Cu. Also the oxygen on barium dosed Cu is, therefore, mobile on the surface leading to what may be termed as 'oxygen spillover'. This is analogous to what has been noted earlier in this lab in the case of alloys such as Cu-Pd and Cu—Sn[29].

We have studied He II photoelectron spectra of adsorbed oxygen on Cu + Ba + O_2. Fig. 11 shows the spectra for clean Cu and after oxygen exposure

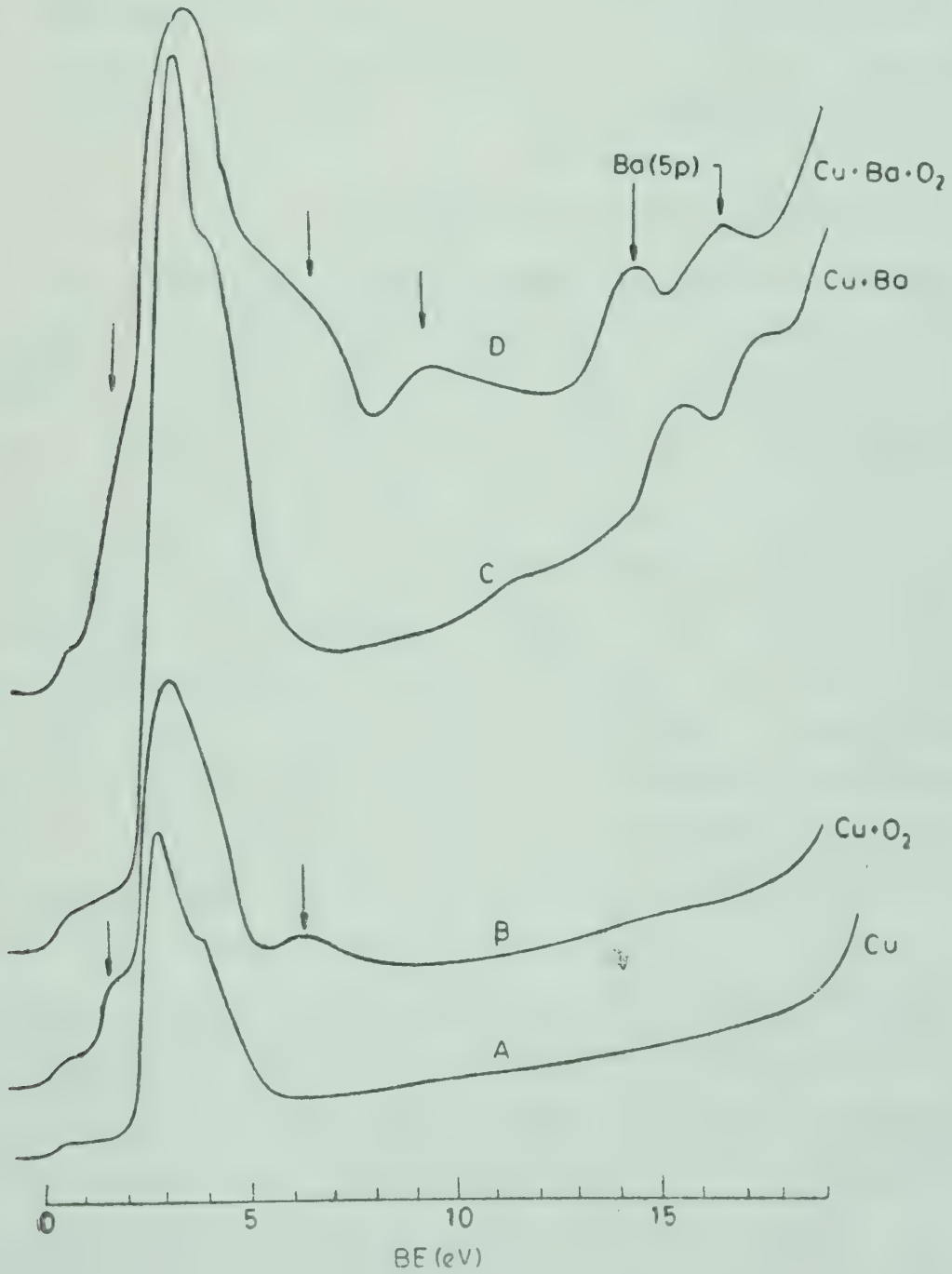

FIG. 11. He II photoelectron spectra of (a) clean copper, (b) after oxygen exposure (2000 L to Cu), (c) after barium coverage on Cu and (d) after oxygen exposure to (E); ($\sigma_{Ba} = 2.0 \times 10^{14}$ atoms/cm², exposure 500L O_2).

to clean as well as barium covered Cu surfaces. A peak at 6.2 eV due to O(2p) and a shoulder at 1.6 eV below E_F are seen on oxygen dosage to clean Cu (Curve B). Similar features have also been observed in the angularly resolved UPS studies on Cu(100)[30] and others. After barium dosage to the clean Cu surface, Ba(5p) peaks at 15.5 and 17.5 eV are clearly observed (Curve C). On subsequent oxygen exposure, two distinct peaks at around 6 eV and 9.2 eV are seen in addition to the shoulder at 1.6 eV below E_F.

These features at 6 eV and 9.2 eV further confirm the presence of two different ypes of oxygen. While the 6 eV emission indicates strongly chemisorbed atomic oxygen, the additional feature at 9.2 eV suggests a weakly bound dissociated oxygen on the surface. Based on both XPS and UPS results, the two oxygen species are characterized as O^{x-} and O^{y-} (x, y, < 2). The Ba(5p) peaks shift to lower binding energy by 1.1 eV on oxygen exposure just as the Ba(3d) peaks do as seen in XPS.

The adsorbed oxygen on potassium dosed Cu shows a very similar trend as the barium dosed surface. O(α) and O(β) peaks at around 530 and 531 eV are observed The intensity of O(α), however, is found to be greater in the case of potassium on Cu. The O(β) peak binding energy is found to increase with increasing σ_K as in the case of barium. This would mean that with increasing alkali coverage (σ_M) the M—O interaction becomes more covalent.

Oxygen on Potassium and Cesium Dosed Platinum

On a clean platinum surface, the initial sticking co-efficient of oxygen is quite low ($\sim$ 0.1) and it is known to decrease exponentially with increasing oxygen coverage. The highest oxygen coverage obtained on Pt(111) is about 0.4[31]. The presence of alkali metal on Pt increases the sticking probability of oxygen.

In their XPS and UPS studies on potassium covered Pt(111)[32], Broden *et al.* have inferred that potassium oxide is not formed on adsorbing oxygen. Two oxygen states were observed which were thought to be due to chemisorbed oxygen and oxide or incorporated atoms. Garfunkel and Somorjai[33] studied coadsorption of potassium and oxygen on Pt(111) by AES, LEED and TDS. In their study, potassium and oxygen were found to to desorb simultaneously indicating strong interactions in the adsorbed overlyer. LEED results on Pt (111) indicated that a planer K_2O layer may be formed by annealing coadsorbed potassium and oxygen to 750 K.

We have studied in detail the adsorption of oxygen on potassium and cesium dosed Pt and have identified two distinct entities of dissociatively chemisorbed oxygen: O(α) with O(1s) at 530 eV associated with Pt and O(β) at 531 eV associatcd with the adsorbed alkali metal. No molecular dioxygen was seen[9].

The high σ_O/σ_K ratio seen in our study indicated that K_2O type of phase is unlikely at room temperature. Beyond 700 K, however, the K--O stoichiometry was found to be in the ratio 2 : 1. This is consistent with the observation made by Garfunkel and Somorjai[33] based on their LEED studies.

As in the case of silver, the saturated oxygen coverage can be greatly increased on platinum. The values of the parameter p_M for potassium and cesium on Pt are given in Table II. The value for the cesium—dosed surface is considerably high and even at rather high cesium coverages ($\sigma_{CS} = 1.5 \times 10^{15}$ atoms/cm^2), oxygen to cesium concentraton ratio is above 3.

TABLE II

Determined values of the parameter p_M

Substrate \ Alkali	K	Cs	Ba
Ag	2.5	3.1	3.8
Pt	2.4	3.5	—
Cu	1.6	—	1.8

THERMAL STABILITY OF ADSORBED OXYGEN ON ALKALI COVERED SURFACES

It was interesting to examine the effect of temperature on the relative stability of the two oxygen species, O(α) and O(β) as this has its bearing on the reactivity and catalytic importance of the adsorbed oxygen. A typical system, that of barium dosed Cu is presented here. The variation in the nature of O(1s) spectra on Cu with and without barium was followed as a function of temperature. There is no significant change in the O(1s) binding energy and intensity as the temperature is increased from 300 to 800K in the case of clean Cu, (see Fig. 12(a)). There is, however, a slight broadening of the O(1s) peak. Contray to this, the O(1s) peak shows marked variation with temperature in the case of barium covered copper. The O(α) peak at 529.6 eV completely disappears at 730K while the 531 eV peak intensity decreases significantly (Fig. 12b). Binding energy of the O(β) peak increases to 531.9 eV as the temperature is increased to 700K and on heating further to 815K, it decreases to 531.1 eV. The variation in surface concentration of oxygen and barium as a function of temperature is shown in Fig. 12(c). The corresponding variation of oxygen in the absence of barium is also given which clearly shows that there is little change in the oxygen concentration as the surface temperature is increased to 700K. In contrast to this, the oxygen on the barium covered surface starts desorbing around 450 K while barium desorbs slowly above 700K[19].

The complete removal of the O(α) peak clearly shows that the oxygen, O^{x-}, associated with Cu is weakly bound and can be desorbed completely at 700K in the presence of barium while it is not so on the clean Cu surface. The increase in the binding energy of O(β) from 531 to 531.9 eV as the temperature is raised from 300 to 700K suggests reduction in Ba—O interaction resulting in more covalent oxygen possibly due to higher surface mobility of this oxygen. Beyond 700K, the barium

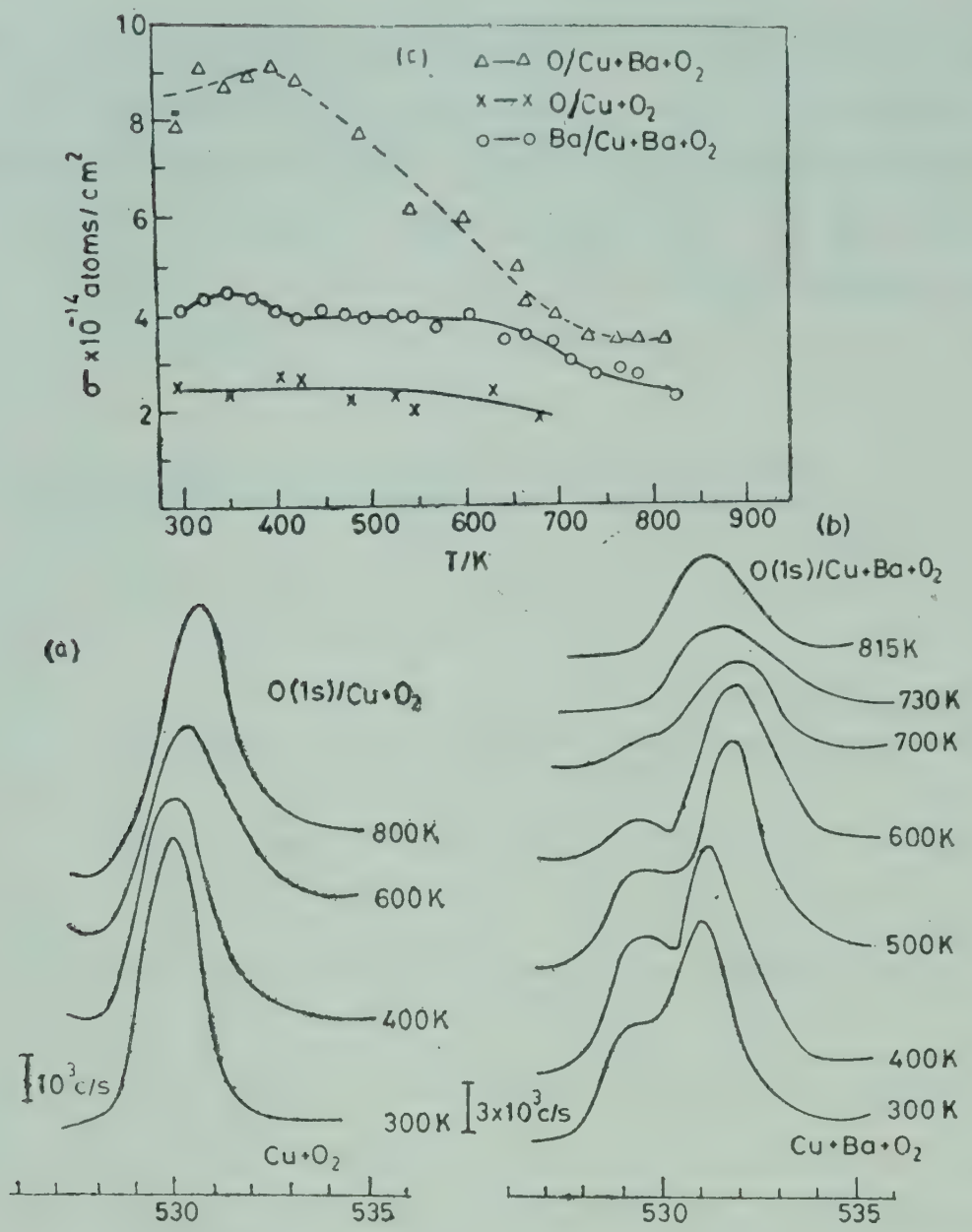

FIG. 12. Variation of the O(1s) spectra with temperature on (a) Copper Covered with Oxygen (3000 L), (b) Copper covered with barium and saturated with oxygen (1000 L) and (c) variation in the surface concentrations of oxygen and barium on the two surfaces.

starts desorbing and the O(β) peak in the higher binding energy region becomes less marked and the O(1s) peak position shifts to a lower value (531.1 eV).

It is to be noted that the oxygen to barium concentration ratio is quite high (close to 2) at 300K which would mean that all the oxygen is not present as the stoichiometric barium oxide, BaO. With increasing temperature, σ_{Ba} remains essentially the same while σ_O falls appreciably resulting in a decrease in the σ_O/σ_{Ba} ratio. Beyond 700K, σ_O/σ_{Ba} is close to unity [Fig. 12(c)]. Therefore, at this temperature, BaO phase could be present on the surface. The decrease in the O(1s) binding energy to 531 eV above 700K could be due to barium oxide formation. At higher temperatures, excess oxygen associated with barium seems to spill over to Cu sites from where it leaves the surface only in presence of barium.

Fig. 13 shows the effect of coadsorbed oxygen on the desorption of potassium and cesium on Ag. It is seen that the alkali metal is more stabilized in the presence of oxygen. Thus the desorption temperatures are raised by about 100° in the case of potassium and by about 60° in the case of cesium when mixed alkali oxygen adlayers are present. The desorption temperature of the alkali metal from the surface, therefore, seems to depend on the presence of chemisorbed oxygen. An

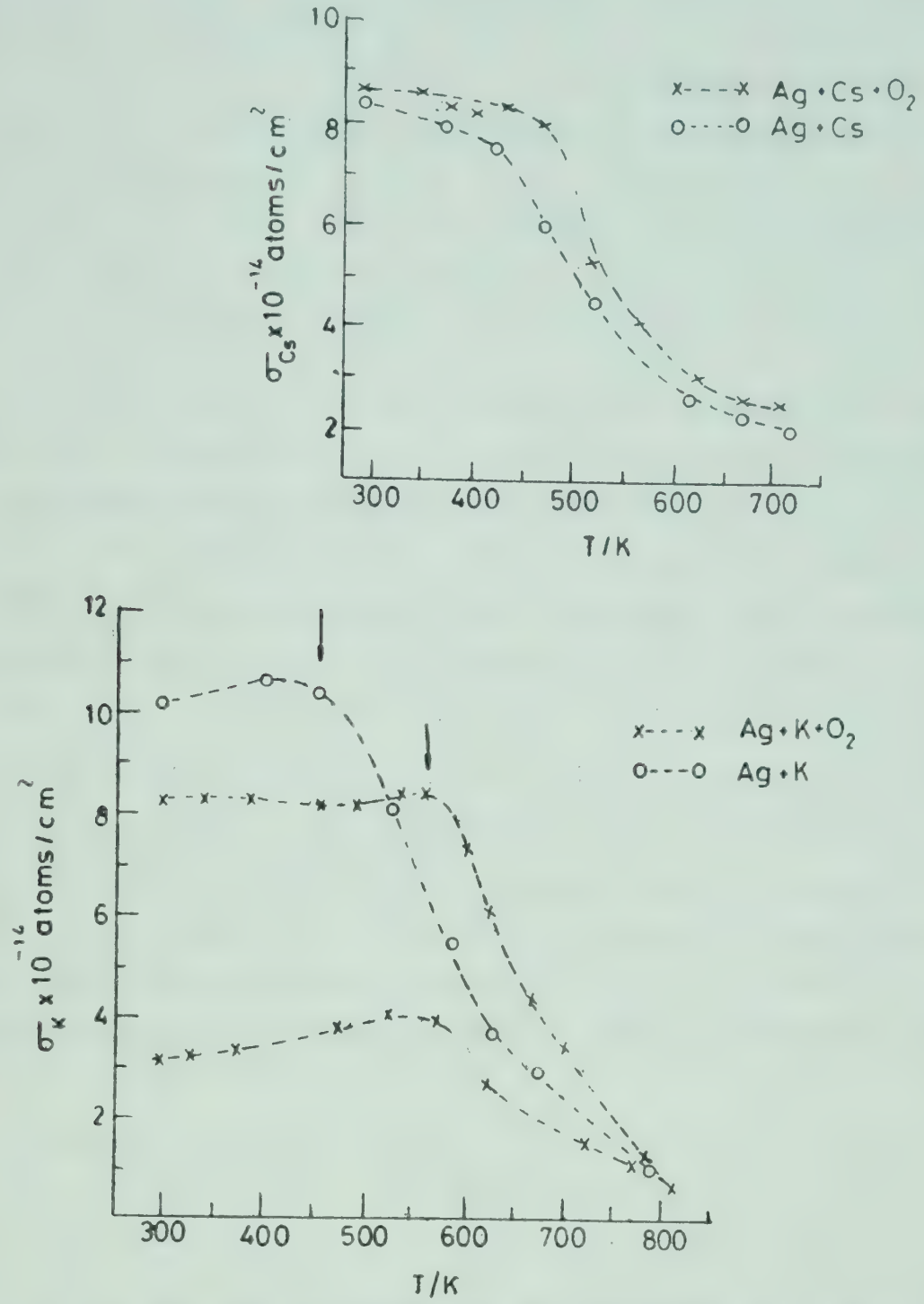

FIG. 13. Variation in the surface concentrations of potassium and cesium as a function of temperature on Ag.

increase in the desorption temperature of rubidium on Ag in the presence of oxygen has been shown in thermal desorption studies[11]. The desorption curves also show that there is an increase in the surface concentration of potassium just before the desorption. This is possibly due to the diffusion of potassium metal atoms into the substrate layers at room temperature and re-diffusion to the surface at elevated temperatures. However in the cesium case, one does not see measurable increase in the surface concentration. Increase in concentrations of potassium, cesium or barium in not seen as the temperature is increased in the case of K/Pt, Cs/Pt and Ba/Cu systems. In the case of potassium dosed Pt, the σ_o/σ_K ratio reduces to about 1 : 2 at higher temperatures (600K) indicating the possibility of K_2O formation[9].

CO and H_2 on alkali-covered Fe, Ni and Pt

CO adsorption on potassium promoted Fe(110)[34] and Fe(100)[35] has been studied employing XPS, UPS and TDS techniques. Saturation CO coverage was found to increase and the sticking probability was found to decrease with increasing initial potassium coverage. He II UPS clearly showed molecular CO with ($1\pi + 5\sigma$) band

at 7.8 eV and 4σ band at 11.4 eV. The corresponding peaks on clean Fe surface are at 7.6 and 10.6 eV respectively. The C(1s) and O(1s) peaks are at 284.0 and 531.2 eV on the potassium dosed surface and at 284.8 and 531.9 eV on the clean Fe surface. However, on heating to about 400K, dissociation of CO was found to occur with C(1s) shifting to 282.3 and the O(1s) to 530.2 eV. The lower binding energies of both C(1s) and O(1s) in presence of potassium for molecular CO show that CO is more strongly chemisorbed on potassium promoted Fe.

Dissociation of CO was shown to occur on potassium promoted Ni, and an increase in the graphitic carbon was found to inhibit the rate of methanation[5]. The extent of dissociation was found to increase with both alkali concentration as well as the electropositive nature of the alkali i.e., in the order, Na < K < Cs. More interes tingly, potassium was found to block hydrogen adsorption. CO dissociation to graphitic carbon was found to increase, thereby lowering the methanation reaction rate as shown by Luftman *et al.*[36] in their TPD studies.

Increase in the adsorption energy of CO from 25 to 36 K cal/mole has been noticed by Crowell *et al.*[37] when sub-monolayers of potassium were pre-adsorbed on Pt(111). CO stretching vibration frequency was found to decrease with increasing potassium coverage from 2120 cm^{-1} to 1400 cm^{-1} (See fig. 14). The bond order of CO was found to be as low as 1.5. The large adsorption energy and the low CO stretching frequency observed in their study, therefore, indicate adsorption of CO in

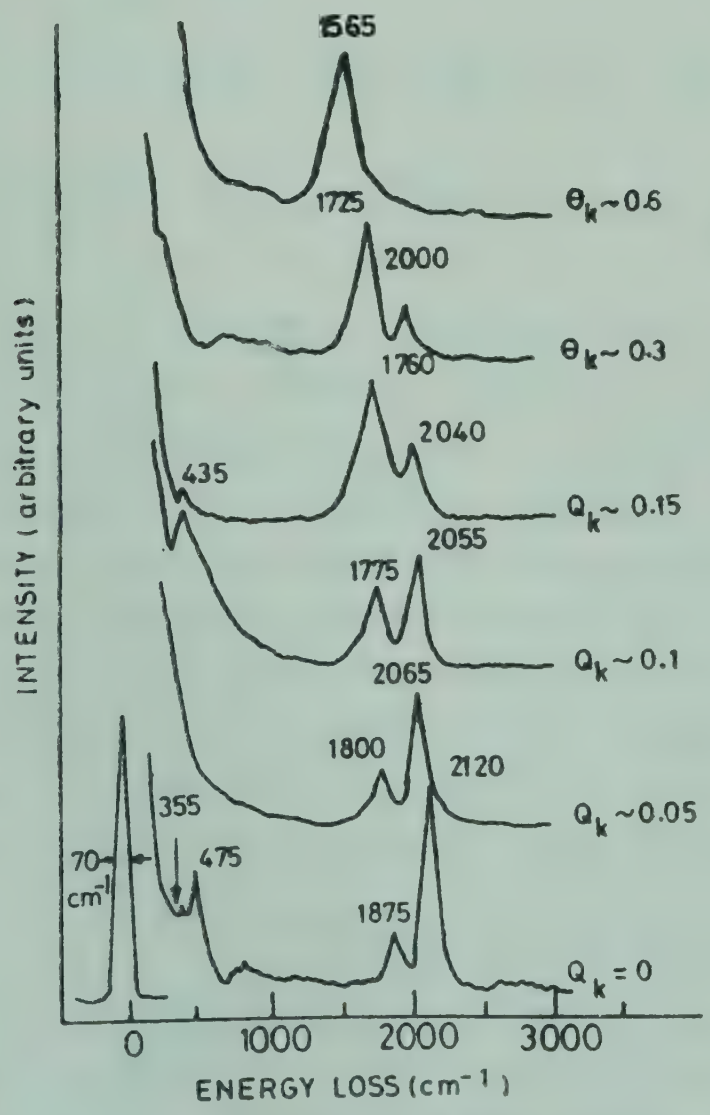

FIG. 14. HREELS spectra for saturation CO exposures with various potassium coverages (from Ref. 37).

the molecular form, with a substantial charge donation from potassium through Pt substrate to the $2\pi^*$ orbital of CO.

CO Interaction with Adsorbed Oxygen on Alkali Covered Surfaces

The presence of dissociatively chemisorbed oxygen and vacant sites for CO adsorption on the metal surface have been shown to be necessary conditions for the oxidation of CO on Pt group metals[38]. The oxidation process has primarily shown a 'clean-off' reaction which is considered to result in the formation of CO_2. Engelhardt *et al.*[39] examined the interaction of CO with oxygen adsorbed on Ag (110); the incoming CO molecules were found to react rapidly with the adsorbed oxygen atoms to form CO_2 which desorbed immediately. Albers *et al.*[40] studied the oxidation of CO in more detail using ellipsometry. The oxidation process was found to differ with the amount of precovered oxygen, but invariably led to a 'clean-off' reaction. In a more recent study, a similar result was seen on Ag(111) when the surface was pre-covered with active oxygen. However when CO was exposed at low temperatures, a new reaction pathway leading to the formation of CO_2 and CO_3 was observed[41]. Kitson and Lambert[4] have shown that molecular dioxygen is not reactive to CO in their TPD studies.

We have studied oxidation of CO on Ag dosed with potassium, cesium and barium[10]. The alkali covered surface was first saturated with oxygen (exposure $>$ 500 L O_2) and then exposed to CO at 300K till there was no further increase in the intensities of the O(1s) and C(1s) peaks.

On this surface with dosed potassium two C(1s) peaks with binding energies at 284.5 and 288.6 eV were observed. The O(1s) peak was found to be symmetric and sharp around 531 eV. On exposure to CO at 80K only one C(1s) peak at 285.0 eV is observed and the O(1s) region shows a shoulder at 532.4 eV. On heating, the intensities of the oxygen and carbon peaks decrease and at 550K the clean surface is observed, the potassium having been desorbed (see fig. 15).

The cesium and barium dosed surfaces also show the $\sim$ 289 eV C(1s) peak on CO exposure at 300K. This peak together with a O(1s) peak at 531.5 eV can be identified as arising from the same surface entity. The concentration ratio of the oxygen to the 289 eV carbon is 3 : 1,indicating a surface carbonate. This assignment is in agreement with the C(1s) line position observed for several metal carbonates such as nickel carbonate[42], cadmimum carbonate and silver carbonate[43]. The He (II) spectra lend further credence to this assignment; the peaks observed at 4.6 and 9.3 eV after exposure to CO agree with those observed for metal carbonate at 4.6 eV (1e″ and 4e″) and 9.0 eV (3e″ and 1a″)[44]. The 4.6 eV peak is due to non bonding O(2p) orbitals. The second intense band at 9.3 eV is produced by the ionization of the 3e and $1a_2$ molecular orbitals, both of which are C(2p) — O(2p) bonding in character. The small shoulder due to the 4a′ molecular orbital of carbonate at 10.6 eV seems to be merged with the second main band.

In XPS, a C(1s) peak is observed at 284.7 eV on potassium and barium-covered surfaces in addition to the carbonate C(1s) peak at 289 eV. However, it is not

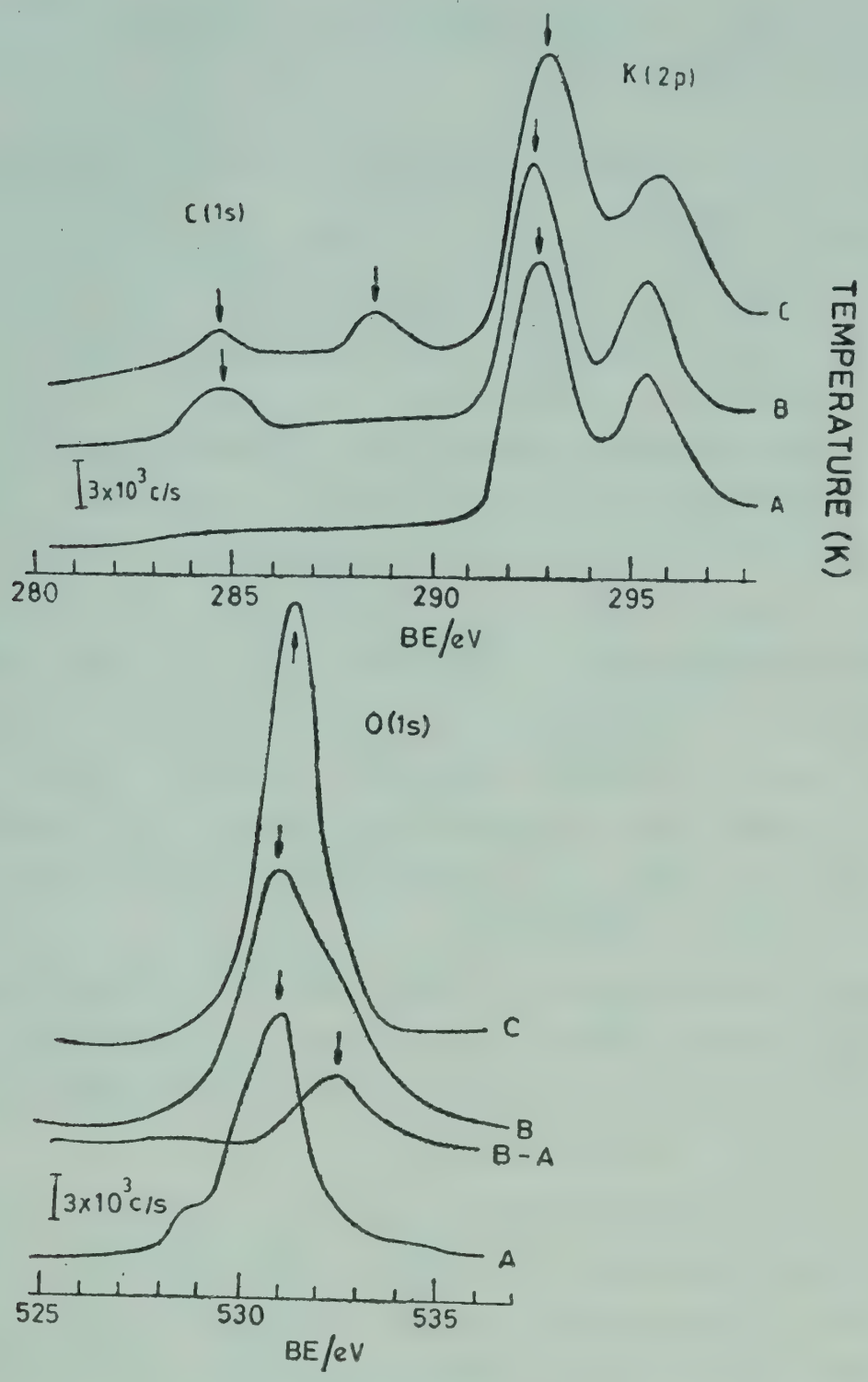

FIG. 15. C(1s), K(2p) and O(1s) spectra: (a) on Ag + K + O_2 (5000L) at 300K, cooled to 80K, (b) Ag + K + O_2 + CO (1000L) at 80K and (c) after warming (b) to 350K ($\sigma_K = 7.3 \times 10^{14}$ atoms/cm^2)

possible to distinguish between molecular and dissociated CO on the basis of the 284.7 eV C(1s) peak position. The O(1s) peak from the carbonate species at 531.5 eV also overlaps with that of adsorbed molecular CO. The highly positive enthalpy of dissociative chemisorption of CO on Ag (334 kJ mol^{-1}) and the small negative value for molecular chemisorption (−27 kJ mol^{-1}) strongly suggest chemisorption of CO in its molecular form. The peak at 531.5 eV, however, is sharp in all three cases, indicating that carbonate is the major oxygen containing species. In the cesium covered surface there is no peak at 284.7 eV suggesting almost total conversion of CO to CO_3. It is also to be noted that an O(1s) peak at 535 eV and C(1s) peak at 292 eV attributable to CO_2(ad.) were not seen in any of the above experiments, even at low temperatures. The O(1s) spectra after adsorption of CO on all three surfaces clearly indicate that both oxide, O^{2-}, and atomic, O^{x-}, types of oxygen react with CO in the formation of the CO_3 species. Although the oxygen to total carbon concentration ratio in the case of potassium-and barium covered surfaces is

2 : 1, the ratio of oxygen to 289 eV carbon is 3 : 1. From the above observations the following reaction sequence for potassium and barium-covered Ag surfaces is suggested :

$$CO(ad.) + O(ad.) + O(ad.) \rightarrow CO_3(ad.) \quad ...(7)$$

$$CO_3(ad.) \rightarrow CO_2(g) + O(ad.) \quad ...(8)$$

$$CO(ad.) + O(ad.) \rightarrow CO_2(g) \quad ...(9)$$

These reactions account for the observed oxygen to total carbon concentration ratios and also for the simultaneous decrease in the C(1s) peaks. The formation of barium carbide is thermodynamically feassible and is known to occur on a barium surface after interaction with CO[45]. Therefore the dissociation of CO cannot be ruled out, although the presence of molecularly chemisorbed CO is more likely on potassium and barium-covered surfaces.

However, in the case of the cesium covered Ag surface, we do not see a C(1s) peak at 284.7 eV and we do see oxygen on the surface after all the carbon has disappeared. It is likely that the large ionic size of Cs^+ (1.69 Å) and the large amount of oxygen on the cesium covered surface hinder the adsorption of an excess of CO. Based on these observations, the following reaction sequence for a cesium-covered Ag surface is suggested.

$$CO(ad.) + O(ad.) + O(ad.) \rightarrow CO_3(ad.) \quad ...(10)$$

$$CO_3(ad.) \rightarrow CO_2(g) + O(ad.) \quad ...(11)$$

$$O(ad.) + O(ad.) \rightarrow O_2(g) \quad ...(12)$$

Interaction of CO with oxygen on K, Ba covered Cu as well as K and Cs covered Pt were also studied. Stable CO_3 formation was not observed in any of these experiments. Also, there was no CO adsorption or dissociation on oxygen saturated surfaces. Thus, only in the case of alkali covered Ag surface, CO adsoption and CO_3 formation are seen.

N_2 on potassium covered Fe

Dissociative chemisorption of nitrogen is considered to be the rate determining step in NH_3 synthesis. The role of potassium in enhancing the dissociation in Fe catalyst has been examined by Ertl *et al.*[2,46]. Compared to the clean Fe surface, the dissociative chemisorption of nitrogen was found to increase 300 fold in presence of a small coverage of potassium ($\sigma_K = 1.5 \times 10^{14}$ atoms/cm^2). Enhanced chemisorption is attributed to the charge transfer from potassium to Fe atoms. An increase in the heat of adsorption of nitrogen by 11.5 K cal/mole is also seen in presence of potassium which simultaneously lowers the activation barrier for dissociation. As a consequence, the effective sticking coefficient for dissociative nitrogen adsorption is markedly increased.

These observations are analogous to those made in the case of CO adsorpion on potassium covered Fe[34]. Pumping of electrons into the antibonding orbital of

N_2 seems to be facilitated due to excess charge over Fe in presence of potassium and the bond order is reduced as is seen in the case of CO on Fe. It would be interesting to see the enhanced dissociation in presence of calcium or barium on Fe in combination with potassium.

Oxidation of ammonia on potassium covered Pt

Extensive amount of work has been done to understand the mechanism of catalytic oxidation of ammonia to nitric oxide. These results have been summarized in a recent review by Temkin[47]. Wire gauge made of Pt-Rh is widely used as a catalyst for this process. The oxidation reaction may be described by Eq. (13).

$$4NH_3 + (3 + 2s)\, O_2 \rightarrow 4s\, NO + 2(1 - s)\, N_2 + 6H_2O;\ 0 < s < 1 \quad ...(13)$$

Here, the selectivity, s, is the fraction of ammonia converted into nitric oxide. It has been shown that s can be raised close to unity by increasing the surface oxygen concentration[48] and also by increasing the sticking probability of ammonia on the surface[47]. We have investigated by means of XPS, the oxidation process on both clean and potassium covered Pt surfaces[49].

The clean Pt surface was first saturated with oxygen at 300K (O_2 exposure 200L) and then cooled to 77K. The surface was then exposed to ammonia. N(1s) and O(ls) spectra were followed as the surface was warmed slowly. Figure 16 shows O(ls) and N(is) spectra on Pt as a function of temperature. A large N(1s) peak at 399.8 eV is characteristic of molecularly chemisorbed ammonia on Pt surface[50]. When the surface is warmed to 80K, it is observed that the excess ammonia condensed on the surface ($\sigma_N = 6 \times 10^{15}$ atoms/cm^2) desorbs and the ammonia chemisorbed on the surface seems to interact with the chemisorbed oxygen. At 80K, the O(1s) peak shifts from 530 eV to 532.5 eV indicating the formation of water on Pt[51]. Also the N(1s) peak shifts to lower binding energy and the N(1s) peak at 398.2 eV corresponding

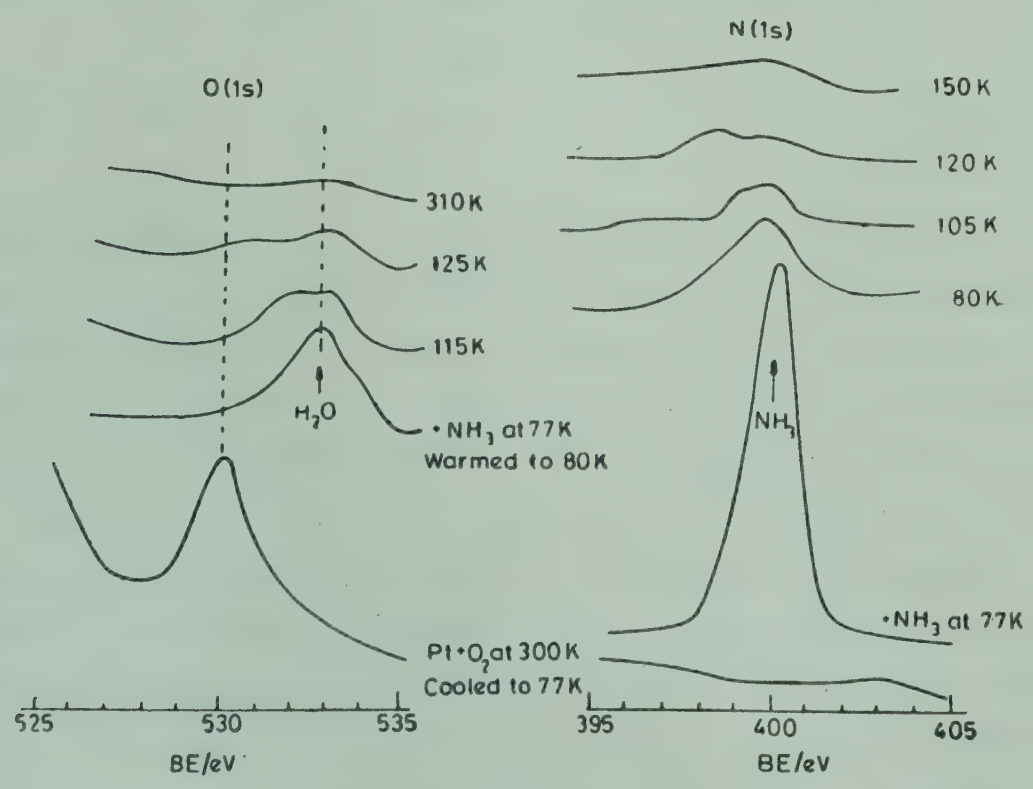

FIG. 16. O(1s) and N(1s) spectra on clean Pt surface before and after NH_3 adsorption as a function of temperature.

to NH species is clearly seen. From this it may be concluded that the reaction on oxygen covered Pt seems to be one of hydrogen abstraction from NH_3 :

$$O(ad) + NH_3(ad) \rightarrow NH(ad) + H_2O(ad) \qquad ...(14)$$

Figure 17 shows O(1s) and N(1s) spectra as a function of temperature on potassium covered Pt surface. On ammonia adsorption at 77K, the N(1s) peak is seen at 400.0 eV, just as in the earlier case with clean Pt. As the temperature is increased, it is interesting to observe that a peak at 400.8 eV develops in the N(1s) region and a shoulder at 532.5 eV is distinctly seen in the O(1s) spectra. At 80K, the N(1s) peak clearly shifts to higher binding energy. Besides, a small N(1s) peak at lower binding energy (398.3 eV) is seen. The N(1s) peak intensity at 400.8 eV decreases as the temperature is raised and a correspondingly large increase in the lower binding energy N(1s) peak is observed. Around 120K, most of the N(1s) peaks disappear and above 150K, water also desorbs. The formation of water definitely proves that the oxygen on potassium covered surface can indeed abstract hydrogen from ammonia.

The σ_O/σ_K ratio drops from 1.5 before ammonia adsorption to about 1.0 after the oxidation indicating thereby that chemisorbed oxygen on potassium covered Pt is utilized during the reaction. The N(1s) peak at 400.8 eV can be attributed to NO formation. This binding energy compares well with the reported N(1s) binding energy at 400.8 eV for NO on Pt(111)[50]. The large surface oxygen concentration seems to favour NO formation. With increase in temperature, the decrease in the NO peak intensity observed here seems to be more due to desorption rather than dissociation, since the surface is still rich in oxygen.

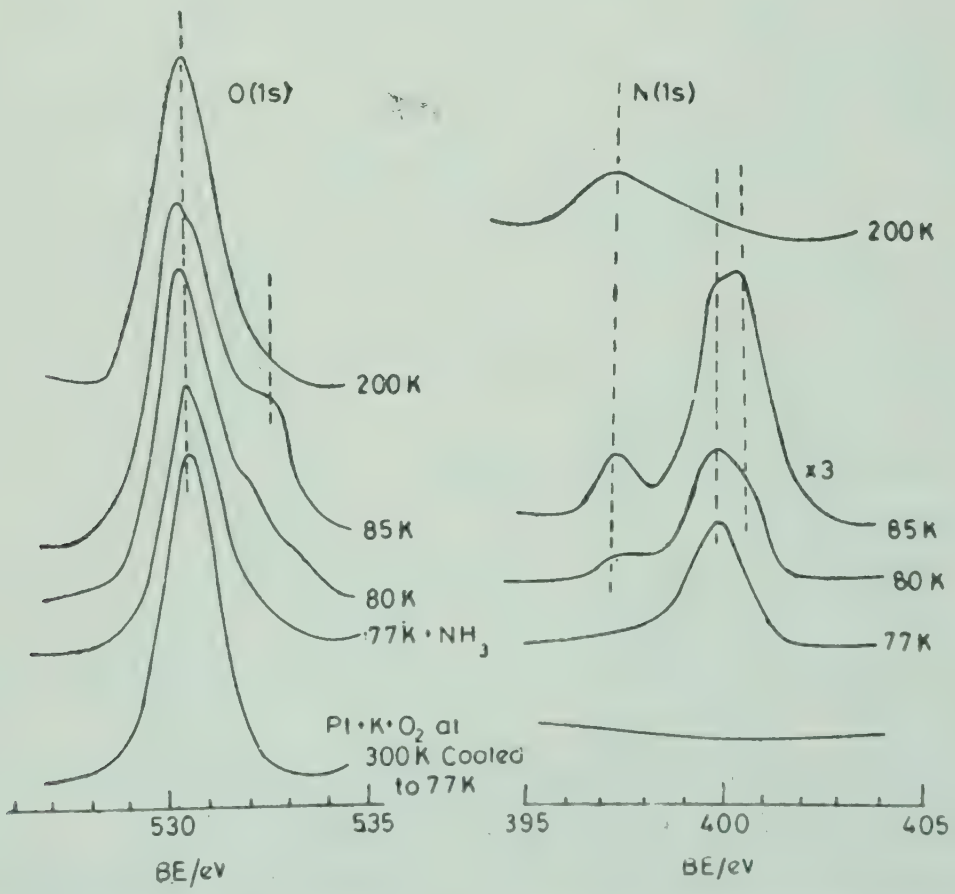

FIG. 17. O(1s) and N(1s) spectra on potassium covered Pt surface before and after ammonia adsorption as a function of temperature.

Based on these results, a comparison of oxidation reactions on a clean Pt surface and on potassium covered Pt surface is quite revealing. Details of surface concentrations of nitrogen and oxygen in presence of potassium have been reported earlier[49]. Our study shows that even at 80K, oxidation of NH_3 to NO occurs on the potassium covered Pt surface saturated with oxygen.

The Effect of Chlorine on Pre-adsorbed Oxygen

Alkali halides are known to promote oxidation on silver catalysts. Earlier studies on the adsorption of chlorine on clean and alkali dosed Ag surfaces have shown its high sticking coefficient. On Ag single crystal surfaces, TDS and LEED studies have primarily shown the formation of chemisorbed atomic chlorine at 300K[52–55]. Our XPS studies on the adsorption of chlorine have shown that characteristic binding energies can be used to identify surface species in the chlorination of Ag. Studies pertaining to silver dosed with two typical metals, potassium and barium, are briefly summarised here.

Fig. 18(a) shows the effect of chlorine exposure to the oxygen saturated Ag surface dosed with potassium. The nature of the O(1s) peaks shows a marked transformation on chlorination. The intensity of O(β) at 531 eV is drastically reduced; O(α) at 529 eV is totally suppressed and O(γ) at 533 eV becomes more prominent and distinct.

Fig. 18(b) shows the Cl(2p) spectra after chlorination of Ag + K + O_2 for different potassium coverages. Curve A shows Cl(2p) spectrum after chlorination

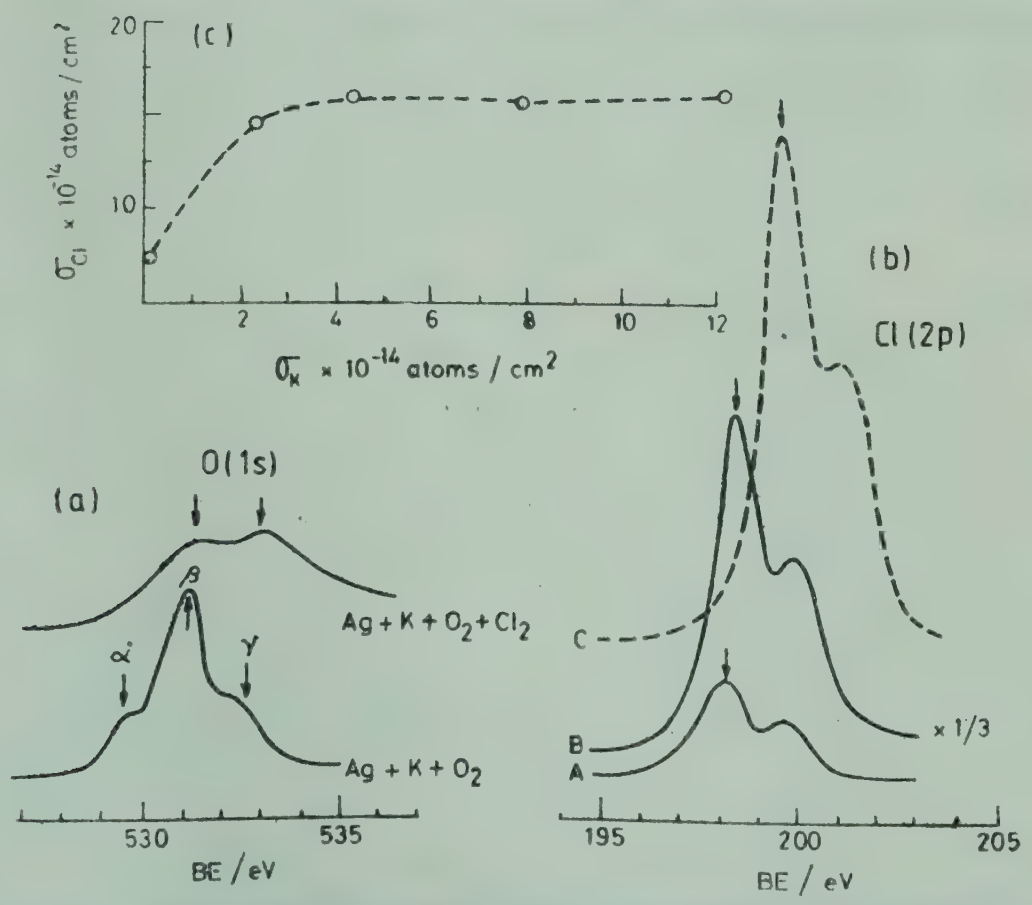

FIG. 18. (a) O(1s) spectra after oxygen dosage (1000L) and after subsequent Cl_2 exposure (1000L) at 300K to K-dosed Ag ($\sigma_K = 8.2 \times 10^{14}$ atoms/cm²).

(b) Cl(2p) spectra on Ag + K + O_2 + Cl_2 for (A) $\sigma_K = O$, (B) $\sigma_K = 4.3 \times 10^{14}$ atoms/cm² and (C) $\sigma_K = 1.2 \times 10^{15}$ atoms/cm².

(c) Variation of saturation chlorine concentration with potassium coverage at 300K.

of clean Ag without any potassium. The Cl($2p_{3/2,\,1/2}$) doublet is clearly observed with binding energies at 198.0 and 199.5 eV. For smaller potassium coverages (curve B), a similar Cl(2p) spectrum is observed, while at higher K coverages (Curve C), a much higher binding energy Cl(2p) is noticed (199.4 eV). The saturated chlorine coverage is greatly enhanced on the potassium dosed Ag surface saturated with oxygen. The surface chlorine concentration, after saturation is found to be independent of potassium coverage [Fig. 18(c)].

The barium covered surface, however, shows certain differences. Fig. 19(a) shows the Cl(2p) spectrum after 10L and 1000L Cl_2 exposure to the oxygen saturated Ag surface dosed with barium ($\sigma_{Ba} = 1.5 \times 10^{15}$ atoms/cm^2). The difference spectrum shown in the figure clearly shows the growth of a low binding energy Cl(2p) doublet for higher doses of chlorine. A composite Cl(2p) peak is shown for another barium dosage along with the curve-fitted resolved peaks into the Cl($2p_{3/2,1/2}$) components. Two distinct Cl(2p) peaks designated, α and β are observed with a separation of about 1.7 eV. The relative growth of Cl(α) and Cl (β) peak as a function of chlorine dosage is shown in fig. 19(c). It is clear that Cl(β) grows exponentially while Cl(α) increases linearly with logarithm of exposure.

It is to be noted that the surface coverage of adsorbed chlorine is greatly increased on the alkali dosed surface as is evident from fig. 18. The suppression of the O(α) and O(β) peaks on chlorination indicate a pronounced decrease in surface concentration of chemisorbed atomic oxygen. One possible reason for the elimination of O(α) associated with Ag is chlorine-induced diffusion of this oxygen

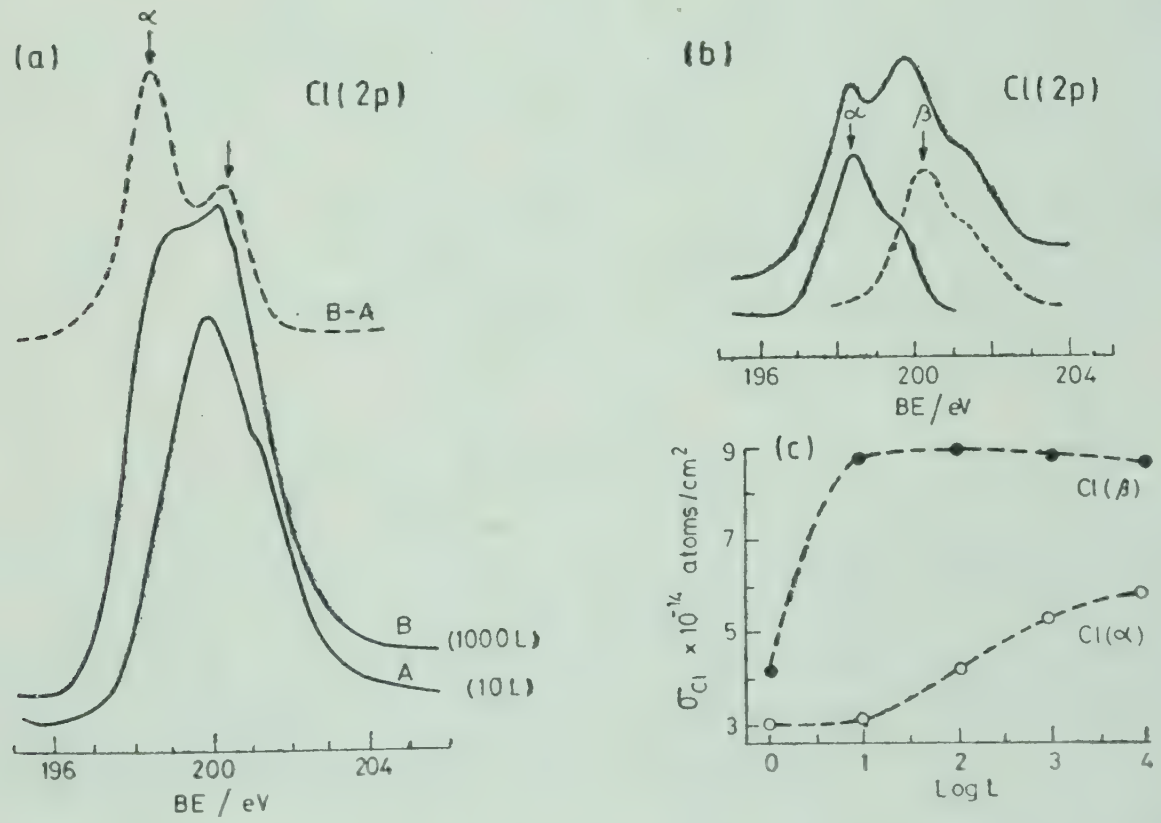

FIG. 19. (a) Cl(2p) specta on Ag + Ba + O_2 after (A) 10L and (B) 1000L Cl_2 exposure at 300K ($\sigma_{Ba} = 1.5 \times 10^{15}$ atoms/cm^2.
(b) Cl(2p) spectrum on Ag + Ba + O_2 + Cl_2 (1000L) and the curve fitted resolved $2p_{3/2,\,1/2}$ components.
(c) Variation in the surface concentrations of Cl(α) and Cl(β) with logarithm of chlorine exposure, (exposure in Langmuirs).

into the sub-surface region. The study of the relative concentrations of the oxygen species on the surface with respect to temperature shows an interesting feature. With decrease in the intensity of Cl(α) at higher temperatures, a corresponding increase in the intensity of O(α) is observed. At 600K, O(α) is found to be quite prominent on the potassium dosed surface. This clearly shows that Cl(ad) induces surface to bulk diffusion of atomic oxygen. A very similar effect is indeed observed on the barium covered surface. Cl(α), in this case desorbs at 725K with simultaneous increase in O(α). Cl(α), associated with Ag, therefore, tends to occupy a highly preferred site on both potassium and barium dosed surfaces.

In addition to the suppression of atomic oxygen, a distinct stabilization of molecular dioxygen occurs on chlorination. The O(γ) peak at 533 eV becomes very prominent and distinct after chlorine dosage. A similar behaviour has been noticed in the case of potassium dosed Ag (100)[53], and also on clean Cu[56].

The nature of Cl(2p) spectra on potassium dosed Ag suggests that adsorbed chlorine is present as a single type of chemisorbed species and is preferentially associated with Ag for coverages of potassium even upto 8×10^{14} atoms/cm^2 as can be seen from the Cl($2p_{3/2}$) peak at 198.2 eV. Further the saturated chlorine coverage is found to be independent of the initial potassium dosage, σ_K, as can be seen from Fig. 19(b). This further asserts association of chlorine with Ag. The higher binding energy Cl(2p) peak observed at around 199 eV for very high potassium coverages ($\sigma_K = 1.5 \times 10^{15}$ atoms/cm^2) could be attributed to KCl. Earlier TDS studies of Lambert also support the above observations. For $\theta_K < 0.5$, a significant amount of AgCl desorption was found to occur in their study even for chlorine coverages as low as $\theta_{Cl} = 0.1$ and for $\theta_K > 0.5$, no AgCl desorption was observed, i.e., all the chlorine desorbed in the form of KCl. The Cl($2p_{3/2}$) binding energy at 199 eV attributed, here, to KCl is nearly the same as that observed for the analogous compound NaCl[57]. Further, in our study, the adsorbed chlorine concentration is found to be in a ratio of about 3 : 1 to the potassium concentration. This also supports the view that the surface chlorine is mostly associated with Ag for lower coverages of potassium.

In the case of the barium dosed surface, however, composite Cl(2p) peaks are observed attributable to Cl(ad) species associated with both Ag as well as barium even for relatively low barium coverages. This is clearly borne out form the curve-fitted resolved peaks (Fig. 19). Also we find that for intial dosages of chlorine, there is an exponential growth in Cl(β). As Cl(β) intensity increases preferentially with increase in σ_{Ba}, it is likely to be due to adsorbed chlorine associated with barium. Even by IL Cl_2 exposure, this barium associated chlorine is found to get saturated. With higher dose of chlorine, linear growth in Cl(α) is observed. The binding energy of Cl(α) is nearly the same as that of Cl(2p) observed on clean Ag. Cl(α) could, therefore, be associated with Ag.

The presence of two Cl(ad) species on the barium dosed surface at relatively low barium coverages is contrary to what is observed on the potassium dosed surface at similar potassium coverages. It is well known that electron transfer from the

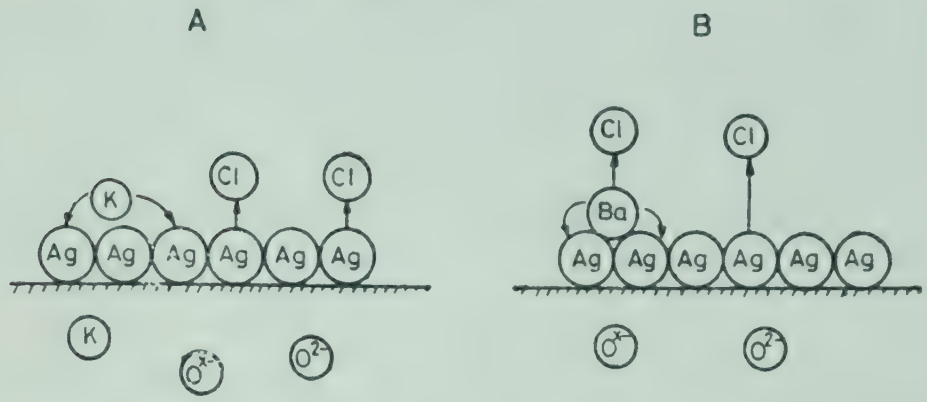

FIG. 20. Schematic diagram of electron transfer showing metal-chlorine interaction in Ag + K + O_2 + Cl_2 and Ag + Ba + O_2 + Cl_2 systems.

alkali to the substrate is responsible for the changes brought about in adsorption phenomena by aikaliadatoms. By electron transfer, silver is thus expected to get enriched in valence electron density thereby facilitating back-transfer to Cl(3p) in the chloridation process. Due to the higher valence occupation in barium compared to potassium, one would expect sufficient charge density to remain on barium, even after electron transfer, to facilitate the formation of Ba—Cl bond. This is schematically shown in fig. 20.

CONCLUDING REMARKS

These studies show that extensive amount of information can be obtained about the changes brought about in the adsorption phenomena by alkali metals by using electron spectroscopic techniques. Identification and characterization of surface species can be made and their reactivity can be examined. Quantitative estimations of surface species and the stoichiometry can be fruitfully used in the understanding of reaction pathways. Temperature programmed desorption using mass spectrometer and the variation of surface concentration with temperature obtained from XPS give complementary information on the nature of adsorbed species.

It is to be noted that the studies carried out so far on the alkali covered surfaces have been limited to adsorption of a single alkali or alkaline earth metal on transition metal surfaces. Of greater catalytic importance will be the study of adsorption of molecules on mixed-alkali-promoted metal surfaces.

ACKNOWLEDGEMENT

We are grateful to Professor C N R Rao for his encouragement and useful discussions. But for his encouragement, we would not have been able to explore the study on alkali covered metal surfaces. Financial assistance from the Department of Science and Technology, Government of India and the Indian National Science Academy is gratefully acknowledged.

REFERENCES

1. Z Paal, G Ertl and S B Lee, *Appl. Surface Sci.* **8** (1981) 231.
2. G Ertl, M Weiss and S B Lee, *Chem. Phys. Lett.* **60** (1979) 391.
3. P A Kilty and W M H Sachtler, *Catal Rev.* **10** (1974) 1.

4. M Kitson and R M Lambert, *Surface Sci.* **109** (1981) 60.
5. C T Campbell and D W Goodman, *Surface Sci.* **123** (1982) 413.
6. J E Davey, *J. Appl. Phys.* **28** (1957) 1031.
7. C N R Rao, *Proc. Indian natn. Sci. Acad.* **47A** (1981) 111.
8. M W Roberts and C S Mc Kee, *Chemistry of the metal gas interface*, Clarendon Press, Oxford, U. K. (1978).
9. M Ayyoob and M S Hegde, *Surface Sci.* **133** (1983) 516.
10. M Ayyoob and M S Hegde, *J. Chem. Soc. Faraday Trans.* **I 88** (1984) 2703.
11. P J Goddard and R M Lambert, *Surface Sci.* **107** (1981) 519.
12. A F Carley and M W Roberts, *Proc. R. Soc. Lond. A* **363** (1978) 403.
13. D Briggs and M P Seah, *Practical Surface Analysis by Auger and X-ray photoelectron spectroscopy*, Wiley, U. K. (1983).
14. L A Gerlach and T N Rhodin, *Surface Sci.* **19** (1970) 403.
15. E V Albano, *Surface Sci.* **141** (1984) 191.
16. S Yashonath and M S Hegde, *Proc. Indian Acad. Sci.* **89** (1980) 489.
17. S Yashonath, P Sen, M S Hegde and C N R Rao, *J. Chem. Soc., Faraday Trans. I* 79 1229 (1983).
18. C N R Rao, D D Sarma and M S Hegde, *Proc. R. Soc. Lond. A* **370** (1980) 269.
19. M Ayyoob and M S Hegde, *Surface Sci.* (In Print) (1984) 140.
20. P V Kamath, D D Sarma and C N R Rao, *Proc. Ind. Acad. Sci.* **93** (1984) 335.
21. R W Joyner and M W Roberts, *Chem. Phys. Lett.* **60** (1979) 459.
22. C N R Rao, P V Kamath and S Yashonath, *Chem. Phys. Lett.* **88** (1982) 13.
23. C Backx, C P M De Groot and P Biloen, *Surface Sci.* **104** (1981) 317.
24. D Briggs, R A Marbrow and R M Lambert, *Surface Sci.* **65** (1977) 314.
25. I E Wacks and R J Madix, *J. Catal.* **53** (1978) 208.
26. S Evans, D E Parry and J M Thomas, *Faraday Disc. Chem. Soc.* **60** (1975) 102.
27. L H Dubois, *Surface Sci.* **119** (1982) 399.
28. C T Au and M W Roberts, *Chem. Phys. Lett.* **74** (1980) 472.
29. T S Sampath Kumar and M S Hegde, *Appl. Surface Sci.* (1984) 20.
30. D T Ling, J N Miller, P A Pianetta, D L Weissman, I Lindau and W E Spicer, *J. Vac. Sci. Technol.* **15** (1978) 495.
31. H P Bonzel and R Ku, *Sarface Sci.* 40 (1973) 85.
32. G Broden, G Pirug and H P Bonzel, *Chem. Phys. Lett.* **73** (1980) 506.
33. E L Garfunkel and G A Somorjai, *Surface Sci.* **115** (1982) 441.
34. G Broden, G Gafner and H P Bonzel, *Surface Sci.* **84** (1979) 295.
35. J Benziger and R J Madix, *Surface Sci.* **94** (1980) 119.
36. H S Luftman, Y M Sun and J M White, *Surface Sci.* **140** (1984) L259.
37. J E Crowell, E L Garfunkel and G A Somorjai, *Surface Sci.* **121** (1982) 303.
38. T Engel and G Ertl, *Adv. Catal.* **28** (1979) 1.
39. H A Engelhardt, A M Bradshaw and D Menzel, *Surface Sci.* **40** (1973) 410.
40. H Albers, W J J Van Der Waal, and G A Bootsma, *Surface Sci.* **68** (1977) 47.
41. T E Felter, W H Weinberg, G Y Lastunshkina, A I Boronin, P A Zhdan, G K Boreskov and and J Hrbek, *Surface Sci.* **118** (1982) 369.
42. L Sabbatini, B. Morelli, P Zambonin and B A De Angelis, *J. Chem. Soc., Faraday Trans. I* **75** (1979) 2628.
43. J S Hammond, S W Gaarenstroom and N Winograd, *Anal. Chem.* **47** (1975) 2193.
44. J A Connor, M Considine and I H Hillier, *J. Chem. Soc. Faraday Trans. II* **74** (1978) 1285.
45. J A T Varhoeven and H V Doveren, *Appl. Surface Sci.* **6** (1980) 225.
46. G Ertl, S B Lee and M Weiss, *Surface Sci.* **114** (1982) 527.

47. M I Temkin, *Adv. Catal.* **28** (1979) 173.
48. J L Gland and V N Korchak, *J. Catal.* **53** (1978) 9.
49. M Ayyoob and M S Hegde, *Ind. J. Chem.* **22A** (1983) 465.
50. G B Fisher, *Chem. Phys. Lett.* **79** (1981) 452.
51. G B Fisher, J L Gland and S J Schmieg, *J. Vac. Sci. Technol.* **20** (1982) 518.
52. D Briggs, R A Marbrow and R M Lambert, *Chem. Phys. Lett.* **53** (1978) 462.
53. M Kitson and R M Lambert, *Surface Sci.* **100** (1980) 368.
54. E Zanazzi, F Jona, D W Jepsen and P M Marcus, *Phys. Rev. B* **14** (1976) 432.
55. R A Marbrow and R M Lambert, *Surface Sci.* **71** (1978) 107.
56. P V Kamath, K Prabhakaran and C N R Rao, *Surface Sci. Lett.* **146** (1984) 55.
57. J A Tossell, *J. Phys. Chem. Solids* **34** (1973) 307.

© *Proc. Indian natn. Sci. Acad.*, **51**, A, No. 1, 1985, pp. 286–289
Printed in India.

FACTORS AFFECTING AUGER SIGNAL IN CMA SYSTEMS*

V C Sahni

Nuclear Physics Division, Bhabha Atomic Research Centre, Bombay-400 085

1. Introduction

Present day experimental study of Auger spectra is most often done using Cylindrical Mirror Analysers (CMA). Essentially the study involves determination of energy distribution $N(E_e)$ of the electrons emerging from a sample and for the ease of identifying the Auger peaks one resorts to electronic differentiation of $N(E_e)$. A CMA system essentially consists of a pair of coaxial cylinders of which the inner one is grounded and the outer one is given a negative potential-ϕ. The electrons originating from a sample placed on the axis of the cylinders pass through an entrance aperture to enter the field region, which is the annular region between the cylinders. Depending on the entrance angle θ, the electron energy E_e, and the voltage ϕ only certain electron pass through the exit aperture and are intercepted by the detector. A schematic diagram illustrating the parameters is given in Fig. 1(a).

Detailed analysis of electron trajectories for this system have been published[1,2]. In addition, the usage of this system for studying Auger spectra has also been published[3], as also some of the factors that influence the Auger peak positions and profile shapes[4,5,6]. In ref. 4 the consequences of sample positioning (relative to single stage CMA) on the signal intensity and energy shifts etc. have been discussed, whereas effects of CMA design distortions—departure from coaxiality, source size etc—have been analysed in ref. 5. The implications of using modulation technique to obtain $N'(E_e)$ electronically have been analysed by several authors and the latest work is due to Anthony and Seah[6]. Thus a lot of ground has been covered in the literature regarding CMA systems. However, the primary resolution function of this analyser has not been discussed adequately. This short note is an attempt to fill this gap. We recall the basic equations of a CMA in the next section and then proceed to a calculation of the resolution function. This is used to provide and understanding of typical line shapes seen in the Auger spectra. Our conclusions are summarised in the last section.

2. Resolution Function of a CMA

The basic equations of an electron moving in a CMA system are very well discussed by Sar-el[1]. Basically one writes the lagrangian equations of motion in cylindrical polar coordinates (r, θ, z), and upon eliminating time one gets the trajectory equation. It can be shown[1] that the distance Z between the source S, of electrons and its image I—located on the common axis of the cylinders, see Fig. 1(a)—is given by

$$Z = 2a \cot \theta \{1 + K \exp(K^2/2) \int_0^k \exp(-u^2/2)\, du\} \qquad \ldots(1)$$

*Paper presented at the Symposium on Physics and Chemistry of Surfaces held at INSA, New Delhi from September 28–30, 1984.

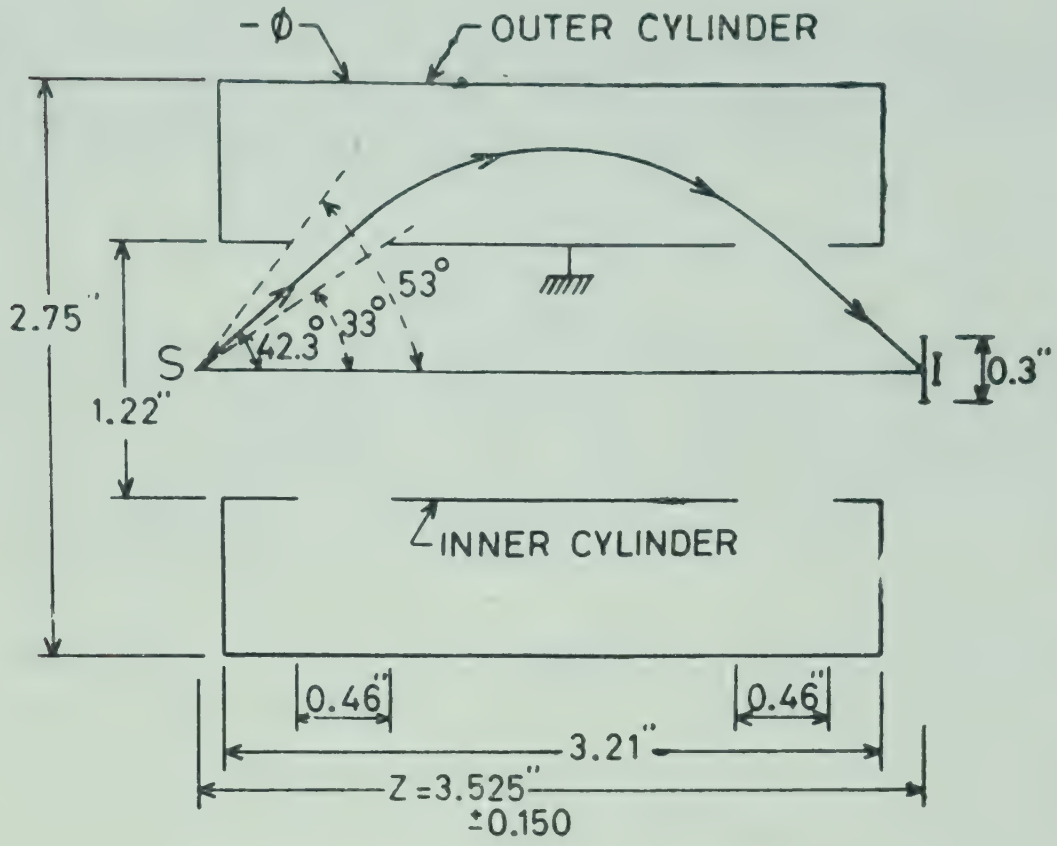

(a)

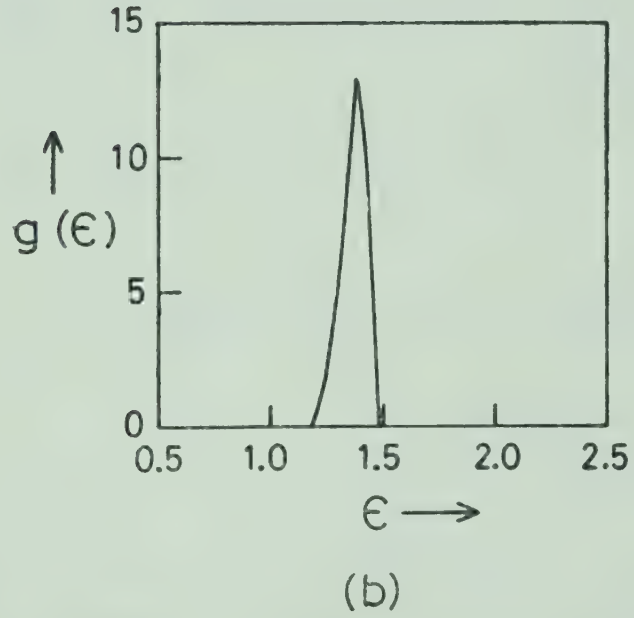

(b)

FIG. 1: (a) Schematic diagram for a CMA showing the electron trajectories starting from the source S to the image I.
(b) Calculated resolusion function $g(\epsilon)$ for the CMA depicted in fig. (a).

where

$$K^2 = 2\epsilon \sin^2 \theta, \ \epsilon = \{E_e/\phi\} \log (b/a) \qquad \ldots(2)$$

Here a and b are radii of the inner and the outer cylinders, E_e is the electron kinetic energy, $-\phi$ is the potential on the outer cylinder; and θ is angle at which electron enters the field region. In Fig. 1(a) we have also indicated the dimensions of an analyzer in use in our laboratory. As is clear from equation (1) Z is a function of ϵ and θ and as such it defines a surface. The range for angle $\theta(\theta_1 \leqslant \theta \leqslant \theta_2)$ is, of course, determined not only by analyser dimensions but also by location of S. Let us consider a polyenergetic, isotropic source of electrons [Fig. 1(a)] and focus attention on the electrons emanating from S entering the field between θ and $\theta + \Delta\theta$.

For simplicity we will ignore any work function corrections to electron energies. Imagine an appropriate cylindrical strip on the inner cylinder through which these electrons pass. One can show that the solid angle subtended by this strip varies with θ as

$$f(\theta) = \sin\theta \qquad \ldots(3)$$

In actual working, one usually intercepts the electrons arriving at I by an electron multiplier which has a finite size. This amounts to the fact that those electrons for which Z lies in a range $[Z_1, Z_2]$ all contribute to the signal. We may, therefore, define a characteristic function $g(\epsilon)$ for a CMA through a conditional integral

$$g(\epsilon) = \int_{Z_1 \leqslant Z(\epsilon,\theta) \leqslant Z_2} f(\theta)\, d\theta \qquad \ldots(4)$$

The function $g(\epsilon)$ contains the complete instrument response, and plays the role of resolution function as discussed below.

It is easy to numerically calculate $g(\epsilon)$ once all the parameters are specified and Fig. 1(b) shows the results for CMA of Fig. 1(a). We may point out that if sample position is changed there is a change in $[\theta_1, \theta_2]$ and $[Z_1, Z_2]$ and a consequent change in $g(\epsilon)$. It is this change in $g(\epsilon)$, which manifests as peak position shift and peak height change observed in ref. 4.

In actual experiments the signal is measured by varying ϕ and so that quantity of interest is

$$I(\phi) = \int_0^\infty g(cE_e/\phi)\, N(E_e)\, dE_e,\ c = \log(b/a)$$

or
$$I(\phi) = (\phi/c) \int_0^\infty g(x)\, N(x\phi/c)\, dx \qquad \ldots(5)$$

Since the signal recording is usually done through electronic differentiation using a modulation voltage μ sin wt and a lock in amplifier one must find the term proportional to μ sin wt in $I(\phi + \mu \sin \text{wt})$. This quantity can be readily shown to be

$$\mu \sin \omega t[(1/c) \int_0^\infty g(x)\, N(x\phi/c)\, dx + (\phi/c) \int_0^\infty g(x)\, N'(x\phi/c)\, (x/c)\, dx] \qquad \ldots(6)$$

It follows from (6) that if $g(\epsilon)$ is replaced by a Dirac delta function we obtain the usual expression given in the literature[7]. However, it is clear that for any detailed analysis of Auger profiles, the shape of resolution function must be included in the discussion.

We might also point in the end a general feature of the resolution function viz. the rise on low energy side is slower compared to fall on the higher energy side (see Fig. 1(b)). This feature is responsible for the longer excursion seen in the peak to peak amplitude on the high energy side, in the usual derivative spectra recorded with CMA's.

3. Summary and Conclusions

We have outlined a way to calculate the resolution function for a CMA and and pointed out how it affects the shapes of Auger spectra recorded using CMA. Detailed account will be published later.

References

1. H Z Sar-el, *Rev. Scientific Instruments* **38** (1967) 1210.
2. V V Zashkvara, M I Korsunskii and O S Kosmachev, *Sov. Physics, Tech. Physics* **11** (1966) 96.
3. P W Palmberg, G K Bohn and J C Tracy, *Appl. Phys. Letters* **15** (1969) 254.
4. E N Sickafus and D M Holloway, *Surface Science* **51** (1975) 131.
5. H E Bishop, J P Coad and J C Riviere, *J. Electron Spectroscopy and Related Phenomena*, **1**, (1973) 389.
6. M T Anthony and M P Seah, *J. Electron Spectroscopy and Retated Phenomena* **32** (1983) 73.
7. F J Kuejers, *Auger Electron Spectroscopy of Alloys*, Ph.D. Thesis (1978) Rijks University, Leiden.

© *Proc. Indian natn. Sci. Acad.*, **51**, A, No. 1, 1985, pp. 290–294.
Printed in India.

DYNAMICS OF SURFACE REACTIONS OF CO, CO_2 C_2H_4 AND CS_4 OVER RUTHENIUM*

R M Iyer

Chemistry Division, Bhabha Atomic Research Centre, Bombay 400 085

It is well known that the catalytic property of a solid is related to the chemical and physical nature of its surface. The surface properties determine the mode of chemisorption of reactants. Consequent perturbations of the geometric and electronic structures of the chemisorbed molecules modifies the reaction path leading to the formation of a specific set of products and involving lesser activation energy. To evaluate catalytic behaviour of a solid it is, therefore, essential to understand the nature of the species formed on its surface at different stages and the modifications that they may undergo under different experimental conditions.

Work has been going on in the Chemistry Division of Bhabha Atomic Research Centre to investigate different aspects of heterogeneous catalysis; of particular interest being the following :

(i) identification of surface species and the dynamics of transformations that they undergo in a catalytic reaction

(ii) mechanism of conversion of CO, CO_2 and CS_2 to hydrocarbons

(iii) mechanisms involved in catalyst poisoning, and

(iv) γ-radiation induced enhancement of catalytic reaction.

A brief account of this work is given below.

A. CO methanation

CO methanation has recently acquired considerable importance as this serves as a route for conversion of coal to fuel gases.

Till about 1976 it was believed that oxygenated complexes such as M = CHOH are active intermediate species in these reactions. In 1976 using labelled CO, Araki and Ponec[1] showed that CH_4 could form directly from an intermediate surface carbon species without involving an oxygenated complex. A lacuna in this study was that these experiments having been conducted under vacuum conditions could not be directly compared with practical high pressure methanation reaction.

At about the same time using a sequential pulse injection method and electron spin resonance technique, we observed the formation of 'active' carbon species over supported Ru catalysts and studied the time and temperature dependent reactivity of carbon thus formed[2].

In these experiments when pulses of CO were injected over supported Ru catalysts formation of CO_2 was found to take place, the yield of which depended on

*Paper presented at the Symposium on Physics and Chemistry of Surfaces held at INSA, New Delhi from September 28–30, 1984.

catalyst temperature and the nature of support material. The formation of CO_2 and its yield indicated that CO disproportionates over catalyst leaving 'carbonaceous' species over catalyst surface according to the equation

$$2CO \rightarrow C + CO_2$$

Electron spin resonance studies confirmed these observations in that a ESR signal with free electron 'g' value was seen when CO was admitted to catalyst kept in the spectrometer cavity at 450 K which diminished on subsequent admission of H_2. These results have confirmed that the interaction of CO results in the formation of active carbon species over catalyst surface which are reactive to hydrogen. The ESR technique therefore is very valuable in the identification of free radicals and other transient species on the surface of the working catalysts.

It was of interest to evaluate the physico-chemical transformation of surface carbon species produced in the reaction and their chemical reactivity towards H_2 and O_2. When subsequent to the injection of a CO pulse over catalyst surface successive pulses of H_2 were injected, the CH_4 formation was observed and the yield of CH_4 from these H_2 pulses depended on several perameters such as catalyst support and temperature and time lapsed between CO and first H_2 injection.Total amount of CH_4 recovered from successive H_2 injections as a function of CO and first H_2 injection is shown in Fig. 1.

The decrease in methane yield with increase in CO-H_2 time interval clearly showed that the surface carbon slowly becomes inert towards H_2. Also, with the increase in catalyst temperature the activity loss was faster. Similar studies have been carried out on CO_2-H_2 and CS_2-H_2 reactions and these studies have helped to delineate the reaction mechanisms involved in these reactions[2,3].

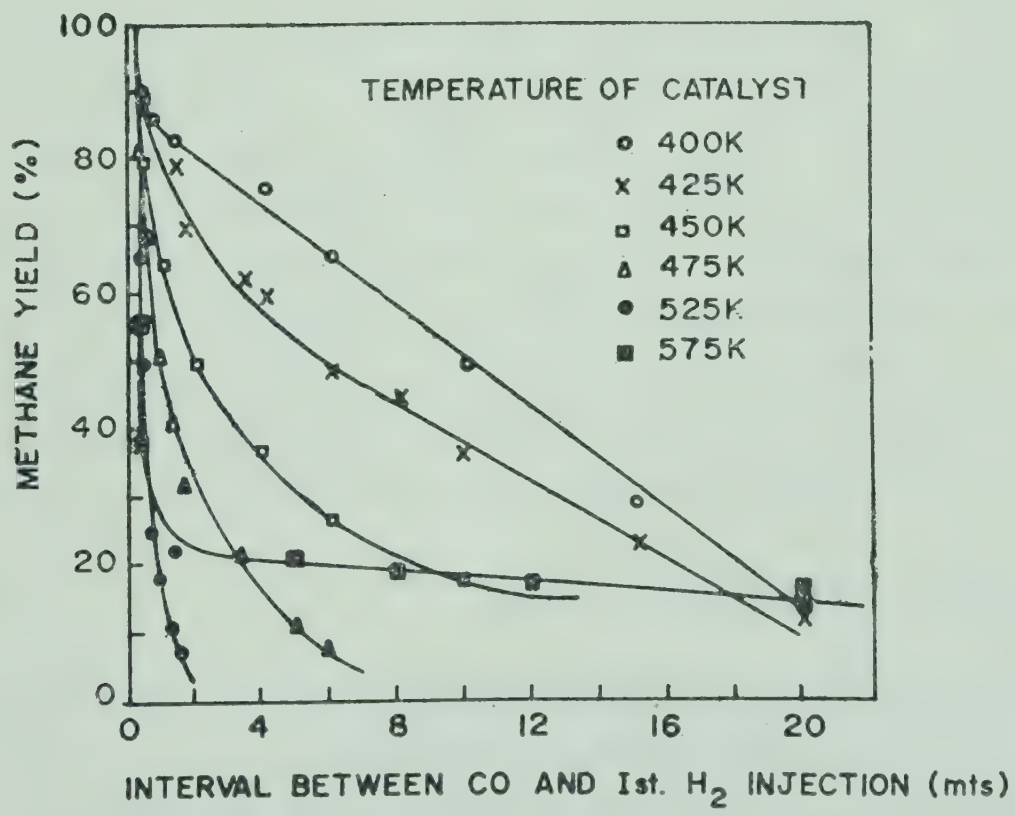

FIG. 1. Total CH_4 yield obtained from successive H_2 injections over Ru/molecular sieves subsequent to the injection of CO pulse with varying CO and first H_2 time interval.

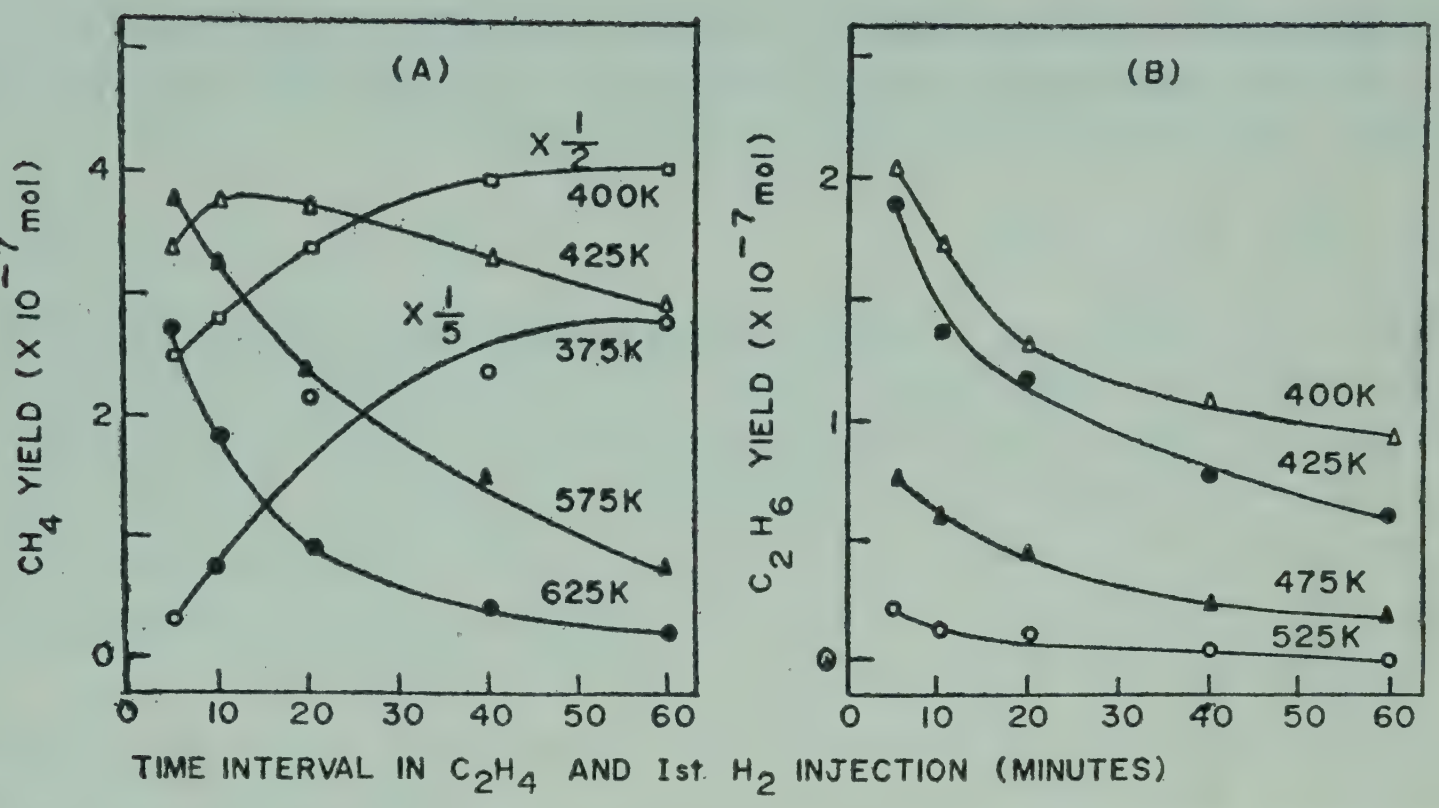

FIG. 2. CH_4 and C_2H_6 yields from first H_2 injection made at different time intervals after an injection of 1.52 μmol of C_2H_4 over Ru/alumina catalyst.

B. C_2H_4 interaction over catalyst surface

Our recent studies[4,5] have shown that interaction of C_2H_4 over supported Ru catalyst surface gives rise to different di-carbon and mono-carbon surface species which undergo changes in a complex manner depending on catalyst temperature and on the nature of catalyst support. Fig. 2 illustrates a typical example of this behaviour. This figure shows the CH_4 and C_2H_6 yields obtained when a hydrogen pulse injection was made over a Ru/Alumina catalyst surface at different temperatures subsequent to a C_2H_4 pulse injection as a function of C_2H_4-H_2 time interval. These data show that upto temperatures of 400 K, CH_4 yield increases with increasing catalyst temperature and also with increasing C_2H_4-H_2 time interval while beyond 425 K, a decrease in CH_4 yield is observed. C_2H_6 yields on the contrary, showed a decreases for all the catalyst temperatures and C_2H_4-H_2 time intervals studied. These and other results obtained in these studies[4,5] have helped in the identification of surface species formed at different stages of the reaction and under different experimental conditions. It has been shown that the di-carbon species formed on the catalyst surface due to disproportionation of C_2H_4 transform with time to a mono-carbon form. Also, both the di-carbon and mono-carbon species subsequently convert to a form that was no more reactive to H_2 and O_2. Detailed kinetics of these transformations has also been evaluated[4].

C. Radiation effect on catalytic reactions

Having established that the lifetime of intermediate 'active' carbon species at a particular temperature is related to its reactivity for H_2, it was of interest to know if it is possible to alter the carbon 'life time' to boost up the catalyst activity. Rise in temperature, which is one such parameter, unfortunately, results in faster inactivation of the carbon species and subsequent coke deposition. Radiations, both

optical and nuclear, are known to cause surface perturbations and ionizations leading to storage of energy in solids depending on its band structure. However, metals are by and large unaffected by γ radiation though the irradiation of wide gap materials results in storage of energy due to trapped electrons and holes which may subsequently be released by thermal stimulation.

Attempts in our laboratory were therefore made to evaluate if the energy storage capacity of insulating materials can be profitably used to augment the catalytic activity of a metal which is otherwise not affected by radiation.

The Ru metal catalysts supported on materials such as molecular sieves, alumina and glassbeads were used for these studies and γ radiation effect on CO-H_2, CO_2-H_2 and CS_2-H_2 reactions was evaluated[6–8]. In all these cases substantial increase in catalytic activity was observed in presence of radiation and Fig. 3 gives a typical data for CO-H_2 reaction over Ru/molecular sieve and Ru/laumina catalysts. It is clear from this data that for Ru/alumina at a typical temperature of 450 K, the CH_4 yield increases from 10% to 50% in presence of radiation. Similarly, in case of CO_2-H_2 reaction large enhancement in catalytic activity was observed in presence of γ radiation.

Thermoluminescence studies[6,7] have helped us to show that the radiation induced enhancement in catalytic activity is due to storage and subsequent thermal release of energy from support material and transport to Ru sites. This provides an additional source of energy at Ru sites for reaction between CO and H_2 molecules.

D. Sulphur poisoning

Another area which was of interest to us is the sulphur poisoning of Ru catalysts[3,8]. To understand the poisoning effect of CS_2, the Ru catalysts exposed to CS_2 were investigated by Auger electron and X-ray photoelectron spectroscopy.

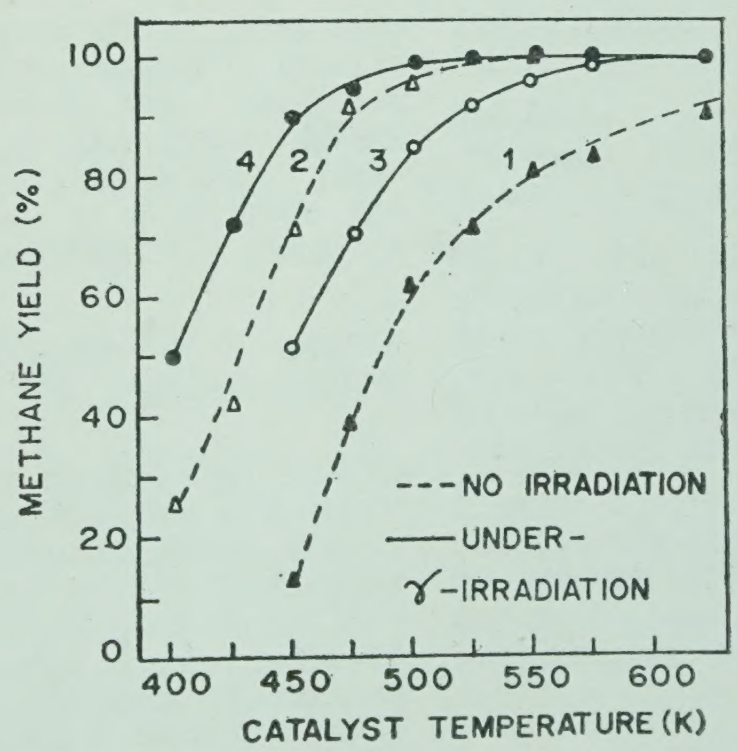

FIG. 3. Effects of γ-irradiation on the activity of Ru/alumina (curves 1,3) and Ru/molecular sieves (curve 2, 4) catalysts for CO methanation reaction at different temperatures.

These data have indicated that sulphur atoms are preferentially deposited over Ru sites which makes the Ru sites unaccessible to the reacting CO and/or H_2 molecules.

These studies further showed that CS_2 disproportionates on Ru to give atomic carbon and sulphur which then get hydrogenated with varying reactivity to produce CH_4 and H_2S. Also, it was observed that the presence of γ-radiation made the Ru catalysts less prone to CS_2 poisoning and extended their life span for CO methanation reaction.

In summary, I would like to add that these studies have revealed the dynamics of surface reactions relevant to catalysis and have provided means to work out complex reaction mechanism involved in these reactions and their kinetic behaviour.

References

1. M Araki, and V Ponec, *J. Catalysis* **44** (1976) 439.
2. N M Gupta, V S Kamble, K Annaji Rao, and R M Iyer, *J. Catalysis* **60** (1979) 57.
3. N M Gupta, V S Kamble, and R M Iyer, *J. Catalysis* **69** (1981) 111.
4. N M Gupta, V S Kamble, and R M Iyer, *J. Catalysis* **88** (1984) 457.
5. V S Kamble, N M Gupta, and R M Iyer, *Proc. of 7th National Symposium on Catalysis* Baroda under publication.
6. N M Gupta, V S Kamble, and R M Iyer, *J. Catalysis* **66** (1980) 101.
7. N M Gupta, V S Kamble, and R M Iyer, *Radiat. Phys. Chem.* **12** (1978) 143.
8. N M Gupta, V S Kamble, and R M Iyer, *J. Catalysis* **81** (1983) 478.

Procedure for submitting manuscript

General : Manuscripts should be sent, *in triplicate* (with 3 sets af illustrations, *one* original and *two* photocopies) to the *Editor of Publications, Proceedings A, Indian National Science Academy, Bahadur Shah Zafar Marg, New Delhi*-110 002.

Submission of the manuscript will be held to imply that it has not been previously published in any form and is not under consideration for publication elsewhere.

Presentation : Articles should be as brief as full documentation allows. They should not usually exceed 12 printed pages (approx. 12.000 words). Review articles may be upto 20 pages. Papers must be written clearly and concisely with consistency in style and spelling (spellings should be according to Oxford Dictionary), and typed double spaced with ample margins on durable bond paper. The usual format is: 'Abstract', 'Key words', Introduction', 'Materials and Methods', 'Results', 'Discussion', and 'Acknowledgement' (if any) and 'References'.

Classification : The exact classification of the paper (e.g., Astrophysics, Inorganic, Organic and Physical Chemistry, Seismology etc.) should be provided at the top of the manuscript.

Title : Title should be brief, specific and informative of the subject discussed. It should not begin with such general words as 'The', 'A', 'Study', 'Effect'. If a paper forms part of a series, this may be indicated through a symbol in the title and a footnote "This is paper X in series. Paper on IX is ref.....". The preceding paper must then be included in the list of references.

Running Title : Should not exceed 50 characters (including spaces).

Keywords : Up to five important key words should be provided for indexing and for information retrieval.

Abbreviations : Non-standard abbreviations used five or more times in the text should be listed in the footnote. Define where first mentioned followed by abbreviation in parentheses. Subsequently, the abbreviations should be used. However, these should be kept to a minimum and should not be used in the titles, key words or abstract.

Abstract : The abstract (typed on a separate page) should summarize the principal findings within 250 words.

Text : The paper must be divided into sections preferably starting with 'Introduction' and ending with 'Discussion' (or 'Acknowledgement', if any). All measurements must be given in SI units. Avoid numbers at the beginning of a sentence or spell them out. The scientific names of plants minerals, and animals should be underlined. Authors of name of taxa should be cited at the first mention of a taxon, but not elsewhere. Accepted common names of plants and animals should neither be capitalized nor placed within quotation marks. Words and phrases of foreign origin in common use need not be underlined (e.g., *et al.*, viz. e.g., i.e., etc.) whereas the rest should be underlined (e.g., *in vitro, in situ*).

Tables : All tables must be numbered serially in roman numerals and placed at the end. The table should have brief titles (*underlined*) and contents should be self-explanatory. Non-standard abbreviations should be used sparingly and defined at the bottom of the table. Also details of the experiment (not mentioned in the text) may be indicated below the table.

Illustrations : Original drawings (in India ink in clean uniform lines on tracing paper or Bristol paper) and sharp photographs (with high contrast and glossy prints) numbered in arabic numerals should be provided. Illustrations on reduction must fit into a minimum of 6.5 cm and a maximum of 12.5 cm width. Labelling of figures should therefore be done keeping in view the reduction (blow-up) into (6.5 cm or 12.5 cm). Magnification should be indicated in the legend be scale or figures (x .....). For composite figures. mounting should be done carefully with even spacing in between. Illustrations should be supported wjth cardboard to avoid damage in transit.

References : References in the text should be cited by number. References at the end of the paper should be listed by number, author's name, title of paper, name of journal (underlined and abbreviated according to the *World List of Scientific Periodicals* Butterworths, London), Vol. no, year of publication and page no. References to book should include : name of author, title of the book (underlined), name of editor if any, preceded by 'Ed(s)', place of publication, publisher, year of publication chapter or pages referred to. References to thesis, the degree, the year for which submitted, the university and the place. Sample citation are given below :

For periodicals
[1]R. H. Fox, *Fund Math.* **34** (1947) 278

For books
[1]H. Rund, *The Differential Geometry of Finsler Spaces*, Springer-Verlage, Berlin (1953) p. 283

Proofs : Proofs will be sent to the author(s) and should be returned to the Editor within 48 hours. Major corrections or alterations will be accepted only at author's expense*. If proofs are not returned within the specified time, they will be read in the Editorial Office and print-ordered.

Reprints : Fifty reprints will be supplied free of charge to the authors. Additional copies should be ordered on the order-from accompanying the proofs. Payment for extra reprints must accompany the order-form.

---

*The recomposition cost will be charged to the author. In case the author desires to withdraw the paper, he shall pay towards the composition charges, if the paper has already been type-set.

Regd. No. 16423/68

Proceedings of the Indian National Science Academy

Vol. 51, Part A, No. 1 JANUARY 1985

CONTENTS *Page*

Experimental Surface Science with Electron Spectroscopies and Cognate Techniques — **C N R Rao** — 1

Theory of Semiconductor Surface Reconstruction — **K C Pandey** — 17

Dynamical Behaviour Atomic Monolayers on Surfaces — **Bal K Agrawal** — 27

Surface Analytical Studies of Optically Selective Oxide Films — **A Banerjee and K L Chopra** — 57

New Concepts in Catalysis : The Impact of Surface Science — **Jerzy Haber** — 76

Theoretical Aspects of Chemisorption by Metals — **T B Grimley** — 98

Auger Electron Spectroscopy and Secondary Ion Mass Spectrometry — **Arun S Nigavekar** — 124

The Impact of Photoelectron Spectroscopy on Surface Chemistry and Catalysis — **M W Roberts** — 165

New Possibilities of NMR Spectroscopy in the Studies of Adsorption and Catalysis — **K I Zamaraev and V M Mastikhin** — 180

Catalytic Chemistry at the Zeolite Surface — **Paul Ratnasamy** — 202

Radiation Processing of Surfaces : Applications of Conversion Electron Mössbauer Spectroscopy — **S B Ögale, S V Ghaisas, S M Kanetkar and V G Bhide** — 211

Surface Chemistry of Alkali—Covered Metals — **M S Hegde and M Ayyoob** — 256

Factors Affecting Auger Signal in CMA Systems — **V S Sahni** — 286

Dynamics of Surface Reactions of CO, CO_2, C_2H_4 and CS_2 — **R M Iyer** — 290

Published by the Executive Secretary, Indian National Science Academy, 1, Bahadur Shah Zafar Marg, New Delhi-110 002, and printed by him at the Kapoor Art Press, A38/3, Mayapuri Industrial Area, Phase I, New Delhi–110 064.